

Switching of Electronic States of Cobalt Dioxolene Complexes Triggered by Spin-Crossover Process and Valence Tautomerism

Dissertation zur Erlangung
des Doktorgrades der Naturwissenschaften (Dr. rer. nat.)
genehmigt vom Fachbereich Chemie
der Technischen Universität Kaiserslautern
(D 386)

vorgelegt von

M. Sc. Ramapada Dolai

Betreuer der Arbeit: Prof. H.-J. Krüger, Ph. D.

Vom Fachbereich Chemie der Technischen Universität Kaiserslautern am
15.05.2019 als Dissertation angenommen.

Tag der wissenschaftlichen Aussprache: 30.01.2020

Dekan: Prof. Dr. Werner R. Thiel

Vorsitzender der Prüfungskommission: Prof. Dr. Christoph van Wüllen

1. Berichterstatter: Prof. Hans-Jörg Krüger, Ph. D.

2. Berichterstatter: Prof. Dr. Werner R. Thiel

Die der vorliegenden Arbeit zugrunde liegenden Experimente wurden in der Zeit von November 2010 bis November 2015 im Fachbereich Chemie der Technischen Universität Kaiserslautern in der Arbeitsgruppe von Herrn Prof. Hans-Jörg Krüger, Ph. D. durchgeführt.

To My Parents and Late Grandfather

Table of Content

Table of Content.....	I
Abbreviations.....	V
List and Abbreviations of Compounds.....	XI
1 Introduction.....	1
1.1 Thermally Induced Spin-Crossover Process.....	2
1.1.1 Spin Transition Behavior.....	8
1.1.2 Comparison Between Iron(II) and Cobalt(II) Systems.....	10
1.1.3 Examples of SCO Active Cobalt(II) Complexes.....	11
1.2 Valence Tautomerism.....	13
1.2.1 Examples of Valence Tautomeric Complexes.....	18
1.3 Closed-Shell Quinonoid and Open-Shell Biradicaloid Systems.....	20
1.4 Singular Value Decomposition.....	22
1.5 Motivation and Target Complex.....	25
2 Results and Discussion.....	31
2.1 Valence Tautomerism in a Cobalt Dioxolene Complex.....	31
2.1.1 Synthesis.....	31
2.1.2 Structural Characterization.....	33
2.1.3 Magnetic Properties.....	40
2.1.3.1 Magnetic Properties in Solid State.....	40
2.1.3.2 Magnetic Properties in Solution State.....	41
2.1.4 Infrared Spectroscopic Properties.....	48
2.1.4.2 Infrared Spectroscopic Properties of the Solid Samples	48
2.1.4.3 Infrared Spectroscopic Properties in the Solution State	51
2.1.5 UV/Vis/NIR Spectroscopic Properties.....	53
2.1.6 Electrochemical Properties.....	74
2.1.7 Brief Summary.....	77

2.2 Switching of Electronic States of Bis(dioxolene) Ligands Triggered by Cobalt(II) Based Temperature-Induced Spin-Crossover and Cobalt-Ligand Based Electron Transfer Processes.....	78
2.2.1 Synthesis.....	79
2.2.2 Structural Characterization.....	82
2.2.3 Magnetic Properties.....	96
2.2.4 Infrared Spectroscopic Properties.....	105
2.2.5 UV/Vis/NIR Spectroscopic Properties.....	112
2.2.6 Electrochemical Properties.....	117
2.2.7 Brief Summary.....	120
2.3 Electronic States of Bis(dioxolene) Ligands and the Interactions Between Metal Ions in Nickel-, Copper- and Zinc-Bis(dioxolene) Complexes.....	121
2.3.1 Synthesis.....	121
2.3.2 Structural Characterization.....	122
2.3.3 Magnetic Properties.....	129
2.3.3.1 Magnetic Properties in Solid State.....	129
2.3.3.2 NMR Spectroscopic Properties.....	131
2.3.3.3 EPR Spectroscopic Properties.....	136
2.3.4 Mass Spectroscopic Properties.....	140
2.3.5 Infrared Spectroscopic Properties.....	142
2.3.6 UV/Vis/NIR Spectroscopic Properties.....	145
2.3.7 Electrochemical Properties.....	157
2.3.8 Brief Summary.....	161
3 Conclusions.....	162
4 Experimental Section.....	166
4.1 Physical Methods.....	166

4.2 Chemicals and Suppliers.....	171
4.3 Synthesis.....	172
4.3.1 Synthesis of 1,2-dichloro-4,5-dimethoxybenzene.....	173
4.3.2 Synthesis of 4,5-dichlorocatechol (H ₂ DCCat).....	174
4.3.3 Synthesis of sodium diphenyl(4,5-dichlorocatecholate)- borate (NaBPh ₂ (DCCat)).....	175
4.3.4 Synthesis of 3,3',4,4'-tetramethoxybiphenyl.....	176
4.3.5 Synthesis of 3,3',4,4'-tetrahydroxybiphenyl	177
4.3.6 Synthesis of 3,3'-dihydroxy-diphenoquinone-(4,4') (H ₂ (SQ-SQ)).....	178
4.3.7 Synthesis of [Co(L-N ₄ tBu ₂)(DCCat)] (1).....	180
4.3.8 Synthesis of [Co(L-N ₄ tBu ₂)(DCCat)]·CH ₂ Cl ₂ (1b).....	181
4.3.9 Synthesis of [Co(L-N ₄ tBu ₂)(DCCat)](BF ₄) (2a).....	182
4.3.10 Synthesis of [Co(L-N ₄ tBu ₂)(DCCat)](BPh ₄) (2b)....	183
4.3.11 Synthesis of [Co(L-N ₄ tBu ₂)(DCCat)](BPh ₄)·2 CH ₂ Cl ₂ (2c).....	185
4.3.12 Synthesis of [Co(L-N ₄ tBu ₂)(DCCat)][BPh ₂ (DCCat)] (2d)..	186
4.3.13 Synthesis of [Co(L-N ₄ tBu ₂)(DCCat)](OTf) (2e).....	188
4.3.14 Synthesis of [Co ₂ (L-N ₄ tBu ₂) ₂ (SQ-SQ)](BPh ₄) ₂ ·4 DMF (3b).....	190
4.3.15 Synthesis of [Co ₂ (L-N ₄ tBu ₂) ₂ (SQ-SQ)](BPh ₄) ₂ (3a).....	193
4.3.16 Synthesis of [Co ₂ (L-N ₄ tBu ₂) ₂ (Cat-SQ)](BF ₄) ₂ ·Et ₂ O (3d)...	194
4.3.17 Synthesis of [Co ₂ (L-N ₄ tBu ₂) ₂ (Cat-SQ)](BF ₄) ₂ (3c).....	195
4.3.18 Synthesis of [Co ₂ (L-N ₄ tBu ₂) ₂ (Cat-SQ)](PF ₆) ₂ (3e).....	196
4.3.19 Synthesis of [Ni ₂ (L-N ₄ tBu ₂) ₂ (SQ-SQ)](BPh ₄) ₂ ·4 DMF (4a).....	197
4.3.20 Synthesis of [Cu ₂ (L-N ₄ tBu ₂) ₂ (SQ-SQ)](BF ₄) ₂ ·Et ₂ O (5a)....	199

4.3.21 Synthesis of $[\text{Zn}_2(\text{L-N}_4\text{tBu}_2)_2(\text{SQ-SQ})](\text{BPh}_4)_2 \cdot 4 \text{ DMF}$ (6b).....	200
4.3.22 Synthesis of $[\text{Zn}_2(\text{L-N}_4\text{tBu}_2)_2(\text{SQ-SQ})](\text{BPh}_4)_2$ (6a).....	202
5 References	203
6 Appendix	215
7 Acknowledgement	333
8 Statutory Explanation	335
9 Curriculum Vitae	336

Abbreviations

Å	Angstrom
<i>a</i>	hyperfine coupling constant
Adj.	adjusted
ATR	attenuated total internal reflectance
a. u.	arbitrary unit
<i>B</i>	magnetic field strength
BQ	benzoquinone
br	broad
ca.	approximately
calcd.	calculated
Cat	catecholate
Cat-Cat	catecholate-catecholate or dideprotonated form of 3,3'-dihydroxy-diphenoquinone-(4,4') with this electronic state
Cat-N-BQ	monoanion of 2-(2-hydroxy-3,5-di- <i>tert</i> -butylphenyl-imino)-4,6-di- <i>tert</i> -butyl-cyclohexa-3,5-dienone
Cat-N-SQ	dianion of 2-(2-hydroxy-3,5-di- <i>tert</i> -butylphenyl-imino)-4,6-di- <i>tert</i> -butyl-cyclohexa-3,5-dienone
Cat-SQ	catecholate-semiquinonate or dideprotonated form of 3,3'-dihydroxy-diphenoquinone-(4,4') with this electronic state
Cp	cyclopentadienyl
CS	closed-shell
CS-OS	closed-shell to open-shell state conversion
CTH	<i>dl</i> -5,7,7,12,14,14-hexamethyl-1,4,8,11-tetraazacyclotetradecane
CV	cyclic voltammogram

d	doublet
D	Debye
DBC	3,5-di- <i>tert</i> -butylcatecholate
DBSQ	3,5-di- <i>tert</i> -butylsemiquinonate
DCBQ	4,5-dichlorobenzoquinone
DCCat	4,5-dichlorocatecholate
DCE	1,2-dichloroethane
DCM	dichloromethane
DCSQ	4,5-dichlorosemiquinonate
dd	doublet of doublet
deg	degree
DHBQ	dideprotonated form of 2,5-dihydroxy-1,4-benzoquinone
DMF	<i>N,N</i> -dimethylformamide
DMSO	dimethyl sulfoxide
dppbm	4,6-di-2'-pyridylpyrimidine
dppe	1,2-bis(diphenylphosphino)ethane
<i>E</i>	potential
EDG	electron-donating group
<i>e.g.</i>	for example
elec	electronic
EPR	electron paramagnetic resonance
ESI	electro-spray ionization
Et	ethyl
Et ₂ O	diethyl ether
Et ₃ N	triethylamine
EtCN	propionitrile
EWG	electron-withdrawing group

exp.	experimental
FIR	far infrared
G	Gibbs free energy
H(SQ-SQ)	monodeprotonated form of 3,3'-dihydroxy-diphenoquinone-(4,4')
H ₂ DCCat	4,5-dichlorocatechol
H ₂ (SQ-SQ)	3,3'-dihydroxy-diphenoquinone-(4,4')
H ₄ (Cat-Cat)	3,3',4,4'-tetrahydroxybiphenyl
HC	hydrocarbon
HOMO	highest occupied molecular orbital
HS	high-spin
HTC	high-temperature component
Hz	hertz
I	current
<i>i.e.</i>	that is
IR	infrared
J	magnetic exchange coupling constant
K	Kelvin
k_B	Boltzmann constant
L	ligand
l	length
LMCT	ligand-to-metal charge-transfer
L-N ₄ Me ₂	<i>N,N'</i> -dimethyl-2,11-diaza[3.3](2,6)pyridinophane
L-N ₄ <i>t</i> Bu ₂	<i>N,N'</i> -di- <i>tert</i> -butyl-2,11-diaza[3.3](2,6)pyridinophane
LS	low-spin
LTC	low-temperature component
LUMO	lowest unoccupied molecular orbital
M	mole per litre

m	multiplet
mA	milliampere
Me	methyl
MeCN	acetonitrile
MeOH	methanol
MHz	megahertz
MLCT	metal-to-ligand charge-transfer
mT	millitesla
mV	millivolt
MW	molecular weight
NaOH	sodium hydroxide
NIR	near infrared
NMR	nuclear magnetic resonance
O_h	octahedral
OS	open-shell
OSS	singlet open-shell state
OST	triplet open-shell state
OTf	trifluoromethane sulfonate
P	spin pairing energy
PHC	polycyclic aromatic hydrocarbon
PhCat	dideprotonated form of 9,10-dihydroxyphenanthrene
ppm	parts per million
R	gas constant
R^2	goodness-of-fit parameter
RMSE	root mean square error
RT	room temperature
s	singlet
s	second (unit of time)

<i>S</i>	spin multiplicity
SCE	secondary calomel electrode
SCO	spin-crossover
sh	shoulder
SOMO	singly occupied molecular orbital
SS_{res}	sum of squared residuals
SQ	semiquinonate
SQ-BQ	semiquinonate-benzoquinone or dideprotonated form of 3,3'-dihydroxy-diphenoquinone-(4,4') with this electronic state
SQ-SQ	semiquinonate-semiquinonate or dideprotonated form of 3,3'-dihydroxy-diphenoquinone-(4,4') with this electronic state
$(\text{SQ-SQ})_{\text{CS}}$	closed-shell form of the semiquinonate-semiquinonate ligand
$(\text{SQ-SQ})_{\text{OS}}$	open-shell form of the semiquinonate-semiquinonate ligand
$(\text{SQ-SQ})_{\text{OSS}}$	singlet open-shell form of the semiquinonate-semiquinonate ligand
SQUID	super conducting quantum interference device
<i>t</i>	triplet
<i>T</i>	temperature
T	transmittance
$T_{1/2}$	spin transition temperature
TBAP	tetrabutylammonium perchlorate
<i>t</i> Bu	<i>tert</i> -butyl
T_c	critical temperature
TCBQ	tetrachloro- <i>o</i> -benzoquinone

THF	tetrahydrofuran
TIP	temperature independent paramagnetism
tpa	bis(6-methyl-2-pyridylmethyl)(2-pyridylmethyl)- amine
tt	triplet of triplet
UV/Vis	ultraviolet/visible
V	volt
vib	vibrational
vs.	versus
VT	valence tautomeric or valence tautomerism
VT _{LS-HS}	valence tautomeric transition from low-spin cobalt(III) catecholate to high-spin cobalt(II) semiquinonate state
VT _{LS-LS}	valence tautomeric transition from low-spin cobalt(III) catecholate to low-spin cobalt(II) semiquinonate state
Y	counter ion
ZFS	zero field splitting
ϵ	molar extinction coefficient
δ	chemical shift
λ	wavelength
χ	magnetic susceptibility
ν	wavenumber
μA	microampere
$^{\circ}\text{C}$	Celsius
μ_{eff}	effective magnetic moment
γ_{HS}	mole fraction of high-spin state
γ_{LS}	mole fraction of low-spin state

List and Abbreviations of Compounds

1	$[\text{Co}(\text{L-N}_{4t}\text{Bu}_2)(\text{DCCat})]$
1a	$[\text{Co}(\text{L-N}_{4t}\text{Bu}_2)(\text{DCCat})] \cdot 3 \text{ MeCN} \cdot \text{H}_2\text{O}$
1b	$[\text{Co}(\text{L-N}_{4t}\text{Bu}_2)(\text{DCCat})] \cdot \text{CH}_2\text{Cl}_2$
2	$[\text{Co}(\text{L-N}_{4t}\text{Bu}_2)(\text{DCCat})]^+$
2a	$[\text{Co}(\text{L-N}_{4t}\text{Bu}_2)(\text{DCCat})](\text{BF}_4)$
2b	$[\text{Co}(\text{L-N}_{4t}\text{Bu}_2)(\text{DCCat})](\text{BPh}_4)$
2c	$[\text{Co}(\text{L-N}_{4t}\text{Bu}_2)(\text{DCCat})](\text{BPh}_4) \cdot 2 \text{ CH}_2\text{Cl}_2$
2d	$[\text{Co}(\text{L-N}_{4t}\text{Bu}_2)(\text{DCCat})][\text{BPh}_2(\text{DCCat})]$
2e	$[\text{Co}(\text{L-N}_{4t}\text{Bu}_2)(\text{DCCat})](\text{OTf})$
3	$[\text{Co}_2(\text{L-N}_{4t}\text{Bu}_2)_2(\text{SQ-SQ})]^{2+}$
3a	$[\text{Co}_2(\text{L-N}_{4t}\text{Bu}_2)_2(\text{SQ-SQ})](\text{BPh}_4)_2$
3b	$[\text{Co}_2(\text{L-N}_{4t}\text{Bu}_2)_2(\text{SQ-SQ})](\text{BPh}_4)_2 \cdot 4 \text{ DMF}$
3c	$[\text{Co}_2(\text{L-N}_{4t}\text{Bu}_2)_2(\text{Cat-SQ})](\text{BF}_4)_2$
3d	$[\text{Co}_2(\text{L-N}_{4t}\text{Bu}_2)_2(\text{Cat-SQ})](\text{BF}_4)_2 \cdot \text{Et}_2\text{O}$
3e	$[\text{Co}_2(\text{L-N}_{4t}\text{Bu}_2)_2(\text{Cat-SQ})](\text{PF}_6)_2$
4	$[\text{Ni}_2(\text{L-N}_{4t}\text{Bu}_2)_2(\text{SQ-SQ})]^{2+}$
4a	$[\text{Ni}_2(\text{L-N}_{4t}\text{Bu}_2)_2(\text{SQ-SQ})](\text{BPh}_4)_2 \cdot 4 \text{ DMF}$
5	$[\text{Cu}_2(\text{L-N}_{4t}\text{Bu}_2)_2(\text{SQ-SQ})]^{2+}$
5a	$[\text{Cu}_2(\text{L-N}_{4t}\text{Bu}_2)_2(\text{SQ-SQ})](\text{BF}_4)_2 \cdot \text{Et}_2\text{O}$
6	$[\text{Zn}_2(\text{L-N}_{4t}\text{Bu}_2)_2(\text{SQ-SQ})]^{2+}$
6a	$[\text{Zn}_2(\text{L-N}_{4t}\text{Bu}_2)_2(\text{SQ-SQ})](\text{BPh}_4)_2$
6b	$[\text{Zn}_2(\text{L-N}_{4t}\text{Bu}_2)_2(\text{SQ-SQ})](\text{BPh}_4)_2 \cdot 4 \text{ DMF}$
6⁺	$[\text{Zn}_2(\text{L-N}_{4t}\text{Bu}_2)_2(\text{Cat-SQ})]^+$
7	$[\text{Zn}(\text{L-N}_{4t}\text{Bu}_2)(-\text{SQ-SQ})]$

1 Introduction

Switching of electronic state of a compound by an external perturbation such as heat, light, pressure, etc., can involve changes in the magnetic properties of the compound. Such switchable compounds have important applications in the field of molecular electronics, electronic storage devices and information processing.^[1–8] Therefore, great interest has been shown by a group of researchers towards the preparation of such compounds and study of the magnetic properties of these compounds.

The changes in the electronic states of the thermally switchable compounds take place due to the application of the external perturbation heat. Among the thermally switchable compounds, spin-crossover complexes^[9–11] and valence tautomeric compounds^[12–14] are extensively studied examples. Sometimes, these processes occur via hysteresis.^[10,15] In a hysteretic spin transition/valence tautomerism, the molecular system can be in one state or another state depending upon the history of the sample.

Apart from the above examples, π -conjugated polycyclic aromatic hydrocarbons (PHCs) with open-shell ground states^[16–22] are the attractive examples which are gathering attention of the researchers due to their unique optical, electronic, magnetic properties, and potential applications in spintronics, organic electronics, energy storage devices and information processing. Thus, it is reasonable to propose that if in a molecular system spin-crossover or valence tautomerism, and open-shell systems coexist, then it enhances the possibility for the observation of unique optical, electronic and magnetic properties of the system which could be different than the usually observable ones for each of the individual system.

1.1 Thermally Induced Spin-Crossover Process

Octahedral complexes of 3d-elements having electronic configurations of $3d^n$ ($n = 4$ to 7) can exist either in their low-spin (LS) or high-spin (HS) states. Depending upon the ligand-field strength of the ligand in an octahedral field, entirely low-spin or entirely high-spin ground state of a metal ion in a complex can be achieved. In an ideal octahedral coordination atmosphere, due to the interaction between the metal and ligand, the d orbitals of the metal ion will split into two different energy levels namely t_{2g} and e_g . Thus, the t_{2g} and e_g orbitals are separated by the ligand-field splitting energy Δ , where $\Delta = 10 Dq$. If $\Delta > P$ ($P =$ spin pairing energy), then low-spin electronic configuration of the metal ion is stabilized, else the high-spin electronic configuration of the metal ion is stabilized for $\Delta < P$ (Figure 1.1).^[9-11] For the case, when both of the energies Δ and P are comparable, so that the ligand-field splitting energy lies near to the crossover point energy (Δ_{crit}), then the low-spin and high-spin state of the metal ion can be interconverted by applying an external perturbation, such as heat, pressure, light etc. This behavior is attributed to the spin-crossover (SCO) phenomenon.

The spin-crossover phenomenon is observed in solid and/or solution state. Spin-crossover behavior in solid state differs from that of the solution state because of the presence of cooperativity in the solid state, such as interaction between the complex molecules or interaction of the complex molecule with the non-coordinated solvent molecules or with the non-coordinated counter ions. On the other hand, such cooperativity is absent in the solution state. The population of the excited states in a temperature-induced spin transition follows the Boltzmann distribution law. The types of spin transitions in the solid state are described below (see discussion in section 1.1.1). Here, spin transition and spin-crossover have the same connotation.

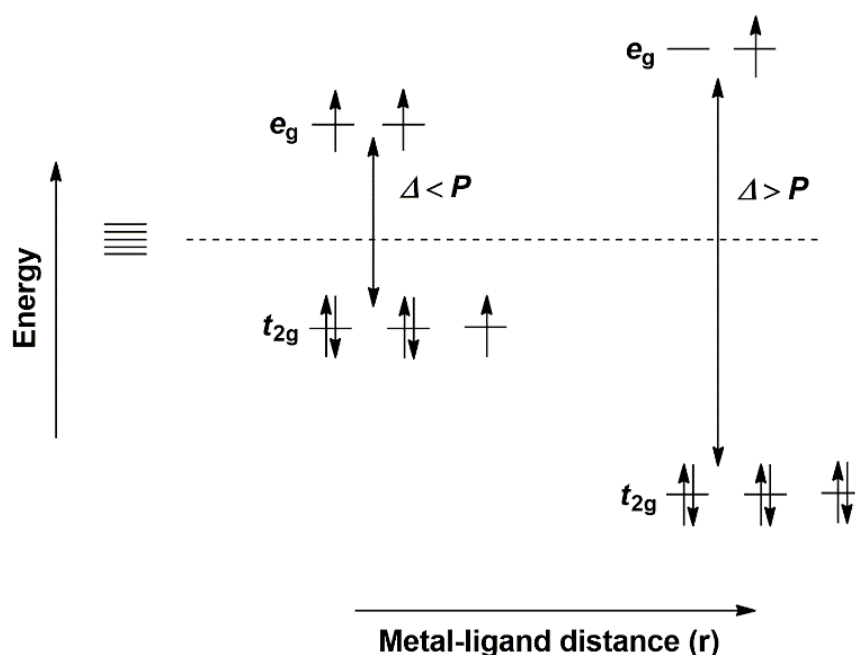


Figure 1.1: Schematic representation of the possible ground states of a d^7 metal ion in an octahedral field.^[9–11]

Cambi and co-workers presented the first spin-crossover complex in 1930.^[23] Therein, the conversion from the low-spin to high-spin state of the complex iron(III) tris(dithiocarbamate) was achieved by changing the temperature. The first iron(II) spin-crossover complex was achieved by *Baker* and *Bobonich* in 1964 for the complex $[\text{Fe}(\text{phen})_2(\text{SCN})_2]$ (phen = 1,10-Phenanthroline).^[24] The first example of spin-crossover phenomenon for a cobalt(II) complex was reported by *Figgins* and *Busch* in 1960.^[25] Afterwards, in 1961, *Stoufer*, *Busch* and *Hadley* reported the cobalt(II) spin-crossover complex $[\text{Co}(\text{PdAdH})_2]\text{I}_2$ (PdAdH = 2,6-pyridinaldihydrazone) with its extensive characterization.^[26] In 1962, *Hogg* and *Wilkins* reported anion-dependence of the magnetism of the salts of $[\text{Co}(\text{terpy})_2]^{2+}$ (terpy = 2,2',2''-terpyridine) and change in magnetism of $[\text{Co}(\text{terpy})_2]\text{Br}_2 \cdot \text{H}_2\text{O}$ by changing temperature.^[27]

Among the SCO complexes, examples of spin-crossover iron(II) complexes are already large,^[28–35] but examples of spin-crossover cobalt(II) complexes are scarce.^[35–55] Most of the spin-crossover active iron(II) and cobalt(II) complexes contain neutral ligands, but the examples of SCO complexes where radical containing ligands are coordinated are rare. Recently, *Krüger* and co-workers have reported a novel class of spin-crossover active iron(II)^[30] and cobalt(II) complexes^[55] where radicals are situated on the co-ligands.

There are several experimental methods available to detect a spin-crossover phenomenon (Table 1.1).^[10,54] Among these methods, X-ray crystallographic structure determination is a very important diagnostic tool because in a spin-crossover process, the metal–ligand bond lengths within the coordination sphere of the complex are changed. The magnetic susceptibility (χT) or effective magnetic moment (μ_{eff}) measurement is one of the important diagnostic tools for the detection of the spin-crossover process. In solid state, the χT value of a complex can be measured in SQUID magnetometer, Faraday or Gouy balance, whereas in solution state, Evans-NMR method is generally applied to measure the magnetic susceptibility. The χT value of a spin-crossover metal complex increases upon transition from low-spin to high-spin state. In the SCO process, the change in the stretching frequency of a metal–ligand bond is observable in vibrational spectrum in the far infrared (FIR) region whereas the changes in stretching frequencies of some characteristic bonds in the coordinated ligand due to the changes in $d\pi\text{--}p\pi$ back bonding strengths are observable in the infrared (IR) region.

Table 1.1: Experimental methods for the detection of a spin-crossover phenomenon and the observed properties in each case.^[10,54]

Method	Observed property	LS	HS
Magnetic measurements	Magnetic susceptibility, effective magnetic moment	Low	High
X-ray structure analysis	Metal to ligand bond lengths	Small	Large
Electronic absorption spectra	Molar extinction coefficient	Small	Large
Calorimetry	Heat capacity	Small	Large
Vibrational spectra	Metal-ligand bond vibrational wavenumber	Small	Large
Volumetric measurement	Partial molar volume	Small	Large
EXAFS spectroscopy	Metal to ligand distances	Small	Large
NMR spectroscopy	Effective magnetic moment, magnetic susceptibility, paramagnetic shift	Small	Large

The electronic configuration of the cobalt(II) ion is d^7 . In an octahedral coordination atmosphere, ^{2S+1}L terms of the free cobalt(II) ion will split according to the Tanabe-Sugano diagram.^[56,57] The Tanabe-Sugano diagram for an octahedral d^7 complex is shown in Figure 1.2 and it is configured by taking the parameters along the x-axis as $10Dq/B$ and y-axis as E/B ($E =$ energy) where B is the Racah parameter.^[53,57] For the low-spin cobalt(II) state, the ground state is doublet (2E), and for the high-spin cobalt(II) state, the ground state is quartet (4T_1).^[54]

The ligand-field strength is also affected by the metal to ligand distances. For a neutral ligand, the $10 Dq$ value can be measured according to the following equation (eq 1.1).^[9]

$$10 Dq(r) \approx \mu/r^6 \quad (1.1)$$

such as ΔG , ΔH and ΔS where ΔS is the difference of entropy and ΔH is the difference of enthalpy between the 4T_1 and 2E states. The change in the Gibbs free energy (ΔG) in a spin-crossover process is related to ΔS and ΔH by the following equation (eq 1.3).

$$\Delta G = \Delta H - T \Delta S \quad (1.3)$$

The spin-crossover process is driven by a positive change in entropy ($\Delta S_{\text{total}} = \Delta S_{\text{elec}} + \Delta S_{\text{vib}} > 0$). The spin transition from doublet 2E to quartet 4T_1 state would lead to the change in spin multiplicity of the cobalt(II) ion ($\Delta S = 1$). Hence, the number of electronic degeneracy is higher in 4T_1 state than that of the 2E state. The approximate value of ΔS_{elec} can be derived from the equation^[10,58]

$$\Delta S_{\text{elec}} = R \ln \frac{(2S+1)_{\text{HS}}}{(2S+1)_{\text{LS}}} \quad (1.4)$$

Thus, ΔS_{elec} value is positive ($\Delta S_{\text{elec}} > 0$). The spin transition leads to the changes in metal to ligand bond lengths, and in high-spin quartet state the metal to ligand bond lengths are larger than the bond lengths in low-spin doublet state. The vibrational levels of the potential wells are closely spaced in high-spin state and widely spaced in low-spin state. Therefore, the density of vibrational levels in the high-spin state is larger than that of the low-spin state. Thus, the ΔS_{vib} is positive ($\Delta S_{\text{vib}} > 0$) and hence, $\Delta S_{\text{total}} =$ positive. The vertical shifts between the potential wells is the difference between the zero point energies for the quartet and doublet states, which is termed as ΔE_{HL}^0 , where $\Delta E_{\text{HL}}^0 = E_{\text{HS}}^0 - E_{\text{LS}}^0$. For a thermally induced spin crossover process, $\Delta E_{\text{HL}}^0 \approx k_{\text{B}}T$ and it falls into the region of the thermal energy.^[9]

The equation involving the thermodynamic parameters is valid, provided, the cooperative effects in the solid state of a complex are not present. For most of the iron(II) SCO complexes, the enthalpy changes are typically in the range of

10–20 kJ mol⁻¹, and entropy changes are in the range of 50–80 J K⁻¹ mol⁻¹.^[59] The values of the thermodynamic parameters associated with a spin-crossover process can be obtained by a curve fitting approach to the spin transition curve and by singular value decomposition of the variable temperature UV/Vis/NIR spectra for the SCO.

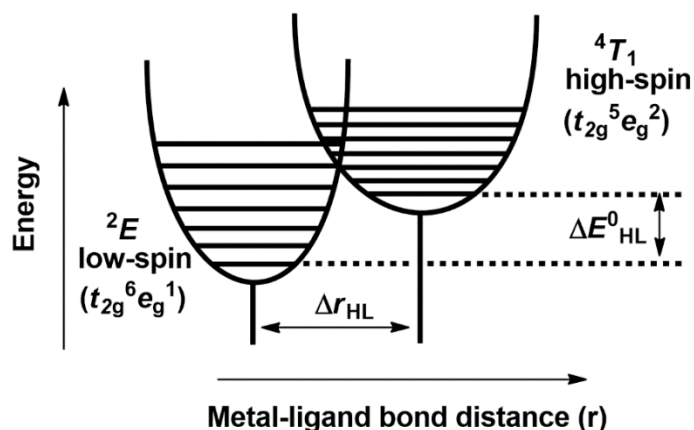


Figure 1.3: Schematic representation of the potential wells of 2E and 4T_1 states of a cobalt(II) spin-crossover complex.^[53]

1.1.1 Spin Transition Behavior

Different types of spin transitions are possible in solid state.^[9,10] The high-spin molar fraction (γ_{HS}) vs. temperature (T) curves which are called as $\gamma_{\text{HS}}(T)$ curves, follow different shapes for various types of spin transitions (Figure 1.4). The spin transition temperature $T_{1/2}$ is the temperature when $\gamma_{\text{HS}} = \gamma_{\text{LS}} = 0.5$. The discussion involving different shapes of the curves in different cases of spin transitions is as following:

- a) Spin transition occurring over a wide range of temperature is called gradual spin transition (Figure 1.4a).
- b) Spin transition occurring in between ≤ 10 K is called abrupt spin transition (Figure 1.4b).

c) Spin transition occurring with a step is called stepwise spin transition (Figure 1.4c).

d) Spin transition where at low temperature some fraction of high-spin molecules are trapped (Figure 1.4d).

e) Abrupt spin transition showing hysteresis (Figure 1.4e).

The spin-crossover process can be continuous or discontinuous. According to the reported spin transition types by *Gütlich et al.*,^[9] types *a*, *b* and *c* are continuous. Only type *e* is discontinuous. Type *d* spin transition can be continuous or discontinuous. Continuous spin transition usually occurs without change in the crystallographic system.^[9,60] There are many examples of discontinuous spin transitions which occur by changes in the crystallographic systems, yet there are also exceptions.^[9,59]

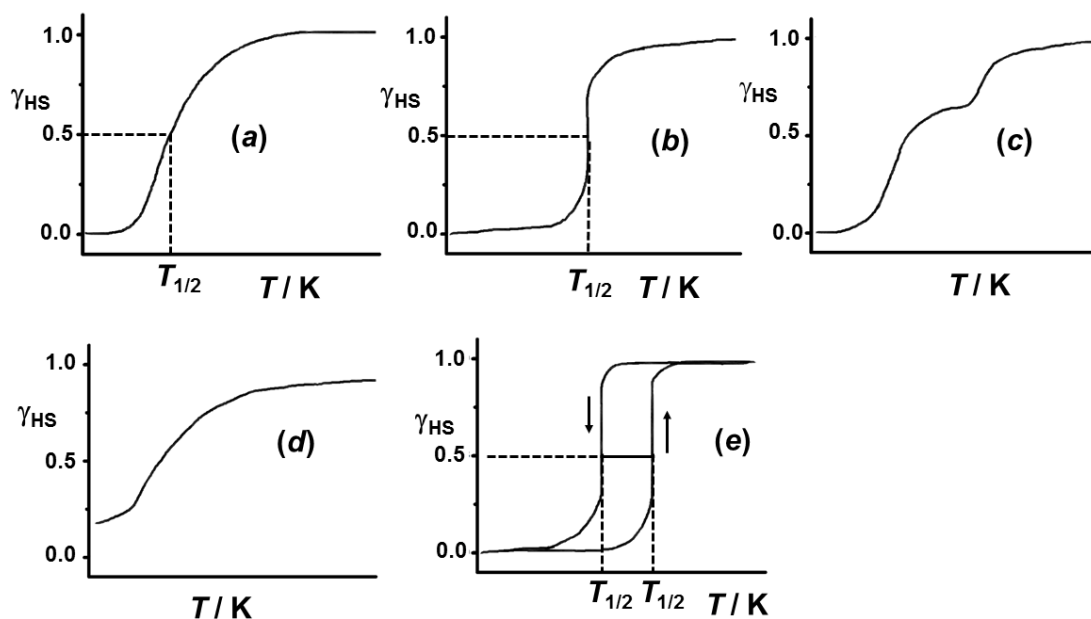


Figure 1.4: Representation of different types of spin transitions. The high-spin molar fraction (γ_{HS}) is plotted along the y-axis and temperature (T) is plotted along the x-axis in each curve.^[9,10]

1.1.2 Comparison Between Iron(II) and Cobalt(II) Systems

Spin transition in an octahedral cobalt(II) system involves only one electron transfer from t_{2g} to e_g level, whereas in an iron(II) system two electron transfer occurs.^[53,54] Therefore, the metal to ligand donor atom bond length change for the spin transition in the cobalt(II) system, is lesser than the change in the metal to ligand donor atom bond length for the spin transition in the iron(II) system, provided the used ligand is same for both the iron(II) and cobalt(II) systems.^[54] Hence, lesser volume change occurs for the cobalt(II) spin transition than that of the iron(II) spin transition. There is also possibility of spin-state mixing through spin-orbit coupling for the cobalt(II) system. Another significant difference between the iron(II) and cobalt(II) systems is the operation of the *Jahn-Teller* distortion. Due to the unsymmetrical occupation of the e_g orbitals, strong *Jahn-Teller* distortion is operative in the low-spin cobalt(II) state, whereas in the high-spin state, it is operative due to the unsymmetrical occupation of the t_{2g} orbitals but to a lesser extent. For an iron(II) system, the *Jahn-Teller* distortion is operative only in high-spin state but to a lesser extent. Therefore, the change of enthalpy (ΔH) and change of entropy (ΔS) in the spin transition of a cobalt(II) system are lesser than that of the iron(II) system, and hence, most of the spin transitions in cobalt(II) systems are of gradual types. Thus, due to the small volume change, spin-orbit coupling accompanied by strong *Jahn-Teller* distortion, a faster spin transition is observed in a cobalt(II) system compared to an iron(II) system.

1.1.3 Examples of SCO Active Cobalt(II) Complexes

In the most cases, the spin-crossover phenomena in octahedral cobalt(II) systems are observed in $[\text{CoN}_6]$ type of complexes containing ligands which have nitrogen donor atoms. Selected examples of such ligands are provided in Figure 1.5; 2,6-pyridindialdihydrazone, α -diimine, 2-pyridylmethanimine,^[26,54] tris-pyridylamine (tpda),^[40,54] 4-substituted-terpy derivatives,^[41–45] 4-terpyridone,^[46] dipyrazine carboxamide,^[47] 2,3,5,6-tetrakis(2-pyridyl)pyrazine (tppz),^[48] 4,4-dimethyl-2,2-bis(2-pyridyl)-oxazolidine-*N*-oxide,^[37] 4,6-bis(2-((6-bromo-pyridine-2-yl)methylene)-hydrazinyl)pyrimidine,^[49] *N,N'*-ethylene bis(3-carboxysalicylaldehyde).^[50–52]

As mentioned earlier, for a low-spin cobalt(II) state, strong *Jahn-Teller* distortion is operative. Depending upon the ligand coordination atmosphere, tetragonal elongation or tetragonal compression along the axial positions of the octahedron occurs. In an octahedral coordination environment, coordination of tridentate planar ligands to the low-spin cobalt(II) center would lead to the tetragonal compression along the axial positions, whereas the combination of an equatorially placed tetradentate planar ligand and axially placed two monodentate ligands would lead to the tetragonal elongation along the axial positions. For the latter case, use of different monodentate ligands in the axial positions determines the ground state of the cobalt(II) ions. Utilization of the phenolic dianion of *N,N'*-ethylene bis(3-carboxysalicylaldehyde) as the tetradentate ligand and monodentate ligands such as 3-methylpyridine, 3-aminopyridine or 3,5-dimethylpyridine would lead to a moderate tetragonal elongation which results in spin-state admixing between the doublet and quartet states of lowest energy.^[52] However, with the use of the above mentioned tetradentate ligand and the monodentate ligands such as, H_2O , pyridine and 4-*tert*-butylpyridine, spin-crossover from low-spin cobalt(II) to high-spin cobalt(II) state is achieved in each case.^[51,52]

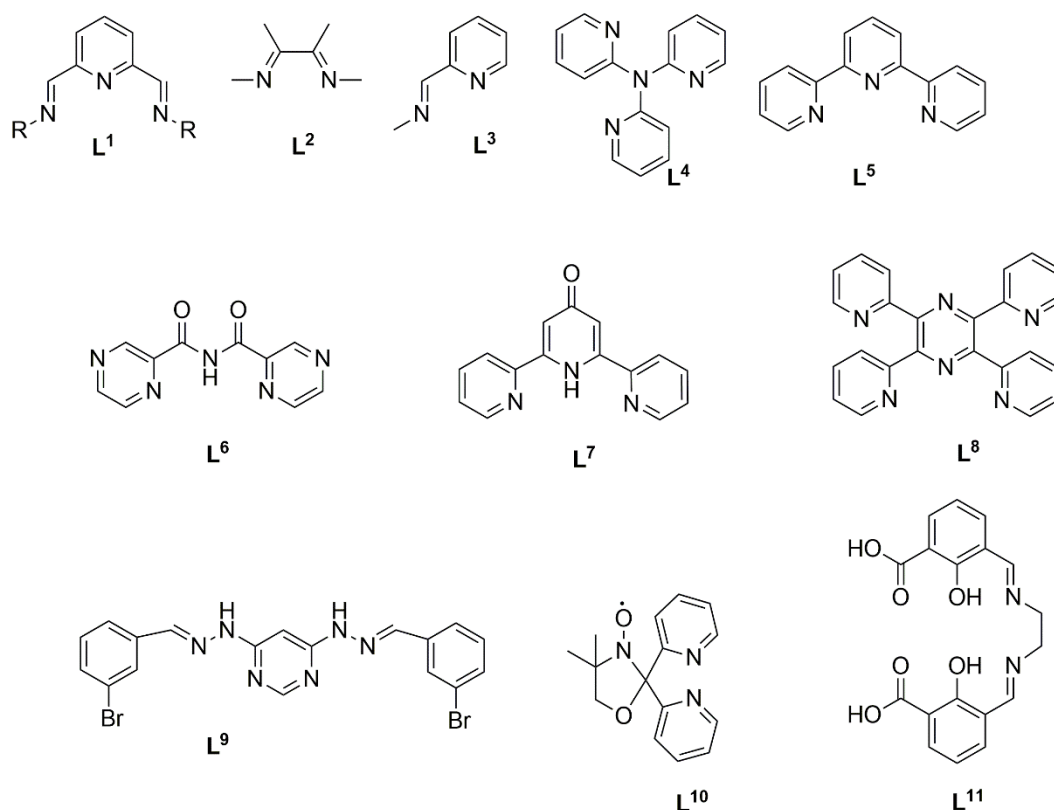


Figure 1.5: Structures and abbreviations of the ligands; L^1 = 2,6-pyridindialdihydrazone ($R = NH_2$). L^2 = α -diimine. L^3 = N -methyl-2-pyridylmethanimine. L^4 = tris-pyridylamine. L^5 = terpyridine. L^6 = dipyrazine carboxamide. L^7 = 4-terpyridone. L^8 = 2,3,5,6-tetrakis-(2-pyridyl)-pyrazine (tppz). L^9 = 4,6-bis(2-((6-bromopyridin-2-yl)methylene)hydrazinyl)pyrimidine. L^{10} = 4,4-dimethyl-2,2-bis(2-pyridyl)-oxazolidine- N -oxide. L^{11} = N,N' -ethylene bis(3-carboxysalicylaldimine).

Due to the *Jahn-Teller* distortion in a d^7 -system, the 2E state will split to 2A and 2B sub-sets and the 4T_1 state will split to 4A and 4E sub-sets (Figure 1.6).^[32,36,52,53,61,62] For a moderate tetragonal elongation, the 2A sub-set of 2E state lies lower in energy than the 4E sub-set of 4T_1 state. However, in a situation, when strong *Jahn-Teller* elongation is operative in an octahedral coordination atmosphere, the 2A sub-set of the 2E state lies lower in energy than the 4A sub-set of the 4T_1 state. Thus, in the case of strong tetragonal elongation, the stabilization of the low-spin doublet state as well as the pseudo-octahedral geometry around the metal center are observed.

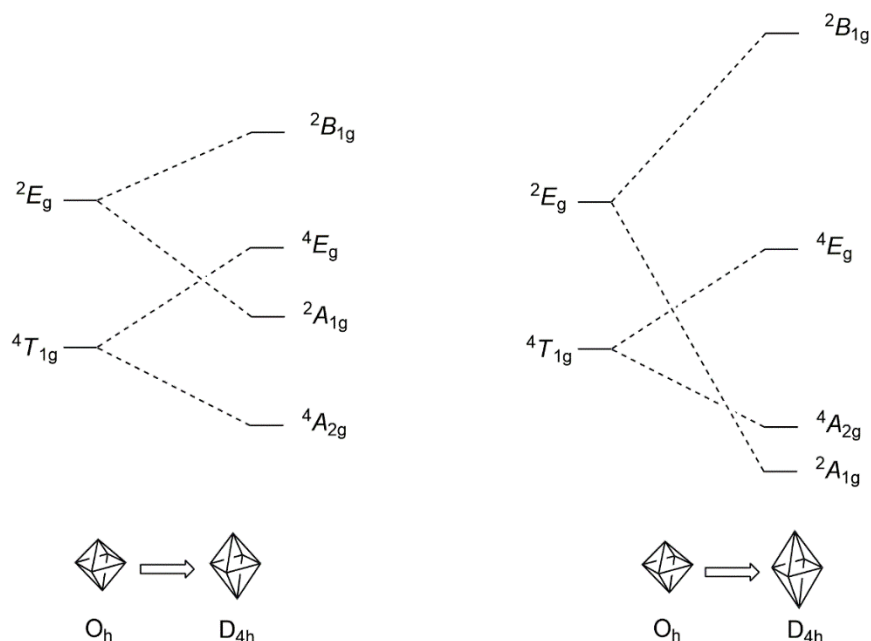


Figure 1.6: Energy level diagram for the splitting of d orbitals of a hexa-coordinated cobalt(II) ion with a quartet ground state in an axially distorted pseudo-octahedral complex where moderate (left) and strong (right) tetragonal elongations occur.^[32,36,52,53,61,62]

1.2 Valence Tautomerism

Valence tautomerism is an intramolecular electron transfer process between a metal ion and a redox-active ligand, which often involves changes in the ground electronic state and redox-state of the metal ion.^[12,13] The redox-active ligands are mainly various types of *o*-dioxolene derivatives. The valence tautomerism happens with the application of an external perturbation, such as heat, light, pressure, etc., when the d orbital energy of a 3d-element is close to the frontier π -orbital energy of the redox-active ligand. The electron transfer in a valence tautomerism (VT) leads to the changes in the oxidation states of the metal and ligand in a metal dioxolene complex, but the overall charge of the complex remains same. Hence, in a valence tautomeric transition, the two species $[M^m \text{Cat}^{2-}]^n$ and $[M^{m-1} \text{SQ}^{\bullet-}]^n$ (m = oxidation state of metal ion, n = overall charge of the complex) are termed as redox isomers with respect to each other.^[15] The *o*-dioxolene unit can coordinate to a metal ion in three

different redox forms, which are catecholate (Cat^{2-}), semiquinonate ($\text{SQ}^{\bullet-}$) and benzoquinone (BQ) (Figure 1.7). Among the three different redox forms of *o*-dioxolene, the catecholate moiety is a strong π - and σ -donors.^[15] The catecholate moiety is also a π -acceptor. Upon oxidation of a metal coordinated catecholate moiety to the semiquinonate moiety, the extent of π -acceptance properties increases and the extent of π -donation properties decreases.^[63] Which one is dominant that depends on the dioxolene system as well as the electronic and oxidation states of the metal ion. Due to the very weak donating property of the benzoquinone, it is replaced by the solvent molecules in solution.^[15] Therefore, synthesis of a metal benzoquinone complex could be extremely difficult. The catecholate, semiquinonate and benzoquinone forms of an *o*-dioxolene ligand have different oxidation states, as well as different magnetic properties. The semiquinonate moiety is paramagnetic, but the catecholate as well as the benzoquinone moieties are diamagnetic.

The coordination of a semiquinonate moiety to a metal center will exhibit interesting magnetic properties. Especially, when the metal center is paramagnetic itself, then coupling between the unpaired electron of the semiquinonate moiety and the unpaired electron residing in the metal center will exhibit interesting magnetic behavior. On the other hand, for a metal bis(dioxolene) complex, in the bis(semiquinonate) redox forms of the ligand, the coupling between the unpaired electrons of the semiquinonate units, as well as the interactions between the unpaired electrons and the metal centers will show interesting magnetic properties. When in a bis(dioxolene) unit the two $\text{SQ}^{\bullet-}$ units are directly linked through a $\text{C}(\text{sp}^2)\text{--C}(\text{sp}^2)$ single bond then *Tschitschibabin* type biradicaloid form^[64] in the bis(dioxolene) unit might be possible.^[65]

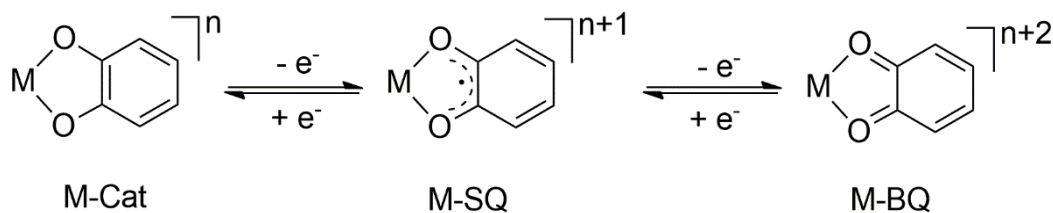


Figure 1.7: Schematic representation of the various possible metal-dioxolene forms.^[15]

Valence tautomeric transitions are mainly observed in the cobalt dioxolene complexes.^[12–15,66–87] However, valence tautomerism also happens in manganese,^[88] iron,^[89] nickel^[90] and rhodium^[91] complexes. Schematic representation of valence tautomerism in a cobalt dioxolene complex is shown in Figure 1.8. In a valence tautomeric transition, transition from a low-spin cobalt(III) catecholate to the low-spin or high-spin cobalt(II) semiquinonate species could occur. However, till date, the valence tautomerism chemistry is involved around the cobalt dioxolene complexes for which the valence tautomeric transition happens from the low-spin cobalt(III) catecholate to high-spin cobalt(II) semiquinonate states of those complexes.^[12–15,66–83] This kind of observation gives an indication that a valence tautomeric transition between the low-spin cobalt(III) catecholate and low-spin cobalt(II) semiquinonate states of a valence tautomeric cobalt dioxolene complex does not occur because the low-spin cobalt(II) semiquinonate state of the complex is not stable. But, based on the recent reports by *Krüger* and co-workers,^[55,92] it could be said that the formation of the low-spin cobalt(II) semiquinonate species is feasible when the ligand-field strength of the utilized ancillary ligand is sufficient to stabilize the low-spin cobalt(II) center. Therefore, isolation of a cobalt dioxolene complex, which could show valence tautomeric transition from low-spin cobalt(III) catecholate to low-spin cobalt(II) semiquinonate state, might be possible.

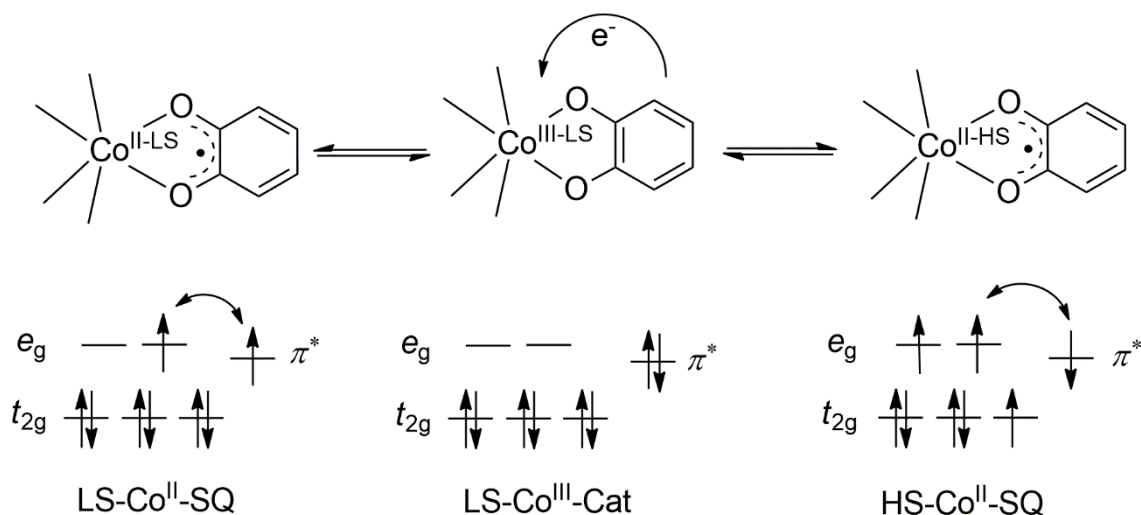


Figure 1.8: Schematic representation of the valence tautomeric transitions in a cobalt dioxolene complex. The spins have been denoted by arrows (\uparrow) and the t_{2g} , e_g , and π^* orbitals in which the electrons reside are denoted by horizontal single lines ($—$). The double headed curved arrows represent the interaction between the unpaired electrons.

Valence tautomeric transition is associated with the changes in the metal–ligand bond lengths as well as changes in the bond lengths in the dioxolene ligand. Therefore, X-ray crystallography is a very important diagnostic tool for the observation of the valence tautomerism. According to the recent reports by *Krüger* and co-workers, a *cis*-octahedral low-spin cobalt(II) semiquinonate complex shows strong MLCT bands in the NIR region,^[55,92] but a *cis*-octahedral cobalt(III) catecholate species only shows weak LMCT bands and d–d transition bands for the $^1A_{1g} \rightarrow ^1T_{1g}$ and $^1A_{1g} \rightarrow ^1T_{2g}$ transitions in *cis*-octahedral cobalt(III) complexes.^[76,77,93,94] On the other hand, a *cis*-octahedral high-spin cobalt(II) semiquinonate chromophore exhibits MLCT bands in the visible region.^[76,77,95] Therefore, UV/Vis/NIR spectroscopy is an important method to detect the valence tautomeric transition. IR spectroscopic technique is a very important diagnostic tool to identify the catecholate redox form of a coordinated dioxolene ligand, because it exhibit strong bands at ca. 1260 and ca. 1475 cm^{-1} , respectively.^[92,96–100]

Among the three redox isomers, low-spin cobalt(III) catecholate species is diamagnetic but low-spin cobalt(II) semiquinonate and high-spin cobalt(II) semiquinonate species are paramagnetic. In a low-spin cobalt(II) semiquinonate species, the unpaired electron of the $SQ^{\bullet-}$ unit is ferromagnetically coupled to the unpaired electron residing in the d_z^2 orbital of the low-spin cobalt(II) center,^[13,33,55,92] whereas in a high-spin cobalt(II) semiquinonate complex, a very weak antiferromagnetic coupling between the semiquinonate moiety and the high-spin cobalt(II) center is expected.^[95] The χT value for a high-spin cobalt(II) semiquinonate species is greater than the value expected for an $S = 1$ species, but lesser than the value expected for an $S = 2$ species.^[92] Therefore, the magnetic susceptibility measurement is an important diagnostic tool.

Similar to the SCO process, the valence tautomeric transition can also be illustrated by an one dimensional potential energy diagram.^[13,79] The potential energy diagram is configured in energy vs. nuclear coordinate diagram (Figure 1.9). The nuclear coordinate is the Co–L bond distance. The potential well of the higher energy high-spin cobalt(II) semiquinonate state is shifted vertically as well as horizontally from the potential well of the low-spin cobalt(III) catecholate state. The vertical difference is the zero point energy difference between the two potential wells and the horizontal difference is the difference in metal to ligand bond length upon VT transition from low-spin cobalt(III) catecholate to high-spin cobalt(II) semiquinonate state. Hence, the total symmetric metal-ligand breathing mode coordinate is approximately equivalent to the nuclear coordinate.

A valence tautomeric transition is also driven due to the gain of entropy. Similar to the SCO process, here also, the entropy change is affected by the change in electronic degeneracy and changes in the metal–ligand bond lengths as well as changes in the bond lengths within the dioxolene unit. The

thermodynamic parameters ΔH and ΔS are found in the range of 14–38 kJ mol⁻¹ and 48–98 J K⁻¹ mol⁻¹, respectively for the valence tautomeric transition from low-spin cobalt(III) catecholate to high-spin cobalt(II) semiquinonate form.^[75,81,101,102] The thermodynamic parameter values for a valence tautomeric transition can be obtained by fitting the transition curve of the valence tautomeric transition and by singular value decomposition of the variable temperature UV/Vis/NIR spectra associated with the valence tautomeric transition.

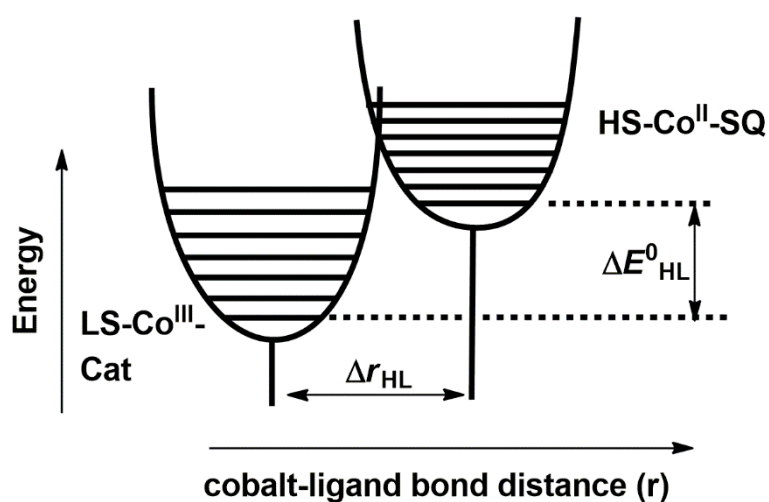


Figure 1.9: Potential energy diagram for the valence tautomeric transition in a cobalt-dioxolene complex.^[13,79]

1.2.1 Examples of Valence Tautomeric Complexes

The observation of valence tautomerism in mononuclear complexes is mainly focused on the [Co(N-N)(diox)₂] (N-N = bidentate ligands, diox = *o*-dioxolene derivatives) type of cobalt complexes. The bidentate ligands, such as 2,2'-bipyridine, 4,4'-biphenyl-2,2'-bipyridine, 4,4'-dimethyl-2,2'-bipyridine, 1,10-phenanthroline, 2,2'-bipyrazine, 2,2'-bipyrimidine have been used to observe valence tautomerism.^[71,72] The valence tautomeric transitions are also observed for dioxolene ligand systems other than 3,5-di-*tert*-butylcatecholate,

which include $[\text{Co}(\text{Cat-N-BQ})(\text{Cat-N-SQ})]^{[73]}$, $[\text{Co}(\text{CTH})(\text{PhCat})](\text{Y})$ ($\text{Y} = \text{I}$, PF_6 , BPh_4),^[74,85] $[\text{Co}(\text{4-papy})_2(\text{diox})_2]$, (4-papy = 4-phenylazopyridine, diox = 3,5-di-*tert*-butylcatecholate).^[75] The occurrences of valence tautomeric transitions in dinuclear complexes are scarcer,^[79] and complexes, such as $[\text{Co}_2(\text{tpa})_2(\text{diox-S-diox})]$, where diox-S-diox = tetra-deprotonated form of the ligand 6,6'-((1,4-phenylenebis-(methylene))bis(sulfanediyl))bis(3,5-di-*tert*-butylbenzene-1,2-diol),^[86] $[\text{Co}_2(\text{tpa})_2(\text{bis}(o\text{-dioxolene}))]$ where bis(*o*-dioxolene) = tetra-deprotonated form of 3,3,3',3'-tetramethyl-1,1'-spirobis(indane-5,5',6,6'-tetrol),^[81] $[\text{Co}_2(\text{CTH})_2(\text{DHBQ})]$,^[82] $[\text{Co}_2(\text{dpbpym})_2(\text{diox})_4]$, (diox = 3,5-di-*tert*-butylcatecholate and/or 3,5-di-*tert*-butylsemiquinonate)^[83] exhibit valence tautomeric transition. Figure 1.10 provides examples of selected dioxolene ligands.

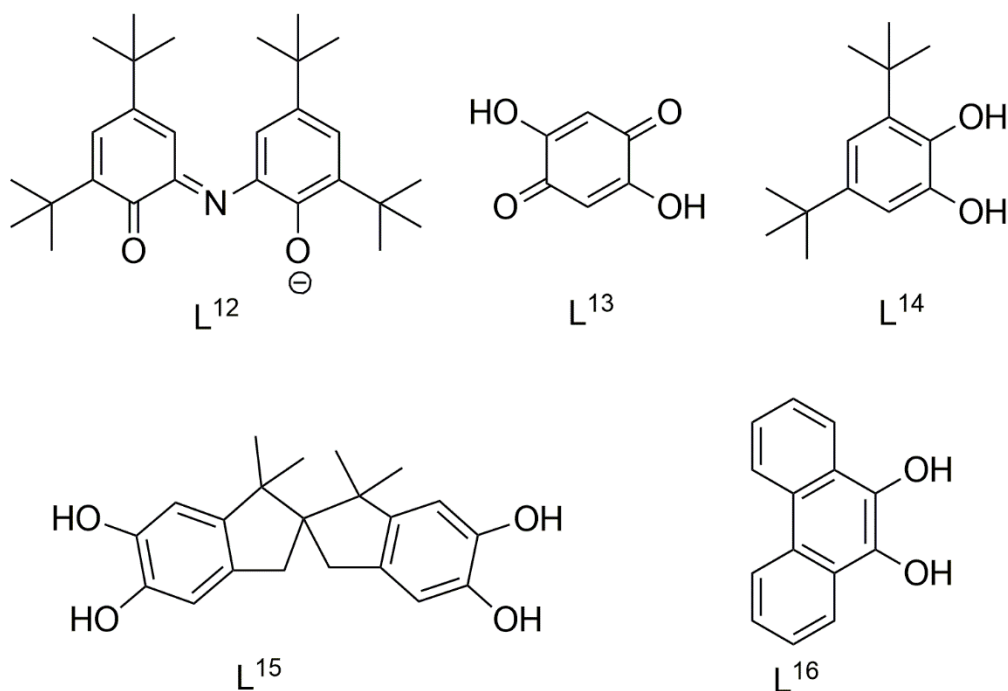


Figure 1.10: Structures and abbreviations of dioxolene ligands. L¹² = monoanion of 2-(2-hydroxy-3,5-di-*tert*-butylphenyl-imino)-4,6-di-*tert*-butyl-cyclohexa-3,5-dienone. L¹³ = 1,4-dihydroxy-benzoquinone. L¹⁴ = 3,5-di-*tert*-butylcatechol. L¹⁵ = 3,3,3',3'-tetramethyl-1,1'-spirobis-(indane-5,5',6,6'-tetrol). L¹⁶ = 9,10-dihydroxyphenanthrene.

1.3 Closed-Shell Quinonoid and Open-Shell Biradicaloid Systems

The biradicaloid concept was first introduced by *Tschitschibabin* in 1907.^[64] The hydrocarbon bis(diphenylmethyl)biphenyl, shown in Figure 1.11, can exist either in quinonoid or biradicaloid form. The biradicaloid form exists in the open-shell state of the hydrocarbon (HC) and the quinonoid form exists in the closed-shell state of the hydrocarbon.

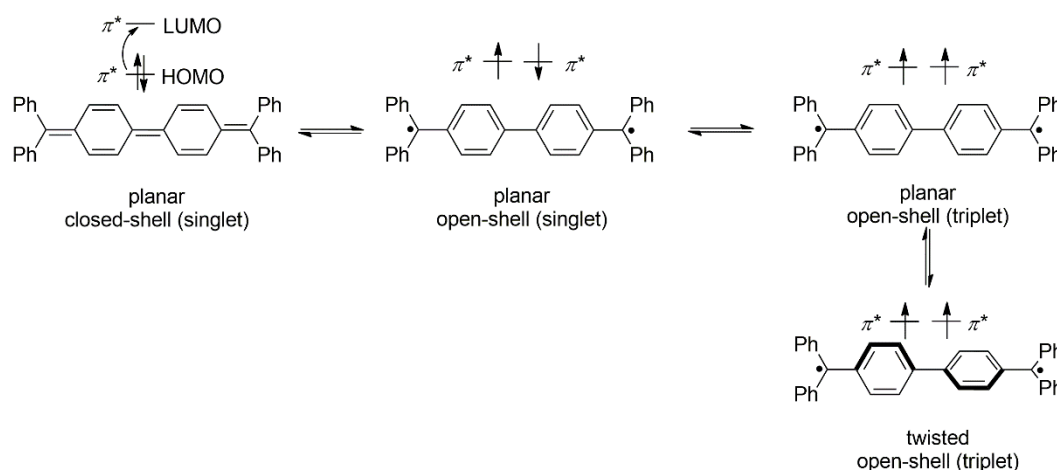


Figure 1.11: Schematic representation of the possible closed-shell and open-shell forms of a PHC. For representation purpose *Tschitschibabin's* hydrocarbon has been chosen. The spins have been denoted by the arrows (\uparrow), and π^* orbitals in which the electrons reside are denoted by the horizontal single lines (—).

Due to the low HOMO–LUMO energy gap of the hydrocarbon, the paired electrons residing in HOMO are unpaired and one electron is promoted to LUMO. Thus, the two unpaired electrons reside in two singly occupied π^* -orbitals. The closed-shell quinonoid form is diamagnetic ($S = 0$), while the spin multiplicity of the open-shell biradicaloid form depends on the orientation of the two unpaired electrons.

In the open-shell singlet state, the two electrons are oriented anti-parallel to each other ($S = 0$), and in the open-shell triplet state, the two electrons are parallel in orientation ($S = 1$). The energy $\Delta E_{\text{CS-OS}}$ required for the closed-shell to open-shell state conversion is overcome by the energy gain due to the

formation of the two aromatic rings in the biphenyl moiety and the stabilization of the radicals by the phenyl rings. Later on, ground state structures of several polycyclic aromatic hydrocarbons (PHCs) have been investigated based on the concept of *Tschitschibabin*. Most of the PHCs have closed-shell ground state, but few *Kekulé* type PHCs have significant amount of biradical characters in their ground states,^[16–22,103–110] and the ground state characters of these types of PHCs are determined by *Clar's* sextet rule.^[111]

PHCs containing open-shell electronic states have potential applications in the field of organic electronics, nonlinear optics, organic conductors, and electronic devices, quantum information processing systems, lithium ion batteries, and organic spintronic.^[16–22] However, PHC containing an open-shell conformation is highly unstable due to its high reactivity. Therefore, synthesis of open-shell hydrocarbon is challenging.

The closed-shell state can be differentiated from the open-shell state by X-ray crystallography,^[22,106,110,112] IR,^[112,113] Raman,^[106,112,114] EPR,^[22,106,112,115] NMR^[20,106,110,112,115] and UV/Vis/NIR.^[20,22,106,110,112,115] Upon conversion from the closed-shell to open-shell state, breaking of a C–C double bond results in the formation of a C–C single bond, that is why, it can be detected by X-ray crystallography.^[22,110] The IR and Raman spectroscopic techniques are also applicable due to the changes in bond lengths.^[113,114] Since, HOMO–LUMO energy gap of a closed-shell species is higher than that of the species which has an open-shell ground state, that is why, the absorption for the HOMO → LUMO transition in a closed-shell species occurs in a higher energy than that of the energy required for the open-shell species.^[20,22] Therefore, UV/Vis/NIR spectroscopy is a very important tool for the identification of open-shell and closed-shell states in PHCs. The closed-shell state is diamagnetic, whereas the open-shell triplet state is paramagnetic. Therefore, these two states can be differentiated by EPR spectroscopy.^[22,115]

1.4 Singular Value Decomposition

Singular value decomposition (SVD) is a linear algebra based mathematical tool by which deconvolution of the overlapping optical spectra can be performed.^[116–121] This tool requires processing of a set of spectra. The SVD provides the spectral features of pure components, and the values of the parameters of an equilibrium model which gives the information; how the pure components are mixed in the analyzed spectra (see mathematical description below).

Let us first consider, the UV/Vis/NIR spectra for n species. At a given wavelength λ with its extinction coefficient $\epsilon(\lambda)$, the spectra can be expressed with the *Beer-Lambert* law by the following equation

$$\mathbf{A}(\lambda) = \frac{\text{Abs}(\lambda)}{l} = C_1\epsilon_1(\lambda) + C_2\epsilon_2(\lambda) + C_3\epsilon_3(\lambda) + C_4\epsilon_4(\lambda) + \dots + C_n\epsilon_n(\lambda) \quad (1.5)$$

Where l is the optical path length and C_i is the concentration of the i^{th} species. When the $\epsilon(\lambda)$ is the vector of the extinction coefficient measured at m wavelengths, then the spectrum of the absorbance of the sample can be represented as $\mathbf{A}(\lambda)$ and it can be written in matrix form as follows:

$$\mathbf{A} = \mathbf{E}\mathbf{C}^T = \begin{bmatrix} \epsilon_1^{\lambda_1} & \epsilon_2^{\lambda_1} & \epsilon_3^{\lambda_1} & \dots & \epsilon_n^{\lambda_1} \\ \epsilon_1^{\lambda_2} & \epsilon_2^{\lambda_2} & \epsilon_3^{\lambda_2} & \dots & \epsilon_n^{\lambda_2} \\ \epsilon_1^{\lambda_3} & \epsilon_2^{\lambda_3} & \epsilon_3^{\lambda_3} & \dots & \epsilon_n^{\lambda_3} \\ \vdots & \vdots & \vdots & \ddots & \vdots \\ \epsilon_1^{\lambda_m} & \epsilon_2^{\lambda_m} & \epsilon_3^{\lambda_m} & \dots & \epsilon_n^{\lambda_m} \end{bmatrix} \cdot \begin{bmatrix} C_1 \\ C_2 \\ C_3 \\ \vdots \\ C_n \end{bmatrix} \quad (1.6)$$

Where \mathbf{E} is the m (wavelength) \times n (species) extinction coefficient matrix column and \mathbf{C} is a row matrix of the concentration of n species. Here, the superscript \mathbf{T} stands for the transpose of the matrix.

The data from a variable temperature UV/Vis/NIR measurement can be organized in a matrix \mathbf{A} as the following way:

$$\mathbf{A} = \begin{bmatrix} A(\lambda_1)^1 & A(\lambda_1)^2 & A(\lambda_1)^3 & \dots & A(\lambda_1)^n \\ A(\lambda_2)^1 & A(\lambda_2)^2 & A(\lambda_2)^3 & \dots & A(\lambda_2)^n \\ A(\lambda_3)^1 & A(\lambda_3)^2 & A(\lambda_3)^3 & \dots & A(\lambda_3)^n \\ \vdots & \vdots & \vdots & \ddots & \vdots \\ A(\lambda_m)^1 & A(\lambda_m)^2 & A(\lambda_m)^3 & \dots & A(\lambda_m)^n \end{bmatrix} \quad (1.7)$$

Where each column of the matrix \mathbf{A} corresponds to the spectrum measured at each temperature. When the spectra are characterized by only two species namely $\mathbf{b1}$ and $\mathbf{b2}$, then the absorbance per wavelength is provided by the following equation

$$\mathbf{A}(\lambda) = f_{b1}\mathbf{a}_{b1}(\lambda) + f_{b2}\mathbf{a}_{b2}(\lambda) + \sum_n \mathbf{w}^n(\lambda) \quad (1.8)$$

Where the $\mathbf{b1}$ component fraction f_{b1} and $\mathbf{b2}$ component fraction f_{b2} are the determinant factors for the overall spectra. The $\mathbf{w}^n(\lambda)$ terms are data from the noise.

The experimental (original) data matrix \mathbf{A} can be decomposed into two factors and written as: $\mathbf{A} = \mathbf{D}\mathbf{F}^T$. As mentioned earlier, the superscript \mathbf{T} stands for the transpose of the matrix, and the \mathbf{D} matrix represents the molar extinction coefficient spectra of pure components, and the \mathbf{F} matrix is composed by the $\mathbf{b1}$ and $\mathbf{b2}$ component fractions. The \mathbf{A} matrix is decomposed into singular values by SVD method; $\mathbf{A} = \mathbf{D}\mathbf{F}^T = \mathbf{U}\mathbf{S}\mathbf{V}^T$. Here $\mathbf{U}^T\mathbf{U} = \mathbf{V}^T\mathbf{V} = \mathbf{I}$ (\mathbf{I} = identity matrix). \mathbf{U} , \mathbf{V} are orthogonal (unitary) and \mathbf{S} is diagonal, and the diagonal values of \mathbf{S} matrix are called singular values of \mathbf{S} .

The important aspect of the SVD is that, the matrix \mathbf{U} (eigenvectors of $\mathbf{A}\mathbf{A}^T$) contains the basis spectra, and the matrix \mathbf{V} (eigenvectors of $\mathbf{A}^T\mathbf{A}$) contains the amplitude vectors. The singular values determine the weight associated with each basis spectra for the overall spectra. The rank of \mathbf{S} is the minimal number of singular values for the data representation. In mathematical term, the rank of a matrix is defined as the maximum number of linearly independent row or column vectors in the matrix. After defining the rank of the \mathbf{S} matrix

(i.e. \mathbf{r}), the original data matrix \mathbf{A} can be rewritten as its rank-defined matrix \mathbf{B} , where $\mathbf{B} = \bar{\mathbf{U}}\bar{\mathbf{S}}\bar{\mathbf{V}}^T$, where $\bar{\mathbf{S}}$ represents the rank-defined matrix containing only the first \mathbf{r} diagonal elements of the singular value matrix \mathbf{S} . The $\bar{\mathbf{U}}$ and $\bar{\mathbf{V}}$ matrices contain only the first \mathbf{r} columns of the \mathbf{U} and \mathbf{V} matrices, respectively. The matrix \mathbf{D} can be rewritten as follows:

$$\mathbf{D} = \bar{\mathbf{U}}\bar{\mathbf{S}}\bar{\mathbf{V}}^T\mathbf{F}^{T+} = \mathbf{U}\mathbf{S}\mathbf{H} \quad (1.9)$$

Where \mathbf{F}^{T+} is the pseudoinverse of \mathbf{F}^T and $\mathbf{H} = \bar{\mathbf{V}}^T\mathbf{F}^{T+}$

Thus,

$$\mathbf{B} = \mathbf{D}\mathbf{F}^T = \bar{\mathbf{U}}\bar{\mathbf{S}}\mathbf{H}\mathbf{F}^T = \bar{\mathbf{U}}\bar{\mathbf{S}}\bar{\mathbf{V}}^T \quad (1.10)$$

Consequently,

$$\bar{\mathbf{V}}^T = \mathbf{H}\mathbf{F}^T \quad (1.11)$$

Thus, \mathbf{H} and \mathbf{F} can be defined by matrix $\bar{\mathbf{V}}$ by curve fitting. For the variable temperature UV/Vis/NIR spectra of a spin-crossover or valence tautomeric complex, the \mathbf{F} matrix is defined from the fractions of low-temperature and high-temperature components provided by the Boltzmann distribution based equilibrium model that is, $\gamma_{\text{HS}} = 1/(e^{\Delta H/RT} \cdot e^{-\Delta S/R} + 1)$, where γ_{HS} corresponds to the molar fraction of high-temperature component. When the spectra are composed of only two species then the two columns of the \mathbf{F} matrix is formed by molar fractions of high-temperature component γ_{HS} and molar fractions of low-temperature component γ_{LS} at different temperatures, provided $\gamma_{\text{HS}} + \gamma_{\text{LS}} = 1$, at each temperature. The \mathbf{F} matrix which minimizes the norm (eq 1.12),^[118,121] can be taken into account for the calculation of spectra of pure components in the \mathbf{D} matrix.

$$\|\bar{\mathbf{S}}(\bar{\mathbf{V}}^T - \mathbf{H}\mathbf{F}^T)\| \quad (1.12)$$

The results obtained from an SVD analysis of the variable temperature UV/Vis/NIR spectra of a compound are strengthened when the results from other analysis of the compound are taken into consideration.^[119]

1.5 Motivation and Target Complex

The ancillary ligand *N,N'*-di-*tert*-butyl-2,11-diaza[3.3](2,6)pyridinophane (L-N₄*t*Bu₂) has been used for the syntheses of the cobalt dioxolene complexes. The coordination mode of the L-N₄*t*Bu₂ ligand with a cobalt(II) ion in an octahedral coordination environment is shown in Figure 1.12. Coordination of this ligand with a metal center provides a pseudo-octahedral geometry around the metal center.^[32,33,55,122,123]

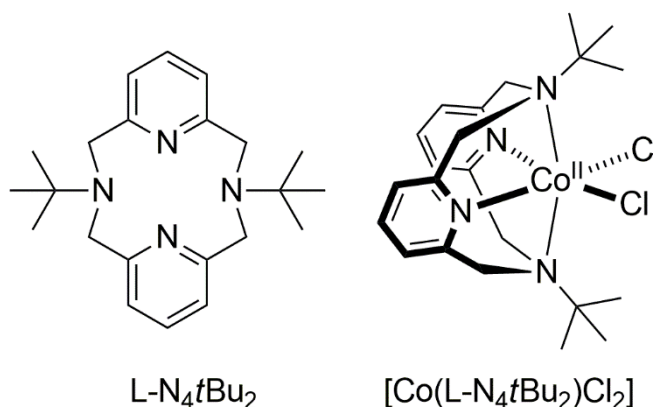


Figure 1.12: Representation of the utilized ancillary ligand L-N₄*t*Bu₂ and coordination mode of the ligand in the complex [Co(L-N₄*t*Bu₂)Cl₂].

The first spin-crossover active cobalt dioxolene complex was reported by *Krüger et al.* in 2010.^[55,92] Therein thermally induced spin transition of the complex [Co(L-N₄*t*Bu₂)(DBSQ)][B(*p*-Cl-Ph)₄] was observed. Few responsible factors which favored the spin-crossover process rather than valence tautomerism are structural and ligand-field strength properties of the L-N₄*t*Bu₂ ligand and the relative redox properties of the coordinated dioxolene ligand vs. [Co(L-N₄*t*Bu₂)] fragment. It can be said that the ligand-field

strength of this specific macrocyclic ligand plays a crucial role for stabilization of the low-spin cobalt(II) semiquinonate species, if we take into account the fact that the cobalt dioxolene complex $[\text{Co}(\text{L-N}_4\text{Me}_2)(\text{DBC})](\text{BPh}_4)\cdot 0.8 \text{ MeCN}\cdot 0.2 \text{ Et}_2\text{O}$, prepared by using $\text{L-N}_4\text{Me}_2$ as an ancillary ligand and 3,5-di-*tert*-butylcatecholate as a dioxolene ligand,^[55,92] has a low-spin cobalt(III) catecholate ground electronic state. The $\text{L-N}_4\text{Me}_2$ ligand differs from the $\text{L-N}_4t\text{Bu}_2$ ligand by the presence of methyl instead of *tert*-butyl substituents at the amine nitrogen atoms of the diazapyridinophane macrocycle. Since, both the macrocyclic ligands coordinate to the cobalt(II) centers in a similar fashion, and both cobalt dioxolene complexes contain same dioxolene moiety, therefore, it is clear that the oxidation of the cobalt(II) ion by the coordinated semiquinonate moiety depends upon the donor strengths of all donor atoms. The σ -donor strengths of the axial donor atoms of the $\text{L-N}_4t\text{Bu}_2$ ligand are reduced considerably compared to the axial donor atoms of the $\text{L-N}_4\text{Me}_2$ ligand due to the steric interactions between the *tert*-butyl groups of $\text{L-N}_4t\text{Bu}_2$ and equatorial ligands. The $\text{Co-N}_{\text{amine}}$ bonds are elongated due to the steric interaction, and as a consequence, σ -donor strengths of the amine nitrogen donor atoms are reduced. Thus, formation of the low-spin cobalt(III) catecholate state of $[\text{Co}(\text{L-N}_4t\text{Bu}_2)(\text{DBSQ})]^+$ is prevented. The redox potential of the coordinated 3,5-di-*tert*-butylcatecholate is such that, during oxidation from the cobalt(II) catecholate species, the dioxolene ligand is oxidized prior to the oxidation of the cobalt(II) ion to generate the cobalt(II) semiquinonate complex. Importantly, the ligand-field strength provided by the $\text{L-N}_4t\text{Bu}_2$ ligand is sufficient to stabilize the low-spin state of the cobalt(II) center in the resulting cobalt(II) semiquinonate species, which led to the isolation of the low-spin cobalt(II) semiquinonate complex.

On the other hand, the complex $[\text{Co}(\text{L-N}_4t\text{Bu}_2)(\text{NCS})_2](\text{BF}_4)$ is an example where the ligand $\text{L-N}_4t\text{Bu}_2$ is coordinated to the low-spin cobalt(III) center.^[32]

Therefore, syntheses of octahedral low-spin cobalt(III) complexes containing $L\text{-N}_4t\text{Bu}_2$ as ancillary ligands are possible. Although, low-spin cobalt(III) catecholate state has not been observed for the complex cation $[\text{Co}(L\text{-N}_4t\text{Bu}_2)(\text{DBSQ})]^+$, it could be observed in a different cobalt dioxolene complex which contains lesser oxidizable dioxolene ligand than DBC^{2-} . Hence, to begin the work for this dissertation, one of the aims was to increase the redox potential of the dioxolene ligand (Figure 1.13), which would force the cobalt(II) ion to oxidize prior to the dioxolene ligand during oxidation from the cobalt(II) catecholate species, so that cobalt(III) catecholate species would be formed. Substitution with electron-withdrawing group in the dioxolene unit would fulfill the requirement. Herein, for the work purpose, 4,5-dichlorocatechol has been used.

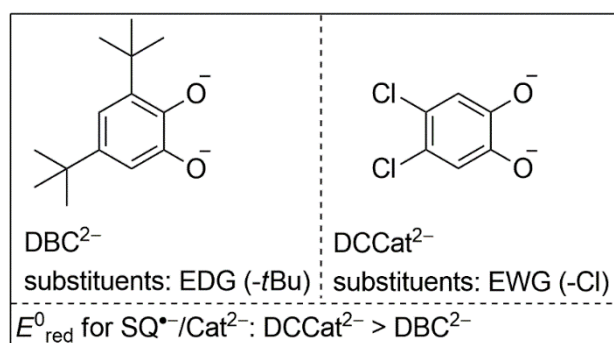


Figure 1.13: Representation of the difference in redox potential between DBC^{2-} and DCCat^{2-} .

It has been found that the $\text{Co}\text{-N}_{\text{axial}}$ bond lengths are about 0.1 Å longer in low-spin cobalt(III) complex containing $L\text{-N}_4t\text{Bu}_2$ as an ancillary ligand than the low-spin cobalt(III) complex containing $L\text{-N}_4\text{Me}_2$ as an ancillary ligand.^[32,55] The elongation of $\text{Co}\text{-N}_{\text{axial}}$ bond lengths results in lowering of energy of the d_z^2 orbital and then, promotion of one electron from the catecholate HOMO to the d_z^2 orbital of cobalt(III) ion becomes feasible with the application of an external perturbation. Therefore, valence tautomerism

could be observed in a low-spin cobalt(III) catecholate complex containing L-N₄tBu₂ as an ancillary ligand and DCCat²⁻ as a dioxolene ligand (Figure 1.14).

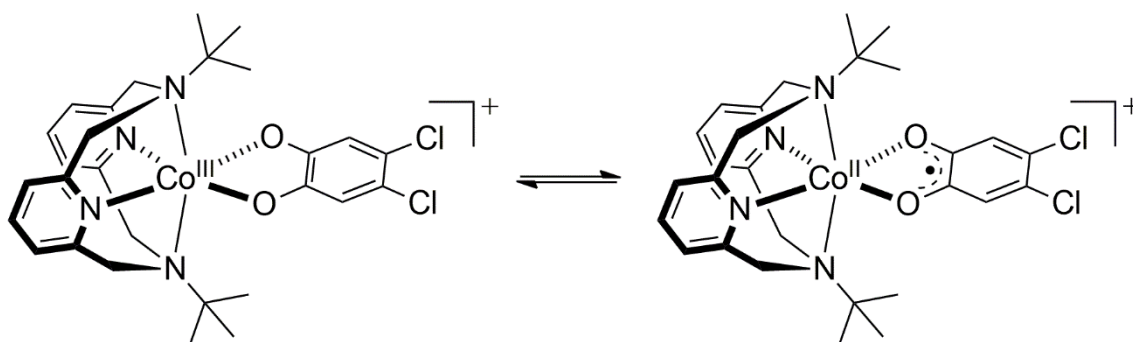


Figure 1.14: Schematic representation of the aimed valence tautomerism in a cobalt dioxolene complex containing DCCat²⁻ as a dioxolene ligand and L-N₄tBu₂ as an ancillary ligand.

If preparation of a valence tautomeric cobalt dioxolene complex with a less oxidizable dioxolene ligand such as DCCat²⁻ become successful, then it would set an example to say that all the three electronic states would be close in energy. Considering this fact, the next aim was set to maximize the possibility for the isolation of low-lying electronic states in cobalt dioxolene complexes, and to achieve that goal a dinuclear cobalt bis(dioxolene) complex was prepared by using a bis(dioxolene) ligand as a bridging ligand, because a bis(dioxolene) ligand with multiple oxidation states would allow accessibility of multiple numbers of low-lying electronic states in a cobalt bis(dioxolene) complex. Therefore, spin-crossover or valence tautomerism or even both processes could be observed. Herein, dideprotonated form of 3,3'-dihydroxydiphenoquinone-(4,4') (H₂(SQ-SQ)) is used as the bis(dioxolene) ligand. The dideprotonated form of H₂(SQ-SQ) which is (SQ-SQ)²⁻ remains in closed-shell form,^[65,124] and the electronic state of the (SQ-SQ)²⁻ ligand is described by semiquinonate-semiquinonate state. The (SQ-SQ)²⁻ ligand can remain in different redox states. Three of the possible redox states are shown in Figure 1.15.

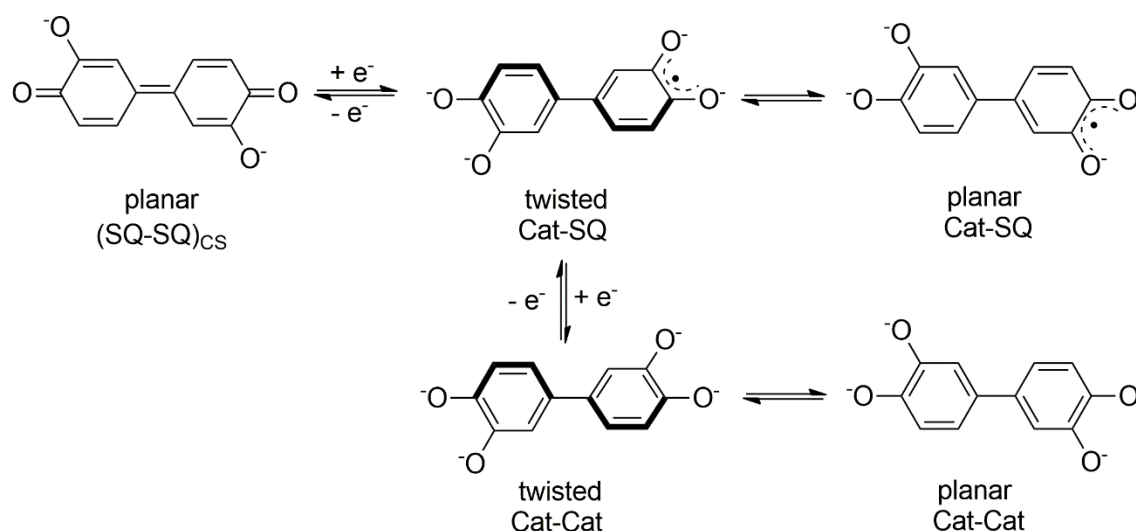


Figure 1.15: Schematic representation of various redox forms of the $(\text{SQ-SQ})^{2-}$ ligand.

The $(\text{SQ-SQ})^{2-}$ ligand can coordinate to two metal centers in its SQ-SQ, Cat-SQ and Cat-Cat redox-states. Coordination of the $(\text{SQ-SQ})^{2-}$ ligand with two cobalt(II) centers containing $\text{L-N}_4\text{tBu}_2$ as ancillary ligands would result in formation of the complex dication $[\{\text{Co}(\text{L-N}_4\text{tBu}_2)\}_2(\text{SQ-SQ})]^{2+}$ which might exhibit valence tautomerism and/or spin-crossover phenomenon (Figure 1.16).

An intramolecular one-electron reduction of the $(\text{SQ-SQ})^{2-}$ ligand by one of the cobalt(II) centers would result in formation of the complex dication $[\{\text{LS}$ or $\text{HS-Co}^{\text{II}}(\text{L-N}_4\text{tBu}_2)\}(\text{Cat-SQ})^{\bullet 3-}\{\text{LS-Co}^{\text{III}}(\text{L-N}_4\text{tBu}_2)\}]^{2+}$ which is redox isomer of the former complex dication. Thus, valence tautomeric transition between the two redox isomers could be possible (Figure 1.16). On the other hand, intramolecular one-electron reduction of $(\text{Cat-SQ})^{\bullet 3-}$ ligand of the latter complex dication by the cobalt(II) center would result in formation of $[\{\text{LS-Co}^{\text{III}}(\text{L-N}_4\text{tBu}_2)\}_2(\text{Cat-Cat})]^{2+}$ which is redox isomer of both the former complex dications. A valence tautomeric transition for this complex dication could also be observed (Figure 1.16).

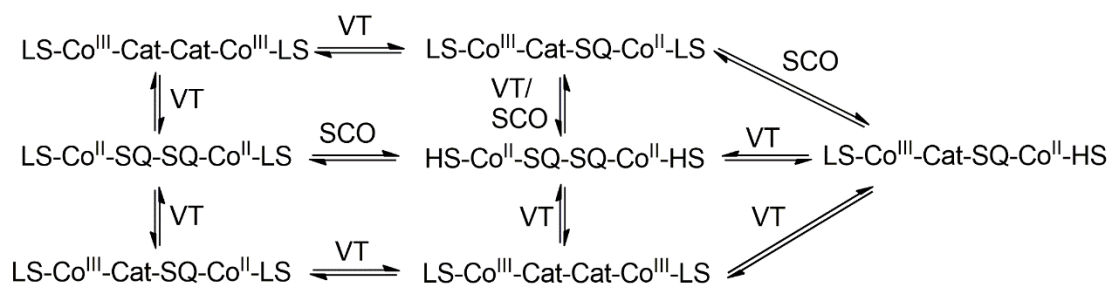


Figure 1.16: Schematic representation of some of the possible electronic states and conversion among these electronic states of $[\{Co(L-N_4tBu_2)\}_2(SQ-SQ)]^{2+}$.

In a situation when the bis(dioxolene) ligand remains in its catecholate-catecholate or catecholate-semiquinonate state, then there are possibilities for the observations of the valence tautomerism together with spin-crossover phenomenon. Furthermore, if the bis(dioxolene) ligand $(SQ-SQ)^{2-}$ is coordinated to the 3d-elements, other than the cobalt(II/III) ion which are nickel(II), copper (II) and zinc(II) ions to prepare the corresponding bis(dioxolene) complexes, and then characterization of them could exhibit interesting magnetic and optical properties. Therefore, nickel(II), copper(II) and zinc(II) bis(dioxolene) complexes have been prepared by using $L-N_4tBu_2$ as ancillary ligands and $(SQ-SQ)^{2-}$ as bis(dioxolene) ligands. An interesting redox behavior is also expected for the complex dication $[\{M(L-N_4tBu_2)\}_2(SQ-SQ)]^{2+}$ where $M = Co(II), Ni(II), Cu(II)$ and $Zn(II)$. In that case, characterization of the reduced or oxidized forms of the complex dication would exhibit interesting magnetic, optical properties. All these expectations have led to the constant growth of interest for the works presented in this dissertation.

2 Results and Discussion

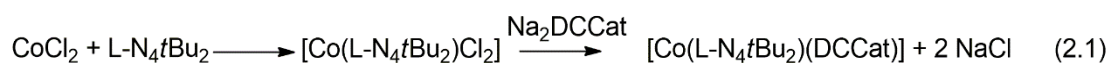
2.1 Valence Tautomerism in a Cobalt Dioxolene Complex

This section describes the valence tautomerism of a mononuclear cobalt dioxolene complex. The discovery of a spin-crossover cobalt dioxolene complex $[\text{Co}(\text{L-N}_4\text{tBu}_2)(\text{DBSQ})][\text{B}(p\text{-Cl-Ph})_4]$ has motivated us to prepare a valence tautomeric cobalt dioxolene complex by using a less oxidizable dioxolene ligand such as DCCat^{2-} instead of DBC^{2-} . The reasons behind the use of less oxidizable dioxolene ligand have been discussed earlier (see discussion in section 1.5).

2.1.1 Synthesis

All compounds were synthesized under an inert atmosphere. The neutral complex was synthesized by reacting 1 equivalent of 4,5-dichlorocatechol with 1 equivalent of $[\text{Co}(\text{L-N}_4\text{tBu}_2)\text{Cl}_2]$ (prepared *in situ* by reacting equimolar solutions of cobalt(II) chloride hexahydrate and $\text{L-N}_4\text{tBu}_2$ in methanol) in the presence of 2 equivalents of sodium hydroxide in methanol. The orange-red complex crystallizes from acetonitrile as solvate $[\text{Co}(\text{L-N}_4\text{tBu}_2)(\text{DCCat})] \cdot 3 \text{ MeCN} \cdot \text{H}_2\text{O}$ (**1a**). Although, single crystal X-ray diffraction was possible with this compound, the crystals became opaque during isolation. Therefore, the crystals were dried in vacuum in order to obtain analytically pure complex of $[\text{Co}(\text{L-N}_4\text{tBu}_2)(\text{DCCat})]$ (**1**) in a 34 % yield. In an alternative way, following analogous synthetic method like above, but crystallization from $\text{DCM}/\text{Et}_2\text{O}$ instead of MeCN afforded orange-red crystals of $[\text{Co}(\text{L-N}_4\text{tBu}_2)(\text{DCCat})] \cdot \text{CH}_2\text{Cl}_2$ (**1b**) in a 76 % yield.

The equation for the synthesis of **1** may be written as



The one-electron oxidized complex $[\text{Co}(\text{L-N}_4\text{tBu}_2)(\text{DCCat})]^+$ is isolated with various counter ions (BF_4^- , BPh_4^- , $\text{BPh}_2(\text{DCCat})^-$, and OTf^-). A list of the synthesized compounds in this section and their employed abbreviations are provided in Table 2.1. Thus, 1 equivalent of **1b** in DCM was treated with 1 equivalent of ferrocenium tetrafluoroborate in nitromethane. The color of the solution changed from orange-red to violet, and then slow diffusion of diethyl ether into the resulting solution afforded $[\text{Co}(\text{L-N}_4\text{tBu}_2)(\text{DCCat})](\text{BF}_4)$ (**2a**) in a 87 % yield.

The equation for the synthesis of **2a** may be written as



The tetraphenylborate salt (**2b**) was prepared by metathesis of 1.02 equivalent of compound **2a** with 1 equivalent of sodium tetraphenylborate in dry acetonitrile. After evaporation of the resulting solution to dryness under vacuum the resulting lilac residue was washed with dry methanol, and then dried in vacuum to afford analytically pure compound of $[\text{Co}(\text{L-N}_4\text{tBu}_2)(\text{DCCat})](\text{BPh}_4)$ (**2b**) in a 88 % yield. Slow diffusion of diethyl ether into a solution of **2b** in DCM yielded X-ray diffraction quality single crystals of $[\text{Co}(\text{L-N}_4\text{tBu}_2)(\text{DCCat})](\text{BPh}_4) \cdot 2 \text{CH}_2\text{Cl}_2$ (**2c**).

The OTf^- as well as $[\text{BPh}_2(\text{DCCat})]^-$ salts were prepared by addition of 1 equivalent of ferrocenium tetrafluoroborate to a solution of 1 equivalent of $[\text{Co}(\text{L-N}_4\text{tBu}_2)(\text{DCCat})]$ in acetonitrile (prepared *in situ* following the same synthetic method as for complex **1**) leading to a change in color of the solution from orange-red to red-violet. Then, after metathesis with 1 equivalent of $\text{Na}[\text{BPh}_2(\text{DCCat})]$, the resulting solution was evaporated to dryness under vacuum. Recrystallization of the residue from $\text{CH}_3\text{NO}_2/\text{Et}_2\text{O}$ afforded crystals of $[\text{Co}(\text{L-N}_4\text{tBu}_2)(\text{DCCat})][\text{BPh}_2(\text{DCCat})]$ (**2d**) in a 33 % yield. Metathesis with NaOTf instead of $\text{Na}[\text{BPh}_2(\text{DCCat})]$, and subsequent recrystallization of

the residue from $\text{CHCl}_3/\text{Et}_2\text{O}$ afforded $[\text{Co}(\text{L}-\text{N}_4\text{tBu}_2)(\text{DCCat})](\text{OTf})$ (**2e**) in a 81 % yield.

The equation for the metathesis reactions may be written as

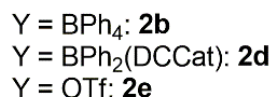


Table 2.1: List and abbreviations of the synthesized cobalt dioxolene compounds.

Compound	Abbreviation
$[\text{Co}(\text{L}-\text{N}_4\text{tBu}_2)(\text{DCCat})]$	1
$[\text{Co}(\text{L}-\text{N}_4\text{tBu}_2)(\text{DCCat})] \cdot 3 \text{ MeCN} \cdot \text{H}_2\text{O}$	1a
$[\text{Co}(\text{L}-\text{N}_4\text{tBu}_2)(\text{DCCat})] \cdot \text{CH}_2\text{Cl}_2$	1b
$[\text{Co}(\text{L}-\text{N}_4\text{tBu}_2)(\text{DCCat})]^+$	2
$[\text{Co}(\text{L}-\text{N}_4\text{tBu}_2)(\text{DCCat})](\text{BF}_4)$	2a
$[\text{Co}(\text{L}-\text{N}_4\text{tBu}_2)(\text{DCCat})](\text{BPh}_4)$	2b
$[\text{Co}(\text{L}-\text{N}_4\text{tBu}_2)(\text{DCCat})](\text{BPh}_4) \cdot 2 \text{ CH}_2\text{Cl}_2$	2c
$[\text{Co}(\text{L}-\text{N}_4\text{tBu}_2)(\text{DCCat})][\text{BPh}_2(\text{DCCat})]$	2d
$[\text{Co}(\text{L}-\text{N}_4\text{tBu}_2)(\text{DCCat})](\text{OTf})$	2e

2.1.2 Structural Characterization

Single crystal X-ray diffraction data for **1a** and **2c** were collected at 150 K, whereas the X-ray diffraction data for **2d** were collected at 150 and 373 K. The crystals of **2c** became opaque at room temperature after isolation. This observation was certainly due to the loss of DCM from the crystal lattice. Therefore, the X-ray crystallographic measurement of **2c** at high temperatures was not successful. Multiple attempts to obtain suitable single crystals of **2b** for measurements at high temperatures by using different combinations of solvents for recrystallization were also unsuccessful. In one of these attempts, however, upon crystallizing the crude product of **2b** from $\text{CH}_3\text{NO}_2/\text{Et}_2\text{O}$, a few crystals suitable for X-ray diffraction were obtained, which, unexpectedly

were identified as complex $[\text{Co}(\text{L-N}_{4t}\text{Bu}_2)(\text{DCCat})][\text{BPh}_2(\text{DCCat})]$ (**2d**) by X-ray structure analysis. Because the crystals of **2d** were suitable for X-ray crystallographic measurement even at higher temperatures, subsequently $\text{Na}[\text{BPh}_2(\text{DCCat})]$ was prepared and used as a metathesis reagent to synthesize larger amounts of analytically pure compound of **2d**.

The perspective view of $[\text{Co}(\text{L-N}_{4t}\text{Bu}_2)(\text{DCCat})]$ is shown in Figure 2.1 and the data for the selected bond lengths and bond angles are provided in Table 2.2. The compound **1a** crystallizes in the monoclinic space group $P12_1/c1$. The cobalt center is coordinated to the four nitrogen donor atoms of the macrocyclic ligand and the two oxygen donor atoms of the ligand DCCat^{2-} . The macrocyclic ligand is folded along the $\text{N}_{\text{amine}}-\text{N}_{\text{amine}}$ axis. The axial positions are occupied by the amine nitrogen donor atoms, whereas the pyridine nitrogen donor atoms occupy the two *cis*-positions in the equatorial plane. The remaining *cis*-positions in the equatorial plane are occupied by the two oxygen donor atoms of the DCCat^{2-} unit. The coordination environment around the metal center is distorted-octahedral because the value of the $\text{N}_{\text{amine}}-\text{Co}-\text{N}_{\text{amine}}$ bond angle is $142.54(8)^\circ$ which deviates from the ideal value of an octahedral $\text{N}_{\text{axial}}-\text{Co}-\text{N}_{\text{axial}}$ bond angle of 180° . The other reason for the consideration of distorted-octahedral geometry is the observation of $\text{N}_{\text{py}}-\text{Co}-\text{N}_{\text{py}}$ and $\text{O}(1)-\text{Co}-\text{O}(2)$ bond angle values of $86.90(9)^\circ$ and $83.00(8)^\circ$, respectively, which deviate from their expected value of 90° , in the case of ideal octahedral coordination geometry.

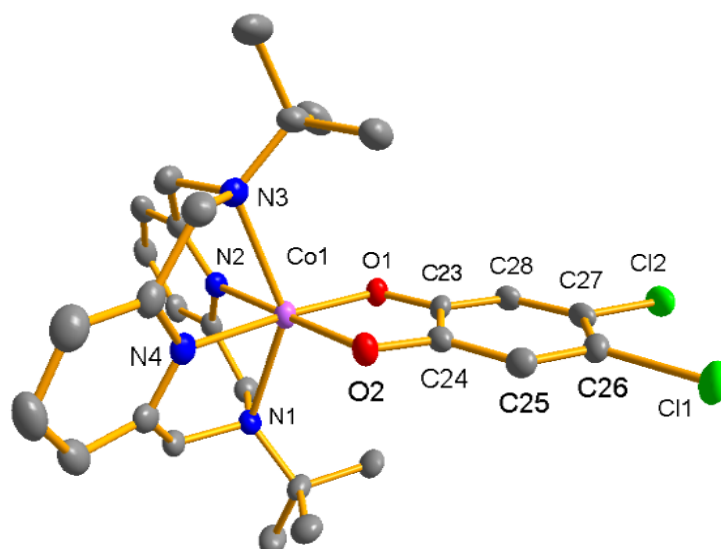


Figure 2.1: Perspective view of $[\text{Co}(\text{L-N}_4\text{tBu}_2)(\text{DCCat})]$ in **1a** showing 50 % thermal ellipsoids at 150 K.

The X-ray diffraction analysis of **1a** reveals that the average of the $\text{Co-N}_{\text{amine}}$ bond lengths is 2.359 Å and the average of the Co-N_{py} bond lengths is 2.063 Å, whereas the average of the Co-O bond lengths is 2.008 Å. These bond lengths fall into the range of metal-ligand bond lengths commonly observed in high-spin cobalt(II) complexes containing $\text{L-N}_4\text{tBu}_2$ as ancillary ligands.^[32,123] The average of the C-O bond lengths is 1.323 Å and the value of the $(\text{O})\text{C-C}(\text{O})$, *i.e.*, $\text{C}(23)\text{-C}(24)$ bond length is 1.434(4) Å. These bond lengths of the dioxolene unit are consistent with the assignment of the redox-state of the dioxolene unit as catecholate state.^[14,33,55] Therefore, the observed bond lengths are consistent with the assignment of the electronic state of the complex as high-spin cobalt(II) catecholate state at 150 K.

Table 2.2: Selected bond lengths [\AA] and bond angles [deg] for **1a** at 150 K.

	1a at 150 K
Co–O(2)	1.999(2)
Co–O(1)	2.017(2)
Co–N(4)	2.064(2)
Co–N(2)	2.062(2)
Co–N(3)	2.347(2)
Co–N(1)	2.371(2)
O(1)–C(23)	1.327(3)
O(2)–C(28)	1.319(3)
C(23)–C(24)	1.434(4)
C(23)–C(28)	1.399(4)
C(24)–C(25)	1.386(4)
C(25)–C(26)	1.397(4)
C(26)–C(27)	1.376(4)
C(27)–C(28)	1.388(4)
O(2)–Co–N(4)	91.99(8)
O(2)–Co–N(2)	178.46(9)
N(4)–Co–N(2)	86.90(9)
O(2)–Co–O(1)	83.00(8)
N(4)–Co–O(1)	174.69(8)
N(2)–Co–O(1)	98.14(9)
O(2)–Co–N(1)	105.66(8)
N(4)–Co–N(1)	77.99(9)
N(2)–Co–N(1)	75.15(9)
O(1)–Co–N(1)	101.61(8)
O(2)–Co–N(3)	100.70(8)
N(4)–Co–N(3)	74.92(9)
N(2)–Co–N(3)	77.99(9)
O(1)–Co–N(3)	107.67(8)
N(1)–Co–N(3)	142.54(8)

The perspective view of the complex cation in **2c** is shown in Figure 2.2 and the data for the selected bond lengths and bond angles are provided in Table 2.3. The compound crystallizes in the orthorhombic space group $P2_12_12_1$.

The perspective view of the complex cation in **2d** is shown in Figure 2.3 and the data for the selected bond lengths and bond angles are provided in Table 2.3. The compound crystallizes in the triclinic space group $P\bar{1}$. The crystal system, space group as well as the various bond lengths and bond angles are temperature invariant.

The coordination modes of the macrocyclic ligand as well as the dioxolene ligand with the cobalt centers of **2c** and **2d** are similar to those in complex **1**. The distorted coordination environments around cobalt centers are evident from the values of the $N_{\text{amine}}\text{-Co-}N_{\text{amine}}$, *i.e.*, $N(1)\text{-Co-}N(3)$ bond angle of $156.4(1)^\circ$ for **2c** and $156.66(6)^\circ$ for **2d** which deviate from the value for a perfect octahedral $N_{\text{axial}}\text{-Co-}N_{\text{axial}}$ bond angle of 180° .

The X-ray diffraction analysis of **2c** and **2d** reveals the averaged $\text{Co-}N_{\text{amine}}$ bond lengths of $(2.138 \pm 0.001) \text{ \AA}$ for **2c** and $(2.140 \pm 0.039) \text{ \AA}$ for **2d**. The averaged $\text{Co-}N_{\text{py}}$ bond lengths are $(1.880 \pm 0.004) \text{ \AA}$ for **2c** and $(1.874 \pm 0.004) \text{ \AA}$ for **2d**. The observed $\text{Co-}N_{\text{amine}}$ and $\text{Co-}N_{\text{py}}$ bond lengths are significantly shorter than the averaged $\text{Co-}N_{\text{py}}$ ($1.915\text{--}1.931 \text{ \AA}$) and $\text{Co-}N_{\text{amine}}$ ($2.316\text{--}2.338 \text{ \AA}$) bond lengths in low-spin cobalt(II) complexes containing $L\text{-}N_4t\text{Bu}_2$ as ancillary ligands.^[32,55,92,122] On the other hand, the averaged $\text{Co-}O$ bond lengths for **2c** and **2d** are $(1.886 \pm 0.010) \text{ \AA}$ and $(1.879 \pm 0.004) \text{ \AA}$, respectively. Similar $\text{Co-}N_{\text{amine/py}}$ bond lengths were also found in a low-spin cobalt(III) complex containing $L\text{-}N_4t\text{Bu}_2$ as an ancillary ligand.^[32] Further, in the coordinated dioxolene moieties, the averaged $\text{C-}O$ bond lengths are 1.343 \AA for **2c** and $(1.337 \pm 0.004) \text{ \AA}$ for **2d**. The values of the $(O)\text{C-}C(O)$, *i.e.*, $C(23)\text{-}C(24)$ bond lengths are in the range of $1.423(6)\text{--}1.414(3) \text{ \AA}$. These bond lengths within the dioxolene units are consistent with the assignment of the redox-states of the dioxolene units as catecholate states.^[14,33,55] Hence, the short $\text{Co-}N_{\text{amine}}$ and $\text{Co-}N_{\text{py}}$ bond

lengths, and the unambiguous assignment of the redox-states of the dioxolene ligands as catecholate states strongly indicate that the electronic states of the cobalt centers in both compounds are best described as low-spin cobalt(III) states.

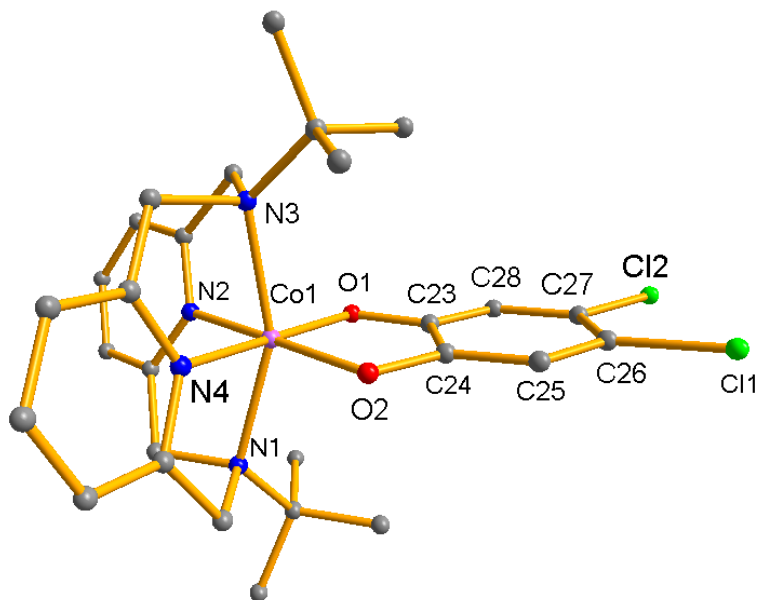


Figure 2.2: Perspective view of $[\text{Co}(\text{L-N}_4\text{tBu}_2)(\text{DCCat})]^+$ in **2c** showing 50% thermal ellipsoids at 150 K.

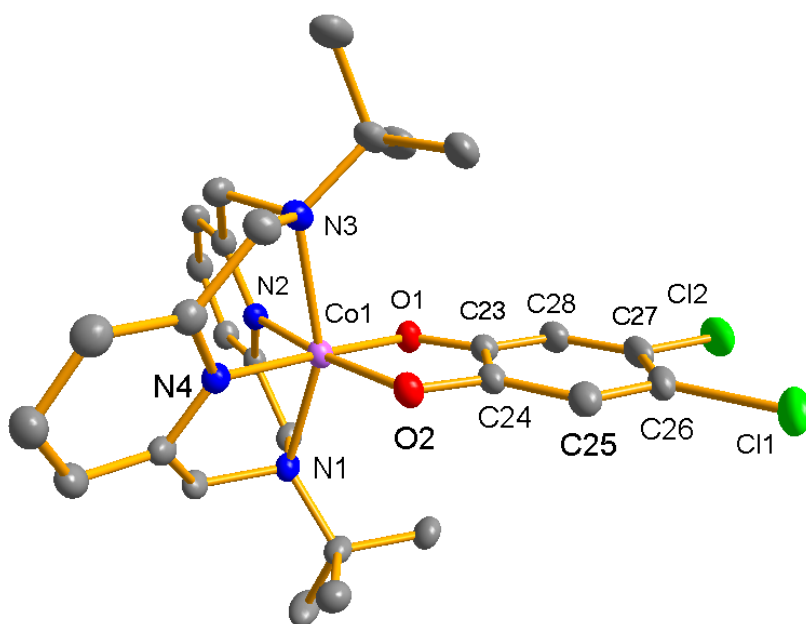


Figure 2.3: Perspective view of $[\text{Co}(\text{L-N}_4\text{tBu}_2)(\text{DCCat})]^+$ in **2d** showing 50% thermal ellipsoids at 150 K.

Table 2.3: Selected bond lengths [\AA] and bond angles [deg] for **2c** at 150 K, and **2d** at 150 and 373 K.

	2c at 150 K	2d at 150 K	2d at 373 K
Co–O(2)	1.876(2)	1.884(1)	1.885(1)
Co–O(1)	1.892(3)	1.875(1)	1.871(2)
Co–N(4)	1.876(2)	1.878(1)	1.885(2)
Co–N(2)	1.884(2)	1.870(1)	1.877(2)
Co–N(3)	2.138(3)	2.101(1)	2.129(2)
Co–N(1)	2.139(4)	2.179(1)	2.198(2)
O(1)–C(23)	1.344(5)	1.334(2)	1.334(3)
O(2)–C(24)	1.341(5)	1.341(2)	1.338(3)
C(23)–C(24)	1.423(6)	1.414(3)	1.408(3)
C(23)–C(28)	1.373(7)	1.392(3)	1.382(4)
C(24)–C(25)	1.382(6)	1.383(3)	1.382(3)
C(25)–C(26)	1.383(7)	1.400(3)	1.391(4)
C(26)–C(27)	1.382(7)	1.381(3)	1.371(4)
C(27)–C(28)	1.403(6)	1.391(3)	1.394(4)
O(2)–Co–N(4)	89.1(1)	91.82(6)	91.94(7)
O(2)–Co–N(2)	177.2(1)	174.04(6)	174.19(7)
N(4)–Co–N(2)	93.0(1)	93.15(6)	92.90(8)
O(2)–Co–O(1)	87.48(9)	87.71(5)	87.41(7)
N(4)–Co–O(1)	176.1(1)	178.27(6)	178.56(8)
N(2)–Co–O(1)	90.5(1)	87.41(6)	87.82(7)
O(2)–Co–N(1)	95.01(9)	94.13(6)	94.39(7)
N(4)–Co–N(1)	79.8(1)	79.74(6)	79.50(7)
N(2)–Co–N(1)	83.5(1)	83.54(6)	83.33(8)
O(1)–Co–N(1)	102.40(9)	101.95(6)	101.83(8)
O(2)–Co–N(3)	101.7(1)	103.24(6)	103.51(7)
N(4)–Co–N(3)	83.9(1)	84.19(6)	83.78(7)
N(2)–Co–N(3)	80.4(1)	80.54(6)	80.24(7)
O(1)–Co–N(3)	94.95(9)	94.30(6)	95.12(7)
N(1)–Co–N(3)	156.4(1)	156.66(6)	155.86(7)

2.1.3 Magnetic Properties

2.1.3.1 Magnetic Properties in Solid State

The magnetic susceptibility measurement of the non-solvated compound **1** was performed with Gouy balance at room temperature. However, the magnetic susceptibility of solvated compound **1a** could not be measured due to the loss of solvent molecules from the crystal lattice. The electronic state of **1** in **1a** at 150 K is high-spin cobalt(II) catecholate which is evident from the X-ray diffraction analysis. If the magnetic moment measurement of **1a** would have been possible then the observed magnetic moment could have been correlated with the X-ray diffraction analysis. Since, the magnetic moment of **1a** could not be measured, therefore, the obtained magnetic susceptibility data for the compound **1** is presented. The molar magnetic susceptibility ($\chi_{\text{M}}T$) value of **1** at 296 K is $2.60 \text{ cm}^3 \text{ K mol}^{-1}$. The effective magnetic moment (μ_{eff}) is $4.56 \mu_{\text{B}}$, and it falls into the range of the commonly observed values ($\mu_{\text{eff}} = 4.3\text{--}5.2 \mu_{\text{B}}$) for high-spin cobalt(II) complexes.^[32,54]

Magnetic susceptibility measurement of **2c** was performed with Gouy balance at room temperature with a grinded sample of the compound. The molar magnetic susceptibility ($\chi_{\text{M}}T$) value at 298 K is $0.017 \text{ cm}^3 \text{ K mol}^{-1}$ ($\mu_{\text{eff}} = 0.368 \mu_{\text{B}}$). Prior to the measurement, it was noticed multiple times that the loss of DCM from crystal lattices of **2c** resulted in change in color of the crystals from green to lilac. Therefore, without knowing the effect of solvent loss from the crystal lattices on the magnetic properties of the compound, it was necessary to monitor the loss of DCM from the compound. During the measurement, the loss of 0.5 molecule of dichloromethane from one complex molecule was observed by recording ^1H NMR of the grinded sample in deuterated acetonitrile (see appendix; Figure A.11). The sample for the NMR measurement was prepared from the grinded sample used for magnetic

moment measurement. Although, an elemental analysis has not been performed to observe the loss of solvent molecules, the probability of the presence of any compound other than **2c** in the sample such as inorganic salts which are NMR silent, is excluded because the crystals of **2c** were obtained by crystallization of analytically pure compound of **2b**. For discussion, any compound other than **2c** is called as impure compound. If impure compound crystallizes or precipitates with **2c** during crystallization, then it would have been noticed by NMR spectroscopy. Therefore, presence of any impure compound with **2c** is excluded. Hence, the $\chi_{\text{M}}T$ value was calculated by adjusting the loss of DCM.

Temperature independent paramagnetism (TIP) phenomenon is expected for some diamagnetic complexes because of mixing of the ground state with the low-lying excited states due to the second order Zeeman effect. The observed $\chi_{\text{M}}T$ value of $0.017 \text{ cm}^3 \text{ K mol}^{-1}$ is in the range of found TIP values for the octahedral low-spin cobalt(III) complexes.^[32,125,126] Therefore, the electronic state of **2** in solid **2c** is best described by low-spin cobalt(III) catecholate state at room temperature.

2.1.3.2 Magnetic Properties in Solution State

^1H NMR spectra of **2b** in $[\text{D}_6]\text{DMSO}$ and $[\text{D}_2]\text{DCM}$ at 295 K are shown in Figure 2.4. The chemical shifts (δ/ppm) in the ^1H NMR spectra are provided in Table 2.4.

^1H NMR in $[\text{D}_6]\text{DMSO}$

The NMR spectrum shows relatively sharp signals in the range between 0 and 9 ppm. The signals corresponding to the protons of the pyridine rings of the macrocycle appear at 8.23 ppm (t, $^3J_{\text{HH}} = 7.8 \text{ Hz}$, 2H; *p*-Py-H) and 7.68 ppm (d, $^3J_{\text{HH}} = 7.8 \text{ Hz}$, 4H; *m*-Py-H). The diastereotopic methylene protons form

an AB system, and the corresponding signals appear at 4.48 ppm (d, $^2J_{\text{HH}} = 16.7$ Hz, 4H; CH₂) and 4.97 ppm (d, $^2J_{\text{HH}} = 16.7$ Hz, 4H; CH₂). The two signals at 1.31 ppm (s, 6H; *t*Bu) and 0.68 ppm (s, 12H; *t*Bu) are observed for the eighteen protons of the *tert*-butyl groups. The reason for the observation of two signals instead of one singlet is the hindered rotation of the *tert*-butyl groups. Only two of the three methyl groups are transferred to each other by swinging oscillation. The singlet at 6.16 ppm (s, 2H; H³/H⁶-DCCat²⁻) originates from the protons of the coordinated DCCat²⁻ unit. The phenyl protons of the BPh₄⁻ anion show signals at 6.79 ppm (t, $^3J_{\text{HH}} = 7.4$ Hz, 4H; *p*-Ph-H), 6.92 ppm (t, $^3J_{\text{HH}} = 7.2$ Hz, 8H; *m*-Ph-H) and 7.20–7.16 ppm (m, 8H; *o*-Ph-H). The attempt to calculate the magnetic susceptibility at room temperature from a sample of **2b** in [D₆]DMSO by Evans-NMR method was unsuccessful because the Evans-NMR measurement did not provide any evidence for the presence of paramagnetic species. If present, it was below the detection limit. Thus, predominately diamagnetic behavior of the complex is evident at 295 K in [D₆]DMSO.

¹H NMR in [D₂]DCM

The ¹H NMR spectrum shows signals in the range +35 to -15 ppm. All the signals are broadened except the signals for the phenyl protons of the BPh₄⁻ counter anion. Therefore, paramagnetic behavior of the complex is evident at 295 K. The magnetic susceptibility of **2b** was measured at 295 K by Evans method.^[127,128]

The measured $\chi_{\text{M}}T$ value of **2b** is 0.65 cm³ K mol⁻¹ ($\mu_{\text{eff}} = 2.28 \mu_{\text{B}}$). Thus, by considering the IR spectroscopic and UV/Vis/NIR studies in [D₂]DCM and DCM, respectively at room temperature (see discussion in sections 2.1.4 and 2.1.5), the observed $\chi_{\text{M}}T$ value is consistent with the presence of low-spin cobalt(III) catecholate (45 % of the molecules) and low-spin cobalt(II)

semiquinonate (55 % of the molecules) forms in the VT_{LS-LS} in $[D_2]DCM$. Presence of high-spin cobalt(II) semiquinonate form is excluded because for a high-spin cobalt(II) semiquinonate complex, the expected χ_{MT} value is $3.3 \text{ cm}^3 \text{ K mol}^{-1}$.^[92,95] Therefore, if smaller amount of high-spin cobalt(II)-semiquinonate complex would be present in solution, then the observed χ_{MT} value would have value higher than $0.65 \text{ cm}^3 \text{ K mol}^{-1}$. The calculation of mole percentages of the two redox isomers in the VT_{LS-LS} equilibrium, is based on the reported χ_{MT} value of $1.16 \text{ cm}^3 \text{ K mol}^{-1}$ for a low-spin cobalt(II) semiquinonate complex,^[33,55] and by considering the χ_{MT} value of $0.017 \text{ cm}^3 \text{ K mol}^{-1}$ for low-spin cobalt(III) catecholate complex.

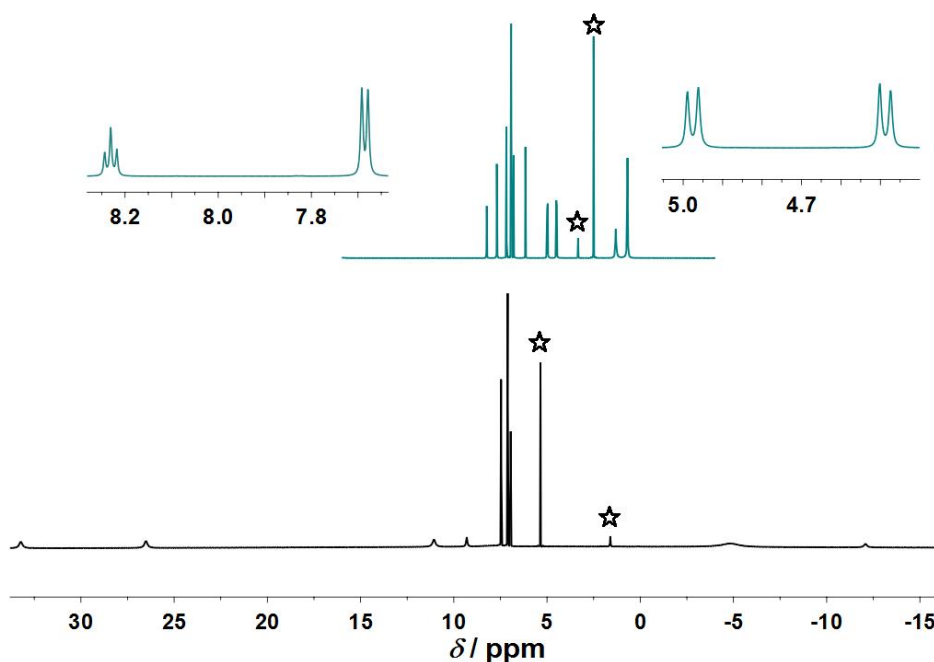


Figure 2.4: ^1H NMR spectra of **2b** in $[D_6]DMSO$ (top) and $[D_2]DCM$ (bottom) at 295 K. Solvent residual and water signals are marked by stars.

The ^1H NMR spectroscopic studies strongly indicate that a valence tautomeric equilibrium, low-spin cobalt(III) catecholate \rightleftharpoons low-spin cobalt(II) semiquinonate, exists in $[D_2]DCM$. The ^1H NMR spectrum in $[D_6]DMSO$ indicates that mostly the low-spin cobalt(III) catecholate form of the complex is present, but a much smaller amount of the low-spin cobalt(II) semiquinonate

form is also present as it is evident by UV/Vis/NIR (see discussion in section 2.1.5).

The variation in the amount of low-spin cobalt(II) semiquinonate complex in the valence tautomeric equilibrium due to the change in solvent, is because of the difference in polarity of DMSO and DCM and the thereby resulting different solute-solvent interactions. The dipole moment of DMSO and DCM are 3.96 D^[129] and 1.60 D,^[130] respectively. The valence tautomerism is occurring to a different extent upon changing the solvent polarity, because the cobalt(III) catecholate and cobalt(II) semiquinonate forms have different charge distributions between the metal ion and the dioxolene unit. Thus, because of the larger charge separation, the low-spin cobalt(III) catecholate form is more stabilized by more polar solvent, whereas the low-spin cobalt(II) semiquinonate form is more stabilized by less polar solvent.

Table 2.4: ¹H NMR data for compound **2b** in [D₆]DMSO and [D₂]DCM at 295 K.

Solvent	δ /ppm
[D ₆]DMSO	8.23 (t, ³ J _{HH} = 7.8 Hz, 2H; <i>p</i> -Py-H), 7.68 (d, ³ J _{HH} = 7.8 Hz, 4H; <i>m</i> -Py-H), 4.97 (d, ² J _{HH} = 16.7 Hz, 4H; CH ₂), 4.48 (d, ² J _{HH} = 16.7 Hz, 4H; CH ₂), 1.31 (s, 6H; <i>t</i> Bu), 0.68 (s, 12H; <i>t</i> Bu), 6.16 (s, 2H; H ³ /H ⁶ -DCCat ²⁻), 6.79 (t, ³ J _{HH} = 7.4 Hz, 4H; <i>p</i> -Ph-H, BPh ₄ ⁻), 6.92 (t, ³ J _{HH} = 7.2 Hz, 8H; <i>m</i> -Ph-H, BPh ₄ ⁻), 7.20–7.16 (m, 8H; <i>o</i> -Ph-H, BPh ₄ ⁻)
[D ₂]DCM	33.23 (4H, br), 26.52 (4H, br), 11.06 (4H, br), 9.31 (2H, br), 7.91 (9H, br), -4.87 (9H, br), -12.08 (2H, br), 6.95 (t, ³ J _{HH} = 7.1 Hz, 4H; <i>p</i> -Ph-H, BPh ₄ ⁻), 7.11 (t, ³ J _{HH} = 7.1 Hz, 8H; <i>m</i> -Ph-H, BPh ₄ ⁻), 7.45–7.41 (m, 8H; <i>o</i> -Ph-H, BPh ₄ ⁻)

Due to the weak solubility of **2b** in [D₂]DCM at low temperatures, variable temperature ¹H NMR spectra were not measured, because the measurement of

the magnetic susceptibility at low concentrations of a complex with rather small amount of paramagnetism would provide inaccurate data. However, the variable temperature ^1H NMR spectra for **2e** were recorded in $[\text{D}_6]\text{DMSO}$ (Figure 2.5 and also see Figure A.14 in appendix), and the data for the measurement are provided in Table 2.5. The signals corresponding to the protons of complex **2** in the ^1H NMR spectra of **2b** and **2e** in $[\text{D}_6]\text{DMSO}$ have the same chemical shifts. Therefore, counter ion effect on valence tautomerism was not observed in $[\text{D}_6]\text{DMSO}$.

Table 2.5: ^1H NMR data of **2e** in $[\text{D}_6]\text{DMSO}$ at 295 and 305 K.

<i>T/K</i>	δ/ppm						
295	8.25	7.69	6.17	4.95	4.46	1.30	0.68
305	8.25	7.71	5.95	5.24	4.85	1.39	0.66

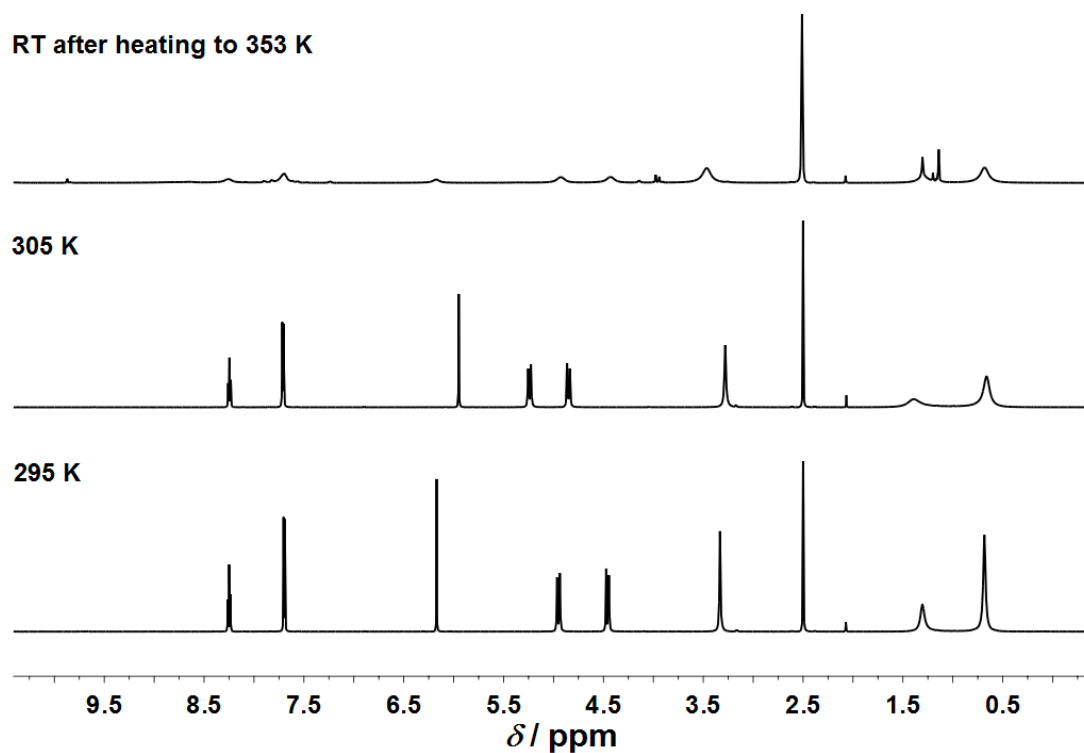


Figure 2.5: Variable temperature ^1H NMR spectra of **2e** in $[\text{D}_6]\text{DMSO}$.

Upon heating the sample from 295 to 305 K, the signal corresponding to the protons of the dioxolene ligand shifts upfield from 6.17 to 5.95 ppm, whereas the signals corresponding to the methylene protons (AB system) shift downfield from 4.95 to 5.24 ppm and from 4.46 to 4.85 ppm. In fact, all of them shift with only slight broadening of the signals. The shifts of the signals indicate that changes in the magnetic properties of the complex **2** are taking place upon heating the sample. The magnetic property change can be correlated with the occurrence of VT_{LS-LS} upon raising the temperature. Above 313 K considerable broadening of all signals is observed (see Figure A.14 and Figure A.15 in appendix).

If we take into account the 1H NMR spectrum of **2b** in $[D_3]MeCN$ and $[D_6]DMSO$ at 295 K (Figure 2.6), then the notable difference between these two NMR spectra is that the signal corresponding to the protons of $DCCat^{2-}$ is shifted more upfield in $[D_3]MeCN$ than that of the signal in $[D_6]DMSO$, whereas the signals corresponding to the methylene protons (AB-system) are shifted downfield in $[D_3]MeCN$ compared to those signals in $[D_6]DMSO$.

It is important to mention that the UV/Vis/NIR spectrum of compound **2b** in MeCN at room temperature shows a higher intensity of the MLCT bands attributed to the low-spin cobalt(II) semiquinonate chromophore than the spectrum of the complex in DMSO at room temperature (see experimental section and discussion in section 2.1.5). Hence, at room temperature the amount of low-spin cobalt(II) semiquinonate complex in the VT_{LS-LS} equilibrium is higher in MeCN than DMSO. This observation by UV/Vis/NIR spectroscopic study is suggesting that in less polar solvent MeCN, the value of the equilibrium constant for the VT_{LS-LS} equilibrium is higher than that of the equilibrium constant in more polar solvent DMSO.

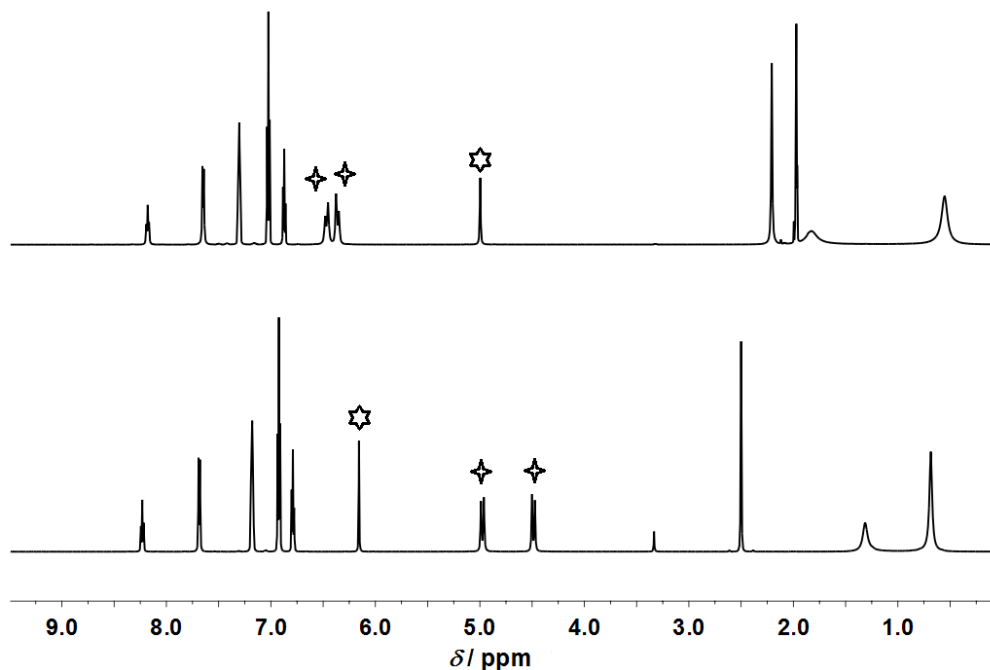


Figure 2.6: ^1H NMR spectra of **2b** in $[\text{D}_3]\text{MeCN}$ (top) and $[\text{D}_6]\text{DMSO}$ (bottom) at 295 K. The six-point and four-point stars are the markers for the signals corresponding to the DCCat^{2-} protons and methylene protons of the $\text{L-N}_4\text{tBu}_2$ ligands, respectively.

If we take into account the shifts of the signals of complex **2** in $[\text{D}_6]\text{DMSO}$ due to the heating, and chemical shift values of the signals corresponding to the complex **2** in $[\text{D}_3]\text{MeCN}$ at room temperature then one of the significant observations is that the increase in the amount of the low-spin cobalt(II) semiquinonate complex in the $\text{VT}_{\text{LS-LS}}$ equilibrium leads to the shifting of the signal corresponding to the dioxolene ligand and AB-protons towards the upfield and downfield, respectively. Since, irrespective of the polarity of the solvent, the valence tautomeric transition from low-spin cobalt(III) catecholate to low-spin cobalt(II) semiquinonate state of **2** is taking place with positive change in temperature (see discussion in section 2.1.5), therefore, upon heating the sample in $[\text{D}_6]\text{DMSO}$ the amount of low-spin cobalt(II) semiquinonate species in the $\text{VT}_{\text{LS-LS}}$ equilibrium would increase and at a particular temperature which is higher than room temperature, in DMSO, the equilibrium constant should be similar with the equilibrium constant in MeCN at room temperature. Until, that value of equilibrium constant is reached, the

signals corresponding to the protons of the dioxolene ligand and methylene protons of the macrocyclic ligand should not be broadened considerably because these signals are not broadened enough in the NMR spectrum in $[D_3]MeCN$ at room temperature. In other words, upon changing the temperature in $[D_6]DMSO$, until unless the signals corresponding to the dioxolene ligand have lower chemical shift values than the chemical shift values of the AB-protons such that NMR features of the complex **2** in $[D_6]DMSO$ at high temperature is similar to that in $[D_3]MeCN$ at room temperature, the signals should not be considerably broadened. The spectrum at 313 K in $[D_6]DMSO$ shows that the AB-protons do not have higher chemical shift values than the protons of the dioxolene ligand but the signals are broad. Therefore, it can be said that decomposition of the sample occurs at high temperature, which in turn could be noticed from the NMR spectrum recorded at room temperature after cooling the sample from 353 K, where the signals are broadened and not similar with the spectrum at 295 K.

2.1.4 Infrared Spectroscopic Properties

2.1.4.1 Infrared Spectroscopic Properties of the Solid Samples

The IR spectra of the KBr pellets of the compounds **1**, **2c** and **2d** are shown in Figure 2.7. All compounds exhibit intense bands at around 1260 and 1475 cm^{-1} . The bands at around 1260 cm^{-1} are markers for the presence of the coordinated dioxolene ligands in their catecholate states,^[92,96–99] whereas the bands at around 1475 cm^{-1} are markers for the presence of the coordinated dioxolene ligands (catecholate or semiquinonate form) in the complexes.^[92]

The significant difference between the IR spectra of **1** and **2c** or **2d** is the presence of a band at 1175 cm^{-1} . Recently, the intense band at around 1175 cm^{-1} of $[Co(L-N_4tBu_2)(DBSQ)][B(p-Cl-Ph)_4]$ has been tentatively assigned to

the characteristic band of the coordinated 3,5-di-*tert*-butylsemiquinonate moiety. But, it is noteworthy that this band might be present with the combination of the dioxolene ligand DBC^{2-} with the $\text{L-N}_4\text{tBu}_2$ ligand.^[92] Since, compound **2c** or **2d** contain 4,5-dichlorocatecholate instead of 3,5-di-*tert*-butylcatecholate as a dioxolene moiety, therefore, it is irrelevant to correlate the observed band at 1175 cm^{-1} to a characteristic band for the coordinated 4,5-dichlorosemiquinonate moiety. Rather, the correlation of the observed bands at 1175 cm^{-1} to the corresponding counter anions of both complexes is relevant because the sodium salts of the counter anions *i.e.*, sodium tetrphenylborate^[131,132] as well as $\text{Na}[\text{BPh}_2(\text{DCCat})]$ (see Figure A.1 in appendix) exhibit bands at around 1175 cm^{-1} in their IR spectra. Hence, one of the reasons for the observation of bands at 1175 cm^{-1} is the presence of the corresponding counter anions.

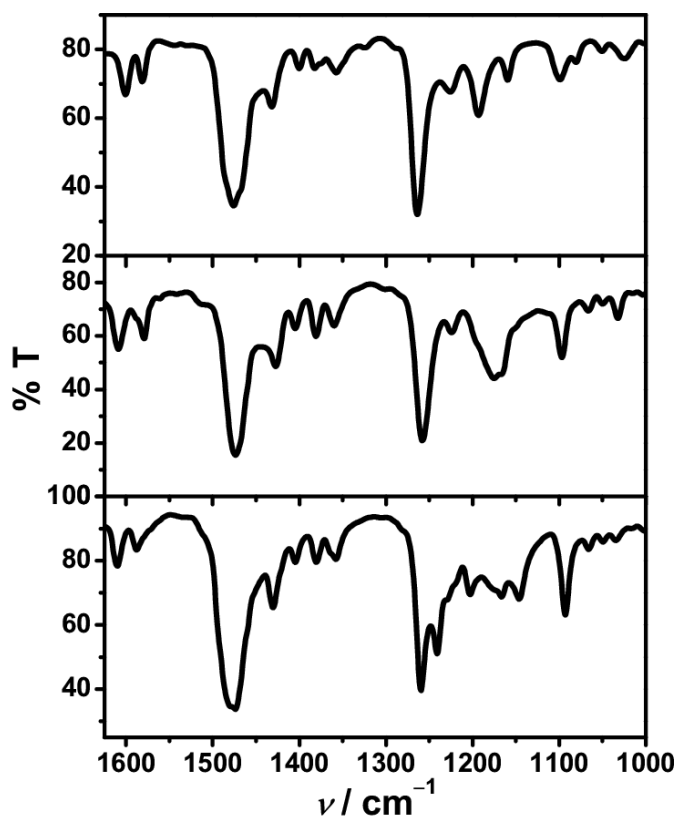


Figure 2.7: IR spectra of compounds **1** (top), **2c** (middle) and **2d** (bottom).

The additional catecholate marker band of the 4,5-dichlorocatecholate moiety which is coordinated to the boron center of the counter anion $[\text{BPh}_2(\text{DCCat})]^-$ in **2d** are also present at 1240 cm^{-1} . The presence of intense band at 1480 cm^{-1} indicate that dioxolene moiety is present in $[\text{BPh}_2(\text{DCCat})]^-$ counter anion.

The assignment of the characteristic bands of the counter anion is based on the IR spectrum of $\text{Na}[\text{BPh}_2(\text{DCCat})]$ where the catecholate marker band is present at 1244 cm^{-1} and the dioxolene marker band is present at 1488 cm^{-1} (see Figure A.1 in appendix). Hence, the higher wavenumber band at 1480 cm^{-1} is assigned to the 4,5-dichlorocatecholate unit of the counter anion and the band at 1473 cm^{-1} is assigned to the 4,5-dichlorocatecholate unit of the complex cation in **2d**.

Table 2.6: Comparison among the IR spectra of **1**, **2c** and **2d** in the range $1610\text{--}1000\text{ cm}^{-1}$. The wavenumbers corresponding to the catecholate and dioxolene marker bands have been highlighted by lighter shading.

	1	2c	2d
ν / cm^{-1}	1601	1607	1609
	1580	1579	1587
	1475	1473	1480, 1473
	1431	1426	1426
	1400	1406	1405
		1380	1381
	1356	1360	1364, 1356
	1265	1258	1258, 1240
	1225	1224	1219
	1192	1195	1203
		1175	1175
	1159	1166	1166
			1145
	1098	1096	1093
	1080	1066	1065

The data for the comparison among the IR spectra of KBr pellets of **1**, **2c** and **2d** are listed in Table 2.6 (see above). All compounds exhibit the typical catecholate marker bands at ca. 1260 cm^{-1} and dioxolene marker bands at ca. 1475 cm^{-1} . These observations support the presence of mostly the catecholate redox forms of the coordinated dioxolene units of the complexes in their KBr pellet samples.

2.1.4.2 Infrared Spectroscopic Properties in the Solution State

Solution state IR spectroscopic studies were performed with **2b**. The IR-spectra have been measured as a thin film in between two NaCl disks at room temperature in DMSO and in a liquid cell with NaCl windows at room temperature in $[\text{D}_2]\text{DCM}$. The spectra are shown in Figure 2.8 and Figure 2.9, respectively. Selected IR bands are provided in Table 2.7.

Table 2.7: Selected data for the IR spectra of **2b** in DMSO and $[\text{D}_2]\text{DCM}$. The catecholate and dioxolene marker bands have been highlighted by lighter shading.

	DMSO	$[\text{D}_2]\text{DCM}$
ν/cm^{-1}	1611	1610
	1580	1580
		1505
	1473	1473
	1434	1435
	1416	1426
	1404	1405
	1382	1382
	1358	1362
	1258	1258
	1225	1224
		1195
	1178	1178
		1165

The characteristic catecholate marker bands of the DCCat^{2-} units are present at 1258 cm^{-1} and the marker bands of the dioxolene units are present at 1475 cm^{-1} in both spectra. The most significant difference between the spectra is the intensity of the band at 1178 cm^{-1} which is higher in $[\text{D}_2]\text{DCM}$ than in DMSO. Since, the tetraphenylborate counter anion also exhibits band at 1175 cm^{-1} , and without knowing the change in intensity of the band at 1175 cm^{-1} for the counter anion in different solvents, it is not clear that the intensity change is affected by the, if any, appearance of a semiquinonate characteristic band of the coordinated dioxolene ligand in DCM. However, most importantly, presence of the significant amount of low-spin cobalt(III) catecholate species in DCM is obvious from the IR spectroscopic studies.

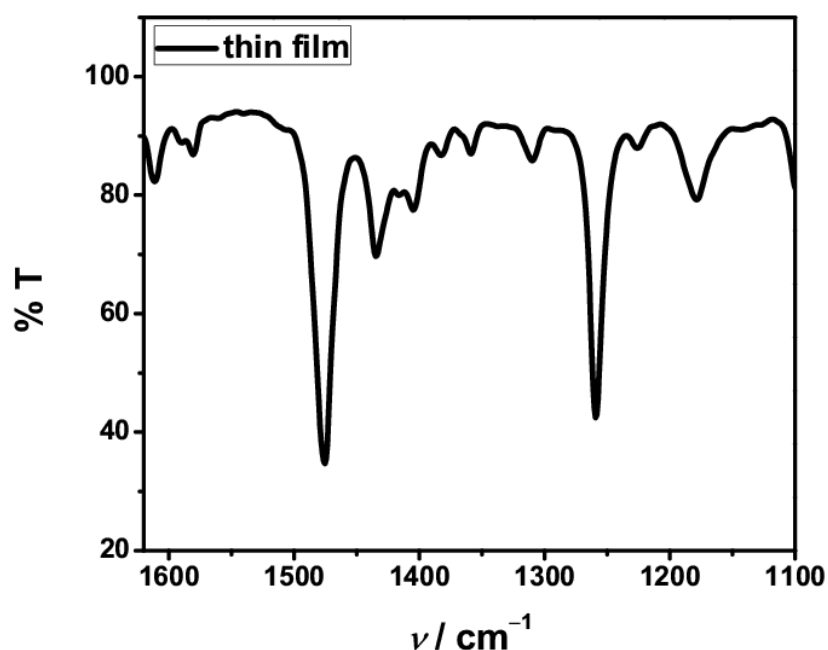


Figure 2.8: IR spectrum of **2b** in DMSO at room temperature. The spectrum was measured from a thin film of the compound prepared in DMSO.

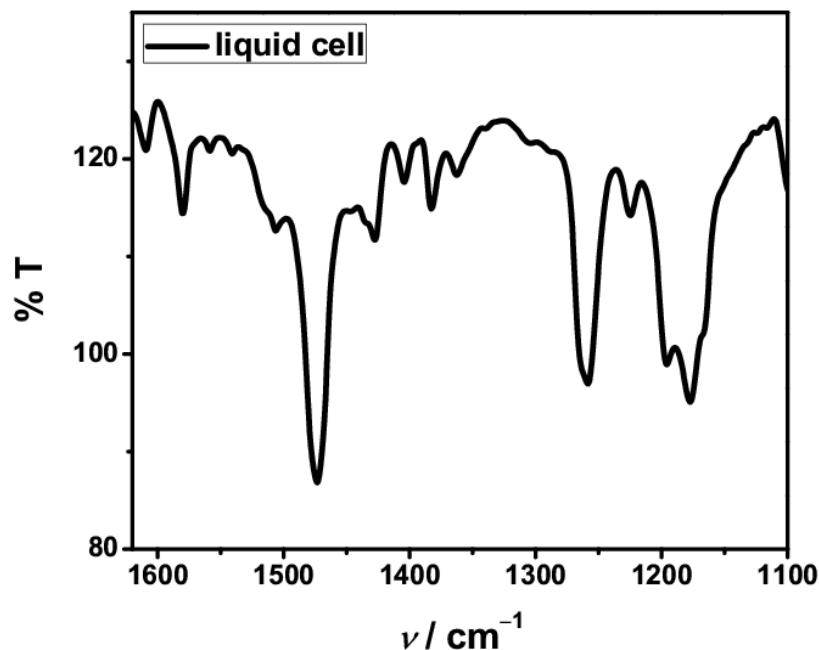


Figure 2.9: IR spectrum of **2b** in $[D_2]DCM$ at room temperature. The spectrum was measured in liquid cell and the sample was prepared from a solution of **2b** in $[D_2]DCM$.

2.1.5 UV/Vis/NIR Spectroscopic Properties

UV/Vis/NIR spectrum of **1** in DCM is shown in Figure 2.10. The spectrum shows a very weak band at 1037 nm ($\epsilon = 16 \text{ M}^{-1} \text{ cm}^{-1}$) which is assigned to the d–d band for the ${}^4T_{1g} \rightarrow {}^4T_{2g}$ transition of the high-spin cobalt(II) ion.^[32,53,122] The relatively intense bands at 551 nm ($\epsilon = 976 \text{ M}^{-1} \text{ cm}^{-1}$), 516 nm (sh, $\epsilon = 1190 \text{ M}^{-1} \text{ cm}^{-1}$), 464 nm ($\epsilon = 1563 \text{ M}^{-1} \text{ cm}^{-1}$) and 380 nm (sh, $\epsilon = 1060 \text{ M}^{-1} \text{ cm}^{-1}$) are most likely due to the LMCT transitions between the $DCCat^{2-}$ and high-spin cobalt(II) center. The assignment of the intense band at 323 nm ($\epsilon = 6627 \text{ M}^{-1} \text{ cm}^{-1}$) is not straightforward because both cobalt(II)–pyridine MLCT transitions^[93,122] and dioxolene based charge transfer transitions are expected in this region.^[63,133] Therefore, if the band at 323 nm is assigned to one of the transitions then the other transition is obscured by that transition. The band at 260 nm ($\epsilon = 11600 \text{ M}^{-1} \text{ cm}^{-1}$) is due to the ligand-based absorption of $L-N_4tBu_2$.^[122]

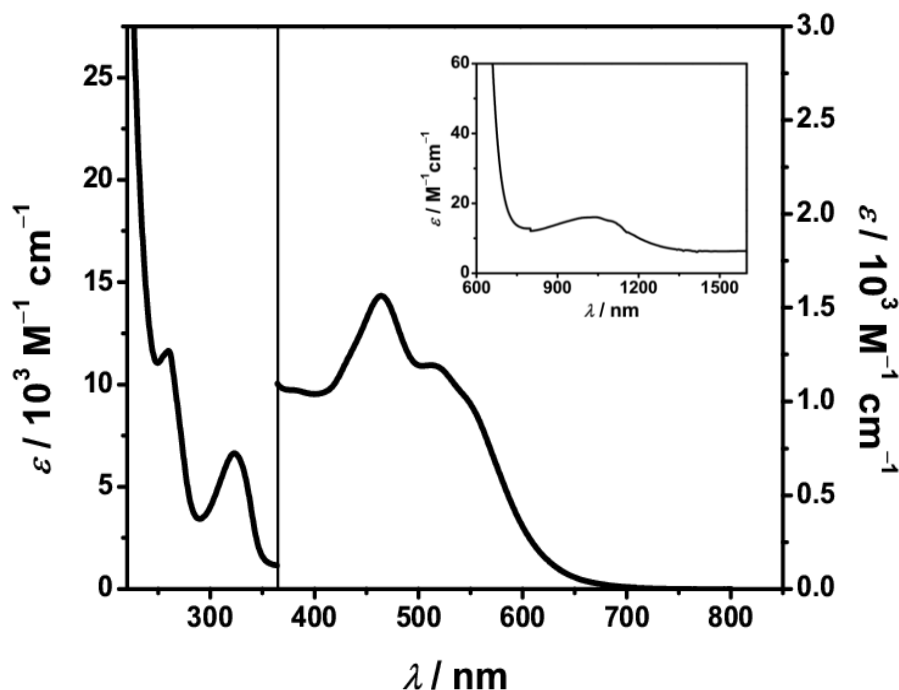


Figure 2.10: UV/Vis/NIR spectrum of $[\text{Co}(\text{L-N}_4\text{tBu}_2)(\text{DCCat})]$ (**1**) in dichloromethane at room temperature. The inset shows the d–d band.

The UV/Vis/NIR spectra of **2b** in DCM, DMSO and MeCN show contrasting intensity pattern of the absorption bands at room temperature, which are consistent with the NMR spectroscopic studies. The UV/Vis/NIR spectra of **2b** in DCM, MeCN and DMSO at 298 K (RT in MeCN) are shown in Figures 2.11, 2.12 and 2.13, respectively. The data for the absorptions are provided in Table 2.8. In order to get insights into the effect of temperature on the valence tautomeric equilibrium, the variable temperature UV/Vis/NIR spectra have been recorded in DCM and MeCN. Since the variable temperature ^1H NMR spectra measurement remained unsuccessful in $[\text{D}_6]\text{DMSO}$, and as the polarity of MeCN ($\mu_{\text{MeCN}} = 3.92 \text{ D}$)^[134] and DMSO ($\mu_{\text{DMSO}} = 3.96 \text{ D}$)^[129] are similar, therefore, in order to observe the changes in magnetic properties of complex **2** in a more polar solvent with a change in temperature, the variable temperature UV/Vis/NIR spectra were recorded in MeCN. The assignment of the absorptions corresponding to the particular chromophore *i.e.*, low-spin cobalt(II) semiquinonate or low-spin cobalt(III) catecholate chromophore is

based on the UV/Vis/NIR features of the low-spin cobalt(II) semiquinonate and low-spin cobalt(III) catecholate complexes, derived by the SVD of the variable temperature UV/Vis/NIR of spectra **2b** in DCM and MeCN (see below in Figure 2.16), and also based on the literature reports.^[33,55,76,92,94]

The bands in the NIR region of the spectra with absorptions at around 1108, 1060, 990 and 938 nm are due to the MLCT transitions from the low-spin cobalt(II) center to the DCSQ^{•-} moiety. The intensity of these bands could be arranged, according to their appearances in the spectra in different solvents, in the following order DCM \gg MeCN $>$ DMSO. Since, a *cis*-octahedral low-spin cobalt(III) catecholate chromophore would exhibit a very weak absorption ($\epsilon \sim 200 \text{ M}^{-1} \text{ cm}^{-1}$) in the NIR region (also see below in Figure 2.16),^[33,76,94] therefore, presence of intense bands in this region for the spectrum in DCM indicates that the NIR spectral features are mainly due to the absorptions of the low-spin cobalt(II) semiquinonate chromophore. The absorptions in the NIR region of the spectra in DMSO and MeCN are originating from the much smaller amount of low-spin cobalt(II) semiquinonate and larger amount of low-spin cobalt(III) catecholate chromophores.

The relatively less intense absorption bands of the spectrum in DCM at 810 and 420 nm are due to the internal $n \rightarrow \pi^*$ and $\pi \rightarrow \pi^*$ charge transfer transitions, respectively, of the DCSQ^{•-} moiety.^[63,94] The bands in the visible region of the spectrum in DCM with absorptions at 630 and 580 nm are originating as a result of the charge transfer bands of the low-spin cobalt(II) semiquinonate chromophore as well as LMCT/charge transfer bands corresponding to the low-spin cobalt(III) catecholate chromophore which is evidenced by the appearance of these bands in the low-temperature and high-temperature components and in particular, the LMCT/charge transfer bands are prominent in the spectra in MeCN and DMSO.

For the spectra in MeCN and DMSO, the bands at around 460 nm is tentatively assigned to the charge transfer transition between the low-spin cobalt(III) ion and catecholate moiety. The bands at around 547 and 505 nm are assigned to LMCT/charge transfer bands between the catecholate moiety and low-spin cobalt(III) centers of the low-spin cobalt(III) catecholate chromophore.^[33]

The assignment of the bands in the UV region of all the spectra is not straightforward because in this region cobalt(II/III)–pyridine MLCT transitions^[32,93,122] as well as ligand-based absorptions for the catecholate and semiquinonate forms of the dioxolene units are expected.^[63,133] The intensity of the bands at around 320 nm could be arranged according to their appearances in the spectra in different solvents in the following order DCM < MeCN < DMSO.

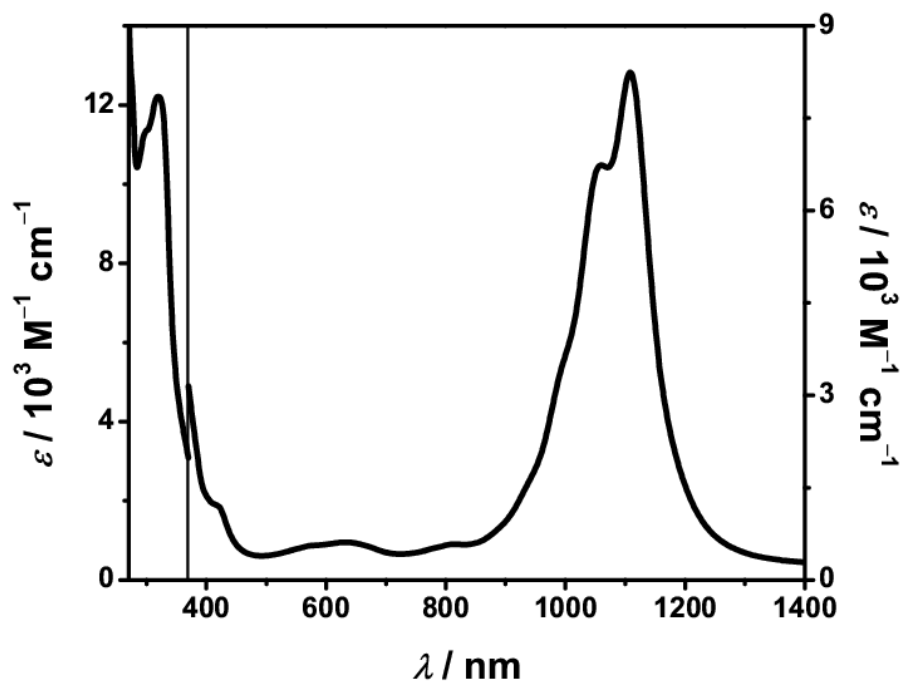


Figure 2.11: UV/Vis/NIR spectrum of **2b** in DCM at 298 K.

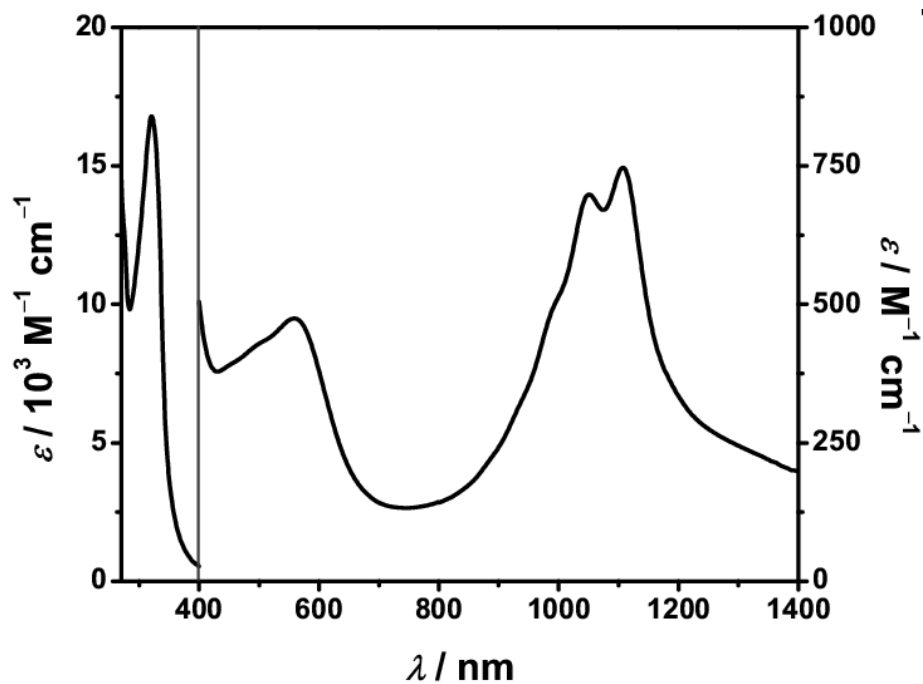


Figure 2.12: UV/Vis/NIR spectrum of **2b** in MeCN at room temperature.

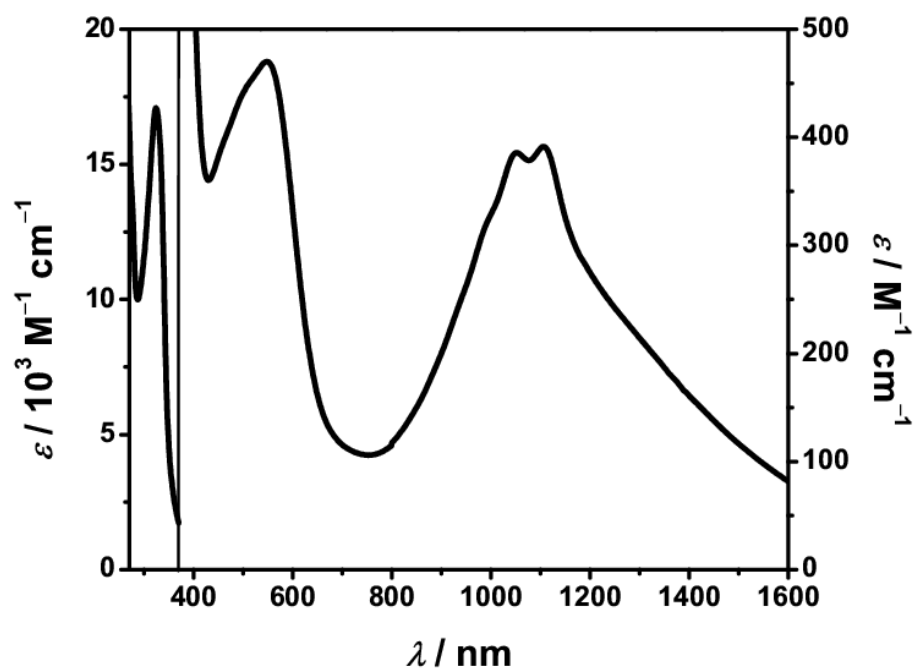


Figure 2.13: UV/Vis/NIR spectrum of **2b** in DMSO at 298 K.

Table 2.8: UV/Vis/NIR data of **2b** in DCM, DMSO and MeCN; λ_{\max} (ϵ).

Solvent (T/K)	λ_{\max}/nm ($\epsilon/\text{M}^{-1} \text{cm}^{-1}$)
DCM (298 K)	1108 (8243), 1060 (6737), 990 (3318), 938 (1581), 810 (580), 630 (614), 580 (558), 420 (1199), 320 (12200), 300 (11300), 274 (12800)
DMSO (298 K)	1106 (391), 1052 (385), 990 (319), 547 (470), 505 (445), 460 (395), 324 (17100), 276 (13700)
MeCN (RT)	1107 (747), 1051 (698), 990 (491), 559 (474), 500 (428), 452 (391), 320 (16800), 275 (12700)

The NIR/Visible spectrum in DCM is fitted with sum of Lorentzian curves (see Figure A.19 in Appendix). The data obtained from the fitting are given in Table A.5 (see in section 6.1.4 in appendix). Also, the data related to the Lorentzian fit of almost all of the discussed UV/Vis/NIR spectra in this section are given in Table A.5. The absorption spectrum recorded in DCM is fitted with sum of five Lorentzian curves with absorption maxima at 1112, 1051, 993, 934 and 803 nm in the NIR region.

The NIR/Visible spectrum recorded in MeCN, is fitted with sum of Lorentzian curves with absorption maxima at 1379, 1190, 1111, 1047, 990, 940 and 807 nm in the NIR region. Among these bands, the two bands at 1379 and 1190 nm could be due to the experimental error and fitting error or broad LMCT band of the predominantly present low-spin cobalt(III) catecholate complex in the $\text{VT}_{\text{LS-LS}}$. In the visible region the spectrum is fitted with sum of three Lorentzian curves with absorption maxima at 573, 506 and 431 nm (see Figure A.20 and Table A.5 in appendix).

The fitting of the NIR/Visible region of the spectrum in DMSO with Lorentzian curves provides peaks at 1384, 1220, 1112, 1047, 991, 894, 570, 511 and 442 nm (see Figure A.21 and Table A.5 in appendix). Among these peaks, the peaks at 1384 and 1220 nm might be due to the experimental and

fitting error or due to the LMCT band of the low-spin cobalt(III) catecholate chromophore which is predominant in the VT_{LS-LS} .

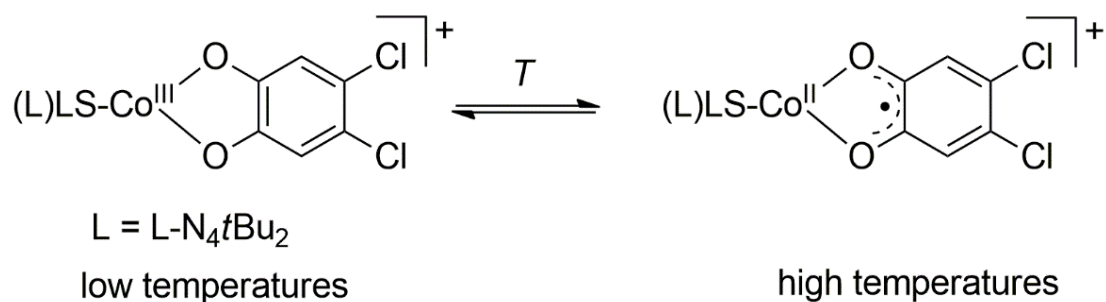
The observation by the UV/Vis/NIR spectroscopic study of **2b** is consistent with those of the NMR and IR spectroscopic studies in different solvents, because at room temperature in DCM, the intensity of the marker bands for the low-spin cobalt(II) semiquinonate chromophore in the NIR region is substantially large due to the predominance of the low-spin cobalt(II) semiquinonate complex in the VT_{LS-LS} equilibrium. Whereas, the low-spin cobalt(III) catecholate complex is present in smaller amount in the equilibrium because the bands corresponding to the low-spin cobalt(III) catecholate chromophore are weaker to an extent such that they are obscured by the relatively intense bands of the low-spin cobalt(II) semiquinonate chromophore in the NIR and visible region, and unapparent in the spectrum.

At room temperature in MeCN and DMSO, the VT_{LS-LS} equilibrium is predominated by the low-spin cobalt(III) catecholate complex because the marker bands for the low-spin cobalt(III) catecholate chromophore in the visible region is apparent and the intensity of the marker bands for the low-spin cobalt(II) semiquinonate complex in the NIR region is much smaller. Therefore, the low-spin cobalt(II) semiquinonate is present in much smaller amount in the VT_{LS-LS} equilibrium in these solvents.

Variable temperature UV/Vis/NIR in DCM and MeCN

The variable temperature UV/Vis/NIR spectra were recorded from the solutions of **2b** in DCM and MeCN (Figures 2.14 and 2.15). The data for the absorption band at 1108 nm in various temperatures have been provided in Table 2.9. The compound was stable in DCM during the measurement and the stability was checked by UV/Vis/NIR (see Figure A.22 in appendix).

The measurement of the UV/Vis/NIR spectra in MeCN with multiple scans at 333 and 343 K and the UV/Vis/NIR spectra representing the solution stability of **2b** during variable temperature UV/Vis/NIR spectra measurement in MeCN, reveal that the compound is slightly decomposing at 343 K but it is stable at 333 K (see in Figures A.23–A.24 in appendix).



Scheme 2.1: Temperature-induced valence tautomeric transition of **2b** in DCM and MeCN.

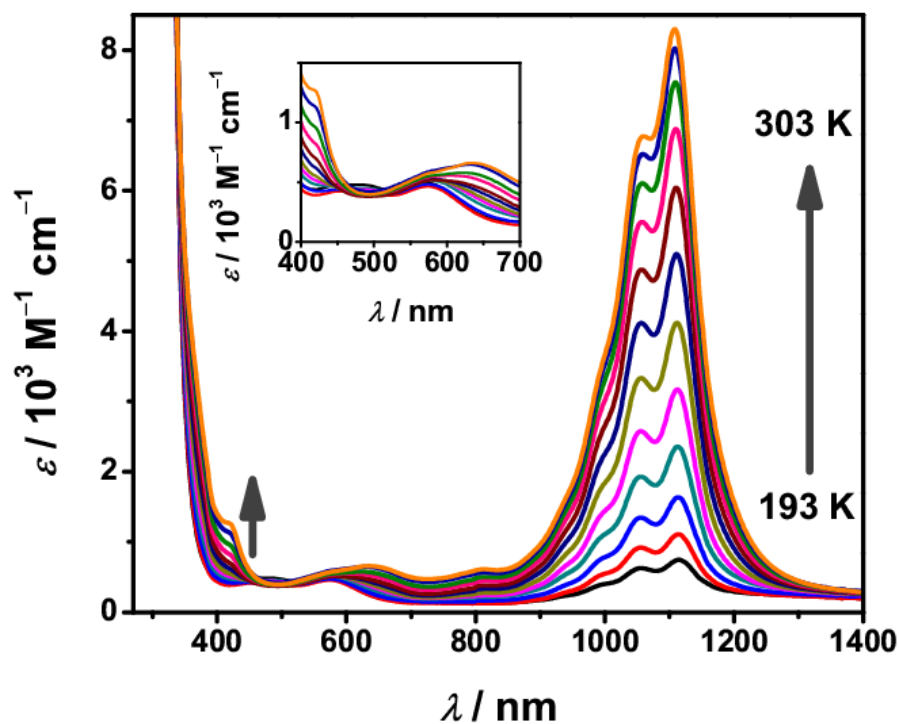


Figure 2.14: Variable temperature UV/Vis/NIR spectra of **2b** in dichloromethane. The inset shows the changes of the bands in the visible region.

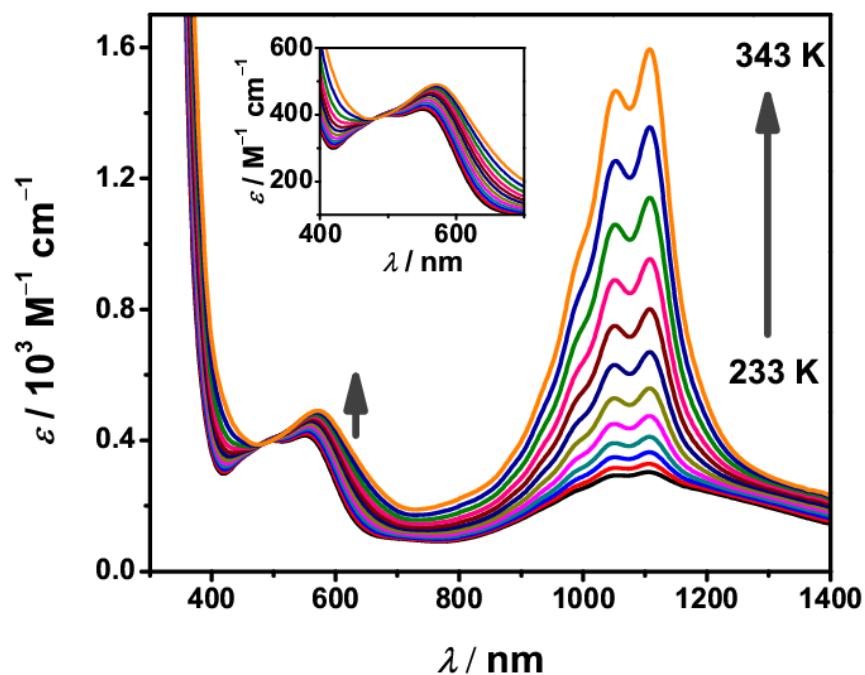


Figure 2.15: Variable temperature UV/Vis/NIR spectra of **2b** in MeCN. The inset shows the changes of the bands in the visible region.

Table 2.9: Variable temperature UV/Vis/NIR data for **2b** in MeCN and DCM: ϵ for $\lambda_{\max} = 1107$ nm (MeCN) and ϵ for $\lambda_{\max} = 1108$ nm (DCM).

Solvent	T/K	$\epsilon/M^{-1} \text{ cm}^{-1}$	Solvent	T/K	$\epsilon/M^{-1} \text{ cm}^{-1}$
MeCN	233	303	DCM	193	746
	243	328		203	1110
	253	364		213	1635
	263	411		223	2356
	273	474		233	3169
	283	558		243	4119
	293	669		253	5097
	303	800		263	6043
	313	954		273	6880
	323	1140		283	7541
	333	1356		293	8027
	343	1594		303	8300

Before the discussion of the spectral changes with the change in temperature, the results from the SVD analyses of the two set of variable temperature UV/Vis/NIR spectra are discussed which are as following: The low- and high-temperature components (LTC and HTC) of the spectra derived by SVD of the both variable temperature UV/Vis/NIR spectra are shown in Figure 2.16. The data for the SVD are given in Table 2.10. A general routine for the SVD is provided in Table A.6 (see appendix). The data for the absorptions of the LTCs and HTC are given in Table 2.11. The Lorentzian fit for the component spectra are shown in Figures A.25–A.28 (see appendix). The spectra for the first three **U** components for each of the SVD analyses are shown in Figures 2.17 and 2.18, respectively. The plots of the first three **V** components vs. *T* (with fit for the the first two components) from each SVD analysis are shown in Figures A.29–A.34 (see appendix). The first two singular values of the each **S** matrix suggest that the first two set of basis spectra corresponds to 98.6 % (for the spectra in MeCN) and 97.9 % (for the spectra in DCM) weights to the observed spectra. The shape of the **V** component vs. *T* plots indicates that, while the first two plots have a similar shape to the γ_{HS} vs. *T* plot for a valence tautomeric transition, the third one does not have any physical meaning interms of a valence tautomeric transition. The NMR spectroscopic study of **2b** is also indicative of the presence of two species in the VT_{LS-LS} equilibrium. The goodness-of-fit parameters for the fitting of **V** component vs. *T* plots are given in Table A.7 (see appendix). Thus, considering all the aspects, it can be inferred that except for the first two components of the **U**, **S** and **V** matrices, the rest are predominated by the corresponding features due to the noise. In addition, the features of the latter components could also arise from the spectral broadening. Therefore, it is concluded that the variable temperature UV/Vis/NIR spectra in each case contain two components.

Table 2.10: The first four singular values, thermodynamic parameters ΔH , ΔS and goodness-of-fit parameter R^2 obtained from the SVD of the variable temperature UV/Vis/NIR spectra of **2b** in DCM and MeCN.^[a]

Solvent	Singular value	Singular value (%)	$\Delta H/\text{kJ mol}^{-1}$	$\Delta S/\text{J K}^{-1} \text{mol}^{-1}$	T/K	R^2 ^[b]
MeCN	4.63×10^4	84.2	20.6	43.4	233	0.987
	7.93×10^3	14.4			243	0.995
	607.24	1.1			253	0.999
	116.08	0.2			263	1
					273	0.999
					283	0.998
					293	0.998
					303	0.998
					313	0.999
					323	1
					333	1
		343	0.999			
DCM	2.12×10^5	82.6	20.9	81.7	193	0.996
	3.90×10^4	15.3			203	0.999
	3.32×10^3	1.3			213	0.999
	927.08	0.4			223	0.998
					233	0.999
					243	0.999
					253	0.999
					263	0.999
					273	1
					283	1
					293	1
		303	0.999			

^[a] The data points have absorbance in the range of 0–1.1.

^[b] Goodness-of-fit parameter for the reconstructed spectrum at each temperature.

Table 2.11: Absorption data for the low-temperature and high-temperature components of the variable temperature UV/Vis/NIR spectra of **2b** in DCM and MeCN.

Solvent	Component	λ_{\max}/nm ($\epsilon/\text{M}^{-1} \text{cm}^{-1}$)
DCM	HTC	1109 (10200), 1058 (8240), 991 (4090), 934 (1804), 814 (668), 637 (722), 579 (603), 420 (1230), 378 (2864)
	LTC ^[a]	573 (474), 486 (448), 446 (407)
MeCN	HTC	1108 (11700), 1053 (10700), 991 (6524), 934 (3377), 805 (1210), 621 (1882), 520 (647), 418 (2240)
	LTC	1148 (236), 553 (427), 489 (397), 449 (342)

^[a] Only UV/Vis bands are considered.

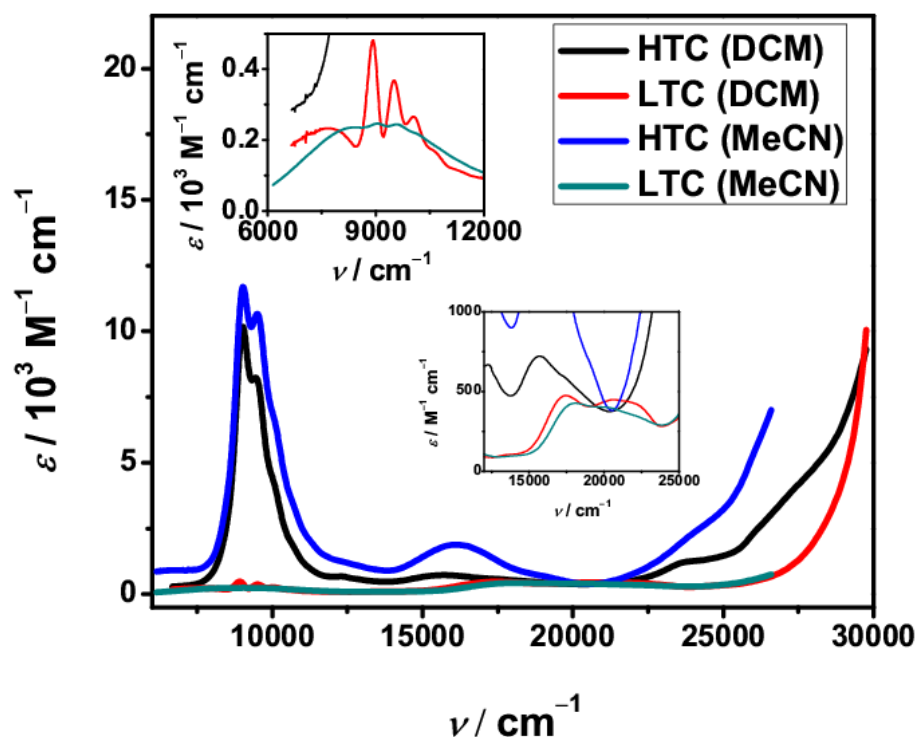


Figure 2.16: The UV/Vis/NIR features corresponding to the HTCs and LTCs derived from the SVD of the variable temperature UV/Vis/NIR spectra of **2b** in DCM and MeCN.

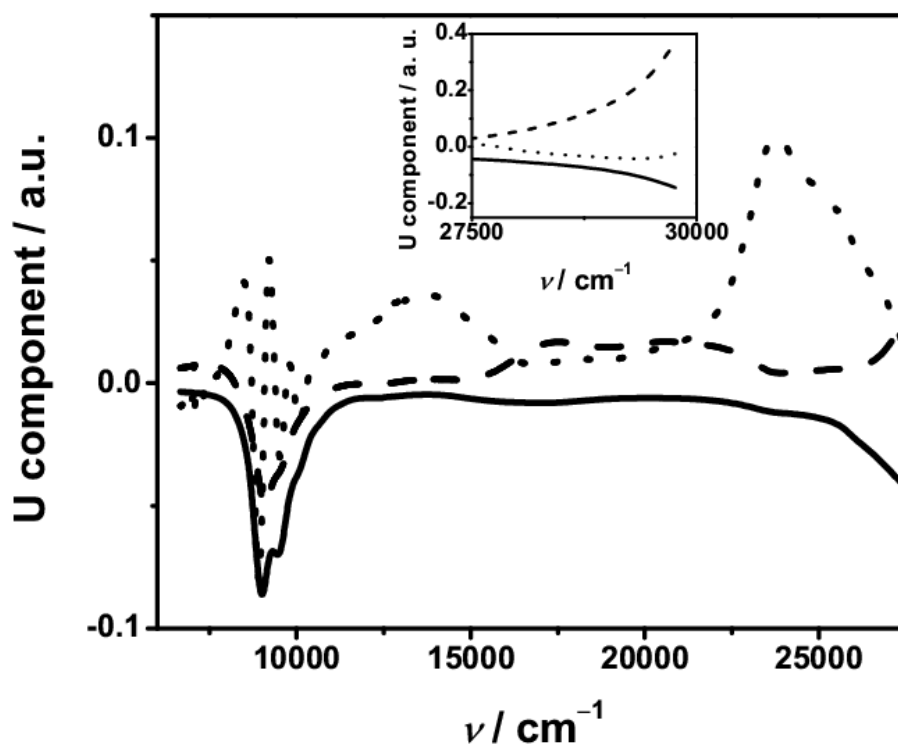


Figure 2.17: Spectra of the first three U components presented in the sequence of solid, dashed and dotted lines for the SVD of the variable temperature UV/Vis/NIR spectra of **2b** in DCM.

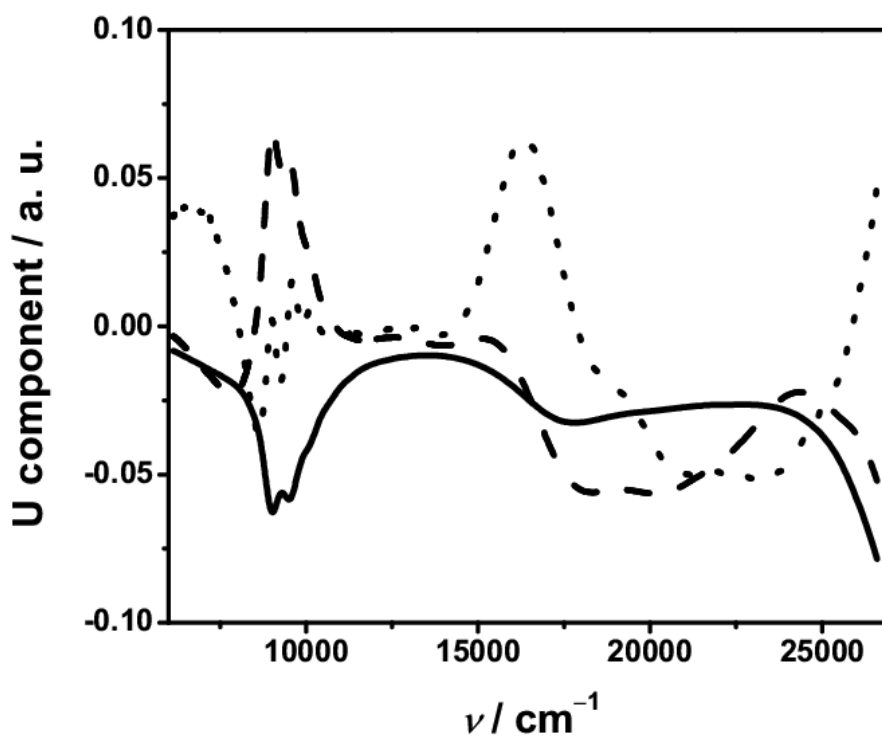


Figure 2.18: Spectra of the first three U components presented in the sequence of solid, dashed and dotted lines for the SVD of the variable temperature UV/Vis/NIR spectra of **2b** in MeCN.

The absorption profiles of the low-temperature components have similarity with those observed for the *cis*-octahedral low-spin cobalt(III) catecholate complexes.^[33,76,94] Note that the appearances of the spikes in the NIR region of the spectra of the low-temperature components could be due to the error of the SVD. The obtained absorption profiles of the high-temperature components closely resemble to the absorption profile for a low-spin cobalt(II) semiquinonate chromophore.^[33,55,92]

The experimental spectra were reconstructed (see Figures A.35–A.40 in appendix). The residuals between the experimental and reconstructed (calculated) spectra for both the measurements are shown in Figures 2.19–2.20. These residuals do not differ substantially from the respective residuals between the original data matrix (**A**) and rank-defined data matrix (**B**) (see appendix; Figures A.41–A.42). The goodness of the reconstruction is shown by calculating the R^2 value the spectrum at each temperature (see above in Table 2.10).

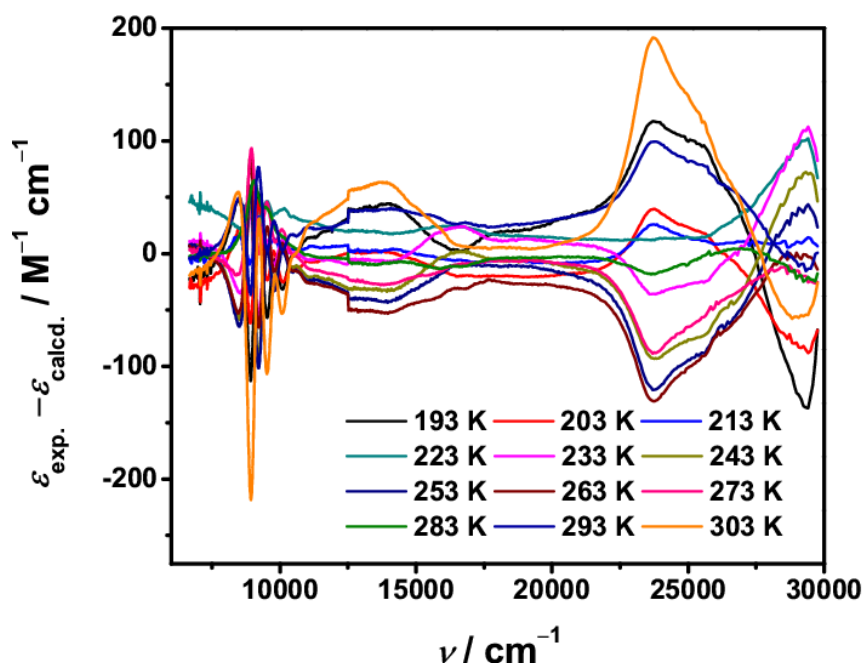


Figure 2.19: Residuals between the experimentally recorded and reconstructed (calculated) spectra obtained by the SVD of the variable temperature UV/Vis/NIR spectra of **2b** in DCM.

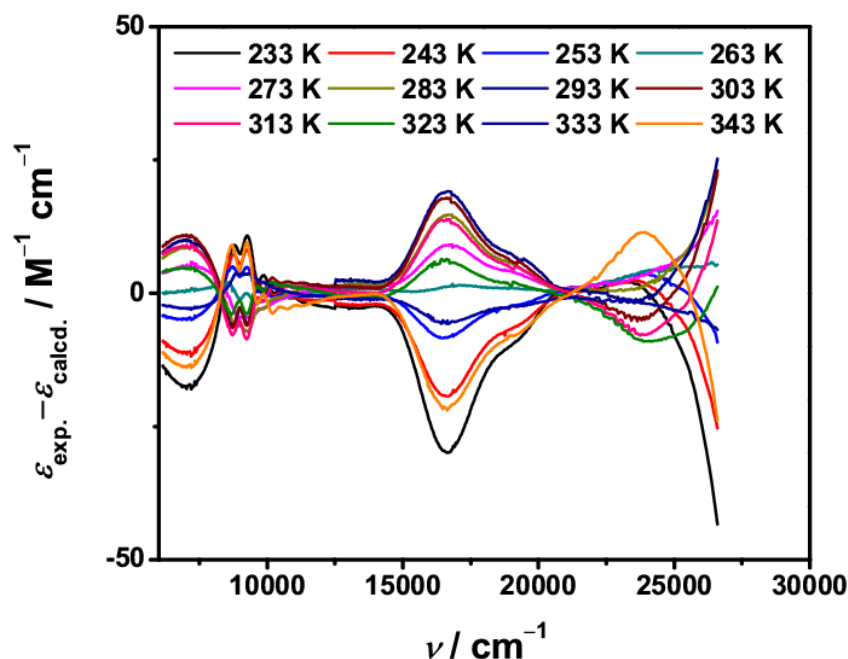


Figure 2.20: Residuals between the experimentally recorded and reconstructed (calculated) spectra obtained by the SVD of the variable temperature UV/Vis/NIR spectra of **2b** in MeCN.

The spectral changes in both measurements are predominated by the changes in intensity for the MLCT bands of the low-spin cobalt(II) semiquinonate chromophore. The intensity of the MLCT bands in the NIR region increases upon increasing the temperature of the solutions. However, the difference between the intensity changes is the extent of changes in the intensity of the MLCT bands which is different for the two measurements. These spectral changes are explained due to the occurrence of a valence tautomeric transition from the low-spin cobalt(III) catecholate to low-spin cobalt(II) semiquinonate state of **2** with positive change in temperature (Scheme 2.1). Increase in the concentration of the low-spin cobalt(II) semiquinonate complex in the valence tautomeric equilibrium leads to the increase in intensity of the MLCT bands. The other features of the spectral changes in DCM include appearance of the charge transfer/LMCT bands corresponding to the low-spin cobalt(III) catecholate chromophore, at low temperatures, with absorption maxima at

452, 500 and 559 nm. These bands remain apparent with slight shift of the absorption maxima values, in the temperature range of 193–243 K. However, upon increasing the temperature these bands become inapparent because they are obscured by the appearance of relatively intense charge transfer bands in the visible region, corresponding to the low-spin cobalt(II) semiquinonate chromophore. For the spectra in MeCN, the charge transfer/LMCT bands in the visible region remain apparent in the temperature range 233–313 K.

The spectrum at each temperature from both measurements has been deconvoluted by Lorentzian function. The deconvoluted spectra are shown in Figures A.43–A.66 and the data obtained from the deconvolution are provided in Table A.5 (see appendix). The molar extinction coefficient for each Lorentzian band, in the NIR region of the spectra in DCM, is plotted vs. temperature (Figure 2.21). For better visibility of the shapes of the curves corresponding to the changes in molar extinction coefficients for the absorption maxima at 993 and 934 nm, a stacked spectra of the curves of Figure 2.21, are shown in Figure A.67 (see appendix). The plot indicates that the percentage of the intensity change for each band upon changing the temperature is similar. In addition, it could be predicted that the intensity change would continue if the temperature is further raised.

The ϵ vs. T plot for the Lorentzian profiles in MeCN at 1111 and 1047 nm is shown in Figure 2.22. The plot suggests that the percentages of changes in intensities of these two absorption bands are similar in the working temperature range of the variable temperature UV/Vis/NIR spectra measurement in MeCN.

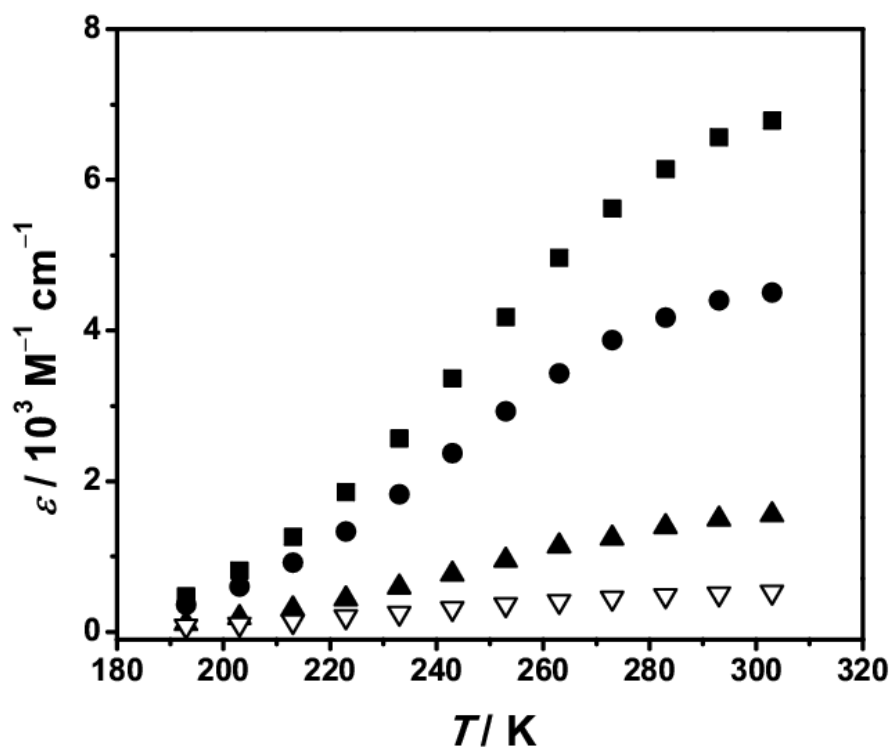


Figure 2.21: ε vs. T plots for the bands at $\lambda_{\max} = 1112$ nm (filled square), $\lambda_{\max} = 1051$ nm (filled circle), $\lambda_{\max} = 993$ nm (filled triangle), $\lambda_{\max} = 934$ nm (unfilled triangle), derived from the Lorentzian fit of the variable temperature UV/Vis/NIR spectra of **2b** in DCM.

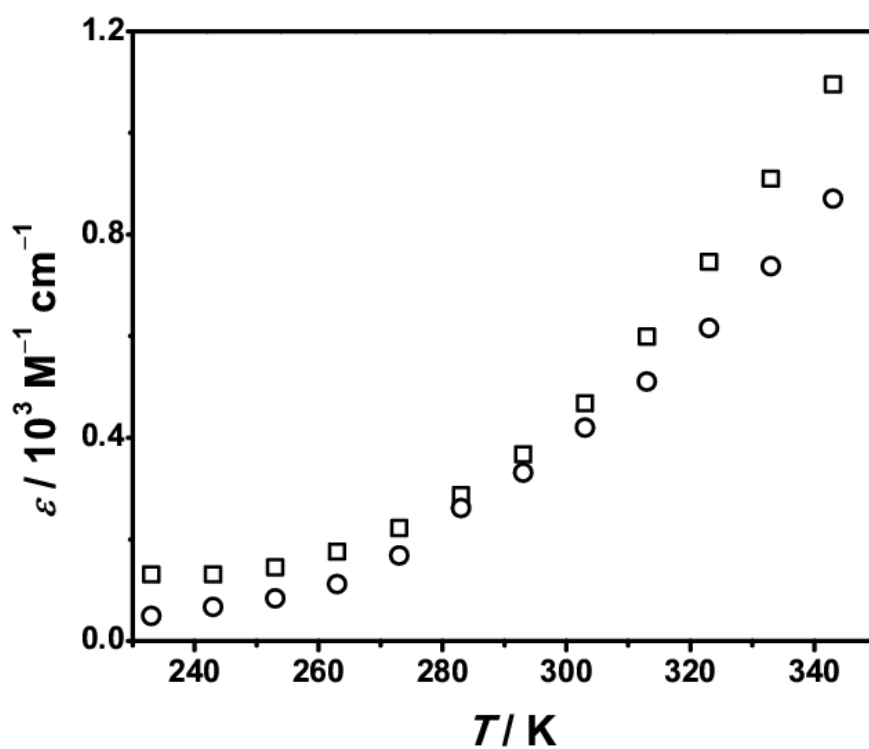


Figure 2.22: ε vs. T plots for the bands at $\lambda_{\max} = 1111$ nm (unfilled square), $\lambda_{\max} = 1047$ nm (unfilled circle), derived from the Lorentzian fit of the variable temperature UV/Vis/NIR spectra of **2b** in MeCN.

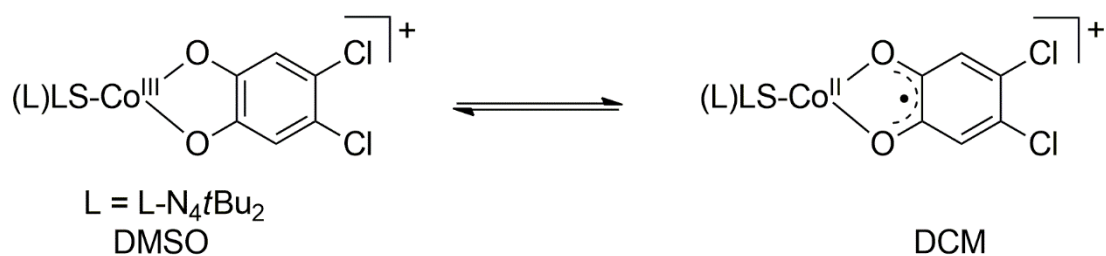
The SVD analyses provide the values of thermodynamic parameters $\Delta H = 20.6 \text{ kJ mol}^{-1}$ and $\Delta S = 43.4 \text{ J K}^{-1} \text{ mol}^{-1}$ ($\Delta S_{\text{elec}} = 9.1 \text{ J K}^{-1} \text{ mol}^{-1}$ and $\Delta S_{\text{vib}} = 34.3 \text{ J K}^{-1} \text{ mol}^{-1}$) for the $\text{VT}_{\text{LS-LS}}$ in MeCN whereas for the same process in DCM, the values of those parameters are $\Delta H = 20.9 \text{ kJ mol}^{-1}$ and $\Delta S = 81.7 \text{ J K}^{-1} \text{ mol}^{-1}$ ($\Delta S_{\text{elec}} = 9.1 \text{ J K}^{-1} \text{ mol}^{-1}$ and $\Delta S_{\text{vib}} = 72.6 \text{ J K}^{-1} \text{ mol}^{-1}$). These values of the thermodynamic parameters indicate that the critical temperature (T_c) of $\text{VT}_{\text{LS-LS}}$ (*i.e.*, the temperature when molar fractions of low-spin cobalt(II) semiquinonate and low-spin cobalt(III) catecholate forms are same) is shifted to higher temperature in MeCN ($T_c = \Delta H/\Delta S = 474 \text{ K}$) than in DCM ($T_c = 257 \text{ K}$). Thus, the $\text{VT}_{\text{LS-LS}}$ of **2b** is mainly affected by the change in ΔS_{vib} which could be explained on the basis of the significant changes in M–L bond vibrations as a result of the solute-solvent interactions which include polarity of the solvents as one of the factors.^[84] Besides, it is likely that the ΔH values for the $\text{VT}_{\text{LS-LS}}$ could remain almost same in these two solvents because *Dei* reported that the ΔH values for the LMCT equilibrium $[\text{Fe}^{\text{III}}(\text{CTH})(\text{DBC})] \rightleftharpoons [\text{Fe}^{\text{II}}(\text{CTH})(\text{DBSQ})]$ are same in 1,2-dichloroethane (DCE) and MeCN.^[135] If the differences in the polarities and number of electron-donor atoms between DCE ($\mu_{\text{DCE}} = 1.47 \text{ D}$)^[136] and MeCN ($\mu_{\text{MeCN}} = 3.92 \text{ D}$)^[134] and differences of the same parameters between DCM ($\mu_{\text{DCM}} = 1.60 \text{ D}$)^[130] and MeCN are considered, then it is very likely that the enthalpy change would be same for the discussed $\text{VT}_{\text{LS-LS}}$ because this equilibrium is similar with the above equilibrium. Besides, there is also an example of the $\text{VT}_{\text{LS-HS}}$ for the complex $[\text{Co}(\text{Cat-N-BQ})(\text{Cat-N-SQ})]$ where the values of the thermodynamic parameters are $\Delta H = 44.4 \text{ kJ mol}^{-1}$ and $\Delta S = 74.4 \text{ J K}^{-1} \text{ mol}^{-1}$ in its solid state and $H = 42 \text{ kJ mol}^{-1}$ and $\Delta S = 140 \text{ J K}^{-1} \text{ mol}^{-1}$ in its solution state.^[69,73] That observation along with the thermodynamic parameters of the other valence tautomeric cobalt dioxolene complexes are indicative of the general fact that a valence tautomeric transition is an entropy driven process.^[73,76,77,80,87,137] The

same conclusion can be reached from the obtained thermodynamic parameters for the VT_{LS-LS} of **2b** in different solvents.

The obtained ΔH and ΔS values for the VT_{LS-LS} of **2b** are significantly smaller than those values ($\Delta H = 31.2 \text{ kJ mol}^{-1}$ and $\Delta S = 125 \text{ J K}^{-1} \text{ mol}^{-1}$) found for the VT_{LS-HS} of the *cis*-octahedral cobalt dioxolene complex $[\text{Co}(\text{Me}_3\text{tpa})(\text{TCCat})](\text{PF}_6)$ (Me_3tpa = tris(2-pyridylmethyl)amine, TCCat = dideprotonated form of tetrachlorocatechol) in its DCM solution.^[76] The finding of the lesser values of the entropy change could be explained due to the fact that the changes in electronic level degeneracy as well as changes in M–L bond lengths are lesser than those for the VT_{LS-HS} . Since, the ΔH value is related to the zero point energy differences between the potential wells of low-energy state and high-energy state,^[71] therefore, it can be inferred that the lesser values of ΔH are consistent with the fact that energy level difference between the high-spin cobalt(II) semiquinonate and low-spin cobalt(III) catecholate state is higher than that of the difference between the low-spin cobalt(II) semiquinonate and low-spin cobalt(III) catecholate state.

UV/Vis/NIR spectra in DCM/DMSO mixtures

In order to gain further insights into the solvent effects on the valence tautomeric equilibrium, the valence tautomerism have been investigated by measuring UV/Vis/NIR spectra of **2b** in DCM/DMSO mixtures. The measurements have been performed by mixing equimolar solutions of the complex in DCM and DMSO in different volume ratio. The data for the absorption band at $1110 \pm 2 \text{ nm}$ in various solvent mixtures have been provided in Table 2.12 and the spectra are shown in Figure 2.23. The enlarged spectra in the NIR region of Figure 2.23 are shown in Figure A.68 (see appendix) to get a better visibility of the bands with small intensity.



Scheme 2.2: Valence tautomeric transition of **2b** due to change in solvent.

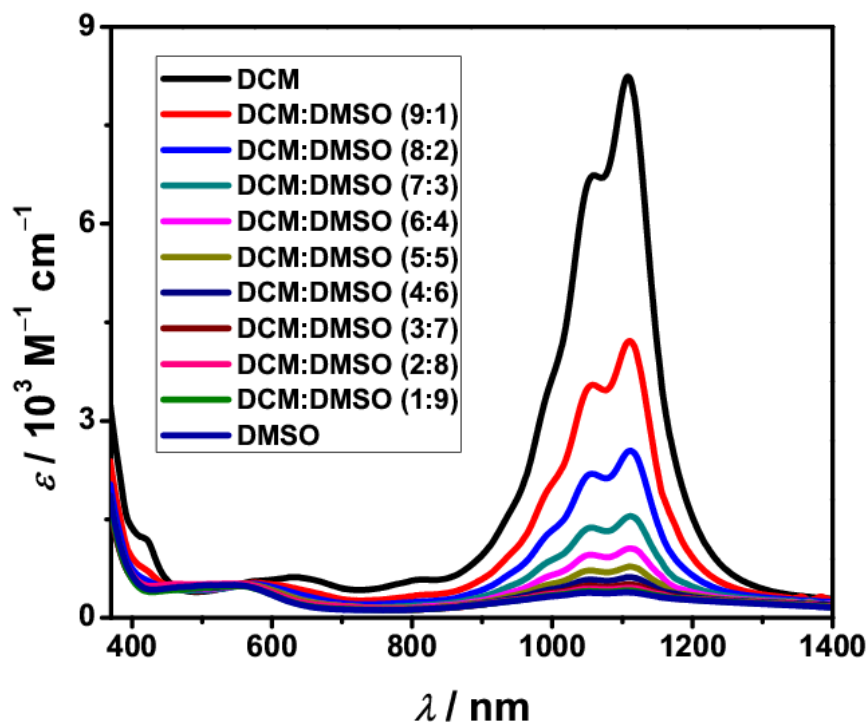


Figure 2.23: UV/Vis/NIR spectra of **2b** in DCM and DMSO and in varying ratio of (DCM/DMSO) mixture at 298 K.

The spectral changes are predominated by the changes of the MLCT bands of the low-spin cobalt(II) semiquinonate chromophore in the NIR region, which is accompanied by the changes in pattern of the bands in the visible region and intensity of the internal $n \rightarrow \pi^*$ and $\pi \rightarrow \pi^*$ charge transfer bands of DCSQ^{•-} moiety at 810 and 420 nm. The increasing amount of DMSO in DCM/DMSO mixture leads to the decrease in intensity of the MLCT bands corresponding to the low-spin cobalt(II) semiquinonate chromophore. The intensity of the charge transfer bands associated with DCSQ^{•-} moiety also decreases. The

marker bands for the low-spin cobalt(III) catecholate chromophore become apparent in the visible region of the spectra when the mixture contains 50 % or more amount of DMSO. Thus, at room temperature, the amount of low-spin cobalt(II) semiquinonate species increases in the VT_{LS-LS} equilibrium with increase in DCM:DMSO volume ratio (Scheme 2.2).

Table 2.12: UV/Vis/NIR data for **2b** in DCM/DMSO mixtures; ϵ for $\lambda_{\max} = 1110 \pm 2$ nm.

Solvent	$\epsilon/M^{-1} \text{ cm}^{-1}$
DCM	8243
DCM:DMSO (9:1)	4212
DCM:DMSO (8:2)	2540
DCM:DMSO (7:3)	1544
DCM:DMSO (6:4)	1054
DCM:DMSO (5:5)	775
DCM:DMSO (4:6)	613
DCM:DMSO (3:7)	505
DCM:DMSO (2:8)	454
DCM:DMSO (1:9)	412
DMSO	383

The effects of the solute-solvent interactions other than polarity of the solvent, on the valence tautomeric transition are reestablished due to the fact that in a DCM/DMSO mixture (5:5) the intensity of the bands is similar to that of the spectrum in MeCN at room temperature. Although there are no data available, about the polarity of solvent mixture of polar and non-polar solvent in different ratio, still it is very unlikely that the DCM/DMSO mixture (5:5) will have a similar polarity with that of MeCN ($\mu = 3.92$ D).

The assignment for the reduction at $E_{1/2} = -1.95$ V is difficult because the reduction can be metal-based irreversible reduction from $[\text{Co}^{\text{II}}(\text{L-N}_4\text{tBu}_2)(\text{DCCat}^{2-})]$ to $[\text{Co}^{\text{I}}(\text{L-N}_4\text{tBu}_2)(\text{DCCat}^{2-})]^-$ or ligand-based irreversible reduction from $[\text{Co}^{\text{II}}(\text{L-N}_4\text{tBu}_2)(\text{DCCat}^{2-})]$ to $[\text{Co}^{\text{II}}(\text{L-N}_4\text{tBu}_2^{\bullet-})(\text{DCCat}^{2-})]^-$.

The CV for the oxidations of **2e** at different scan rates are shown in Figure 2.24 and the data are provided in Table A.8 (see in section 6.1.5 in appendix). The oxidation which is occurring at $E_{1/2} = 711$ mV is due to the redox process involving one-electron oxidation from $[\text{Co}^{\text{III}}(\text{L-N}_4\text{tBu}_2)(\text{DCCat}^{2-})]^+$ to $[\text{Co}^{\text{III}}(\text{L-N}_4\text{tBu}_2)(\text{DCSQ}^{\bullet-})]^{2+}$. Although similar to this potential, the oxidation of the complex $[\text{Co}^{\text{II}}(\text{L-N}_4\text{tBu}_2)(\text{MeCN})_2]^{2+}$ occurs,^[122] but still the peak is assigned to the former redox process due to the fact that there is a presence of second oxidation peak at 1.60 V (third for **2b**) in the CV of **2e** which accounts for the irreversible oxidation of the formed low-spin cobalt(III) semiquinonate to low-spin cobalt(III) benzoquinone species. The formed low-spin cobalt(III) benzoquinone species dissociates to DCBQ and $[\text{Co}^{\text{III}}(\text{L-N}_4\text{tBu}_2)(\text{MeCN})_2]^{3+}$. The irreversible anodic potential at 938 mV in the CV of **2b** is assigned to the irreversible oxidation of BPh_4^- counter anion.

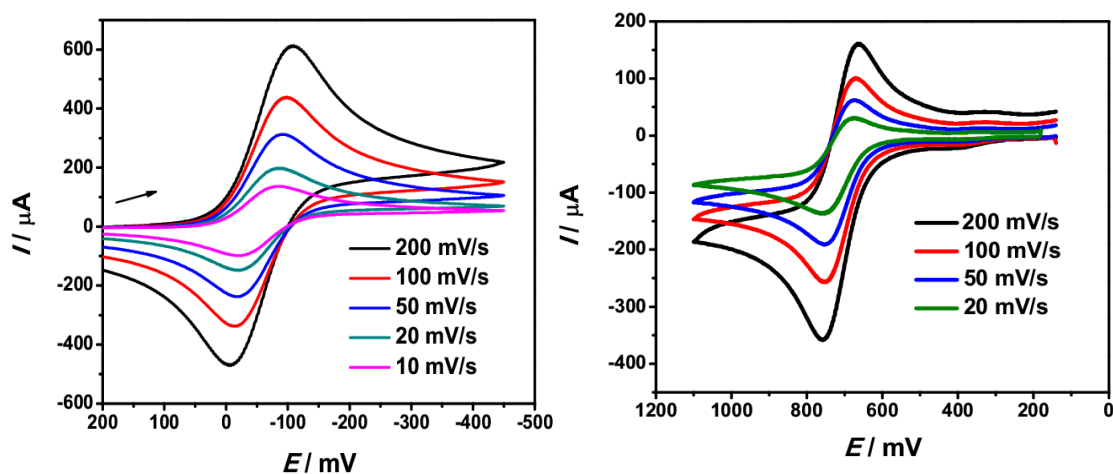


Figure 2.24: Cyclic voltammograms for first the reductive processes of **2b** (left) and first oxidative processes of **2e** (right) at different scan rates in 0.2 M TBAP/MeCN.

The comparison between the observed electrochemistry of **2b** and previously reported $[\text{Co}(\text{L-N}_{4t}\text{Bu}_2)(\text{DBSQ})][\text{B}(p\text{-Cl-Ph})_4]$ ^[33] reveals the effect of the presence of electronegative substituents in DCCat^{2-} unit. Here, one-electron oxidation of the high-spin cobalt(II) catecholate species resulted in formation of the low-spin cobalt(III) catecholate species, whereas the use of 3,5-di-*tert*-butylcatecholate as a dioxolene ligand resulted in formation of the corresponding low-spin cobalt(II) semiquinonate species from one-electron oxidation of the corresponding high-spin cobalt(II) catecholate species

The oxidation of high-spin cobalt(II) catecholate species occurs at $E_{1/2} = -626$ mV for the case where DBC^{2-} is dioxolene ligand,^[33,92] while with the use of DCCat^{2-} as dioxolene ligand the oxidation occurs at $E_{1/2} = -56$ mV. The higher oxidation potential of the $\text{HS-Co}^{\text{II}}\text{-DCCat}$ species than the $\text{HS-Co}^{\text{II}}\text{-DBC}$ species is the reason behind the observation of valence tautomerism for **2b**.

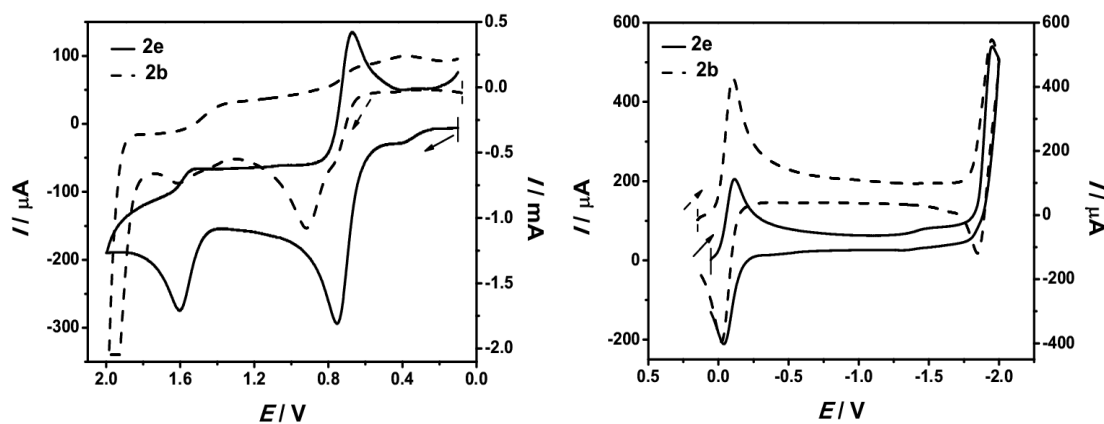


Figure 2.25: Cyclic voltammograms for the oxidative processes (left) and reductive processes (right) of **2b** and **2e** in 0.2 M TBAP/MeCN at $\nu = 100$ mV/s.

From the electrochemical point of view, the stabilization of the low-spin cobalt(III) semiquinonate species was not observed in the CV of $[\text{Co}(\text{L-N}_{4t}\text{Bu}_2)(\text{DBSQ})][\text{B}(p\text{-Cl-Ph})_4]$, but the observation of the formation of the low-spin cobalt(III) semiquinonate species for complex **2** can be explained, also, due to the presence of electronegative substituents because the radical of

the DCSQ^{•-} moiety in the low-spin cobalt(III) semiquinonate species is stabilized by the chloride substituents. Hence, the formation of the low-spin cobalt(III) catecholate species and the stabilization of the radical in one-electron oxidized low-spin cobalt(III) semiquinonate complex are explained by the presence of electronegative substituents in the dioxolene unit of **2**.

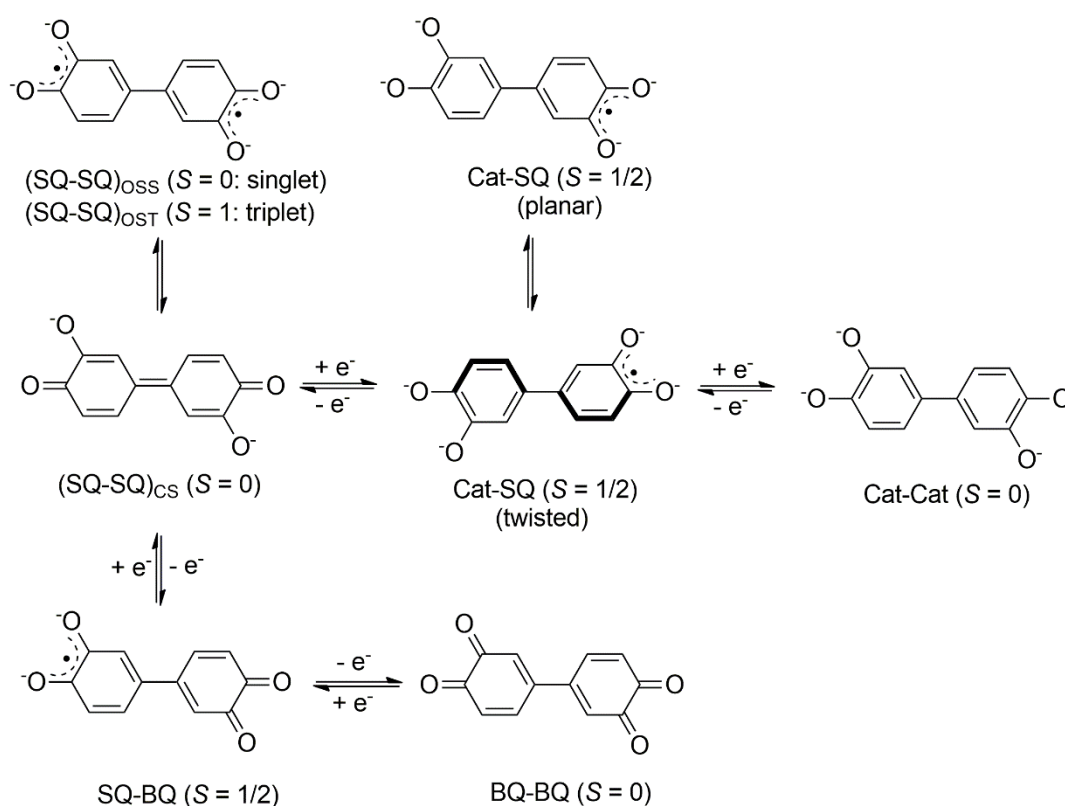
2.1.7 Brief Summary

In summary, UV/Vis/NIR, NMR and IR spectroscopic studies demonstrate that although the electronic state of **2** in compound **2b** in the solid state can be described by low-spin cobalt(III) catecholate state over the temperature range from low temperature to room temperature, the electronic state can be switched in solution state by changing the polarity of the utilized solvents and temperature. The change of entropy due to the solute-solvent interactions upon dissolution of the complex in different solvents plays one of the roles. While at room temperature in DCM, the VT_{LS-LS} equilibrium is predominated by the low-spin cobalt(II) semiquinonate species, in MeCN and DMSO, it is predominated by the low-spin cobalt(III) catecholate species. In DCM and MeCN, temperature-induced incomplete valence tautomerism from low-spin cobalt(III) catecholate to low-spin cobalt(II) semiquinonate state of **2b** is observed, but the critical temperature for the process VT_{LS-LS} is higher in MeCN than in DCM. The spin-state of the cobalt(II) ion in neutral cobalt(II) catecholate complex **1a** is high-spin state, but for the one-electron oxidized complex **2**, in its dissolved state, the low-spin state of the cobalt(II) ion is observed in the low-spin cobalt(II) semiquinonate complex. This displays that upon decreasing the π -donation properties and increasing the π -acceptance properties of the dioxolene ligand coordinated to the cobalt(II) ion, *i.e.*, by oxidizing DCCat²⁻ to DCSQ^{•-}, the spin-state of the cobalt(II) ion is switched from the high-spin to low-spin state.

2.2 Switching of Electronic States of Bis(dioxolene) Ligands Triggered by Cobalt(II) Based Temperature-Induced Spin-Crossover and Cobalt-Ligand Based Electron Transfer Processes

This section describes the changes in electronic states of cobalt bis(dioxolene) complexes. As described earlier, providing the right choice of ligands, *Krüger* and co-workers discovered the first spin-crossover cobalt dioxolene complex $[\text{Co}(\text{L-N}_4\text{tBu}_2)(\text{DBSQ})][\text{B}(p\text{-Cl-Ph})_4]$ in 2010.^[55,92] The key factors for the isolation of the above spin-crossover complex are the sufficient ligand-field strength provided by the ancillary ligand $\text{L-N}_4\text{tBu}_2$ and higher reduction potential of $\text{Co}^{\text{III}}/\text{Co}^{\text{II}}$ redox couple than the $\text{DBSQ}^{\bullet-}/\text{DBC}^{2-}$ redox couple in the complex $[\text{Co}(\text{L-N}_4\text{tBu}_2)(\text{DBSQ})]^+$. On the other hand, when redox potentials of the $\text{SQ}^{\bullet-}/\text{Cat}^{2-}$ and $\text{Co}^{\text{III}}/\text{Co}^{\text{II}}$ redox couples are comparable then valence tautomeric complexes could be isolated (see discussion in section 1.5). Following this principle and by using $\text{L-N}_4\text{tBu}_2$ as the ancillary ligand and DCCat^{2-} which is less oxidizable compared to DBC^{2-} , as the co-ligand, synthesis of complex **2b** was successful which shows a valence tautomerism between the low-spin cobalt(III) catecholate and low-spin cobalt(II) semiquinonate states which is different than the usually observed valence tautomeric transition from a low-spin cobalt(III) catecholate to high-spin cobalt(II) semiquinonate state (see discussion in section 2.1). Then, the focus was shifted towards the investigation of electronic interactions between cobalt centers and a bis(dioxolene) ligand in a cobalt bis(dioxolene) complex. Although, at the start of this work, there were some reports of cobalt bis(dioxolene) complexes,^[79,81–83,86] but none of the reports provides an example where at least one of the cobalt(II) centers possess a low-spin state. Since, it was found, by using $\text{L-N}_4\text{tBu}_2$ as an ancillary ligand, low-spin cobalt(II) semiquinonate complex could be isolated, therefore, in the hope of accessing the low-spin state of the cobalt(II) ion in a cobalt bis(dioxolene)

complex, the cobalt bis(dioxolene) complex was prepared, which contains $L-N_4tBu_2$ as ancillary ligands and a bis(dioxolene) ligand which is the dideprotonated form of 3,3'-dihydroxy-diphenylquinone-(4,4') ($H_2(SQ-SQ)$), as co-ligand. The bis(dioxolene) ligand is redox-active and it could coordinate to two metal centers in its various redox forms. The different redox-states of the bis(dioxolene) ligand are shown below (Scheme 2.4). Herein, the findings related to the discovery of a novel class of cobalt bis(dioxolene) complexes are discussed.



Scheme 2.4: The possibility of the various redox forms of the bis(dioxolene) ligand and their abbreviations which are according to their redox-states as well as spin-states.

2.2.1 Synthesis

All the compounds were synthesized under an inert atmosphere. The compound **3b** was synthesized by employing two synthetic methods. In the first method, the compound was prepared by two-electron oxidation of the *in situ* generated dark red colored complex $[Co_2(L-N_4tBu_2)_2(Cat-Cat)]$ (prepared

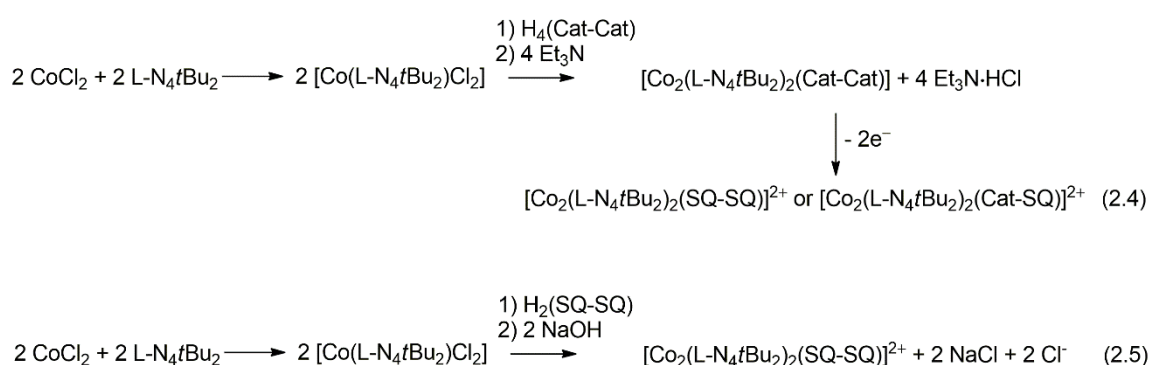
by reacting 2 equivalents of $[\text{Co}(\text{L-N}_{4t}\text{Bu}_2)\text{Cl}_2]$ with 1 equivalent of 3,3',4,4'-tetrahydroxybiphenyl in presence of 4 equivalents of triethylamine. The $[\text{Co}(\text{L-N}_{4t}\text{Bu}_2)\text{Cl}_2]$ was prepared *in situ* by reacting equimolar solutions of $\text{CoCl}_2 \cdot 6 \text{H}_2\text{O}$ and $\text{L-N}_{4t}\text{Bu}_2$ in methanol) by 2 equivalents of ferrocenium tetrafluoroborate in methanol. After metathesis of the resulting solution with 2 equivalents of sodium tetraphenylborate a dark green precipitate was formed. Multiple recrystallizations of the precipitate from $\text{MeCN}/\text{Et}_2\text{O}$ and then $\text{DMF}/\text{Et}_2\text{O}$, led to the isolation of $[\text{Co}_2(\text{L-N}_{4t}\text{Bu}_2)_2(\text{SQ-SQ})](\text{BPh}_4)_2 \cdot 4 \text{DMF}$ (**3b**) in a 50 % yield.

By an alternative second method, compound **3b** was prepared by avoiding the oxidation step. A solution of 1 equivalent of 3,3'-dihydroxy-diphenylquinone-(4,4') and 2 equivalents of sodium hydroxide in methanol was added to a violet solution of the complex $[\text{Co}(\text{L-N}_{4t}\text{Bu}_2)\text{Cl}_2]$ (2 equivalents) prepared *in situ* in methanol. The resulting reaction mixture was stirred and heated to reflux temperatures for multiple times. Then metathesis with 2 equivalents of sodium tetraphenylborate resulted in the formation of a dark green precipitate. Following two recrystallizations of the precipitate from $\text{DMF}/\text{Et}_2\text{O}$, the compound **3b** was isolated in a 45 % yield. Drying of **3b** at 100 °C *in vacuo* afforded $[\text{Co}_2(\text{L-N}_{4t}\text{Bu}_2)_2(\text{SQ-SQ})](\text{BPh}_4)_2$ (**3a**) in a 97 % yield.

The tetrafluoroborate as well as hexafluorophosphate salts were prepared by following procedures: The dark red solution of the complex $[\text{Co}_2(\text{L-N}_{4t}\text{Bu}_2)_2(\text{Cat-Cat})]$ was prepared *in situ* in methanol (prepared by following same method as above), and the solution was purged by pure dioxygen in presence of excess sodium tetrafluoroborate. The color of the solution immediately changed from dark red to dark green. A dark green colored solid began to precipitate from the solution. Multiple recrystallizations of the precipitate under an inert atmosphere from $\text{MeCN}/\text{Et}_2\text{O}$ produced an olive-green colored compound of $[\text{Co}_2(\text{L-N}_{4t}\text{Bu}_2)_2(\text{Cat-SQ})](\text{BF}_4)_2 \cdot \text{Et}_2\text{O}$ (**3d**) in a

47 % yield. The non-solvated compound $[\text{Co}_2(\text{L-N}_4\text{tBu}_2)_2(\text{Cat-SQ})](\text{BF}_4)_2$ (**3c**) was prepared by drying of **3d** at room temperature in vacuo. Use of potassium hexafluorophosphate instead of sodium tetrafluoroborate as metathesis reagent yielded the compound $[\text{Co}_2(\text{L-N}_4\text{tBu}_2)_2(\text{Cat-SQ})](\text{PF}_6)_2$ (**3e**) in a 41 % yield. A list of the abbreviations used for the prepared compounds is provided in Table 2.13.

A schematic illustration of the synthesis of the compounds is provided in Scheme 2.5.



Scheme 2.5: Synthesis of different salts of **3**.

Table 2.13: List of abbreviations for the synthesized cobalt bis(dioxolene) complexes

Compound	Abbreviation
$[\text{Co}_2(\text{L-N}_4\text{tBu}_2)_2(\text{SQ-SQ})]^{2+}$	3
$[\text{Co}_2(\text{L-N}_4\text{tBu}_2)_2(\text{SQ-SQ})](\text{BPh}_4)_2$	3a
$[\text{Co}_2(\text{L-N}_4\text{tBu}_2)_2(\text{SQ-SQ})](\text{BPh}_4)_2 \cdot 4 \text{DMF}$	3b
$[\text{Co}_2(\text{L-N}_4\text{tBu}_2)_2(\text{Cat-SQ})](\text{BF}_4)_2$	3c
$[\text{Co}_2(\text{L-N}_4\text{tBu}_2)_2(\text{Cat-SQ})](\text{BF}_4)_2 \cdot \text{Et}_2\text{O}$	3d
$[\text{Co}_2(\text{L-N}_4\text{tBu}_2)_2(\text{Cat-SQ})](\text{PF}_6)_2$	3e

2.2.2 Structural Characterization

The single crystal X-ray diffraction data for compound **3b** were collected at five different temperatures in the temperature range between 100 and 300 K at intervals of 50 K, whereas the single crystal X-ray diffraction data for compound **3d** were only collected at 150 K. The X-ray diffraction data of **3e**·solv (solv = unidentified solvent molecules) were collected at 150 K from a single crystal obtained by *n*-pentane diffusion into a dilute solution of **3e** in DCM. Although, the X-ray diffraction data is not of a high quality and the reproducibility of the crystals remains as a question,^[138] still, the data is discussed in order to clarify some metal–dioxolene bond nature found in compound **3d** (see below).

Perspective view of complex **3** in **3b** is shown in Figure 2.26 and the selected bond lengths and bond angles for **3b** are provided in Table 2.14 (100–200 K) and Table 2.15 (250–300 K). The compound **3b** crystallizes in the triclinic space group $P\bar{1}$. From the variable temperature X-ray diffraction analysis, it is evident that the crystal system and space group remain unaltered at all temperatures. Each cobalt center is coordinated to the four nitrogen donor atoms of the L-N₄tBu₂ ligand, and two *ortho*-oxygen donor atoms of one half of the bis(dioxolene) ligand. The macrocyclic ligand is folded along the N_{amine}–N_{amine} axis. The N(1)–Co–N(3) bond angle value of 149.51(9)° at 100 K which deviates from a perfect N_{axial}–Co–N_{axial} bond angle value of 180°, indicating that the coordination geometry around each cobalt center is best described as a distorted-octahedron. The two amine nitrogen donor atoms of L-N₄tBu₂ occupy the two axial positions, whereas both the pyridine nitrogen donor atoms of L-N₄tBu₂ occupy the equatorial positions (*cis*-positions) and the other two equatorial positions (*cis*-positions) are occupied by the two *ortho*-oxygen donor atoms of one half of the bis(dioxolene) ligand. The complex molecule shows a crystallographic inversion center in the center of

the C(26)–C(26A) bond which links both dioxolene rings in the bis(dioxolene) ligand. Thus, the asymmetric unit contains half of the complex cation, one BPh_4^- counter anion and two DMF molecules.

Figure 2.27 shows a graphical representation of the changes in selected bond lengths of the complex **3b** due to the change in temperature. For the two cobalt centers, the average of the Co– N_{py} bond lengths at 100 K is 1.930 Å, and upon increasing the temperature the value increases and at the temperatures 150, 200, 250 and 300 K, the averaged Co– N_{py} bond lengths are 1.978, 2.006, 2.018 and 2.023 Å, respectively. The average of the Co– N_{amine} bond lengths is 2.339 Å at 100 K and the value remains almost unchanged with increase in the temperature from 100 to 300 K. These bond length changes are consistent with the assignment of the electronic configurations of the two cobalt centers as low-spin electronic configurations at low temperatures and high-spin electronic configurations at high temperatures.^[32,55,92,123]

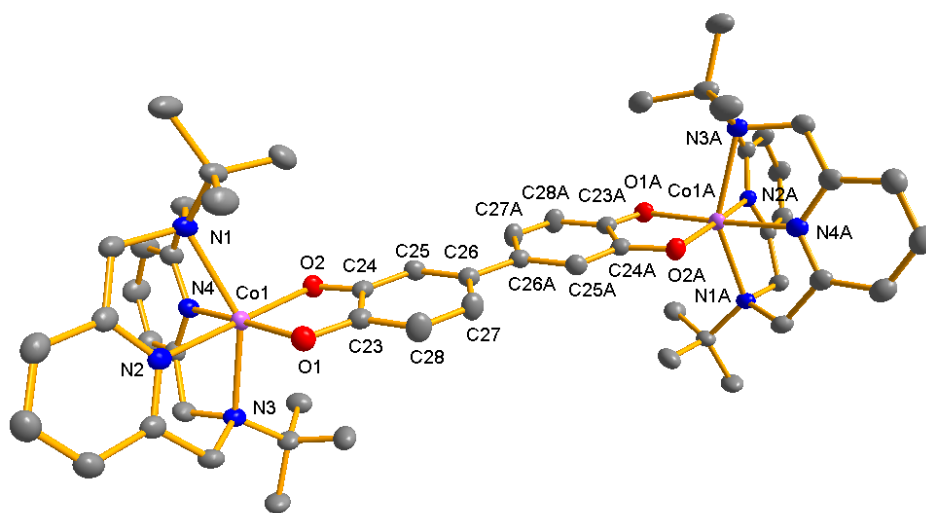


Figure 2.26: Perspective view of $[\text{Co}_2(\text{L-N}_4\text{tBu}_2)_2(\text{SQ-SQ})]^{2+}$ in **3b**, showing 50 % thermal ellipsoids at 100 K.

The Co–O(1) bond length is 1.911(1) Å at 100 K, and upon increasing the temperature this bond length increases and at the temperatures 150, 200, 250 and 300 K, the Co–O(1) bond lengths are 1.993(1), 2.044(1), 2.065(1) and 2.074(1) Å, respectively. Whereas the Co–O(2) bond length is 1.922(1) Å at 100 K, and upon increasing the temperature this bond length also increases and at the temperatures 150, 200, 250 and 300 K, the Co–O(2) bond lengths are 1.958(1), 1.982(1), 1.990(1) and 1.995(1) Å, respectively. The bond lengths of Co–O(1) and Co–O(2) at 100 K fall into the range of observed Co–O bond lengths for a low-spin cobalt(II) semiquinonate complex.^[55,92] Since, the redox-states of the cobalt centers are temperature invariant, therefore, the increase in the Co–O bond lengths upon increasing the temperature also indicates that the spin-states of the cobalt(II) centers are changed from low-spin to high-spin states.

Since, the two Co–O bond lengths are unequal at high temperatures, therefore, the two C(sp²)–O bonds of the bis(dioxolene) unit do not possess same bond order at high temperatures. The bond order changes of the C–O bonds of the (SQ-SQ)²⁻ ligand would entail the change in other bond lengths within the bis(dioxolene) ligand and thus, accompany the change in the electronic state of it (Scheme 2.4). Therefore, the changes in lengths of the various bonds within the bis(dioxolene) ligand are discussed. The discussion is as following: The C(26)–C(26A) bond length is 1.461(4) Å at 100 K, and upon increasing the temperature, the length of this bond decreases and at the temperatures 150, 200, 250 and 300 K, the C(26)–C(26A) bond lengths are 1.445(4), 1.439(4), 1.432(4) and 1.433(4) Å, respectively. The bond lengths of 1.433(4) and 1.461(4) Å fall into the range of commonly observed C(sp²)–C(sp²) double bond and C(sp²)–C(sp²) single bond, respectively.^[22,110]

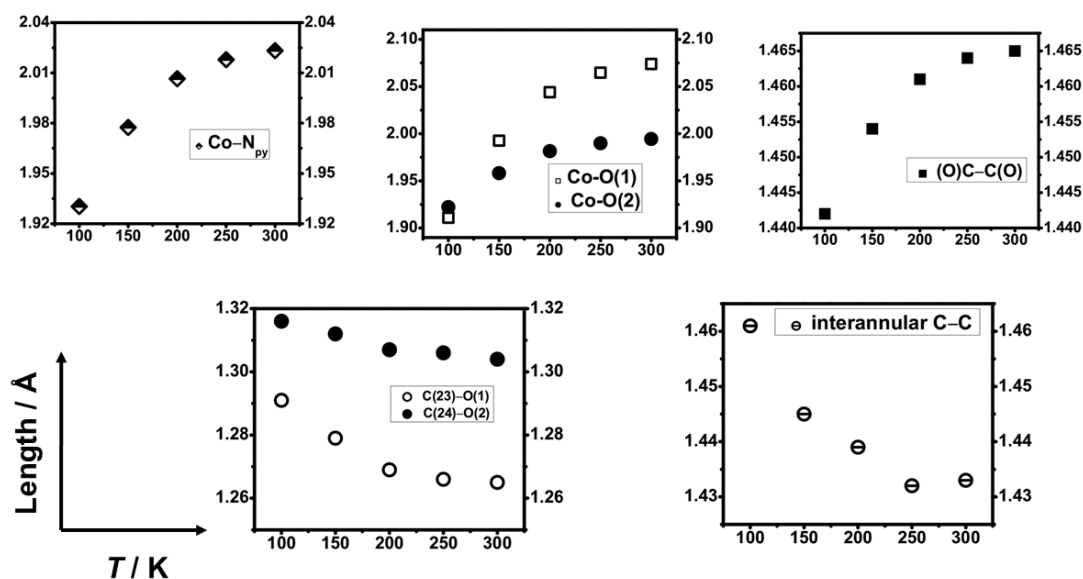


Figure 2.27: Temperature dependence of the Co–N_{py} and Co–O bond lengths as well as the C–O, interannular C–C and (O)C–C(O) bond lengths of **3b**.

The lengths of the C(24)–O(2) and C(23)–O(1) bonds are 1.316(2) and 1.291(2) Å, respectively at 100 K, and upon increasing the temperature, both bond lengths decrease. The C(24)–O(2) bond lengths are 1.312(2), 1.307(2), 1.306(2), 1.304(3) Å at 150, 200, 250, 300 K, respectively, whereas the C(23)–O(1) bond lengths are 1.279(2), 1.269(2), 1.266(2), 1.265(3) Å at 150, 200, 250, 300 K, respectively. The averaged C–O bond lengths of 1.304 Å at 100 K is consistent with the assignment of the C–O bonds to the carbon–oxygen semiquinonate bonds.^[14,55] However, the lengths of the C(23)–O(1) and C(24)–O(2) bonds at 300 K are consistent with the assignment of these bonds to the C(sp²)–O double bond and C(sp²)–O single bond, respectively.^[139]

In the asymmetric unit: The (O)C–C(O) bond length, *i.e.*, C(23)–C(24) bond length also increases upon increasing the temperature. The (O)C–C(O) bond lengths are 1.442(2), 1.454(3), 1.461(3), 1.464(3) and 1.465(3) Å at 100, 150, 200, 250 and 300 K, respectively. The bond length of 1.442(2) Å for the

(O)C–C(O) bond falls into the range for commonly observed values for more localized π -bonding characters of metal coordinated *o*-semiquinonate radicals.^[13,55] The bond length of 1.465(3) Å falls into the range for commonly observed C(sp²)–C(sp²) single bond.^[22,110]

The detailed investigations of the bond length changes in the bis(dioxolene) unit due to variation in temperature display that the bis(dioxolene) unit is in an open-shell biradicaloid form at low temperatures and in a closed-shell quinonoid form at high temperatures. Therefore, at low temperatures, the structural property of the complex **3** in **3b** is best described as two low-spin cobalt(II) centers bridged by a biradicaloid form of the bis(dioxolene) unit. Whereas at high temperatures, it is best described as two high-spin cobalt(II) centers bridged by a closed-shell quinonoid form of the bis(dioxolene) unit. Thus, by considering the X-ray crystallographic measurements at different temperatures, the conversion between these two structural forms of the complex is described as spin-crossover from LS-Co^{II}-(SQ-SQ)_{OS}-Co^{II}-LS to HS-Co^{II}-(SQ-SQ)_{CS}-Co^{II}-HS state.

Table 2.14: Selected bond lengths [\AA] and bond angles [deg] for **3b** at 100, 150 and 200 K.

	<i>T</i> = 100 K	<i>T</i> = 150 K	<i>T</i> = 200 K
Co(1)–O(1)	1.911(1)	1.993(1)	2.044 (1)
Co(1)–O(2)	1.922(1)	1.958(1)	1.982(1)
Co(1)–N(2)	1.927(1)	1.975(1)	2.007(2)
Co(1)–N(4)	1.934(2)	1.980(2)	2.006(2)
Co(1)–N(3)	2.339(1)	2.341(1)	2.342(2)
Co(1)–N(1)	2.341(1)	2.335(2)	2.338(2)
O(1)–C(23)	1.291(2)	1.279(2)	1.269(2)
O(2)–C(24)	1.316(2)	1.312(2)	1.307(2)
C(23)–C(28)	1.411(3)	1.417(3)	1.427(3)
C(23)–C(24)	1.442(2)	1.454(3)	1.461(3)
C(24)–C(25)	1.392(3)	1.385(3)	1.384(3)
C(25)–C(26)	1.402(3)	1.409(3)	1.410(3)
C(26)–C(27)	1.435(3)	1.442(3)	1.444(3)
C(27)–C(28)	1.360(3)	1.353(3)	1.344(3)
C(26)–C(26A)	1.461(4)	1.445(4)	1.439(4)
Co(1)–Co(1A)	11.542	11.634	11.693
O(2)–Co(1)–O(1)	84.69(5)	82.68(5)	81.42(5)
O(2)–Co(1)–N(4)	93.54(5)	95.83(6)	97.35(6)
O(1)–Co(1)–N(4)	176.40(6)	176.25(6)	176.36(6)
O(2)–Co(1)–N(2)	176.16(5)	174.84(6)	173.88(6)
O(1)–Co(1)–N(2)	91.98(6)	92.61(6)	92.89(6)
N(4)–Co(1)–N(2)	89.89(6)	88.99(6)	88.46(6)
O(2)–Co(1)–N(3)	96.43(5)	105.64(6)	106.48(6)
O(1)–Co(1)–N(3)	104.47(5)	96.95(6)	97.35(6)
N(4)–Co(1)–N(3)	80.86(6)	80.11(6)	79.67(6)
N(2)–Co(1)–N(3)	77.77(6)	76.96(6)	76.36(6)
O(2)–Co(1)–N(1)	97.84(5)	99.01(6)	99.75(6)
O(1)–Co(1)–N(1)	105.50(5)	106.46(6)	106.89(6)
N(4)–Co(1)–N(1)	77.82(6)	77.15(6)	76.68(6)
N(2)–Co(1)–N(1)	81.18(6)	80.24(6)	79.68(6)
N(3)–Co(1)–N(1)	149.91(5)	147.87(6)	146.56(6)

Table 2.15: Selected bond lengths [\AA] and bond angles [deg] for **3b** at 250 and 300 K.

	<i>T</i> = 250 K	<i>T</i> = 300 K
Co(1)–O(1)	2.065(1)	2.074(1)
Co(1)–O(2)	1.990 (1)	1.995(1)
Co(1)–N(2)	2.019(2)	2.023(2)
Co(1)–N(4)	2.017(2)	2.023(2)
Co(1)–N(3)	2.347(2)	2.345(2)
Co(1)–N(1)	2.338(2)	2.341(2)
O(1)–C(23)	1.266(2)	1.265(3)
O(2)–C(24)	1.306(2)	1.304(3)
C(23)–C(28)	1.423(3)	1.425(3)
C(23)–C(24)	1.464(3)	1.465(3)
C(24)–C(25)	1.384(3)	1.382(3)
C(25)–C(26)	1.410(3)	1.406(3)
C(26)–C(27)	1.445(3)	1.446(3)
C(27)–C(28)	1.343(3)	1.342(3)
C(26)–C(26A)	1.432(4)	1.433(4)
Co(1)–Co(1A)	11.709	11.718
O(2)–Co(1)–O(1)	80.98(5)	80.64(6)
O(2)–Co(1)–N(4)	97.89(6)	98.25(7)
O(1)–Co(1)–N(4)	176.61(7)	177.03(7)
O(2)–Co(1)–N(2)	173.49(7)	173.31(7)
O(1)–Co(1)–N(2)	92.90(6)	92.98(6)
N(4)–Co(1)–N(2)	88.35(7)	88.22(7)
O(2)–Co(1)–N(3)	106.73(6)	106.73(7)
O(1)–Co(1)–N(3)	97.84(6)	98.31(7)
N(4)–Co(1)–N(3)	79.36(6)	79.34(7)
N(2)–Co(1)–N(3)	76.14(6)	76.06(7)
O(2)–Co(1)–N(1)	100.11(6)	100.48(7)
O(1)–Co(1)–N(1)	106.65(6)	106.36(7)
N(4)–Co(1)–N(1)	76.68(6)	76.53(7)
N(2)–Co(1)–N(1)	79.46(7)	79.27(7)
N(3)–Co(1)–N(1)	146.07(6)	145.77(7)

The single crystal X-ray diffraction data for **3d** were collected at 150 K. The perspective view of **3** in **3d** is shown in Figure 2.28 and the data for the selected bond lengths and bond angles of **3d** are provided in Table 2.16. The compound crystallizes in the monoclinic space group $P2_1/c$. The identification of the solvent molecule in the crystal as diethyl ether and the determination of its content in the crystal are based on NMR spectroscopic results (see Figure A.90 in appendix) and elemental analysis. The data provided in Table 2.16 are modified data obtained from manipulation of the originally collected X-ray diffraction data by SQUEEZE option in the program PLATON. The coordination mode of each cobalt center with the nitrogen donor atoms of the macrocyclic ligand L-N_{4t}Bu₂, and two of the *ortho*-oxygen donor atoms of one half of the bis(dioxolene) ligand, is similar to the coordination mode of the cobalt center in **3b**. Here, also, the coordination geometry around each cobalt center is a distorted-octahedral because the N_{amine}-Co-N_{amine} bond angle value is 153.02(6)°, which deviates from an ideal octahedral N_{axial}-Co-N_{axial} bond angle value of 180°. A center of symmetry is situated in the center of C(26)-C(26A) bond which connects the two dioxolene rings of the bis(dioxolene) ligand. Thus, the asymmetric unit contains half of the complex and one BF₄⁻ counter anion.

For the two cobalt centers, the average of the Co-N_{amine} bond lengths is 2.247 Å and the average of the Co-N_{py} bond lengths is 1.898 Å, whereas the average of the Co-O bond lengths is 1.884 Å. The C-O, (O)C-C(O), C(26)-C(26A) bond lengths in the bis(dioxolene) ligand are 1.322(2), 1.423(3), 1.485(4) Å, respectively. Among these bond lengths, the bond length of 1.485(4) Å for C(26)-C(26A) bond is in the range for C(sp²)-C(sp²) single bond between the biphenyl units.^[22,110] Table 2.17 provides the selected data for a low-spin cobalt(III) catecholate complex and a low-spin cobalt(II) semiquinonate complex containing L-N_{4t}Bu₂ as ancillary ligands, and the average

cobalt–ligand donor atom (Co–L) bond lengths of these two redox isomers. All the observed Co–L bond lengths of **3d** are similar to the arithmetic average of the Co–L bond lengths of a low-spin cobalt(III) catecholate complex and a low-spin cobalt(II) semiquinonate complex. Thus, one of the explanations from the observed bond lengths is that low-spin cobalt(III) and low-spin cobalt(II) centers are bridged by the (Cat-SQ)^{•3-} ligand which is one-electron reduced redox form of the (SQ-SQ)²⁻ ligand, and the electronic state of the complex **3** in **3d** is LS-Co^{III}-Cat-SQ-Co^{II}-LS at 150 K.

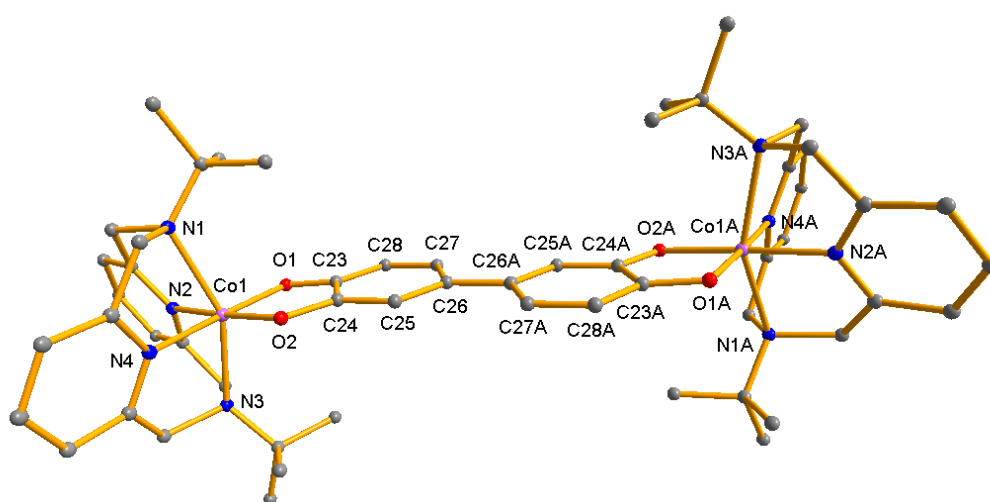


Figure 2.28: Perspective view of $[\text{Co}_2(\text{L-N}_4\text{tBu}_2)_2(\text{Cat-SQ})]^{2+}$ in **3d**, showing 50 % thermal ellipsoids at 150 K.

Another explanation of the structural data can be due to the equal mixtures of complexes $[\{\text{LS-Co}^{\text{III}}\text{-L-N}_4\text{tBu}_2\}(\text{Cat-Cat})^{4-}\{\text{LS-Co}^{\text{III}}\text{-L-N}_4\text{tBu}_2\}]^{2+}$ and $[\{\text{LS-Co}^{\text{II}}\text{-L-N}_4\text{tBu}_2\}(\text{SQ-SQ})_{\text{OS}}^{2-}\{\text{LS-Co}^{\text{II}}\text{-L-N}_4\text{tBu}_2\}]^{2+}$. However, the magnetic data exclude this possibility (see discussion in section 2.2.3). The X-ray diffraction data of **3e**·solv (see below) suggest that the radical is situated on the semiquinonate site of $[\{\text{LS-Co}^{\text{III}}\text{-L-N}_4\text{tBu}_2\}(\text{Cat-SQ})^{\bullet 3-}\{\text{LS-Co}^{\text{II}}\text{-L-N}_4\text{tBu}_2\}]^{2+}$ and the semiquinonate and catecholate halves of the (Cat-SQ)^{•3-} moiety are coordinated to the low-spin cobalt(II) and low-spin cobalt(III) ions, respectively.

Table 2.16: Selected bond lengths [\AA] and bond angles [deg] for **3d** at 150 K.

	$T = 150 \text{ K}$
Co(1)–O(2)	1.881(1)
Co(1)–O(1)	1.887(2)
Co(1)–N(2)	1.895(1)
Co(1)–N(4)	1.901(2)
Co(1)–N(3)	2.245(2)
Co(1)–N(1)	2.249(2)
O(1)–C(23)	1.322(2)
O(2)–C(24)	1.331(2)
C(23)–C(28)	1.392(3)
C(23)–C(24)	1.423(3)
C(24)–C(25)	1.385(3)
C(25)–C(26)	1.399(3)
C(26)–C(27)	1.416(3)
C(26)–C(26A)	1.485(4)
Co(1)–Co(1A)	11.472
O(2)–Co(1)–O(1)	86.66(6)
O(2)–Co(1)–N(2)	176.77(6)
O(1)–Co(1)–N(2)	90.43(6)
O(2)–Co(1)–N(4)	92.16(6)
O(1)–Co(1)–N(4)	178.10(6)
N(2)–Co(1)–N(4)	90.79(6)
O(2)–Co(1)–N(3)	102.75(6)
O(1)–Co(1)–N(3)	96.75(6)
N(2)–Co(1)–N(3)	78.97(6)
N(4)–Co(1)–N(3)	82.06(6)
O(2)–Co(1)–N(1)	96.84(6)
O(1)–Co(1)–N(1)	102.79(6)
N(2)–Co(1)–N(1)	82.43(6)
N(4)–Co(1)–N(1)	78.82(6)
N(3)–Co(1)–N(1)	153.02(6)

Table 2.17: Selected Co–N, C–O bond lengths [\AA] for low-spin cobalt(III) catecholate and low-spin cobalt(II) semiquinonate^[55] complexes containing L-N₄tBu₂ as ancillary ligand and arithmetic average of the corresponding bond lengths observed in these two redox isomers [\AA].

Bond	Length/ \AA for LS-Co(III)-Cat ^[a]	Length/ \AA for LS-Co(II)-SQ	Arithmetic average length/ \AA
Co–N _{amine}	2.138	2.339	2.238
Co–N _{py}	1.880	1.931	1.905
Co–O	1.879	1.890	1.884
C–O	1.343	1.313	1.328

^[a] The bond lengths which are observed for compounds **2c**, **2d** and **3e**·solv have been provided.

The perspective view of **3** in **3e**·solv is shown in Figure 2.29, and the data for the selected bond lengths and bond angles are given in Table 2.18. The compound **3e**·solv crystallizes in the monoclinic space group *P121/n1*. The coordination mode of each cobalt center with one L-N₄tBu₂ and one-half of the bis(dioxolene) ligand is similar to the cobalt centers of **3** in **3b** and **3d**. The coordination environment around each cobalt center is a distorted-octahedron which is confirmed by the deviation of the N_{amine}–Co–N_{amine} bond angle values (150.0(2)–155.0(2) \AA) from a perfect N_{axial}–Co–N_{axial} bond angle value of 180°. In contrast to the crystal structures of **3b** and **3d**, the crystal structure of **3** in **3e**·solv does not show any center of symmetry in the center of C(27)–C(33) bond which links the two dioxolene rings of the bis(dioxolene) ligand. Thus, the asymmetric unit contains the whole complex, two hexafluorophosphate counter anions and unidentified solvent molecules.

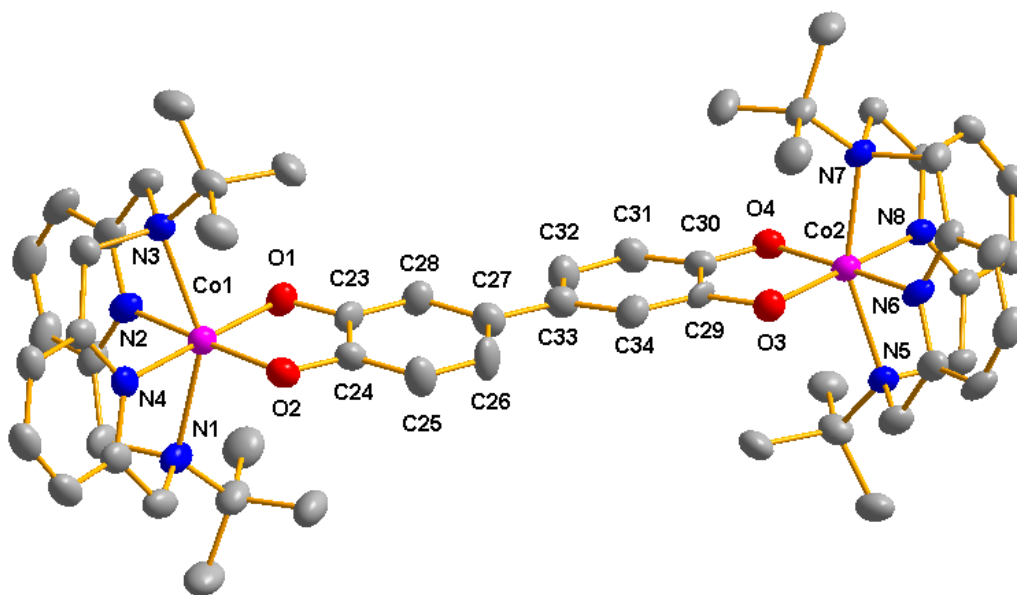


Figure 2.29: Perspective view of $[\text{Co}_2(\text{L-N}_4\text{tBu}_2)_2(\text{Cat-SQ})]^{2+}$ in $3\mathbf{e}\cdot\text{solv}$, showing 50 % thermal ellipsoids at 150 K.

In order to simplify the discussion, the asymmetric unit is divided into two parts *i.e.* first half and second half of the asymmetric unit where the first half contains one cobalt dioxolene unit and the second half contains the other cobalt dioxolene unit. In the first half of the asymmetric unit, the $\text{Co}(1)\text{-N}_{\text{amine}}$ and $\text{Co}(1)\text{-N}_{\text{py}}$ bond lengths are in the range of 2.315(5)–2.333(5) Å and 1.928(5)–1.918(5) Å, respectively. The $\text{Co}(1)\text{-(O)}$ and C-O bond lengths are in the range of 1.897(4)–1.907(5) Å and 1.304(7)–1.325(8) Å, respectively. These bond lengths are consistent with the assignment of the electronic configuration and oxidation state of the cobalt center as the low-spin cobalt(II).^[55,92] The bond lengths within the dioxolene unit are 1.403(9), 1.426(9), 1.387(9), 1.376(10), 1.416(9) and 1.406(9) Å for the $\text{C}(23)\text{-C}(28)$, $\text{C}(23)\text{-C}(24)$, $\text{C}(24)\text{-C}(25)$, $\text{C}(25)\text{-C}(26)$, $\text{C}(26)\text{-C}(27)$ and $\text{C}(27)\text{-C}(28)$ bonds, respectively. These bond lengths are typical for a metal coordinated *ortho*-semiquinonate ligand.^[55,92] From the above discussion of bond lengths, it can be firmly said that the first half of the asymmetric unit contains a low-spin cobalt(II) semiquinonate moiety.

In the second half of the asymmetric unit, the Co(2)–N_{amine} and Co(2)–N_{py} bond lengths are in the range of 2.146(5)–2.170(5) Å and 1.885(5)–1.890(5) Å, respectively. The Co(2)–(O) and C–O bond lengths are in the range of 1.871(4)–1.892(4) Å and 1.336(7)–1.339(7) Å, respectively. These bond lengths are similar with the observed Co–L bond lengths in complex **2b** which has a low-spin cobalt(III) catecholate ground electronic state. The bond lengths within the dioxolene unit are 1.422(9), 1.376(9), 1.380(9), 1.411(9), 1.412(9) and 1.382(9) Å for the C(29)–C(30), C(30)–C(31), C(31)–C(32), C(32)–C(33), C(33)–C(34) and C(29)–C(34) bonds, respectively. These bond lengths are typical for a metal coordinated catecholate ligand.^[55,92]

The C(27)–C(33) bond length is 1.472(9) Å and it falls into the range for commonly observed length of C(sp²)–C(sp²) single bond between biphenyl units.^[22,110] From the above discussion related to the various bond lengths, it can be conclusively said that the second half of the asymmetric unit contains a low-spin cobalt(III) catecholate moiety, and it is linked with the low-spin cobalt(II) semiquinonate moiety by a C(sp²)–C(sp²) single bond. Thus, the electronic state of **3** in **3e**·solv can be best described by LS-Co^{III}-Cat-SQ-Co^{II}-LS state at 150 K.

Table 2.18: Selected bond lengths [\AA] and bond angles [$^\circ$] of **3** in **3e**·solv at 150 K.

First half of the asymmetric unit		Second half of the asymmetric unit	
Co(1)–O(2)	1.907(5)	Co(2)–O(3)	1.871(4)
Co(1)–O(1)	1.897(4)	Co(2)–O(4)	1.892(4)
Co(1)–N(2)	1.928(5)	Co(2)–N(8)	1.885(5)
Co(1)–N(4)	1.918(5)	Co(2)–N(6)	1.890(5)
Co(1)–N(3)	2.315(5)	Co(2)–N(7)	2.146(5)
Co(1)–N(1)	2.333(5)	Co(2)–N(5)	2.170(5)
O(1)–C(23)	1.304(7)	C(29)–O(3)	1.336(7)
O(2)–C(24)	1.325(8)	C(30)–O(4)	1.339(7)
C(23)–C(28)	1.403(9)	C(29)–C(30)	1.422(9)
C(23)–C(24)	1.426(9)	C(30)–C(31)	1.376(9)
C(24)–C(25)	1.387(9)	C(31)–C(32)	1.380(9)
C(25)–C(26)	1.376(10)	C(32)–C(33)	1.411(9)
C(26)–C(27)	1.416(9)	C(33)–C(34)	1.412(9)
C(27)–C(28)	1.406(9)	C(29)–C(34)	1.382(9)
C(27)–C(33)	1.472(9)	C(33)–C(27)	1.472(9)
Co(1)–Co(2)	11.480	Co(2)–Co(1)	11.480
O(2)–Co(1)–O(1)	85.4(2)	O(3)–Co(2)–N(8)	177.0(2)
O(2)–Co(1)–N(2)	175.9(2)	O(3)–Co(2)–N(6)	88.4(2)
O(1)–Co(1)–N(2)	90.9(2)	N(8)–Co(2)–N(6)	94.1(2)
O(2)–Co(1)–N(4)	92.7(2)	O(3)–Co(2)–O(4)	87.9(2)
O(1)–Co(1)–N(4)	177.9(2)	N(8)–Co(2)–O(4)	89.6(2)
N(2)–Co(1)–N(4)	91.1(2)	N(6)–Co(2)–O(4)	176.2(2)
O(2)–Co(1)–N(3)	103.8(2)	O(3)–Co(2)–N(7)	101.9(2)
O(1)–Co(1)–N(3)	98.3(2)	N(8)–Co(2)–N(7)	80.1(2)
N(2)–Co(1)–N(3)	78.2(2)	N(6)–Co(2)–N(7)	84.1(2)
N(4)–Co(1)–N(3)	81.3(2)	O(4)–Co(2)–N(7)	95.5(2)
O(2)–Co(1)–N(1)	98.3(2)	O(3)–Co(2)–N(5)	95.3(2)
O(1)–Co(1)–N(1)	103.4(2)	N(8)–Co(2)–N(5)	83.4(2)
N(2)–Co(1)–N(1)	81.0(2)	N(6)–Co(2)–N(5)	79.7(2)
N(4)–Co(1)–N(1)	77.7(2)	O(4)–Co(2)–N(5)	101.6(2)
N(3)–Co(1)–N(1)	150.0(2)	N(7)–Co(2)–N(5)	155.0(2)

2.2.3 Magnetic Properties

The magnetic susceptibility data for **3b** were collected with a SQUID magnetometer in the temperature range 2–300 K. The repeated measurements with two different batches of the sample display reproducibility of the observed magnetic properties. The $\chi_M T$ vs. T plots from the repeated measurements are shown in Figure 2.30. The plot corresponding to the measurement in the temperature range 2–300 K refers to the measurement of the first batch of sample. The plots corresponding to the measurements in the temperature ranges 2–295 K and 2–320 K refer to the measurement of the second batch of sample.

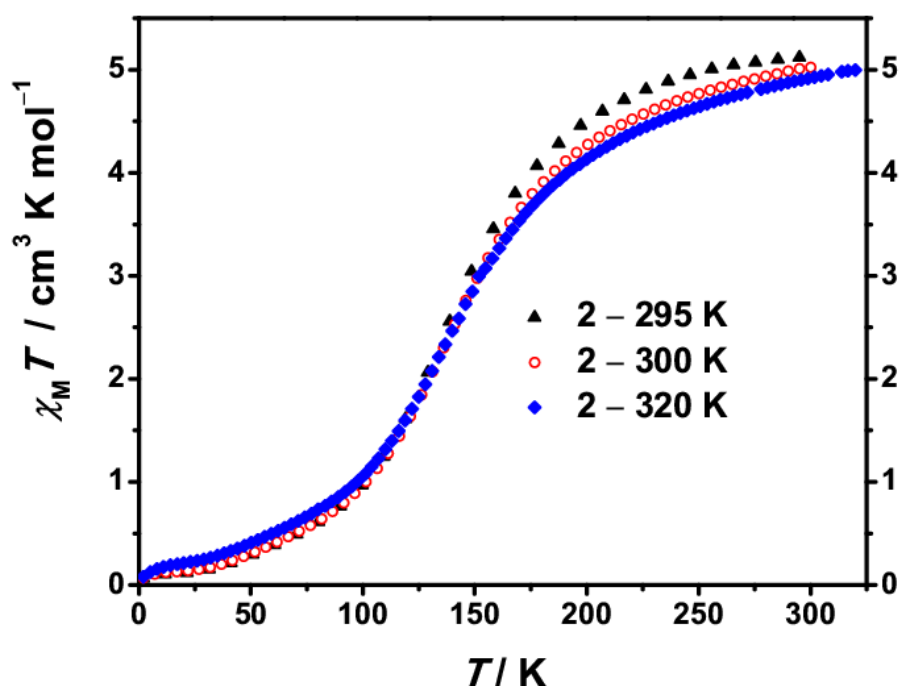
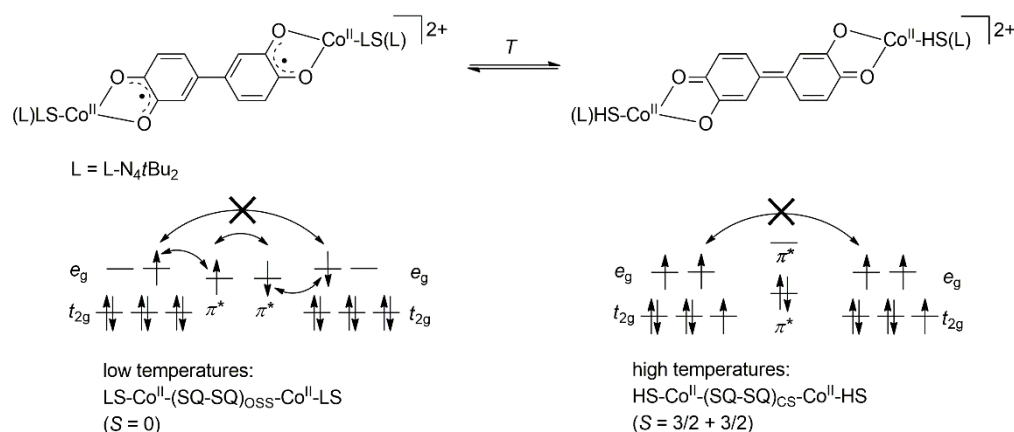


Figure 2.30: Variation of $\chi_M T$ product with temperature for solid **3b**. The empty red circles correspond to the one batch of sample. The filled black triangle and filled blue diamonds correspond to another batch of sample.

To discuss the magnetic properties, the $\chi_M T$ vs. T plot is divided into two parts: The $\chi_M T$ value of $0.107 \text{ cm}^3 \text{K mol}^{-1}$ remains almost unchanged over the temperature range 6–30 K, and this value corresponds to an $S = 0$ species.

Hence, if the data of the X-ray crystal structure determination at low temperatures are taken into account, then the diamagnetic state can only be explained for the case when strong antiferromagnetic coupling between the two unpaired electrons in the open-shell biradicaloid form of the bis(dioxolene) unit exists (*i.e.*, the bis(dioxolene) ligand is in an open-shell singlet electronic state), and each unpaired electron of the low-spin cobalt(II) center is ferromagnetically coupled to the unpaired electron in the *o*-dioxolene half of the bis(dioxolene) unit (Scheme 2.6). The ferromagnetic coupling between the low-spin cobalt(II) center and semiquinonate moiety is taken into account instead of the antiferromagnetic coupling because the unpaired electron of the low-spin cobalt(II) ion resides in the σ -antibonding d_z^2 orbital, whereas the unpaired electron of semiquinonate radical is situated in a π^* -molecular orbital. Since, both the orbitals are orthogonal to each other, a ferromagnetic coupling between the low-spin cobalt(II) ion and the semiquinonate radical is expected.^[55,92]



Scheme 2.6: Temperature-induced spin transitions for the cobalt(II) centers accompanied by singlet open-shell to closed-shell state conversion for the bis(dioxolene) ligand in solid state of **3b**. The double headed curved arrows represent the interaction between the unpaired electrons.

However, the most significant changes in magnetic susceptibility occur over the temperature range 30–300 K. The $\chi_M T$ value gradually increases upon

increasing the temperature from 30 K, and at 300 K the curve almost reaches a plateau where the $\chi_M T$ value is $5.01 \text{ cm}^3 \text{ K mol}^{-1}$. From the variable temperature structural characterization, it is evident that at high temperatures, two high-spin cobalt(II) centers are bridged by the closed-shell quinonoid form of the bis(dioxolene) unit. The $\chi_M T$ value of $5.01 \text{ cm}^3 \text{ K mol}^{-1}$ ($\mu_{\text{eff}} = 6.33 \mu_B$) corresponds to the expected value for two very weakly interacting or non-interacting high-spin cobalt(II) ions bridged by the diamagnetic closed-shell quinonoid form of the bis(dioxolene) unit ($S = 2 \times 3/2$).^[32,54] Therefore, the increase in the $\chi_M T$ value strongly suggests the spin transition for the two cobalt(II) ions is accompanied by the singlet open-shell to singlet closed-shell state conversion of the bis(dioxolene) unit (SQ-SQ)²⁻.

The emergence of any other electronic state except these two electronic states is discarded because the curves corresponding to the variation of the bond lengths with temperature (Figure 2.27) and the curve corresponding to the variation of $\chi_M T$ with T (Figure 2.30) have similar shapes in the temperature range of 100–300 K.

The temperature dependence of the magnetic susceptibility for the non-solvated compound **3c** is shown in Figure 2.31. The measurements with one substance in the temperature range 2–350 K display reproducibility of the observed magnetic properties. The measurement of the substance was started at 295 K, and then temperature was gradually decreased to 2 K (curve corresponding to the temperature range 295–2 K). Then, the temperature was gradually increased to 350 K. After that the temperature was again gradually decreased to 2 K (curve corresponding to the temperature range 2–350 K).

To discuss the magnetic properties, the $\chi_M T$ vs. T plot is divided into two parts: In the temperature range 30–175 K, the curve shows a plateau with $\chi_M T$ value of $1.112 \text{ cm}^3 \text{ K mol}^{-1}$. This $\chi_M T$ value is in the range for expected values for a

low-spin cobalt(II) semiquinonate ($S = 1$) complexes.^[55] Therefore, the possibility of equal mixtures of LS-Co^{III}-Cat-Cat-Co^{III}-LS and LS-Co^{II}-(SQ-SQ)_{OSS}-Co^{II}-LS states is discarded. Below 30 K, the $\chi_M T$ value falls to a value of $0.18 \text{ cm}^3 \text{ K mol}^{-1}$ and this is attributed due to the zero field splitting.^[55]

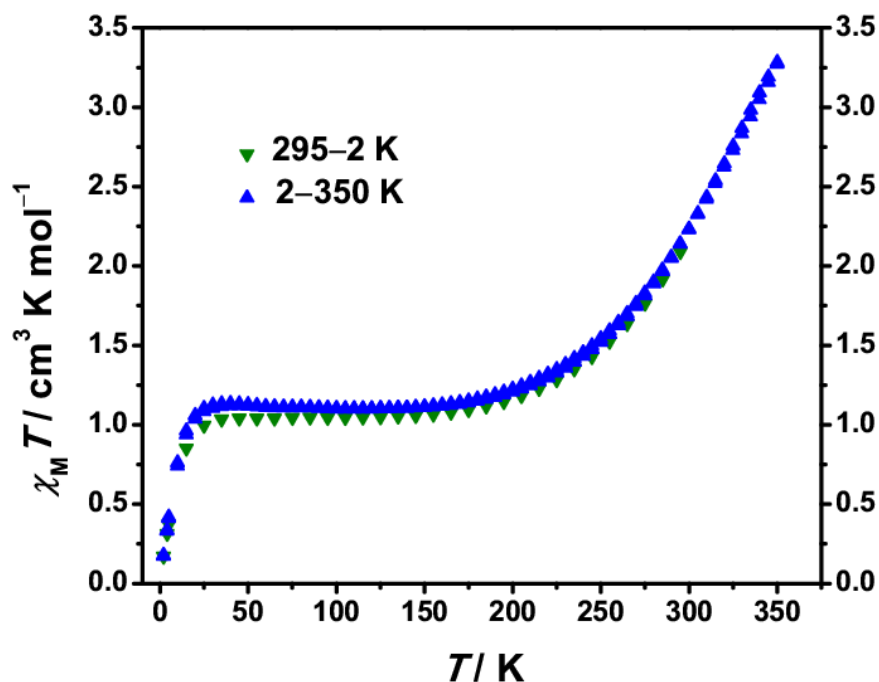
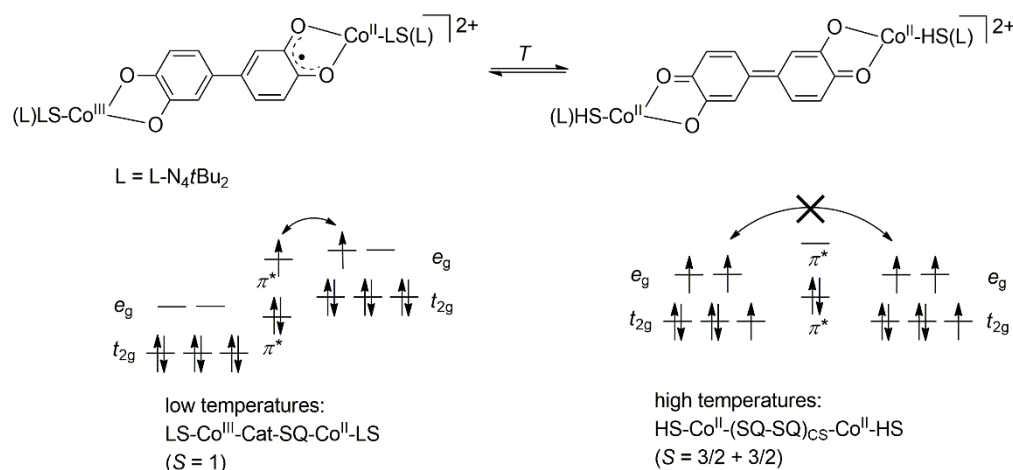


Figure 2.31: Variation of $\chi_M T$ product with temperature for solid **3c**.

However, after raising the temperature from 175 to 350 K, there is a continuous increase in the $\chi_M T$ value, and at 350 K, the $\chi_M T$ value is $3.29 \text{ cm}^3 \text{ K mol}^{-1}$ ($\mu_{\text{eff}} = 5.13 \mu_B$). The responsible process for the changes in the electronic states is incomplete at 350 K. There are two reasonable possibilities for such changes in the electronic states. The first possibility arises from the observed magnetic data, is that, after 175 K upon increasing the temperature the low-spin cobalt(III) catecholate half of the complex undergoes valence tautomeric conversion and converts to high-spin cobalt(II) semiquinonate state, whereas the low-spin cobalt(II) center of the low-spin cobalt(II) semiquinonate half undergoes spin transition, and the low-spin cobalt(II) semiquinonate half converts to high-spin cobalt(II) semiquinonate state. Thus,

the changes in the electronic and redox-states of the cobalt centers lead to the change in electronic state of the bis(dioxolene) unit from catecholatesemiquinonate state to closed-shell semiquinonatesemiquinonate state (Scheme 2.7).



Scheme 2.7: Temperature-induced valence tautomeric transition for the low-spin cobalt(III) center accompanied by spin transition for the cobalt(II) center and redox-state changes of the bis(dioxolene) unit from catecholatesemiquinonate to closed-shell semiquinonatesemiquinonate state in solid state of **3c**. The double headed curved arrows represent the interaction between the unpaired electrons.

The second possibility is the conversion from LS-Co^{III}-Cat-SQ-Co^{II}-LS to LS-Co^{III}-Cat-SQ-Co^{II}-HS state. If the possibility of the existence of LS-Co^{III}-Cat-SQ-Co^{II}-HS state is assumed, then the maximum $\chi_M T$ value should reach a plateau near the value of 3.3–3.5 cm³ K mol⁻¹,^[95] but the plateau has not started at 350 K. Thus, it is likely that the excited state of **3c** will have higher $\chi_M T$ value than 3.29 cm³ K mol⁻¹.

Furthermore, the (Cat-SQ)^{•3-} unit and (SQ-SQ)_{CS}²⁻ units can be differentiated by infrared spectroscopy. The ATR spectra of the compounds **3c** and **3d** support the existence of HS-Co^{II}-(SQ-SQ)_{CS}-Co^{II}-HS state at high temperatures (see the discussion in section 2.2.4). Thus, the infrared spectroscopic investigation is also pointing towards the excited state of the

complex to be the HS-Co^{II}-(SQ-SQ)_{CS}-Co^{II}-HS state. Nonetheless, it is evident that the ground electronic state of **3c** is LS-Co^{III}-Cat-SQ-Co^{II}-LS and one of the possible excited states is HS-Co^{II}-(SQ-SQ)_{CS}-Co^{II}-HS state (Scheme 2.7).

The high-spin molar fraction vs. temperature plot of compound **3b** is shown in Figure 2.32. The γ_{HS} values at different temperatures have been calculated from the observed $\chi_{\text{M}}T$ value at those temperatures, and by considering the $\chi_{\text{M}}T$ values of 0.112 ($\chi_{\text{M}}T_{\text{LS}}$) and 5.20 cm³ K mol⁻¹ ($\chi_{\text{M}}T_{\text{HS}}$) for entirely LS-Co^{II}-(SQ-SQ)_{OSS}-Co^{II}-LS and HS-Co^{II}-(SQ-SQ)_{CS}-Co^{II}-HS complexes, respectively. Note that, here, the high-spin molar fraction refers to the sum of the molar fractions of the two high-spin cobalt(II) ions. The consideration of the $\chi_{\text{M}}T_{\text{LS}}$ value of 0.112 cm³ K mol⁻¹ is based on the observation of a plateau with this value in the temperature range 2–30 K where **3b** exists entirely in LS-Co^{II}-(SQ-SQ)_{OSS}-Co^{II}-LS state (Figure 2.30). The consideration of $\chi_{\text{M}}T_{\text{HS}}$ value of 5.20 cm³ K mol⁻¹ is based on the fact that the observed $\chi_{\text{M}}T$ value for complex **1** is 2.60 cm³ K mol⁻¹ which has a ground electronic state of high-spin cobalt(II) catecholate (see discussion in section 2.1.3). Hence, for two non-interacting or weakly interacting high-spin cobalt(II) ions in complex **3b**, the expected value would be ca. 5.20 cm³ K mol⁻¹. Further, the $\chi_{\text{M}}T$ vs T plot of **3b** shows that the curve is reaching to a plateau at 300 K ($\chi_{\text{M}}T = 5.01$ cm³ K mol⁻¹). Thus, approximately the $\chi_{\text{M}}T_{\text{HS}}$ value is considered as 5.20 cm³ K mol⁻¹. From the below plot (Figure 2.32), the $T_{1/2}$ value is found to be 141 K. A least-squares fitting of the γ_{HS} vs. T plot by the equation 2.6 provides the ΔH and ΔS values of 5.8 ± 0.3 kJ mol⁻¹ and 41.2 ± 1.3 J K⁻¹ mol⁻¹, respectively.

$$\gamma_{\text{HS}} = 1/(e^{\Delta H/RT} \cdot e^{-\Delta S/R} + 1) \quad (2.6)$$

The goodness-of-fit data are provided in Table 2.19. These values of the enthalpy and entropy changes are in the range of those values for the SCO cobalt(II) complexes.^[32,54]

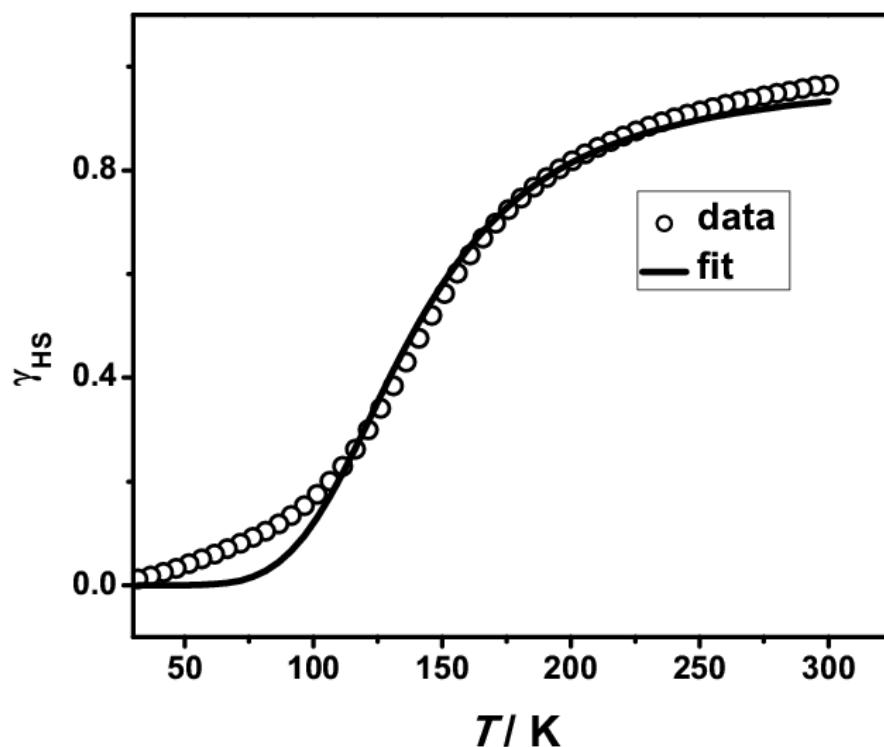


Figure 2.32: The high-spin molar fraction γ_{HS} vs. T plot for solid **3b**.

The high-spin molar fraction vs. temperature plot in the temperature range 150–350 K for solid **3c** is shown in Figure 2.33. For the calculation of γ_{HS} values, the $\chi_{\text{M}}T$ value for the pure LS-Co^{III}-Cat-SQ-Co^{II}-LS complex is considered as $1.112 \text{ cm}^3 \text{ K mol}^{-1}$ because with this value a plateau is observed in the $\chi_{\text{M}}T$ vs. T plot of **3c** in the temperature range 30–175 K where complex **3c** exists entirely in LS-Co^{III}-Cat-SQ-Co^{II}-LS state. Whereas, as described earlier, the $\chi_{\text{M}}T$ value for the pure HS-Co^{II}-(SQ-SQ)_{CS}-Co^{II}-HS complex is considered as $5.20 \text{ cm}^3 \text{ K mol}^{-1}$. The $T_{1/2}$ value for the conversion of the LS-Co^{III}-Cat-SQ-Co^{II}-LS to HS-Co^{II}-(SQ-SQ)_{CS}-Co^{II}-HS complex is found to be 350 K. A least-squares fitting of the plot by the equation 2.6, provides the thermodynamic parameters $\Delta H = 17.3 \pm 0.5 \text{ kJ mol}^{-1}$ and $\Delta S = 48.9 \pm 0.6 \text{ J K}^{-1} \text{ mol}^{-1}$. The goodness-of-fit data are provided in Table 2.19. These values of the thermodynamic parameters neither fall into the commonly observed values of those parameters for SCO cobalt(II) complexes nor for the $\text{VT}_{\text{LS-HS}}$

of cobalt dioxolene complexes. This kind of observation could be explained on the basis of the fact that in complex **3c**, the two linked cobalt dioxolene moieties undergo different transitions that are, the low-spin cobalt(III) catecholate half exhibits VT_{LS-HS} whereas the low-spin cobalt(II) semiquinonate site undergoes spin transition. The values of the thermodynamic parameters for one of the transitions would be different than the other one because the ΔS value would be different for the two processes due to the fact that the changes in M–L bond lengths and number of unpaired electrons in a valence tautomeric transition differ from those for an SCO process.^[15,32,54,81] For, the case herein, the curve fitting approach could provide the averaged or in between values for the ΔH and ΔS of the SCO and VT_{LS-HS} processes.

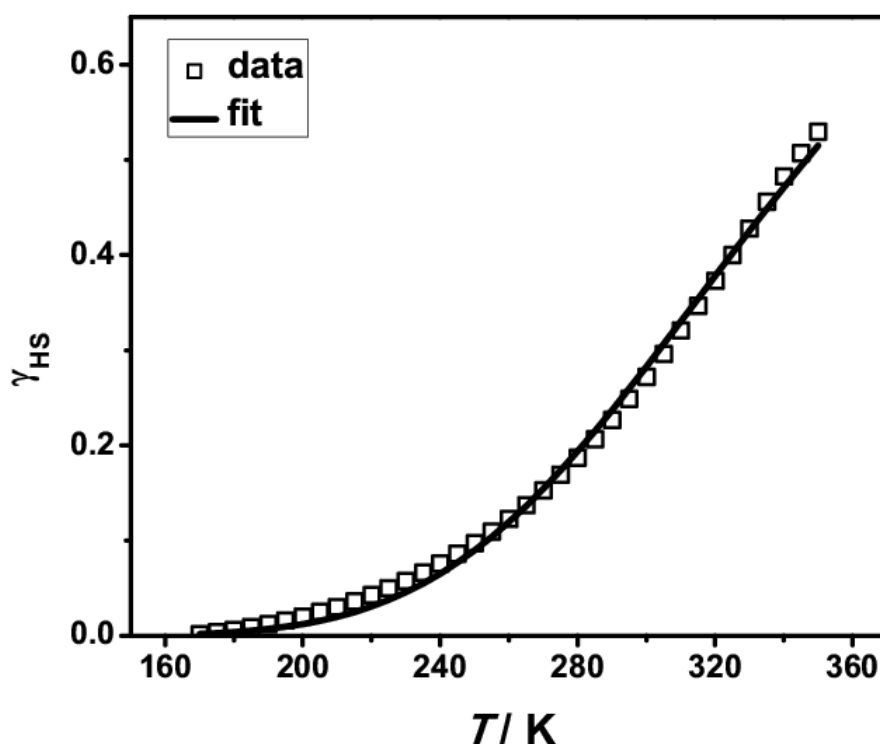


Figure 2.33: The high-spin molar fraction γ_{HS} vs. T plot for solid **3c**.

Table 2.19: Goodness-of-fit and thermodynamic parameter data for the fitting of the γ_{HS} vs. T plots of solid **3b** and **3c**.

Compound	SS _{res}	Adj. R^2	RMSE	$\Delta H/\text{kJ mol}^{-1}$	$\Delta S/\text{J K}^{-1} \text{mol}^{-1}$
3b (solid)	0.062	0.991	0.034	5.8 ± 0.3	41.2 ± 1.3
3c (solid)	2.7×10^{-3}	0.997	8.5×10^{-3}	17.3 ± 0.5	48.9 ± 0.6

^1H NMR spectrum of the compound **3a** in $[\text{D}_3]\text{MeCN}$ at 293 K shows broad signals in the range between +100 ppm and -60 ppm (Figure 2.34). The peaks (δ/ppm) are listed in the Table 2.20, and also in the experimental section.

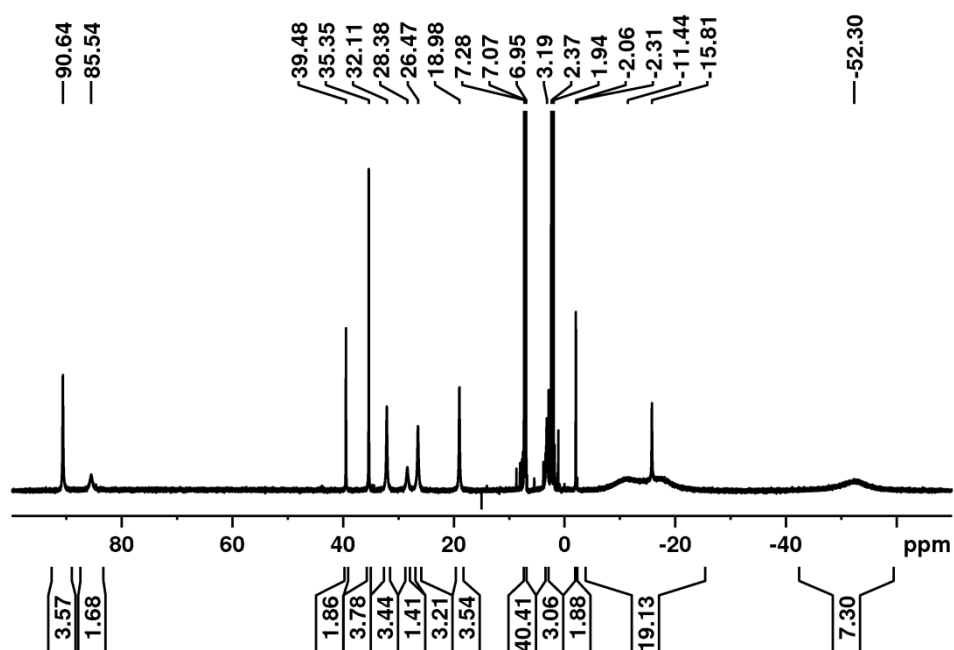


Figure 2.34: ^1H NMR spectrum of the compound **3a** at 293 K in $[\text{D}_3]\text{MeCN}$.

The $\chi_{\text{M}}T$ value measured from a solution of **3a** in $[\text{D}_3]\text{MeCN}$ is $5.07 \text{ cm}^3 \text{ K mol}^{-1}$ at 293 K. This value is in agreement with the assignment of electronic state of dissolved $[\text{Co}_2(\text{L-N}_4t\text{Bu}_2)_2(\text{SQ-SQ})]^{2+}$ complex as $\text{HS-Co}^{\text{II}}-(\text{SQ-SQ})_{\text{CS}}-\text{Co}^{\text{II}}-\text{HS}$ state at 293 K.

Table 2.20: ^1H NMR data for $[\text{Co}_2(\text{L-N}_4t\text{Bu}_2)_2(\text{SQ-SQ})]^{2+}$ of **3a** at 293 K in $[\text{D}_3]\text{MeCN}$.

Solvent	δ/ppm
$[\text{D}_3]\text{MeCN}$	90.64 (br), 85.54 (br), 39.48 (br), 35.35 (br), 32.11 (br), 28.38 (br), 26.47 (br), 18.98 (br), 3.19 (br), -2.06 (br), -2.31 (br), -11.08 (br), -15.81 (br), -17.56 (br), -52.30 (br)

2.2.4 Infrared Spectroscopic Properties

Infrared spectroscopy performed on compounds **3a**, **3b**, **3c**, and **3d** has provided invaluable insights into the electronic states of the bis(dioxolene) ligands of the compounds at room temperature. The ATR spectra of the compounds **3a** and **3b** are shown in Figure 2.35. The spectra of **3a** and **3b** show intense bands at around 1504 and 1520 cm^{-1} . Tentative assignment of these bands requires discussion about the appearance of the different stretching modes of L-N₄tBu₂ ligand, BPh₄⁻ counter anion, DMF in infrared spectra. The discussion is as following: (1) Since, the IR spectrum of the complex $[\text{Co}(\text{L-N}_4t\text{Bu}_2)(\text{MeCN})_2](\text{ClO}_4)_2$ does not exhibit any bands in the region 1550–1500 cm^{-1} ,^[32] therefore, the above bands are not assigned to any kind of stretching mode related to the L-N₄tBu₂ ligand. (2) As, compound **3a** does not exhibit the bands corresponding to DMF (see Figure A.75 in appendix), and is prepared by drying of **3b** in vacuum, therefore, the above bands for the compounds are not originating from DMF. (3) The copper bis(dioxolene) complex **5a** which contains the (SQ-SQ)_{CS}²⁻ ligand but does not contain BPh₄⁻ counter anions and DMF, also shows intense bands in the above energy region with similar intensity pattern (see Figure A.121 in appendix). In both complexes **3b** and **5a**, the metal ions are divalent. So, the bands related to the macrocyclic ligand L-N₄tBu₂ would exhibit similar IR features for both the compounds. Therefore, on the basis of crystallographic data of **3b** at 300 K, the presence of the bands at around 1504 and 1520 cm^{-1}

for complexes **3a** and **3b** could only be linked to the presence of the (SQ-SQ)_{CS}²⁻ ligand in the complexes. In other words, the bands could be used as the marker bands for the presence of the (SQ-SQ)_{CS}²⁻ ligand in the synthesized metal bis(dioxolene) complexes. The Gaussian fit of the ATR spectra in the range 1500–1550 cm⁻¹, shows presence of one Gaussian peak at 1505 cm⁻¹ for **3b**, whereas two Gaussian peaks at 1502 and 1528 cm⁻¹, for **3a** are found in that range (see Figures A.80–A.81 in appendix). Although, in the ATR spectrum of **3b**, a shoulder could be seen at around 1520 cm⁻¹ which has a lesser bandwidth than the bandwidth of the shoulder at 1522 cm⁻¹ for **3a**, but a Gaussian peak is not found at around 1522 cm⁻¹ for **3b**. This kind of anomaly is explained as following: The IR spectrum of DMF shows a medium band at 1504 cm⁻¹.^[132] Since, the complex **3b** contains 4 DMF molecules in its crystal lattice, therefore, in its ATR spectrum, a band corresponding to the DMF molecules would be present at around 1504 cm⁻¹. Additionally, the marker band for the (SQ-SQ)_{CS}²⁻ ligand is also present at the at around 1504 cm⁻¹. Thus, the total intensity of the band at 1504 cm⁻¹ in the ATR spectrum of **3b** is the sum of the intensity of the bands corresponding to the DMF molecules and (SQ-SQ)_{CS}²⁻ ligand. Therefore, the intensity ratio of the bands at 1504 to 1520 cm⁻¹ in the ATR spectrum of **3b** differs to the intensity ratio of those bands in the ATR spectrum of **3a** and that ratio is such that the bandwidth of the band at 1520 cm⁻¹ for **3b** become much smaller compared to that of the bandwidth for **3a**. Thus, from the Gaussian fitting of the ATR spectrum of **3b**, only one peak is found instead of two peaks, in the wavenumber range 1500–1550 cm⁻¹. Note that it has been observed that during deconvolution of the IR spectra, when the stretching frequencies of two IR bands are separated by up to maximal value of ca. 20 cm⁻¹ and if one of the bands is significantly weaker than the other band, then the Gaussian fit could provide only one peak corresponding to the intense band.

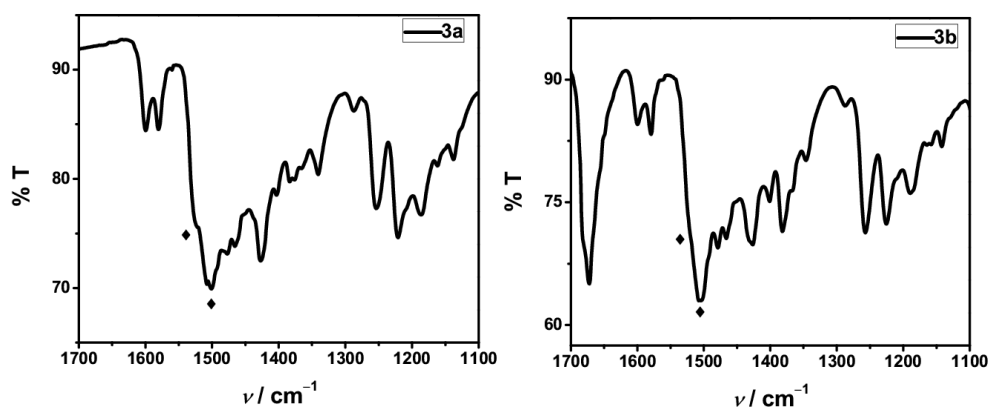


Figure 2.35: ATR spectra of **3a** (left) and **3b** (right) at RT. The bands associated with the closed-shell form of the bis(dioxolene) ligand are marked by filled diamonds.

The ATR spectra of the compounds **3c** and **3d** are shown in Figure 2.36. Both the spectra have similar type of characteristic bands. In the spectra, the catecholate marker bands of the catecholate halves of $(\text{Cat-SQ})^{\bullet 3-}$ ligands are present at 1265 cm^{-1} . The assignment of this band to the catecholate marker band is based on the following observation: Each of the complexes **5a**, **3a** and **3b** exhibit two bands at around 1280 and 1250 cm^{-1} in the range of 1300 – 1250 cm^{-1} in their ATR spectra. Whereas **3c** exhibit three bands at 1282 , 1265 and 1249 cm^{-1} , and **3d** exhibit three bands at 1281 , 1266 and 1250 cm^{-1} (see experimental section). Thus, this observation along with the IR spectroscopic study of the complex **2** (see discussion in the above section 2.1.4), X-ray crystallographic data of **3d** at 150 K and SQUID data of **3c** in the temperature range 2 – 350 K suggest that the band at 1265 cm^{-1} can only be correlated with the marker band for the catecholate halves of the $(\text{Cat-SQ})^{\bullet 3-}$ ligands. According to the observation in the IR spectra of complex **2**, another dioxolene marker band with similar intensity to the band at 1265 cm^{-1} , should be observed at around 1475 cm^{-1} . In the ATR spectra (Figure 2.36), that band, if present is obscured by the relatively intense band at 1465 cm^{-1} . The band at 1465 cm^{-1} is correlated with the presence of the macrocyclic ligand $\text{L-N}_4t\text{Bu}_2$ in **3c** and **3d** because the complexes $[\text{Co}(\text{L-N}_4t\text{Bu}_2)(\text{MeCN})_2](\text{ClO}_4)_2$ and

[Co(L-N₄tBu₂)Cl₂] exhibit medium bands at around 1465 cm⁻¹ in their IR spectra.^[32] These observations strongly support the existence of catecholate-semiquinonate states of the bis(dioxolene) ligands in significant amounts in both compounds **3c** and **3d**, at room temperature. At room temperature, the existence of closed-shell quinonoid forms of the bis(dioxolene) ligands in **3c** and **3d** is supported by the observation of the (SQ-SQ)_{CS}²⁻ marker bands at 1501 cm⁻¹. The Gaussian fitting of the ATR spectra reveal that two Gaussian bands at 1502 and 1522 cm⁻¹ are present in the range 1500–1550 cm⁻¹ (see Figures A.82–A.83 in appendix). The Gaussian bands at 1268 cm⁻¹ are the marker bands for the catecholate halves of the (Cat-SQ)^{•3-} units. Therefore, without the X-ray structure data of **3d** at high temperature, the electronic states of **3** in **3c** and **3d** could be described by HS-Co^{II}-(SQ-SQ)_{CS}-Co^{II}-HS state at high temperatures. The possibility of existence of LS-Co^{II}-(SQ-SQ)_{CS}-Co^{II}-HS is discarded because the state does not exist for **3b**.

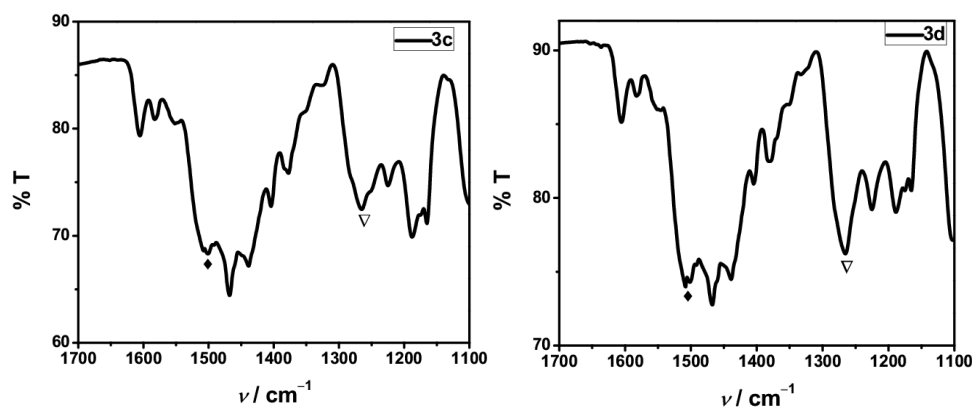


Figure 2.36: ATR spectra of **3c** (left) and **3d** (right) at RT. The bands associated with the (Cat-SQ)^{•3-} moieties are marked by triangles and the bands associated with the (SQ-SQ)_{CS}²⁻ moieties are marked by filled diamonds.

Although in ATR sampling technique a slight mechanical pressure is applied on the crystals, therefore, the question remains whether crystals of **3d** loses diethyl ether due to application of the pressure. But inspection of ATR spectra of **3c** and **3d** reveals difference in intensity pattern of the bands in the spectra. The sample for ATR measurement of **3c** was prepared by drying of **3d** in vacuum. Therefore, considering the IR spectrum of diethyl ether,^[132] if **3c** and **3d** have the same molecular property, then the band which is lower in energy than 1200 cm^{-1} would have been most affected, *i.e.*, the intensity of the bands in this region would have been lower than the intensity of the catecholate C–O band. In addition, it has been observed that **3d** does not lose diethyl ether completely upon storage at room temperature for more than two weeks. It has also been observed that during drying of **3d** in vacuum at RT, the crystals do not lose crystallinity. Therefore, it is justified to say that **3c** and **3d** have similar molecular property but not the same.

The KBr pellet IR spectra of **3b** and **3d** are shown in Figure 2.37 and Figure 2.38, respectively. The bands at 1507 and 1520 cm^{-1} are the marker bands for the $(\text{SQ-SQ})_{\text{CS}}^{2-}$ unit. The catecholate marker band of the $(\text{Cat-SQ})^{3-}$ unit, which are observed in the ATR spectrum of **3d**, is also observed in its KBr pellet IR spectrum. The band at 1260 cm^{-1} in the IR spectrum of **3d** is assigned to the marker band for the catecholate half of the coordinated $(\text{Cat-SQ})^{3-}$ moiety.

One of the differences between the ATR and KBr pellet spectra of **3d**, are that the intensity of the $(\text{SQ-SQ})_{\text{CS}}^{2-}$ marker bands is higher in the KBr pellet spectrum than the observed intensity in ATR spectrum. The Gaussian fit of the KBr pellet IR spectra of **3b** and **3d** shows that for compound **3b**, one Gaussian band at 1504 cm^{-1} is present, and for compound **3d** two Gaussian bands at 1504 and 1525 cm^{-1} are present (see Figures A.84–A.85 in appendix).

The reason for the observation of one Gaussian band instead of two Gaussian bands for compound **3b** in the range of 1500–1550 cm^{-1} , is same as described for the observation in its ATR spectrum (see above). In the deconvoluted spectra of **3d**, the Gaussian band at 1259 cm^{-1} is the catecholate marker band. Thus, on the basis of X-ray diffraction, magnetic susceptibility data and comparison with the ATR spectral data, it can be inferred that at room temperature, the complex **3** exists, mainly, in $\text{HS-Co}^{\text{II}}\text{-(SQ-SQ)}_{\text{CS}}\text{-Co}^{\text{II}}\text{-HS}$ state in the KBr pellet of **3b**, whereas in the KBr pellet of **3d**, it exhibit a VT/SCO equilibrium between the $\text{LS-Co}^{\text{III}}\text{-Cat-SQ-Co}^{\text{II}}\text{-LS}$ and $\text{HS-Co}^{\text{II}}\text{-(SQ-SQ)}_{\text{CS}}\text{-Co}^{\text{II}}\text{-HS}$ states.

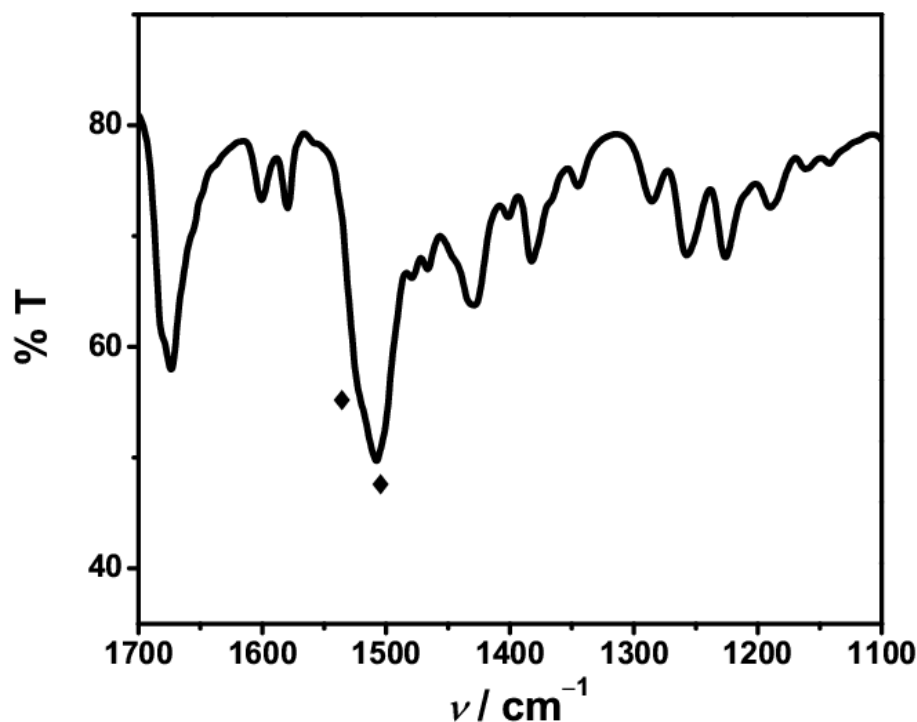


Figure 2.37: IR spectrum of KBr pellet of compound **3b**. The bands associated with the $(\text{SQ-SQ})_{\text{CS}}^{2-}$ moieties are marked by filled diamonds.

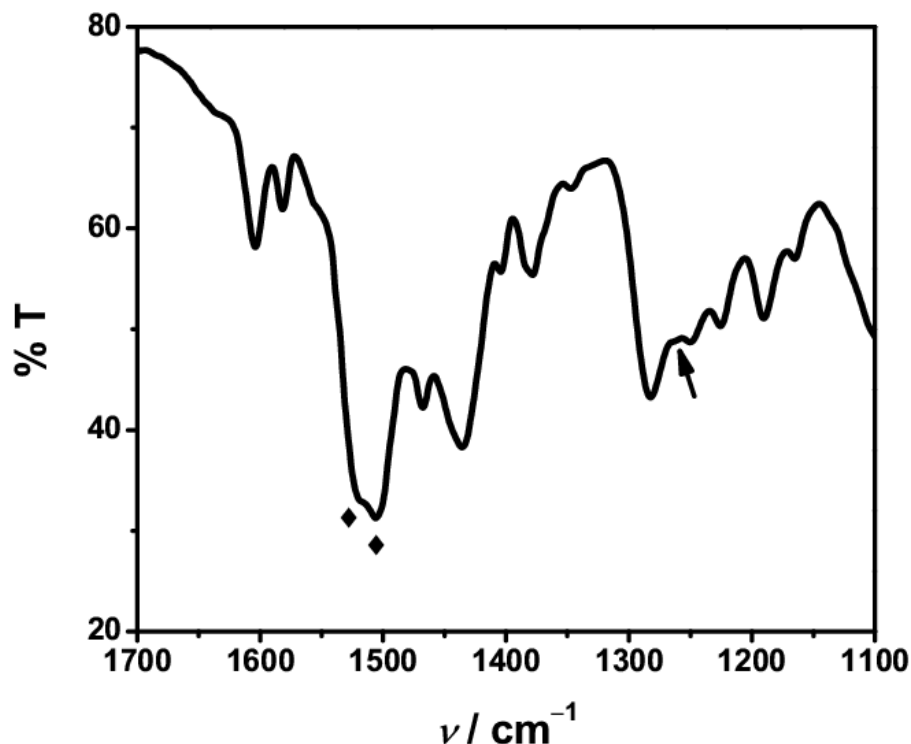


Figure 2.38: IR spectrum of KBr pellet of compound **3d**. The bands associated with the $(\text{SQ-SQ})_{\text{CS}}^{2-}$ moiety are marked by filled diamonds and the arrow is pointed towards the marker band of catecholite half of the $(\text{Cat-SQ})^{3\bullet-}$ moiety.

Keeping in mind that, temperature-induced intramolecular electron transfer in a mixed-valence system *e.g.*, in a class II mixed-valence system, was observed by *Lancaster et al.* by variable temperature EPR spectroscopy,^[140,141] it is worthwhile to mention about the possibility of such electron transfer in $(\text{Cat-SQ})^{3\bullet-}$ ligands of the complexes **3c** and **3d** because the $(\text{Cat-SQ})^{3\bullet-}$ ligand is also a mixed-valence system. The presence of catecholite marker bands at around 1265 cm^{-1} in the IR spectra of the compounds at room temperature indicates that if the electron transfer is happening in the $(\text{Cat-SQ})^{3\bullet-}$ ligand at room temperature, then the electron transfer rate is faster than IR spectroscopic time scale because in case of the electron transfer *i.e.*, delocalization, the catecholite marker bands would not have appeared in the IR spectra.

2.2.5 UV/Vis/NIR Spectroscopic Properties

The solution state properties of $[\text{Co}_2(\text{L-N}_4\text{tBu}_2)_2(\text{SQ-SQ})]^{2+}$ have been investigated by variable temperature UV/Vis/NIR spectroscopy along with NMR spectroscopy. The variable temperature UV/Vis/NIR spectra of **3a** in EtCN are presented in Figure 2.39. The variable temperature UV/Vis/NIR spectra of **3d** are superimposable with this spectra (see appendix; Figure A.96). Therefore, any kind of counter ion effects on solution state properties are discarded. The Gaussian fit of the spectra are shown in Figures A.98–A.105 and the data found from the fitting are given in Table A.16 (see in section 6.2.4 in appendix).

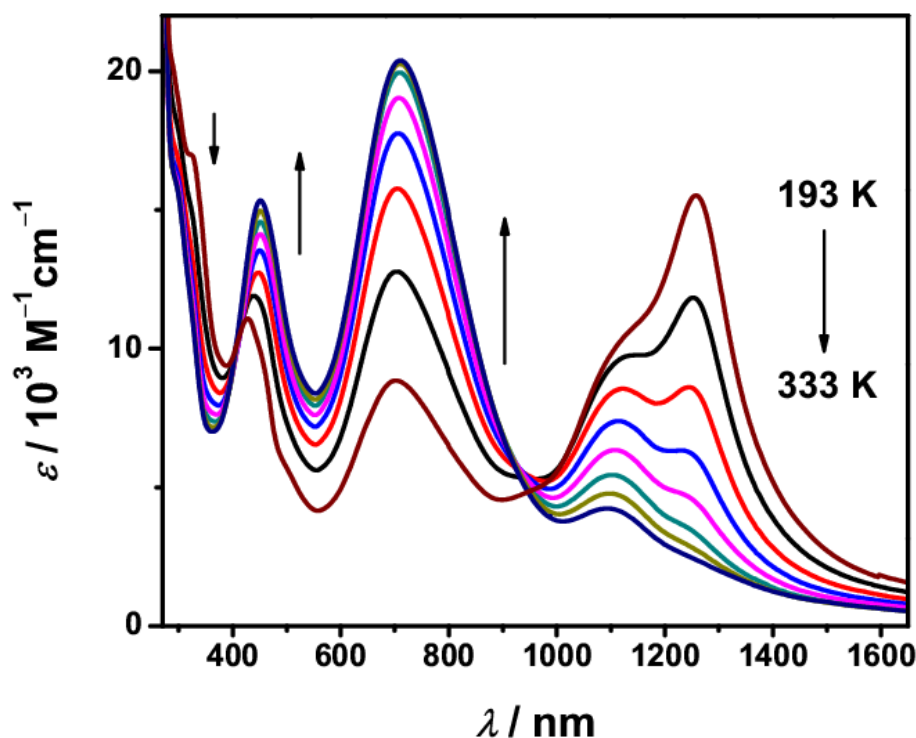


Figure 2.39: Variable temperature UV/Vis/NIR of compound **3a** in propionitrile.

The discussion related to the spectral changes become simple if, at first, the results of the SVD of the variable temperature UV/Vis/NIR spectra are considered. Therefore, those results are discussed as following: The data

obtained from the SVD are provided in Table 2.21. The singular values of the **S** matrix show that the first two components corresponds to the 97.6 % weights of the first two basis spectra to the overall spectra. The spectral features of the first three **U** components are shown in Figure 2.40. The first two **V** component vs. *T* plots have the shape of γ_{HS} vs. *T* plot for an SCO/VT process, whereas the third one does not have any physical significance in terms of an SCO/VT process (see Figures A.106–A.108 in appendix). Thus, based on the shapes of the **V** component vs. *T* plots and singular values, it is concluded that the spectra contain two components. The statistical parameters showing goodness-of-fit of the **V** components are provided in Table A.17 (see appendix). The absorption profiles of the pure components of the spectra are shown in Figure 2.41 and the absorption data are provided in Table 2.22. The Gaussian fit of the component spectra are shown in Figures A.109–A.110 and the data are provided in Table A.16 (see appendix). Except for the first two components of the **U**, **S** and **V** matrices, the rest are predominated by the features due to the noise and in addition, they could be due to the spectral broadening.

Table 2.21: The first four singular values, thermodynamic parameters ΔH , ΔS and goodness-of-fit parameter R^2 obtained from the SVD of the variable temperature UV/Vis/NIR spectra of **3a** in EtCN.^[a]

Singular value	Singular value (%)	$\Delta H/\text{kJ mol}^{-1}$	$\Delta S/\text{J K}^{-1} \text{ mol}^{-1}$	<i>T</i> /K	R^2 [b]
8.68×10^5	78.3	12.8	59.8	193	0.995
2.14×10^5	19.3			213	0.999
1.98×10^4	1.8			233	0.997
3.91×10^3	0.3			253	0.998
				273	0.999
				293	0.999
				313	0.999
				333	0.998

^[a] The data points have absorbance in the range of 0–1.1.

^[b] Goodness-of-fit parameter for the reconstructed (calculated) spectrum at each temperature

Table 2.22: Absorption data for the low- and high-temperature components (LTC and HTC) of the variable temperature UV/Vis/NIR spectra of **3a** in EtCN.

Component	λ_{\max}/nm ($\epsilon/\text{M}^{-1} \text{cm}^{-1}$)
HTC	1089 (4415), 709 (22200), 453 (15700)
LTC	1257 (22400), 1175 (16300), 975 (6000), 684 (3400), 645 (3110), 502 (3160), 462 (6076), 418 (10200), 357 (20400)

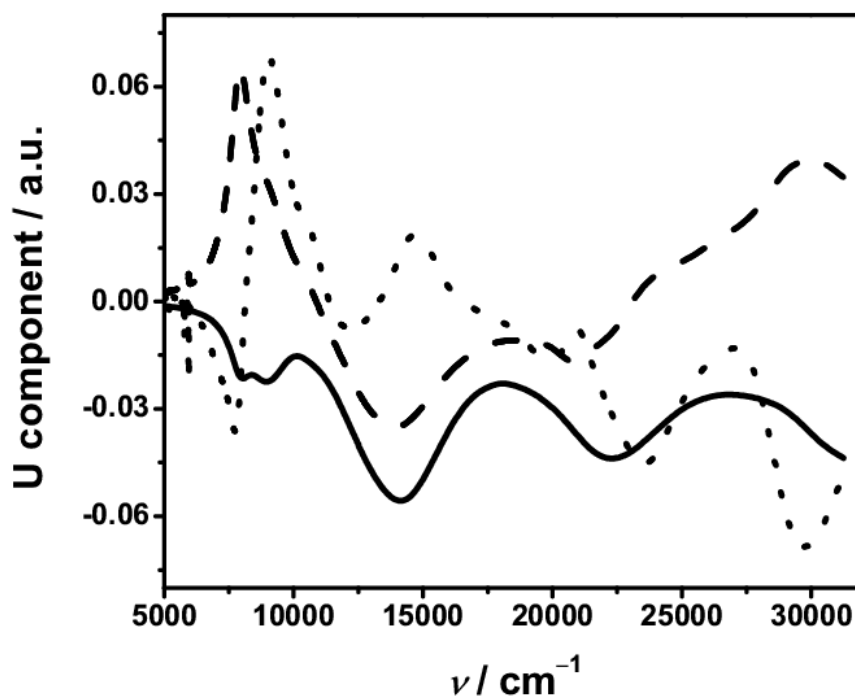


Figure 2.40: Spectra of the first three **U** components, in the sequence of solid, dashed and dotted lines, for the SVD of variable temperature UV/Vis/NIR of compound **3a** in EtCN.

Based on the magnetic susceptibility value of **3a** at room temperature, the absorption profile of the HTC is assigned to the HS-Co^{II}-(SQ-SQ)_{CS}-Co^{II}-HS chromophore. While the bands in the UV and Visible regions are assigned to the various possible $\pi \rightarrow \pi^*$ transitions of the bis(dioxolene) ligand, the relatively weak band in the NIR region with absorption at 1089 nm is tentatively assigned to the charge transfer transition between the high-spin cobalt(II) centers and (SQ-SQ)_{CS}²⁻ ligand. Among these bands, the intense

band with absorption at 709 nm is assigned to the HOMO–LUMO transition ($\pi \rightarrow \pi^*$) of the (SQ-SQ) $_{CS}^{2-}$ ligand.

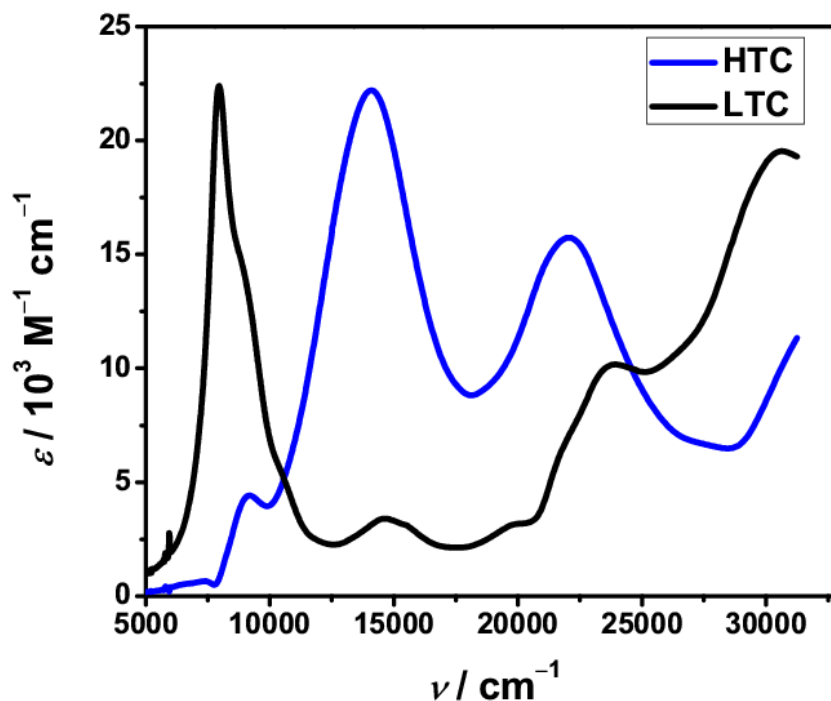


Figure 2.41: UV/Vis/NIR spectral features corresponding to the LTC and HTC obtained by the SVD of the variable temperature UV/Vis/NIR spectra of **3a** in EtCN.

Assignment of the absorption profile of the LTC to a particular chromophore is difficult without a theoretical calculation. However, the NIR spectral features that is, the pattern of the bands has similarity with the NIR spectral features for a low-spin cobalt(II) semiquinonate chromophore.^[33,55,92] Therefore, at least occurrence of an SCO process for one of the cobalt(II) centers is obvious.

The experimental spectra were reconstructed by SVD (see appendix; Figures A.111–A.112). The residuals between the experimental and reconstructed spectra are shown in Figure 2.42. These residuals do not differ substantially from the residuals between the original data matrix **A** and rank-defined data matrix **B** (see appendix; Figure A.113).

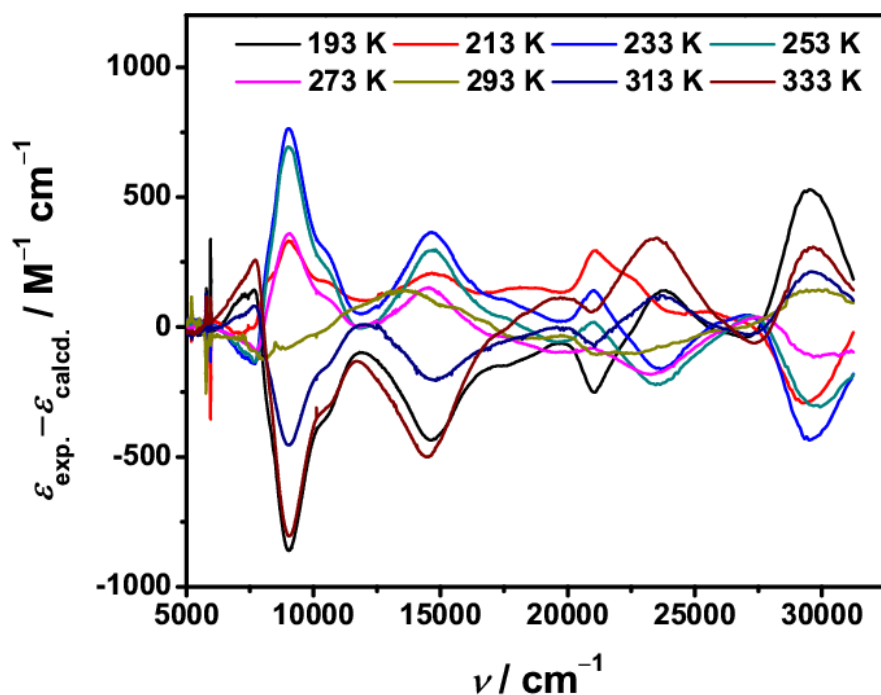
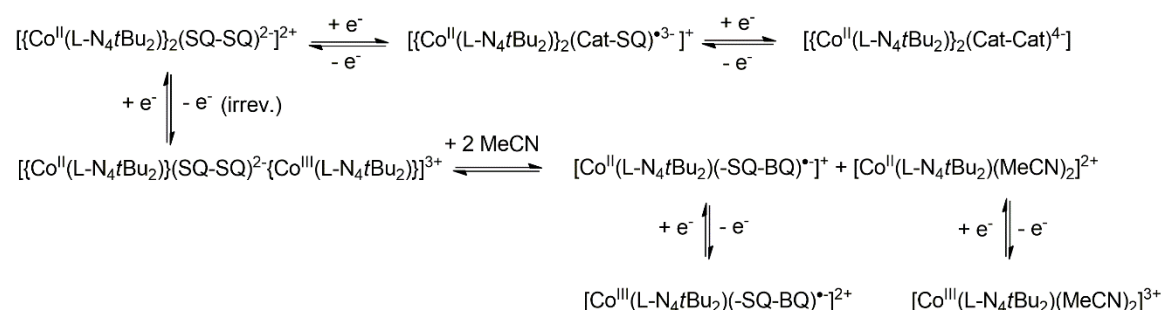


Figure 2.42: Residuals between the experimentally recorded and reconstructed spectra obtained by the SVD of the variable temperature UV/Vis/NIR spectra of **3a** in EtCN.

The spectral changes are consistent with increases in the intensity of the bands corresponding to the HTC with increase in temperature. The intensity of the bands of the LTC decreases with increase in temperature. The SVD provides the thermodynamic parameters of $\Delta H = 12.8 \text{ kJ mol}^{-1}$ and $\Delta S = 59.8 \text{ J K}^{-1} \text{ mol}^{-1}$ for the conversion from the low energy to high energy state of dissolved **3**. These thermodynamic parameters are also indicative for the SCO processes of cobalt(II) centers because the enthalpy change value falls into the range for commonly observed enthalpy change values of SCO cobalt(II) complexes.^[32,54] The entropy change value is somewhat higher than those observed for the SCO cobalt(II) complexes in their solid states.^[32,54] This observation could be due to the change in ΔS_{vib} as a result of the solute-solvent interactions (see discussion in section 2.1.5).

2.2.6 Electrochemical Properties

The redox properties of **3e** have been investigated by cyclic voltammetry. The cyclic voltammogram of compound **3e** is shown in Figure 2.43. The cyclic voltammograms for reductive and oxidative processes at different scan rates are presented in Figure 2.44. The cyclic voltammetry data are provided in Table A.18 (see in section 6.2.5 in appendix). The involved processes are outlined in Scheme 2.8. The CV for the reductive processes shows two redox couples at $E_{1/2}$ values of -112 and -552 mV at a scan rate $\nu = 100$ mV/s.



Scheme 2.8: Redox processes for compound **3e**.

The redox process occurring at $E_{1/2} = -112$ mV is assigned to the ligand-based one-electron reduction from $(\text{SQ-SQ})^{2-}$ to $(\text{Cat-SQ})^{\bullet 3-}$ and the reduction at $E_{1/2} = -552$ mV is assigned to the ligand-based one-electron reduction from $(\text{Cat-SQ})^{\bullet 3-}$ to $(\text{Cat-Cat})^{4-}$. The $i_{\text{pa}}/i_{\text{pc}}$ value for each reduction is ≈ 1 and the ΔE values for first and second set of reductions are in the range of 72–80 mV at scan rate $\nu = 100$ mV/s, respectively. Therefore, these two reductions are considered as reversible redox processes.

The CV for the oxidations show three redox processes at $E_{\text{pa}} = 360$ mV, $E_{1/2} = \text{ca. } 571$ mV and $E_{1/2} = 709$ mV at a scan rate $\nu = 100$ mV/s. The differential pulse voltammetry (DPV) of compound **3e** has helped to explain the oxidations (see appendix; Figure A.114). Although, the resolution of the DPV curve is not good, still the explanation of the oxidative processes is better

understood from the DPV. The oxidation at $E_{\text{pa}} = 360$ mV is irreversible, whereas the oxidations at $E_{1/2} = \text{ca. } 571$ mV and $E_{1/2} = 709$ mV are quasi-reversible.

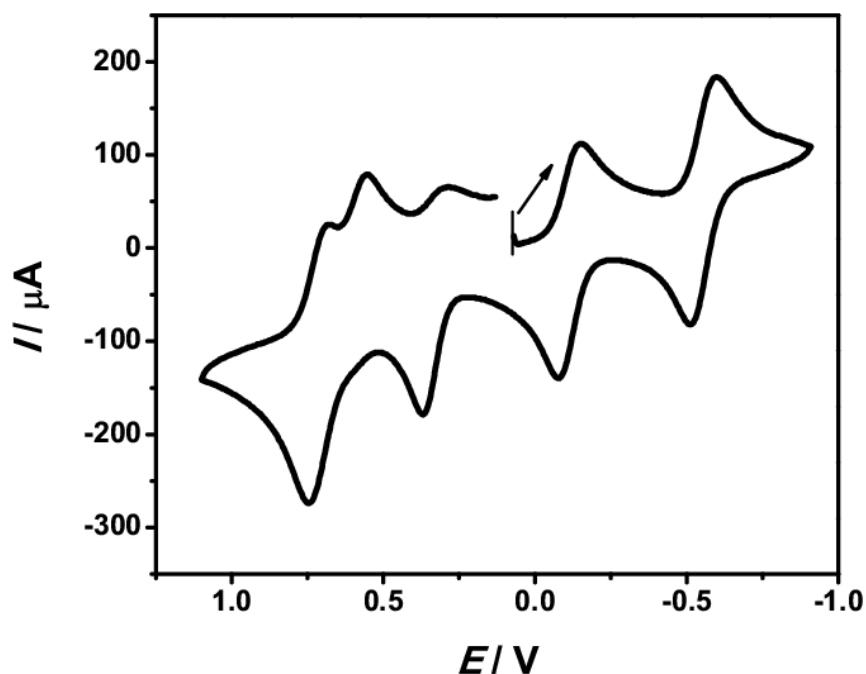


Figure 2.43: Cyclic voltammogram of **3e** in 0.2 M TBAP/MeCN at $\nu = 100$ mV/s.

The redox process at $E_{\text{pa}} = 360$ mV at a scan rate $\nu = 100$ mV/s, is assigned to the irreversible oxidation from $[\{\text{Co}^{\text{II}}(\text{L-N}_4\text{tBu}_2)\}(\text{SQ-SQ})^{2-}\{\text{Co}^{\text{II}}(\text{L-N}_4\text{tBu}_2)\}]^{2+}$ to $[\{\text{Co}^{\text{II}}(\text{L-N}_4\text{tBu}_2)\}(\text{SQ-SQ})^{2-}\{\text{Co}^{\text{III}}(\text{L-N}_4\text{tBu}_2)\}]^{3+}$. The direct oxidation product is unstable and dissociates to $[\text{Co}^{\text{II}}(\text{L-N}_4\text{tBu}_2)(-\text{SQ-BQ})^{\bullet-}]^+$ and $[\text{Co}^{\text{II}}(\text{L-N}_4\text{tBu}_2)(\text{MeCN})_2]^{2+}$.

The oxidation at $E_{1/2} = \text{ca. } 571$ mV is assigned to the one-electron oxidation from $[\text{Co}^{\text{II}}(\text{L-N}_4\text{tBu}_2)(-\text{SQ-BQ})^{\bullet-}]^+$ to $[\text{Co}^{\text{III}}(\text{L-N}_4\text{tBu}_2)(-\text{SQ-BQ})^{\bullet-}]^{2+}$. The oxidation at $E_{1/2} = 709$ mV is assigned to the one-electron oxidation from $[\text{Co}^{\text{II}}(\text{L-N}_4\text{tBu}_2)(\text{MeCN})_2]^{2+}$ to $[\text{Co}^{\text{III}}(\text{L-N}_4\text{tBu}_2)(\text{MeCN})_2]^{3+}$.^[122] The second

oxidation is tentatively assigned to a quasi-reversible redox process ($\Delta E = \text{ca. } 62 \text{ mV}$ at $\nu = 100 \text{ mV/s}$).

The third oxidation is also quasi-reversible because the CV of the $[\text{Co}(\text{L-N}_4\text{tBu}_2)(\text{MeCN})_2]^{2+}$ complex shows a quasi-reversible oxidation at around 709 mV .^[122]

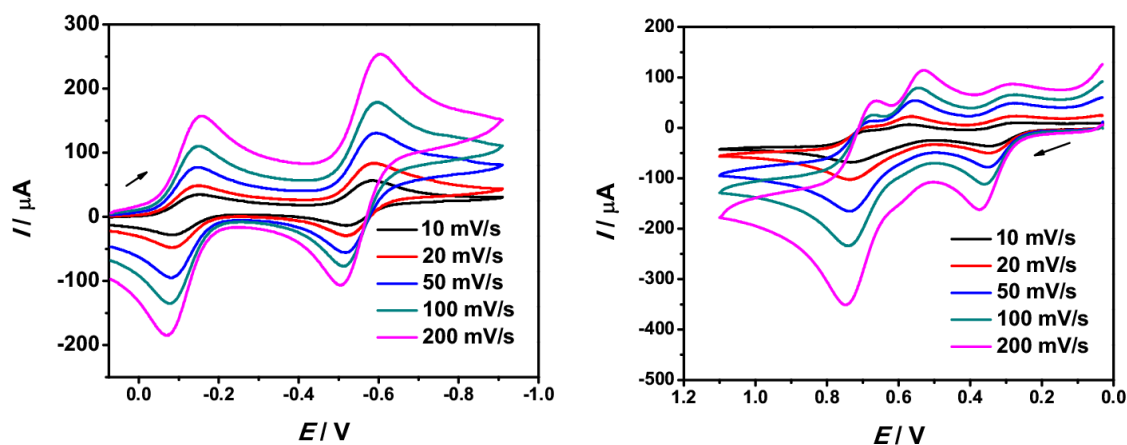


Figure 2.44: Cyclic voltammograms for the reductive (left) and oxidative (right) processes of **3e** at different scan rates in 0.2 M TBAP/MeCN.

2.2.7 Brief Summary

In summary, the structural and magnetic data unambiguously reveal that the electronic state of the bis(dioxolene) ligand of solid **3b** is switched between open-shell singlet and closed-shell singlet which is triggered by cobalt(II) based spin-crossover process. This observation has opened up new ways to manipulate the electronic state of an organic moiety. On the other hand, intramolecular redox reaction between one of the cobalt(II) ions and (SQ-SQ)²⁻ ligand has resulted in the transfer of one electron from the cobalt(II) ion to the bis(dioxolene) ligand in each of the compounds **3c** and **3d** in their solid states. As a consequence for each of **3c** and **3d**, LS-Co^{III}-Cat-SQ-Co^{II}-LS electronic state is achieved at low temperatures, whereas at high temperatures the electronic states of **3c** and **3d** are best described as HS-Co^{II}-(SQ-SQ)_{CS}-Co^{II}-HS electronic states. Based on the infrared spectroscopic investigation, it is apparent that, if any electron transfer is occurring at room temperature between the dioxolene moieties of the (Cat-SQ)^{•3-} ligand of the LS-Co^{III}-Cat-SQ-Co^{II}-LS complex then the electron transfer rate is faster than IR time scale. The X-ray crystallographic measurement of **3e**·solv indicates that the electronic state of **3** in **3e**·solv is LS-Co^{III}-Cat-SQ-Co^{II}-LS at 150 K.

The solution state properties of complex **3** are independent of counter ions. On the basis of variable temperature UV/Vis/NIR spectroscopy and NMR-spectroscopy, we could say that in solution state, at least one of the cobalt(II) centers of **3** undergoes spin transition. Whether the spin transition is accompanied by change in the redox-state of the bis(dioxolene) ligand from catecholate-semiquinonate to closed-shell semiquinonate-semiquinonate state or change in the electronic configuration of the bis(dioxolene) ligand from open-shell semiquinonate-semiquinonate to closed-shell semiquinonate-semiquinonate state, remain unclear.

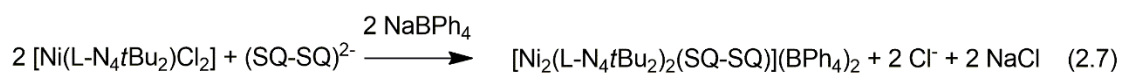
2.3 Electronic States of Bis(dioxolene) Ligands and the Interactions Between Metal Ions in Nickel-, Copper- and Zinc-Bis(dioxolene) Complexes

In order to investigate the electronic interactions between the metal centers bridged by the bis(dioxolene) ligand (SQ-SQ)²⁻ and the effect of the coordinated metal ions on the electronic states of the bridging ligand, other than cobalt(II) ions, the nickel(II), copper(II) and zinc(II) bis(dioxolene) complexes **4**, **5** and **6**, respectively, have been synthesized and characterized.

2.3.1 Synthesis

The nickel bis(dioxolene) complex was synthesized by following an analogous synthetic procedure (second method) for complex **3**, but starting with the isolated complex [Ni(L-N₄tBu₂)Cl₂] instead of the *in situ* prepared complex [Co(L-N₄tBu₂)Cl₂] afforded dark green crystals of [Ni₂(L-N₄tBu₂)₂(SQ-SQ)](BPh₄)₂·4 DMF (**4a**) in a 45 % yield

The equation for the synthesis of **4** may be written as



The compound **5a** was synthesized by following a similar synthetic method as for compound **3d**, but starting with CuCl₂·2 H₂O instead of CoCl₂·6 H₂O and oxidizing the *in situ* prepared [Cu₂(L-N₄tBu₂)₂(Cat-Cat)] with ferrocenium tetrafluoroborate instead of dioxygen afforded yellow-green crystals of [Cu₂(L-N₄tBu₂)₂(SQ-SQ)](BF₄)₂·Et₂O (**5a**) in a 43 % yield.

The compound **6b** was synthesized by following the first synthetic method developed for compound **3b** but starting with ZnCl₂ instead of CoCl₂·6 H₂O afforded dark green crystals of [Zn₂(L-N₄tBu₂)₂(SQ-SQ)](BPh₄)₂·4 DMF (**6b**)

in a 48 % yield. The non-solvated compound $[\text{Zn}_2(\text{L-N}_4\text{tBu}_2)_2(\text{SQ-SQ})](\text{BPh}_4)_2$ (**6a**) was obtained by drying of **6b** in vacuo at 100 °C. The list and abbreviations of the synthesized compounds are provided in Table 2.23.

The equation for the synthesis of complexes **5** and **6** may be written as

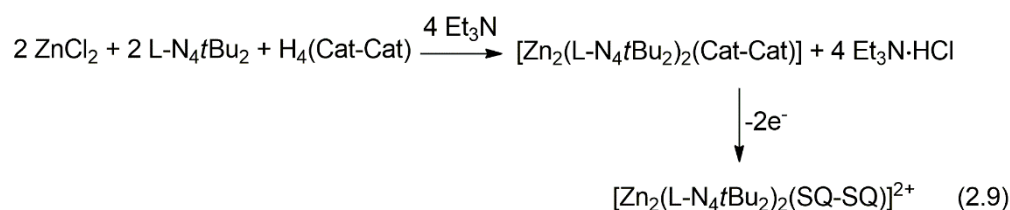
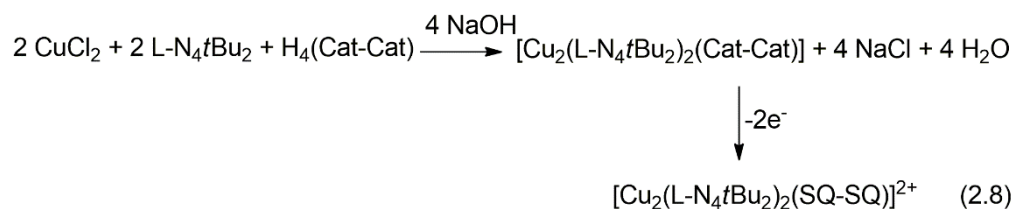


Table 2.23: List and the abbreviations for the synthesized and discussed compounds.

Compound	Abbreviation
$[\text{Ni}_2(\text{L-N}_4\text{tBu}_2)_2(\text{SQ-SQ})]^{2+}$	4
$[\text{Ni}_2(\text{L-N}_4\text{tBu}_2)_2(\text{SQ-SQ})](\text{BPh}_4)_2 \cdot 4 \text{ DMF}$	4a
$[\text{Cu}_2(\text{L-N}_4\text{tBu}_2)_2(\text{SQ-SQ})]^{2+}$	5
$[\text{Cu}_2(\text{L-N}_4\text{tBu}_2)_2(\text{SQ-SQ})](\text{BF}_4)_2 \cdot \text{Et}_2\text{O}$	5a
$[\text{Zn}_2(\text{L-N}_4\text{tBu}_2)_2(\text{SQ-SQ})](\text{BPh}_4)_2$	6a
$[\text{Zn}_2(\text{L-N}_4\text{tBu}_2)_2(\text{SQ-SQ})](\text{BPh}_4)_2 \cdot 4 \text{ DMF}$	6b
$[\text{Zn}_2(\text{L-N}_4\text{tBu}_2)_2(\text{SQ-SQ})]^{2+}$	6
$[\text{Zn}_2(\text{L-N}_4\text{tBu}_2)_2(\text{Cat-SQ})^{\bullet 3-}]^+$	6^{•-}
$[\text{Zn}(\text{L-N}_4\text{tBu}_2)(-\text{SQ-SQ})]$	7

2.3.2 Structural Characterization

The single crystal X-ray diffraction data for compounds **4a** and **6b** were collected at 100 and 295 K, whereas the X-ray diffraction data for compound **5a** were collected at 150 K. The analysis of the data for compounds **4a** and **6b** suggests that the structural properties at 100 and 295 K are identical. The

perspective views of the complex cations of the complexes are shown in Figure 2.45 and selected bond lengths and angles in these compounds are provided in Tables 2.24–2.26. The compounds **4a** and **6b** crystallize in the triclinic space group $P\bar{1}$ and their structures are isomorphous with that of **3b**. Compound **5a** crystallizes in the monoclinic space group $P2_1/c$. The diethyl ether molecule in compound **5a** is disordered. The identification and content of diethyl ether is based on the elemental analysis. The data provided in Table 2.25 are modified data obtained by the SQUEEZE option in the program PLATON. The structure of **5a** is isomorphous with the structure of **3d**.

The metal centers in **4a**, **5a** and **6b** are coordinated to the ligand donor atoms in a similar fashion as the cobalt centers in compound **3b** or **3d**. Also, the distorted-octahedral coordination spheres around the metal centers are demonstrated by the substantial deviation of the $N_{\text{amine}}\text{--M--}N_{\text{amine}}$ bond angles (found in the range of $144.62(5)\text{--}149.20(6)^\circ$) from the ideal value of 180° . For each complex, the two halves of the complex cations are related by a crystallographic inversion center located in the middle of the C(26)–C(26A) bond which links the two dioxolene units of the bridging ligand. Thus, each asymmetric unit of **4a** and **6b** contains half of the complex cation, one BPh_4^- anion and two DMF molecules. The asymmetric unit of **5a** contains half of the complex cation and one BF_4^- anion.

The $\text{M--}N_{\text{amine}}$ bond lengths are in the ranges of $2.301(2)\text{--}2.314(2)$, $2.426(3)\text{--}2.431(3)$, $2.355(1)\text{--}2.392(2)$ Å for **4**, **5** and **6**, respectively. The $\text{M--}N_{\text{py}}$ bond lengths are in the ranges of $1.983(2)\text{--}1.986(2)$, $1.970(3)\text{--}1.983(3)$, $2.040(1)\text{--}2.053(2)$ Å for **4**, **5** and **6**, respectively. The observed $\text{M--}N_{\text{amine}}$ and $\text{M--}N_{\text{py}}$ bond lengths are consistent with the assignment of the oxidation states of the metal centers as (+II) states.^[122]

In the bis(dioxolene) units of the complexes, the interannular C–C bond lengths determined at different temperatures are in the ranges of 1.432(4)–1.429(4) and 1.422(3)–1.421(3) Å for complexes **4** and **6**, respectively. These bond lengths are consistent with the range of the bond lengths commonly observed for C(sp²)–C(sp²) double bonds in such quinoidal molecules.^[22,110] Although, the bridging C–C bond length of 1.447(7) Å for complex **5** is longer than the above bond lengths, still the SQUID data of **5a** suggest that the bis(dioxolene) unit of complex **5** exists in closed-shell quinonoid form (see discussion in section 2.3.3).

The lengths of the C(23)–O(1) bonds are in the ranges of 1.262(3)–1.263(2) and 1.255(2)–1.257(2) Å for **4** and **6**, respectively. The value of the C(23)–O(1) bond length in complex **5** is 1.243(4) Å. The C(24)–O(2) bond lengths are found in the ranges of 1.299(2)–1.300(2) and 1.297(2)–1.298(2) Å for **4** and **6**, respectively. For complex **5**, the C(24)–O(2) bond length is 1.304(4) Å. The (O)C–C(O) bond lengths are in the ranges of 1.464(3)–1.470(3) and 1.469(2)–1.475(2) Å, for complexes **4** and **6**, respectively. The (O)C–C(O) bond length in complex **5** is 1.459(5) Å. These bond lengths are in accordance with the assignment of the electronic states of the bis(dioxolene) ligands in these complexes as closed-shell semiquinonate-semiquinonate states which is supported by the observation of similar bond lengths in the bis(dioxolene) ligand of **3b** at high temperatures.

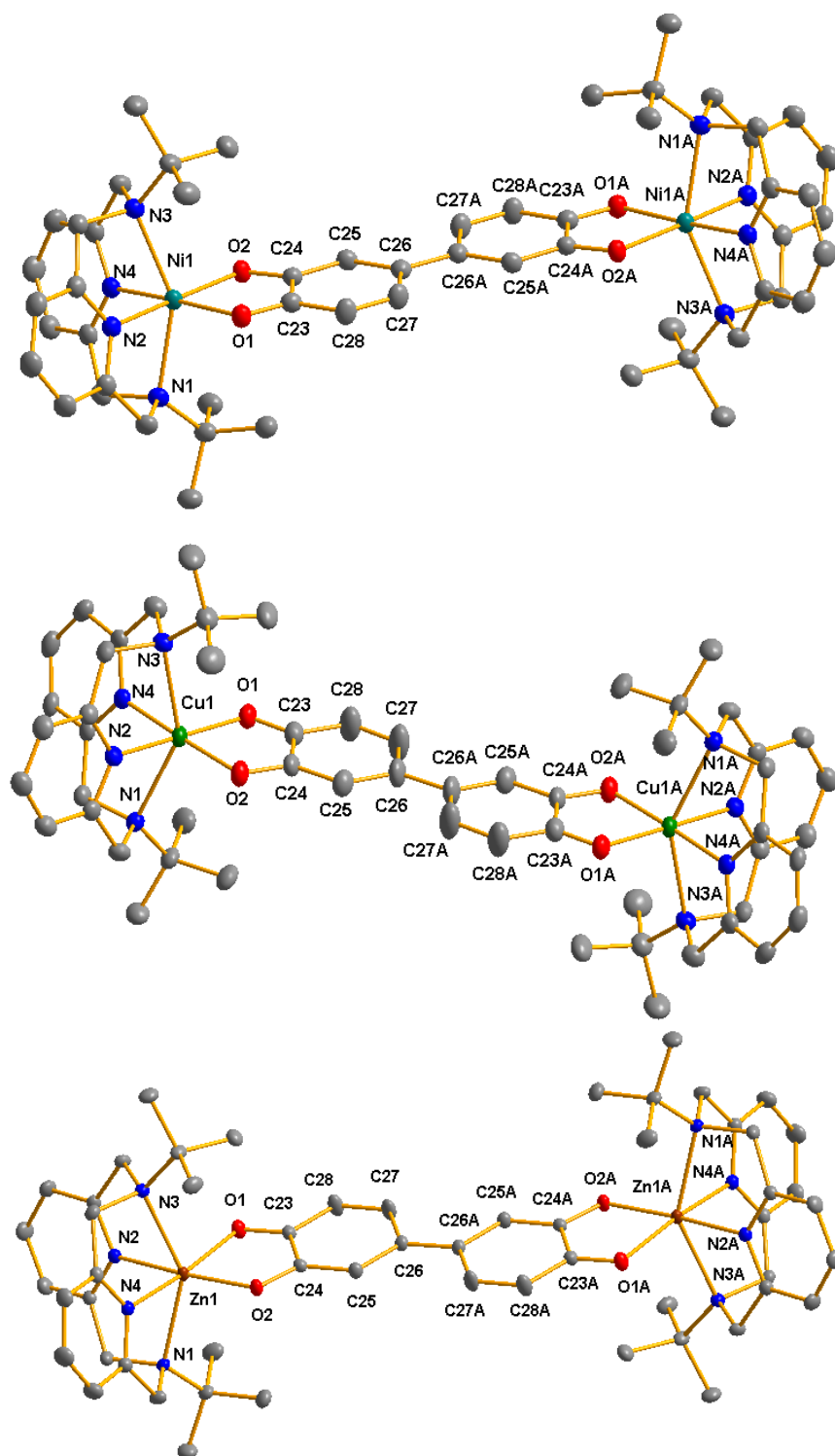


Figure 2.45: Perspective views of **4** (top), **5** (middle), **6** (bottom) in compounds **4a**, **5a** and **6b**, respectively, employing thermal ellipsoids of 50% probability, and omitting all hydrogen atoms for the purpose of clarity.

Table 2.24: Selected bond lengths [\AA] and bond angles [deg] for **4a**.

	<i>T</i> = 100 K	<i>T</i> = 295 K
Ni(1)–O(2)	2.015(1)	2.014(1)
Ni(1)–O(1)	2.049(1)	2.058(2)
Ni(1)–N(4)	1.985(2)	1.985(2)
Ni(1)–N(2)	1.983(2)	1.986(2)
Ni(1)–N(3)	2.302(2)	2.314(2)
Ni(1)–N(1)	2.301(2)	2.306(2)
O(1)–C(23)	1.263(2)	1.262(3)
O(2)–C(24)	1.299(2)	1.300(2)
C(23)–C(28)	1.429(3)	1.427(3)
C(23)–C(24)	1.470(3)	1.464(3)
C(24)–C(25)	1.387(3)	1.382(3)
C(25)–C(26)	1.409(3)	1.409(3)
C(26)–C(27)	1.449(3)	1.443(3)
C(27)–C(28)	1.347(3)	1.339(3)
C(26)–C(26A)	1.432(4)	1.429(4)
O(2)–Ni(1)–O(1)	81.47(5)	81.07(5)
O(2)–Ni(1)–N(4)	95.80(6)	96.48(6)
O(1)–Ni(1)–N(4)	175.50(6)	176.58(7)
O(2)–Ni(1)–N(2)	174.18(6)	173.84(6)
O(1)–Ni(1)–N(2)	93.02(6)	92.95(6)
N(4)–Ni(1)–N(2)	89.82(6)	89.56(7)
O(2)–Ni(1)–N(3)	104.97(6)	104.77(6)
O(1)–Ni(1)–N(3)	96.45(6)	97.74(6)
N(4)–Ni(1)–N(3)	80.76(6)	80.53(7)
N(2)–Ni(1)–N(3)	77.39(6)	77.37(7)
O(2)–Ni(1)–N(1)	98.73(6)	99.41(7)
O(1)–Ni(1)–N(1)	106.38(6)	105.10(6)
N(4)–Ni(1)–N(1)	77.51(6)	77.60(7)
N(2)–Ni(1)–N(1)	80.97(6)	80.65(7)
N(3)–Ni(1)–N(1)	149.20(6)	148.93(6)

Table 2.25: Selected bond lengths [\AA] and bond angles [deg] for **5a**.

	$T = 150 \text{ K}$
Cu(1)–O(2)	1.950(2)
Cu(1)–O(1)	2.029(2)
Cu(1)–N(4)	1.983(3)
Cu(1)–N(2)	1.970(3)
Cu(1)–N(3)	2.426(3)
Cu(1)–N(1)	2.431(3)
O(1)–C(23)	1.243(4)
O(2)–C(24)	1.304(4)
C(23)–C(28)	1.437(5)
C(23)–C(24)	1.459(5)
C(24)–C(25)	1.393(5)
C(25)–C(26)	1.392(5)
C(26)–C(27)	1.450(6)
C(27)–C(28)	1.349(6)
C(26)–C(26A)	1.447(7)
O(2)–Cu(1)–O(1)	83.0(1)
O(2)–Cu(1)–N(4)	95.9(1)
O(1)–Cu(1)–N(4)	178.9(1)
O(2)–Cu(1)–N(2)	176.2(1)
O(1)–Cu(1)–N(2)	93.3(1)
N(4)–Cu(1)–N(2)	87.7(1)
O(2)–Cu(1)–N(3)	104.7(1)
O(1)–Cu(1)–N(3)	99.9(2)
N(4)–Cu(1)–N(3)	79.6(1)
N(2)–Cu(1)–N(3)	76.6(1)
O(2)–Cu(1)–N(1)	100.7(1)
O(1)–Cu(1)–N(1)	104.5(1)
N(4)–Cu(1)–N(1)	76.3(1)
N(2)–Cu(1)–N(1)	79.4(2)
N(3)–Cu(1)–N(1)	146.45(9)

Table 2.26: Selected bond lengths [\AA] and bond angles [deg] for **6b**.

	<i>T</i> = 100 K	<i>T</i> = 295 K
Zn(1)–O(2)	1.988(1)	1.986(1)
Zn(1)–O(1)	2.130(1)	2.149(1)
Zn(1)–N(4)	2.053(2)	2.051(2)
Zn(1)–N(2)	2.040(1)	2.045(1)
Zn(1)–N(3)	2.389(1)	2.392(2)
Zn(1)–N(1)	2.355(1)	2.370(2)
O(1)–C(23)	1.257(2)	1.255(2)
O(2)–C(24)	1.298(2)	1.297(2)
C(23)–C(28)	1.435(2)	1.434(3)
C(23)–C(24)	1.475(2)	1.469(2)
C(24)–C(25)	1.383(2)	1.379(2)
C(25)–C(26)	1.414(2)	1.415(2)
C(26)–C(27)	1.452(2)	1.443(3)
C(27)–C(28)	1.347(2)	1.342(3)
C(26)–C(26A)	1.422(3)	1.421(3)
O(2)–Zn(1)–O(1)	80.62(5)	79.96(5)
O(2)–Zn(1)–N(4)	100.02(5)	101.05(6)
O(1)–Zn(1)–N(4)	173.80(5)	175.93(6)
O(2)–Zn(1)–N(2)	172.14(5)	171.24(5)
O(1)–Zn(1)–N(2)	91.76(5)	91.44(5)
N(4)–Zn(1)–N(2)	87.76(5)	87.65(6)
O(2)–Zn(1)–N(3)	106.92(5)	106.97(6)
O(1)–Zn(1)–N(3)	95.65(5)	97.51(6)
N(4)–Zn(1)–N(3)	78.24(5)	78.42(6)
N(2)–Zn(1)–N(3)	75.58(5)	75.60(6)
O(2)–Zn(1)–N(1)	101.22(5)	101.92(6)
O(1)–Zn(1)–N(1)	109.89(5)	107.66(5)
N(4)–Zn(1)–N(1)	76.11(5)	76.06(6)
N(2)–Zn(1)–N(1)	79.45(5)	79.00(6)
N(3)–Zn(1)–N(1)	144.62(5)	144.45(5)

2.3.3 Magnetic Properties

2.3.3.1 Magnetic Properties in Solid State

The magnetic susceptibility data of compounds **4a**, **5a** and **6b** were collected in the temperature range of 2–300 K with a SQUID magnetometer. The $\chi_{\text{M}}T$ vs. T plots are shown in Figures 2.46–2.48.

As it can be seen from the $\chi_{\text{M}}T$ vs. T plot of **4a** (Figure 2.46), the $\chi_{\text{M}}T$ value is $2.52 \text{ cm}^3 \text{ K mol}^{-1}$ at 295 K which is somewhat higher than the expected spin-only value for two non-interacting $S = 1$ spin centers. Upon decreasing the temperature, the value decreases to $2.29 \text{ cm}^3 \text{ K mol}^{-1}$ at 50 K. Below 50 K, the $\chi_{\text{M}}T$ value decreases abruptly and reaches a value of $0.07 \text{ cm}^3 \text{ K mol}^{-1}$ at 2 K. Since, the X-ray diffraction data suggest that at all temperatures two nickel(II) centers are bridged by the (SQ-SQ) $_{\text{CS}}^{2-}$ ligand. Therefore, this type of variation of $\chi_{\text{M}}T$ value with temperature implies that an antiferromagnetic coupling between the two spins of the nickel(II) centers exists. The best-fit for the data gives values for the coupling constant $J = -2.764 \text{ cm}^{-1}$ and for $g = 2.267$. The equation for the SQUID data fit is given in the experimental section. On the basis of crystal structure data, it can be firmly said that the small negative value of J is indicative of a very weak antiferromagnetic coupling between the two nickel(II) ions.

The $\chi_{\text{M}}T$ vs. T plot of **5a** is shown in Figure 2.47. The SQUID data was collected in the temperature range 2–295 K. At 295 K, the $\chi_{\text{M}}T$ value is $0.90 \text{ cm}^3 \text{ K mol}^{-1}$ which is slightly higher than the expected value for two non-interacting $S = 1/2$ spin carriers. Upon cooling the sample from 295 to 55 K, the $\chi_{\text{M}}T$ value decreases to a value of $0.84 \text{ cm}^3 \text{ K mol}^{-1}$ from the value of $0.90 \text{ cm}^3 \text{ K mol}^{-1}$. On cooling the sample, further, from 55 to 2 K, an abrupt decrease of the $\chi_{\text{M}}T$ value was observed and the $\chi_{\text{M}}T$ value at 2 K is $0.04 \text{ cm}^3 \text{ K mol}^{-1}$. If the crystal structure data of **5a** is taken into account then such

variation of $\chi_M T$ with temperature strongly suggest that an antiferromagnetic coupling between the copper(II) ions exists. The best-fit of the data is achieved for the coupling constant $J = -4.634 \text{ cm}^{-1}$ and for $g = 2.19$. Based on the X-ray crystal structure data, the small negative value of J can only be correlated with the existence of a very weak antiferromagnetic coupling between the two copper(II) ions.

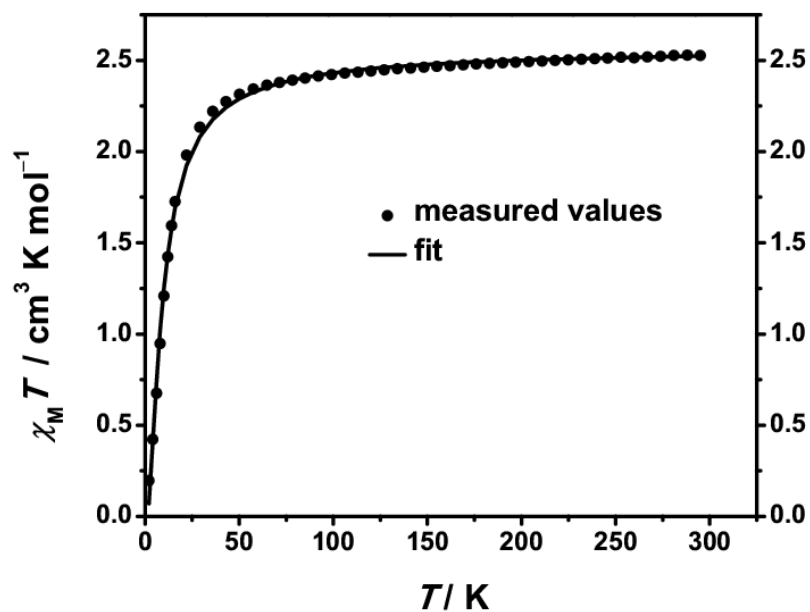


Figure 2.46: Variation of the product $\chi_M T$ with temperature for solid **4a**.

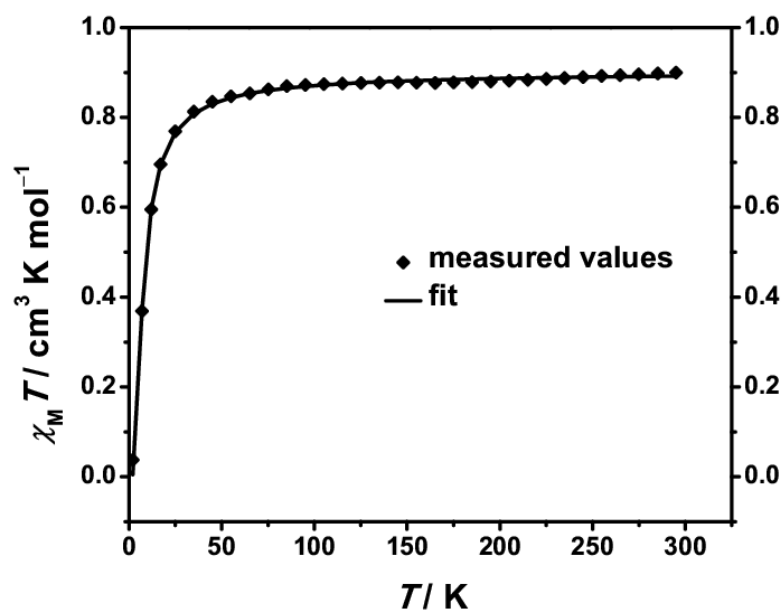


Figure 2.47: Variation of the product $\chi_M T$ with temperature for solid **5a**.

The variation of $\chi_M T$ with temperature for compound **6b** is shown in Figure 2.48. This type of $\chi_M T$ vs. T plot is typical for a diamagnetic complex. Based on the observation from X-ray crystallographic measurement and the SQUID data, the existence of temperature invariant diamagnetic $\text{Zn}^{\text{II}}\text{-(SQ-SQ)}_{\text{CS}}\text{-Zn}^{\text{II}}$ electronic state in compound **6b** is obvious.

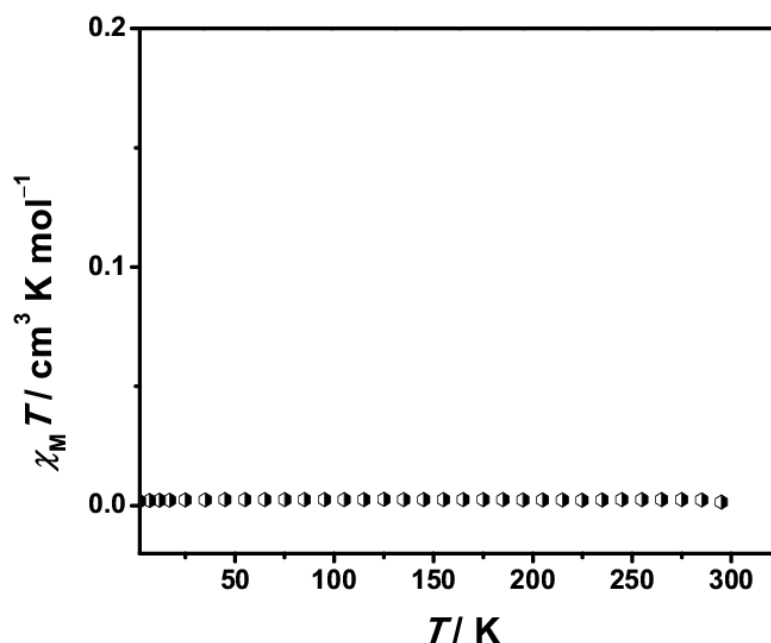


Figure 2.48: Variation of the product $\chi_M T$ with temperature for solid **6b**.

2.3.3.2 NMR Spectroscopic Properties

The ^1H NMR spectra of complexes **6a** and **6b** were measured in $[\text{D}_3]\text{MeCN}$ and $[\text{D}_6]\text{DMSO}$. The spectra are shown in Figures 2.49 and 2.50. The NMR data are provided in Table 2.27.

The ^1H NMR spectra show the presence of signals corresponding to the two $\text{L-N}_4\text{tBu}_2$ ligands but the signals corresponding to the bis(dioxolene) unit are absent. The difference between the two NMR spectra is that all the signals of the NMR spectrum in $[\text{D}_3]\text{MeCN}$ are sharp whereas in $[\text{D}_6]\text{DMSO}$, the signals corresponding to the pyridyl protons are sharp but the signals corresponding to the methylene and *tert*-butyl protons are broad.

The symmetry of complex **6** must be taken into account for a clear assignment of the signals. The discussion related to the symmetry of the complex **6** is as following: The complex molecule has C_{2h} symmetry. The principal axis *i.e.* C_2 axis is perpendicular to the plane in which the pyridine nitrogen donor atoms and oxygen donor atoms lie, and passes through the middle of the interannular carbon–carbon bond. Thus, the symmetry for one-half of the complex **6** can be described by C_s symmetry. Therefore, the protons of the four methylene groups of one $L-N_4tBu_2$ ligand where two protons of each CH_2 group are diastereotopic, would exhibit two AB splitting patterns. Here, one AB pattern is observed for the CH_2 pair lying above and below the σ -plane, and the other AB pattern is observed for the other CH_2 pair lying above and below the σ -plane. The *para*- and *meta*-pyridyl protons of one pyridine ring are not symmetrically equivalent with those protons of the other pyridine ring of one $L-N_4tBu_2$ ligand. Therefore, two signals are observed for each of the *para*- and *meta*-pyridyl protons.

In the 1H NMR spectrum of complex **6a** in $[D_3]MeCN$, the signal corresponding to the four *tert*-butyl groups of two $L-N_4tBu_2$ ligands appear as a singlet at 1.14 ppm (s, 36H). Each of the doublets at 3.52 ppm (d, $^2J_{HH} = 16.4$ Hz, 4H; CH_2) and 3.51 ppm (d, $^2J_{HH} = 16.8$ Hz, 4H; CH_2) is observed for the symmetrically equivalent four protons of the methylene groups of two $L-N_4tBu_2$ ligands. If the pair of doublets at 3.52 and 3.51 ppm is considered as the signals corresponding to the two A protons of the two AB systems, then a pair of doublets should also be found for the two B protons of the two AB systems. That pair of doublets is observed in the range of 4.64–4.52 ppm which looks like a doublet at a glance. However, a close look to the so-called doublet indicates that each of the line of this doublet has a shoulder. Hence, it can be said that there is a pair of doublets in the range of 4.64–4.52 ppm.

Here, the signals are represented as a doublet at 4.58 ppm (d, $^2J_{\text{HH}} = 16.4$ Hz, 8H; CH₂). The protons of the pyridine rings render two sets of signals at 7.82 ppm (t, $^3J_{\text{HH}} = 7.8$ Hz, 2H; *p*-PyH) and 7.80 ppm (t, $^3J_{\text{HH}} = 7.7$ Hz, 2H; *p*-Py-H). These signals are assigned to the two pairs of symmetrically equivalent *para*-pyridyl protons of the two L-N₄tBu₂ ligands. The expected two sets of doublets for the *meta*-pyridyl protons are merged with the multiplet corresponding to the *ortho*-phenyl protons of the BPh₄⁻ anions. Therefore, the signals corresponding to the *meta*-pyridyl protons are represented as a multiplet. The signals in the range 7.27–7.23 ppm (m, 8H; *m*-PyH) are assigned to two pairs of four symmetrically equivalent *meta*-pyridyl protons of the two L-N₄tBu₂ ligands.

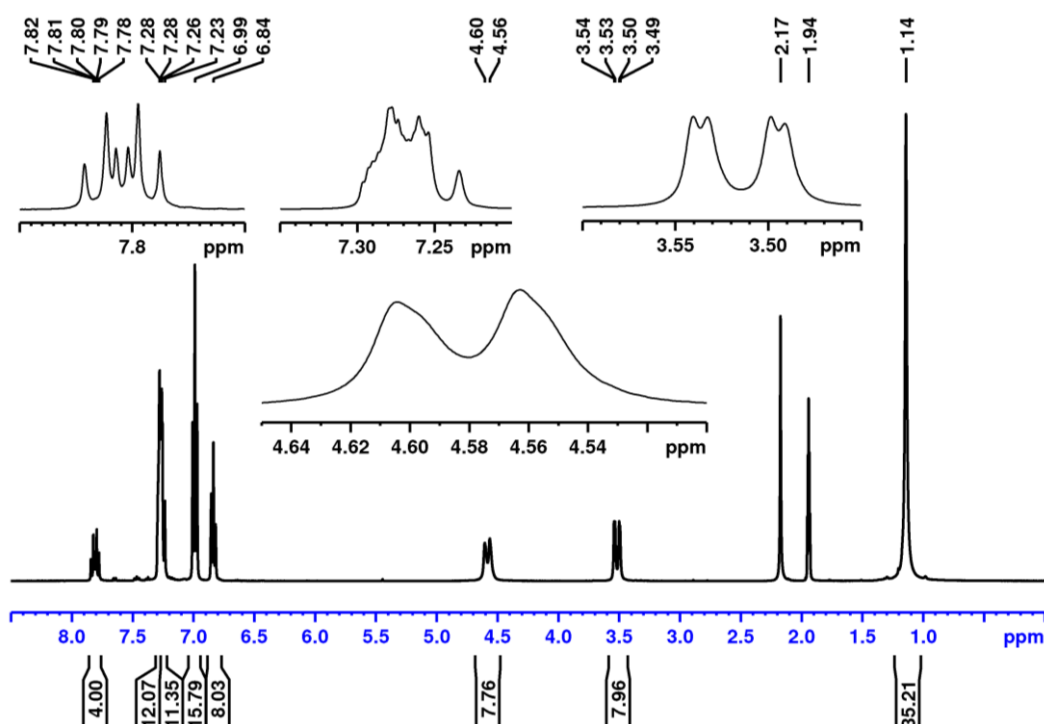


Figure 2.49: ¹H NMR of **6a** in [D₃]MeCN at RT. The insets show some peaks which are expanded for better visibility.

A comparison between the NMR spectra in [D₆]DMSO and [D₃]MeCN shows that the chemical shifts for the above mentioned protons are similar in both spectra. The integration of the protons of the pyridine rings and *tert*-butyl

groups are consistent with the integration of BPh_4^- anions but the integration of BPh_4^- anions does not match with the integration of methylene protons (Figure 2.50). The broadening of the signals corresponding to the methylene protons could be due to the dynamic effect and generation of the one-electron reduced species of complex **6** in its solution (see discussion in section 2.3.3.3).

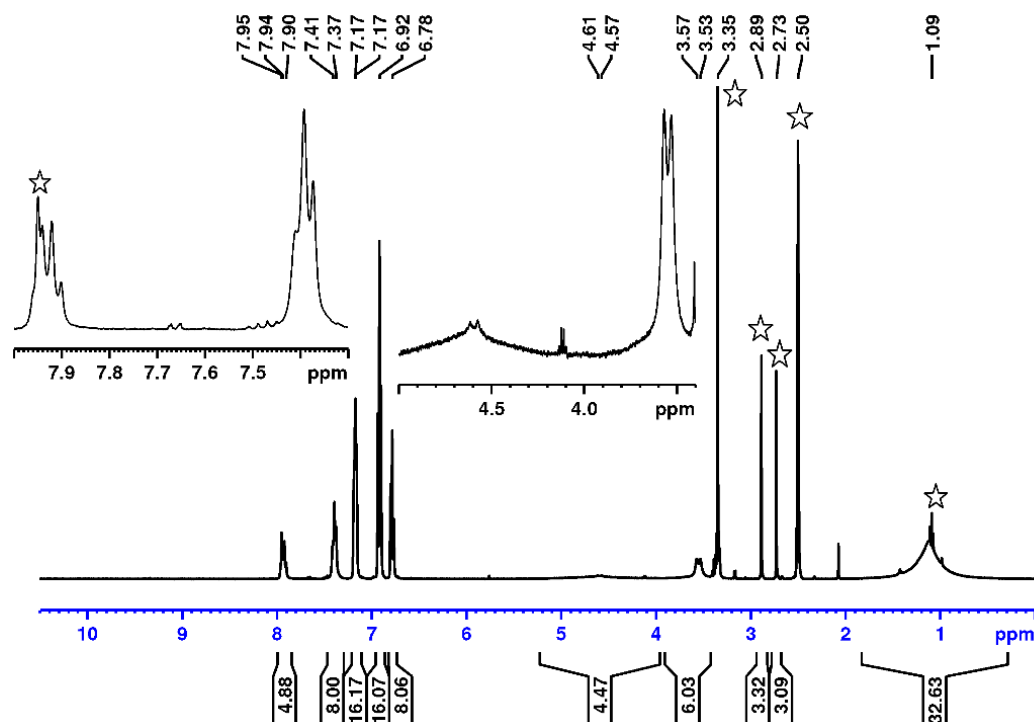


Figure 2.50: ^1H NMR of **6b** in $[\text{D}_6]\text{DMSO}$ at RT. The insets show some peaks which are expanded for better visibility. The solvent residual and water signals are marked by stars. The inconsistent integration of DMF protons is due to the sample preparation technique.

The ^1H NMR spectra reveal that the bis(dioxolene) ligand is not replaced fully or partially by solvent molecules because coordination of solvent molecules to form a mixture of $2 \times [\text{Zn}(\text{L-N}_4\text{tBu}_2)(\text{solv})_2]^{2+}$ and $(\text{SQ-SQ})^{2-}$ would have rendered one-set of signals for each of the *para*- and *meta*-pyridyl protons, and the methylene protons would have displayed one AB splitting pattern due to the C_{2v} symmetry of the $[\text{Zn}(\text{L-N}_4\text{tBu}_2)(\text{MeCN-D}_3)_2]^{2+}$ complex. Additionally, $(\text{SQ-SQ})^{2-}$ would have exhibited signals in the diamagnetic range because the UV/Vis/NIR spectrum of the $(\text{SQ-SQ})^{2-}$ ligand suggests that

the ligand exists in its closed-shell state. On the other hand, if partial replacement of the bis(dioxolene) ligand takes place and a mixture of $[\text{Zn}(\text{L-N}_4\text{tBu}_2)(\text{solv})_2]^{2+}$ and $[\text{Zn}(\text{L-N}_4\text{tBu}_2)(-\text{SQ-SQ})]$ species is formed, then signals for the $(\text{SQ-SQ})^{2-}$ ligand of the latter complex should have been observed.

The ^1H NMR spectra do not show any indication for the occurrence of any dissociation reaction or equilibrium because in the spectrum, the integration value of the pyridyl protons are consistent with the integration value of tetraphenylborate counter anions when the integrations are performed by considering the number of protons for only complex **6**. However, the UV/Vis/NIR spectroscopic study of the complex **6b** reveals that an equilibrium between complex **6** and unidentified species exists in the solution of **6** (see discussion in section 2.3.6). Therefore, it could be said that the rate of the backward reaction of that equilibrium is faster than the NMR time scale.

Table 2.27: Data for the ^1H NMR of **6a** (400 MHz, $[\text{D}_3]\text{MeCN}$, RT) and **6b** (400 MHz, $[\text{D}_6]\text{DMSO}$, RT).

Compound (solvent)	δ/ppm
6a ($[\text{D}_3]\text{MeCN}$)	7.82 (t, $^3J_{\text{HH}} = 7.8$ Hz, 2H; <i>p</i> -Py-H), 7.80 (t, $^3J_{\text{HH}} = 7.7$ Hz, 2H; <i>p</i> -Py-H), 7.27–7.23 (m, 8H; <i>m</i> -Py-H), 4.58 (d, $^2J_{\text{HH}} = 16.4$ Hz, 8H; CH_2), 3.52 (d, $^2J_{\text{HH}} = 16.4$ Hz, 4H; CH_2), 3.51 (d, $^2J_{\text{HH}} = 16.8$ Hz, 4H; CH_2), 1.14 (s, 36H; <i>t</i> Bu), 6.83 (t, $^3J_{\text{HH}} = 7.2$ Hz, 8H; <i>p</i> -Ph-H, BPh_4^-), 6.98 (t, $^3J_{\text{HH}} = 7.5$ Hz, 16H; <i>m</i> -Ph-H, BPh_4^-), 7.29–7.25 (m, 16H; <i>o</i> -Ph-H, BPh_4^-)
6b ($[\text{D}_6]\text{DMSO}$)	7.95–7.90 (m, 4H; <i>p</i> -Py-H), 7.41–7.37 (m, 8H; <i>m</i> -Py-H), 4.59 (br, 4H; CH_2), 3.55 (d, $^2J_{\text{HH}} = 15.6$ Hz, 6H; CH_2), 1.09 (br, 36H; <i>t</i> Bu), 6.78 (t, $^3J_{\text{HH}} = 7.2$ Hz, 8H; <i>p</i> -Ph-H, BPh_4^-), 6.91 (t, $^3J_{\text{HH}} = 7.2$ Hz, 16H; <i>m</i> -Ph-H, BPh_4^-), 7.19–7.15 (m, 16H; <i>o</i> -Ph-H, BPh_4^-)

Since, the expected signals for the case when the replacement of the bis(dioxolene) ligand by solvent molecules occur, are not observed, therefore, the absence of the signals corresponding to the $(\text{SQ-SQ})_{\text{CS}}^{2-}$ ligand is most likely due to the dynamic effect and the presence of a paramagnetic substance which is evidenced by the EPR spectra of complex **6b**. The EPR spectra reveal that the paramagnetic substance is the one-electron reduced species of complex **6**.

2.3.3.3 EPR Spectroscopic Properties

The measurement of EPR spectrum of **6b** ($c = 6 \text{ mM}$) in 0.2 M TBAP/acetonitrile at room temperature shows an EPR signal at a g value of 2.005 but with a very low intensity (Figure 2.51), which is indicative of the presence of very small amount of $\mathbf{6}^{\bullet-}$. So, one of the explanations for the incoherent observation in the NMR spectrum, is the presence of $\mathbf{6}^{\bullet-}$ with dissolved **6**.

Next aim was to know the origin of the paramagnetic species. The first thought was that the small amount of paramagnetic species could be present in the sample due to generation of $\mathbf{6}^{\bullet-}$ during its synthesis and could not be separated from the desired compound by crystallization technique such that it remained as a contamination with the desired compound. The second thought was that, the coordinating solvent such as MeCN might coordinate to the metal center or centers, and the dissociated products might itself be a paramagnetic species or as a result of instability of the dissociated product, the complex $\mathbf{6}^{\bullet-}$ was generated. Here, the instability refers to the decomposition of the dissociated product to $\mathbf{6}^{\bullet-}$ or due to the dissociated product's redox property, some kind of redox reactions were going on in solution state, thus the product $\mathbf{6}^{\bullet-}$ was generated.

If the first thought stands true, then EPR signals with similar intensity would be observed in better coordinating solvent than MeCN such as DMF. Therefore, the EPR spectrum of compound **6b** ($c = 6$ mM) was also recorded in 0.2 M TBAP/DMF (Figure 2.52). The similarity between the EPR spectra, recorded in MeCN and DMF, was that both spectra show signals at a g value of 2.005 but the intensity of the signal was higher in DMF than in MeCN. In addition, the intensity of the signal of the EPR spectrum, recorded in DMF, increased with time (Figure 2.53). Therefore, the second thought seems to be a valid reason for the observation of EPR signals.

In the redox series of complex **6**, the one-electron reduced and oxidized species of **6** would be EPR active. After performing the cyclic voltammograms of the complex **6b**, in 0.2 M TBAP/DMF and in 0.2 M TBAP/MeCN (see discussion in section 2.3.7), it was found that the one-electron reduced species $[\text{Zn}_2(\text{L-N}_4\text{tBu}_2)_2(\text{Cat-SQ})^{\bullet 3-}]^+$ (**6^{•-}**) could be synthesized electrochemically. Thus, the one-electron reduced species was synthesized electrochemically. However, any attempt to synthesize the oxidized complex $[\text{Zn}_2(\text{L-N}_4\text{tBu}_2)_2(\text{SQ-BQ})^{\bullet -}]^{3+}$ (**6^{•+}**) was not made because the irreversible oxidation of complex **6** occurred at higher redox potential than the anodic potential value for the irreversible oxidation of BPh_4^- anion.

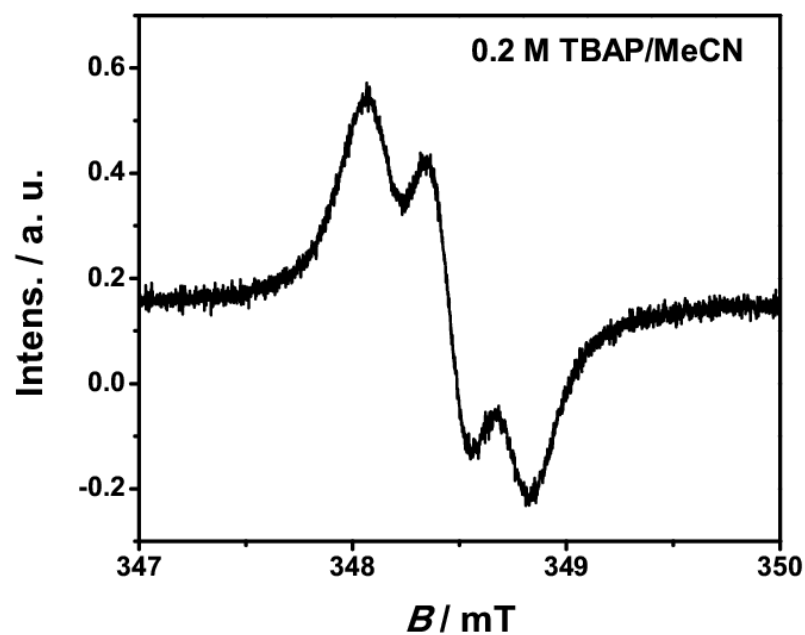


Figure 2.51: EPR spectrum of dissolved **6b** (concentration = 6×10^{-3} M) in 0.2 M TBAP/MeCN at room temperature.

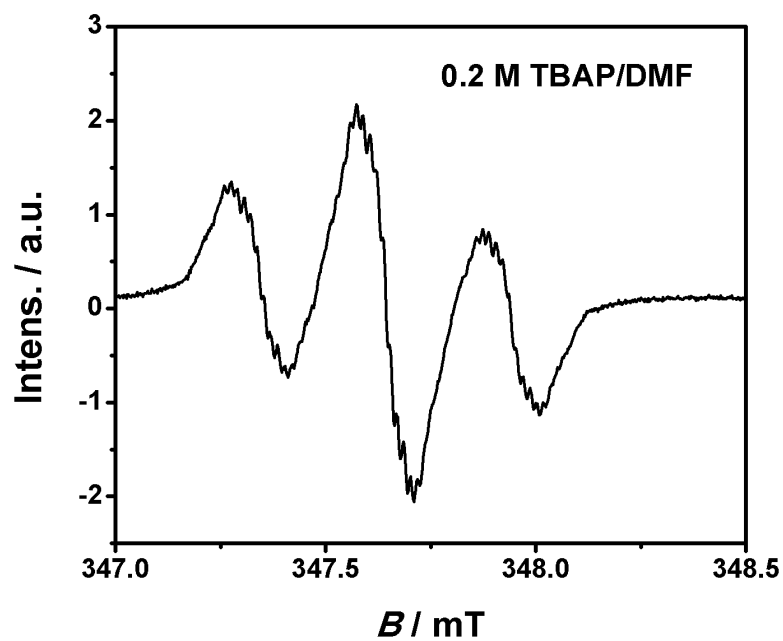


Figure 2.52: EPR spectrum of dissolved **6b** (concentration = 6×10^{-3} M) in 0.2 M TBAP/DMF at room temperature.

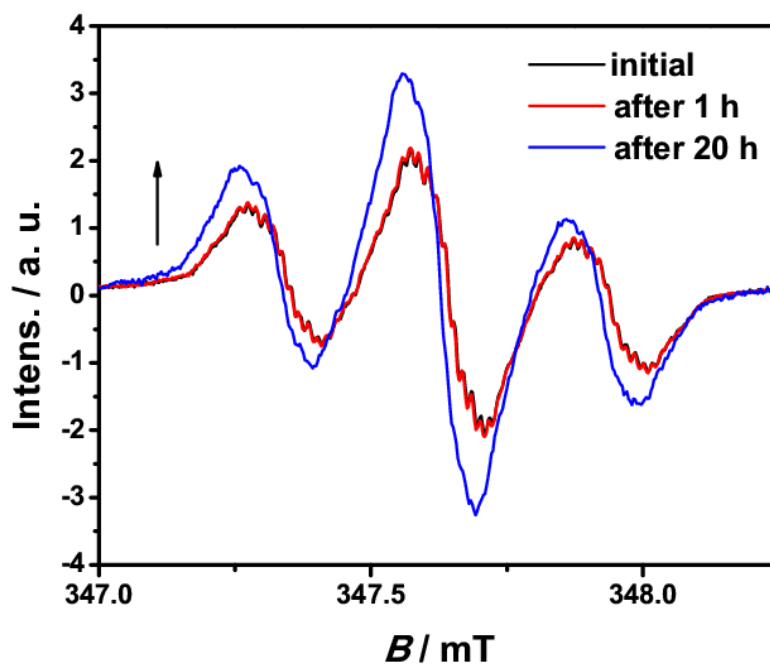


Figure 2.53: EPR spectra of dissolved **6b** (concentration = 6×10^{-3} M) in 0.2 M TBAP/DMF at room temperature. The spectra show the changes in intensity of the signals with time.

The EPR spectrum of the one-electron reduced species $[\text{Zn}_2(\text{L-N}_4t\text{Bu}_2)_2(\text{Cat-SQ})^{\bullet 3-}]^+$ (**6 \bullet**) is shown in Figure 2.54. The isotropic signal is centered at a g value of 2.005. The simulation of the EPR spectrum reveal that the unpaired electron is coupled with six ^1H nuclei of $(\text{Cat-SQ})^{\bullet 3-}$ ligand and four amine ^{14}N nuclei of two $\text{L-N}_4t\text{Bu}_2$ ligands. There are total six ^1H nuclei (3×2 equivalent nuclei). The coupling constants for ^1H , a_{H} are 8.12, 1.46 and 0.86 MHz. The coupling constants are in the decreasing order for the ^1H nuclei at 2/2', 5/5' and 6/6' positions of the bis(dioxolene) ligand. There are total eight ^{14}N nuclei (2×4 equivalent nuclei). However, only coupling to the amine nitrogen nuclei is observed. The coupling constant a_{Namine} is 0.38 MHz. The coupling to the ^{14}N nuclei of pyridine rings is not observed. If there is any coupling between the radical and pyridine nitrogen nuclei then that coupling is too weak to be observed. The simulation of the EPR spectrum strongly indicates that the radical is delocalized over the entire $(\text{Cat-SQ})^{\bullet 3-}$ moiety. The

electronic absorption spectrum of one-electron reduced species ($\mathbf{6}^{\bullet-}$) also supports this assignment.

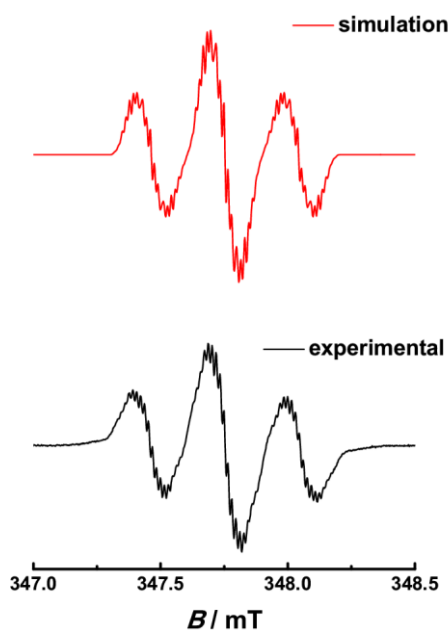


Figure 2.54: EPR spectrum of the one-electron reduced species of dissolved $\mathbf{6b}$ in 0.2 M TBAP/DMF at room temperature.

The solution state EPR spectrum pattern of $\mathbf{6b}$ is very similar with the EPR pattern of $[\text{Zn}_2(\text{L-N}_4t\text{Bu}_2)_2(\text{Cat-SQ})^{\bullet 3-}]^+$, therefore, the EPR active species for the dissolved $\mathbf{6}$ is $\mathbf{6}^{\bullet-}$. However, currently, there is no evidence to propose the mechanism for the formation of the complex $\mathbf{6}^{\bullet-}$ in the solution of $\mathbf{6}$, and it remains unclear.

2.3.4 Mass Spectroscopic Properties

The ESI-MS spectra of $\mathbf{6b}$ in MeCN are shown in Figure 2.55. An intense peak is found at $m/z = 525.20$ and moderate peaks are found at m/z values of 451.20 and 631.22. The peak at $m/z = 525.20$ is assigned to the molecular ion peak for $[\text{Zn}_2(\text{L-N}_4t\text{Bu}_2)_2(\text{SQ-SQ})]^{2+}$ ($\mathbf{6}$) fragment because the observed experimental molecular ion peak is matching with the simulated peak (calcd. $m/z = 525.20$). Thus, the ESI-MS spectra suggest that the coordination of the

bis(dioxolene) ligand to two $[\text{Zn}(\text{L-N}_4\text{tBu}_2)]^{2+}$ fragments is not totally perturbed in the solution of the complex **6b**. In other words, the complex **6** does not dissociate or disproportionate completely in its acetonitrile solution.

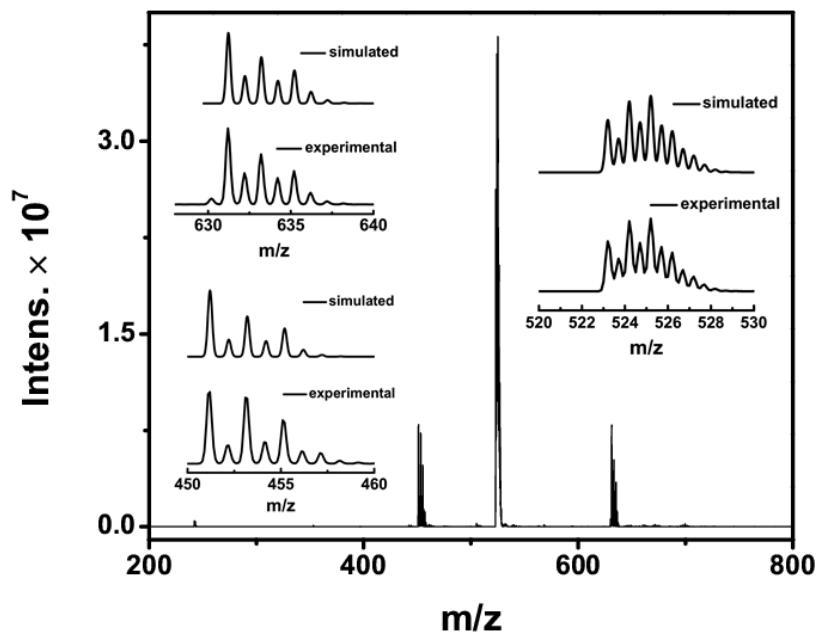
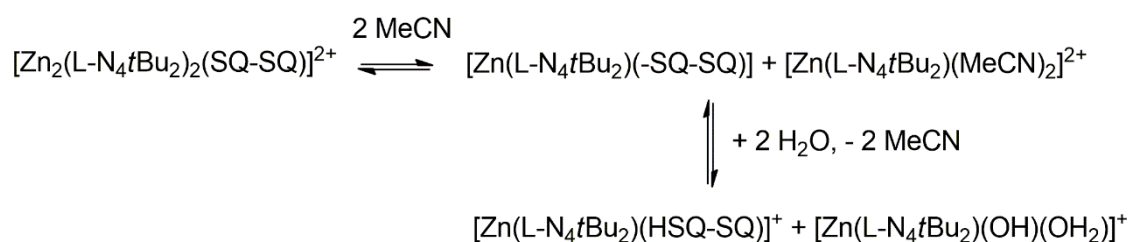


Figure 2.55: ESI-MS spectra of **6b** in MeCN. The inset on the right side shows experimental and simulated spectra at $m/z = 525.20$. The insets on the left side show experimental and simulated spectra at $m/z = 451.21$ (bottom) and 631.23 (top).

The molecular ion peak at $m/z = 451.20$ (calcd. $m/z = 451.21$) corresponds to the $[\text{Zn}(\text{L-N}_4\text{tBu}_2)(\text{OH})(\text{OH}_2)]^+$ fragment. The molecular ion peak at $m/z = 631.22$ (calcd. $m/z = 631.23$) corresponds to the $[\text{Zn}(\text{L-N}_4\text{tBu}_2)(\text{HSQ-SQ})]^+$ fragment. The proposed mechanism for the formation of these two complexes is outlined in Scheme 2.9. The formation of these two complexes could be possible due to the dissociation of complex **6** to $[\text{Zn}(\text{L-N}_4\text{tBu}_2)(-\text{SQ-SQ})]$ (**7**) and $[\text{Zn}(\text{L-N}_4\text{tBu}_2)(\text{MeCN})_2]^{2+}$ and then reaction with water. However, formation of these two complexes in solution would not explain the observation by EPR and NMR spectroscopy because both the dissociated products would be diamagnetic. The UV/Vis/NIR spectrum of complex **6** also does not indicate that the $[\text{Zn}(\text{L-N}_4\text{tBu}_2)(\text{HSQ-SQ})]^+$ complex is present in MeCN.

The presence of water in the reaction medium might be due to the solvent used. Further attempts to record the ESI-MS spectrum in a condition where water would be excluded, exclusively from the reaction medium, were not made because the NMR spectrum of complex **6** in $[D_3]MeCN$ did not show signals corresponding to the $[Zn(L-N_4tBu_2)(OH)(OH_2)]^+$ and $[Zn(L-N_4tBu_2)(HSQ-SQ)]^+$ complexes (see discussion in section 2.3.3.2). Although, the inclusion of water into the reaction medium was unintentional, but presence of water led to the identification of $[Zn(L-N_4tBu_2)(-SQ-SQ)]$ as one of the dissociated products because being a neutral complex, it would not have shown peaks in the ESI-MS spectrum. Rather, abstraction of a proton from the water molecule led to the formation of the positively charged $[Zn(L-N_4tBu_2)(HSQ-SQ)]^+$ complex which displayed the corresponding molecular ion peak. Thus, the mass spectrometry indicates that there could be occurrence of dissociation of complex **6** in MeCN in presence of water.



Scheme 2.9: Dissociation of complex **6**, and reaction of the dissociated products with water.

2.3.5 Infrared Spectroscopic Properties

The infrared spectroscopic investigations for **4a**, **5a** and **6b** were performed with KBr pellet sampling techniques (Figures 2.56, 2.57 and 2.58) at room temperature. The IR spectroscopic investigation for **5a** was also performed with ATR sampling technique (see Figure A.121 in section 6.3.2 in appendix). The ATR and KBr pellet IR spectra are similar. The reason for using the ATR sampling technique is to compare the spectrum of **5a** with those of **3c** and **3d**,

and thereby detect the differences between these spectra. In order to compare the IR spectra features of the complexes **3b**, **4a**, **5a** and **6b**, a stacked spectra representing the KBr pellet spectra of these compounds are shown in Figures A.124–A.125 and the IR data of all the compounds are given in Table A.24 (see in section 6.3.2 in appendix). The IR spectra of KBr pellets of **4a**, **5a** and **6b** are similar with the KBr pellet spectrum of **3b** at room temperature. The intense bands at 1504 and 1519 cm^{-1} (**4a**), 1505 cm^{-1} (**5a**), 1515 and 1532 cm^{-1} (**6b**) in the IR spectra of all the complexes are tentatively assigned to the marker bands for the $(\text{SQ-SQ})_{\text{CS}}^{2-}$ ligand. The deconvolution of the IR spectra of these compounds by Gaussian function also shows that for compound **4a**, two bands at 1502 and 1519 cm^{-1} , compound **5a**, one intense band at 1507 cm^{-1} and compound **6b**, two bands at 1514 and 1533 cm^{-1} are present in the range of 1500–1550 cm^{-1} (see Figures A.126–A.128 in section 6.3.2 in appendix).

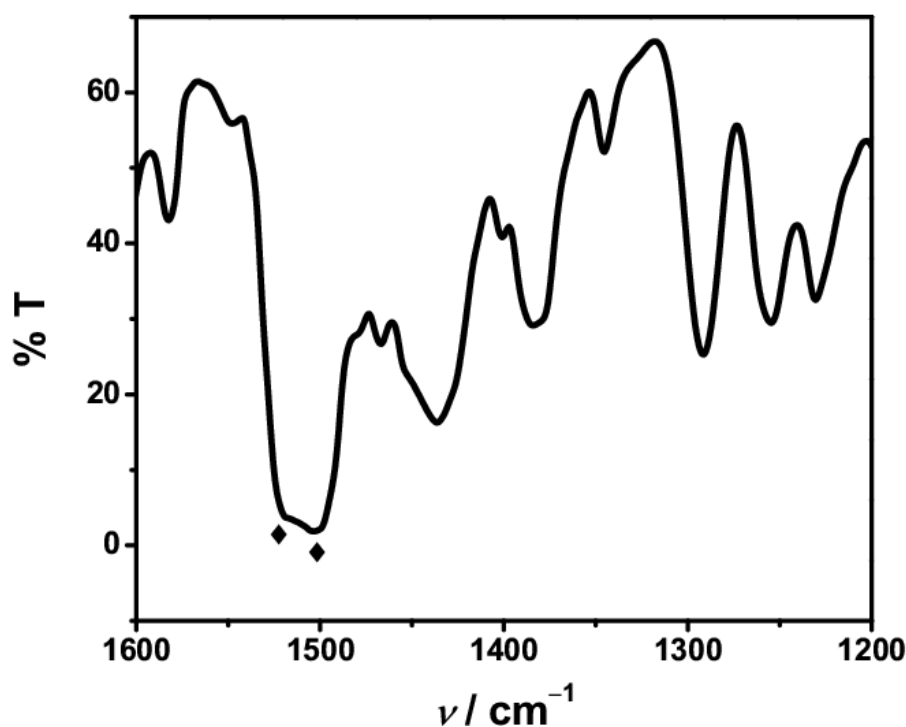


Figure 2.56: IR spectrum of **4a** in KBr pellet at room temperature, showing the bands associated with closed-shell semiquinonate-semiquinonate ligand marked by filled diamonds.

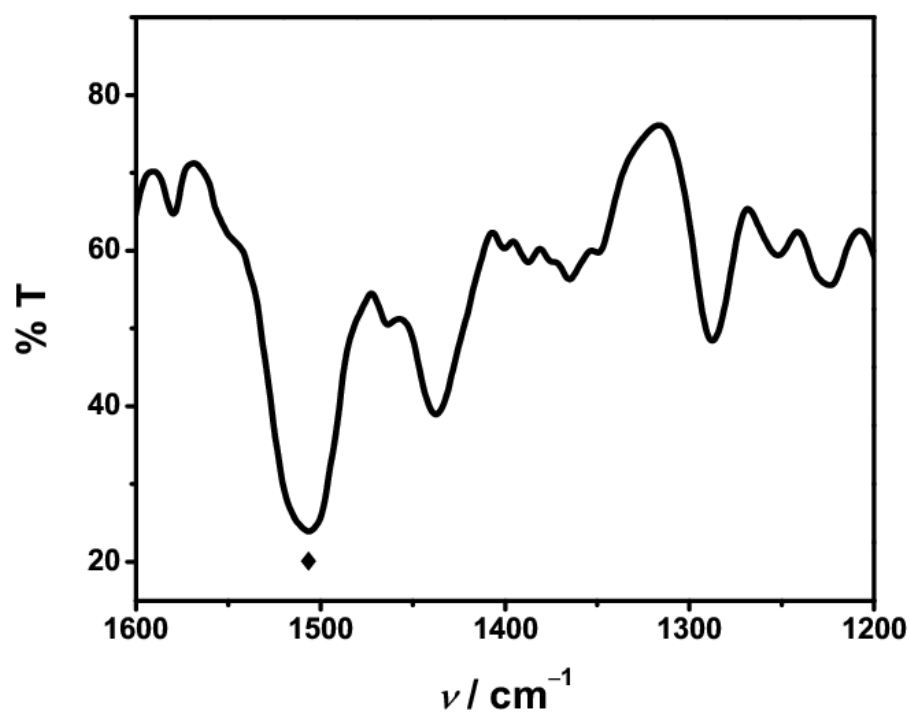


Figure 2.57: IR spectrum of **5a** in KBr pellet at room temperature, showing the bands associated with closed-shell semiquinonate-semiquinonate ligand marked by filled diamonds.

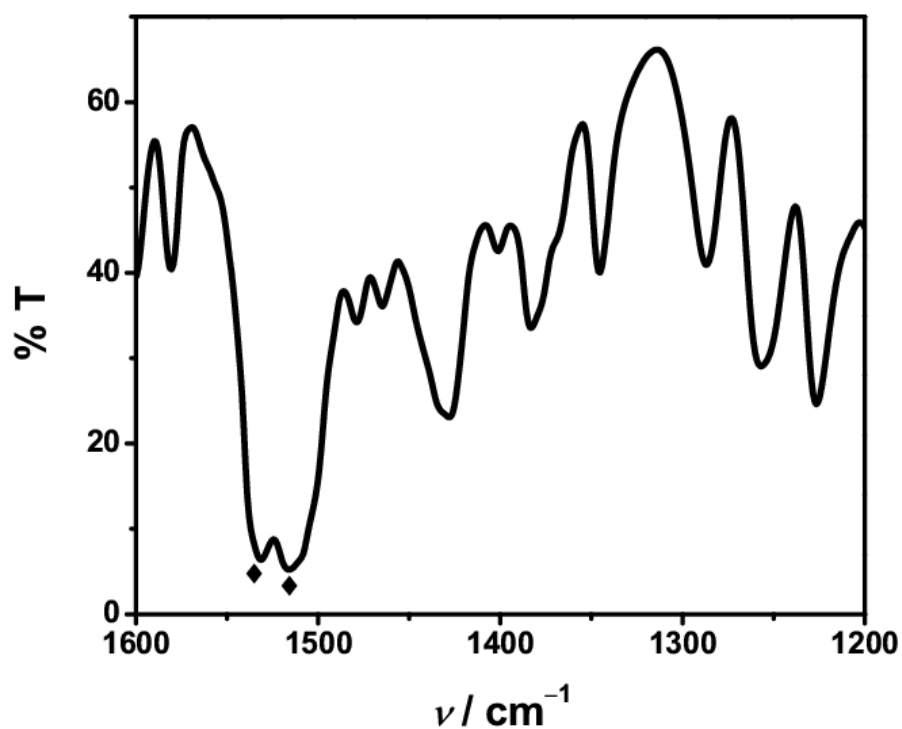


Figure 2.58: IR spectrum of **6b** in KBr pellet at room temperature, showing the bands associated with closed-shell semiquinonate-semiquinonate ligand marked by filled diamonds.

2.3.6 UV/Vis/NIR Spectroscopic Properties

The UV/Vis/NIR spectra of **4a**, **5a** and **6b** are presented in Figures 2.59–2.61. All these spectra were recorded in acetonitrile at room temperature. The UV/Vis/NIR data are provided in Table 2.28. The spectra are fitted with sum of Gaussian peaks. The Gaussian peaks are shown in Figures A.129–A.131 (see in section 6.3.3 in appendix). The found data from the Gaussian fitting such as molar extinction coefficient, absorption maxima and area under the peaks are given in Table A.25 (see in section 6.3.3 in appendix).

The UV/Vis spectrum of 3,3'-dihydroxy-diphenoquinone-(4,4') and Gaussian fit of the spectrum (see Figures A.92–A.93 in section 6.2.4 in appendix) have helped to understand and assign the various absorptions which are observed for the bis(dioxolene) ligand (SQ-SQ)_{CS}²⁻ of the above complexes. The absorption maxima values are given in Table 2.28. The spectrum shows two bands with absorption maxima at 474 nm (13100 M⁻¹ cm⁻¹), 413 nm (12800 M⁻¹ cm⁻¹). These values are in agreement with the reported values.^[124] The Gaussian fit of the UV/Vis spectrum provide absorption maxima at 485 and 415 nm in the visible region. All these peaks are assigned to $\pi \rightarrow \pi^*$ transitions.

In order to see the UV/Vis/NIR spectral changes of H₂(SQ-SQ) upon deprotonation, the UV/Vis/NIR spectrum was recorded from a solution containing mixture of sodium hydroxide and H₂(SQ-SQ) in 1,4-dioxane and methanol (see Figure A.94 in section 6.2.4 in the appendix). The spectrum shows intense absorptions at 699 and 426 and 336 nm. The main components from the Gaussian fitting are found at 708, 426 and 333 nm (see Figure A.95 in section 6.2.4 in appendix). There remains always a question whether the H₂(SQ-SQ) ligand was fully or partially deprotonated. However, based on the UV/Vis/NIR spectrum of the metal bis(dioxolene) complexes, it can be said that the spectral feature corresponds to the closed-shell bis(dioxolene) ligand.

The compounds **4a**, **5a** and **6b** show intense bands at around 700, 522 (sh), 465 nm which are assigned to the ligand-based absorptions of the (SQ-SQ)_{CS}²⁻ moiety. The main peaks of the Gaussian fit of the UV/Vis/NIR spectra of these complexes are found at around 705, 465 and 300 nm. All these absorptions are assigned to the $\pi \rightarrow \pi^*$ transitions of the bis(dioxolene) ligands in their closed-shell states. Among these bands, the bands at around 705 nm are assigned to the HOMO–LUMO transitions of the (SQ-SQ)_{CS}²⁻ ligands of these compounds. The bands in the UV region at around 295 and 330 nm are tentatively assigned to the ligand-based absorptions corresponding to the (SQ-SQ)_{CS}²⁻ ligand. The bands at around 310 nm in the spectra of **4a** and **5a** are tentatively assigned to the (Ni^{II}/Cu^{II})–pyridine MLCT transition.^[122]

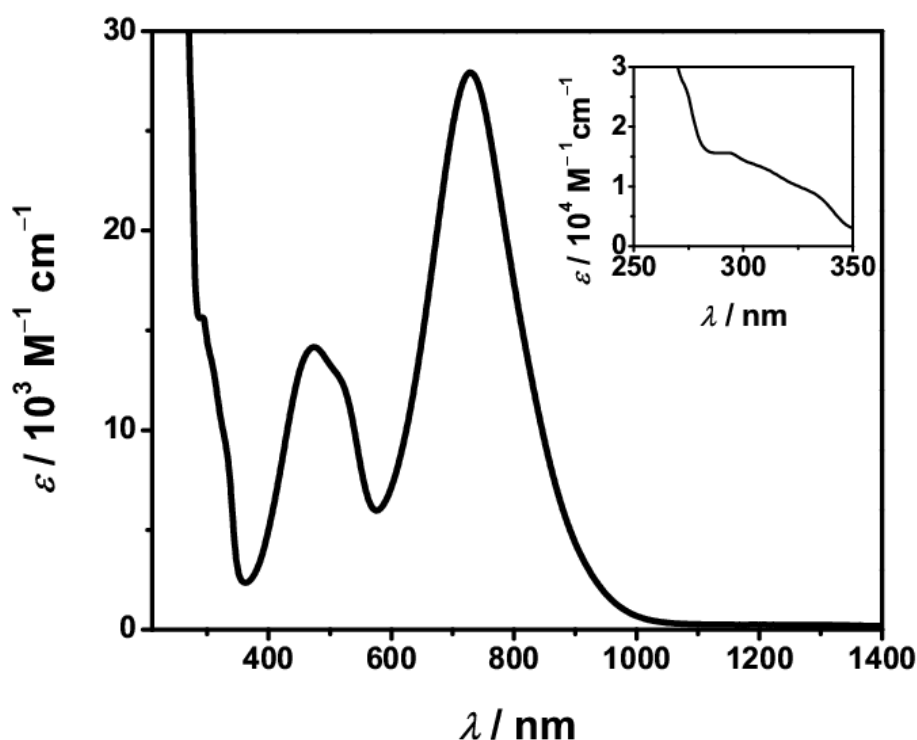


Figure 2.59: UV/Vis/NIR spectrum of **4a** in MeCN at RT. The inset shows the bands in UV region.

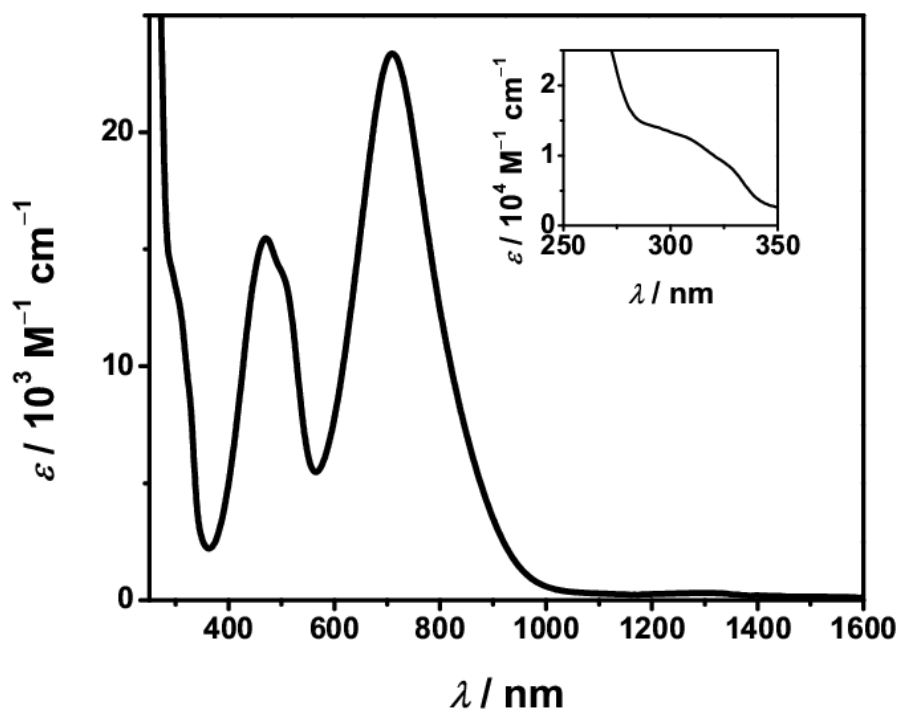


Figure 2.60: UV/Vis/NIR spectrum of complex **5a** in MeCN at RT. The inset shows the bands in the UV region.

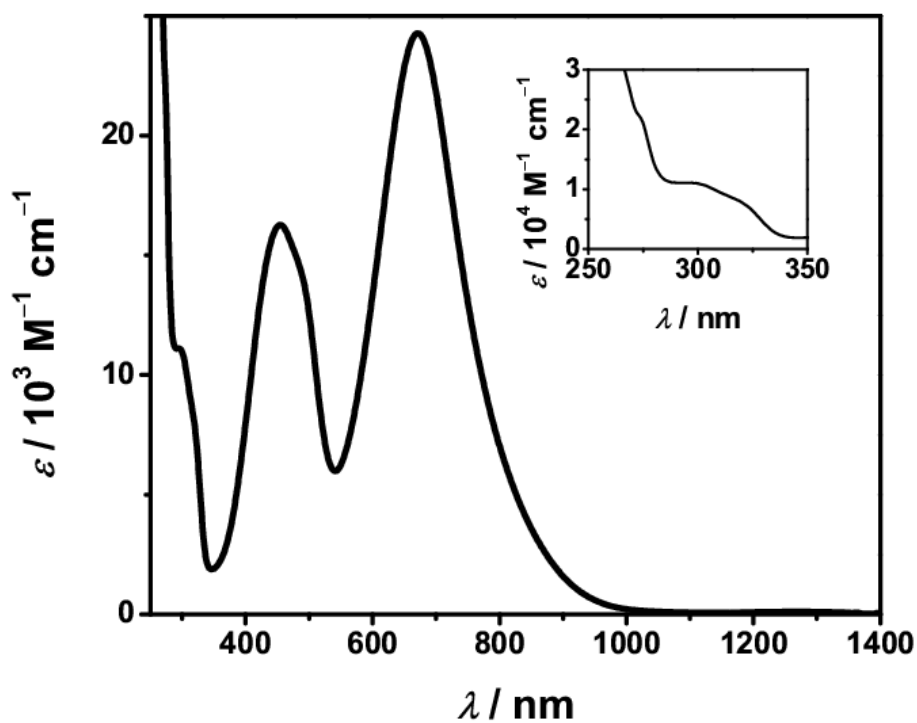


Figure 2.61: UV/Vis/NIR spectrum of **6b** in MeCN at RT. The inset shows the bands in the UV region.

Table 2.28: UV/Vis/NIR data of H₂(SQ-SQ), (SQ-SQ)_{CS}²⁻, **4a**, **5a**, **6b** and **6^{•-}** at room temperature.

Compound (solvent)	λ_{\max}/nm ($\epsilon/\text{M}^{-1} \text{cm}^{-1}$)
H ₂ (SQ-SQ) (1,4-dioxane)	474 (13100), 413 (12800)
(SQ-SQ) ²⁻ (1,4-dioxane) ^[a]	699 (1), 426 (0.69), 336 (0.76)
4a (MeCN)	727 (27900), 522 (12200), 475 (14200), 332 (8900), 310 (12800), 294 (15600)
5a (MeCN)	709 (23300), 508 (13600), 471 (15500), 330 (7700), 310 (12200), 294 (14000)
6b (MeCN)	671 (24300), 495 (13400), 455 (16300), 322 (7340), 300 (11000)
6b (DMF, 293 K)	1271 (1340), 857 (23100), 796 (21000), 700 (12200), 480 (6000), 465 (6800), 449 (7200), 354 (12500)
6b (DMF, 213 K)	1271 (2900), 867 (18000), 786 (17500), 707 (16800), 506 (7000), 478 (11300), 460 (12200), 449 (12300), 357 (9600)
6b (DMSO, RT)	1271 (710), 870 (8300), 691 (17400), 504 (8700), 483 (11000), 455 (12100), 360 (4850)
6^{•-} (DMF)	1279 (26100), 1063 (8710), 615 (3430), 569 (6740), 529 (5080), 476 (32116), 463 (34400), 450 (36518), 334 (5776), 313 (11300), 294 (17800), 274 (32500)

^[a] The relative intensities of the absorption maxima are given in the parentheses with respect to the maximum at 699 nm.

In order to compare the UV/Vis/NIR features of the complexes, their UV/Vis/NIR spectra are again shown in Figure 2.62. The spectra reveal that all the bands corresponding to the $\pi \rightarrow \pi^*$ transitions in the visible/NIR region of the spectra are red-shifted. The spectra in Figure 2.63 show very weak bands in the NIR region. The weak NIR bands for complexes **4a** and **5a** are tentatively assigned to the SOMO–LUMO transitions corresponding to the one-electron reduced species of the respective complexes. For complex **6b**, the weak NIR band is assigned to the SOMO–LUMO transition of its one-electron reduced species.

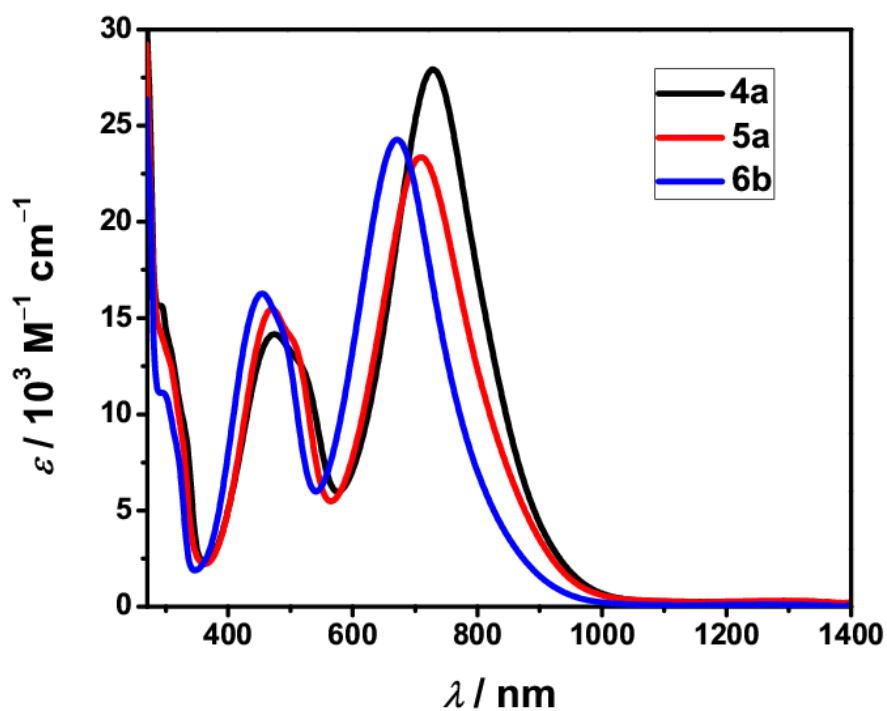


Figure 2.62: UV/Vis/NIR spectra for the MeCN solutions of **4a**, **5a** and **6b** at RT.

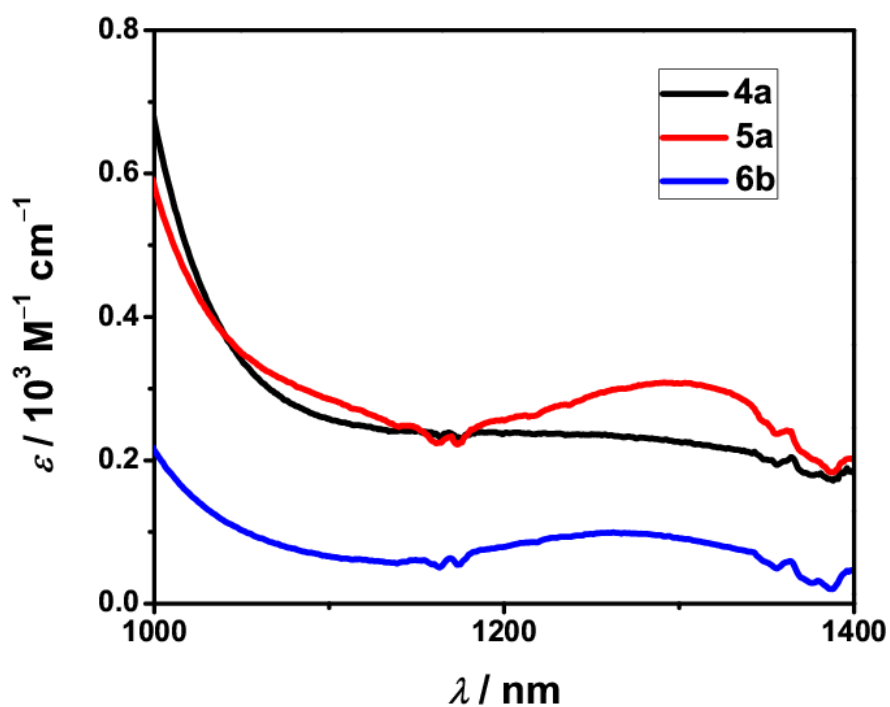


Figure 2.63: NIR spectra of the MeCN solutions of **4a**, **5a** and **6b** at RT. The spectra are plotted by the adjustment of the above Figure 2.62.

After observing the distinct NMR spectra of complex **6** in $[\text{D}_3]\text{MeCN}$ and $[\text{D}_6]\text{DMSO}$, and a sufficiently resolved EPR signal in TBAP/DMF, in the hope

to observe different UV/Vis/NIR features in DMSO and DMF than MeCN, the UV/Vis/NIR spectra of compound **6b** were recorded in DMSO and DMF. The spectra of **6b** in those solvents are shown in Figure 2.64. The data for the absorption are shown in Table 2.28 (see above). The concentration of the samples of **6b** in MeCN, DMSO and DMF are given in Table 2.29.

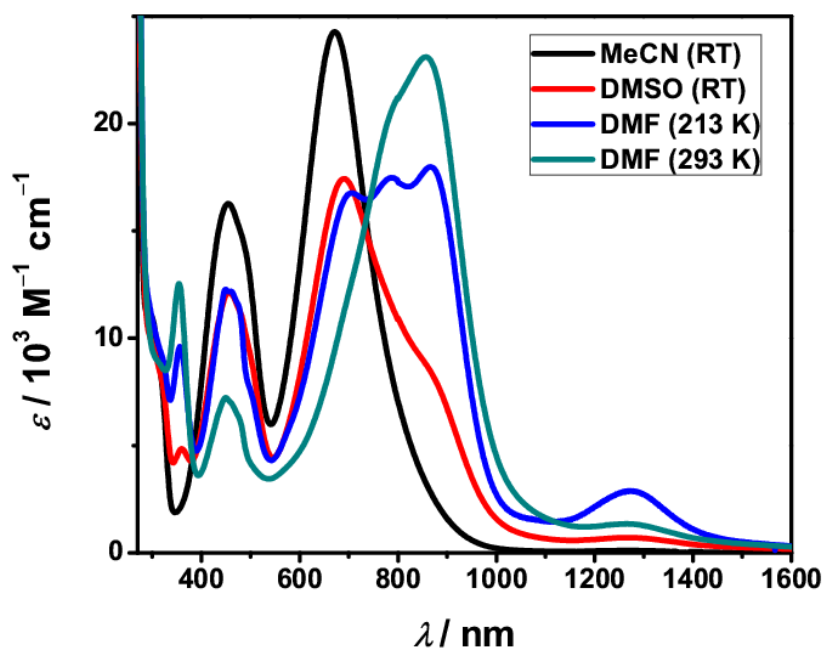


Figure 2.64: UV/Vis/NIR spectrum of **6b** in MeCN and DMSO at RT, and in DMF at 293 K.

The spectra in DMSO and DMF reveal that in addition to the bands for $(\text{SQ-SQ})_{\text{CS}}^{2-}$, at room temperature, new bands at around 870 and 691 nm are present and they are almost absent in the spectrum in MeCN. The intensity of these new bands is smaller at 213 K in the spectrum in DMF compared to that of the spectrum in DMF at 293 K, but the bands corresponding to the HOMO–LUMO transition of $(\text{SQ-SQ})_{\text{CS}}^{2-}$ are intense compared to the intensity of these bands in the spectrum in DMF at 293 K. The presence of $\mathbf{6}^{\bullet-}$ in the solutions of **6b** in DMF and DMSO to a much smaller amount is evidenced by the appearance of the bands at 1271 and 480 nm which are observed in the UV/Vis/NIR spectrum of $\mathbf{6}^{\bullet-}$ (see Figure 2.69).

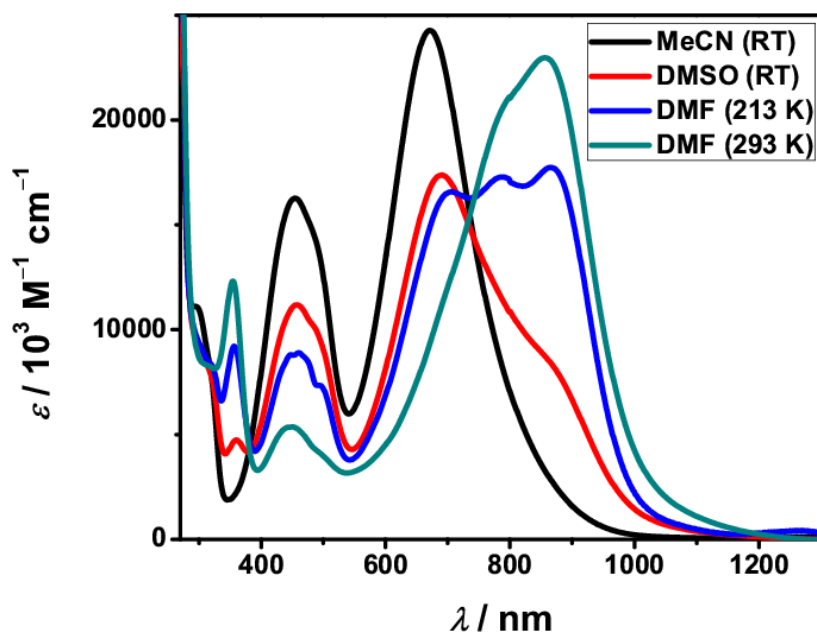


Figure 2.65: UV/Vis/NIR spectra of **6b** in MeCN and DMSO at room temperature and DMF at 213 and 293 K. The spectra in DMSO and DMF are the spectra obtained after subtraction of the UV/Vis/NIR spectrum of **6^{•-}** from them.

After subtracting the UV/Vis/NIR spectrum of **6^{•-}** from the spectra of **6b** in DMF and DMSO, the obtained spectra shown in Figure 2.65 have been deconvoluted by Gaussian function. The Gaussian fit of the reduced species subtracted UV/Vis/NIR spectrum in DMSO shows main components at 863, 689, 454, 359 and 294 nm (see Figure A.132 in section 6.3.3 in appendix). While Gaussian fit of the reduced species subtracted UV/Vis/NIR spectrum in DMF at 293 K, shows main components at 886, 821, 719, 452, 355 and 323 nm (see Figure A.133 in section 6.3.3 in appendix). The Gaussian fit of the UV/Vis/NIR spectrum at 213 K in DMF, confirms the presence of the main components at 880, 793, 711, 459 and 359 nm (see Figure A.134 in section 6.3.3 in appendix).

Table 2.29: Concentration of **6b** in different solvents for the measurement of the UV/Vis/NIR spectra.

Solvent	Concentration (M)
MeCN	5.25×10^{-5}
DMF	3.33×10^{-5}
DMSO	3.68×10^{-5}

If the ESI-MS spectra of **6b** in MeCN is considered then it is tempting to assign the above mentioned new bands to the corresponding bands for the complex $[\text{Zn}(\text{L-N}_4\text{tBu}_2)(\text{-SQ-SQ})]$ (**7**). However, without a theoretical calculation, the assignment based only on the ESI-MS spectroscopy could be wrong. Therefore, for the discussion purpose, the complex which remains in an equilibrium with complex **6** in its dissolved state is interpreted as unidentified product.

The UV/Vis/NIR spectra shown in Figure 2.64 were also analyzed by SVD. The data obtained from the SVD are provided in Table 2.30. The spectral features for the **U** components are shown in Figure 2.66. Based on the singular values of the **S** matrix, it can be inferred that the spectra contain three components. One of the first two **U** components corresponds to the $\text{Zn}^{\text{II}}(\text{-SQ-SQ})_{\text{CS}}\text{-Zn}^{\text{II}}$ chromophore, while the other **U** component corresponds to the absorption profile of the unidentified product which remains in equilibrium with complex **6**. The third **U** component corresponds to the absorption profile of the complex **6^{•-}**. The fourth **U** components have spectral feature which would be expected as a result of the absorption maxima shift in different solvents owing to solvatochromic shift, and also due to the noise. In addition, if any oxidized product of complex **6** is generating in solution, then the absorption profile of that product would correspond to the spectral feature of the fourth **U** component. Likewise to the SVD of the variable temperature UV/Vis/NIR spectra of complexes **2b** and **3a**, the spectra were not reconstructed because any equilibrium model to compute the **F** matrix is not

applicable to the spectra due to the fact that two processes are occurring simultaneously; one of them is a reversible process and the other one is an irreversible process.

Table 2.30: The four singular values obtained from the SVD of the UV/Vis/NIR spectra of **6b** in MeCN, DMSO and DMF.

Singular value	Singular value (%)
6.104×10^5	70.99
2.136×10^5	24.85
2.167×10^4	2.52
1.405×10^4	1.63

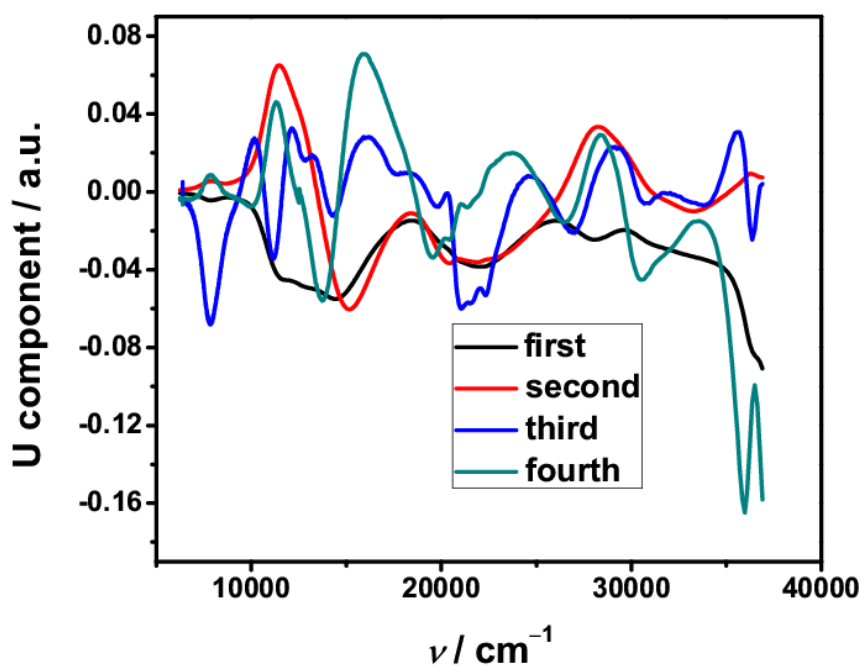


Figure 2.66: The four U components obtained by the SVD of the UV/Vis/NIR spectra of **6b** in MeCN (RT), DMSO (RT) and DMF (213 and 293 K).

The formation of $\mathbf{6}^{\bullet-}$ is not completely hindered by lowering the temperature and is evidenced by the observation of spectral changes in the NIR region where the intensity of band at 1279 nm corresponding to the SOMO–LUMO ($\pi^* \rightarrow \pi^*$) transition of the (Cat-SQ) $^{\bullet-}$ unit of the one-electron reduced species $\mathbf{6}^{\bullet-}$ increases even after cooling the sample in DMF (Figure 2.64). Therefore,

the UV/Vis/NIR spectral changes of complex **6** in DMF were monitored with time (Figure 2.67). The spectral features in the NIR region and near UV region of the spectrum recorded after storage of the sample for 24 h, have similarity with the spectral features of $\mathbf{6}^{\bullet-}$ in these regions. The intensity of the bands in the visible region decreases over the time, whereas the intensity of the bands in the NIR and near UV region increases over the time. Thus the spectral changes are suggesting that at least generation of one-electron reduced complex $\mathbf{6}^{\bullet-}$ is taking place in solution of **6** in DMF.

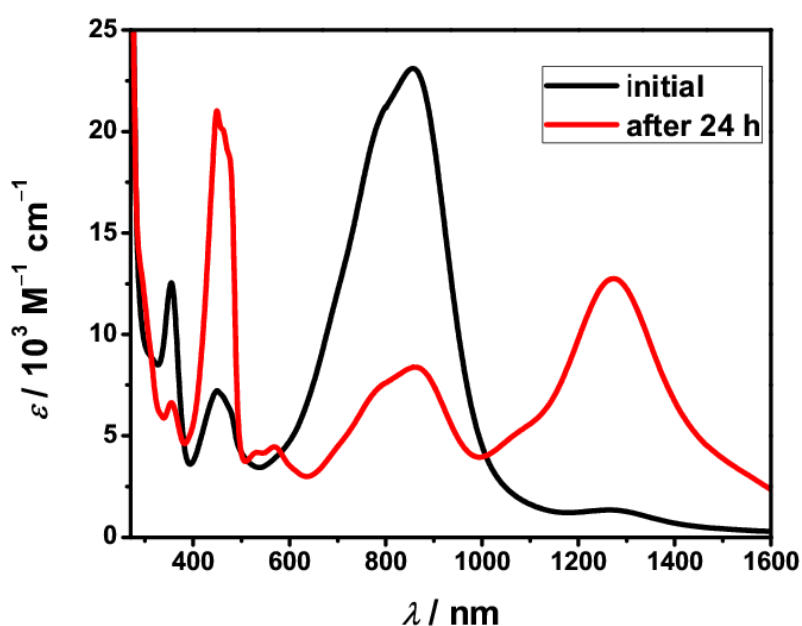


Figure 2.67: The changes in the UV/Vis/NIR spectra of complex **6b** with time. The spectrum, measured initially, was measured at 293 K. The spectrum, recorded after 24 h, was measured at room temperature.

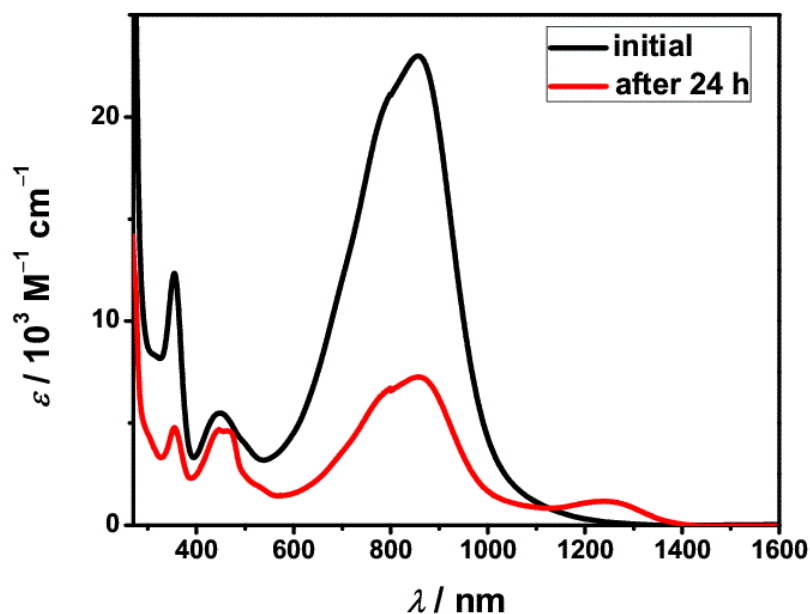


Figure 2.68: UV/Vis/NIR spectra of **6b** showing stability at RT/293 K. The spectra are obtained after subtraction of the corresponding spectra in Figure 2.67 by the UV/Vis/NIR spectrum of **6^{•-}**.

The UV/Vis/NIR spectrum of **6^{•-}** in 0.2 M TBAP/DMF is shown in Figure 2.69. The complex **6^{•-}** was prepared by electrochemical reduction of **6b** in 0.2 M TBAP/DMF. The absorption maxima values are listed in Table 2.28 (see above). The one-electron reduction of complex **6** means the addition of one electron to the LUMO of the closed-shell semiquinonate-semiquinonate moiety. Since, the electronic levels of complex **6** differ from complex **6^{•-}**, therefore the UV/Vis/NIR spectral features of these complexes are different to each other. The spectrum of **6** does not show any band in the NIR region, whereas **6^{•-}** shows bands in the NIR region at 1279 and 1063 nm. The band corresponding to the HOMO–LUMO transition of the bis(dioxolene) ligand of **6b** (at 671 nm in acetonitrile) is absent in the spectrum of **6^{•-}**.

Gaussian fit of the UV/Vis/NIR spectrum of **6^{•-}** shows main components at 1502 1283, 1116, 568, 480, 467, 452, 442, 414 and 282 nm (see Figure A.135 in section 6.3.3 in appendix). The band at 1283 nm is assigned to the SOMO–LUMO ($\pi^* \rightarrow \pi^*$) transition of the (Cat-SQ)^{•3-} unit. The pattern of

intense bands in the NIR and near UV region and pattern of the relatively weak bands in the visible region are typical for a vibronic progression. Thus, strong electronic communication exists between the dioxolene moieties of the bis(dioxolene) ligand. All the bands in the visible region are assigned to the ligand-based absorptions. The catecholate-semiquinonate based absorptions are similar with the class III mixed valence type catecholate-semiquinonate based ligand-based absorptions.^[142]

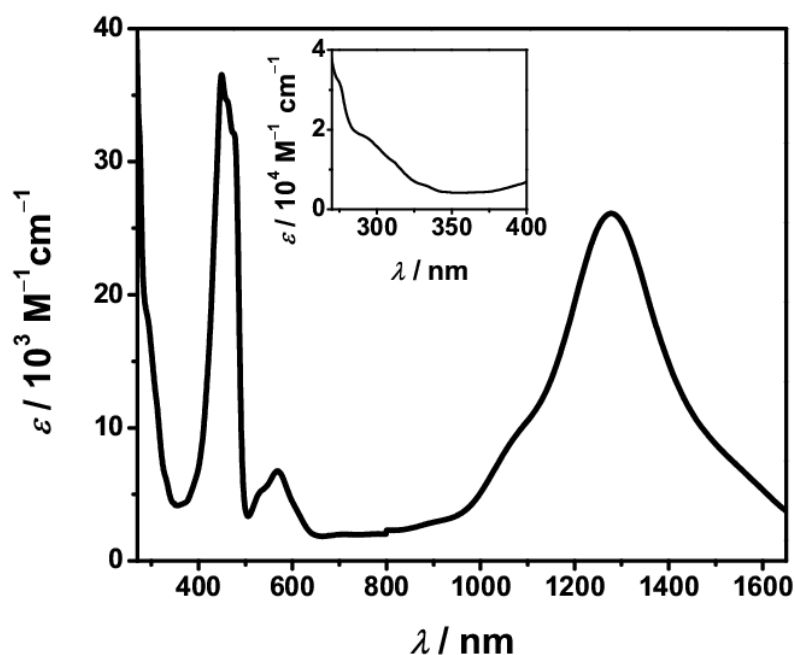


Figure 2.69: UV/Vis/NIR spectrum of **6**^{•-} in 0.2 M TBAP/DMF at RT. The inset shows the bands in the UV region.

The above discussion implies that an equilibrium exists between the complex **6** and unidentified species in the solution state of complex **6**. Most likely, a theoretical calculation could provide the chemical structure of the unidentified species. From the UV/Vis/NIR study of the metal bis(dioxolene) complexes in MeCN, the HOMO–LUMO energy gaps of the coordinated bis(dioxolene) ligands in these complexes can be derived by the unit conversion for energy. A comparison of ligand-based absorptions among the complexes **3**, **4**, **5** and **6** shows that the $\Delta E_{\text{HOMO-LUMO}}$ of closed-shell semiquinonate-semiquinonate

ligands of these complexes could be arranged in the order of $\Delta E_{\text{HOMO-LUMO}}$ for **4** $<$ $\Delta E_{\text{HOMO-LUMO}}$ for **3** or $\Delta E_{\text{HOMO-LUMO}}$ for **5** $<$ $\Delta E_{\text{HOMO-LUMO}}$ for **6**. This comparison in fact implies that the corresponding open-shell semiquinonate-semiquinonate ligand must have lower $\Delta E_{\text{HOMO-LUMO}}$ than 1.70 eV because, the $\Delta E_{\text{HOMO-LUMO}}$ for complex **4** is 1.70 eV, yet the bis(dioxolene) unit of **4** is in closed-shell semiquinonate-semiquinonate state. This comparison is also in accordance with the existence of the bis(dioxolene) ligand of dissolved **3** in its closed-shell semiquinonate-semiquinonate state at room temperature because the HOMO–LUMO energy gap of the bis(dioxolene) ligand of dissolved **3** is 1.74 eV (calculated from the UV/Vis/NIR spectra of complex **3a** in EtCN at 333 K).

2.3.7 Electrochemical Properties

The redox properties of the compounds **4a**, **5a** and **6b** have been investigated by cyclic voltammetry in 0.2 M TBAP/MeCN. The cyclic voltammograms for the compounds **4a**, **5a** and **6b** are shown in Figures 2.70, 2.71 and 2.72, respectively. The cyclic voltammetry data are provided in Table A.26 (see in section 6.3.4 in appendix). All the given potentials are vs. SCE. All complexes show two redox couples which are due to the two sequential one-electron reductive processes. Both reductions are ligand-based, and the reductions are assigned to one-electron reduction from (SQ-SQ)_{CS}²⁻ to (Cat-SQ)^{•3-} for the first reduction and one-electron reduction from (Cat-SQ)^{•3-} to (Cat-Cat)⁴⁻ for the second reduction (Scheme 2.10). For compounds **4a**, **5a** and **6b**, at scan rate $\nu = 100$ mV/s, the $E_{1/2}$ values for the first reductions are -176 , 45 and -120 mV, respectively. Whereas the $E_{1/2}$ values for the second reductions are -650 , -450 and -526 mV, respectively.

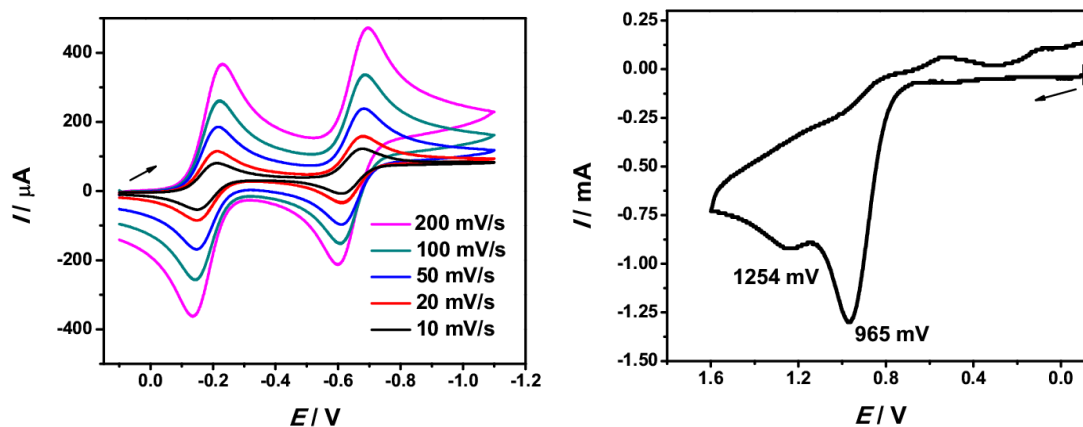


Figure 2.70: Cyclic voltammograms for the first reductive processes (left) at different scan rates and oxidative processes (right) at $v = 100$ mV/s of **4a** in 0.2 M TBAP/MeCN.

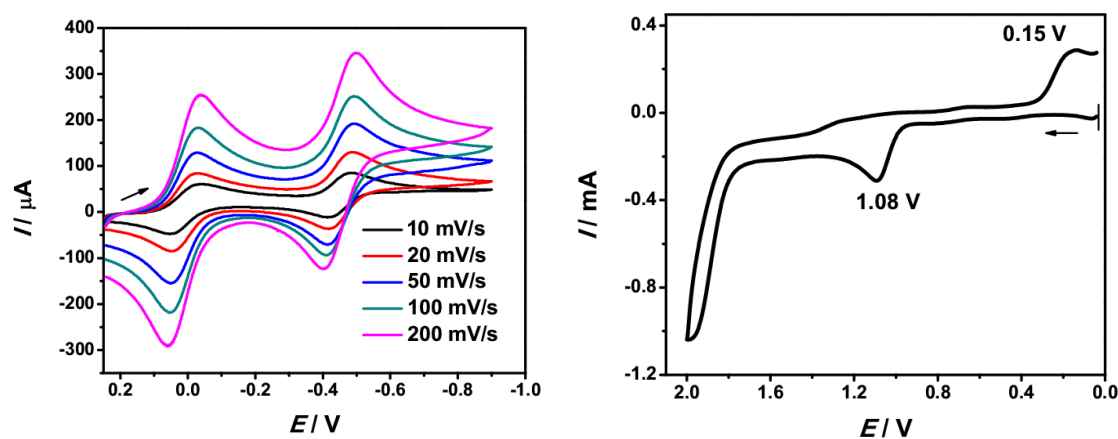


Figure 2.71: Cyclic voltammograms for the first reductive processes (left) at different scan rates and oxidative processes (right) at $v = 100$ mV/s of **5a** in 0.2 M TBAP/MeCN.

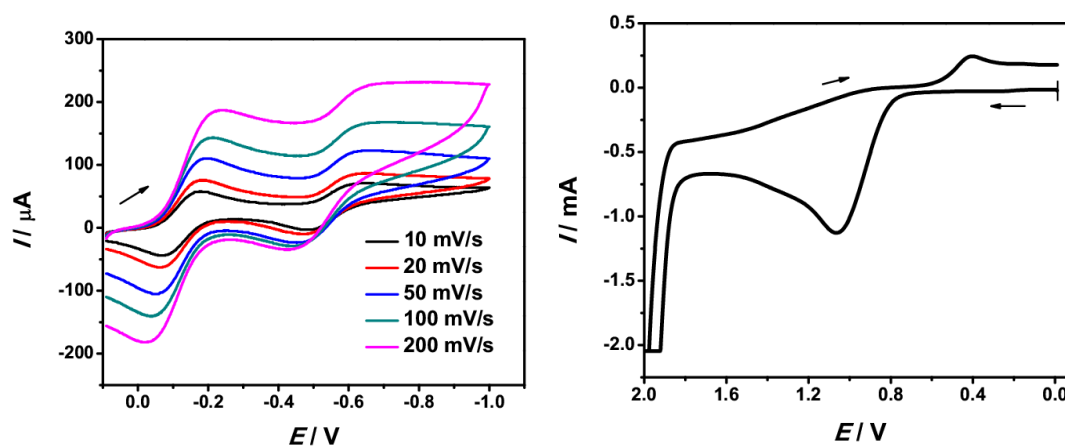


Figure 2.72: Cyclic voltammograms for the first reductive processes (left) at different scan rates and oxidative processes (right) at $v = 100$ mV/s of **6b** in 0.2 M TBAP/MeCN.

The cyclic voltammetry measurements of compound **6b** were also performed in DMF. The CV recorded in DMF is shown in Figure 2.73. The CV in DMF shows two sequential one-electron reductions at $E_{1/2} = -65$ mV and $E_{1/2} = -540$ mV, and both reductions are ligand-based. There should be two reduction peaks for the one-electron reduction. One of them for the undissociated complex **6** and the other one for the unidentified complex which remains in equilibrium with **6** in its dissolved state, but those peaks are not observed. This kind of observation could be due to the following reason: 1) The amount of the unidentified complex is such large that only the one-electron reduction is observed for that complex. 2) The rate of the backward reaction of the equilibrium is faster than cyclic voltammetry time scale.

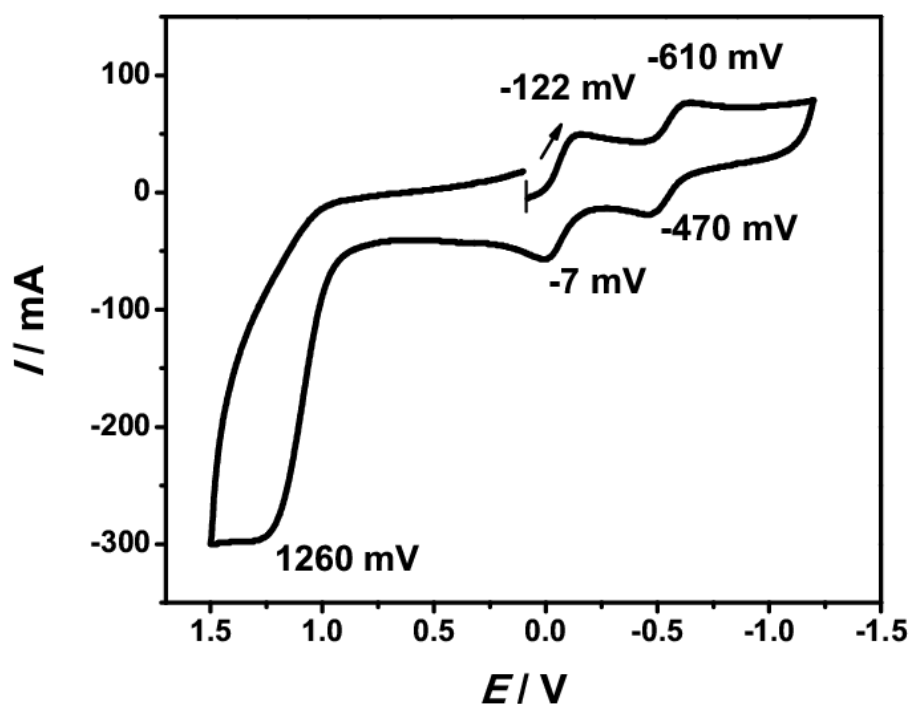


Figure 2.73: Cyclic voltammogram of **6b** in 0.2 M TBAP/DMF at scan rate $\nu = 100$ mV/s

2.3.8 Brief Summary

In summary, the synthesis and characterization of the complexes reveal that for each complex, the two metal ions are bridged by closed-shell form of the (SQ-SQ)²⁻ ligand. Unlike, the cobalt bis(dioxolene) complex **3b**, the electronic states of the bis(dioxolene) ligands are not switched by varying the temperature. The magnetic exchange coupling between the paramagnetic metal ions are antiferromagnetic but very weak. The UV/Vis/NIR spectroscopic investigation reveals that the HOMO–LUMO energy gap of the (SQ-SQ)_{CS}²⁻ ligand is different in each complex. The UV/Vis/NIR spectra of complex **6** in different solvents and different temperature in DMF suggest that an equilibrium exists between complex **6** and unidentified species. The equilibrium is affected by the changes in temperature and coordinating properties of the solvents. The UV/Vis/NIR spectra also show that, unknown type of redox reaction is taking place, and the one-electron reduced species **6**^{•-} is generating in the dissolved state of **6**.

3 Conclusions

The presented works explore the conversion between the low-lying electronic states of spin-crossover and valence tautomeric cobalt dioxolene complexes. The cobalt dioxolene complexes have been synthesized by using a suitable ancillary ligand L-N₄tBu₂ and the dioxolene ligands DCCat²⁻ and (SQ-SQ)²⁻ as co-ligands. Most of the complexes have been characterized by X-ray crystallographic and magnetic measurements as well as NMR, UV/Vis/NIR and IR spectroscopic studies.

The complex [Co(L-N₄tBu₂)(DCCat)] (**1**) shows existence of the temperature invariant high-spin cobalt(II) catecholate state. To the best of our knowledge, this is the first cobalt(II) catecholate complex which is characterized by X-ray crystallographic, magnetic, UV/Vis/NIR and IR measurements. One-electron oxidation of **1** has yielded the complex [Co(L-N₄tBu₂)(DCCat)](BPh₄) (**2b**). The solid state properties of **2b** are best described by the low-spin cobalt(III) catecholate state of the complex, but the solution state properties of the complex **2b** are best described by the valence tautomeric transition from the low-spin cobalt(III) catecholate to low-spin cobalt(II) semiquinonate state. The VT_{LS-LS} is occurring due to the changes in polarity of the utilized solvents, temperature and entropy due to solute-solvent interactions of the complex in these solvents. In a more polar solvent, the valence tautomeric equilibrium is predominated by the low-spin cobalt(III) catecholate species, whereas in a less polar solvent, the valence tautomeric equilibrium is predominated by the low-spin cobalt(II) semiquinonate species.

Regardless of the polarity of the utilized solvents, the valence tautomeric transition from the low-spin cobalt(III) catecholate to low-spin cobalt(II) semiquinonate state always occurs with positive change in temperature, but the critical temperature for the valence tautomeric transition is much lower in less polar solvent DCM compared to that in more polar solvent MeCN. To the

best of our knowledge, this is the first cobalt dioxolene complex which exhibits valence tautomeric transition from a low-spin cobalt(III) catecholate to low-spin cobalt(II) semiquinonate state rather than the usually observed valence tautomeric transition from a low-spin cobalt(III) catecholate to high-spin cobalt(II) semiquinonate state.

The detailed investigation of the solid state properties of the cobalt bis(dioxolene) complexes reveals that, the coordinated $(\text{SQ-SQ})^{2-}$ ligand shows conversion from its singlet open-shell biradicaloid to closed-shell quinonoid form due to the changes in the spin-states of the coordinated cobalt(II) centers from low-spin to high-spin states in **3b**. Thus, the solid state properties of **3b** are best described by the temperature-induced spin-crossover processes for the cobalt(II) centers accompanied by the open-shell to closed-shell state conversion of the bis(dioxolene) ligand $(\text{SQ-SQ})^{2-}$. To the best of our knowledge, this is the first instance, where electronic configuration of a coordinated organic moiety is switched by metal induced spin-crossover processes. In addition, to the best of our knowledge, this is the first cobalt bis(dioxolene) complex which shows spin-crossover phenomenon rather than valence tautomerism.

The complexes $[\text{Co}_2(\text{L-N}_4\text{tBu}_2)_2(\text{Cat-SQ})](\text{BF}_4)_2 \cdot \text{Et}_2\text{O}$ (**3d**) and $[\text{Co}_2(\text{L-N}_4\text{tBu}_2)_2(\text{Cat-SQ})](\text{PF}_6)_2 \cdot \text{solv}$ (**3e-solv**) were isolated with a slight modification to the synthetic method of **3b**. For these complexes, it is observed that the redox activity between the $(\text{SQ-SQ})^{2-}$ ligand and cobalt(II) centers has triggered an intramolecular electron transfer between one of the cobalt(II) centers and the $(\text{SQ-SQ})^{2-}$ unit. In these complexes, at low temperatures, the low-spin cobalt(III) and low-spin cobalt(II) centers are bridged by the $(\text{Cat-SQ})^{\bullet 3-}$ unit, which is one electron reduced form of the $(\text{SQ-SQ})^{2-}$ unit. The redox-state of the $(\text{Cat-SQ})^{\bullet 3-}$ ligand is catecholate-semiquinonate state. The X-ray crystallography of **3e-solv** suggests that the catecholate site of the (Cat-

SQ)^{•3-} unit is coordinated to the low-spin cobalt(III) center, whereas semiquinonate site is coordinated to the low-spin cobalt(II) center. The radical of the (Cat-SQ)^{•3-} ligand is situated at the semiquinonate site. At high temperatures for the complexes **3c** and **3d**, the two high-spin cobalt(II) centers are bridged by the diamagnetic closed-shell quinonoid form of the bis-dioxolene unit (SQ-SQ)²⁻. The solid state properties of the complex **3c** and **3d** are best described by the temperature induced valence tautomeric transition for the low-spin cobalt(III) center accompanied by spin-crossover process for the cobalt(II) center from LS-Co^{III}-Cat-SQ-Co^{II}-LS to HS-Co^{II}-(SQ-SQ)_{CS}-Co^{II}-HS state, and change in the redox-state of the bis(dioxolene) ligand from (Cat-SQ)^{•3-} to (SQ-SQ)_{CS}²⁻. To the best of our knowledge, this is the first cobalt bis(dioxolene) complex where simultaneously spin-crossover for the cobalt(II) center and valence tautomerism for the low-spin cobalt(III) center are achieved.

The solution state properties of the cobalt bis(dioxolene) complexes **3a** and **3d** are identical and have been observed by UV/Vis/NIR spectroscopy. The electronic state of dissolved **3** at room temperature is HS-Co^{II}-(SQ-SQ)_{CS}-Co^{II}-HS. The variable temperature UV/Vis/NIR spectra of the complexes reveal that at least, one of the cobalt(II) centers undergoes temperature-induced spin transition. However, the responsible process is unknown at the moment due to lack of the theoretical calculations. The discovery of these novel class of cobalt bis(dioxolene) complexes opens up new ways to manipulate the electronic states of coordinated organic moieties by the changes in spin- and redox-states of the metal centers.

The nickel(II), copper(II) and zinc(II) centers of the complexes **4a**, **5a** and **6b**, respectively, do not exhibit temperature-induced changes in the electronic configurations of the coordinated (SQ-SQ)²⁻ ligands from their closed-shell quinonoid to open-shell biradicaloid configurations. For nickel(II) and

copper(II) bis(dioxolene) complexes, the two paramagnetic metal ions are bridged by the $(\text{SQ-SQ})_{\text{CS}}^{2-}$ ligands and they are very weakly antiferromagnetically coupled. The electronic state of complex **6b** is described by the temperature invariant $\text{Zn}^{\text{II}}-(\text{SQ-SQ})_{\text{CS}}-\text{Zn}^{\text{II}}$ state.

The solution state properties of zinc bis(dioxolene) complex **6b** indicate that an equilibrium between complex **6** and unidentified species exists. The equilibrium is affected by the changes in temperature and coordinating properties of the utilized solvents. Additionally, the one-electron reduced species **6^{•-}** is generating in solution of **6** in different solvents by an unknown type of redox reaction. Currently, due to lack of enough experimental evidences, the mechanism for that redox reaction and the chemical structure of the unidentified species cannot be proposed. In addition, as a future scope, a theoretical calculation could be helpful to identify the unidentified species in the above mentioned equilibrium.

4 Experimental Section

4.1 Physical Methods

The elemental analyses were performed in the analytic section of the Department of Chemistry at Technische Universität Kaiserslautern. The instruments used were either Elemental Analyzer EA2400CHN from PerkinAlmer or vario MICRO cube from Elementar Analysensysteme GmbH.

The nuclear magnetic resonance (NMR) spectra were measured in FT-NMR instruments DPX200, DPX400 or Avance 600 from Bruker. In the caption of the spectrum where temperature is not mentioned, therein it is meant that the spectrum was recorded at room temperature. The resonance signals of the residual protons of the deuterated solvents were used as an internal standard. Solution magnetic susceptibility measurements were performed by the Evans method using coaxial NMR tubes. The value of the measured shift was the value for the shift between the residual signals of the solvent. The magnetic susceptibility was calculated using the following equation (eq 4.1).^[128]

$$\chi_g = \frac{3\Delta f}{4\pi f m} + \chi_0 \quad (4.1)$$

Where χ_g = mass susceptibility of the solute (cm³/g), Δf = observed frequency shift of reference resonance (Hz), f = spectrometer frequency (Hz), χ_0 = mass susceptibility of solvent (cm³/g), m = mass of substance per cm³ of solution.

The NMR spectra were simulated and plotted by TOPSPIN 3.0, 3.1 or 3.5 from the company Bruker, and for the overlay of NMR plots the Mestrenova software was used.

The crystal structure measurements were performed by Dr. Harald Kelm of the Department of Chemistry at Technische Universität Kaiserslautern. The

measurements were performed by the instrument Oxford Diffraction Gemini S Ultra. The crystal structure data were solved by the program SIR97.^[143] Structure refinement was performed with the help of the program SHELLXL-97.^[144] The figures of the crystal structures are for the perspective views of the complex cations in the complexes showing 50 % thermal ellipsoids and atom numbering scheme. The hydrogen atoms are omitted for the purpose of clarity.

The SQUID measurements were performed by Dr. S. Demeshko in the research group of Prof. F. Meyer of the Department of Chemistry, University of Göttingen, Germany. Temperature-dependent magnetic susceptibility measurements were carried out with a Quantum-Design MPMS-XL-5 SQUID magnetometer equipped with a 5 Tesla magnet in the mentioned temperature ranges K at a magnetic field of 0.5 T (T = Tesla). The powdered sample was poured into a gel bucket and fixed in a non-magnetic sample holder. Each raw data file for the measured magnetic moment was corrected for the diamagnetic contribution of the sample holder and the gel bucket. The molar susceptibility data were corrected for the diamagnetic contribution.

Experimental data for the complexes were modelled by using a fitting procedure to the appropriate Heisenberg-Dirac-van-Vleck (HDvV) spin Hamiltonian for isotropic exchange coupling and Zeeman splitting, equation (4.2).

$$\hat{H} = -2J\hat{S}_1 \cdot \hat{S}_2 + g\mu_B(\vec{S}_1 + \vec{S}_2)B \quad (4.2)$$

Temperature-independent paramagnetism (TIP) and a Curie-behaved paramagnetic impurity (PI) with spin $S = 1/2$ were included according to $\chi_{\text{calc}} = (1 - PI) \cdot \chi_{\text{mono}} + PI \cdot \chi_{\text{mono}} + TIP$

The room temperature magnetic moment measurement was performed by a magnetic balance of the type Magway MSB Mk1 from Sherwood Scientific Ltd. The complex $[\text{HgCo}(\text{SCN})_4]$ was used as the standard reference complex. The diamagnetic correction during the calculation of the magnetic moment was performed. The diamagnetic susceptibility of a complex $\chi_{\text{dia}} = 1/2 \text{ MW} \times 10^{-6} \text{ cm}^3 \text{ mol}^{-1}$. The spin only value of the effective magnetic moment was calculated according to the following formula: $\mu_S = g\sqrt{S(S+1)} \mu_B$ ($g = 2.0023 \approx 2$, Landé-factor (gyromagnetic factor) of the electron, $S = \frac{n}{2}$, spin multiplicity, $n =$ number of unpaired electrons, $\mu_B =$ Bohr Magneton). For complexes containing more than one non-interacting magnetic centers the formula is written as $\mu_S = \sqrt{\sum_i \mu_{S,i}^2}$. The effective magnetic moment was calculated with the following equation by using the product $\chi_M T$; $\mu_{\text{eff}} = 2.828\sqrt{\chi_M T} \mu_B$. The least-squares fitting of the χ_{HS} vs. T plots were performed by the MATLAB software (The MathWorks, Inc.) using the trust-region-reflective algorithm.

The electronic absorption (UV/Vis/NIR) spectra were recorded by a Varian Cary 5000 UV/Vis/NIR-Spectrophotometer. All the measurements were performed in solution state. For the variable temperature UV/Vis/NIR spectra measurements, the concentration of the solution was calculated at each temperature by calculating the density of the solvent at that temperature. The density of a solvent at temperature T (d_T) was determined by the equation: $d_T = d_s / \{1 + \alpha (T_s - T)\}$,^[145] $d_s =$ density at a known temperature T_s (e.g. 25 °C), $\alpha =$ volumetric coefficient of thermal expansion of the solvent. For MeCN, $d_s = 0.786 \text{ g/cm}^3$, $\alpha = 1.38 \times 10^{-3} \text{ K}^{-1}$. For DCM, $d_s = 1.325 \text{ g/cm}^3$, $\alpha = 1.4 \times 10^{-3} \text{ K}^{-1}$. For EtCN, $d_s = 0.772 \text{ g/cm}^3$, $\alpha = 1.34 \times 10^{-3} \text{ K}^{-1}$.

For the variable temperature UV/Vis/NIR spectra, Unisoku UnispeKs cryostat was used. Deconvolution of the UV/Vis/NIR spectra was performed by the program MagicPlot. The SVD of the variable temperature UV/Vis/NIR spectra was performed, with the input and help from Prof. Hans-Jörg Krüger of the Department of Chemistry at Technische Universität Kaiserslautern, by the MATLAB software (The MathWorks, Inc.).

The EPR spectra were recorded by an X-Band EPR-Spectrometer Elexsys E580 from Bruker. There was a general cavity of the type Standard Resonator ER4102ST. The spectra at room temperature were measured with a solution of complex in a screw capped flat cell. The simulation of the EPR spectra was performed with the input and help received from Prof. Hans-Jörg Krüger, by using the program EasySpin version 5.2.25.^[146]

Electrochemical experiments were performed in the solution state of the complex by a potentiostat/galvanostat 273A from Princeton Applied Research. The solution contains tetrabutylammonium perchlorate as the electrolyte (strength = 0.2 M). Three electrodes were used; among these two platinum electrodes were used as working electrode and counter electrode and the third electrode was the saturated calomel electrode, used as the reference electrode. The measurements were performed inside a glove box under nitrogen atmosphere at room temperature. During coulometric method the counter electrode was replaced by a platinum net. The peak current ratio was determined by the Nicholson method: $\frac{i_{pa}}{i_{pc}} = \frac{i_{a0}}{i_{pc}} + \frac{0.485i_{\lambda 0}}{i_{pc}} + 0.086$. The half-wave potential ($E_{1/2}$) was determined by using the equation: $E_{\frac{1}{2}} = \frac{E_{pa} + E_{pc}}{2}$, E_{pa} = anodic peak potential, E_{pc} = cathodic peak potential. The potential difference was calculated by using the equation: $\Delta E = (E_{pa} - E_{pc})$. The

potentials are given against the calomel electrode (vs. SCE). The value of the half-wave potential of Fc^+/Fc couple was found to be 430 mV (vs. SCE).

The ESI-MS spectra were recorded by a Bruker Esquire 6000plus ion trap spectrometer in the research group of Prof. Dr. Gereon Niedner-Schatteburg, in the Department of Chemistry at Technische Universität Kaiserslautern.

The IR spectra of the solid samples were recorded by using either KBr pellet sampling techniques or ATR sampling techniques. The KBr pellet IR spectra were recorded by an IR-Spectrometer of the type FT/IR-6100 from JASCO. The IR spectra of ATR sampling technique were recorded on the crystalline sample of the complexes and the measurements were carried out with a Perkin Elmer FT-ATR-IR 1000 spectrometer equipped with a diamond coated ZnSe-window. The Gaussian deconvolution of the IR and ATR spectra have been performed by plotting the IR curves in terms of absorbance vs. wavenumber, followed by baseline subtraction by the software Origin Pro 8.0. Then the baseline subtracted spectra were deconvoluted by Gaussian function in the software MagicPlot.

The solution state IR spectra were recorded in between two NaCl disks by an IR-Spectrometer of the type FT/IR-6100 from JASCO. The sample for the IR spectrum in DMSO was taken in between two NaCl disks ($c = \text{ca. } 8.5 \times 10^{-2}$ M). The IR spectrum in $[\text{D}_2]\text{DCM}$ was recorded by taking the sample ($c = 6.61 \times 10^{-3}$ M) inside a liquid cell with NaCl windows.

4.2 Chemicals and Suppliers

ABCR: $\text{CoCl}_2 \cdot 6 \text{H}_2\text{O}$, $\text{NiCl}_2 \cdot 6 \text{H}_2\text{O}$, $\text{CuCl}_2 \cdot 2 \text{H}_2\text{O}$, ZnCl_2 , sodium tetraphenylborate, dichloromethane, magnesium.

Acros Organics: acetone, *N,N*-dimethylformamide, sodium hydroxide, anhydrous sodium sulfate, triethylamine, potassium bromide, dichloromethane, nitromethane, toluene, propionitrile.

Sigma Aldrich: sodium tetraphenylborate, $[\text{D}_3]\text{MeCN}$, 4-bromoveratrole, $[\text{D}_6]\text{DMSO}$.

euriso-top: $[\text{D}]\text{CHCl}_3$, $[\text{D}_6]\text{DMSO}$, $[\text{D}_2]\text{DCM}$, $[\text{D}_4]\text{MeOH}$.

Fisher Scientific: acetonitrile, chloroform, *n*-hexane, methanol, sodium bicarbonate.

All the other chemicals were either prepared or obtained from the Chemikalienausgabe des Fachbereichs Chemie of Technische Universität Kaiserslautern.

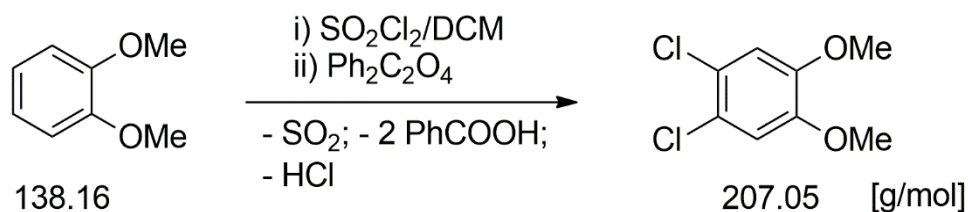
4.3 Synthesis

All the air sensitive syntheses were performed under pure nitrogen atmosphere by using standard Schlenk techniques, and in the degassed solvents. Dry solvents were used for the air and moisture sensitive reactions. The solvents were dried by refluxing the solvents, over a time period of ca. 3×8 h with drying agents. The drying agents were calcium oxide for methanol, calcium hydride for acetonitrile, mixture of sodium and benzophenone for THF and sodium amalgam for diethyl ether.

The compounds which were synthesized by using a modified literature procedure are described in the synthetic part. The following compounds were synthesized according to literature procedures.

- 1) *N,N'*-di-*tert*-butyl-2,11-diaza[3.3](2,6)pyridinophane (L-N₄*t*Bu₂)^[147]
- 2) [Ni(L-N₄*t*Bu₂)Cl₂] \cdot MeCN^[147]
- 3) diphenylborinic acid (Ph₂BOH)^[148,149]

4.3.1 Synthesis of 1,2-dichloro-4,5-dimethoxybenzene



The compound was synthesized from a modified literature procedure.^[150] At 0 °C, sulfuryl dichloride (26.8 g, 0.20 mol) was slowly and cautiously added to a solution of 1,2-dimethoxybenzene (13.8 g, 0.10 mol) in dichloromethane (100 mL). Then the resulting solution was cautiously treated with solid benzoyl peroxide (242 mg, 1 mmol) and the resulting reaction mixture was stirred at 35 °C for 6 h, and after that the solution was washed with 5 % sodium bicarbonate solution (200 mL) followed by water (250 mL). The organic layer was then dried over anhydrous sodium sulfate and filtered. The filtrate was evaporated to dryness in a rotary evaporator to obtain a crude product of the desired compound which was dissolved in hot methanol (25 mL). Storage of the solution at room temperature afforded a colorless crystalline compound (5.1 g). The obtained crystalline compound was again redissolved in warm petroleum ether (100 mL) and upon standing at room temperature, a colorless crystalline compound of 1,2-dichloro-4,5-dimethoxybenzene was obtained (2.72 g). The volume of the mother liquor was reduced (40 mL) to obtain another portion of the compound (1.33 g).

MW ($\text{C}_8\text{H}_8\text{Cl}_2\text{O}_2$) = 207.05 g/mol

Yield = 19 % (4.05 g, 19 mmol)

Characterization:

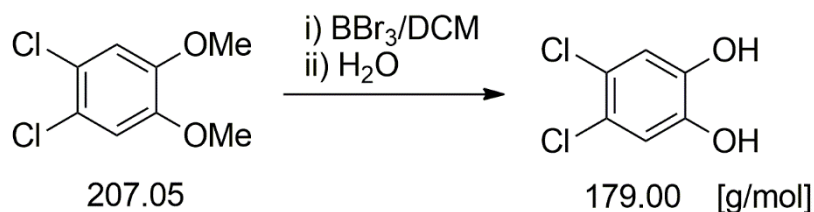
Elemental analysis: (Calculated for $\text{C}_8\text{H}_8\text{Cl}_2\text{O}_2$)

Calculated: C = 46.41 %, H = 3.89 %

Found: C = 46.60 %, H = 3.81 %

^1H NMR (400 MHz, $[\text{D}]\text{CHCl}_3$, RT): δ = 6.89 (s, 2H; H^3/H^6), 3.85 ppm (s, 6H; CH_3 , $\text{OMe}^4/\text{OMe}^5$).

4.3.2 Synthesis of 4,5-dichlorocatechol (H_2DCCat)



The compound was synthesized from a modified literature procedure.^[151] Under an inert atmosphere, 1,2-dichloro-4,5-dimethoxybenzene (2.07 g, 10 mmol) was dissolved in dichloromethane (100 mL) and then a solution of BBr_3 in DCM (25 mL, 25 mmol) was slowly added to the solution at 0 °C. The resulting reaction mixture was stirred for 3 h at ambient temperature. After that the solvent was removed in a rotary evaporator. The resulting oily natured residue was redissolved in ethyl acetate (75 mL) and then washed with brine (100 mL). Then the organic layer was filtered over anhydrous sodium sulfate and the volume of the filtrate was reduced in a rotary evaporator to obtain a sticky type of grey solid which was recrystallized from ethyl acetate/*n*-hexane (1:250). For recrystallization; the solution was stored at -30 °C to yield a colorless crystalline compound which was dried in vacuum to obtain an analytically pure compound of 4,5-dichlorocatechol.

MW ($\text{C}_6\text{H}_4\text{Cl}_2\text{O}_2$) = 179.00 g/mol

Yield = 62 % (1.12 g, 6.25 mmol)

Characterization:

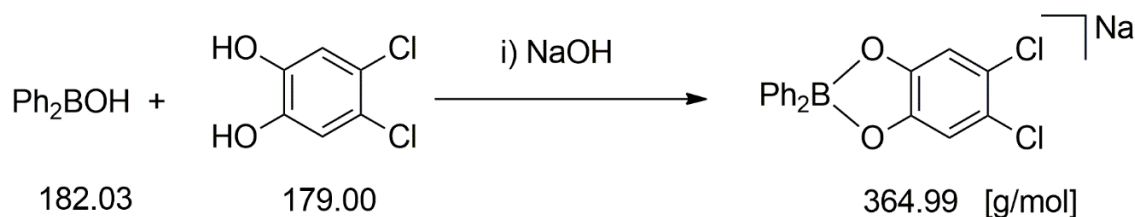
Elemental analysis: (Calculated for $\text{C}_6\text{H}_4\text{Cl}_2\text{O}_2$)

Calculated: C = 40.26 %, H = 2.25 %

Found: C = 40.36 %, H = 2.29 %

^1H NMR (400 MHz, $[\text{D}_4]\text{MeOH}$, RT): $\delta = 6.85$ ppm (s, 2H; H^3/H^6 - H_2DCCat).

4.3.3 Synthesis of sodium diphenyl(4,5-dichlorocatecholate)borate ($\text{NaBPh}_2(\text{DCCat})$)



Under an atmosphere of pure nitrogen, solid 4,5-dichlorocatechol (89.5 mg, 0.50 mmol) was added to a solution of diphenylborinic acid (91 mg, 0.50 mmol) in toluene (25 mL). After addition of methanol (1 mL), sodium hydroxide (10 mg, 0.25 mmol) was added to the solution. After stirring the resulting reaction mixture for 1 h at ambient temperature, the solution was evaporated to dryness in vacuum for 3 h to obtain a colorless solid compound. Then the solid compound was redissolved in ethyl acetate (20 mL) and filtered through celite. The filtrate was evaporated to dryness in vacuum to afford a sticky type of colorless solid compound. This crude product was used without further purification, and for the metathesis reaction purpose, the compound was prepared *in situ*.^[152]

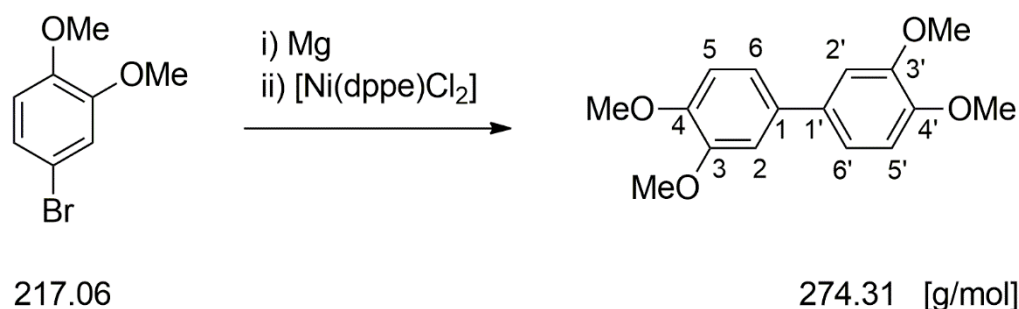
MW ($\text{C}_{18}\text{H}_{12}\text{BCl}_2\text{NaO}_2$) = 364.99 g/mol

Characterization:

^1H NMR (600 MHz, $[\text{D}_3]\text{MeCN}$, RT): $\delta = 7.38$ (d, $^3J_{\text{HH}} = 6.8$ Hz, 4H; *o*-Ph-H), 7.13 (t, $^3J_{\text{HH}} = 7.4$ Hz, 4H; *m*-Ph-H), 7.03 (tt, $^3J_{\text{HH}} = 7.4$ Hz, $^4J_{\text{HH}} = 1.3$ Hz, 2H; *p*-Ph-H) 6.46 ppm (s, 2H; H^3/H^6 - DCCat^{2-}).

IR (KBr pellet, RT): $\nu = 3570, 3378, 3065, 3048, 3015, 3001, 1647, 1622, 1596, 1488, 1452, 1431, 1369, 1355, 1244, 1228, 1216, 1197, 1180, 1146, 1099, 1068, 957, 937, 917, 896, 877, 850, 836, 810, 750, 706, 646, 615, 588$ cm^{-1} .

4.3.4 Synthesis of 3,3',4,4'-tetramethoxybiphenyl



The compound was synthesized according to a modified literature procedure.^[153,154] Under an atmosphere of pure nitrogen, a solution of 4-bromoveratrole (10.85 g, 50 mmol) in dry THF (75 mL) was first treated with Magnesium turnings (1.20 g, 50 mmol), and then the solution was warmed to initiate the Grignard reaction, and then stirred until the Grignard reaction was completed. After cooling down to room temperature, the Grignard solution was slowly added to another solution of 4-bromoveratrole (10.85 g, 50 mmol) and $[\text{Ni}(\text{dppe})\text{Cl}_2]$ (528 mg, 1 mmol) in dry THF (75 mL) at 0 °C. The color of the resulting solution became dark brown, and the resulting reaction mixture was stirred overnight and then saturated solution of ammonium chloride (10 mL) was added to quench the reaction. The obtained solution was extracted with dichloromethane (3×50 mL) and washed with water (2×100 mL). The combined organic layer was dried over anhydrous sodium sulfate and the volume of the filtrate was reduced in a rotary evaporator. The resulting oily natured residue was recrystallized from hot methanol (50 mL) to obtain a colorless solid compound of 3,3',4,4'-tetramethoxybiphenyl.

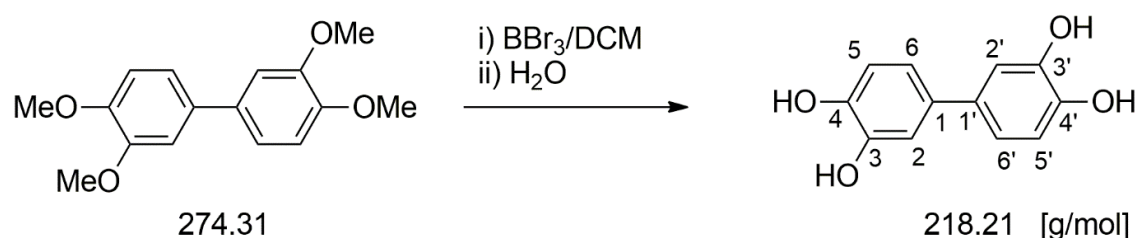
MW ($C_{16}H_{18}O_4$) = 274.31 g/mol

Yield = 30 % (4.10 g, 15 mmol)

Characterization:

1H NMR (400 MHz, $[D]CHCl_3$, RT): δ = 6.93 (d, $^3J_{HH}$ = 8.3 Hz, 2H; $H^5/H^{5'}$), 7.06 (d, $^4J_{HH}$ = 2.1 Hz, 2H; $H^2/H^{2'}$), 7.09 (dd, $^3J_{HH}$ = 8.3 Hz, $^4J_{HH}$ = 2.0 Hz, 2H; $H^6/H^{6'}$), 3.91 (s, 6H; $OMe^4/OMe^{4'}$), 3.95 ppm (s, 6H; $OMe^3/OMe^{3'}$).

4.3.5 3,3',4,4'-tetrahydroxybiphenyl (H_4 (Cat-Cat))



The compound was synthesized according to a reported procedure.^[155] Under an atmosphere of pure nitrogen, a solution of BBr_3 in DCM (50 mL, 50 mmol) was slowly added to a solution of 3,3',4,4'-tetramethoxybiphenyl (2.74 g, 10 mmol) in dichloromethane (50 mL) at -78 °C. The resulting reaction mixture was warmed to room temperature and stirred overnight. Then water (100 mL) was slowly added to the reaction mixture and the resulting solution was extracted with diethyl ether (3×50 mL). The combined organic layer was dried over anhydrous sodium sulfate and the volume of the filtrate was reduced in a rotary evaporator. The obtained grey solid was recrystallized from ethyl acetate/*n*-hexane (10:90) to obtain an off-white colored amorphous (non-crystalline solid) compound of 3,3',4,4'-tetrahydroxybiphenyl.

MW ($C_{12}H_{10}O_4$) = 218.21 g/mol

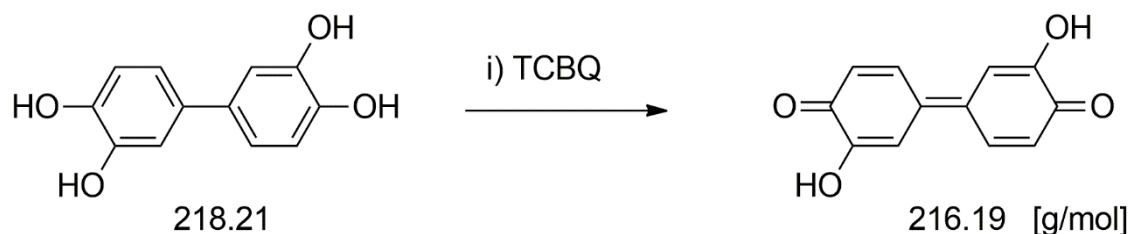
Yield = 91 % (2.00 g, 9.1 mmol)

Characterization:Elemental analysis: (Calculated for C₁₂H₁₀O₄)

Calculated: C = 66.05 %, H = 4.62 %

Found: C = 65.98 %, H = 4.92 %

¹H NMR (400 MHz, [D₄]MeOH, RT): δ = 6.76 (d, ³J_{HH} = 8.2 Hz, 2H; H⁵/H^{5'}), 6.84 (dd, ³J_{HH} = 8.2 Hz, ⁴J_{HH} = 2.1 Hz, 2H; H⁶/H^{6'}), 6.94 ppm (d, ⁴J_{HH} = 2.1 Hz, 2H; H²/H^{2'}).

4.3.6 3,3'-dihydroxy-diphenoquinone-(4,4') (H₂(SQ-SQ))

The compound was synthesized by following a modified literature procedure.^[124] Under an atmosphere of pure nitrogen, a colorless solution of 3,3',4,4'-tetrahydroxybiphenyl (436 mg, 2 mmol) in 1,4-dioxane (5 mL) was added dropwise to a red solution of tetrachloro-*o*-benzoquinone (1 g, 4.1 mmol) in 1,4-dioxane (5 mL) and then the reaction mixture was stirred until a dark brown solid was formed. The solid was collected by filtration and then washed with diethyl ether (60 mL). The obtained dark brown solid was dried in high vacuum at 100 °C for 4 h. The obtained compound was used for further reaction without any further purification.

MW (C₁₂H₈O₄) = 216.19 g/mol

Yield = ca. 85 % (370 mg, ca. 1.71 mmol)

Characterization:

Elemental analysis: (Calculated for C₁₂H₈O₄)^[a]

Calculated: C = 66.67 %, H = 3.73 %

Found: C = 65.71 %, H = 3.63 %

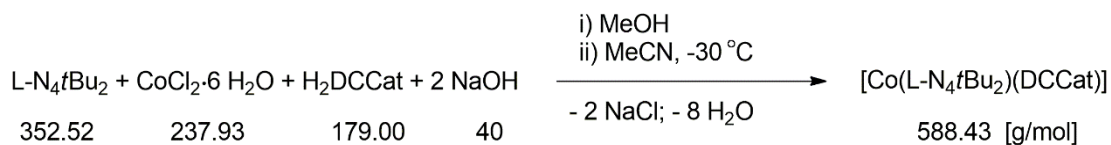
IR (KBr pellet, RT): ν = 3299, 1643, 1603, 1563, 1449, 1398, 1254, 1237, 1129, 961, 854, 827, 746, 675, 599, 560, 546, 465 cm⁻¹.

UV/Vis/NIR (1,4-dioxane, RT): λ_{\max} (ϵ) = 474 (13100), 413 nm (12800 M⁻¹ cm⁻¹).

¹H NMR (400 MHz, [D₆]DMSO, RT): δ = 10.01 (s, 1H), 9.40 (s, 1H), 7.70 (d, J_{HH} = 9.8 Hz, 1H), 7.26 (d, J_{HH} = 8.1 Hz, 1H), 7.21 (s, 1H), 6.86 (d, J_{HH} = 7.4 Hz, 1H), 6.54 (s, 1H), 6.47 ppm (d, J_{HH} = 10.3 Hz, 1H).

^[a] The substantial deviation of the elemental analysis from the calculated values can be explained; as in the ¹H NMR spectrum recorded in [D₆]DMSO, the peak corresponding to the protons of 1,4-dioxane is present at 3.56 ppm (see Figures A.88–A.89 in appendix). The ratio of the solvent molecule to the compound molecule cannot be identified exactly due to the decomposition of the compound in dimethyl sulfoxide. Therefore, the peaks corresponding to the compound cannot be assigned exactly.

4.3.7 Synthesis of [Co(L-N₄tBu₂)(DCCat)] (1)



Under an atmosphere of pure nitrogen, CoCl₂·6 H₂O (119 mg, 0.50 mmol) and L-N₄tBu₂ (176 mg, 0.50 mmol) were mixed in methanol (30 mL). Then the reaction mixture was heated to reflux temperatures for multiple times to obtain a violet solution. After cooling down to room temperature, a solution of 4,5-dichlorocatechol (89.5 mg, 0.50 mmol) and sodium hydroxide (40 mg, 1 mmol) in methanol (10 mL) was added to the violet solution. The color of the resulting solution changed to orange-red, and then the solution was refluxed for further 30 minutes, which resulted in formation of orange-red colored solid compound along with darkening of color of the solution. Then the suspension was evaporated to dryness under vacuum and the obtained orange-red residue was redissolved in hot acetonitrile (100 mL) and filtered through celite. The filtrate was stored at -30 °C for one week to afford orange-red crystals (67.1 mg) of [Co(L-N₄tBu₂)(DCCat)]·3 MeCN·H₂O (**1a**). Another portion of the crystals (31.5 mg) was obtained by reducing the volume of the mother liquor (25 mL) and storage of the solution at -30 °C. The crystals became opaque during isolation and therefore, the compound was dried in vacuum to obtain an analytically pure compound of [Co(L-N₄tBu₂)(DCCat)] (**1**).

MW (C₂₈H₃₄Cl₂CoN₄O₂) = 588.43 g/mol

Yield = 34 % (98.6 mg, 0.17 mmol)

Characterization:

Elemental analysis: (Calculated for C₂₈H₃₄Cl₂CoN₄O₂)

Calculated: C = 57.15 %, H = 5.82 %, N = 9.52 %

Found: C = 57.01 %, H = 5.81 %, N = 9.61 %

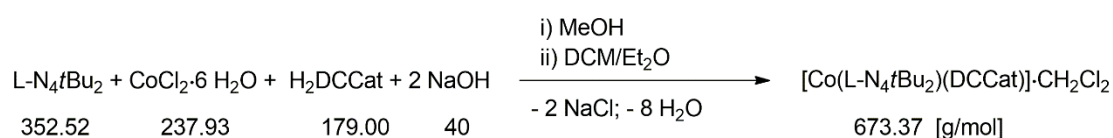
X-ray crystal structure analysis of **1a**: high-spin cobalt(II) catecholate at 150 K.

χ_{MT} for solid **1** (296 K) = 2.60 cm³ K mol⁻¹.

IR (KBr pellet, RT): ν = 2971, 2915, 1601, 1580, 1475, 1431, 1400, 1356, 1265, 1225, 1192, 1159, 1098, 1080, 1050, 1024, 1002, 963, 936, 913, 843, 819, 783, 773, 733, 716, 676, 666, 514 cm⁻¹.

UV/Vis/NIR (DCM, RT): λ_{\max} (ϵ) = 1037 (16), 551 (976), 516 (1190), 464 (1563), 380 (1060), 323 (6627), 260 nm (11600 M⁻¹ cm⁻¹).

4.3.8 Synthesis of [Co(L-N₄tBu₂)(DCCat)]·CH₂Cl₂ (**1b**)



Under an atmosphere of pure nitrogen, CoCl₂·6 H₂O (238 mg, 1 mmol) and L-N₄tBu₂ (352 mg, 1 mmol) were mixed in methanol (30 mL) and then, the reaction mixture was heated to reflux temperatures for multiple times to obtain a violet solution. After cooling down to room temperature, a solution of 4,5-dichlorocatechol (179 mg, 1 mmol) and sodium hydroxide (80 mg, 2 mmol) in methanol (10 mL) was added to the violet solution. The color of the solution changed to orange-red, and then the solution was refluxed for 30 minutes, which resulted in formation of orange-red colored solid compound along with darkening of color of the solution. After cooling down to room temperature, the suspension was evaporated to dryness under vacuum and the obtained orange-red residue was redissolved in dichloromethane (75 mL). The resulting solution was filtered through celite. Slow diffusion of diethyl ether into the filtrate yielded orange-red crystals of the compound [Co(L-N₄tBu₂)(DCCat)]·CH₂Cl₂ (**1b**).

MW ($C_{29}H_{36}Cl_4CoN_4O_2$) = 673.37 g/mol

Yield = 76 % (510 mg, 0.76 mmol)

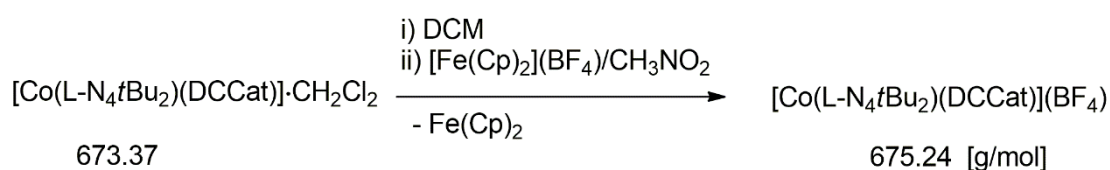
Characterization:

Elemental analysis: (Calculated for $C_{29}H_{36}Cl_4CoN_4O_2$)

Calculated: C = 51.73 %, H = 5.39 %, N = 8.32 %

Found: C = 51.91 %, H = 5.41 %, N = 8.29 %

4.3.9 Synthesis of $[Co(L-N_4tBu_2)(DCCat)](BF_4)$ (**2a**)



Under an atmosphere of pure nitrogen, the compound **1b** (505 mg, 0.75 mmol) was dissolved in dichloromethane (100 mL) to obtain an orange-red solution. Then a solution of ferrocenium tetrafluoroborate (204 mg, 0.75 mmol) in nitromethane (5 mL) was added to the orange-red solution. The color of the resulting solution changed to violet from orange-red. Slow diffusion of diethyl ether into the violet solution afforded greenish colored crystalline compound. This compound was dried in the vacuum to yield an analytically pure lilac colored compound of $[Co(L-N_4tBu_2)(DCCat)](BF_4)$ (**2a**).

MW ($C_{28}H_{34}BCl_2CoF_4N_4O_2$) = 675.24 g/mol

Yield = 87 % (442 mg, 0.65 mmol)

Characterization:

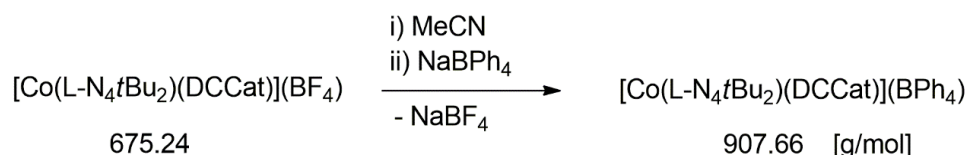
Elemental analysis: (Calculated for $C_{28}H_{34}BCl_2CoF_4N_4O_2$)

Calculated: C = 49.80 %, H = 5.08 %, N = 8.30 %

Found: C = 49.80 %, H = 5.18 %, N = 8.26 %

IR (KBr pellet, RT): $\nu = 2978, 2930, 2889, 1612, 1589, 1475, 1438, 1407, 1381, 1360, 1257, 1224, 1174, 1098, 1083, 1057, 1037, 940, 890, 837, 791, 781, 755, 703, 680, 577, 533, 521, 485, 454, 425, 417, 402 \text{ cm}^{-1}$.

4.3.10 Synthesis of [Co(L-N₄tBu₂)(DCCat)](BPh₄) (**2b**)



Under an atmosphere of pure nitrogen, a solution of sodium tetraphenylborate (171 mg, 0.50 mmol) in dry acetonitrile (5 mL) was added to a red-violet solution of **2a** (344 mg, 0.51 mmol) in dry acetonitrile (75 mL). After stirring for 15 minutes, the resulting solution was evaporated to dryness under vacuum. The obtained lilac residue was washed with dry methanol. Then the solid was dried in vacuum to obtain an analytically pure lilac colored compound of [Co(L-N₄tBu₂)(DCCat)](BPh₄) (**2b**).

MW (C₅₂H₅₄BCl₂CoN₄O₂) = 907.66 g/mol

Yield = 88 % (402 mg, 0.44 mmol)

Characterization:

Elemental analysis: (Calculated for C₅₂H₅₄BCl₂CoN₄O₂)

Calculated: C = 68.81 %, H = 6.00 %, N = 6.17 %

Found: C = 68.63 %, H = 6.05 %, N = 6.06 %

IR (KBr pellet, RT): $\nu = 3053, 3033, 2996, 2981, 1609, 1579, 1474, 1427, 1405, 1380, 1360, 1258, 1224, 1195, 1175, 1166, 1096, 1065, 1049, 1032, 937, 913, 888, 836, 791, 779, 733, 706, 678, 624, 612, 575, 541, 526, 516, 487, 482, 468, 442, 431, 423 \text{ cm}^{-1}$.

Selected IR bands (DMSO, thin film): $\nu = 1611, 1580, 1473, 1434, 1416, 1404, 1382, 1358, 1258, 1225, 1178 \text{ cm}^{-1}$.

Selected IR bands ([D₂]DCM, liquid cell): $\nu = 1610, 1580, 1505, 1473, 1435, 1426, 1405, 1382, 1362, 1258, 1224, 1195, 1178, 1165 \text{ cm}^{-1}$.

¹H NMR (600 MHz, [D₆]DMSO, 295 K): $\delta = 8.23$ (t, $^3J_{\text{HH}} = 7.8 \text{ Hz}$, 2H; *p*-Py-H), 7.68 (d, $^3J_{\text{HH}} = 7.8 \text{ Hz}$, 4H; *m*-Py-H), 4.97 (d, $^2J_{\text{HH}} = 16.7 \text{ Hz}$, 4H; CH₂), 4.48 (d, $^2J_{\text{HH}} = 16.7 \text{ Hz}$, 4H; CH₂), 1.31 (s, 6H; *t*Bu), 0.68 (s, 12H; *t*Bu), 6.16 (s, 2H; H³/H⁶-DCCat²⁻), 6.79 (t, $^3J_{\text{HH}} = 7.4 \text{ Hz}$, 4H; *p*-Ph-H, BPh₄⁻), 6.92 (t, $^3J_{\text{HH}} = 7.2 \text{ Hz}$, 8H; *m*-Ph-H, BPh₄⁻), 7.20–7.16 ppm (m, 8H; *o*-Ph-H, BPh₄⁻).

¹H NMR (400 MHz, [D₃]MeCN, RT): $\delta = 8.15$ (t, $^3J_{\text{HH}} = 7.8 \text{ Hz}$, 2H; *p*-Py-H), 7.61 (d, $^3J_{\text{HH}} = 7.8 \text{ Hz}$, 4H; *m*-Py-H), 6.35 (d, $^2J_{\text{HH}} = 16.5 \text{ Hz}$, 4H; CH₂), 6.21 (d, $^2J_{\text{HH}} = 16.4 \text{ Hz}$, 4H; CH₂), 5.04 (s, 2H; H³/H⁶-DCCat²⁻), 1.76 (br, 6H; *t*Bu), 0.53 (s, 12H; *t*Bu), 6.84 (tt, $^3J_{\text{HH}} = 7.2 \text{ Hz}$, $^4J_{\text{HH}} = 1.6 \text{ Hz}$, 4H; *p*-Ph-H, BPh₄⁻), 6.99 (t, $^3J_{\text{HH}} = 7.4 \text{ Hz}$, 8H; *m*-Ph-H, BPh₄⁻), 7.30–7.24 ppm (m, 8H; *o*-Ph-H, BPh₄⁻).

¹H NMR (600 MHz, [D₂]DCM, 295 K): $\delta = 33.23$ (4H, br), 26.52 (4H, br), 11.06 (4H, br), 9.31 (2H, br), 7.91 (9H, br), -4.87 (9H, br), -12.08 (2H, br), 6.95 (t, $^3J_{\text{HH}} = 7.1 \text{ Hz}$, 4H; *p*-Ph-H, BPh₄⁻), 7.11 (t, $^3J_{\text{HH}} = 7.1 \text{ Hz}$, 8H; *m*-Ph-H, BPh₄⁻), 7.45–7.41 ppm (m, 8H; *o*-Ph-H, BPh₄⁻).

Evans-NMR method (600 MHz, [D₂]DCM, 295 K): $\chi_{\text{M}}T = 0.65 \text{ cm}^3 \text{ K mol}^{-1}$.

UV/Vis/NIR (DCM, 298 K): $\lambda_{\text{max}} (\epsilon) = 1108 (8243), 1060 (6737), 990 (3318), 938 (1581), 810 (580), 630 (614), 580 (558), 420 (1199), 320 (12200), 300 (11300), 274 \text{ nm} (12800 \text{ M}^{-1} \text{ cm}^{-1})$.

UV/Vis/NIR (DMSO, 298 K): $\lambda_{\text{max}} (\epsilon) = 1106 (391), 1052 (385), 990 (319), 547 (470), 505 (445), 460 (395), 324 (17100), 276 \text{ nm} (13700 \text{ M}^{-1} \text{ cm}^{-1})$.

UV/Vis/NIR (MeCN, RT): $\lambda_{\text{max}} (\epsilon) = 1107 (747), 1051 (698), 990 (491), 559 (474), 500 (428), 452 (391), 320 (16800), 275 \text{ nm} (12700 \text{ M}^{-1} \text{ cm}^{-1})$.

Cyclic voltammetry:

Reductions at $\nu = 100$ mV/s: $E_{1/2} = -56$ mV vs. SCE (reversible), $E_{pc} = -1.95$ V vs. SCE (irreversible).

Oxidations at $\nu = 100$ mV/s: $E_{1/2} = 715$ mV vs. SCE (reversible), $E_{pa} = 938$ mV vs. SCE (irreversible), $E_{pa} = 1.60$ V vs. SCE (irreversible).

4.3.11 Synthesis of [Co(L-N₄tBu₂)(DCCat)](BPh₄)·2 CH₂Cl₂ (**2c**)

Under an atmosphere of pure nitrogen, the compound **2b** (120 mg, 0.132 mmol) was dissolved in dichloromethane (75 mL) to obtain a green and clear solution. Slow diffusion of diethyl ether into the green solution yielded green crystals of the compound [Co(L-N₄tBu₂)(DCCat)](BPh₄)·2 CH₂Cl₂ (**2c**) suitable for X-ray diffraction.

MW (C₅₄H₅₈BCl₆CoN₄O₂) for **2c** = 1077.53 g/mol

Yield = 46 % (63.1 mg, 0.061 mmol); the molecular weight is adjusted according to the calculation of loss of 0.5 DCM per complex by NMR spectroscopic measurement.

Characterization:

X-ray crystal structure analysis: low-spin cobalt(III) catecholate at 150 K.

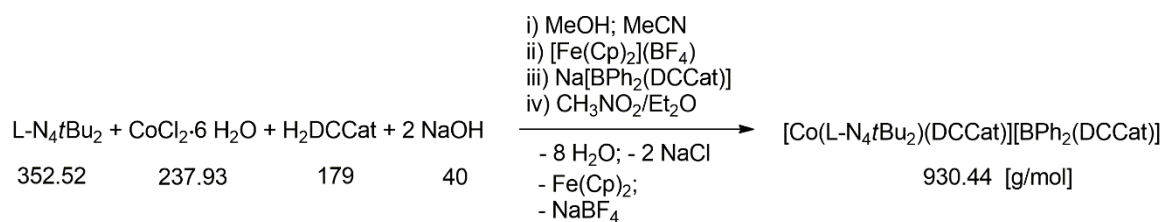
χ_{MT} for solid [Co(L-N₄tBu₂)(DCCat)](BPh₄)·1.5 CH₂Cl₂ (298 K): 0.017 cm³ K mol⁻¹.

IR (KBr pellet, RT): $\nu = 3053, 3033, 2996, 2980, 1607, 1579, 1473, 1426, 1406, 1380, 1360, 1258, 1224, 1195, 1175, 1166, 1096, 1066, 1050, 1031, 937, 912, 888, 837, 790, 779, 734, 706, 677, 624, 612, 575, 543, 525, 513, 487, 475, 468, 453, 420$ cm⁻¹.

¹H NMR for **2c** (400 MHz, [D₃]MeCN, RT): $\delta = 8.15$ (t, ³J_{HH} = 7.8 Hz, 2H; *p*-Py-H), 7.61 (d, ³J_{HH} = 7.8 Hz, 4H; *m*-Py-H), 6.29 (d, ²J_{HH} = 16.5 Hz, 4H; CH₂), 6.15 (d, ²J_{HH} = 16.4 Hz, 4H; CH₂), 5.08 (s, 2H; H³/H⁶-DCCat²⁻), 1.76

(br, 6H; *t*Bu), 0.54 ppm (s, 12H; *t*Bu), 6.84 ppm (tt, $^3J_{\text{HH}} = 7.2$ Hz, $^4J_{\text{HH}} = 1.6$ Hz, 4H; *p*-Ph-H, BPh₄⁻), 6.99 (t, $^3J_{\text{HH}} = 7.4$ Hz, 8H; *m*-Ph-H, BPh₄⁻), 7.30–7.24 ppm (m, 8H; *o*-Ph-H, BPh₄⁻).

4.3.12 Synthesis of [Co(L-N₄*t*Bu₂)(DCCat)][BPh₂(DCCat)] (2d)



Under an atmosphere of pure nitrogen, CoCl₂·6 H₂O (238 mg, 1 mmol) and L-N₄*t*Bu₂ (352 mg, 1 mmol) were mixed in methanol (30 mL). The resulting reaction mixture was heated to reflux temperatures for multiple times to obtain a violet solution. Then, to this violet solution, a solution of 4,5-dichlorocatechol (179 mg, 1 mmol) and sodium hydroxide (80 mg, 2 mmol) in methanol (10 mL) was added. The color of the resulting solution changed from violet to orange-red. The orange-red solution was refluxed for further 30 minutes, which resulted in formation of orange-red colored solid compound along with darkening of color of the solution. After cooling down to room temperature, the suspension was evaporated to dryness under vacuum. The obtained residue was redissolved in hot MeCN (120 mL) and the resulting solution was filtered through celite. After cooling down to room temperature, solid ferrocenium tetrafluoroborate (272 mg, 1 mmol) was added to the filtrate to produce a red-violet solution. Then *in situ* prepared Na[BPh₂(DCCat)] (prior to use prepared *in situ* in another reaction set up; by reacting 1 mmol of Ph₂BOH, 1 mmol of H₂DCCat and 0.50 mmol of NaOH in toluene/methanol (25:1), and then by evaporation of the reaction mixture to dryness under vacuum) in MeCN (10 mL) was added. The resulting solution was evaporated to dryness under vacuum and the obtained solid residue was redissolved in

nitromethane (50 mL) and the resulting solution was filtered through celite. Slow diffusion of diethyl ether into the filtrate afforded the lilac crystals of [Co(L-N₄tBu₂)(DCCat)][BPh₂(DCCat)] (**2d**). The compound was dried in vacuum in order to obtain analytically pure compound of **2d**.

MW (C₄₆H₄₆BCl₄CoN₄O₄) = 930.44 g/mol

Yield = 33 %. (310 mg, 0.333 mmol)

Characterization:

Elemental analysis: (Calculated for C₄₆H₄₆BCl₄CoN₄O₄)

Calculated: C = 59.38 %, H = 4.98 %, N = 6.02 %

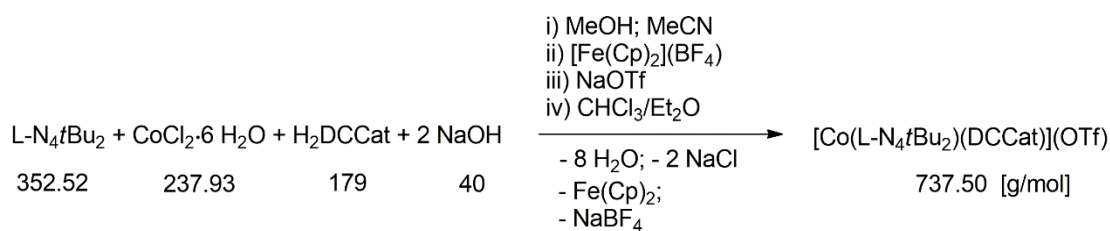
Found: C = 59.47 %, H = 5.07 %, N = 6.19 %

X-ray crystal structure analysis: low-spin cobalt(III) catecholate at 150 and 373 K.

IR (KBr pellet, RT): ν = 3080, 3059, 3045, 3034, 3013, 2996, 2981, 2966, 2927, 2876, 1609, 1587, 1480, 1473, 1426, 1405, 1381, 1364, 1356, 1258, 1240, 1219, 1203, 1175, 1166, 1145, 1093, 1065, 1049, 1034, 998, 940, 911, 884, 866, 835, 788, 780, 757, 749, 732, 702, 675, 643, 614, 582, 571, 543, 530, 523, 510, 485, 460, 452, 441, 433, 419 cm⁻¹.

¹H NMR (400 MHz, [D₃]MeCN, RT): δ = 8.15 (t, ³J_{HH} = 7.8 Hz, 2H; *p*-Py-H), 7.61 (d, ³J_{HH} = 7.8 Hz, 4H; *m*-Py-H), 6.29 (d, ²J_{HH} = 16.5 Hz, 4H; CH₂), 6.14 (d, ²J_{HH} = 16.4 Hz, 4H; CH₂), 5.07 (s, 2H; H³/H⁶-DCCat²⁻), 1.76 (br, 6H; *t*Bu), 0.53 ppm (s, 12H; *t*Bu), 7.38 (dd, ³J_{HH} = 8.3 Hz, ⁴J_{HH} = 1.3 Hz, 4H; *o*-Ph-H, BPh₂(DCCat)⁻), 7.12 Hz (tt, ³J_{HH} = 7.6 Hz, ⁴J_{HH} = 1.5 Hz, 4H; *m*-Ph-H, BPh₂(DCCat)⁻), 7.03 (tt, ³J_{HH} = 7.2 Hz, ⁴J_{HH} = 1.5 Hz, 2H; *p*-Ph-H, BPh₂(DCCat)⁻), 6.45 ppm (s, 2H; H³/H⁶-DCCat²⁻, BPh₂(DCCat)⁻).

4.3.13 Synthesis of [Co(L-N₄tBu₂)(DCCat)](OTf) (2e)



Under an inert atmosphere, CoCl₂·6 H₂O (119 mg, 0.50 mmol) and L-N₄tBu₂ (176 mg, 0.50 mmol) were mixed in methanol (15 mL), and refluxed for 30 minutes to produce a violet solution. To this solution, addition of a solution containing 4,5-dichlorocatechol (89.5 mg, 0.50 mmol) and NaOH (40 mg, 1 mmol) in methanol (10 mL) resulted in change in color of the solution from violet to orange-red. This orange-red solution was refluxed for further 30 minutes, which resulted in formation of orange-red colored solid compound along with darkening of color of the solution. The suspension was evaporated to dryness under vacuum, then the resulting residue was redissolved in hot MeCN (70 mL) and filtered through celite. After cooling down to room temperature, addition of solid ferrocenium tetrafluoroborate (136 mg, 0.50 mmol) to the filtrate resulted in change in color of the solution from orange-red to red-violet. The resulting red-violet solution was treated with solid NaOTf (86 mg, 0.50 mmol) and stirred for 15 minutes. Then the resulting solution was evaporated to dryness under vacuum to obtain a lilac residue. The residue was redissolved in chloroform (40 mL) and filtered through celite. Slow diffusion of diethyl ether into the filtrate afforded a lilac colored crystalline compound which was dried in vacuum to afford an analytically pure compound of [Co(L-N₄tBu₂)(DCCat)](OTf) (**2e**).

MW (C₂₉H₃₄Cl₂CoF₃N₄O₅S) = 737.50 g/mol

Yield = 81 % (298 mg, 0.404 mmol)

Characterization:

Elemental analysis: (Calculated for $C_{29}H_{34}Cl_2CoF_3N_4O_5S$)

Calculated: C = 47.23 %, H = 4.65 %, N = 7.60 %

Found: C = 46.89 %, H = 4.69 %, N = 7.60 %

IR (KBr pellet, RT): $\nu = 3090, 2976, 2946, 2924, 2884, 1612, 1591, 1475, 1439, 1407, 1381, 1360, 1276, 1256, 1224, 1166, 1098, 1068, 1051, 1031, 941, 891, 836, 794, 780, 754, 711, 703, 679, 637, 573, 516, 486, 453, 412$ cm^{-1} .

Cyclic voltammetry:

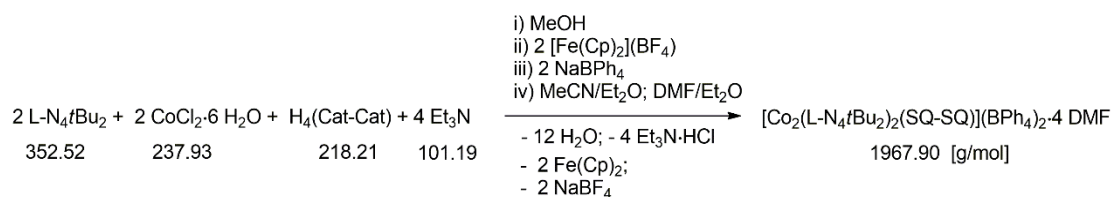
Reductions at $\nu = 100$ mV/s: $E_{1/2} = -58$ mV vs. SCE (reversible), $E_{pc} = -1.95$ V vs. SCE (irreversible).

Oxidations at $\nu = 100$ mV/s: $E_{1/2} = 711$ mV vs. SCE (reversible), $E_{pa} = 1.60$ V vs. SCE (irreversible).

1H NMR (600 MHz, $[D_6]$ DMSO, 295 K): $\delta = 8.25$ (t, $^3J_{HH} = 7.8$ Hz, 2H; *p*-Ph-H), 7.69 (d, $^3J_{HH} = 7.8$ Hz, 4H; *m*-Py-H), 6.17 (s, 2H; H^3/H^6 -DCCat $^{2-}$), 4.95 (d, $^2J_{HH} = 16.7$ Hz, 4H; CH $_2$), 4.46 (d, $^2J_{HH} = 16.6$ Hz, 4H; CH $_2$), 1.30 (s, 6H; *t*Bu), 0.68 ppm (s, 12H; *t*Bu).

4.3.14 Synthesis of $[\text{Co}_2(\text{L-N}_4\text{tBu}_2)_2(\text{SQ-SQ})](\text{BPh}_4)_2 \cdot 4 \text{ DMF}$ (**3b**)

First method:



Under an atmosphere of pure nitrogen, a solution of $\text{CoCl}_2 \cdot 6 \text{ H}_2\text{O}$ (238 mg, 1 mmol) and $\text{L-N}_4\text{tBu}_2$ (352 mg, 1 mmol) in methanol (40 mL) was refluxed for 30 minutes. The resulting violet solution was first treated with solid 3,3',4,4'-tetrahydroxybiphenyl (109 mg, 0.50 mmol) and then with triethylamine (280 μL , 2 mmol). The color of the solution changed to dark red, and the solution was refluxed for further 30 minutes. After cooling down to room temperature, solid ferrocenium tetrafluoroborate (272 mg, 1 mmol) was added to the dark red solution. Then the color of the solution changed to dark green and after addition of solid sodium tetraphenylborate (342 mg, 1 mmol) to the dark green solution, dark green colored solid was formed. The solid was collected by filtration and washed with diethyl ether (20 mL). Slow diffusion of diethyl ether into a solution of the solid in acetonitrile (30 mL) afforded crystalline compound. This crystalline compound was dissolved in DMF (50 mL) and slow diffusion of diethyl ether into the solution produced dark green crystals. Recrystallization of the obtained crystals from DMF/ Et_2O yielded dark green crystals of $[\text{Co}_2(\text{L-N}_4\text{tBu}_2)_2(\text{SQ-SQ})](\text{BPh}_4)_2 \cdot 4 \text{ DMF}$ (**3b**).

MW ($\text{C}_{116}\text{H}_{138}\text{B}_2\text{Co}_2\text{N}_{12}\text{O}_8$) = 1967.90 g/mol

Yield = 50 % (490 mg, 0.25 mmol)

Characterization:

Elemental analysis: (Calculated for $C_{116}H_{138}B_2Co_2N_{12}O_8$)

Calculated: C = 70.80 %, H = 7.07 %, N = 8.54 %

Found: C = 70.87 %, H = 6.89 %, N = 8.35 %

X-ray crystal structure analysis:

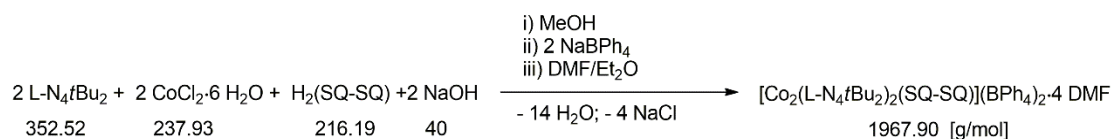
At 100 K = LS-Co^{II}-(SQ-SQ)_{OS}-Co^{II}-LS.

At 300 K = HS-Co^{II}-(SQ-SQ)_{CS}-Co^{II}-HS.

SQUID: $T_{1/2} = 141$ K.

IR (KBr pellet, RT): $\nu = 3052, 3037, 3010, 2978, 2922, 2852, 1673, 1600, 1580, 1521, 1507, 1479, 1465, 1428, 1401, 1382, 1345, 1285, 1257, 1225, 1190, 1159, 1142, 1086, 1030, 936, 908, 882, 843, 826, 787, 778, 743, 733, 706, 658, 623, 612, 578, 567, 519, 490, 475, 466, 457, 446, 437, 430, 416, 408$ cm⁻¹.

ATR (RT): $\nu = 3052, 3012, 2980, 2923, 2852, 1672, 1600, 1579, 1520, 1504, 1479, 1466, 1426, 1401, 1381, 1346, 1288, 1256, 1229, 1189, 1164, 1142, 1084, 1030, 1014, 936, 909, 881, 840, 826, 788, 778, 741, 734, 705, 657$ cm⁻¹.

Second method:

Under an atmosphere of pure nitrogen, a solution of $\text{CoCl}_2 \cdot 6 \text{ H}_2\text{O}$ (119 mg, 0.50 mmol) and $\text{L-N}_4\text{tBu}_2$ (176 mg, 0.50 mmol) in methanol (25 mL) was refluxed for 30 minutes. The resulting violet solution was treated with a dark green solution of $\text{H}_2(\text{SQ-SQ})$ (54 mg, 0.25 mmol) and sodium hydroxide (20 mg, 0.50 mmol) in warm methanol (50 mL). The color of the solution changed to dark green. The solution was heated to reflux temperatures for multiple times and after cooling down to room temperature, solid sodium tetraphenylborate (171 mg, 0.50 mmol) was added to produce a dark green solid. Then green solid was collected by filtration and washed with diethyl ether (20 mL). Slow diffusion of diethyl ether into a solution of the solid in DMF (25 mL) produced dark green crystals. Recrystallization of the obtained crystals from DMF/ Et_2O afforded dark green crystals of $[\text{Co}_2(\text{L-N}_4\text{tBu}_2)_2(\text{SQ-SQ})](\text{BPh}_4)_2 \cdot 4 \text{ DMF}$ (**3b**).

MW ($\text{C}_{116}\text{H}_{138}\text{B}_2\text{Co}_2\text{N}_{12}\text{O}_8$) = 1967.90 g/mol

Yield = 45 % (221 mg, 0.112 mmol)

Characterization:

Elemental analysis: (Calculated for $\text{C}_{116}\text{H}_{138}\text{B}_2\text{Co}_2\text{N}_{12}\text{O}_8$)

Calculated: C = 70.80 %, H = 7.07 %, N = 8.54 %

Found: C = 70.70 %, H = 7.20 %, N = 8.18 %

4.3.15 Synthesis of [Co₂(L-N₄tBu₂)₂(SQ-SQ)](BPh₄)₂ (**3a**)

The compound **3b** (196.7 mg, 0.10 mmol) was dried at 100 °C under high vacuum for 6 h to afford an analytically pure compound of [Co₂(L-N₄tBu₂)₂(SQ-SQ)](BPh₄)₂ (**3a**).

MW (C₁₀₄H₁₁₀B₂Co₂N₈O₄) = 1675.53 g/mol

Yield = 97 % (162.3 mg, 0.097 mmol)

Characterization:

Elemental analysis: (Calculated for C₁₀₄H₁₁₀B₂Co₂N₈O₄)

Calculated: C = 74.55 %, H = 6.62 %, N = 6.69 %

Found: C = 74.25 %, H = 6.61 %, N = 6.62 %

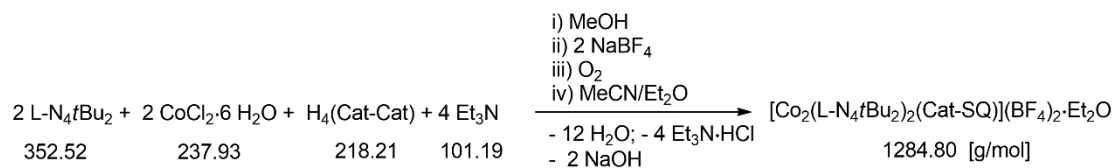
ATR (RT): ν = 3052, 3033, 3026, 3012, 2980, 2907, 1599, 1580, 1522, 1501, 1492, 1477, 1465, 1427, 1403, 1383, 1365, 1345, 1287, 1253, 1220, 1185, 1161, 1137, 1076, 1031, 1015, 934, 907, 897, 881, 838, 785, 772, 747, 732, 702 cm⁻¹.

¹H NMR (400 MHz, [D₃]MeCN, 293 K): δ = 90.64 (br), 85.54 (br), 39.48 (br), 35.35 (br), 32.11 (br), 28.38 (br), 26.47 (br), 18.98 (br), 3.19 (br), -2.06 (br), -2.31 (br), -11.08 (br), -15.81 (br), -17.56 (br), -52.30 (br), 6.94 (t, ³J_{HH} = 7.2 Hz, 8H; *p*-Ph-H, BPh₄⁻), 7.06 (t, ³J_{HH} = 7.3 Hz, 16H; *m*-Ph-H, BPh₄⁻), 7.31–7.26 ppm (m, 16H; *o*-Ph-H, BPh₄⁻).

Evans-NMR method (600 MHz, [D₃]MeCN, 293 K): $\chi_M T$ = 5.07 cm³ K mol⁻¹.

UV/Vis/NIR (EtCN, 293 K): λ_{\max} (ϵ) = 1260 (3296), 1100 (5447), 709 (19500), 450 (14600), 324 (11600), 296 nm (15900 M⁻¹ cm⁻¹).

4.3.16 Synthesis of $[\text{Co}_2(\text{L-N}_4\text{tBu}_2)_2(\text{Cat-SQ})](\text{BF}_4)_2 \cdot \text{Et}_2\text{O}$ (**3d**)



Under an atmosphere of pure nitrogen, a solution of $\text{CoCl}_2 \cdot 6 \text{ H}_2\text{O}$ (238 mg, 1 mmol) and $\text{L-N}_4\text{tBu}_2$ (352 mg, 1 mmol) in methanol (30 mL) was refluxed for 30 minutes. The resulting violet solution was first treated with solid 3,3',4,4'-tetrahydroxybiphenyl (109 mg, 0.50 mmol), and then with triethylamine (280 μL , 2 mmol). The color of the solution changed to dark red, which was refluxed for further 30 minutes. After cooling down to room temperature, the solution was exposed to air for 5 minutes. The color of the solution changed to light green and then excess solid sodium tetrafluoroborate (150 mg, 1.37 mmol) was added. Then the solution was purged with pure dioxygen for 2 minutes, after that the color of the solution changed to dark green and a dark green colored solid was formed. The resulting reaction mixture was stirred for 15 minutes and then the solid was collected by filtration and then at first washed with methanol (20 mL) followed by diethyl ether (20 mL). Slow diffusion of diethyl ether under an inert atmosphere into a solution of the solid in acetonitrile (30 mL) afforded olive-green crystals. Recrystallization of the crystals from acetonitrile/diethyl ether produced olive-green crystals of $[\text{Co}_2(\text{L-N}_4\text{tBu}_2)_2(\text{Cat-SQ})](\text{BF}_4)_2 \cdot \text{Et}_2\text{O}$ (**3d**).

MW ($\text{C}_{60}\text{H}_{80}\text{B}_2\text{Co}_2\text{F}_8\text{N}_8\text{O}_5$) = 1284.80 g/mol

Yield = 47 % (302 mg, 0.235 mmol)

Characterization:

Elemental analysis: (Calculated for $\text{C}_{60}\text{H}_{80}\text{B}_2\text{Co}_2\text{F}_8\text{N}_8\text{O}_5$)

Calculated: C = 56.09 %, H = 6.28 %, N = 8.72 %

Found: C = 55.81 %, H = 6.37 %, N = 8.47 %

X-ray crystal structure analysis: LS-Co^{III}-Cat-SQ-Co^{II}-LS at 150 K.

ATR (RT): $\nu = 2971, 2923, 1604, 1582, 1501, 1467, 1439, 1404, 1380, 1368, 1351, 1281, 1266, 1250, 1225, 1191, 1175, 1165, 1103, 1047, 1031, 939, 911, 879, 841, 829, 791, 778, 709, 680, \text{cm}^{-1}$.

IR (KBr pellet, RT): $\nu = 2970, 2923, 1603, 1581, 1520, 1506, 1467, 1436, 1402, 1376, 1368, 1283, 1260, 1250, 1225, 1190, 1165, 1121, 1083, 1056, 1033, 938, 908, 848, 827, 791, 777, 751, 729, 708, 673, 647, 619, 580, 565, 519, 450, 418 \text{ cm}^{-1}$.

UV/Vis/NIR (EtCN, 293 K): $\lambda_{\text{max}} (\epsilon) = 1260 (2990), 1100 (5466), 709 (20600), 450 (14400), 324 (11900), 296 \text{ nm} (16200 \text{ M}^{-1} \text{ cm}^{-1})$.

4.3.17 Synthesis of [Co₂(L-N₄tBu₂)₂(Cat-SQ)](BF₄)₂ (**3c**)

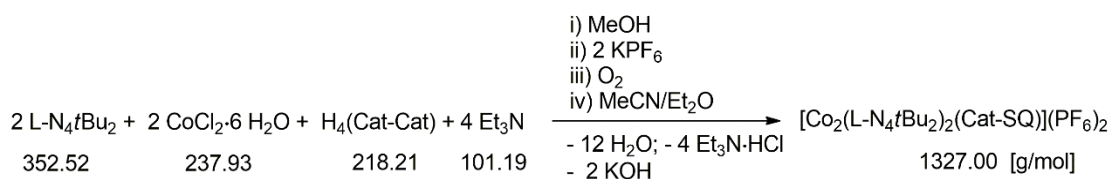
Upon drying of compound **3d** in vacuum at room temperature, the compound [Co₂(L-N₄tBu₂)₂(Cat-SQ)](BF₄)₂ (**3c**) was obtained. The loss of diethyl ether was confirmed by NMR spectroscopic investigation (see Figure A.91 in Appendix).

Characterization:

SUID: $T_{1/2} = 350 \text{ K}$.

ATR (RT): $\nu = 2972, 2924, 1605, 1581, 1501, 1467, 1438, 1404, 1383, 1369, 1350, 1282, 1265, 1249, 1225, 1187, 1174, 1164, 1103, 1047, 1032, 938, 910, 890, 879, 841, 829, 791, 778, 743, 709, 681 \text{ cm}^{-1}$.

4.3.18 Synthesis of $[\text{Co}_2(\text{L-N}_4\text{tBu}_2)_2(\text{Cat-SQ})](\text{PF}_6)_2$ (**3e**)



Under an atmosphere of pure nitrogen, a solution of $\text{CoCl}_2 \cdot 6 \text{ H}_2\text{O}$ (238 mg, 1 mmol) and $\text{L-N}_4\text{tBu}_2$ (352 mg, 1 mmol) in methanol (30 mL) was refluxed for 30 minutes. The resulting violet solution was first treated with solid 3,3',4,4'-tetrahydroxybiphenyl (109 mg, 0.50 mmol), and then with triethylamine (280 μL , 2 mmol). The color of the solution changed to dark red, which was refluxed for further 30 minutes. After cooling down to room temperature, the dark red solution was exposed to air for 5 minutes and then excess solid KPF_6 (200 mg, 1.08 mmol) was added to this solution. Then pure dioxygen was passed through the solution for 2 minutes until the color of the solution changed to dark green, and a dark green solid began to precipitate. The resulting reaction mixture was stirred for 1 h at room temperature to produce a dark green solid which was collected by filtration and washed with methanol (25 mL) followed by diethyl ether (20 mL). Under an inert atmosphere, slow diffusion of diethyl ether into a solution of the solid in acetonitrile (60 mL) afforded a green crystalline compound. Recrystallization of the crystals from acetonitrile/diethyl ether afforded a green crystalline compound. This crystalline compound was dried in vacuum at room temperature to obtain an analytically pure green colored crystalline compound of $[\text{Co}_2(\text{L-N}_4\text{tBu}_2)_2(\text{Cat-SQ})](\text{PF}_6)_2$ (**3e**).

MW ($\text{C}_{56}\text{H}_{70}\text{Co}_2\text{F}_{12}\text{N}_8\text{O}_4\text{P}_2$) = 1327.00 g/mol

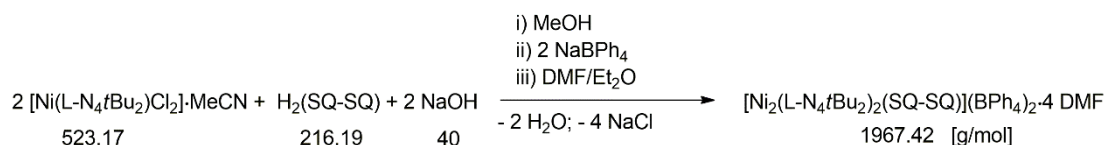
Yield = 41 % (270 mg, 0.203 mmol)

Characterization:Elemental analysis: (Calculated for C₅₆H₇₀Co₂F₁₂N₈O₄P₂)

Calculated: C = 50.69 %, H = 5.32 %, N = 8.44 %

Found: C = 50.63 %, H = 5.14 %, N = 8.14 %

Cyclic voltammetry:

Reductions at $\nu = 100$ mV/s: $E_{1/2} = -112$ mV vs. SCE (reversible), $E_{1/2} = -552$ mV vs. SCE (reversible).Oxidations at $\nu = 100$ mV/s: $E_{pa} = 360$ mV vs. SCE (irreversible), $E_{1/2} = ca. 571$ mV vs. SCE (quasi-reversible), $E_{1/2} = 709$ mV vs. SCE (quasi-reversible).**4.3.19 Synthesis of [Ni₂(L-N₄tBu₂)₂(SQ-SQ)](BPh₄)₂·4 DMF (4a)**

Under an atmosphere of pure nitrogen, a solution of [Ni(L-N₄tBu₂)Cl₂] \cdot MeCN (131 mg, 0.25 mmol) in methanol (25 mL) was treated with a dark green solution of H₂(SQ-SQ) (27 mg, 0.125 mmol) and sodium hydroxide (10 mg, 0.25 mmol) in warm methanol (30 mL), and the resulting dark green solution was heated to reflux temperatures for multiple times. After cooling down to room temperature, solid sodium tetraphenylborate (86 mg, 0.25 mmol) was added to the solution to obtain a dark green solid, which was collected by filtration and washed with diethyl ether (20 mL). Slow diffusion of diethyl ether into a solution of the solid in DMF (25 mL) afforded dark green crystals. Recrystallization of the crystals from DMF/Et₂O yielded dark green crystals of [Ni₂(L-N₄tBu₂)₂(SQ-SQ)](BPh₄)₂·4 DMF (**4a**).

MW ($C_{116}H_{138}B_2Ni_2N_{12}O_8$) = 1967.42 g/mol

Yield = 45 % (110 mg, 0.056 mmol)

Characterization:

Elemental analysis: (Calculated for $C_{116}H_{138}B_2Ni_2N_{12}O_8$)

Calculated: C = 70.82 %, H = 7.07 %, N = 8.54 %

Found: C = 70.69 %, H = 7.03 %, N = 8.27 %

X-ray crystal structure analysis: $Ni^{II}-(SQ-SQ)_{CS}-Ni^{II}$ (temperature invariant)

SQUID: $J = -2.764 \text{ cm}^{-1}$

IR (KBr pellet, RT): $\nu = 3053, 3036, 3010, 2994, 2979, 2920, 2853, 1673, 1603, 1582, 1519, 1504, 1479, 1467, 1435, 1401, 1384, 1377, 1344, 1292, 1255, 1231, 1188, 1157, 1134, 1090, 1075, 1034, 1011, 964, 936, 907, 884, 847, 825, 789, 778, 744, 733, 705, 678, 658, 624, 612, 579, 570, 520, 484, 471, 464, 452, 439, 418, 407 \text{ cm}^{-1}$.

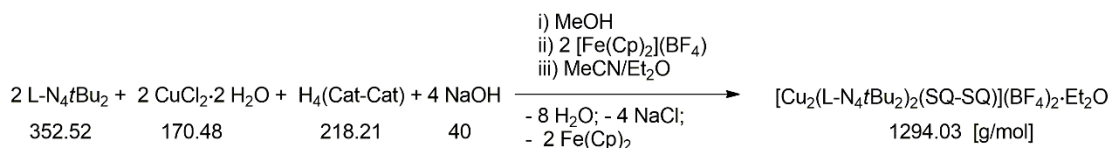
UV/Vis/NIR (MeCN, RT): $\lambda_{\text{max}} (\epsilon) = 727 (27900), 522 (12200), 475 (14200), 332 (8900), 310 (12800), 294 \text{ nm} (15600 \text{ M}^{-1} \text{ cm}^{-1})$.

Cyclic voltammetry:

Reductions at $\nu = 100 \text{ mV/s}$: $E_{1/2} = -176 \text{ mV vs. SCE}$ (reversible), $E_{1/2} = -650 \text{ mV vs. SCE}$ (reversible).

Oxidations at $\nu = 100 \text{ mV/s}$: $E_{\text{pa}} = 965 \text{ mV vs. SCE}$ (irreversible), $E_{\text{pa}} = 1.25 \text{ V vs. SCE}$ (irreversible).

4.3.20 Synthesis of $[\text{Cu}_2(\text{L-N}_{4t}\text{Bu}_2)_2(\text{SQ-SQ})](\text{BF}_4)_2 \cdot \text{Et}_2\text{O}$ (**5a**)



Under an atmosphere of pure nitrogen, $\text{CuCl}_2 \cdot 2 \text{ H}_2\text{O}$ (86 mg, 0.50 mmol) was mixed with $\text{L-N}_{4t}\text{Bu}_2$ (176 mg, 0.50 mmol) in methanol (20 mL) and refluxed for 15 minutes to obtain a green solution. To this green solution, solid 3,3',4,4'-tetrahydroxybiphenyl (54.5 mg, 0.25 mmol) was added. Then solid sodium hydroxide (40 mg, 1 mmol) was added to the reaction mixture to afford a greenish brown solution which was refluxed for further 15 minutes. After cooling down to room temperature, solid ferrocenium tetrafluoroborate (136 mg, 0.50 mmol) was added to the greenish brown solution to obtain a dark green solution. Then, the solvent was removed under vacuum. The resulting residue was redissolved in acetonitrile (25 mL) and filtered through celite. Slow diffusion of diethyl ether into the filtrate yielded yellow-green crystals. Recrystallization of the crystals from $\text{MeCN/Et}_2\text{O}$ afforded yellow-green crystals of $[\text{Cu}_2(\text{L-N}_{4t}\text{Bu}_2)_2(\text{SQ-SQ})](\text{BF}_4)_2 \cdot \text{Et}_2\text{O}$ (**5a**).

MW ($\text{C}_{60}\text{H}_{80}\text{B}_2\text{Cu}_2\text{F}_8\text{N}_8\text{O}_5$) = 1294.03 g/mol

Yield = 43 % (141 mg, 0.108 mmol)

Characterization:

Elemental analysis: (Calculated for $\text{C}_{60}\text{H}_{80}\text{B}_2\text{Cu}_2\text{F}_8\text{N}_8\text{O}_5$)

Calculated: C = 55.69 %, H = 6.23 %, N = 8.66 %

Found: C = 55.71 %, H = 6.42 %, N = 8.25 %

X-ray crystal structure analysis: $\text{Cu}^{\text{II}}-(\text{SQ-SQ})_{\text{CS}}-\text{Cu}^{\text{II}}$ at 150 K.

SQUID: $J = -4.634 \text{ cm}^{-1}$

ATR (RT): $\nu = 3085, 3052, 2971, 2920, 2895, 2855, 1603, 1583, 1502, 1479, 1466, 1438, 1426, 1401, 1384, 1376, 1370, 1348, 1284, 1254, 1230, 1195, 1174, 1165, 1089, 1046, 1032, 997, 974, 966, 938, 901, 884, 850, 836, 823, 803, 791, 778, 771, 751, 711 \text{ cm}^{-1}$.

IR (KBr pellet, RT): $\nu = 3083, 3049, 2971, 2920, 2895, 2853, 1603, 1579, 1505, 1463, 1437, 1400, 1387, 1374, 1365, 1349, 1288, 1251, 1223, 1195, 1166, 1057, 1034, 938, 923, 884, 850, 827, 791, 775, 751, 711, 687, 680, 646, 587, 575, 537, 519, 505, 479, 467, 456, 434, 424, 411, 404 \text{ cm}^{-1}$.

UV/Vis/NIR (MeCN, RT): $\lambda_{\text{max}} (\epsilon) = 709 (23300), 508 (13600), 471 (15500), 330 (7700), 310 (12200), 294 \text{ nm} (14000 \text{ M}^{-1} \text{ cm}^{-1})$.

Cyclic voltammetry:

Reductions at $\nu = 100 \text{ mV/s}$: $E_{1/2} = 45 \text{ mV vs. SCE (reversible)}$, $E_{1/2} = -450 \text{ mV vs. SCE (reversible)}$.

Oxidation at $\nu = 100 \text{ mV/s}$: $E_{\text{pa}} = 1.08 \text{ V vs. SCE (irreversible)}$.

4.3.21 Synthesis of $[\text{Zn}_2(\text{L-N}_4\text{tBu}_2)_2(\text{SQ-SQ})](\text{BPh}_4)_2 \cdot 4 \text{ DMF}$ (**6b**)



Under an atmosphere of pure nitrogen, ZnCl_2 (136 mg, 1 mmol) was mixed with $\text{L-N}_4\text{tBu}_2$ (352 mg, 1 mmol) in methanol (25 mL) and refluxed for 15 minutes to obtain a colorless solution. To this colorless solution, solid 3,3',4,4'-tetrahydroxybiphenyl (109 mg, 0.50 mmol) was added. Then, after addition of triethylamine (280 μL , 2 mmol), the reaction mixture was refluxed for further 15 minutes. After cooling down to room temperature, solid ferrocenium tetrafluoroborate (272 mg, 1 mmol) was added to the colorless solution to obtain a dark green solution. Then solid sodium tetraphenylborate

(342 mg, 1 mmol) was added to the dark green solution to produce a dark green precipitate. The precipitate was collected by filtration and washed with diethyl ether (20 mL). Slow diffusion of diethyl ether into the solution of the solid in acetonitrile (30 mL) afforded crystalline compound which was dissolved in DMF (60 mL) and slow diffusion of diethyl ether into this solution yielded dark green crystals of $[\text{Zn}_2(\text{L-N}_4t\text{Bu}_2)_2(\text{SQ-SQ})](\text{BPh}_4)_2 \cdot 4 \text{ DMF}$ (**6b**).

MW ($\text{C}_{116}\text{H}_{138}\text{B}_2\text{N}_{12}\text{O}_8\text{Zn}_2$) = 1980.79 g/mol

Yield = 48 % (475 mg, 0.24 mmol)

Characterization:

Elemental analysis: (Calculated for $\text{C}_{116}\text{H}_{138}\text{B}_2\text{N}_{12}\text{O}_8\text{Zn}_2$)

Calculated: C = 70.34 %, H = 7.02 %, N = 8.49 %

Found: C = 70.27 %, H = 7.01 %, N = 8.22 %

X-ray crystal structure analysis: $\text{Zn}^{\text{II}}-(\text{SQ-SQ})_{\text{CS}}-\text{Zn}^{\text{II}}$ (temperature invariant)

SQUID = diamagnetic

^1H NMR (400 MHz, $[\text{D}_6]$ DMSO, RT): δ = 7.95–7.90 (m, 4H; *p*-Py-H), 7.41–7.37 (m, 8H; *m*-Py-H), 4.59 (br, 4H; CH_2), 3.55 (d, $^2J_{\text{HH}} = 15.6$ Hz, 6H; CH_2), 1.09 (br, 36H; *t*Bu), 6.78 (t, $^3J_{\text{HH}} = 7.2$ Hz, 8H; *p*-Ph-H, BPh_4^-), 6.91 (t, $^3J_{\text{HH}} = 7.2$ Hz, 16H; *m*-Ph-H, BPh_4^-), 7.19–7.15 ppm (m, 16H; *o*-Ph-H, BPh_4^-).

IR (KBr pellet, RT): ν = 3052, 3036, 3010, 2979, 2921, 2855, 1671, 1600, 1580, 1532, 1515, 1478, 1465, 1428, 1401, 1382, 1368, 1345, 1286, 1257, 1226, 1192, 1157, 1142, 1084, 1030, 935, 911, 898, 883, 844, 829, 790, 779, 742, 733, 659, 625, 611, 579, 567, 515, 445, 424, 410, 401 cm^{-1} .

UV/Vis/NIR (MeCN, RT) = 671 (24300), 495 (13400), 455 (16300), 322 (7340), 300 nm ($11000 \text{ M}^{-1} \text{ cm}^{-1}$).

ESI-MS (MeCN): m/z = Calculated for $[\text{Zn}_2(\text{L-N}_4\text{tBu}_2)_2(\text{SQ-SQ})]^{2+}$: 525.20; Found 525.20.

Cyclic voltammetry:

Reductions at $\nu = 100$ mV/s: $E_{1/2} = -120$ mV vs. SCE (quasi-reversible), $E_{1/2} = -526$ mV vs. SCE (quasi-reversible).

Oxidations at $\nu = 100$ mV/s: $E_{\text{pa}} = 1.05$ V vs. SCE (irreversible), $E_{\text{pa}} = 1.35$ V vs. SCE (irreversible).

4.3.22 Synthesis of $[\text{Zn}_2(\text{L-N}_4\text{tBu}_2)_2(\text{SQ-SQ})](\text{BPh}_4)_2$ (**6a**)

The compound **6b** was grinded and dried in high vacuum at 100 °C for 8 h to obtain an analytically pure compound of $[\text{Zn}_2(\text{L-N}_4\text{tBu}_2)_2(\text{SQ-SQ})](\text{BPh}_4)_2$ (**6a**). The absence of solvent molecules in the obtained compound was confirmed by NMR spectroscopy.

MW ($\text{C}_{104}\text{H}_{110}\text{B}_2\text{N}_8\text{O}_4\text{Zn}_2$) = 1688.42 g/mol

Characterization:

Elemental analysis: (Calculated for $\text{C}_{104}\text{H}_{110}\text{B}_2\text{N}_8\text{O}_4\text{Zn}_2$)

Calculated: C = 73.98 %, H = 6.57 %, N = 6.64 %

Found: C = 73.68 %, H = 6.59 %, N = 6.58 %

^1H NMR (400 MHz, $[\text{D}_3]\text{MeCN}$, RT): $\delta = 7.82$ (t, $^3J_{\text{HH}} = 7.8$ Hz, 2H; *p*-Py-H), 7.80 (t, $^3J_{\text{HH}} = 7.7$ Hz, 2H; *p*-Py-H), 7.27–7.23 (m, 8H; *m*-Py-H), 4.58 (d, $^2J_{\text{HH}} = 16.4$ Hz, 8H; CH_2), 3.52 (d, $^2J_{\text{HH}} = 16.4$ Hz, 4H; CH_2), 3.51 (d, $^2J_{\text{HH}} = 16.8$ Hz, 4H; CH_2), 1.14 (s, 36H; *t*Bu), 6.83 (t, $^3J_{\text{HH}} = 7.2$ Hz, 8H; *p*-Ph-H, BPh_4^-), 6.98 (t, $^3J_{\text{HH}} = 7.5$ Hz, 16H; *m*-Ph-H, BPh_4^-), 7.29–7.25 ppm (m, 16H; *o*-Ph-H, BPh_4^-).

5 References

- [1] O. Kahn, C. Jay Martinez, *Science* **1998**, 279, 44–48.
- [2] J.-F. Letard, P. Guionneau, L. Goux-Capes, *Top. Curr. Chem.* **2004**, 235, 221–249.
- [3] C. Atmani, F. El Hajj, S. Benmansour, M. Marchivie, S. Triki, F. Conan, V. Patinec, H. Handel, G. Dupouy, C. J. Gómez-García, *Coord. Chem. Rev.* **2010**, 254, 1559–1569.
- [4] O. Sato, *Acc. Chem. Res.* **2003**, 36, 692–700.
- [5] Y.-L. Bai, J. Tao, R.-B. Huang, L.-S. Zheng, S.-L. Zheng, K. Oshida, Y. Einaga, *Chem. Commun.* **2008**, 1753–1755.
- [6] J. Olgún, S. Brooker, in *Spin-Crossover Materials: Properties and Applications* (Ed. M. A. Halcrow), J. Wiley And Sons, Inc., **2013**, pp. 77–113.
- [7] O. Kahn, J. Kröber, C. Jay, *Adv. Mater.* **1992**, 4, 718–728.
- [8] A. Dei, D. Gatteschi, C. Sangregorio, L. Sorace, *Acc. Chem. Res.* **2004**, 37, 827–835.
- [9] P. Gütlich, A. Hauser, H. Spiering, *Angew. Chem. Int. Ed.* **1994**, 33, 2024–2054.
- [10] P. Gütlich, H. A. Goodwin, *Top. Curr. Chem.* **2004**, 233, 01–47.
- [11] A. Hauser, *Top. Curr. Chem.* **2004**, 233, 49–58.
- [12] R. M. Buchanan, C. G. Pierpont, *J. Am. Chem. Soc.* **1980**, 102, 4951–4957.

- [13] D. A. Shultz, in *Magnetism: Molecules to Materials II: Molecule-Based Materials* (Eds. J. S. Miller, M. Drillon), Wiley-VCH **2001**, pp. 281–306.
- [14] C. G. Pierpont, *Coord. Chem. Rev.* **2001**, 216-217, 99–125.
- [15] D. N. Hendrickson, C. G. Pierpont, *Top. Curr. Chem.* **2004**, 234, 63–95.
- [16] Y. Morita, S. Suzuki, K. Sato, T. Takui, *Nat. Chem.* **2011**, 3, 197–204.
- [17] Z. Sun, Q. Ye, C. Chi, J. Wu, *Chem. Soc. Rev.* **2012**, 41, 7857–7889.
- [18] Z. Sun, J. Wu, *Pure Appl. Chem.* **2014**, 86, 529–537.
- [19] Z. Sun, Z. Zeng, J. Wu, *Acc. Chem. Res.* **2014**, 47, 2582–2591.
- [20] Z. Sun, K.-W. Huang, J. Wu, *J. Am. Chem. Soc.* **2011**, 133, 11896–11899.
- [21] D. Luo, S. Lee, B. Zheng, Z. Sun, W. Zeng, K.-W. Huang, K. Furukawa, D. Kim, R. D. Webster, J. Wu, *Chem. Sci.* **2014**, 5, 4944–4952.
- [22] Y. Su, X. Wang, X. Zheng, Z. Zhang, Y. Song, Y. Sui, Y. Li, X. Wang, *Angew. Chem. Int. Ed.* **2014**, 53, 2857–2861.
- [23] L. Cambi, L. Szegö, *Chem. Ber.* **1931**, 64, 2591–2598.
- [24] W. A. Baker, H. M. Bobonich, *Inorg. Chem.* **1964**, 3, 1184–1188.
- [25] P. E. Figgins, D. H. Busch, *J. Am. Chem. Soc.* **1960**, 82, 820–824.
- [26] R. C. Stoufer, D. H. Busch, W. B. Hadley, *J. Am. Chem. Soc.* **1961**, 83, 3732–3734.
- [27] R. Hogg, R. G. Wilkins, *J. Chem. Soc.* **1962**, 341–350.
- [28] Y. García, V. Niel, M. C. Muñoz, J. A. Real, *Top. Curr. Chem.* **2004**, 233, 229–257.

- [29] H. A. Goodwin, *Top. Curr. Chem.* **2004**, 233, 59–90.
- [30] M. Schmitz, M. Seibel, H. Kelm, S. Demeshko, F. Meyer, H.-J. Krüger, *Angew. Chem. Int. Ed.* **2014**, 53, 5988–5992.
- [31] H.-J. Krüger, *Coord. Chem. Rev.* **2009**, 253, 2450–2459.
- [32] S. Reh, *Synthese Und Charakterisierung von Cobalt(II)-, Eisen(II)- Und Eisen(III)-Komplexen Mit Interessanten Magnetischen Eigenschaften*, Ph. D. Dissertation, Technische Universität Kaiserslautern, **2013**.
- [33] M. Graf, *Untersuchungen Zu Spincrossover Und Valenztautomerie an Eisen (II)- Bzw. Kobalt (II)-Komplexen*, Ph. D. Dissertation, Technische Universität Kaiserslautern, **2009**.
- [34] P. Gütlich, A. B. Gaspar, Y. Garcia, *Beilstein J. Org. Chem.* **2013**, 9, 342–391.
- [35] K. S. Murray, in *Spin-Crossover Materials: Properties and Applications* (Ed. M. A. Halcrow), *John Wiley and Sons, Inc.*, **2013**, pp. 1–43.
- [36] J. Zarembowitch, *New. J. Chem.* **1992**, 16, 255.
- [37] I. A. Gass, S. Tewary, G. Rajaraman, M. Asadi, D. W. Lupton, B. Mobaraki, G. Chastanet, J.-F. Létard, K. S. Murray, *Inorg. Chem.* **2014**, 53, 5055–5066.
- [38] S. Hayami, Y. Komatsu, T. Shimizu, H. Kamihata, Y. H. Lee, *Coord. Chem. Rev.* **2011**, 255, 1981–1990.
- [39] D. H. Busch, in *Cobalt* (Ed. R.S. Young), *Chapter 6*, ACS Monograph Series, Reinhold Publ. Corp. New York, N. Y., **1960**.
- [40] E. S. Kucharski, W. R. McWhinnie, A. H. White, *Aust J Chem* **1978**, 31, 2647.

- [41] S. Hayami, D. Urakami, Y. Kojima, H. Yoshizaki, Y. Yamamoto, K. Kato, A. Fuyuhiko, S. Kawata, K. Inoue, *Inorg. Chem.* **2010**, *49*, 1428–1432.
- [42] S. Hayami, K. Hashiguchi, G. Juhász, M. Ohba, H. Ōkawa, Y. Maeda, K. Kato, K. Osaka, M. Takata, K. Inoue, *Inorg. Chem.* **2004**, *43*, 4124–4126.
- [43] S. Hayami, Y. Shigeyoshi, M. Akita, K. Inoue, K. Kato, K. Osaka, M. Takata, R. Kawajiri, T. Mitani, Y. Maeda, *Angew. Chem. Int. Ed.* **2005**, *44*, 4899–4903.
- [44] Y. Komatsu, K. Kato, Y. Yamamoto, H. Kamihata, Y. H. Lee, A. Fuyuhiko, S. Kawata, S. Hayami, *Eur. J. Inorg. Chem.* **2012**, 2769–2775.
- [45] S. Hayami, K. Murata, D. Urakami, Y. Kojima, M. Akita, K. Inoue, *Chem. Commun.* **2008**, 6510–6512.
- [46] A. B. Gaspar, M. C. Muñoz, V. Niel, J. A. Real, *Inorg. Chem.* **2001**, *40*, 9–10.
- [47] M. G. Cowan, J. Olguín, S. Narayanaswamy, J. L. Tallon, S. Brooker, *J. Am. Chem. Soc.* **2012**, *134*, 2892–2894.
- [48] J. Palion-Gazda, A. Świtlicka-Olszewska, B. Machura, T. Grancha, E. Pardo, F. Lloret, M. Julve, *Inorg. Chem.* **2014**, *53*, 10009–10011.
- [49] S.-Q. Wu, Y.-T. Wang, A.-L. Cui, H.-Z. Kou, *Inorg. Chem.* **2014**, *53*, 2613–2618.
- [50] J. Zarembowitch, O. Kahn, *Inorg. Chem.* **1984**, *23*, 589–593.
- [51] J. Zarembowitch, R. Claude, O. Kahn, *Inorg. Chem.* **1985**, *24*, 1576–1580.
- [52] P. Thuéry, J. Zarembowitch, *Inorg. Chem.* **1986**, *25*, 2001–2008.

- [53] I. Krivokapic, M. Zerara, M. L. Daku, A. Vargas, C. Enachescu, C. Ambrus, P. Tregenna-Piggott, N. Amstutz, E. Krausz, A. Hauser, *Coord. Chem. Rev.* **2007**, *251*, 364–378.
- [54] H. A. Goodwin, *Top. Curr. Chem.* **2004**, *234*, 23–47.
- [55] M. Graf, G. Wolmershäuser, H. Kelm, S. Demeschko, F. Meyer, H.-J. Krüger, *Angew. Chem. Int. Ed.* **2010**, *49*, 950–953.
- [56] Y. Tanabe, S. Sugano, *J. Phys. Soc. Japan* **1954**, *9*, 766.
- [57] S. Sugano, Y. Tanabe, H. Kamimura, *Pure and Applied Physics: A Series of Monographs and Textbooks*, **1970**, V. 33.
- [58] R. Clérac, F. A. Cotton, K. R. Dunbar, T. Lu, C. A. Murillo, X. Wang, *J. Am. Chem. Soc.* **2000**, *122*, 2272–2278.
- [59] E. König, G. Ritter, S. K. Kulshreshtha, *Chem. Rev.* **1985**, *85*, 219–234.
- [60] E. König, *Prog. Inorg. Chem.* **1987**, *35*, 527.
- [61] A. Bayri, A. R. Bahadır, F. M. Avcu, Ö. Aytakin, *Transit. Met. Chem.* **2005**, *30*, 987–991.
- [62] F. Lloret, M. Julve, J. Cano, R. Ruiz-García, E. Pardo, *Inorg. Chim. Acta* **2008**, *361*, 3432–3445.
- [63] C. Benelli, A. Dei, D. Gatteschi, L. Pardi, *Inorg. Chem.* **1989**, *28*, 1476–1480.
- [64] A. E. Tschitschibabin, *Chem. Ber.* **1907**, *40*, 1810–1819.
- [65] G. A. Abakumov, V. K. Cherkasov, V. I. Nevodchikov, V. A. Kuropatov, B. C. Noll, C. G. Pierpont, *Inorg. Chem.* **1998**, *37*, 6117–6119.
- [66] P. Gutlich, A. Dei, *Angew. Chem. Int. Ed.* **1997**, *36*, 2734–2736.

- [67] O.-S. Jung, D. H. Jo, Y.-A. Lee, B. J. Conklin, C. G. Pierpont, *Inorg. Chem.* **1997**, *36*, 19–24.
- [68] A. S. Attia, O.-S. Jung, C. G. Pierpont, *Inorg. Chim. Acta* **1994**, *226*, 91–98.
- [69] A. Caneschi, A. Cornia, A. Dei, *Inorg. Chem.* **1998**, *37*, 3419–3421.
- [70] S. K. Larsen, C. G. Pierpont, *J. Am. Chem. Soc.* **1988**, *110*, 1827–1832.
- [71] D. M. Adams, D. N. Hendrickson, *J. Am. Chem. Soc.* **1996**, *118*, 11515–11528.
- [72] D. M. Adams, A. Dei, A. L. Rheingold, D. N. Hendrickson, *Angew. Chem. Int. Ed.* **1993**, *32*, 880–882.
- [73] O. Cador, F. Chabre, A. Dei, C. Sangregorio, J. Van Slageren, M. G. F. Vaz, *Inorg. Chem.* **2003**, *42*, 6432–6440.
- [74] A. Caneschi, A. Dei, F. F. de Biani, P. Gütlich, V. Ksenofontov, G. Levchenko, A. Hofer, F. Renz, *Chem. Eur. J.* **2001**, *7*, 3926–3930.
- [75] A. Witt, F. W. Heinemann, S. Sproules, M. M. Khusniyarov, *Chem. Eur. J.* **2014**, *20*, 11149–11162.
- [76] A. Dei, A. Feis, G. Poneti, L. Sorace, *Inorg. Chim. Acta* **2008**, *361*, 3842–3846.
- [77] A. Beni, A. Dei, S. Laschi, M. Rizzitano, L. Sorace, *Chem. Eur. J.* **2008**, *14*, 1804–1813.
- [78] P. Dapporto, A. Dei, G. Poneti, L. Sorace, *Chem. Eur. J.* **2008**, *14*, 10915–10918.
- [79] O. Sato, J. Tao, Y.-Z. Zhang, *Angew. Chem. Int. Ed.* **2007**, *46*, 2152–2187.

- [80] G. Poneti, M. Mannini, L. Sorace, P. Sainctavit, M.-A. Arrio, A. Rogalev, F. Wilhelm, A. Dei, *Chem Phys Chem* **2009**, *10*, 2090–2095.
- [81] K. G. Alley, G. Poneti, P. S. D. Robinson, A. Nafady, B. Moubaraki, J. B. Aitken, S. C. Drew, C. Ritchie, B. F. Abrahams, R. K. Hocking, K. S. Murray, A. M. Bond, H. H. Harris, L. Sorace, C. Boskovic, *J. Am. Chem. Soc.* **2013**, *135*, 8304–8323.
- [82] C. Carbonera, A. Dei, J.-F. Létard, C. Sangregorio, L. Sorace, *Angew. Chem. Int. Ed.* **2004**, *43*, 3136–3138.
- [83] N. G. R. Hearn, J. L. Korčok, M. M. Paquette, K. E. Preuss, *Inorg. Chem.* **2006**, *45*, 8817–8819.
- [84] E. Evangelio, C. Rodriguez-Blanco, Y. Coppel, D. N. Hendrickson, J. P. Sutter, J. Campo, D. Ruiz-Molina, *Solid State Sci.* **2009**, *11*, 793–800.
- [85] A. Bencini, A. Caneschi, C. Carbonera, A. Dei, D. Gatteschi, R. Righini, C. Sangregorio, J. Van Slageren, *J. Mol. Struct.* **2003**, *656*, 141–154.
- [86] G. Poneti, M. Mannini, B. Cortigiani, L. Poggini, L. Sorace, E. Otero, P. Sainctavit, R. Sessoli, A. Dei, *Inorg. Chem.* **2013**, *52*, 11798–11805.
- [87] D. M. Adams, A. Dei, A. L. Rheingold, D. N. Hendrickson, *J. Am. Chem. Soc.* **1993**, *115*, 8221–8229.
- [88] A. S. Attia, C. G. Pierpont, *Inorg. Chem.* **1997**, *36*, 6184–6187.
- [89] I. Ratera, D. Ruiz-Molina, F. Renz, J. Ensling, K. Wurst, C. Rovira, P. Gülich, J. Veciana, *J. Am. Chem. Soc.* **2003**, *125*, 1462–1463.
- [90] Y. Shimazaki, F. Tani, K. Fukui, Y. Naruta, O. Yamauchi, *J. Am. Chem. Soc.* **2003**, *125*, 10512–10513.
- [91] G. A. Abakumov, G. A. Razuvaev, V. I. Nevodchikov, V. K. Cherkasov, *J. Organomet. Chem.* **1988**, *341*, 485–494.

- [92] F. Rupp, K. Chevalier, M. Graf, M. Schmitz, H. Kelm, A. Grün, M. Zimmer, M. Gerhards, C. van Wüllen, H.-J. Krüger, R. Diller, *Chem. Eur. J.* **2017**, *23*, 2119–2132.
- [93] A. B. P. Lever, *Inorganic Electronic Spectroscopy*, Elsevier, Amsterdam, **1984**.
- [94] C. Benelli, A. Dei, D. Gatteschi, L. Pardi, *Inorg. Chim. Acta* **1989**, *163*, 99–104.
- [95] A. Caneschi, A. Dei, D. Gatteschi, V. Tangoulis, *Inorg. Chem.* **2002**, *41*, 3508–3512.
- [96] C. Benelli, A. Dei, D. Gatteschi, L. Pardi, *Inorg. Chem.* **1988**, *27*, 2831–2836.
- [97] P. A. Wicklund, D. G. Brown, *Inorg. Chem.* **1976**, *15*, 396–400.
- [98] M.-A. Haga, E. S. Dodsworth, A. B. P. Lever, *Inorg. Chem.* **1986**, *25*, 447–453.
- [99] M. W. Lynch, M. Valentine, D. N. Hendrickson, *J. Am. Chem. Soc.* **1982**, *104*, 6982–6989.
- [100] F. Rupp, K. Chevalier, M. M. N. Wolf, H.-J. Krüger, C. van Wüllen, Y. Nosenko, G. Niedner-Schatteburg, C. Riehn, R. Diller, *EPJ Web Conf.* **2013**, *41*, 05045.
- [101] C. G. Pierpont, O.-S. Jung, *Inorg. Chem.* **1995**, *34*, 4281–4283.
- [102] O.-S. Jung, D. H. Jo, Y.-A. Lee, Y. S. Sohn, C. G. Pierpont, *Inorg. Chem.* **1998**, *37*, 5875–5880.
- [103] C. Lambert, *Angew. Chem. Int. Ed.* **2011**, *50*, 1756–1758.
- [104] Z. Sun, J. Wu, *J. Mater. Chem.* **2012**, *22*, 4151–4160.

- [105] A. Shimizu, M. Uruichi, K. Yakushi, H. Matsuzaki, H. Okamoto, M. Nakano, Y. Hirao, K. Matsumoto, H. Kurata, T. Kubo, *Angew. Chem. Int. Ed.* **2009**, *48*, 5482–5486.
- [106] M. Abe, *Chem. Rev.* **2013**, *113*, 7011–7088.
- [107] L. Salem, C. Rowland, *Angew. Chem. Int. Ed.* **1972**, *11*, 92–111.
- [108] F. Breher, *Coord. Chem. Rev.* **2007**, *251*, 1007–1043.
- [109] M. Abe, J. Ye, M. Mishima, *Chem. Soc. Rev.* **2012**, *41*, 3808.
- [110] A. Konishi, Y. Hirao, M. Nakano, A. Shimizu, E. Botek, B. Champagne, D. Shiomi, K. Sato, T. Takui, K. Matsumoto, H. Kurata, T. Kubo, *J. Am. Chem. Soc.* **2010**, *132*, 11021–11023.
- [111] E. Clar, *The Aromatic Sextet*, Wiley, London, **1972**.
- [112] S. Das, J. Wu, in *Polycyclic Arenes and Heteroarenes*, Wiley-VCH, **2015**, pp. 1–36.
- [113] Y. Kobayashi, K. Shima, K. Mutoh, J. Abe, *J. Phys. Chem. Lett.* **2016**, *7*, 3067–3072.
- [114] M.-D. Li, P. J. Hanway, T. R. Albright, A. H. Winter, D. L. Phillips, *J. Am. Chem. Soc.* **2014**, *136*, 12364–12370.
- [115] Z. Zeng, Y. M. Sung, N. Bao, D. Tan, R. Lee, J. L. Zafra, B. S. Lee, M. Ishida, J. Ding, J. T. López Navarrete, Y. Li, W. Zeng, D. Kim, K.-W. Huang, R. D. Webster, J. Casado, J. Wu, *J. Am. Chem. Soc.* **2012**, *134*, 14513–14525.
- [116] R. I. Shrager, R. W. Handler, *Anal. Chem.* **1982**, *54*, 1147–1152.
- [117] R. I. Shrager, *Siam J. Alg. Disc. Meth.* **1984**, *5*, 351–358.
- [118] R. I. Shrager, *Chemom. Intell. Lab. Syst.* **1986**, *1*, 59–70.

- [119] R. W. Hendler, R. I. Schragar, *J. Biochem. Biophys. Methods* **1994**, *28*, 1–33.
- [120] A. L. Galo, M. F. Colombo, *J. Spectrosc.* **2013**, *Article ID*, 7.
- [121] K. D. Vandegriff, R. I. Shragar, *Methods Enzymol.* **1994**, *232*, 460–485.
- [122] J. R. Khusnutdinova, J. Luo, N. P. Rath, L. M. Mirica, *Inorg. Chem.* **2013**, *52*, 3920–3932.
- [123] S. P. Meneghetti, P. J. Lutz, J. Fischer, J. Kress, *Polyhedron* **2001**, *20*, 2705–2710.
- [124] L. Horner, K.-H. Weber, *Chem. Ber.* **1963**, *96*, 1568–1578.
- [125] R. Carlin, *Magnetochemistry*, Springer-Verlag, Berlin, **1985**.
- [126] O. Kahn, *Molecular Magnetism*, Wiley-VCH, New York, **1993**.
- [127] D. F. Evans, *J. Chem. Soc.* **1959**, 2003–2005.
- [128] E. M. Schubert, *J. Chem. Educ.* **1992**, *69*, 62.
- [129] S. E. McLain, A. K. Soper, A. Luzar, *J. Chem. Phys.* **2006**, *124*, 074502.
- [130] R. J. Myers, W. D. Gwinn, *J. Chem. Phys.* **1952**, *20*, 1420.
- [131] “Infrared spectral data from the Bio-Rad/Sadtler (IR data collection was obtained from Bio-Rad Laboratories, Philadelphia, PA (US))”.
- [132] “Integrated spectral database system of organic compounds (data were obtained from the National Institute of Advanced Industrial Science and Technology (Japan)),” **2016**.
- [133] M. D. Stallings, M. M. Morrison, D. T. Sawyer, *Inorg. Chem.* **1981**, *20*, 2655–2660.
- [134] S. A. Rackley, R. J. Butcher, M. Römheld, S. M. Freund, T. Oka, *J. Mol. Spectrosc.* **1982**, *92*, 203–217.

- [135] A. Dei, *Inorg. Chem.* **1993**, *32*, 5730–5733.
- [136] N. Shiratori, H. Takahashi, K. Higashi, *Bull. Chem. Soc. Jpn.* **1975**, *48*, 1423–1426.
- [137] E. Evangelio, D. Ruiz-Molina, *Eur. J. Inorg. Chem.* **2005**, 2957–2971.
- [138] The single crystal X-ray diffraction data were collected at least two times. However, a single crystal was always not obtained by the described method. The data is discussed on the basis of the fact that this particular crystal structure exists.
- [139] Y. Mulyana, K. G. Alley, K. M. Davies, B. F. Abrahams, B. Moubaraki, K. S. Murray, C. Boskovic, *Dalt. Trans.* **2014**, *43*, 2499–2511.
- [140] K. Lancaster, *Intramolecular Electron Transfer in Mixed-Valence Triarylamines*, Ph. D. Dissertation, Georgia Institute of Technology, **2009**.
- [141] K. Lancaster, S. A. Odom, S. C. Jones, S. Thayumanavan, S. R. Marder, J.-L. Bredas, V. Coropceanu, S. Barlow, *J. Am. Chem. Soc.* **2009**, *131*, 1717–1723.
- [142] A. Bencini, C. A. Daul, A. Dei, F. Mariotti, H. Lee, D. A. Shultz, L. Sorace, *Inorg. Chem.* **2001**, *40*, 1582–1590.
- [143] Á. Altomare, M. C. Burla, M. Camalli, G. L. Cascarano, C. Giacovazzo, A. Guagliardi, A. G. G. Moliterini, G. Polidori, R. Spagna, *J. Applied Crystallogr.* **1999**, *32*, 115–119.
- [144] G. M. Sheldrick, *Acta Crystallogr. Sect. A* **2008**, *64*, 112–122.
- [145] “https://www.engineeringtoolbox.com/volumetric-temperature-expansion-d_315.html,”.
- [146] S. Stoll, A. Schweiger, *J. Magn. Reson.* **2006**, *178*, 42–55.

- [147] H.-J. Krüger, 2,11-diaza[3.3](2,6)pyridinophane - *A Unique Class of Ligands*, Habilitationsschrift, Universität Hamburg, **1997**.
- [148] T. M. El Dine, J. Rouden, J. Blanchet, *Chem. Commun.* **2015**, *51*, 16084–16087.
- [149] A. Hofer, G. Kovacs, A. Zappatini, M. Leuenberger, M. A. Hediger, M. Lochner, *Bioorganic Med. Chem.* **2013**, *21*, 3202–3213.
- [150] R. Willstätter, H. E. Müller, *Chem. Ber.* **1911**, *44*, 2182–2191.
- [151] J. J. Li, M. B. Norton, E. J. Reinhard, G. D. Anderson, S. A. Gregory, P. C. Isakson, C. M. Koboldt, J. L. Masferrer, W. E. Perkins, K. Seibert, Y. Zhang, B. S. Zweifel, D. B. Reitz, *J. Med. Chem.* **1996**, *39*, 1846–1856.
- [152] Herein, the firm establishment of the described synthetic procedure for the salt Na[BPh₂(DCCat)] is not made because the ¹H NMR and IR spectra of the salt were recorded only once from one batch of sample. However, the complex **2d** was successfully prepared by the described method for the complex.
- [153] M. Iyoda, H. Otsuka, K. Sato, N. Nisato, M. Oda, *Bull. Chem. Soc. Jpn.* **1990**, *63*, 80–87.
- [154] L. F. Joulie, E. Schatz, M. D. Ward, F. Weber, L. J. Yellowlees, *J. Chem. Soc. Dalt. Trans.* **1994**, 799–804.
- [155] C. B. Stevens, J. M. Hanna, R. K. Lammi, *Bioorganic Med. Chem. Lett.* **2013**, *23*, 1703–1706.

6 Appendix

List of contents

6 Appendix.....	215
List and Abbreviations of Compounds.....	216
6.1 Valence Tautomerism in a Cobalt Dioxolene Complex.....	217
6.1.1 Crystal Data.....	217
6.1.2 Infrared Spectra.....	222
6.1.3 NMR Spectra.....	226
6.1.4 UV/Vis/NIR Spectra.....	231
6.1.5 Cyclic Voltammograms.....	267
6.2 Switching of Electronic States of Bis(dioxolene) Ligands Triggered by Cobalt(II) Based Temperature-Induced Spin- Crossover and Cobalt-Ligand Based Electron Transfer Processes.....	270
6.2.1 Crystal Data.....	270
6.2.2 Infrared Spectra.....	278
6.2.3 NMR Spectra.....	285
6.2.4 UV/Vis/NIR Spectra.....	288
6.2.5 Cyclic Voltammograms.....	302
6.3 Electronic States of Bis(dioxolene) Ligands and the Interactions Between Metal Ions in Nickel-, Copper- and Zinc- Bis(dioxolene) Complexes.....	307
6.3.1 Crystal Data.....	307
6.3.2 Infrared Spectra.....	313
6.3.3 UV/Vis/NIR Spectra.....	320
6.3.4 Cyclic Voltammograms.....	326

List and abbreviations of compounds

1	[Co(L-N ₄ tBu ₂)(DCCat)]
1a	[Co(L-N ₄ tBu ₂)(DCCat)]·3 MeCN·H ₂ O
1b	[Co(L-N ₄ tBu ₂)(DCCat)]·CH ₂ Cl ₂
2	[Co(L-N ₄ tBu ₂)(DCCat)] ⁺
2a	[Co(L-N ₄ tBu ₂)(DCCat)](BF ₄)
2b	[Co(L-N ₄ tBu ₂)(DCCat)](BPh ₄)
2c	[Co(L-N ₄ tBu ₂)(DCCat)](BPh ₄)·2 CH ₂ Cl ₂
2d	[Co(L-N ₄ tBu ₂)(DCCat)][BPh ₂ (DCCat)]
2e	[Co(L-N ₄ tBu ₂)(DCCat)](OTf)
3	[Co ₂ (L-N ₄ tBu ₂) ₂ (SQ-SQ)] ²⁺
3a	[Co ₂ (L-N ₄ tBu ₂) ₂ (SQ-SQ)](BPh ₄) ₂
3b	[Co ₂ (L-N ₄ tBu ₂) ₂ (SQ-SQ)](BPh ₄) ₂ ·4 DMF
3c	[Co ₂ (L-N ₄ tBu ₂) ₂ (Cat-SQ)](BF ₄) ₂
3d	[Co ₂ (L-N ₄ tBu ₂) ₂ (Cat-SQ)](BF ₄) ₂ ·Et ₂ O
3e	[Co ₂ (L-N ₄ tBu ₂) ₂ (Cat-SQ)](PF ₆) ₂
4	[Ni ₂ (L-N ₄ tBu ₂) ₂ (SQ-SQ)] ²⁺
4a	[Ni ₂ (L-N ₄ tBu ₂) ₂ (SQ-SQ)](BPh ₄) ₂ ·4 DMF
5	[Cu ₂ (L-N ₄ tBu ₂) ₂ (SQ-SQ)] ²⁺
5a	[Cu ₂ (L-N ₄ tBu ₂) ₂ (SQ-SQ)](BF ₄) ₂ ·Et ₂ O
6	[Zn ₂ (L-N ₄ tBu ₂) ₂ (SQ-SQ)] ²⁺
6a	[Zn ₂ (L-N ₄ tBu ₂) ₂ (SQ-SQ)](BPh ₄) ₂
6b	[Zn ₂ (L-N ₄ tBu ₂) ₂ (SQ-SQ)](BPh ₄) ₂ ·4 DMF
6^{•+}	[Zn ₂ (L-N ₄ tBu ₂) ₂ (Cat-SQ)] ⁺
7	[Zn(L-N ₄ tBu ₂)(-SQ-SQ)]

6.1 Valence Tautomerism in a Cobalt Dioxolene Complex

6.1.1 Crystal Data

Crystallographic data of compounds **1a** and **2c** were collected at 150(2) K, whereas for compound **2d**, the data were collected at 150(2) and 373(2) K. The data were collected by an Oxford Diffraction Gemini S Ultra type of instrument using graphite-monochromatized Cu- K_{α} ($\lambda = 1.54184 \text{ \AA}$) or Mo- K_{α} ($\lambda = 0.70173 \text{ \AA}$) radiation. The crystal structures were solved by direct methods implemented in the SIR 97 program package and refined using the full-matrix least-squares method on F^2 with SHELXL-97 package. The hydrogen atoms were located geometrically and refined using Riding model. As the temperature factor, 1.5 times value for hydrogen atoms of CH_3 groups and for all other hydrogen atoms 1.2 times value of the equivalent isotropic temperature factor of that atom used, to which the respective hydrogen atom is bonded. All non-hydrogen atoms were refined with anisotropic displacement parameters.

Table A.1: Crystal data and structure refinement for **1a** at 150 K.

Identification code	11240ocu
Empirical formula	C ₃₄ H ₄₅ Cl ₂ CoN ₇ O ₃
Formula weight [g mol ⁻¹]	729.60
Temperature [K]	150(2)
λ [Å]	1.54184
Crystal system	monoclinic
Space group	<i>P</i> 12 ₁ / <i>c</i> 1
<i>a</i> [Å]	9.8824(2)
<i>b</i> [Å]	17.9052(3)
<i>c</i> [Å]	20.4354(4)
α [deg]	90
β [deg]	93.959(2)
γ [deg]	90
<i>V</i> [Å ³]	3607.34(12)
<i>Z</i>	4
ρ_{calcd} [g cm ⁻³]	1.343
$\mu(\text{Cu-}K\alpha)$ [mm ⁻¹]	5.443
<i>F</i> (000)	1532
Crystal size [mm ³]	0.52 × 0.14 × 0.06
θ [deg]	3.29–62.63
Reflections collected	13489
Independent reflections	5768
<i>R</i> _{int}	0.0379
Absorption correction	semi-empirical from equivalents
Max. and min. transmission	0.7360 and 0.1641
Refinement method	full-matrix least-squares on <i>F</i> ²
Data/restraints/parameters	5768/2/439
GOOF on <i>F</i> ²	0.975
Final <i>R</i> indices [<i>I</i> > 2σ(<i>I</i>)]	<i>R</i> 1 = 0.0441, <i>wR</i> 2 = 0.1140
<i>R</i> indices (all data)	<i>R</i> 1 = 0.0562, <i>wR</i> 2 = 0.1205
Largest diff. peak and hole [e Å ⁻³]	0.574 and -0.522

Table A.2: Crystal data and structure refinement for **2c** at 150 K.

Identification code	13129ocu
Empirical formula	C ₅₄ H ₅₈ BCl ₆ CoN ₄ O ₂
Formula weight [g mol ⁻¹]	1077.48
Temperature [K]	150(2)
λ [Å]	1.54184
Crystal system	orthorhombic
Space group	<i>P</i> 2 ₁ 2 ₁ 2 ₁
<i>a</i> [Å]	11.4049(2)
<i>b</i> [Å]	18.0459(3)
<i>c</i> [Å]	25.3194(5)
α [deg]	90
β [deg]	90
γ [deg]	90
<i>V</i> [Å ³]	5211.03(16)
<i>Z</i>	4
ρ_{calcd} [g cm ⁻³]	1.373
$\mu(\text{Cu-}K_{\alpha})$ [mm ⁻¹]	5.763
<i>F</i> (000)	2240
Crystal size [mm ³]	0.49 × 0.18 × 0.18
θ [deg]	3.49–62.67
Reflections collected	21404
Independent reflections	8123
<i>R</i> _{int}	0.0384
Absorption correction	analytical
Max. and min. transmission	0.4236 and 0.1645
Refinement method	full-matrix least-squares on <i>F</i> ²
Data/restraints/parameters	8123/0/619
GOOF on <i>F</i> ²	1.029
Final <i>R</i> indices [<i>I</i> > 2σ(<i>I</i>)]	<i>R</i> 1 = 0.0412, <i>wR</i> 2 = 0.1046
<i>R</i> indices (all data)	<i>R</i> 1 = 0.0436, <i>wR</i> 2 = 0.1070
Largest diff. peak and hole [e Å ⁻³]	0.870 and -0.602

Table A.3: Crystal data and structure refinement for **2d** at 150 K.

Identification code	14088o.
Empirical formula	$C_{46}H_{46}BCl_4CoN_4O_4$
Formula weight [g mol ⁻¹]	930.41
Temperature [K]	150(2)
λ [Å]	0.71073
Crystal system	triclinic
Space group	$P\bar{1}$
a [Å]	11.5510(4)
b [Å]	13.3150(5)
c [Å]	14.7470(5)
α [deg]	91.152(3)
β [deg]	93.026(3)
γ [deg]	110.143(3)
V [Å ³]	2124.64(14)
Z	2
ρ_{calcd} [g cm ⁻³]	1.454
$\mu(\text{Mo-K}\alpha)$ [mm ⁻¹]	0.706
$F(000)$	964
Crystal size [mm ³]	0.310 × 0.200 × 0.090
θ [deg]	2.769–29.00
Reflections collected	21016
Independent reflections	11282
R_{int}	0.0307
Absorption correction	semi-empirical from equivalents
Max. and min. transmission	1.00000 and 0.92337
Refinement method	full-matrix least-squares on F^2
Data/restraints/parameters	11282/0/547
GOOF on F^2	1.018
Final R indices [$I > 2\sigma(I)$]	$R1 = 0.0411$, $wR2 = 0.0902$
R indices (all data)	$R1 = 0.0587$, $wR2 = 0.0998$
Largest diff. peak and hole [e Å ⁻³]	0.473 and -0.413

Table A.4: Crystal data and structure refinement for **2d** at 373 K.

Identification code	14091ocb
Empirical formula	$C_{46}H_{46}BCl_4CoN_4O_4$
Formula weight [g mol ⁻¹]	930.41
Temperature [K]	373(2)
λ [Å]	1.54184
Crystal system	triclinic
Space group	$P\bar{1}$
a [Å]	11.6723(5)
b [Å]	13.5082(6)
c [Å]	14.8708(4)
α [deg]	91.117(3)
β [deg]	92.960(3)
γ [deg]	110.006(4)
V [Å ³]	2198.55(16)
Z	2
ρ_{calcd} [g cm ⁻³]	1.405
$\mu(\text{Cu-}K\alpha)$ [mm ⁻¹]	5.683
$F(000)$	964
Crystal size [mm ³]	0.320 × 0.260 × 0.130
θ [deg]	3.485–62.581
Reflections collected	15075
Independent reflections	6984
R_{int}	0.0233
Absorption correction	analytical
Max. and min. transmission	0.530 and 0.208
Refinement method	full-matrix least-squares on F^2
Data/restraints/parameters	6984/0/547
GOOF on F^2	1.027
Final R indices [$I > 2\sigma(I)$]	$R1 = 0.0371$, $wR2 = 0.0945$
R indices (all data)	$R1 = 0.0431$, $wR2 = 0.0992$
Largest diff. peak and hole [e Å ⁻³]	0.186 and -0.329

6.1.2 Infrared Spectra

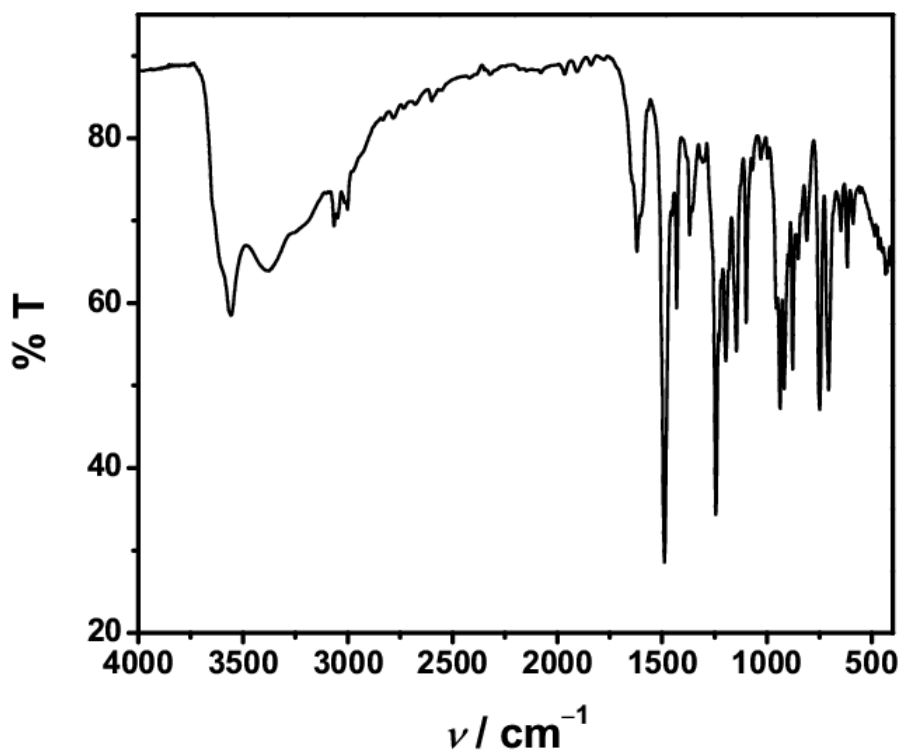


Figure A.1: IR spectrum of Na[BPh₂(DCCat)] in KBr pellet at RT.

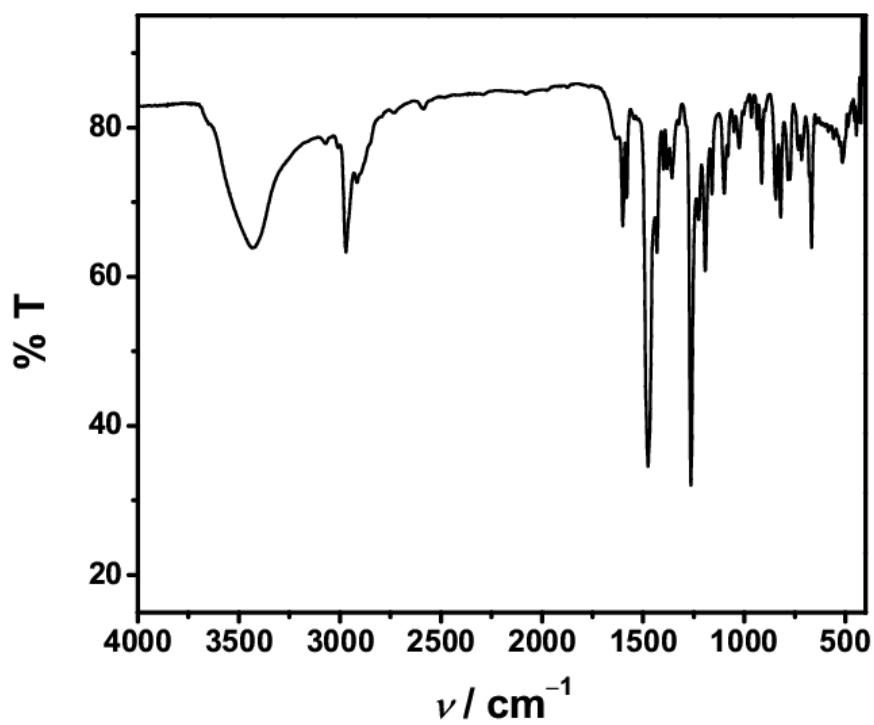


Figure A.2: IR spectrum of [Co(L-N₄tBu₂)(DCCat)] (1) in KBr pellet at RT.

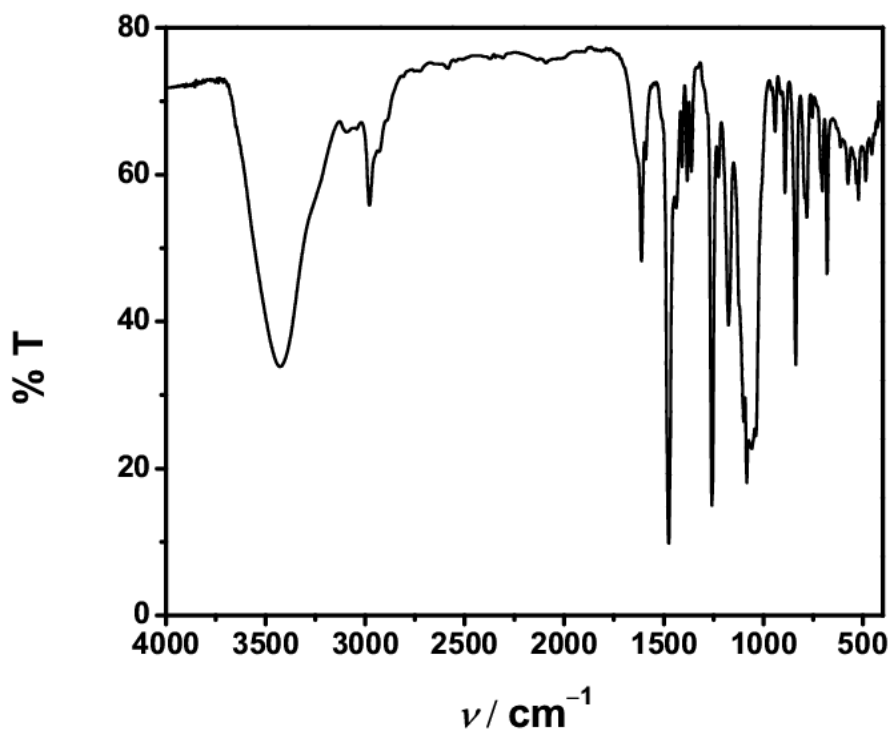


Figure A.3: IR spectrum of $[\text{Co}(\text{L-N}_{4t}\text{Bu}_2)(\text{DCCat})](\text{BF}_4)$ (**2a**) in KBr pellet at RT.

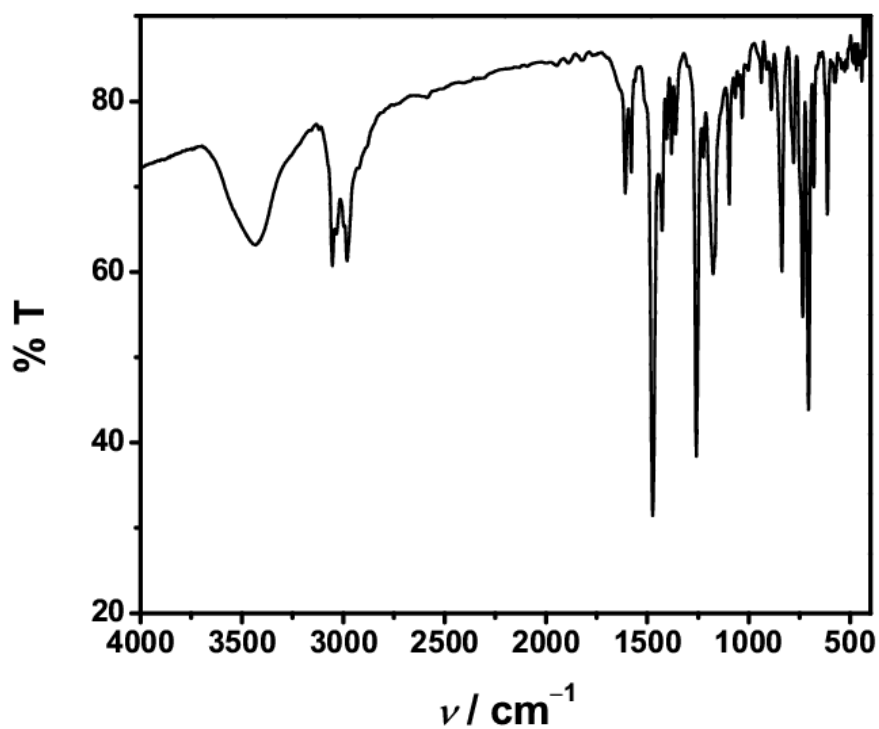


Figure A.4: IR spectrum of $[\text{Co}(\text{L-N}_{4t}\text{Bu}_2)(\text{DCCat})](\text{BPh}_4)$ (**2b**) in KBr pellet at RT.

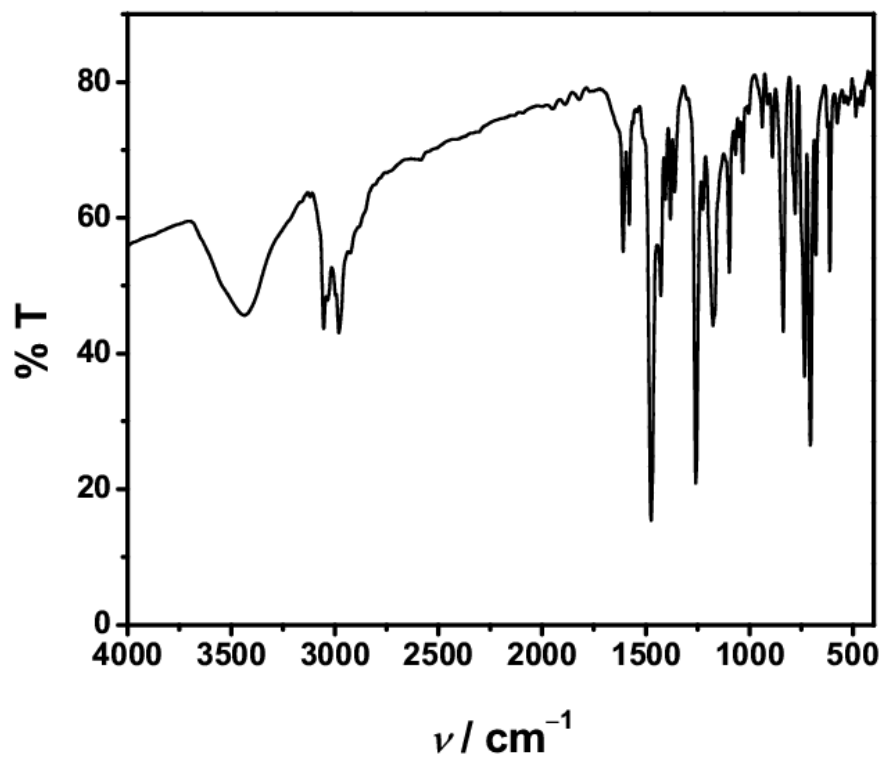


Figure A.5: IR spectrum $[\text{Co}(\text{L-N}_4\text{tBu}_2)(\text{DCCat})](\text{BPh}_4) \cdot 2 \text{CH}_2\text{Cl}_2$ (**2c**) in KBr pellet at RT.

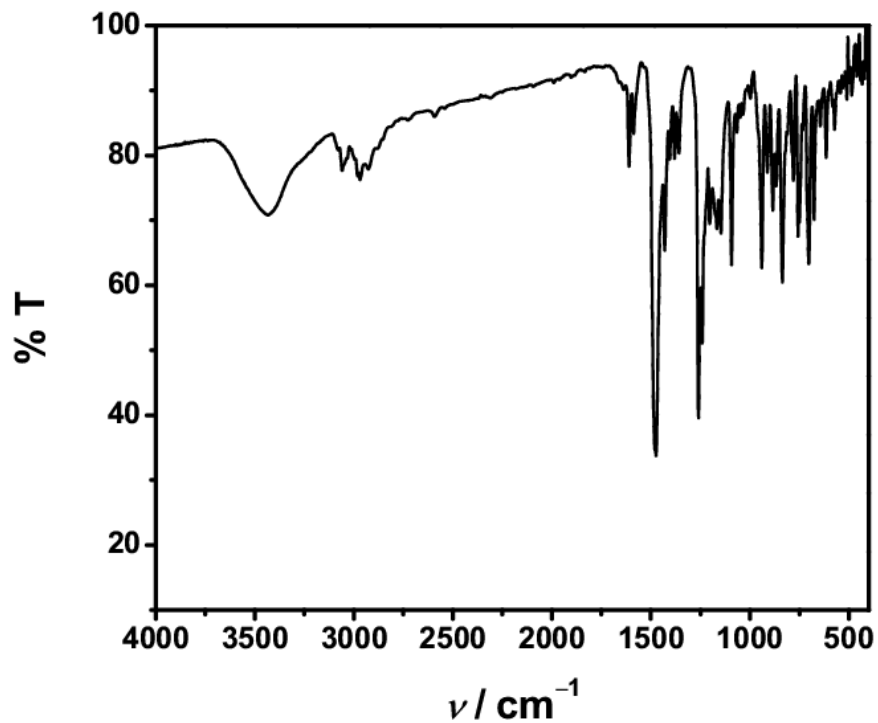


Figure A.6: IR spectrum $[\text{Co}(\text{L-N}_4\text{tBu}_2)(\text{DCCat})][\text{BPh}_2(\text{DCCat})]$ (**2d**) in KBr pellet at RT.

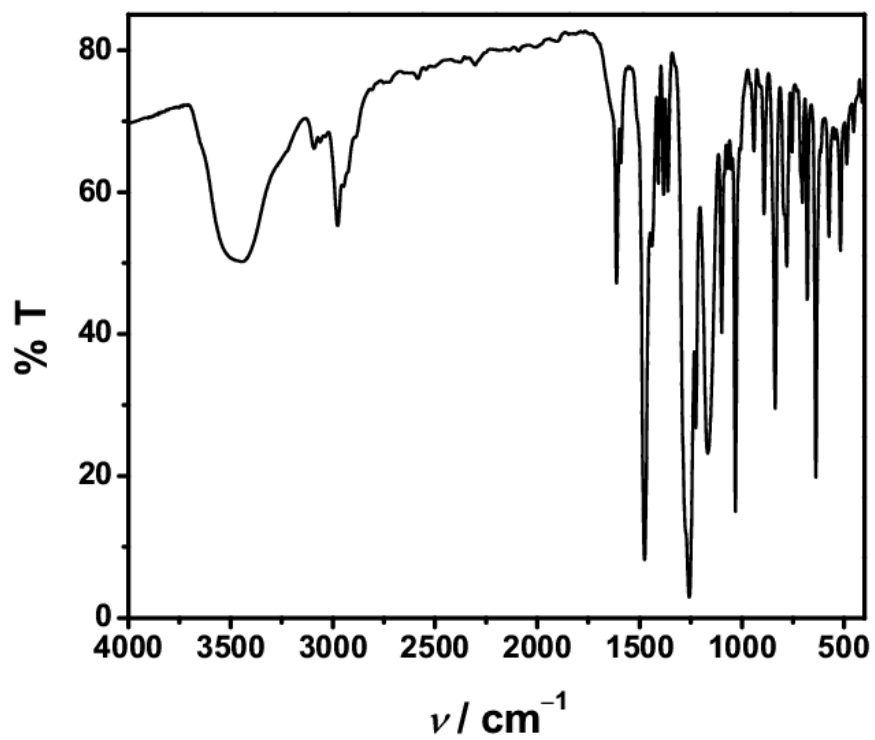


Figure A.7: IR spectrum $[\text{Co}(\text{L-N}_4\text{tBu}_2)(\text{DCCat})](\text{OTf})$ (**2e**) in KBr pellet at RT.

6.1.3 NMR Spectra

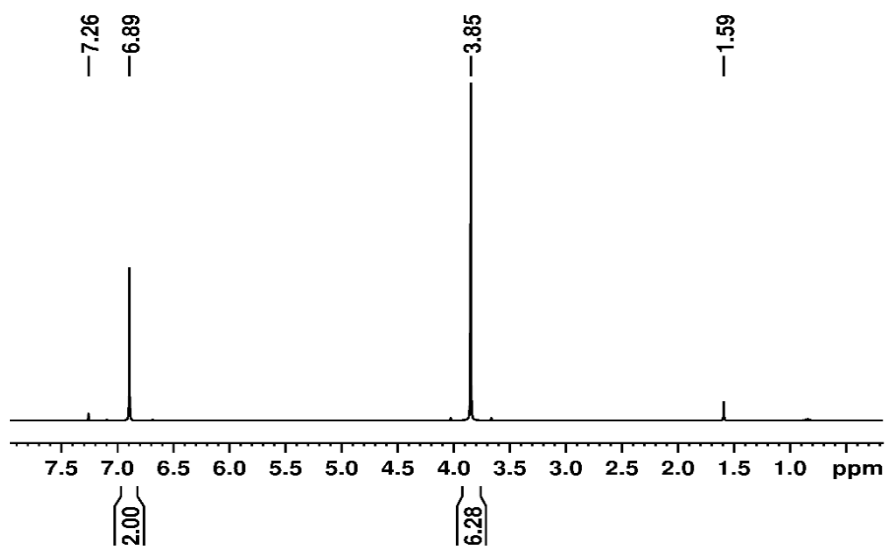


Figure A.8: ^1H NMR spectrum of 1,2-dichloro-4,5-dimethoxybenzene in $[\text{D}]\text{CHCl}_3$ at RT.

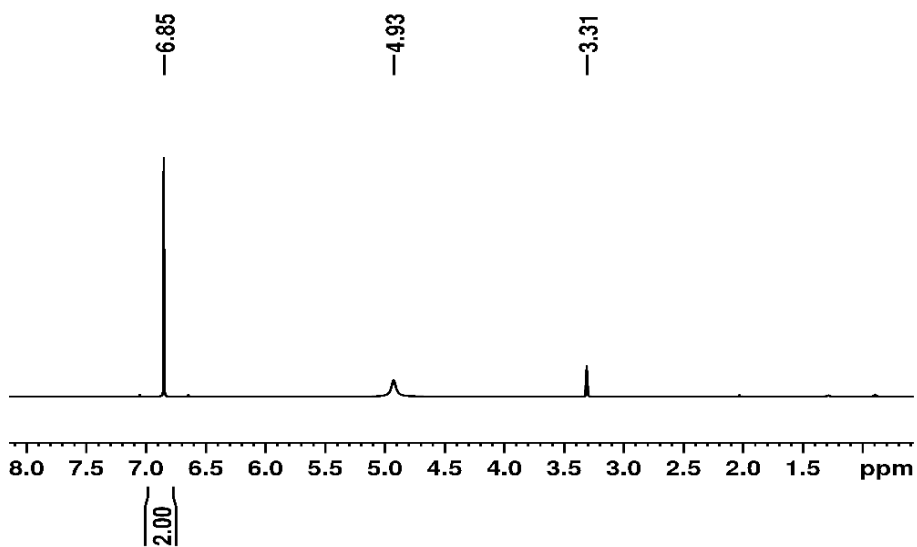


Figure A.9: ^1H NMR spectrum of 4,5-dichlorocatechol (H_2DCCat) in $[\text{D}_4]\text{MeOH}$ at RT.

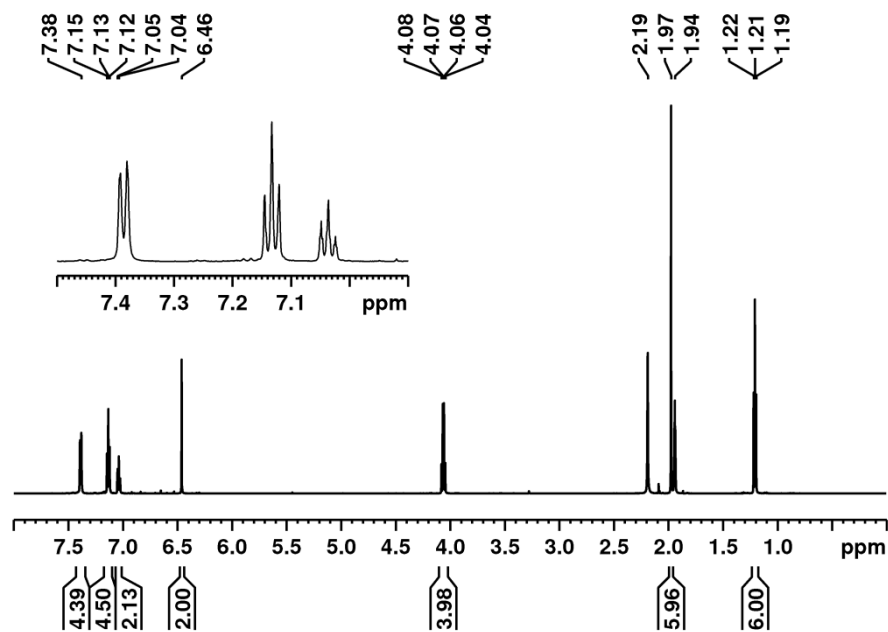


Figure A.10: ¹H NMR spectrum of Na[BPh₂(DCCat)] in [D₃]MeCN at RT.

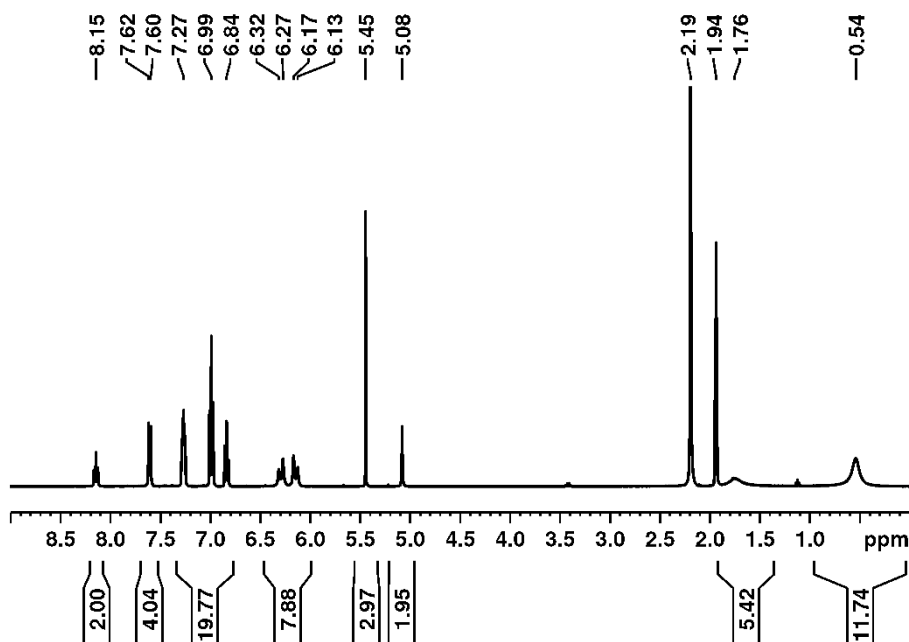


Figure A.11: ¹H NMR spectrum of **2c** in [D₃]MeCN at RT. The spectrum was recorded from the sample prepared for the magnetic moment measurement of the compound.

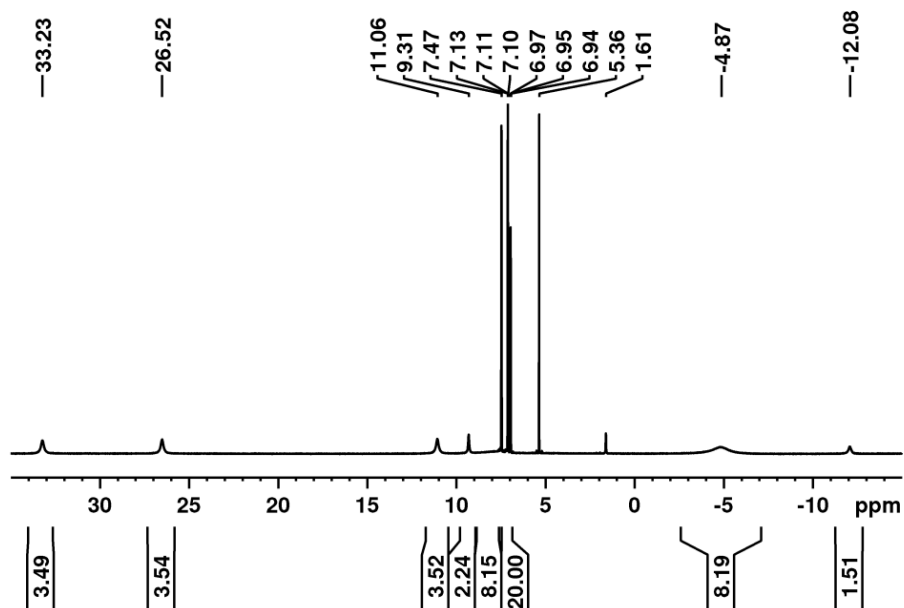


Figure A.12: ^1H NMR spectrum of **2b** in $[\text{D}_2]\text{DCM}$ at 295 K.

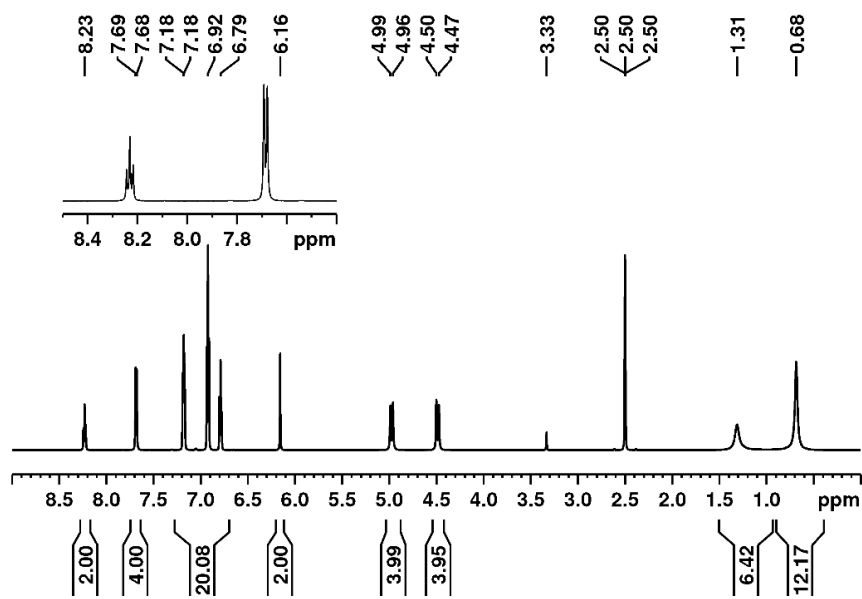


Figure A.13: ^1H NMR spectrum of **2b** in $[\text{D}_6]\text{DMSO}$ at 295 K.

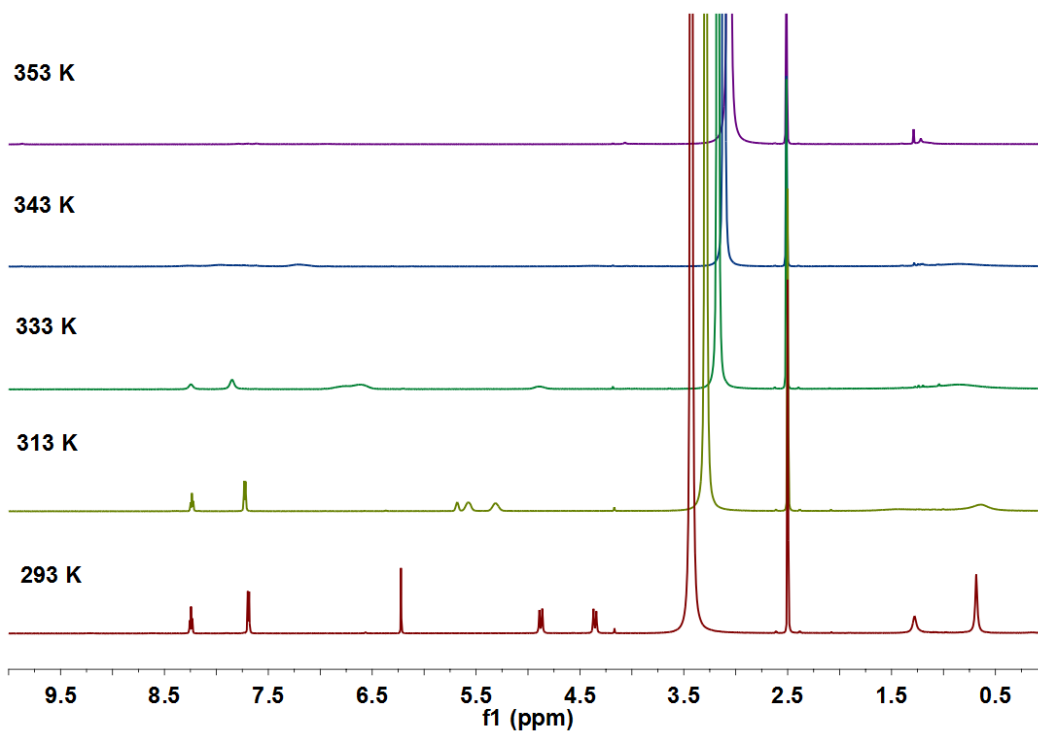


Figure A.14: Variable temperature ¹H NMR spectra of **2e** in [D₆]DMSO.

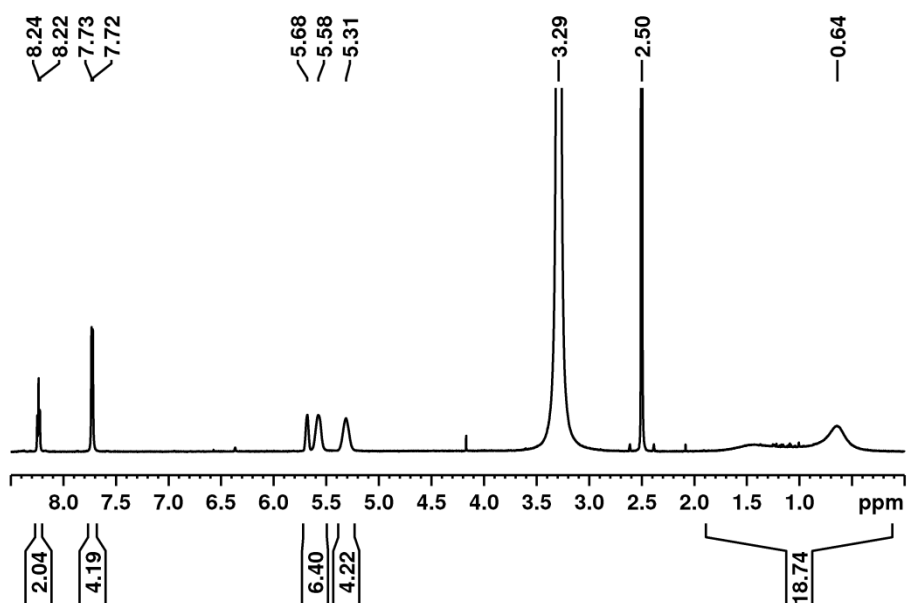


Figure A.15: ¹H NMR spectrum of **2e** in [D₆]DMSO at 313 K. This spectrum is provided for a better view of signal broadening and it refers to the spectrum of 313 K of the above spectra.

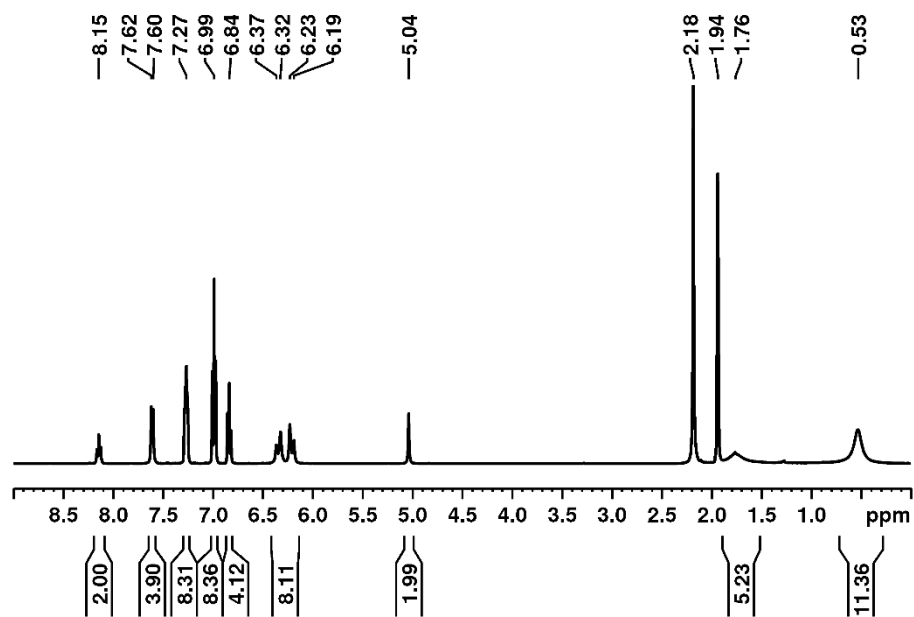


Figure A.16: ^1H NMR spectrum of **2b** in $[\text{D}_3]\text{MeCN}$ at RT.

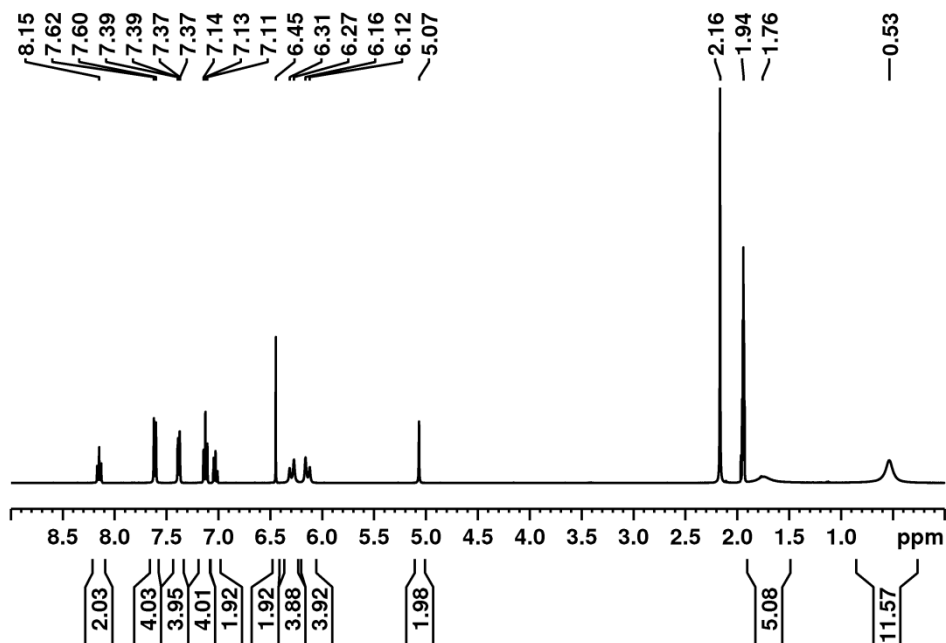


Figure A.17: ^1H NMR spectrum of **2d** in $[\text{D}_3]\text{MeCN}$ at RT.

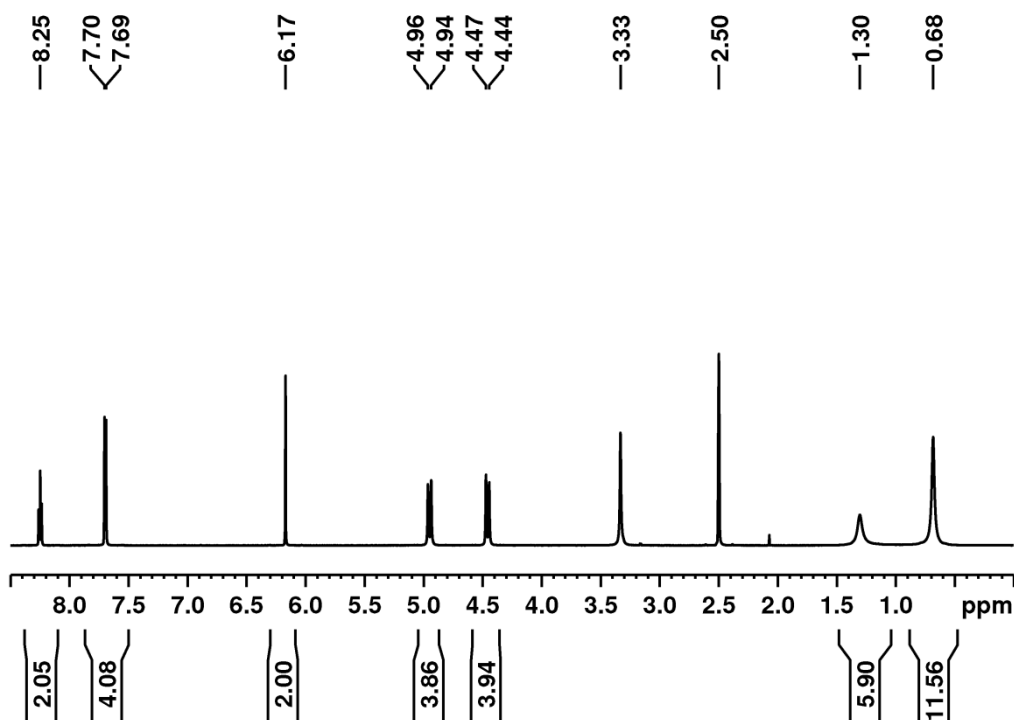


Figure A.18: ^1H NMR spectrum of **2e** in $[\text{D}_6]\text{DMSO}$ at 295 K.

6.1.4 UV/Vis/NIR Spectra

The spectra which are fitted by Lorentzian function are shown in Figure A.19–Figure A.21, and Figure A.43–Figure A.66. The adjusted R^2 values for almost all of the fit are 0.999. If the adjusted R^2 value is less than 0.999, then that value is provided in the caption of the corresponding Figure. The blue solid line in each UV/Vis/NIR spectrum represents the range of the spectrum used for the Lorentzian fitting. The orange-red dashed line in each fitted spectrum corresponds to the sum of Lorentzian peaks. The Lorentzian peaks are represented as black solid lines. The data obtained from the fitting are provided in Table A.5.

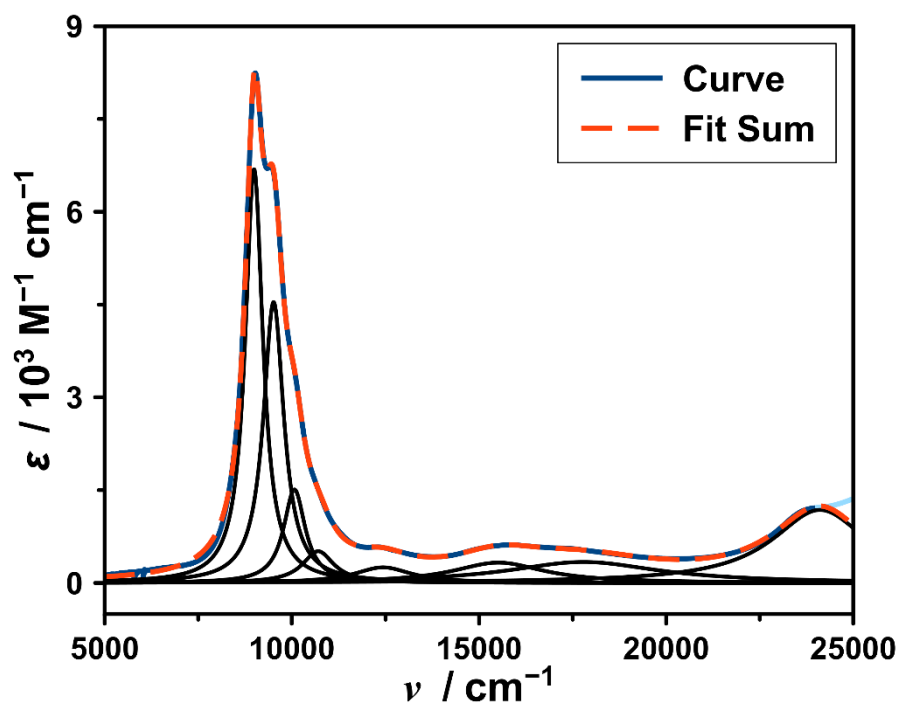


Figure A.19: Lorentzian fit of the NIR/Visible spectrum of **2b** in DCM at 298 K.

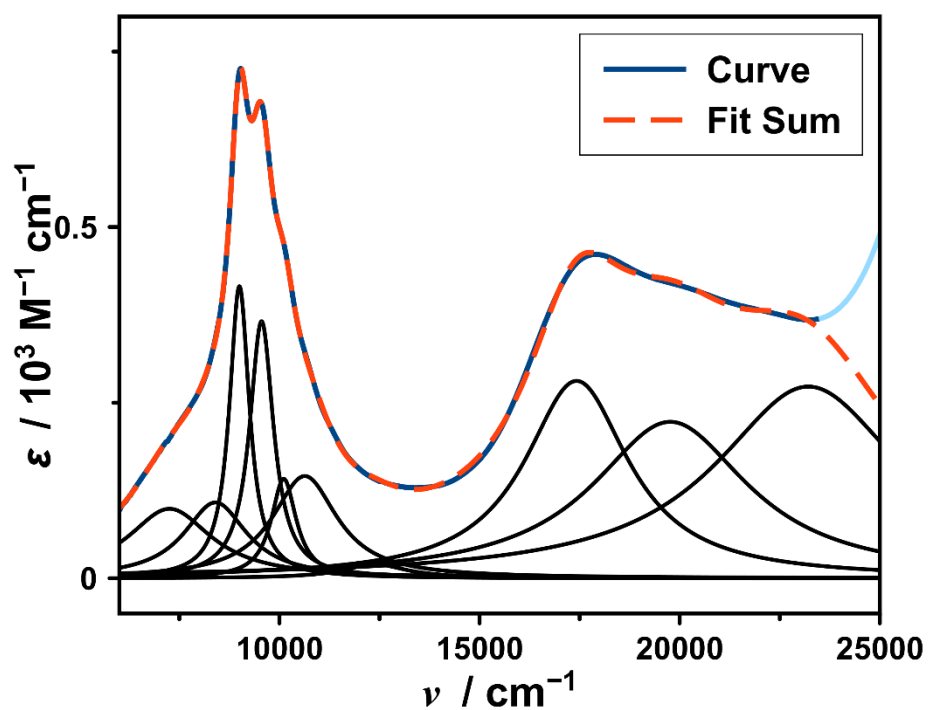


Figure A.20: Lorentzian fit of the NIR/Visible spectrum of **2b** in MeCN at RT.

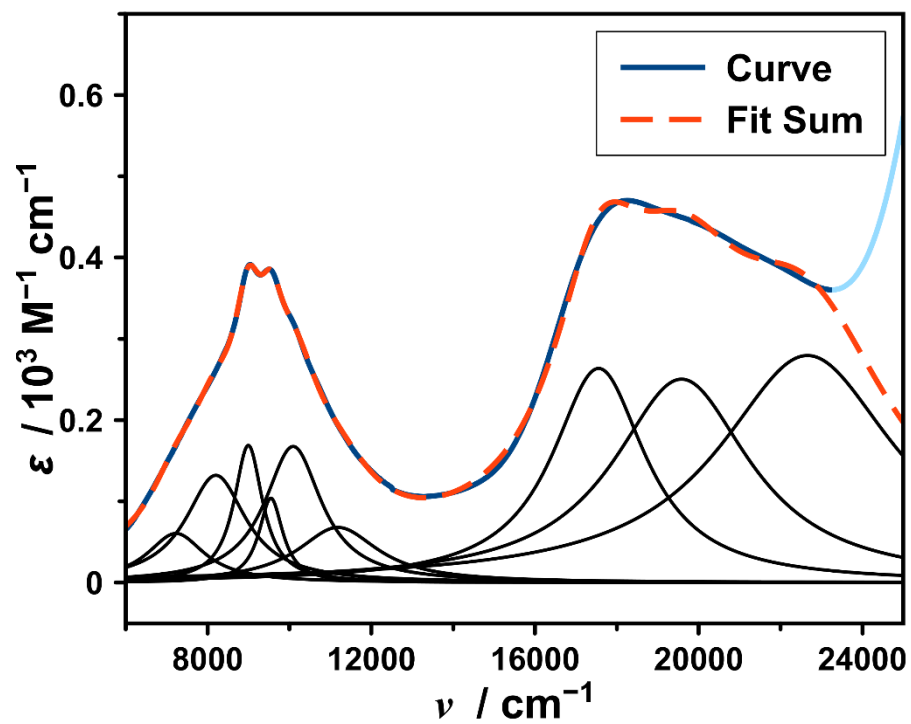


Figure A.21: Lorentzian fit of the NIR/Visible spectrum of **2b** in DMSO at 298 K.

Table A.5: The absorption maximum (ν/cm^{-1}), molar extinction coefficient ($\epsilon/\text{M}^{-1}\text{cm}^{-1}$) and area under the Lorentzian peaks ($\text{area}/\text{M}^{-1}\text{cm}^{-2}$) for the Lorentzian fit of the UV/Vis/NIR spectra of compound **2b** in different solvents and temperatures.

Solvent (T / K)	ν (ϵ)	ν (area $\times 10^{-6}$)
LTC (DCM) ^[a]	7531 (193), 9379 (607), 17243 (347), 19907 (208), 22212 (305)	7531 (1.31), 9379 (0.23), 17243 (1.43), 19907 (1.33), 22212 (2.30)
HTC (DCM) ^[a]	8986 (8387), 9509 (5674), 10065 (1960), 10699 (656), 12433 (319), 15553 (520), 18014 (335), 23946 (1185)	8986 (7.30), 9509 (5.71), 10065 (2.09), 10699 (0.98), 12433 (0.87), 15553 (2.25), 18014 (1.90), 23946 (5.40)
LTC (MeCN) ^[b]	7908 (126), 9702 (177), 17636 (271), 19928 (245), 22931 (236)	7908 (0.47), 9702 (0.90), 17636 (1.08), 19928 (1.50), 22931 (1.88)
HTC (MeCN) ^[c]	8987 (8916), 9541 (6974), 10086 (2494), 10585 (1621), 12394 (488), 15694 (1107), 16892 (909), 24819 (2929)	8987 (8.71), 9541 (7.62), 10086 (2.75), 10585 (4.05), 12394 (1.87), 15694 (4.15), 16892 (3.72), 24819 (14.0)
DCM (193 K) ^[a]	8953 (473), 9503 (359), 10057 (108), 10506 (80), 13230 (50), 17303 (349), 20341 (284), 22541 (232), 24338 (208), 7819 (180)	8953 (0.36), 9503 (0.35), 10057 (0.90), 10506 (0.20), 13230 (~ 0), 17303 (1.62), 20341 (2.0), 22541 (1.36), 24338 (0.79), 7819 (1.08)
DCM (203 K) ^[a]	8956 (815), 9505 (602), 10061 (191), 10548 (106), 12808 (37), 17242 (344), 20293 (248), 22455 (205), 24216 (192), 7572 (156)	8956 (0.64), 9505 (0.59), 10061 (0.17), 10548 (0.22), 12808 (0.11), 17242 (1.62), 20293 (1.72), 22455 (1.15), 24216 (0.71), 7572 (0.84)
DCM (213 K) ^[a]	8959 (1262), 9505 (922), 10063 (302), 10590 (144), 12415 (45), 17212 (359), 20370 (242), 22535 (196), 24277 (224), 7316 (158)	8959 (1.0), 9505 (0.90), 10063 (0.28), 10590 (0.28), 12415 (0.19), 17212 (1.88), 20370 (1.73), 22535 (1.13), 24277 (0.87), 7316 (0.80)

DCM (223 K) ^[a]	8962 (1858), 9507 (1335), 10068 (436), 10602 (205), 12453 (65), 17140 (404), 20362 (210), 22497 (208), 24346 (287), 7032 (184)	8962 (1.49), 9507 (1.31), 10068 (0.40), 10602 (0.40), 12453 (0.25), 17140 (2.44), 20362 (1.37), 22497 (1.23), 24346 (1.24), 7032 (0.93)
DCM (233 K) ^[a]	8966 (2568), 9509 (1830), 10069 (594), 10613 (253), 12441 (82), 15793 (80), 17203 (365), 20231 (215), 22518 (206), 24280 (316), 6971 (138)	8966 (2.09), 9509 (1.81), 10069 (0.55), 10613 (0.45), 12441 (0.30), 15793 (0.30), 17203 (2.0), 20231 (1.58), 22518 (1.25), 24280 (1.30), 6971 (0.48)
DCM (243 K) ^[a]	8970 (3368), 9510 (2372), 10071 (766), 10627 (312), 12387 (99), 15732 (131), 17262 (346), 20030 (180), 22302 (190), 24134 (384), 6904 (120)	8970 (2.78), 9510 (2.38), 10071 (0.73), 10627 (0.54), 12387 (0.32), 15732 (0.52), 17262 (1.88), 20030 (1.20), 22302 (1.11), 24134 (1.63), 6904 (0.29)
DCM (253 K) ^[a]	8973 (4178), 9510 (2928), 10073 (947), 10646 (365), 12362 (123), 15704 (180), 17356 (321), 20417 (180), 24116 (536), 6866 (106)	8973 (3.49), 9510 (2.95), 10073 (0.92), 10646 (0.62), 12362 (0.36), 15704 (0.74), 17356 (1.74), 20417 (1.37), 24116 (3.37), 6866 (0.15)
DCM (263 K) ^[a]	8976 (4964), 9510 (3434), 10075 (1138), 10670 (407), 12338 (155), 15657 (244), 17475 (309), 20443 (168), 23994 (621), 6837 (92)	8976 (4.15), 9510 (3.50), 10075 (1.14), 10670 (0.63), 12338 (0.43), 15657 (1.04), 17475 (1.58), 20443 (1.15), 23994 (3.31), 6837 (0.09)
DCM (273 K) ^[a]	8980 (5620), 9511 (3873), 10073 (1243), 10665 (452), 12402 (178), 15530 (240), 17281 (311), 20004 (143), 24218 (772)	8980 (4.82), 9511 (3.98), 10073 (1.28), 10665 (0.73), 12402 (0.52), 15530 (1.0), 17281 (1.80), 20004 (1.28), 24218 (4.42)
DCM (283 K) ^[a]	8984 (6152), 9511 (4172), 10071 (1395), 10684 (482), 12414	8984 (5.40), 9511 (4.29), 10071 (1.47), 10684 (0.76),

	(221), 15647 (338), 17915 (318), 24243 (943)	12414 (0.66), 15647 (1.57), 17915 (2.19), 24243 (5.67)
DCM (293 K) ^[a]	8988 (6565), 9512 (4401), 10068 (1494), 10698 (510), 12470 (252), 15615 (411), 18043 (327), 24104 (1151)	8988 (5.86), 9512 (4.49), 10068 (1.61), 10698 (0.79), 12470 (0.73), 15615 (1.98), 18043 (2.19), 24104 (5.94)
DCM (303 K) ^[a]	8991 (6788), 9512 (4507), 10065 (1550), 10703 (531), 15511 (440), 17990 (326), 23986 (1220)	8991 (6.17), 9512 (4.60), 10065 (1.70), 10703 (0.82), 15511 (2.05), 17990 (2.04), 23986 (5.75)
DCM (298 K) ^[d]	8991 (6686), 9512 (4538), 10067 (1509), 10710 (512), 12456 (252), 15558 (328), 18028 (338), 24017 (1180)	8991 (6.01), 9512 (4.73), 10067 (1.65), 10710 (0.81), 12456 (0.73), 15558 (1.54), 18028 (2.64), 24017 (5.75)
DMSO (298 K) ^[e]	8994 (168), 9546 (103), 10089 (167), 11184 (68), 17554 (263), 19580 (250), 22658 (279), 7226 (60), 8201 (131)	8994 (0.22), 9546 (0.11), 10089 (0.44), 11184 (0.25), 17554 (1.14), 19580 (1.60), 22658 (2.30), 7226 (0.16), 8201 (0.37)
MeCN (RT) ^[e]	7252 (98), 8399 (107), 8998 (415), 9552 (365), 10105 (141), 10631 (145), 12387 (32), 17420 (280), 19759 (222), 23209 (272)	7252 (0.39), 8399 (0.32), 8998 (0.40), 9552 (0.41), 10105 (0.17), 10631 (0.45), 12387 (0.06), 17420 (1.39), 19759 (1.66), 23209 (2.42)
MeCN (233K) ^[e]	7195 (48), 8126 (123), 9012 (131), 9582 (49), 10073 (111), 10967 (59), 17690 (248), 19912 (235), 22756 (236)	7195 (0.11), 8126 (0.33), 9012 (0.22), 9582 (0.51), 10073 (0.31), 10967 (0.29), 17690 (0.98), 19912 (1.53), 22756 (1.87),
MeCN (243 K) ^[e]	7196 (52), 8177 (134), 9009 (131), 9559 (67), 10050 (125), 11009 (59), 17646 (254), 19870 (233), 22773 (238)	7196 (0.13), 8177 (0.39), 9009 (0.18), 9559 (0.68), 10050(0.34), 11009 (0.28), 17646 (1.03), 19870 (1.52), 22773 (1.91)
MeCN (253 K) ^[e]	7194 (57), 8210 (138), 9006 (145), 9546 (84),	7194 (0.16), 8210 (0.42), 9006 (0.17), 9546 (0.82), 10029

	10029 (139), 11012 (59), 17958 (257), 19826 (231), 22808 (242)	(0.37), 11012 (0.28), 17958 (1.08), 19826 (1.54), 22808 (1.99)
MeCN (263 K) ^[e]	7194 (64), 8235 (138), 9003 (176), 9540 (112), 10033 (148), 10968 (66), 17551 (262), 19788 (229), 22861 (245)	7194 (0.19), 8235 (0.44), 9003 (0.19), 9540 (0.11), 10033 (0.37), 10968 (0.31), 17551 (1.14), 19788 (1.55), 22861 (2.05)
MeCN (273 K) ^[e]	7211 (73), 8275 (134), 9001 (222), 9541 (168), 10071 (125), 10729 (99), 17504 (269), 19751 (227), 22924 (249)	7211 (0.24), 8275 (0.43), 9001 (0.22), 9541 (0.17), 10071 (0.23), 10729 (0.45), 17504 (1.19), 19751 (1.57), 22924 (2.13)
MeCN (283 K) ^[e]	7274 (96), 8347 (125), 8995 (287), 9550 (262), 10105 (124), 10704 (115), 12149 (24), 17459 (278), 19754 (224), 23046 (252)	7274 (0.36), 8347 (0.38), 8995 (0.28), 9550 (0.30), 10105 (0.17), 10704 (0.34), 12149 (0.08), 17459 (1.29), 19754 (1.60), 23046 (2.17)
MeCN (293 K) ^[e]	7275 (105), 8380 (116), 8994 (367), 9549 (331), 10103 (136), 10654 (138), 12205 (24), 17407 (286), 19740 (222), 23165 (259),	7275 (0.42), 8380 (0.35), 8994 (0.35), 9549 (0.38), 10103 (0.17), 10654 (0.41), 12205 (0.08), 17407 (1.39), 19740 (1.63), 23165 (2.25),
MeCN (303 K) ^[e]	7363 (128), 8433 (90), 8991 (468), 9547 (420), 10102 (160), 10630 (158), 12132 (28), 17362 (292), 19743 (217), 23317 (267)	7363 (0.56), 8433 (0.22), 8991 (0.44), 9547 (0.48), 10102 (0.19), 10630 (0.45), 12132 (0.09), 17362 (1.49), 19743 (1.64), 23317 (2.34)
MeCN (313 K) ^[e]	7496 (149), 8412 (54), 8988 (599), 9545 (511), 10098 (190), 10612 (180), 12153 (30), 17315 (301), 19736 (211), 23473 (282)	7496 (0.73), 8412 (0.08), 8988 (0.58), 9545 (0.58), 10098 (0.22), 10612 (0.51), 12153 (0.09), 17315 (1.60), 19736 (1.63), 23473 (2.47)
MeCN (323 K) ^[e]	7506 (150), 8405 (46), 8987 (746), 9544 (616), 10094 (219), 10586 (208), 12196 (31), 17262 (309), 19723 (201), 23658 (206)	7506 (0.78), 8405 (0.05), 8987 (0.72), 9544 (0.70), 10094 (0.24), 10586 (0.60), 12196 (0.09), 17262 (1.72), 19723 (1.60), 23658 (2.67)

MeCN (333 K) ^[e]	7441 (141), 8407 (47), 8986 (910), 9542 (738), 10091 (251), 10555 (243), 12258 (33), 17206 (316), 19691 (187), 23894 (348)	7441 (0.77), 8407 (0.04), 8986 (0.89), 9542 (0.83), 10091 (0.27), 10555 (0.71), 12258 (0.09), 17206 (1.86), 19691 (1.54), 23894 (3.01)
MeCN (343 K) ^[f]	7317 (128), 8414 (53), 8986 (1096), 9541 (871), 10088 (276), 10516 (286), 12315 (37), 17142 (323), 19622 (169), 24151 (411),	7317 (0.72), 8414 (0.04), 8986 (1.08), 9541 (0.98), 10088 (0.30), 10516 (0.86), 12315 (0.09), 17142 (2.02), 19622 (1.44), 24151 (3.52),

^[a] Wavenumber range 6666–24000 cm⁻¹. ^[b] Wavenumber range 6000–24000 cm⁻¹.

^[c] Wavenumber range 7500–24000 cm⁻¹. ^[d] Wavenumber range 5000–24000 cm⁻¹.

^[e] Wavenumber range 6000–23500 cm⁻¹. ^[f] Wavenumber range 6000–23300 cm⁻¹.

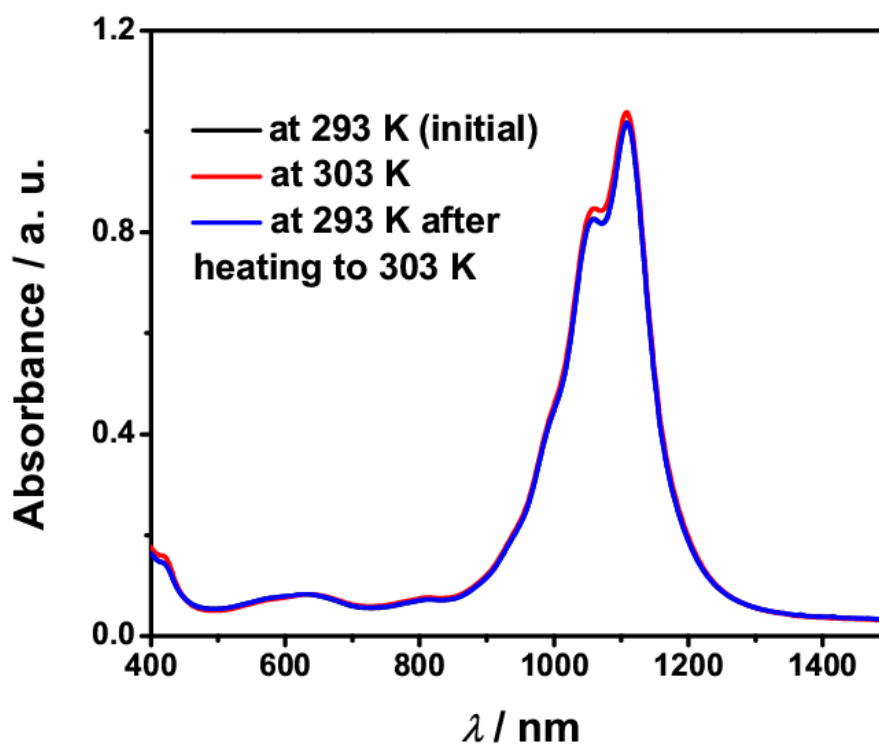


Figure A.22: Solution stability of **2b** during measurement of the variable temperature UV/Vis/NIR spectra in DCM.

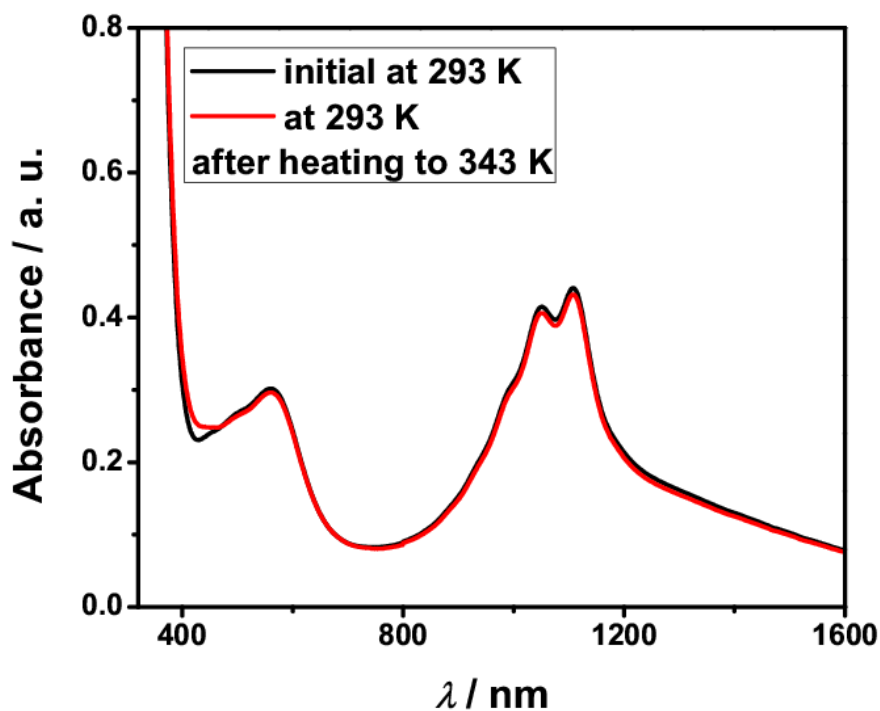


Figure A.23: UV/Vis/NIR spectra of **2b** in MeCN representing the solution stability at high temperature.

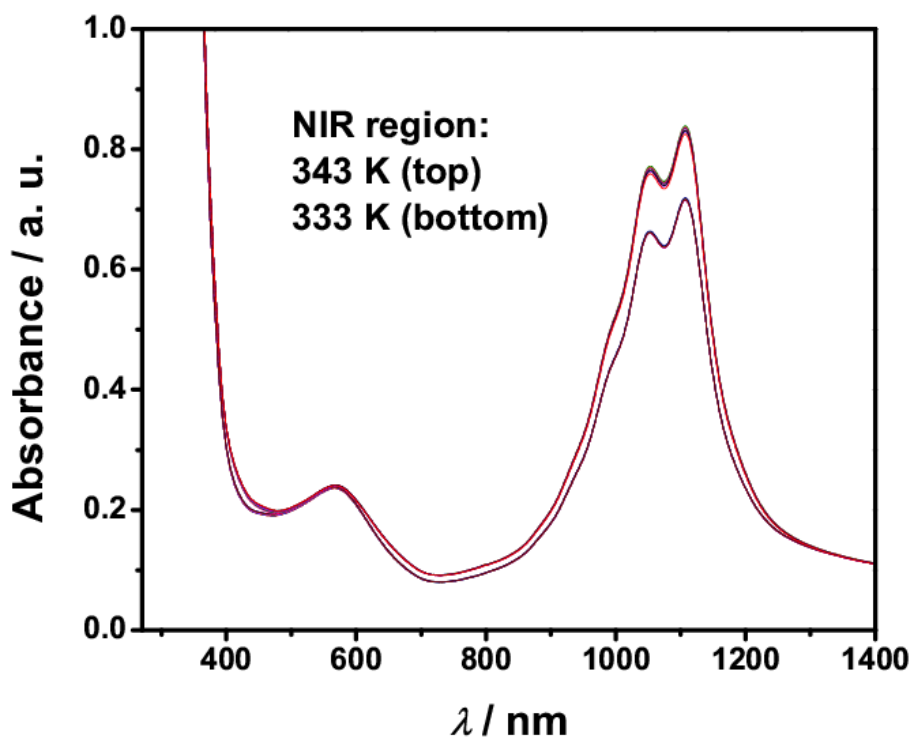


Figure A.24: UV/Vis/NIR spectra of **2b** in MeCN at 333 K and 343 K measured from a sample of **2b** to check the stability of the compound. At each temperature 8 scans; each scan at interval of 15 minutes was performed.

Table A.6: MATLAB script for the SVD of the variable temperature UV/Vis/NIR spectra.**a) Input data format**

$$\text{data} = \begin{bmatrix} NA & NA & NA & \dots & NA \\ NA & T_1 & T_2 & \dots & T_n \\ v_1 & \varepsilon_{11} & \varepsilon_{12} & \dots & \varepsilon_{1n} \\ v_2 & \varepsilon_{21} & \varepsilon_{22} & \dots & \varepsilon_{2n} \\ \vdots & \vdots & \vdots & \ddots & \vdots \\ v_m & \varepsilon_{m1} & \varepsilon_{m2} & \dots & \varepsilon_{mn} \end{bmatrix}$$

NA values are left blank. T_n stands for the temperature for the n^{th} measurement.

b) Main script

1. `[m,n] = size(data);`
2. `T = data(2,2:n); % temperature`
3. `wl = data(3:m,1);`
4. `abs = data(3:m,2:n);`
5. `figure(1)`
6. `plot(wl,abs); % view data`
7. `[U,S1,V] = svd(abs,0); % SVD compute`
8. `diag_S1=diag(S1); % weight of the basis spectra`
9. `percent_S1 = 100*diag_S1/sum(diag_S1);`
10. `B=U(:,1:2)*S1(1:2,1:2)*V(:,1:2)'; % reduced data for two components`
11. `SV = S1(1:2,1:2)*V(:,1:2)';`
12. `SV=SV';`
13. `x=[T', SV(:,1), SV(:,2)];`
14. `par = [12000 40]; % initial guess of the parameters`
15. `lb=[8000 25]; ub=[];`
16. `SV=SV';`
17. `options=optimoptions('lsqcurvefit','Algorithm','trust-region-reflective');`

```
18. par =lsqcurvefit(@myfun,par,x,SV,lb,ub,options) % call myfun.m to
    optimize
19. clear x
20. R=8.314;
21. F=zeros(length(T),2);% compute the F matrix
22. F(:,1)=(1./(((exp(par(1)./(R*T)))*exp(-par(2)./R))+1));
23. F(:,2)=1-F(:,1); H = V(:,1:2)*pinv(F)';
24. fitV=H*F'; err=V(:,1:2)-fitV;
25. err1sqsum=sum(err(1,:).^2);err2sqsum=sum(err(2,:).^2); % SSres
26. avgv1=mean(V(:,1)); avgv2=mean(V(:,2));
27. err1t=V(1,:)-avgv1; err2t=V(2,:)-avgv2;
28. err1tsq=sum((err1t).^2); err2tsq=sum((err2t).^2); % SStotal
29. [a,b]=size(V);
30. RMSE1=sqrt(err1sqsum/a);RMSE2=sqrt(err2sqsum/a); % RMSError
31. clear a; clear b;
32. figure(2)
33. plot(T,fitV,T,V(:,1:2)','o');
34. nc = 2; % number of principal component
35. D_calcd=(U(:,1:nc)*S1(1:nc,1:nc)*V(:,1:nc)')*pinv(F)'; % spectra of
    pure components
36. figure(3)
37. plot(wl,D_calcd);
38. nc = 2;
39. abs_calcd = U(:,1:nc)*S1(1:nc,1:nc)*H*F'; % recalculated spectra
40. resid=abs-abs_calcd;
41. figure(4)
42. plot(wl,resid); %residual between experimental and calculated spectra
43. clear m; clear n
```

```
44. %-----% R^2 calculation for the reconstruction
45. x = abs;
46. [m,n] = size(x); avg = mean(x);
47. avgx=avg(ones(m,1),:);
48. k = (abs-avgx); % for calculation of SStotal
49. Sp=(x-abs_calcd); % residuals
50. sum_Sp= sum((Sp(:,1:n).^2)); % SSres
51. sumk=sum((k(:,1:n).^2)); %% SStotal
52. Rsq = 1-(sum_Sp./sumk); % R^2 values for each plot
53. figure(5)
54. plot(Rsq,'p');
55. figure(6)
56. plot(wl,abs,wl,abs_calcd,'--'); % comparison between experimental and
    reconstructed spectra
57. clear x
```

c) myfun

```
1. function y = myfun(par,x)
2. R = 8.314;
3. F(:,1) = (1 ./((exp(par(1) ./ (R*x(:,1))))*exp(-par(2) ./ R))+1)); F(:,2)= 1-
    F(:,1);
4. y = [x(:,2) x(:,3)]'*pinv(F')*F';
5. end
```

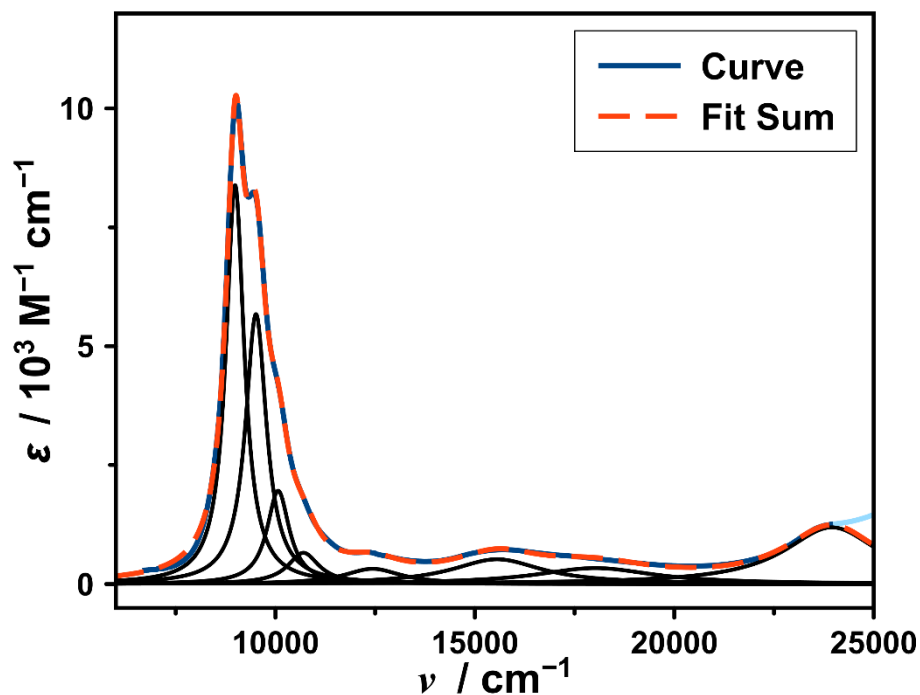


Figure A.25: Lorentzian fit of the UV/Vis/NIR spectral features corresponding to the high-temperature component in the variable temperature UV/Vis/NIR spectra of **2b** in DCM.

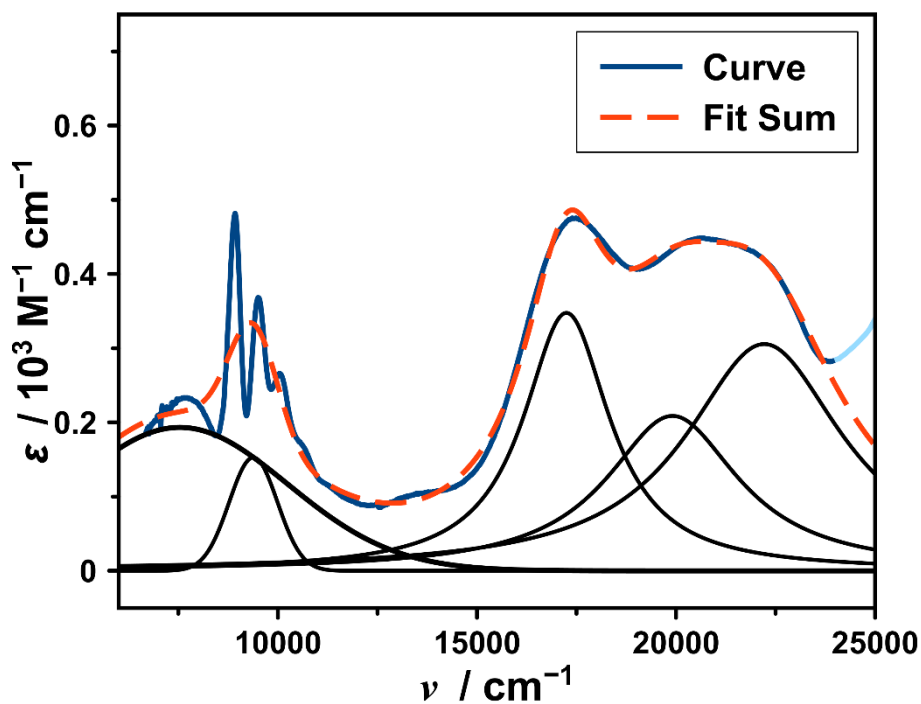


Figure A.26: Lorentzian fit of the UV/Vis/NIR spectral features corresponding to the low-temperature component in the variable temperature UV/Vis/NIR spectra of **2b** in DCM. Adj. R^2 of the fit is 0.907.

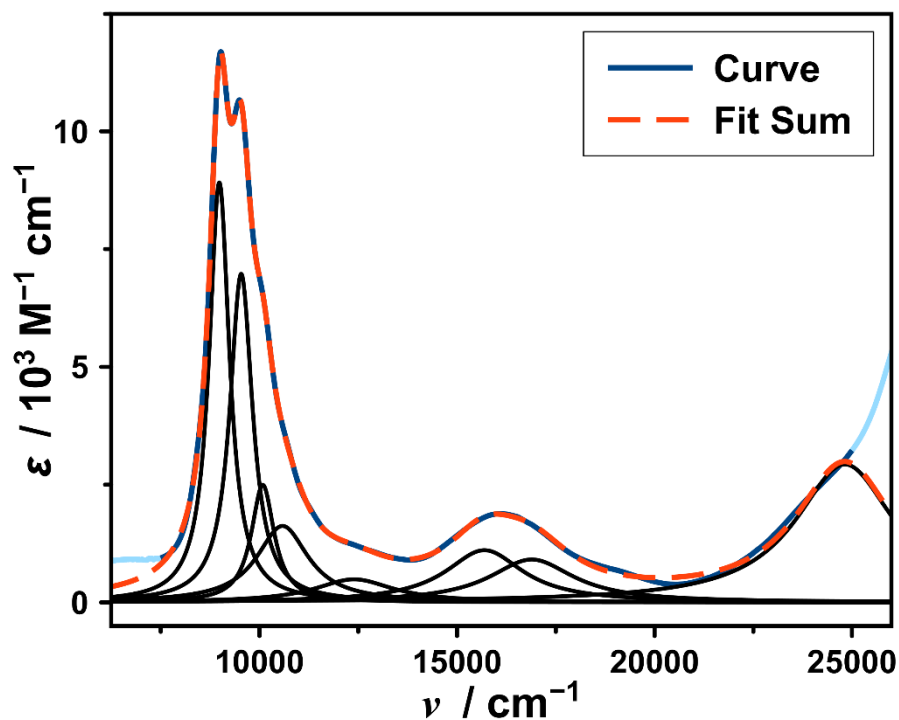


Figure A.27: Lorentzian fit of the UV/Vis/NIR spectral features corresponding to the high-temperature component in the variable temperature UV/Vis/NIR spectra of **2b** in MeCN.

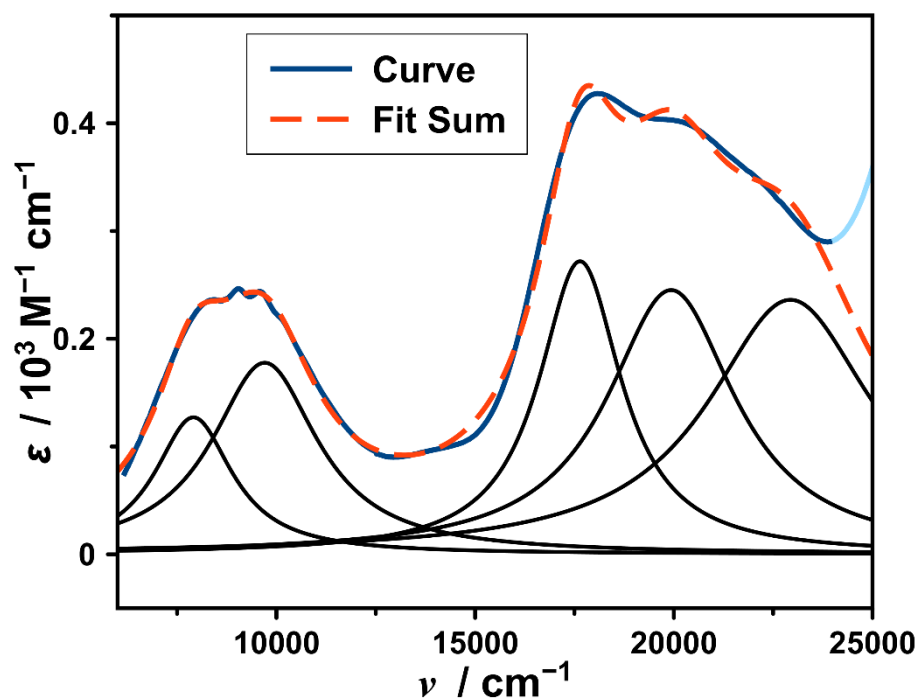


Figure A.28: Lorentzian fit of the UV/Vis/NIR spectral features corresponding to the low-temperature component in the variable temperature UV/Vis/NIR spectra of **2b** in MeCN. Adj. R^2 of the fit is 0.996.

Table A.7: Goodness-of-fit data for the fitting of the **V** component vs. T plots, obtained from the SVD of the variable temperature UV/Vis/NIR spectra of **2b** in DCM and MeCN; sum of squared residuals (SS_{res}) and root mean square error (RMSE).

UV/Vis/NIR spectra	V component	SS_{res}	RMSE
DCM	V component 1	4.5×10^{-5}	1.9×10^{-3}
	V component 2	5.4×10^{-4}	6.7×10^{-3}
MeCN	V component 1	2.7×10^{-5}	1.5×10^{-3}
	V component 2	3.5×10^{-3}	1.7×10^{-2}

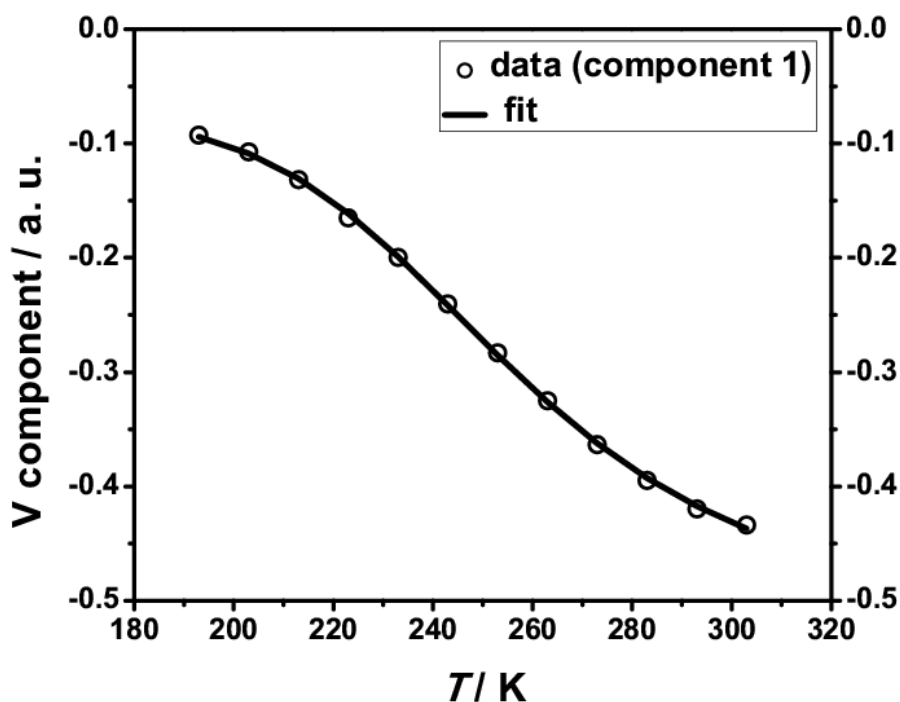


Figure A.29: V component (first) vs. T plot and its fit obtained from the SVD of the variable temperature UV/Vis/NIR spectra of **2b** in DCM.

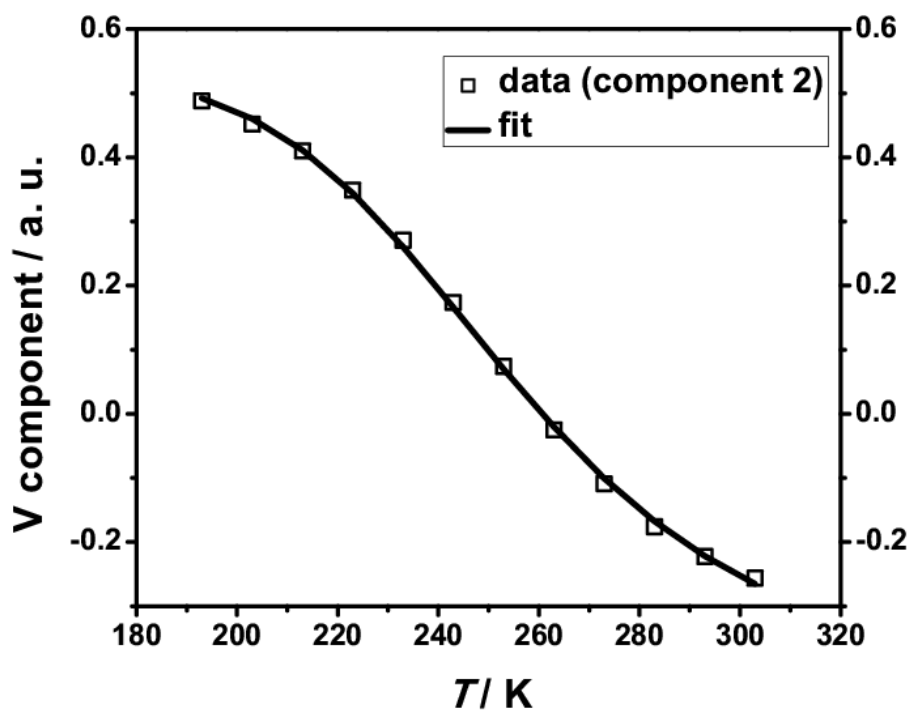


Figure A.30: V component (second) vs. T plot and its fit obtained from the SVD of the variable temperature UV/Vis/NIR spectra of **2b** in DCM.

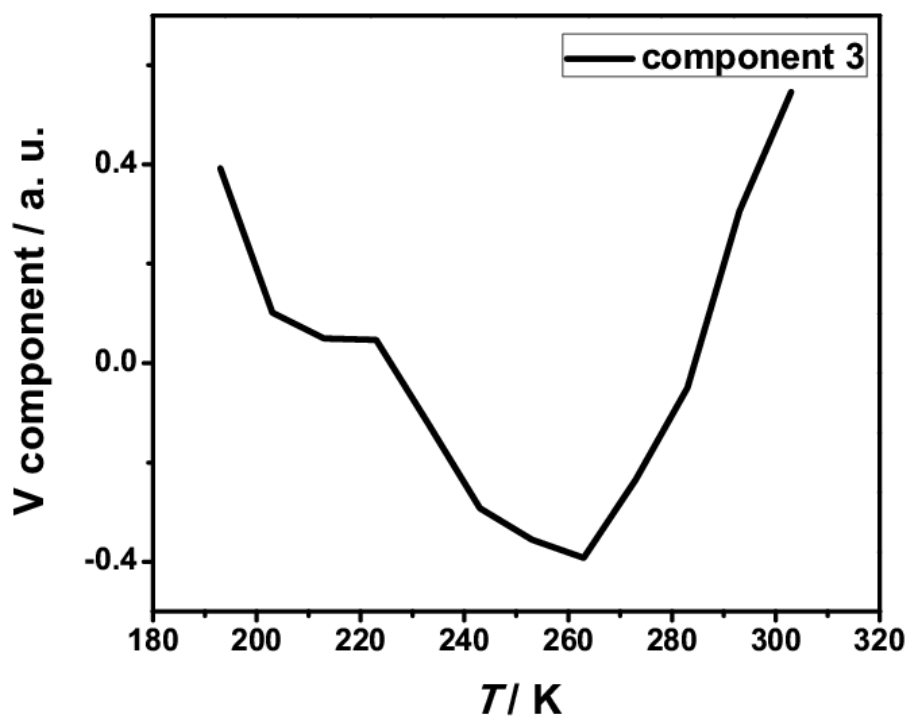


Figure A.31: V component (third) vs. T plot derived from the SVD of the variable temperature UV/Vis/NIR spectra of **2b** in DCM.

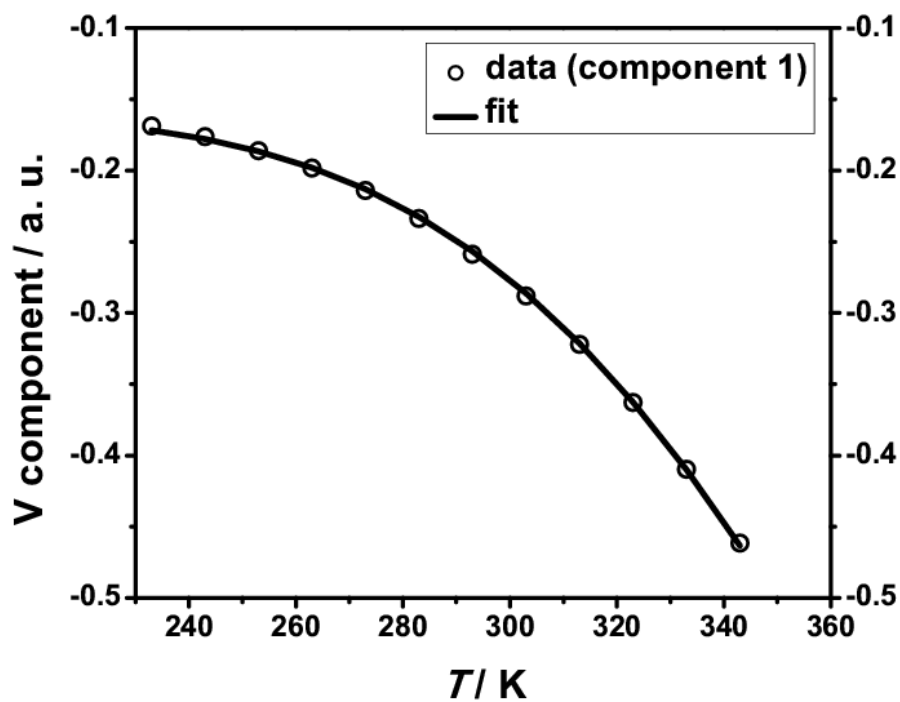


Figure A.32: V component (first) vs. T plot and its fit derived from the SVD of the variable temperature UV/Vis/NIR spectra of **2b** in MeCN.

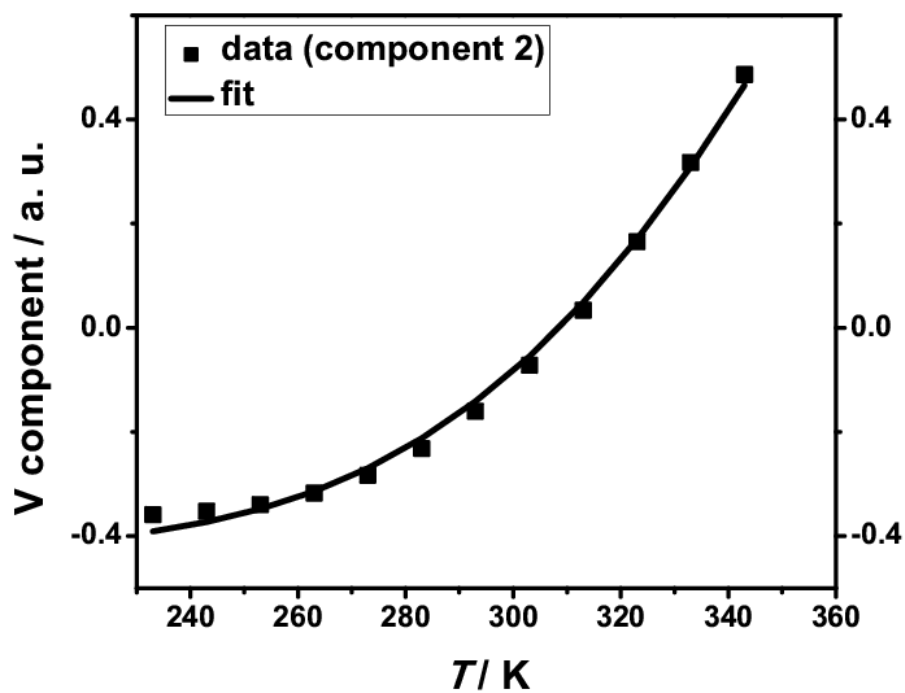


Figure A.33: V component (second) vs. T plot and its fit derived from the SVD of the variable temperature UV/Vis/NIR spectra of **2b** in MeCN.

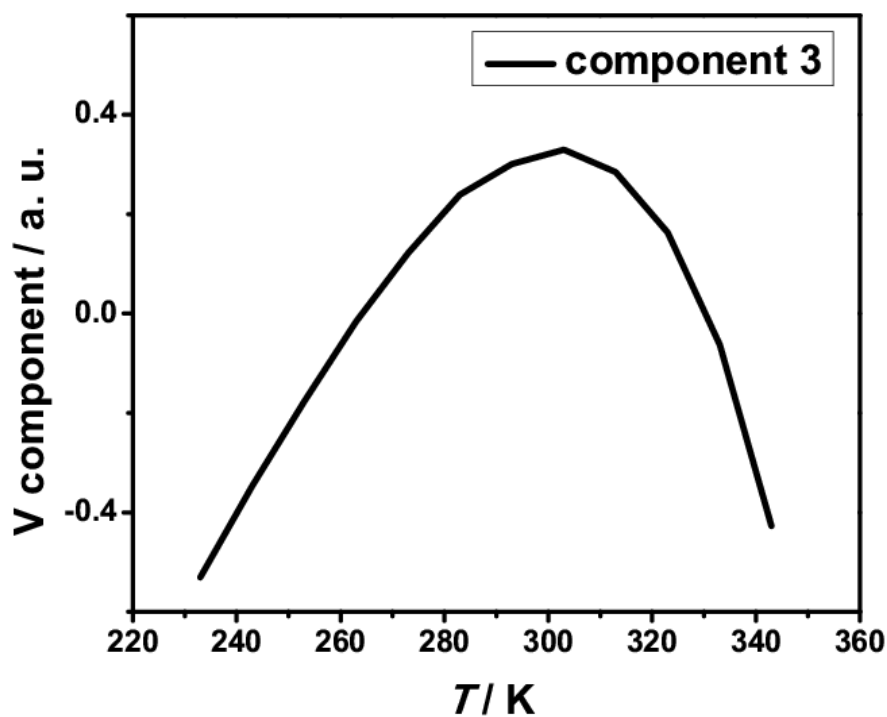


Figure A.34: V component (third) vs. T plot derived from the SVD of the variable temperature UV/Vis/NIR spectra of **2b** in MeCN.

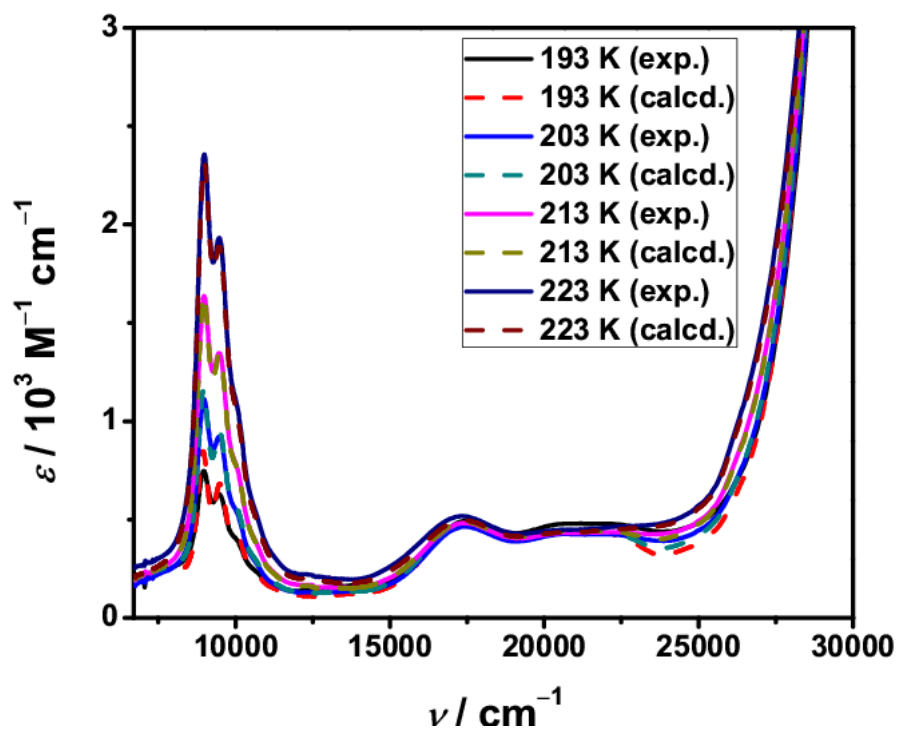


Figure A.35: Experimental and reconstructed (calculated) UV/Vis/NIR spectra of **2b** in DCM at 193, 203, 213 and 223 K.

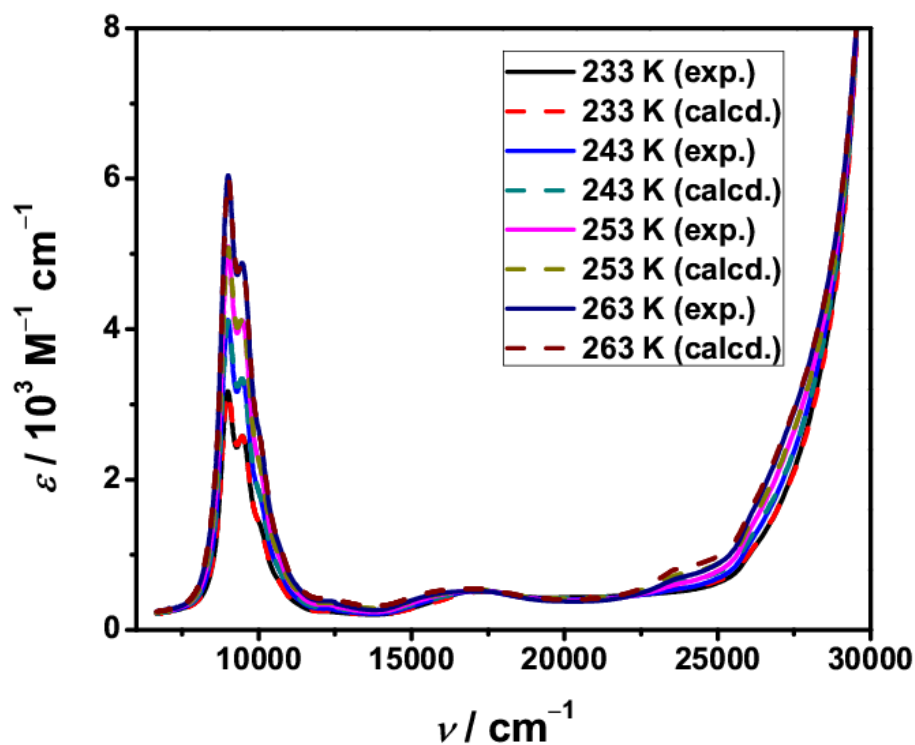


Figure A.36: Experimental and reconstructed (calculated) UV/Vis/NIR spectra of **2b** in DCM at 233, 243, 253 and 263 K.

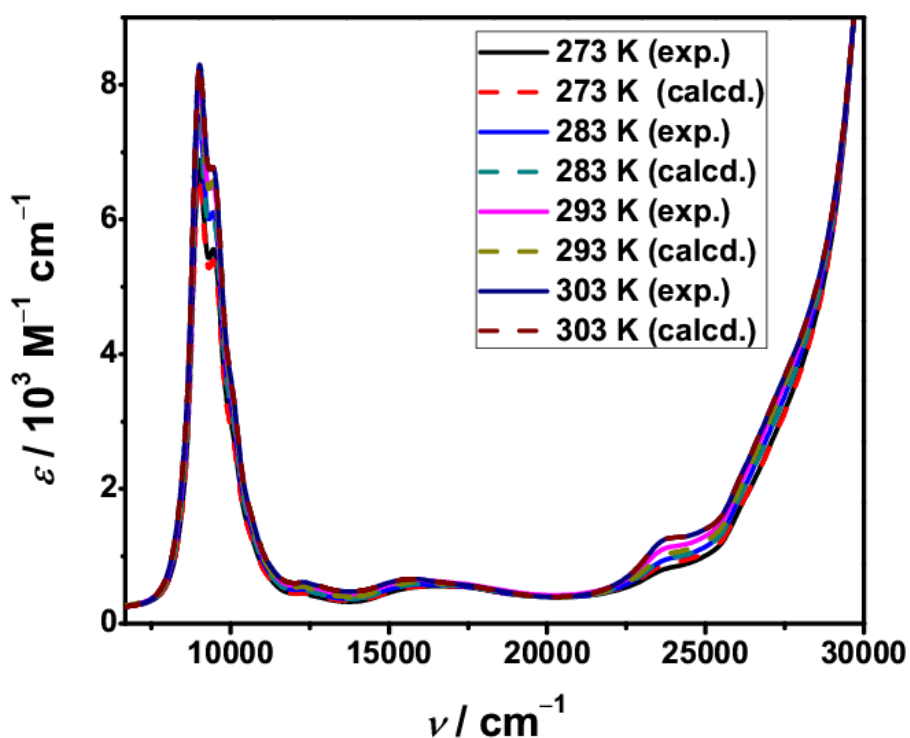


Figure A.37: Experimental and reconstructed (calculated) UV/Vis/NIR spectra of **2b** in DCM at 273, 283, 293 and 303 K.

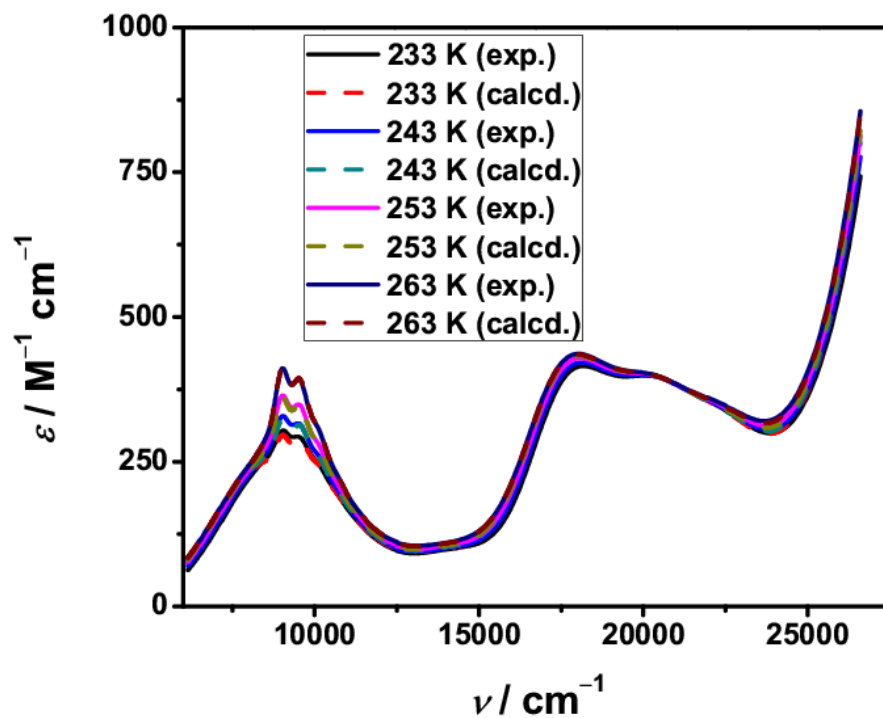


Figure A.38: Experimental and reconstructed (calculated) UV/Vis/NIR spectra of **2b** in MeCN at 233, 243, 253 and 263 K.

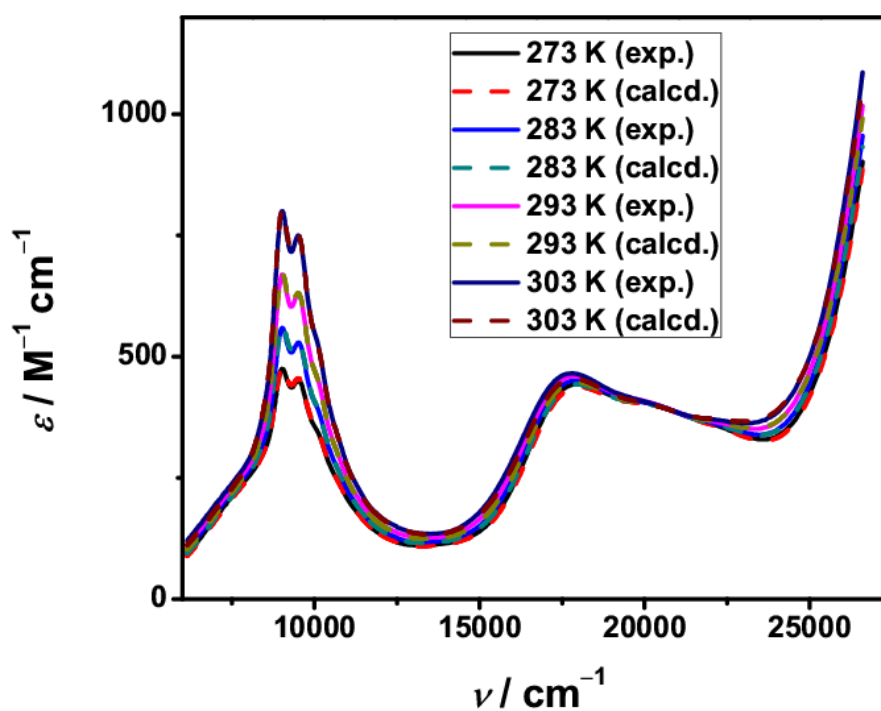


Figure A.39: Experimental and reconstructed (calculated) UV/Vis/NIR spectra of **2b** in MeCN at 273, 283, 293 and 303 K.

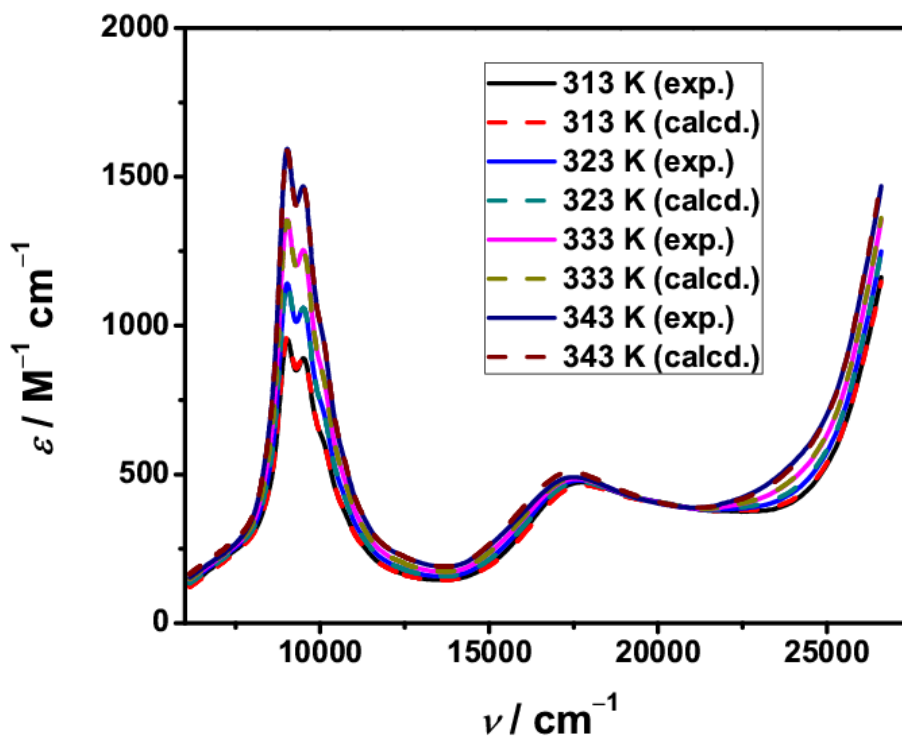


Figure A.40: Experimental and reconstructed (calculated) UV/Vis/NIR spectra of **2b** in MeCN at 313, 323, 333 and 343 K.

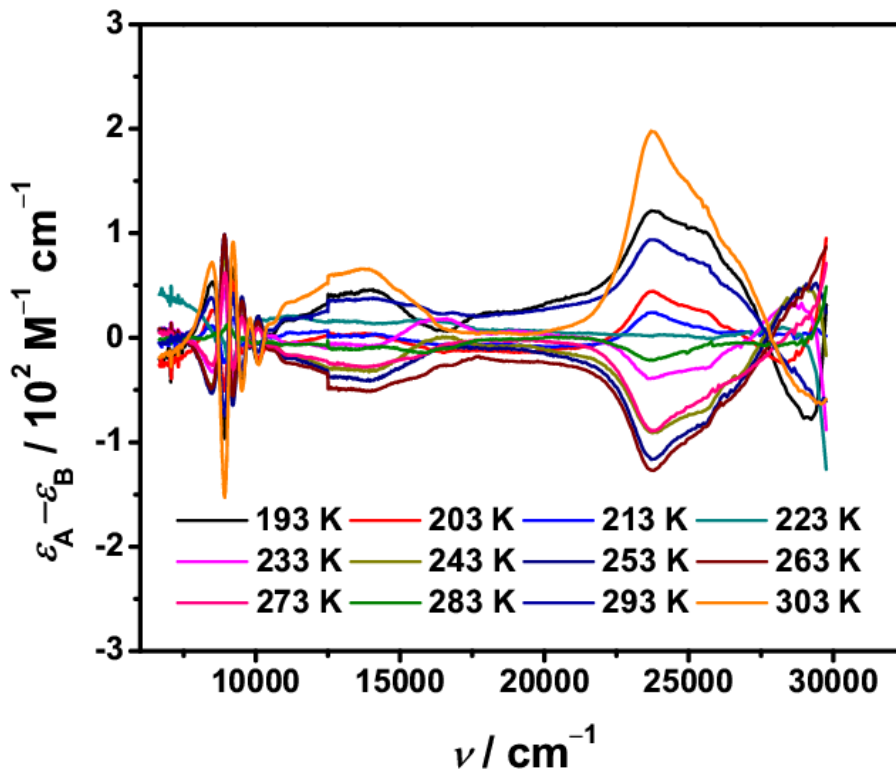


Figure A.41: Residuals between the original data matrix (A) and rank-defined data matrix (B) for the SVD of the variable temperature UV/Vis/NIR spectra of **2b** in DCM.

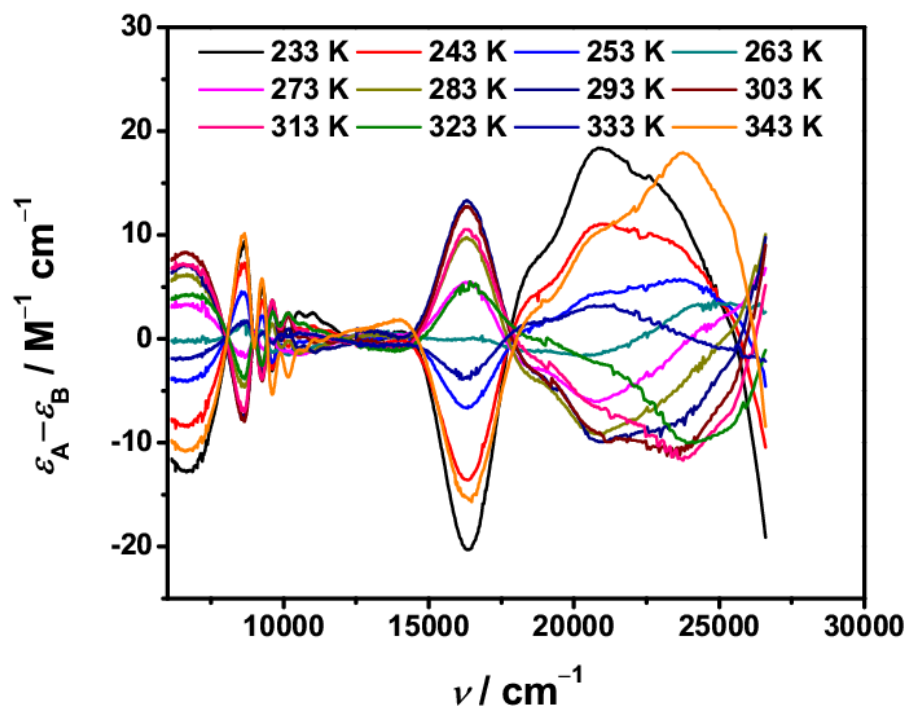


Figure A.42: Residuals between the original data matrix (**A**) and rank-defined data matrix (**B**) for the SVD of the variable temperature UV/Vis/NIR spectra of **2b** in MeCN.

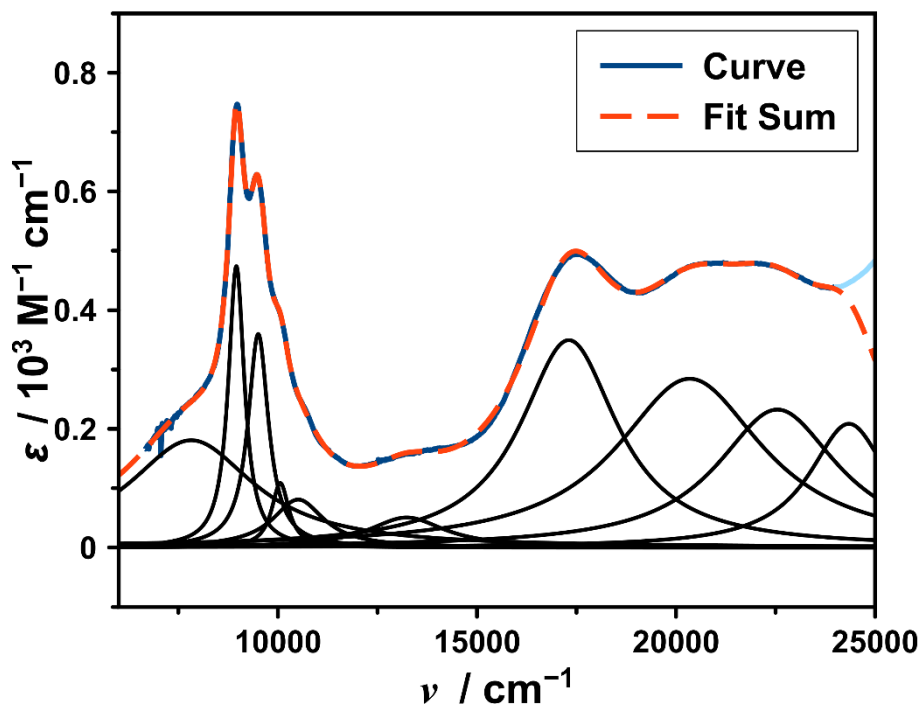


Figure A.43: Lorentzian fit of the NIR/Visible spectrum of **2b** in DCM at 193 K.

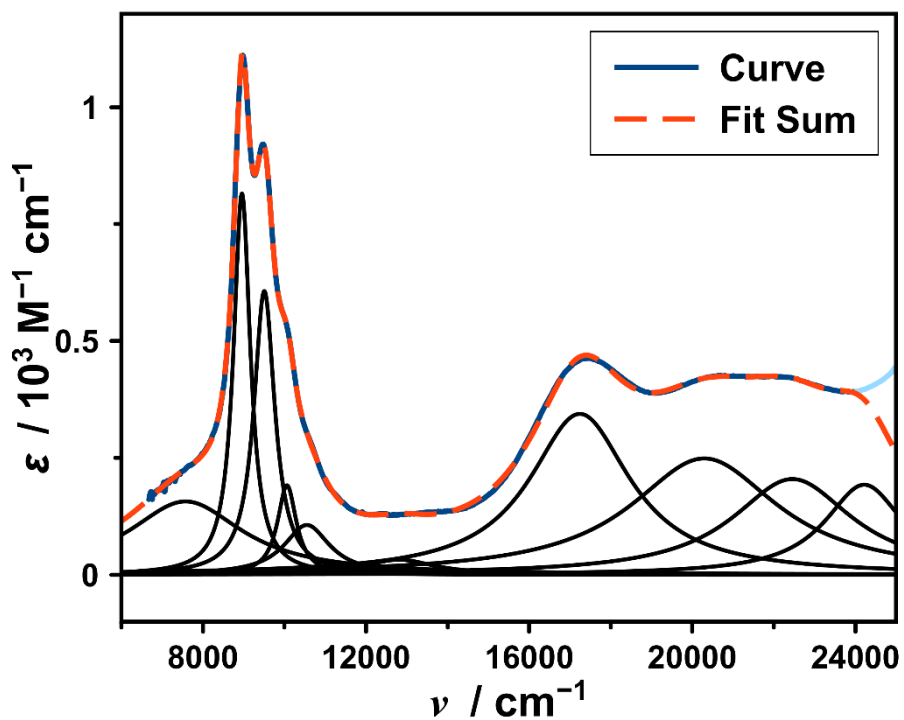


Figure A.44: Lorentzian fit of the NIR/Visible spectrum of **2b** in DCM at 203 K.

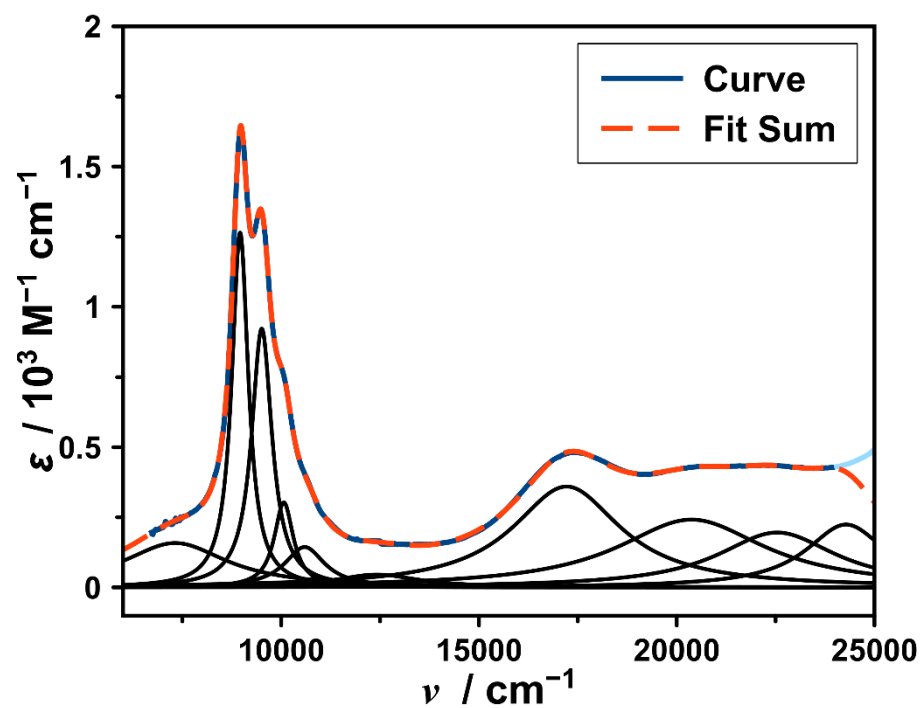


Figure A.45: Lorentzian fit of the NIR/Visible spectrum of **2b** in DCM at 213 K.

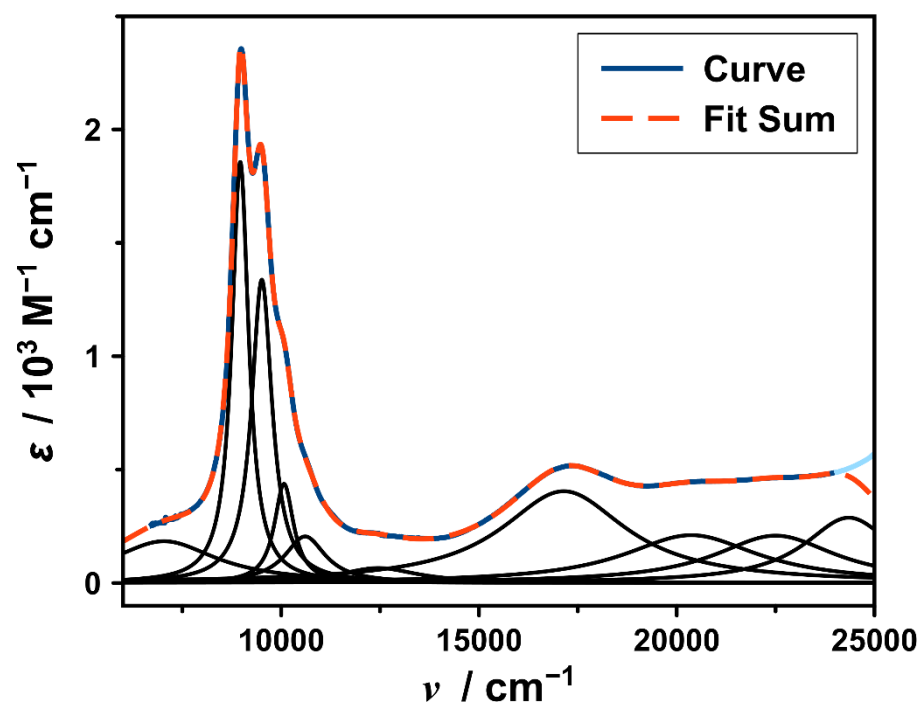


Figure A.46: Lorentzian fit of the NIR/Visible spectrum of **2b** in DCM at 223 K.

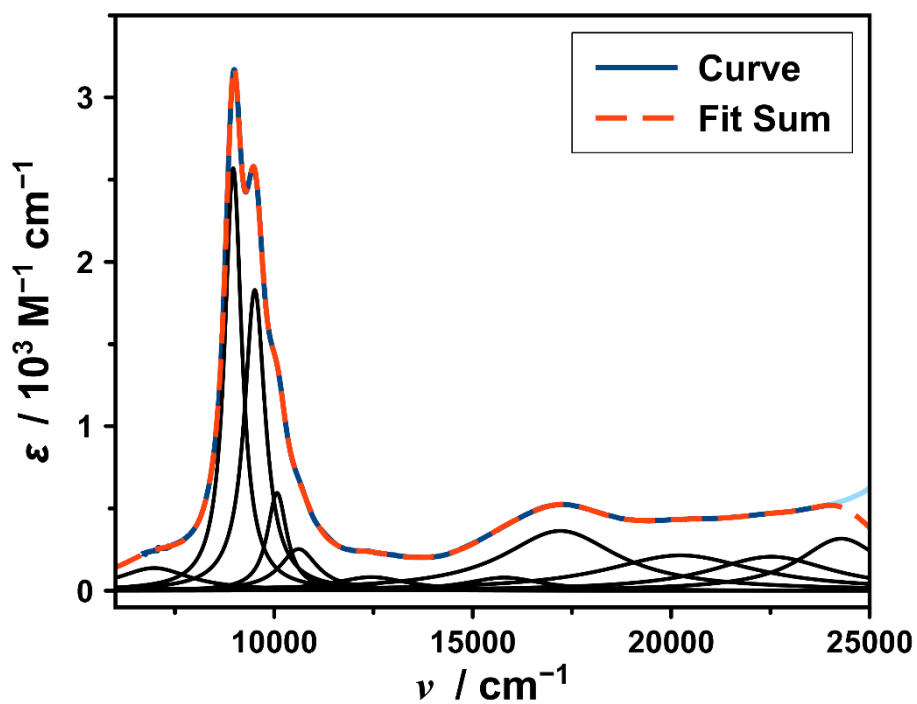


Figure A.47: Lorentzian fit of the NIR/Visible spectrum of **2b** in DCM at 233 K.

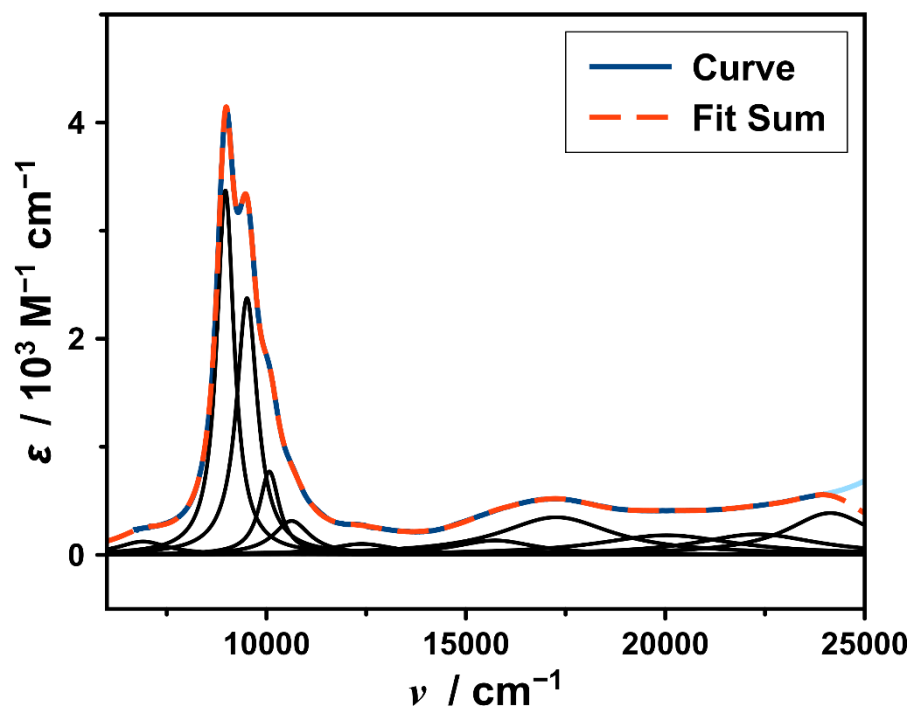


Figure A.48: Lorentzian fit of the NIR/Visible spectrum of **2b** in DCM at 243 K.

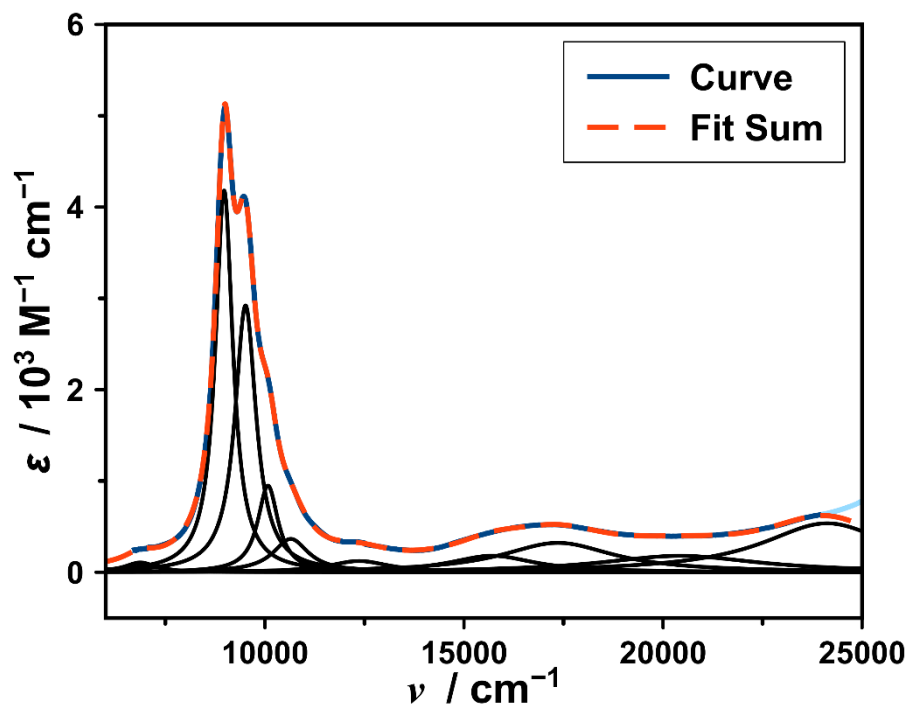


Figure A.49: Lorentzian fit of the NIR/Visible spectrum of **2b** in DCM at 253 K.

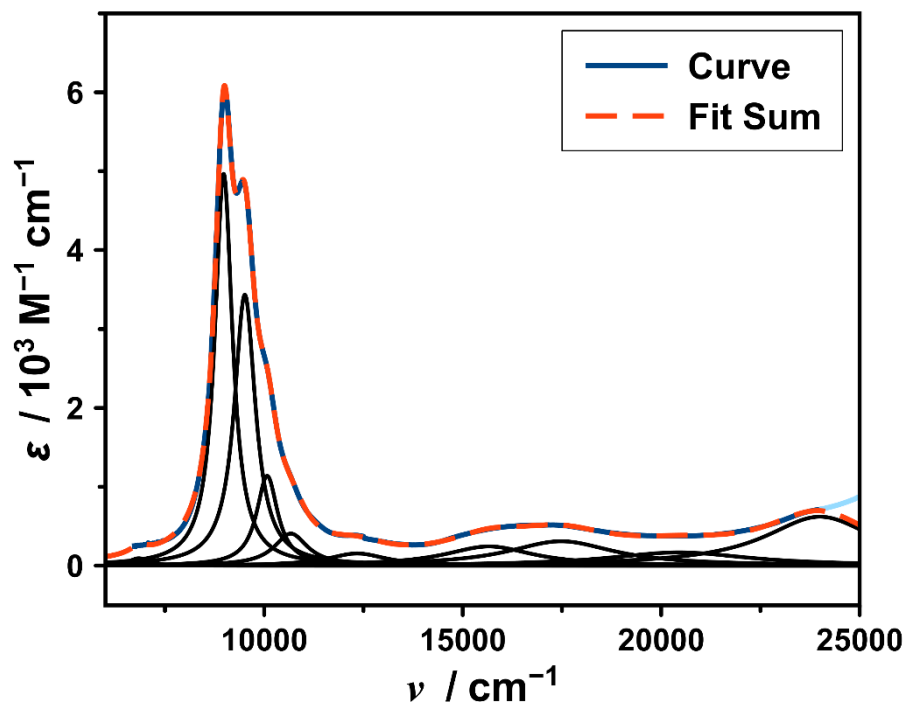


Figure A.50: Lorentzian fit of the NIR/Visible spectrum of **2b** in DCM at 263 K.

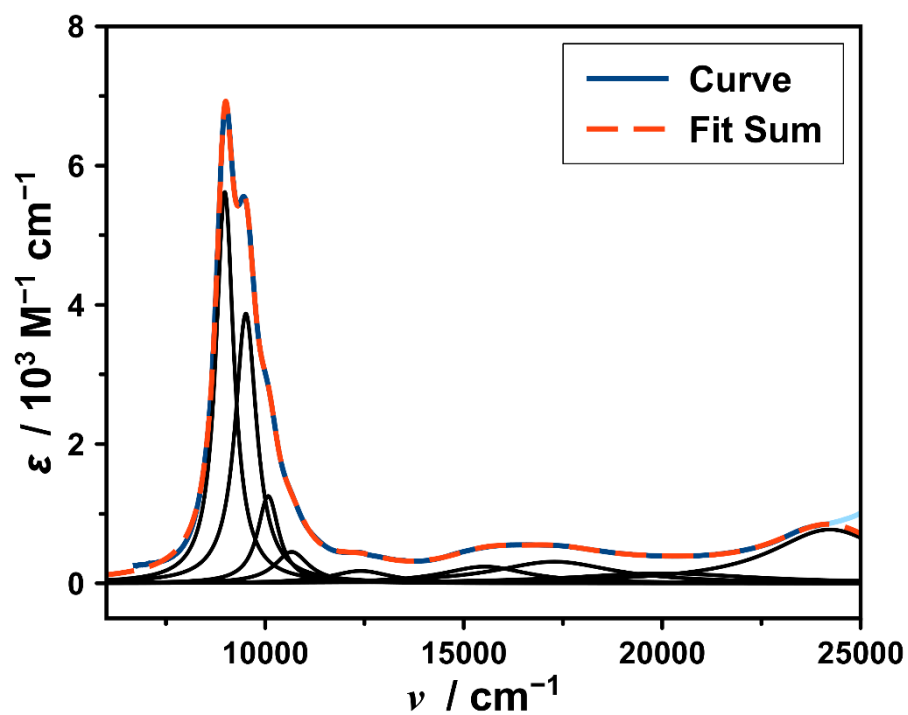


Figure A.51: Lorentzian fit of the NIR/Visible spectrum of **2b** in DCM at 273 K.

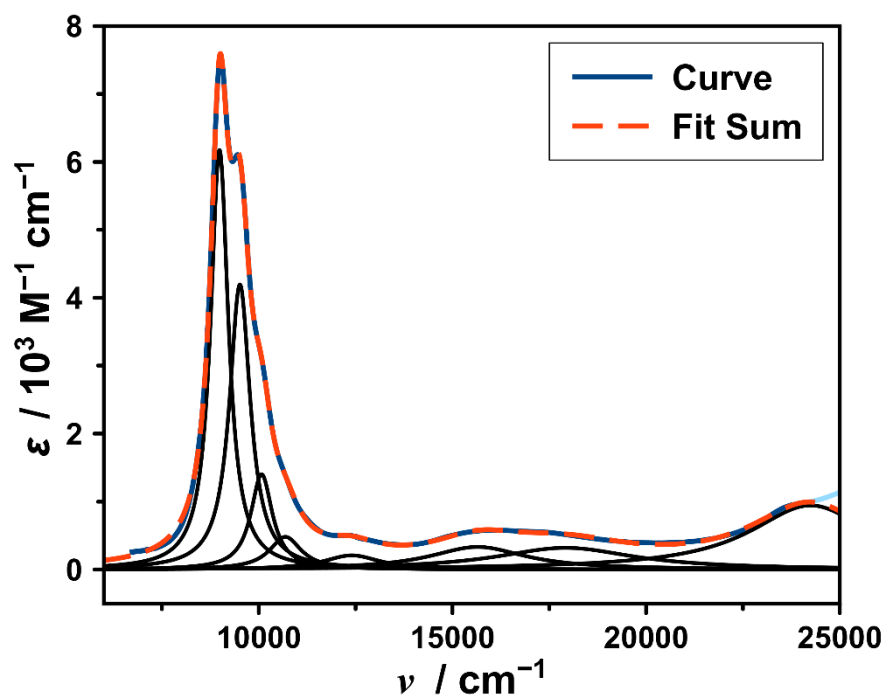


Figure A.52: Lorentzian fit of the NIR/Visible spectrum of **2b** in DCM at 283 K.

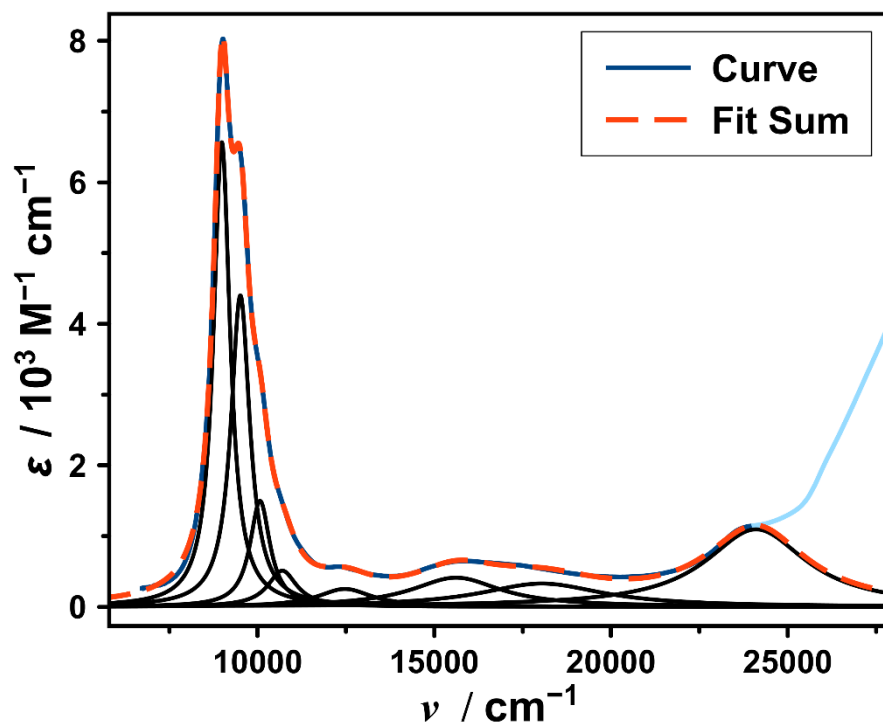


Figure A.53: Lorentzian fit of the NIR/Visible spectrum of **2b** in DCM at 293 K.

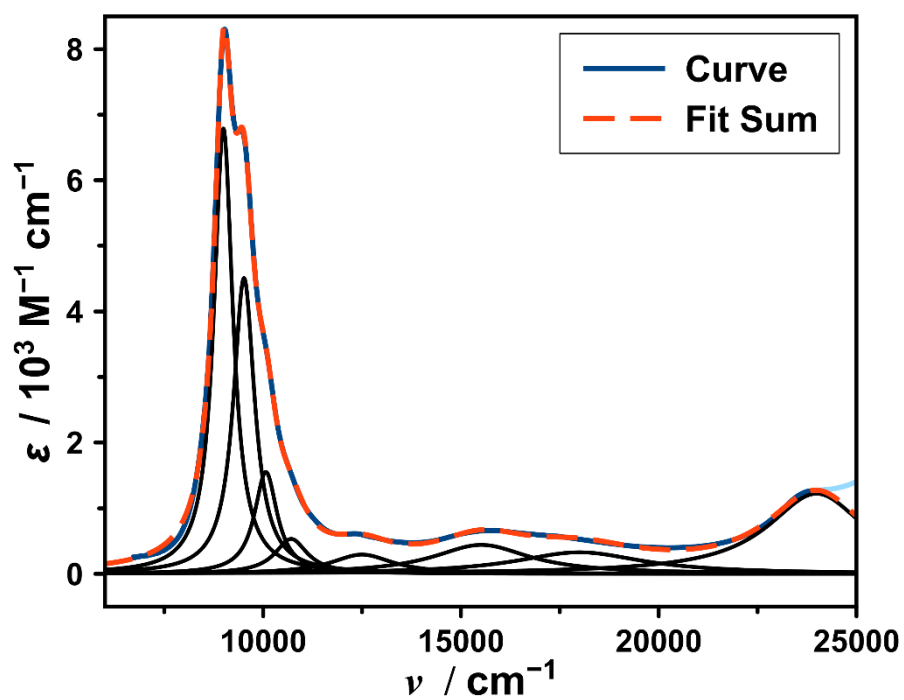


Figure A.54: Lorentzian fit of the NIR/Visible spectrum of **2b** in DCM at 303 K.

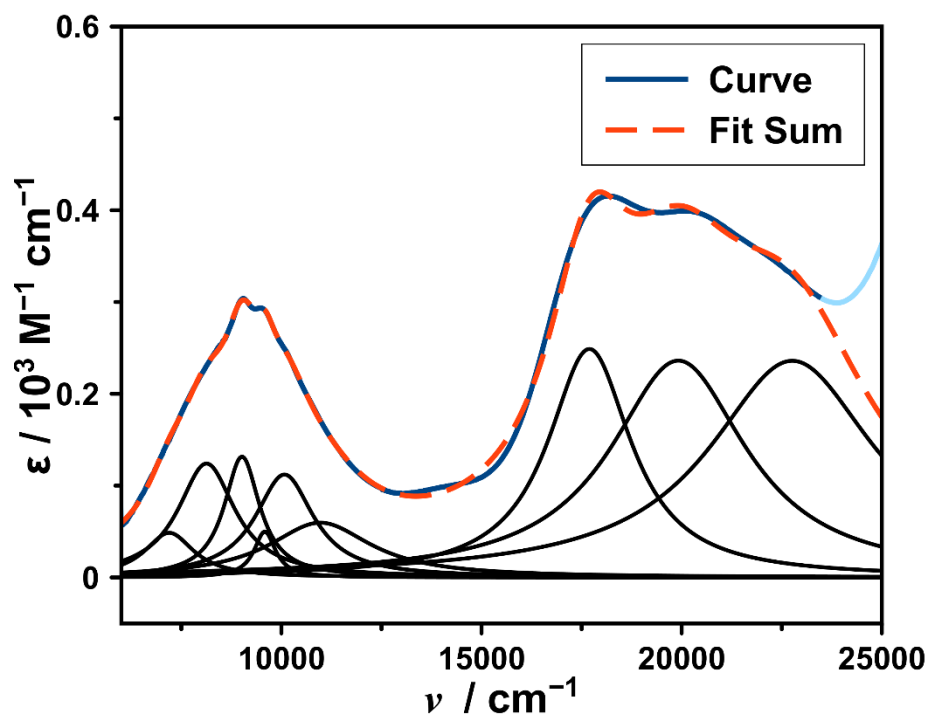


Figure A.55: Lorentzian fit of the NIR/Visible spectrum of **2b** in MeCN at 233 K.

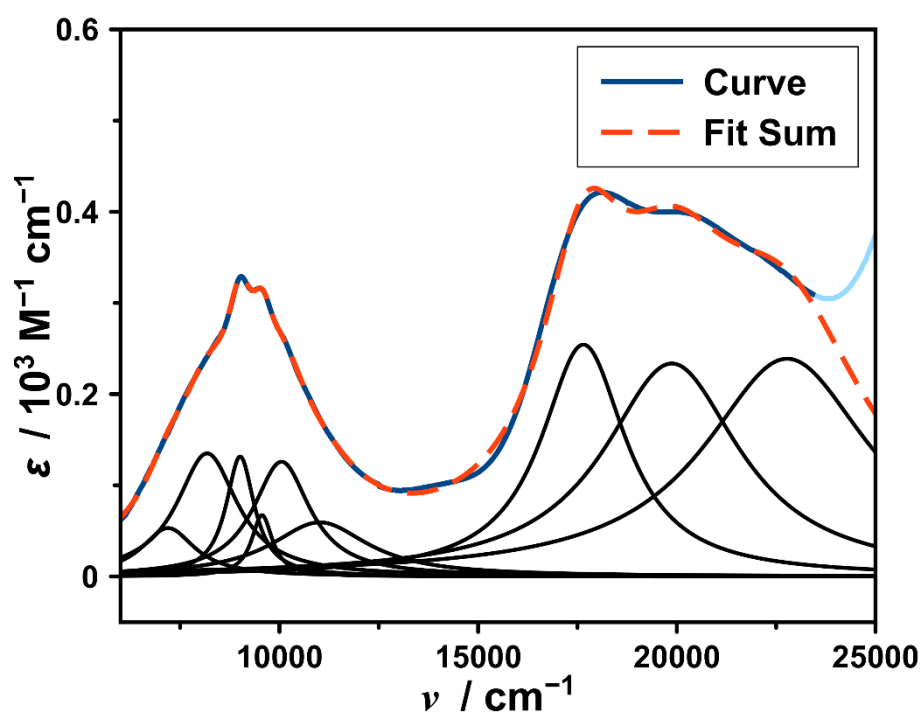


Figure A.56: Lorentzian fit of the NIR/Visible spectrum of **2b** in MeCN at 243 K.

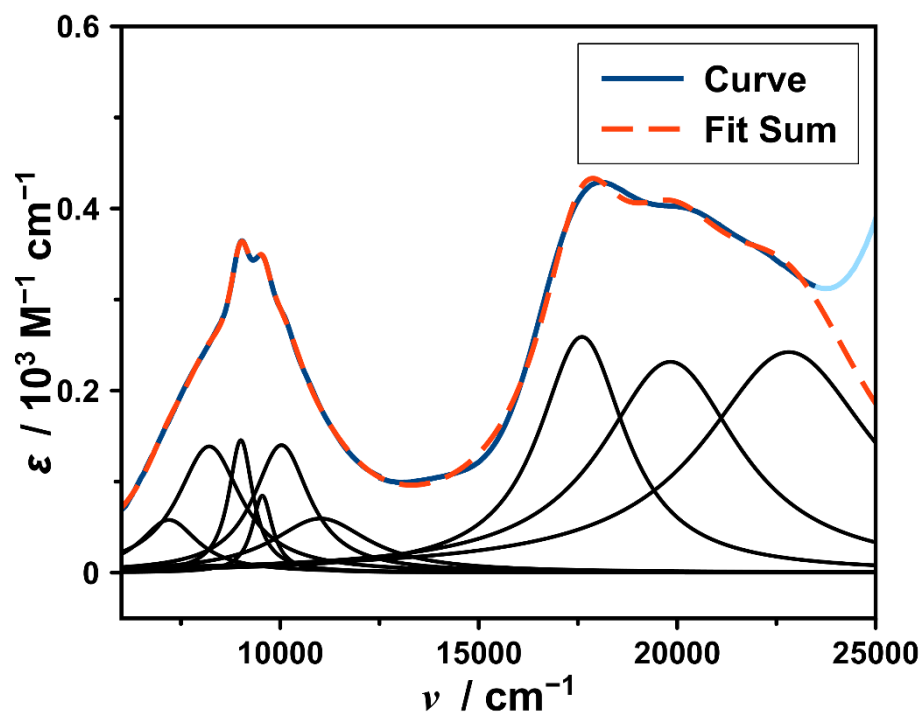


Figure A.57: Lorentzian fit of the NIR/Visible spectrum of **2b** in MeCN at 253 K.

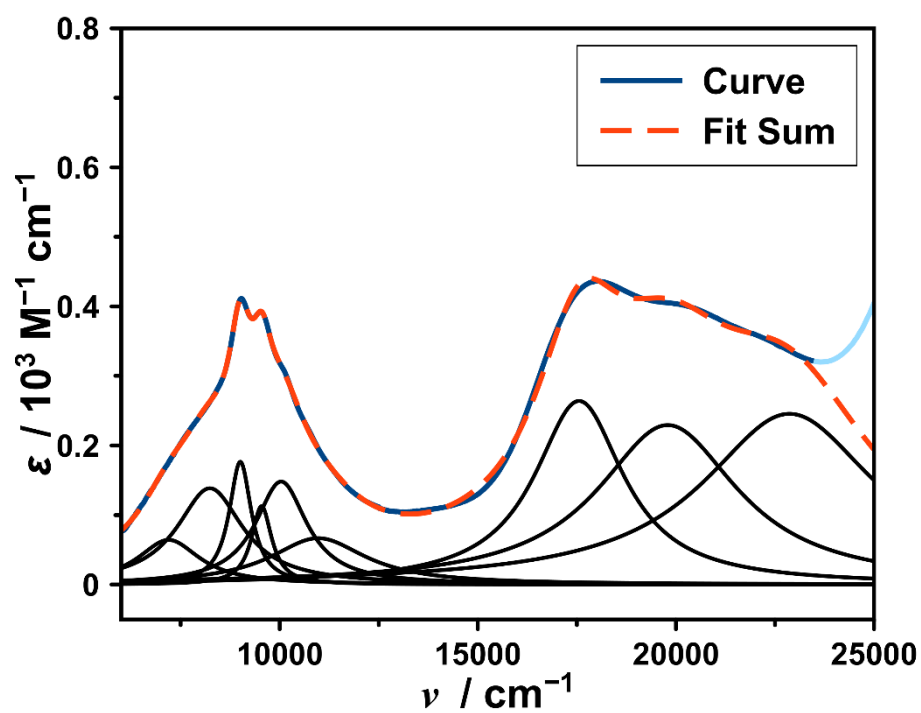


Figure A.58: Lorentzian fit of the NIR/Visible spectrum of **2b** in MeCN at 263 K.

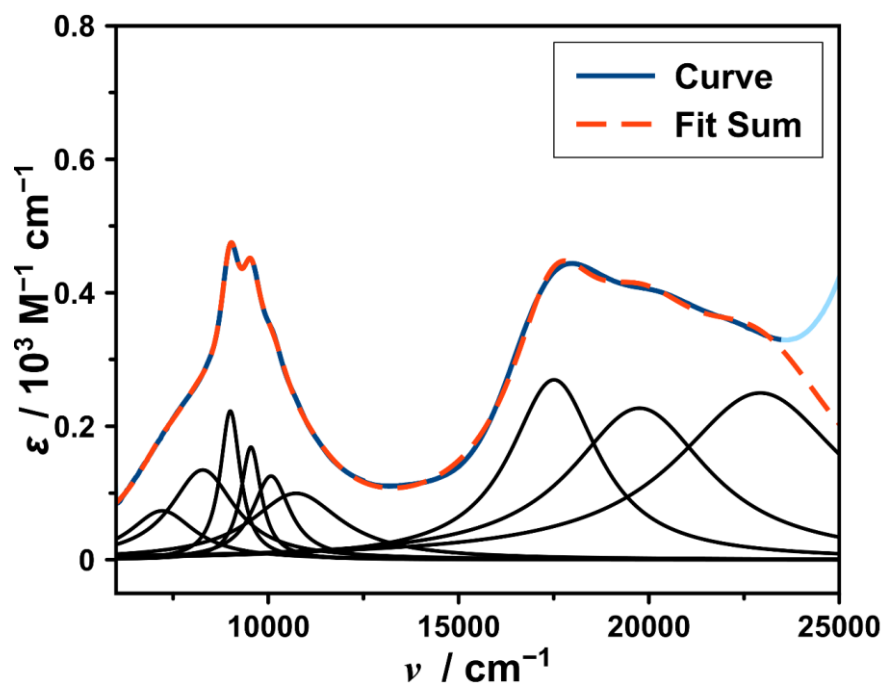


Figure A.59: Lorentzian fit of the NIR/Visible spectrum of **2b** in MeCN at 273 K.

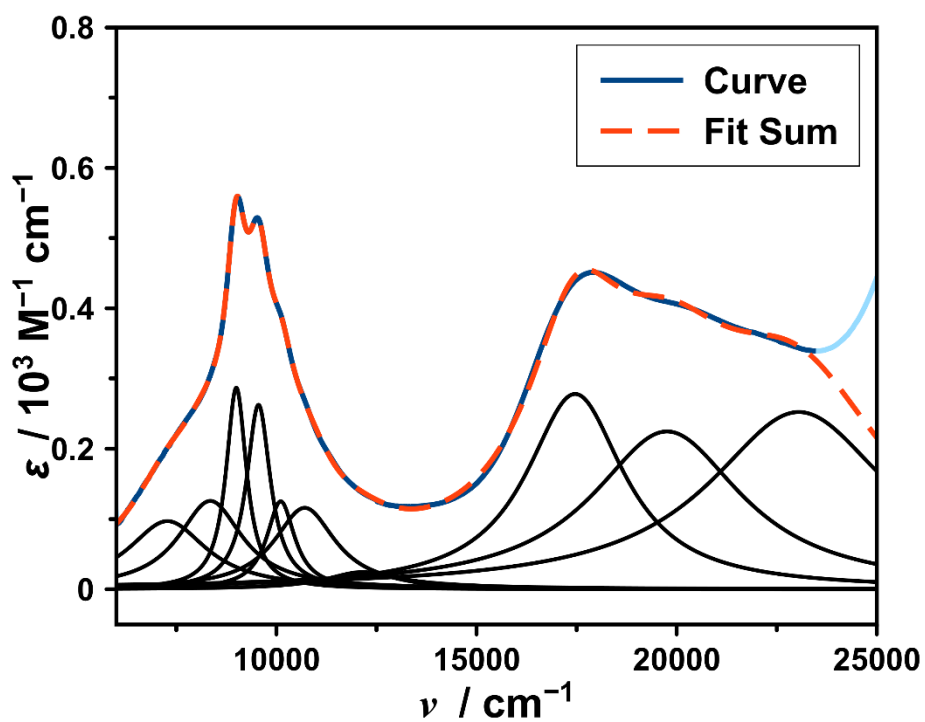


Figure A.60: Lorentzian fit of the NIR/Visible spectrum of **2b** in MeCN at 283 K.

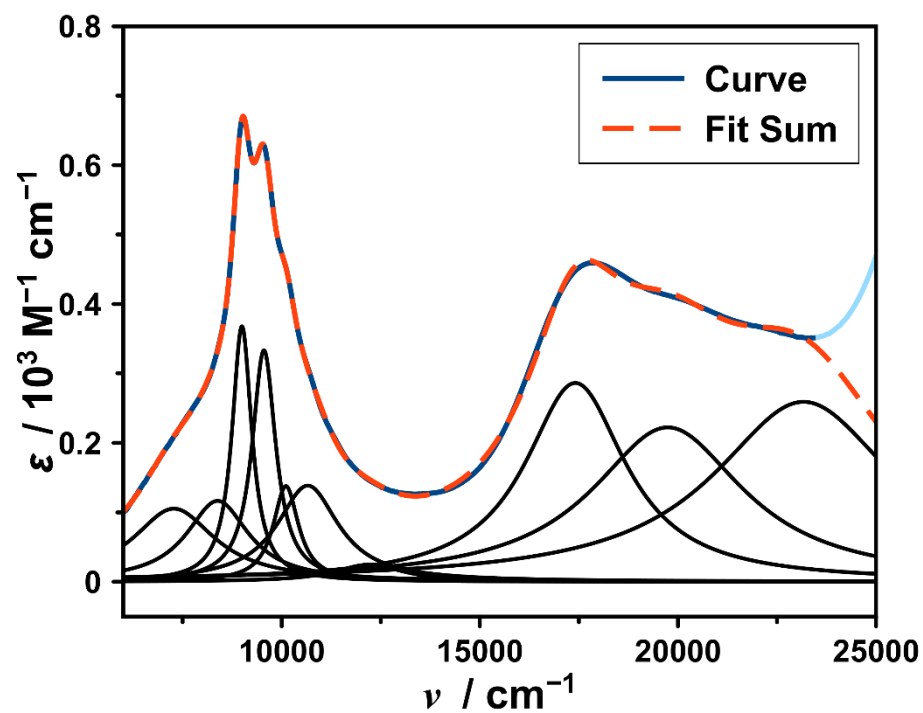


Figure A.61: Lorentzian fit of the NIR/Visible spectrum of **2b** in MeCN at 293 K.

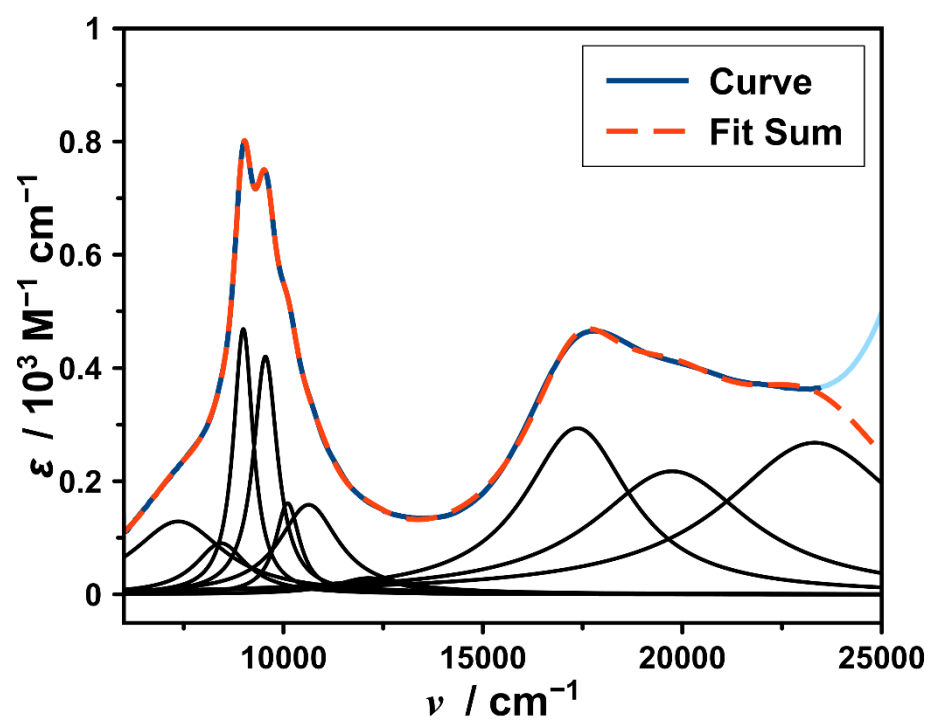


Figure A.62: Lorentzian fit of the NIR/Visible spectrum of **2b** in MeCN at 303 K.

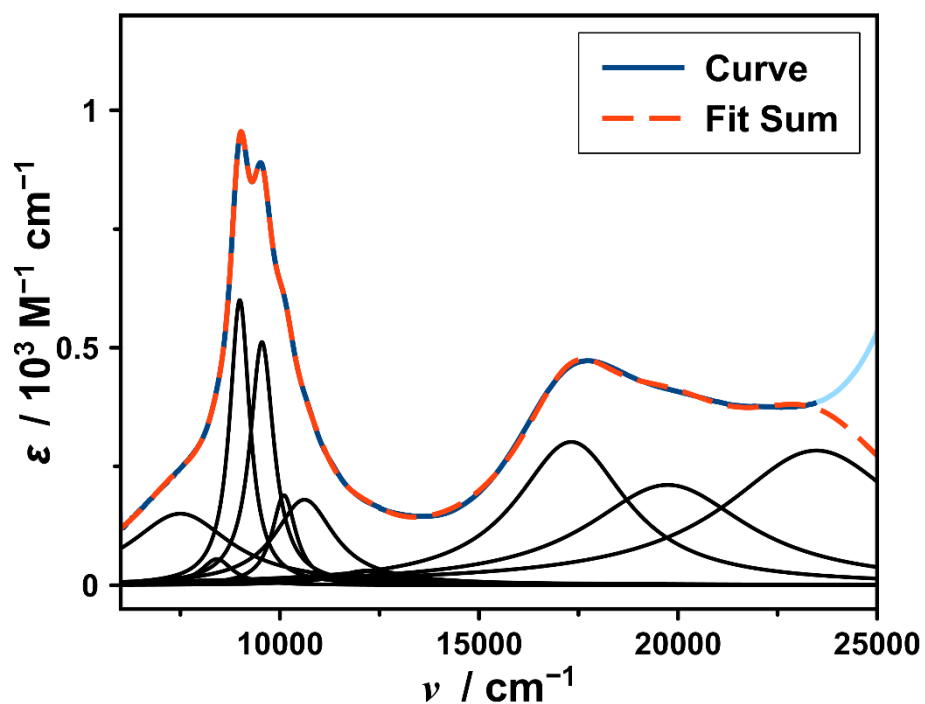


Figure A.63: Lorentzian fit of the NIR/Visible spectrum of **2b** in MeCN at 313 K.

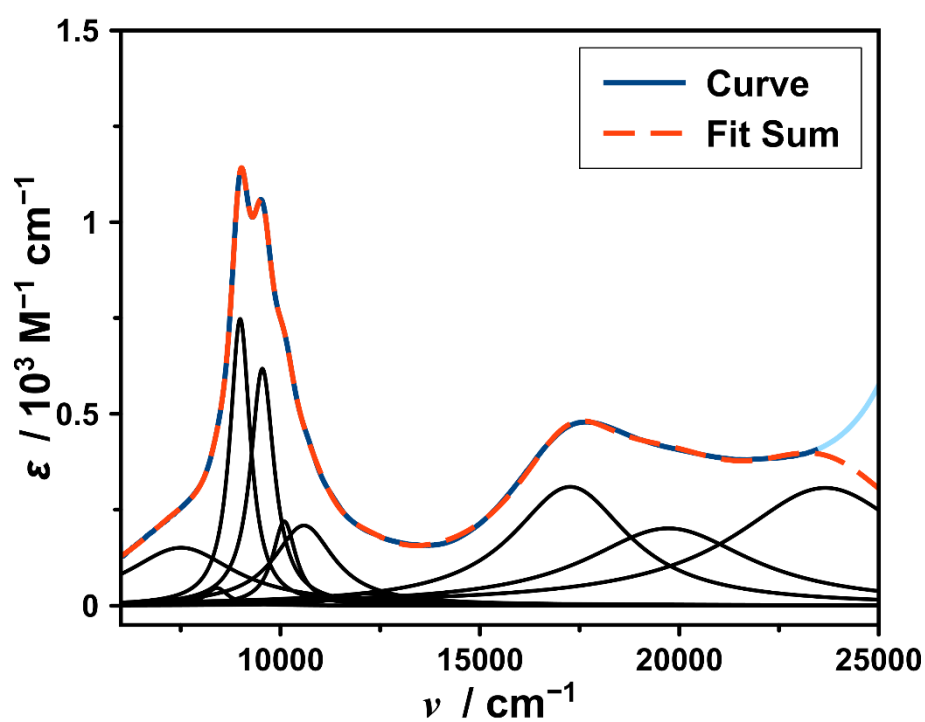


Figure A.64: Lorentzian fit of the NIR/Visible spectrum of **2b** in MeCN at 323 K.

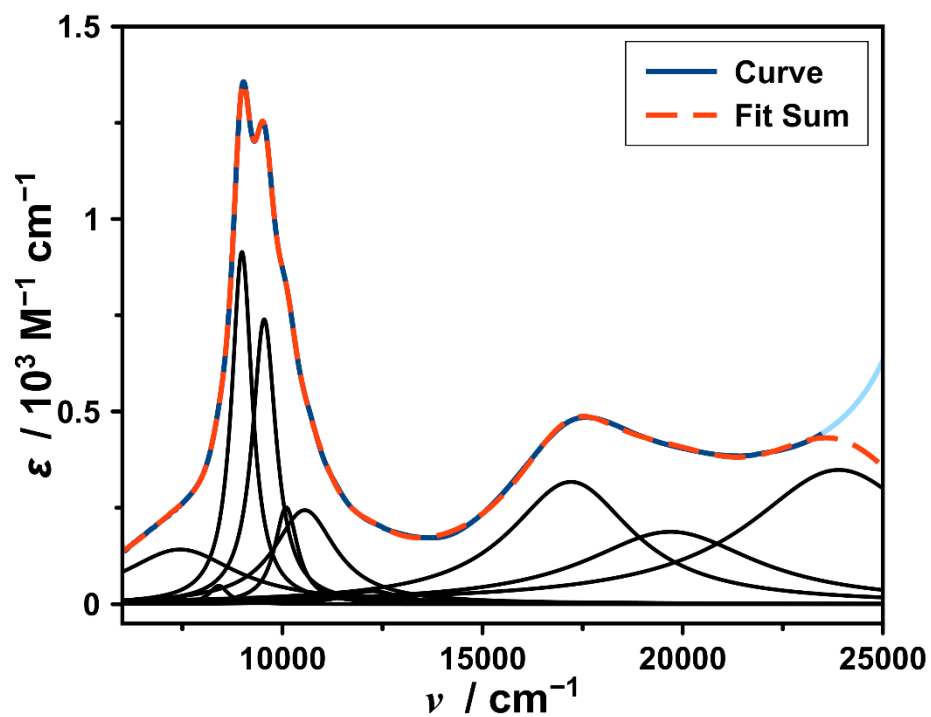


Figure A.65: Lorentzian fit of the NIR/Visible spectrum of **2b** in MeCN at 333 K.

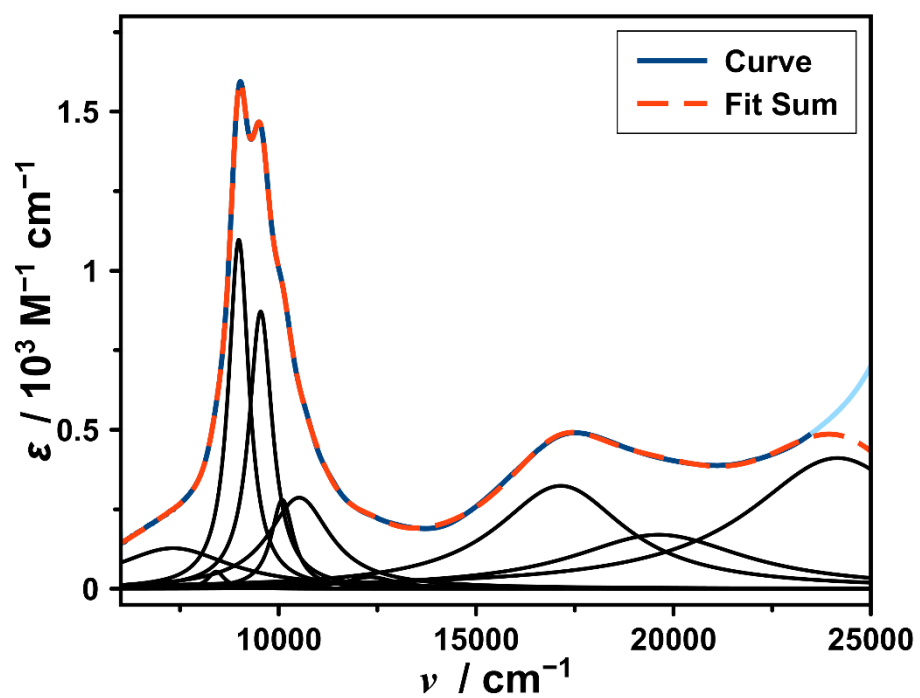


Figure A.66: Lorentzian fit of the NIR/Visible spectrum of **2b** in MeCN at 343 K.

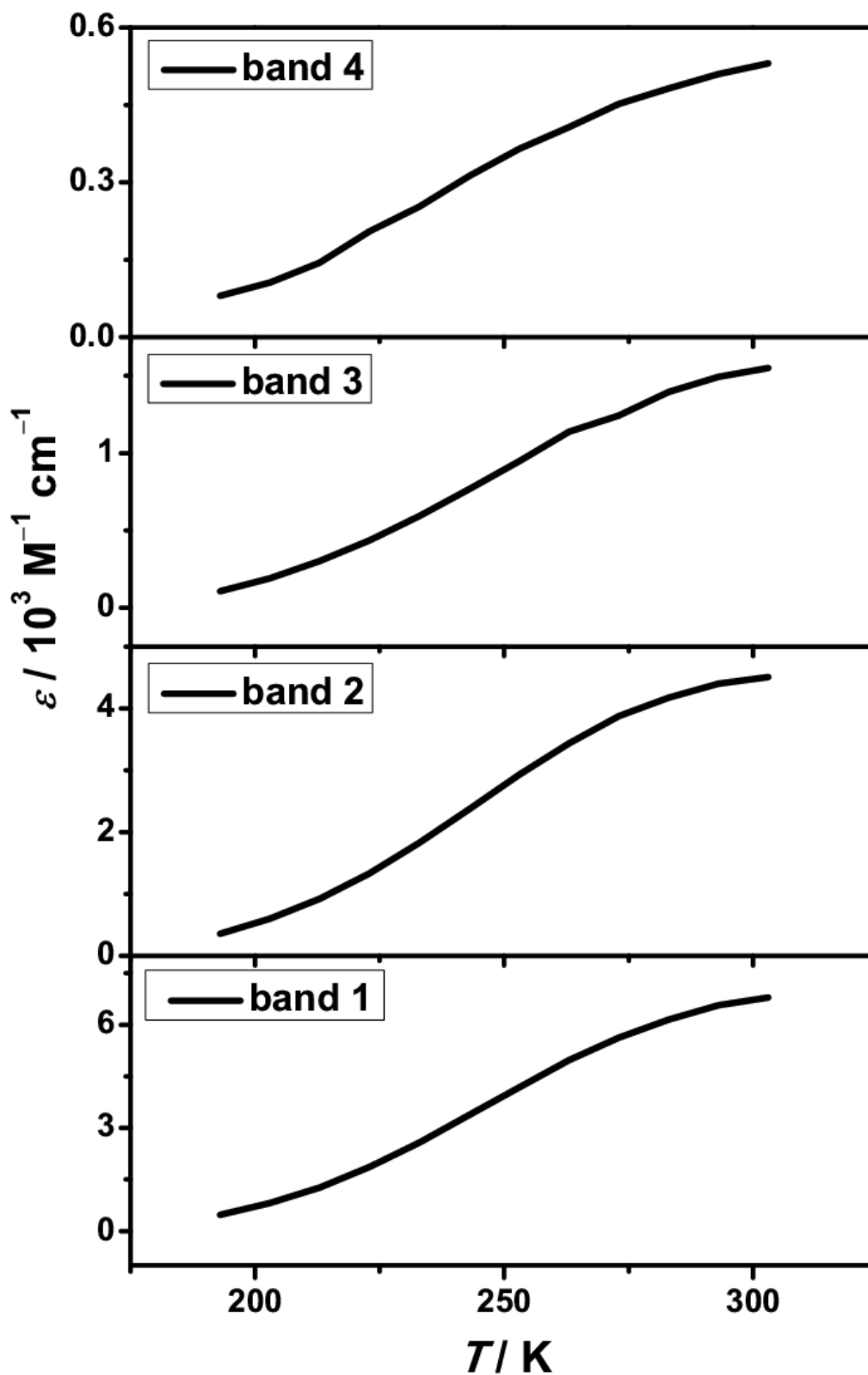


Figure A.67: ϵ vs. T plots for the bands at $\lambda_{\text{max}} = 1112 \text{ nm}$ (band 1), $\lambda_{\text{max}} = 1051 \text{ nm}$ (band 2), $\lambda_{\text{max}} = 993 \text{ nm}$ (band 3), $\lambda_{\text{max}} = 934 \text{ nm}$ (band 4), derived from the Lorentzian fit of the variable temperature UV/Vis/NIR spectra of **2b** in DCM.

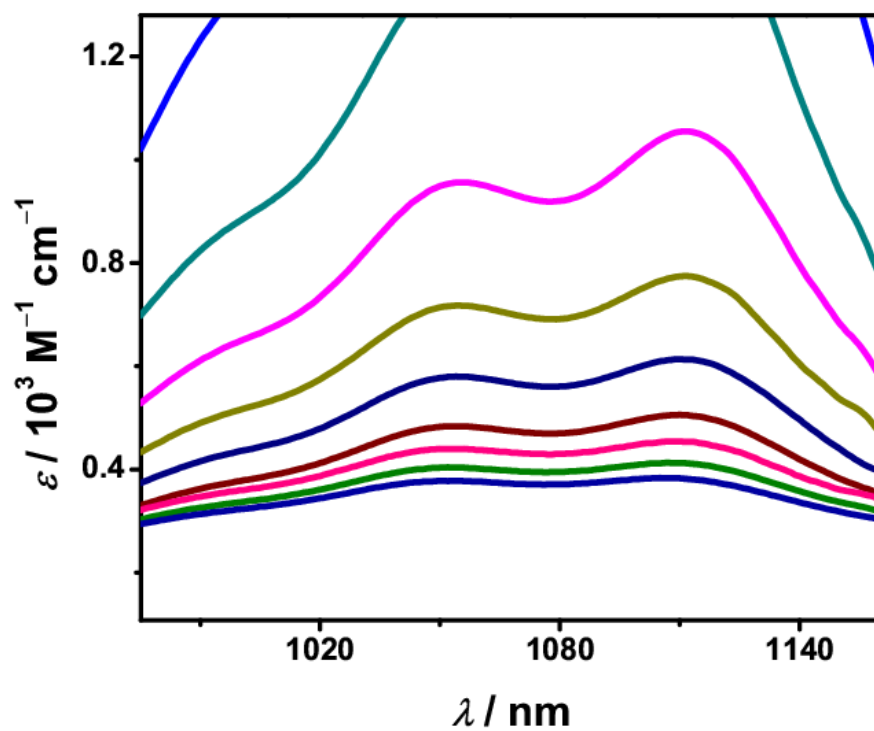


Figure A.68: Expanded spectra in the NIR region for the UV/Vis/NIR spectra of **2b** in DCM and DMSO and in varying ratio of (DCM/DMSO) mixture at 298 K.

6.1.5 Cyclic Voltammograms

Table A.8: Cyclic voltammetry data for the first reduction of **2b** and first oxidation of **2e**; Half-wave potential ($E_{1/2}$), difference between peak potentials (ΔE), peak current ratio (i_{pa}/i_{pc}), scan rate (ν).

	$\nu/\text{mV s}^{-1}$	$E_{1/2}/\text{mV}$	$\Delta E/\text{mV}$	i_{pa}/i_{pc}
Reduction 1	200	-56	103	1
	100	-56	86	1
	50	-54	76	0.99
	20	-53	66	0.97
	10	-53	58	0.96
Oxidation 1	200	711	94	1.05
	100	711	84	1.01
	50	713	79	0.99
	20	716	87	1.01

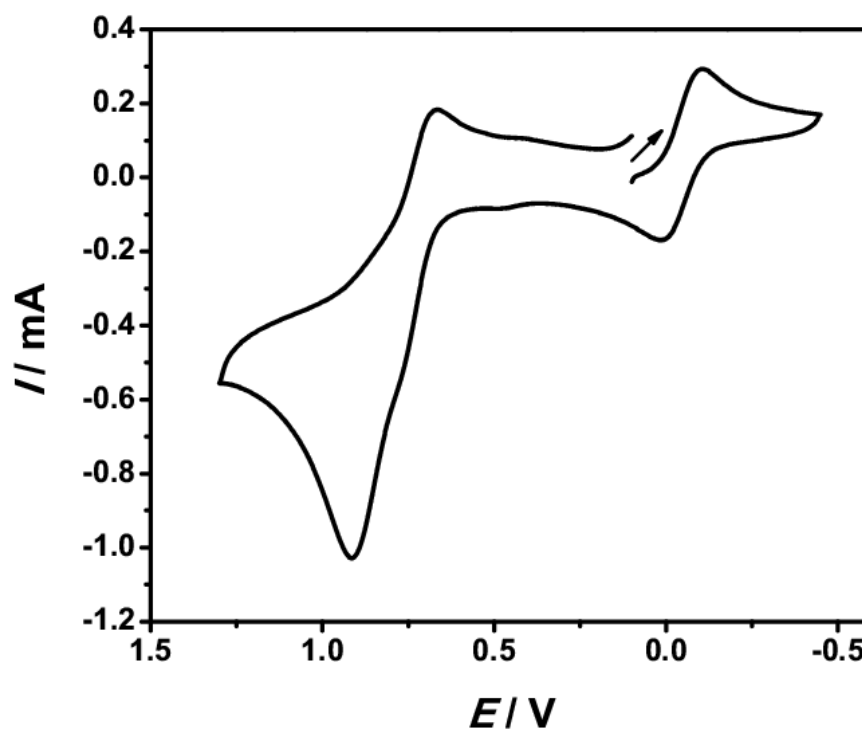


Figure A.69: Cyclic voltammogram of **2b** in 0.2 M TBAP/MeCN at scan rate $\nu = 100$ mV/s.

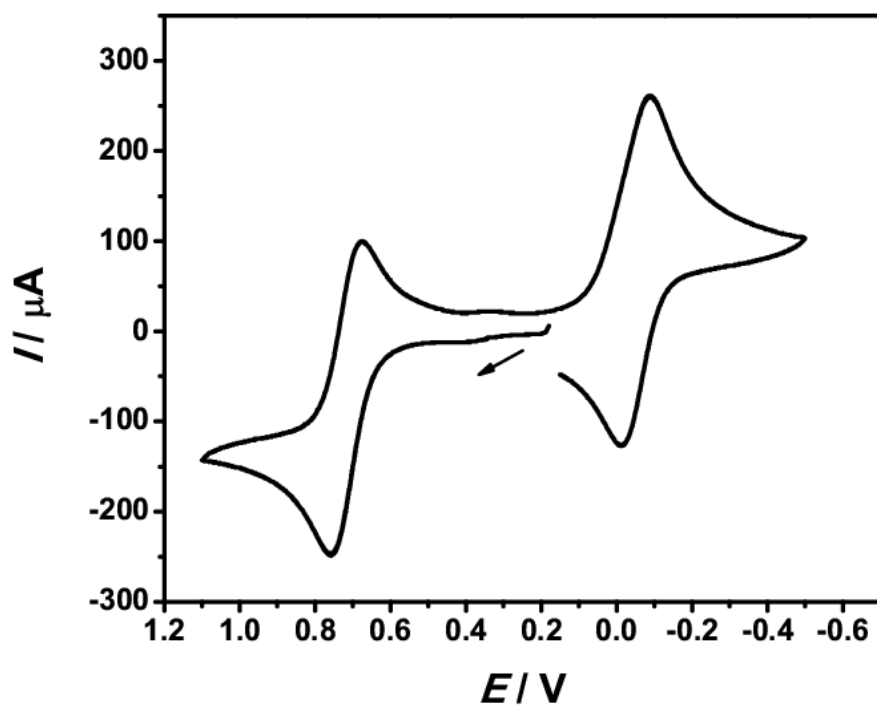


Figure A.70: Cyclic voltammogram of $2e$ in 0.2 M TBAP/MeCN at scan rate $v = 100$ mV/s.

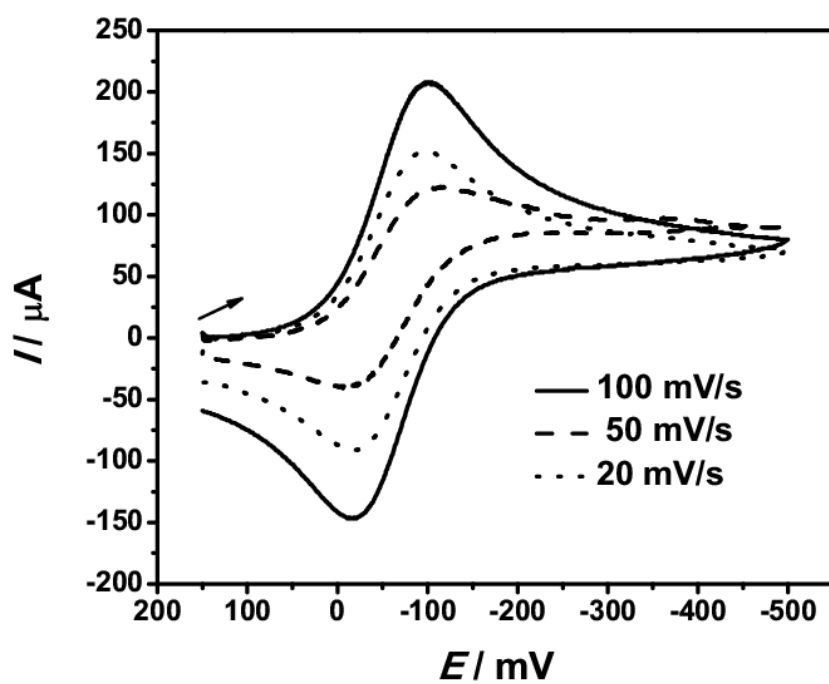


Figure A.71: Cyclic voltammograms for the first reductive processes of $2e$ at different scan rates in 0.2 M TBAP/MeCN.

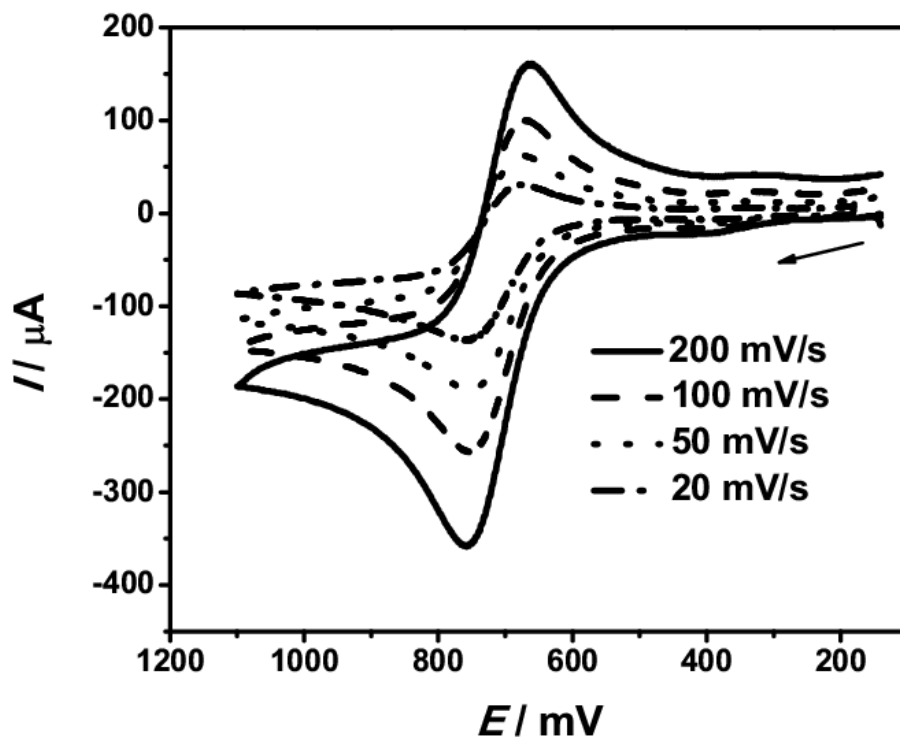


Figure A.72: Cyclic voltammograms for the first oxidative processes of **2e** in 0.2 M TBAP/MeCN at different scan rates.

6.2 Switching of the Electronic States of Bis(dioxolene) Ligands Triggered by Cobalt(II) Based Temperature-Induced Spin-Crossover and Cobalt-Ligand Based Electron Transfer Processes

6.2.1 Crystal Data

X-ray crystallographic data for compound **3b** were collected in the temperature range 100(2)–300(2) K and for compound **3d** and **3e**·solv the data were collected at 150 K. The data were collected by an Oxford Diffraction Gemini S Ultra type of instrument using graphite-monochromatized Cu- K_{α} ($\lambda = 1.54184 \text{ \AA}$) or Mo- K_{α} ($\lambda = 0.71073 \text{ \AA}$) radiation. The crystal structures were solved by direct methods implemented in the SIR 97 program package and refined using the full-matrix least-squares method on F^2 with SHELXL-97 package. The hydrogen atoms were located geometrically and refined using Riding model. For the temperature factor, 1.5 times value for hydrogen atoms of CH₃ groups and for all other hydrogen atoms 1.2 times value of the equivalent isotropic temperature factor of that atom used, to which the respective hydrogen atom is bonded. All non-hydrogen atoms were refined with anisotropic displacement parameters.

Table A.9: Crystal data and structure refinement for **3b** at 100 K.

Identification code	14264ocu
Empirical formula	C ₅₈ H ₆₉ BCoN ₆ O ₄
Formula weight [g mol ⁻¹]	983.93
Temperature [K]	100(2)
λ [Å]	1.54184
Crystal system	triclinic
Space group	$P\bar{1}$
a [Å]	9.6267(3)
b [Å]	15.1529(6)
c [Å]	18.8180(6)
α [deg]	100.948(3)
β [deg]	95.389(2)
γ [deg]	104.477(3)
V [Å ³]	2580.47(16)
Z	2
ρ_{calcd} [g cm ⁻³]	1.266
$\mu(\text{Cu-}K\alpha)$ [mm ⁻¹]	3.019
$F(000)$	1046
Crystal size [mm ³]	0.450 × 0.110 × 0.110
θ [deg]	3.476–62.775
Reflections collected	20370
Independent reflections	8204
R_{int}	0.0202
Absorption correction	analytical
Max. and min. transmission	0.745 and 0.447
Refinement method	full-matrix least-squares on F^2
Data/restraints/parameters	8204/0/641
GOOF on F^2	1.031
Final R indices [$I > 2\sigma(I)$]	$R1 = 0.0363$, $wR2 = 0.0962$
R indices (all data)	$R1 = 0.0376$, $wR2 = 0.0975$
Largest diff. peak and hole [e Å ⁻³]	0.504 and -0.362

Table A.10: Crystal data and structure refinement for **3b** at 150 K.

Identification code	14260ocu
Empirical formula	$C_{58}H_{69}BCoN_6O_4$
Formula weight [g mol ⁻¹]	983.93
Temperature [K]	150(2)
λ [Å]	1.54184
Crystal system	triclinic
Space group	$P\bar{1}$
a [Å]	9.6704(3)
b [Å]	15.1962(6)
c [Å]	18.9248(7)
α [deg]	100.554(3)
β [deg]	96.042(3)
γ [deg]	104.713(3)
V [Å ³]	2610.46(17)
Z	2
ρ_{calcd} [g cm ⁻³]	1.252
$\mu(\text{Cu-}K\alpha)$ [mm ⁻¹]	2.985
$F(000)$	1046
Crystal size [mm ³]	0.450 × 0.110 × 0.110
θ [deg]	4.305–62.655
Reflections collected	20687
Independent reflections	8305
R_{int}	0.0193
Absorption correction	analytical
Max. and min. transmission	0.747 and 0.460
Refinement method	full-matrix least-squares on F^2
Data/restraints/parameters	8305/0/641
GOOF on F^2	1.038
Final R indices [$I > 2\sigma(I)$]	$R1 = 0.0392$, $wR2 = 0.1047$
R indices (all data)	$R1 = 0.0408$, $wR2 = 0.1062$
Largest diff. peak and hole [e Å ⁻³]	0.493 and -0.421

Table A.11: Crystal data and structure refinement for **3b** at 200 K.

Identification code	14261ocu
Empirical formula	C ₅₈ H ₆₉ BCoN ₆ O ₄
Formula weight [g mol ⁻¹]	983.93
Temperature [K]	200(2)
λ [Å]	1.54184
Crystal system	triclinic
Space group	$P\bar{1}$
a [Å]	9.7148(3)
b [Å]	15.2263(7)
c [Å]	19.0171(8)
α [deg]	100.333(4)
β [deg]	96.380(3)
γ [deg]	104.797(3)
V [Å ³]	2638.95(19)
Z	2
ρ_{calcd} [g cm ⁻³]	1.238
$\mu(\text{Cu-}K_{\alpha})$ [mm ⁻¹]	2.952
$F(000)$	1046
Crystal size [mm ³]	0.450 × 0.110 × 0.110
θ [deg]	3.465–62.780
Reflections collected	18080
Independent reflections	8389
R_{int}	0.0204
Absorption correction	analytical
Max. and min. transmission	0.745 and 0.415
Refinement method	full-matrix least-squares on F^2
Data/restraints/parameters	8389/8/641
GOOF on F^2	1.042
Final R indices [$I > 2\sigma(I)$]	$R1 = 0.0413$, $wR2 = 0.1117$
R indices (all data)	$R1 = 0.0434$, $wR2 = 0.1136$
Largest diff. peak and hole [e Å ⁻³]	0.429 and -0.430

Table A.12: Crystal data and structure refinement for **3b** at 250 K.

Identification code	14262ocu
Empirical formula	$C_{58}H_{69}BCoN_6O_4$
Formula weight [g mol ⁻¹]	983.93
Temperature [K]	250(2)
λ [Å]	1.54184
Crystal system	triclinic
Space group	$P\bar{1}$
a [Å]	9.7496(2)
b [Å]	15.2368(7)
c [Å]	19.1195(7)
α [deg]	100.243(4)
β [deg]	96.416(3)
γ [deg]	104.693(3).
V [Å ³]	2666.63(17)
Z	2
ρ_{calcd} [g cm ⁻³]	1.225
$\mu(\text{Cu-}K\alpha)$ [mm ⁻¹]	2.922
$F(000)$	1046
Crystal size [mm ³]	0.450 × 0.110 × 0.110
θ [deg]	3.459–62.677
Reflections collected	17649
Independent reflections	8440
R_{int}	0.0181
Absorption correction	analytical
Max. and min. transmission	0.744 and 0.448
Refinement method	full-matrix least-squares on F^2
Data/restraints/parameters	8440/8/639
GOOF on F^2	1.024
Final R indices [$I > 2\sigma(I)$]	$R1 = 0.0423$, $wR2 = 0.1157$
R indices (all data)	$R1 = 0.0451$, $wR2 = 0.1186$
Largest diff. peak and hole [e Å ⁻³]	0.424 and -0.435

Table A.13: Crystal data and structure refinement for **3b** at 300 K.

Identification code	14263ocu
Empirical formula	C ₅₈ H ₆₉ BCoN ₆ O ₄
Formula weight [g mol ⁻¹]	983.93
Temperature [K]	300(2)
λ [Å]	1.54184
Crystal system	triclinic
Space group	$P\bar{1}$
a [Å]	9.7883(3)
b [Å]	15.2452(7)
c [Å]	19.2278(8)
α [deg]	100.150(4)
β [deg]	96.375(3)
γ [deg]	104.600(3)
V [Å ³]	2696.51(19)
Z	2
ρ_{calcd} [g cm ⁻³]	1.212
$\mu(\text{Cu-K}\alpha)$ [mm ⁻¹]	2.889
$F(000)$	0.450 × 0.110 × 0.110
Crystal size [mm ³]	1046
θ [deg]	3.452–62.670
Reflections collected	18305
Independent reflections	8548
R_{int}	0.0196
Absorption correction	analytical
Max. and min. transmission	0.745 and 0.445
Refinement method	full-matrix least-squares on F^2
Data/restraints/parameters	8548/8/639
GOOF on F^2	1.016
Final R indices [$I > 2\sigma(I)$]	$R1 = 0.0464$, $wR2 = 0.1304$
R indices (all data)	$R1 = 0.0506$, $wR2 = 0.1346$
Largest diff. peak and hole [e Å ⁻³]	0.403 and -0.477

Table A.14: Crystal data and structure refinement for **3d** at 150 K.

Identification code	14311o_sq
Empirical formula	C ₅₆ H ₇₀ B ₂ Co ₂ F ₈ N ₈ O ₄
Formula weight [g mol ⁻¹]	1210.68
Temperature [K]	150(2)
λ [Å]	0.71073
Crystal system	monoclinic
Space group	<i>P</i> 2 ₁ / <i>c</i>
<i>a</i> [Å]	21.0374(6)
<i>b</i> [Å]	11.9243(3)
<i>c</i> [Å]	13.7109(4)
α [deg]	90
β [deg]	103.968(3)
γ [deg]	90
<i>V</i> /Å ³	3337.76(17)
<i>Z</i>	2
ρ_{calcd} [g cm ⁻³]	1.205
$\mu(\text{Cu-}K\alpha)$ [mm ⁻¹]	0.564
<i>F</i> (000)	1260
Crystal size/mm ³	0.430 × 0.300 × 0.120
θ [deg]	2.787–29.994
Reflections collected	19132
Independent reflections	9724
<i>R</i> _{int}	0.0336
Absorption correction	semi-empirical from equivalents
Max. and min. transmission	1.00000 and 0.94767
Refinement method	full-matrix least-squares on <i>F</i> ²
Data/restraints/parameters	9724/0/367
GOOF on <i>F</i> ²	1.000
Final <i>R</i> indices [<i>I</i> > 2σ(<i>I</i>)]	<i>R</i> 1 = 0.0458, <i>wR</i> 2 = 0.1107
<i>R</i> indices (all data)	<i>R</i> 1 = 0.0742, <i>wR</i> 2 = 0.1241
Largest diff. peak and hole [e Å ⁻³]	0.537 and -0.444

Table A.15: Crystal data and structure refinement for **3e**·solv at 150 K.

Identification code	12093oc
Empirical formula	C ₄₅ H ₄₅ Cl ₀ Co _{1.13} F ₀ N _{4.50} O _{2.25} P ₀
Formula weight [g mol ⁻¹]	751.15
Temperature [K]	150(2)
Wavelength [Å]	1.54184
Crystal system	Monoclinic
Space group	<i>P</i> 121/ <i>n</i> 1
<i>a</i> [Å]	14.2421(3)
<i>b</i> [Å]	12.8057(2)
<i>c</i> [Å]	40.8007(8)
α [deg]	90
β [deg]	98.7(2)
γ [deg]	90
<i>V</i> /Å ³	7354.7(2)
<i>Z</i>	8
ρ_{calcd} [g cm ⁻³]	1.357
$\mu(\text{Cu-}K\alpha)$ [mm ⁻¹]	4.445
F(000)	3159
Crystal size/mm ³	x ? x ? x ?
θ [deg]	3.16 to 62.68
Reflections collected	34619
Independent reflections	11715
<i>R</i> _{int}	0.0575
Absorption correction	Semi-empirical from equivalents
Max. and min. transmission	1 and 0.30775
Refinement method	Full-matrix least-squares on <i>F</i> ²
Data/restraints/parameters	11715 / 0 / 805
GOOF on <i>F</i> ²	0.993
Final <i>R</i> indices [<i>I</i> > 2σ(<i>I</i>)]	<i>R</i> 1 = 0.0909, <i>wR</i> 2 = 0.2661
<i>R</i> indices (all data)	<i>R</i> 1 = 0.1219, <i>wR</i> 2 = 0.2973
Largest diff. peak and hole [e Å ⁻³]	1.373 and -0.844

6.2.2 Infrared Spectra

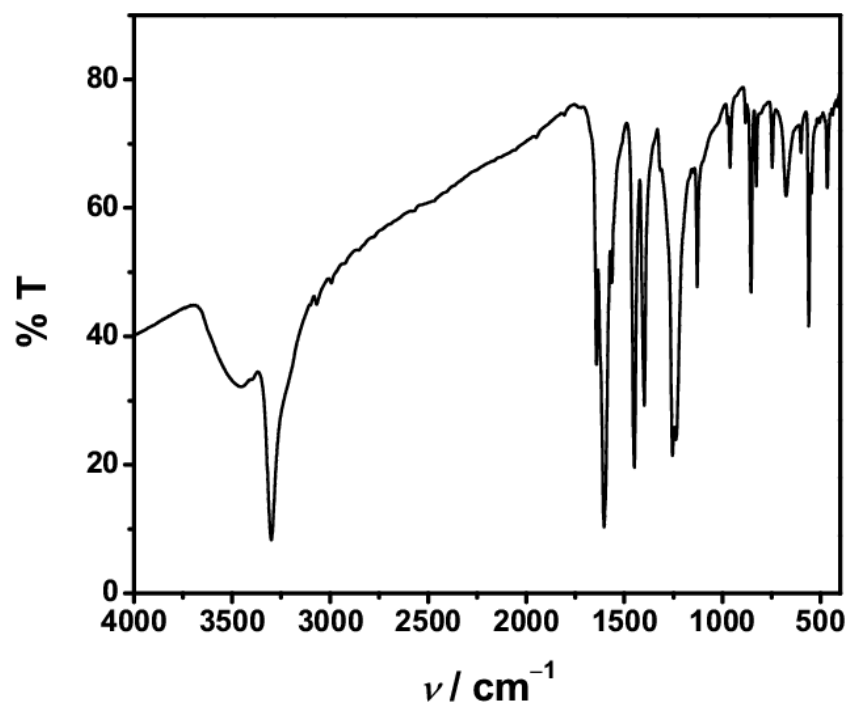


Figure A.73: IR spectrum of 3,3'-dihydroxy-diphenoquinone-(4,4') ($\text{H}_2(\text{SQ-SQ})$) in KBr pellet at RT.

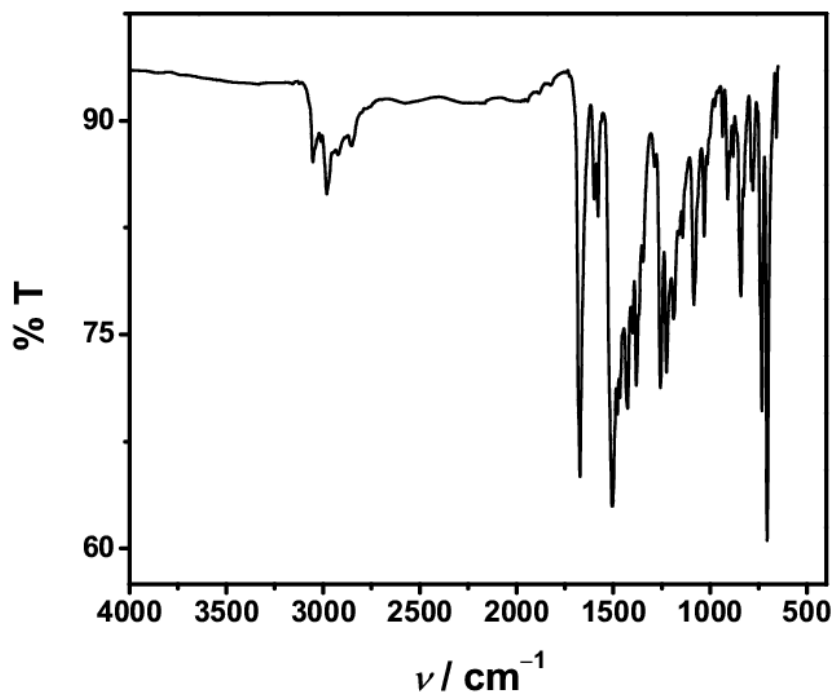


Figure A.74: ATR spectrum of $[\text{Co}_2(\text{L-N}_4\text{tBu}_2)(\text{SQ-SQ})](\text{BPh}_4)_2 \cdot 4 \text{ DMF}$ (**3b**) at RT.

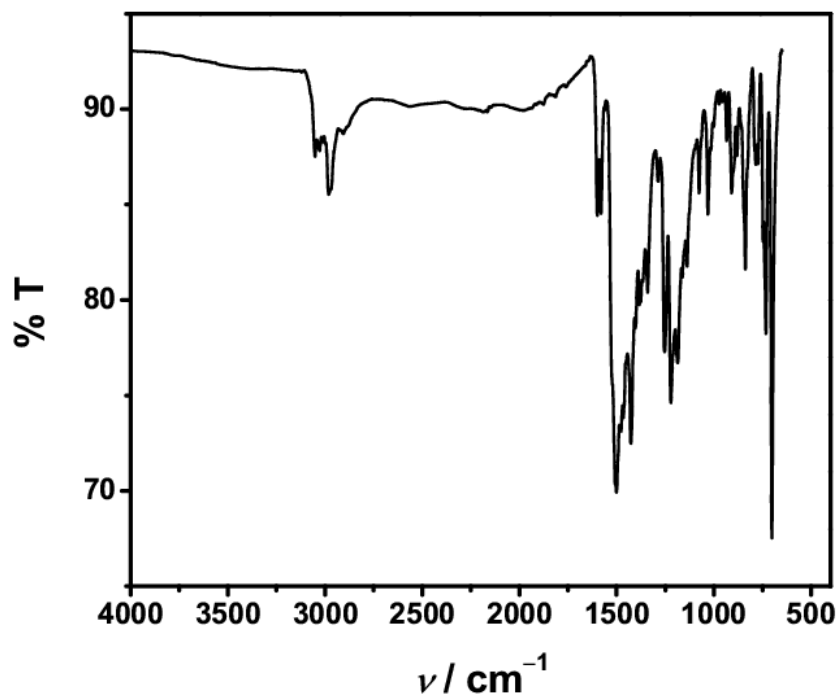


Figure A.75: ATR spectrum of $[\text{Co}_2(\text{L-N}_4\text{tBu}_2)_2(\text{SQ-SQ})](\text{BPh}_4)_2$ (**3a**) at RT.

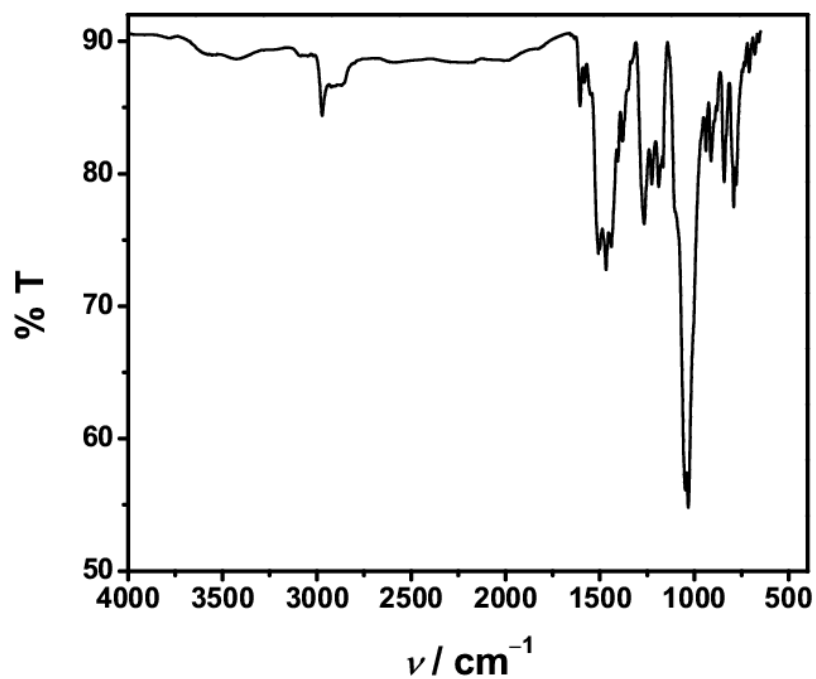


Figure A.76: ATR spectrum of $[\text{Co}_2(\text{L-N}_4\text{tBu}_2)_2(\text{Cat-SQ})](\text{BF}_4)_2 \cdot \text{Et}_2\text{O}$ (**3d**) at RT.

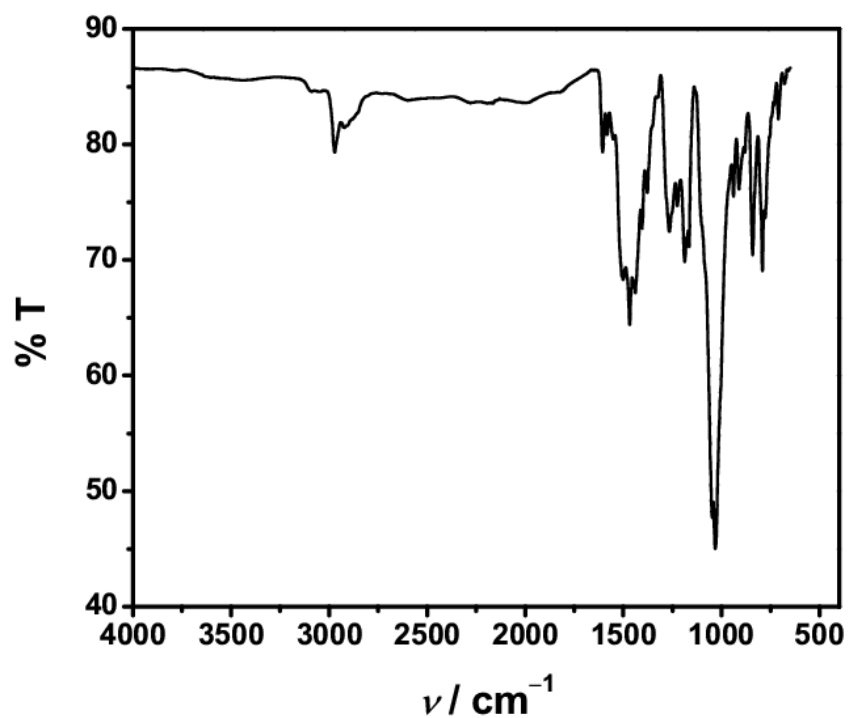


Figure A.77: ATR spectrum of $[\text{Co}_2(\text{L-N}_4\text{tBu}_2)(\text{Cat-SQ})](\text{BF}_4)_2$ (**3c**) at RT.

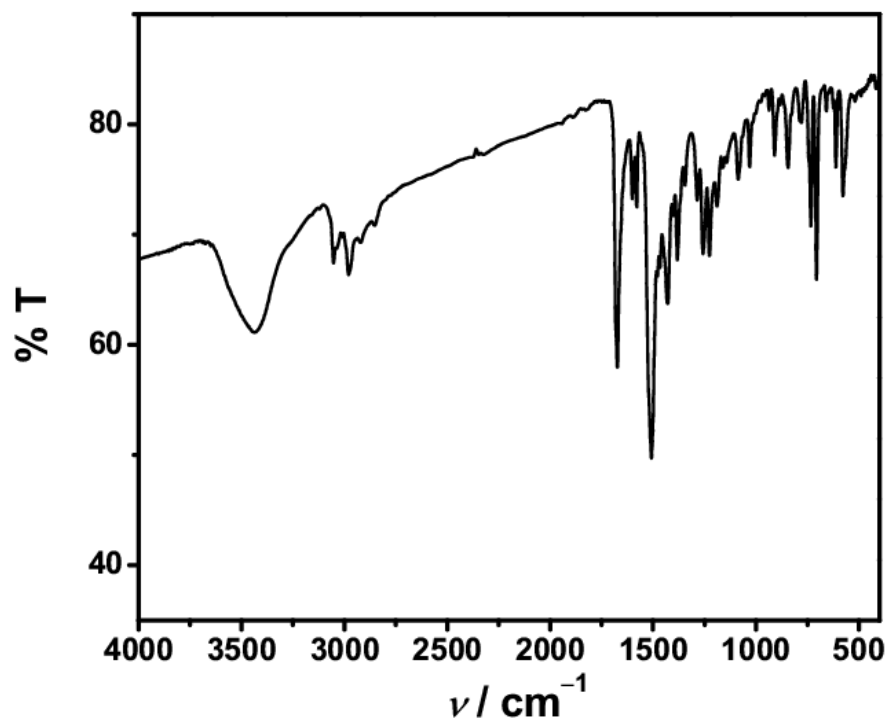


Figure A.78: IR spectrum of $[\text{Co}_2(\text{L-N}_4\text{tBu}_2)(\text{SQ-SQ})](\text{BPh}_4)_2 \cdot 4 \text{ DMF}$ (**3b**) in KBr pellet at RT.

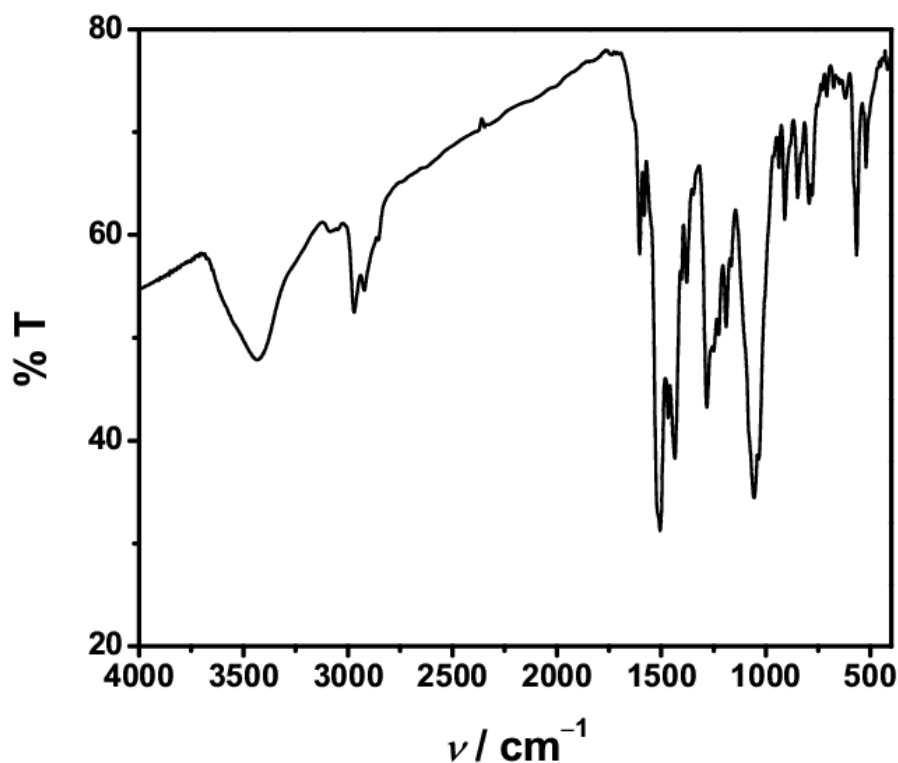


Figure A.79: IR spectrum of $[\text{Co}_2(\text{L-N}_4\text{tBu}_2)_2(\text{Cat-SQ})](\text{BF}_4)_2 \cdot \text{Et}_2\text{O}$ (**3d**) in KBr pellet at RT.

Deconvolution of the IR Spectra

The Gaussian fit of the IR spectra of the complexes **3a**, **3b**, **3c** and **3d** are shown in Figures A.80–A.85. The Gaussian peaks are represented mainly as black solid lines. However, the peaks which are of interest are shown as red and green solid lines. The sum of the fitted spectrum is shown by orange-red dashed line. The IR spectrum in the range of the data points used for the deconvolution is shown by blue solid lines.

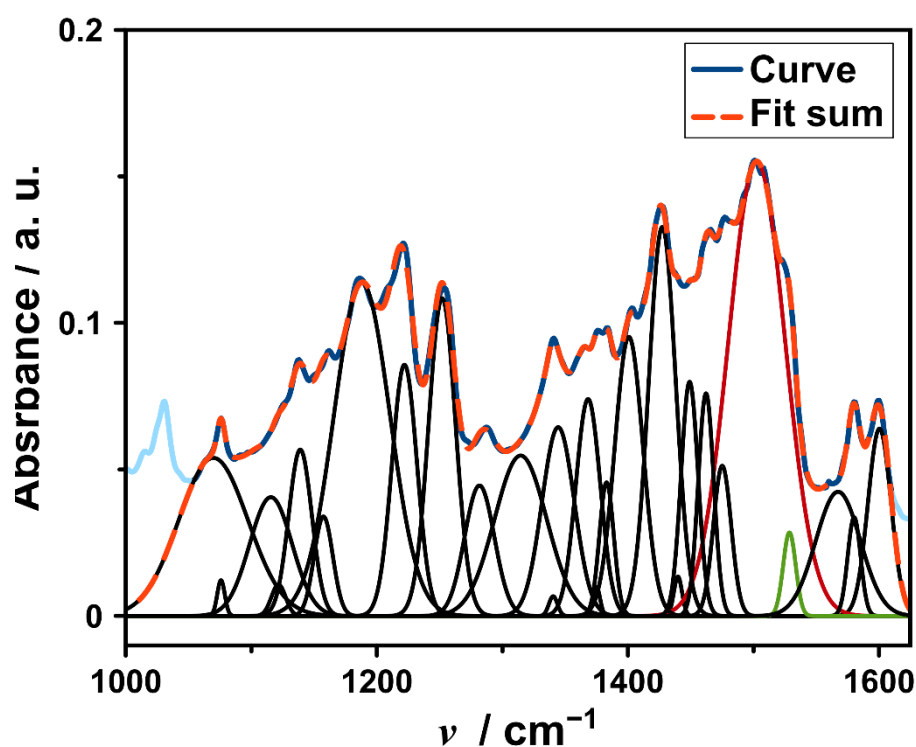


Figure A.80: Deconvoluted ATR spectrum of $[\text{Co}_2(\text{L-N}_4\text{tBu}_2)_2(\text{SQ-SQ})](\text{BPh}_4)_2$ (**3a**) at RT; Deconvolution was performed in the wavenumber range of 1053–1610 cm^{-1} . Adj. R^2 of fit is 0.998.

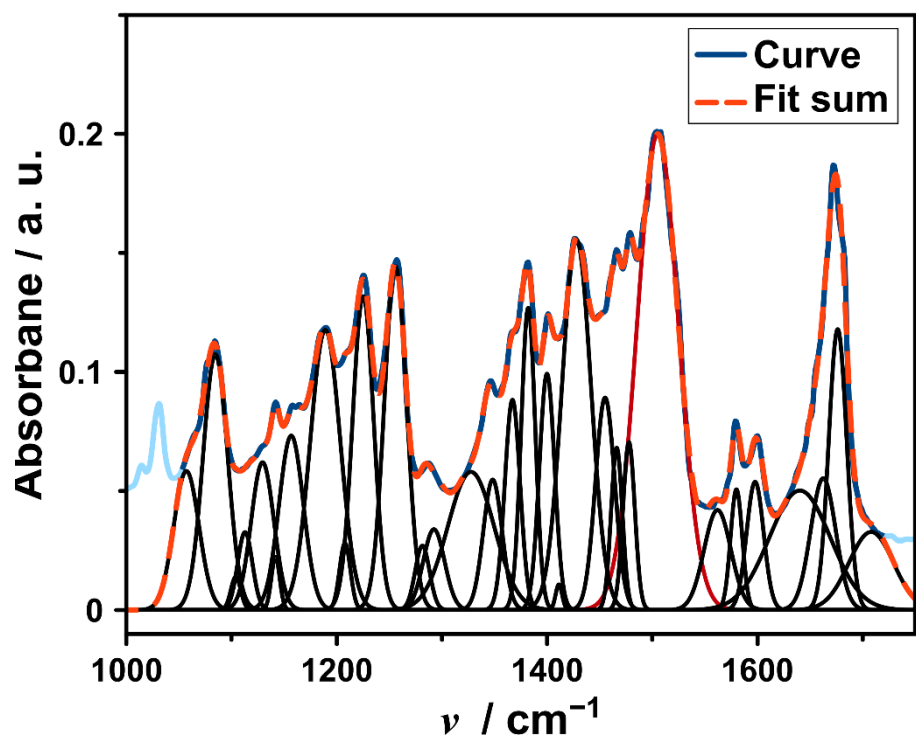


Figure A.81: Deconvoluted ATR spectrum of $[\text{Co}_2(\text{L-N}_4\text{tBu}_2)_2(\text{SQ-SQ})](\text{BPh}_4)_2 \cdot 4 \text{ DMF}$ (**3b**) at RT; Deconvolution was performed in the wavenumber range of 1053–1720 cm^{-1} and Adj. R^2 of fit is 0.997.

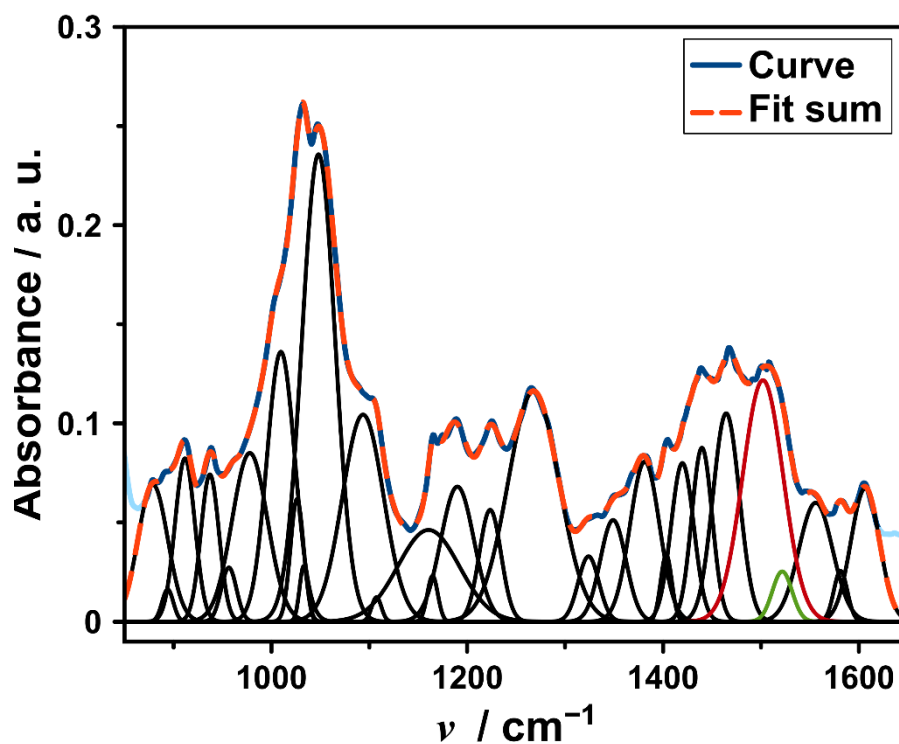


Figure A.82: Deconvoluted ATR spectrum of $[\text{Co}_2(\text{L-N}_4\text{tBu}_2)_2(\text{Cat-SQ})](\text{BF}_4)_2$ (**3c**) at RT; Deconvolution was performed in the wavenumber range of 870–1620 cm^{-1} and Adj. R^2 of the fit is 0.999.

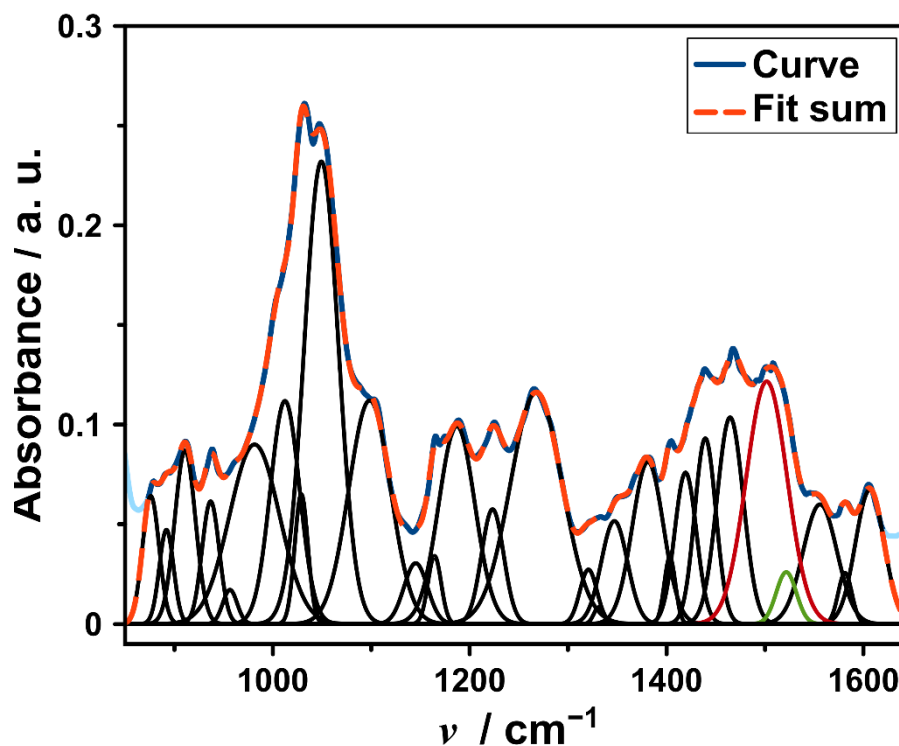


Figure A.83: Deconvoluted ATR spectrum of $[\text{Co}_2(\text{L-N}_4\text{tBu}_2)_2(\text{Cat-SQ})](\text{BF}_4)_2 \cdot \text{Et}_2\text{O}$ (**3d**) at RT; Deconvolution was performed in the wavenumber range of 873–1620 cm^{-1} and Adj. R^2 of the fit is 0.999.

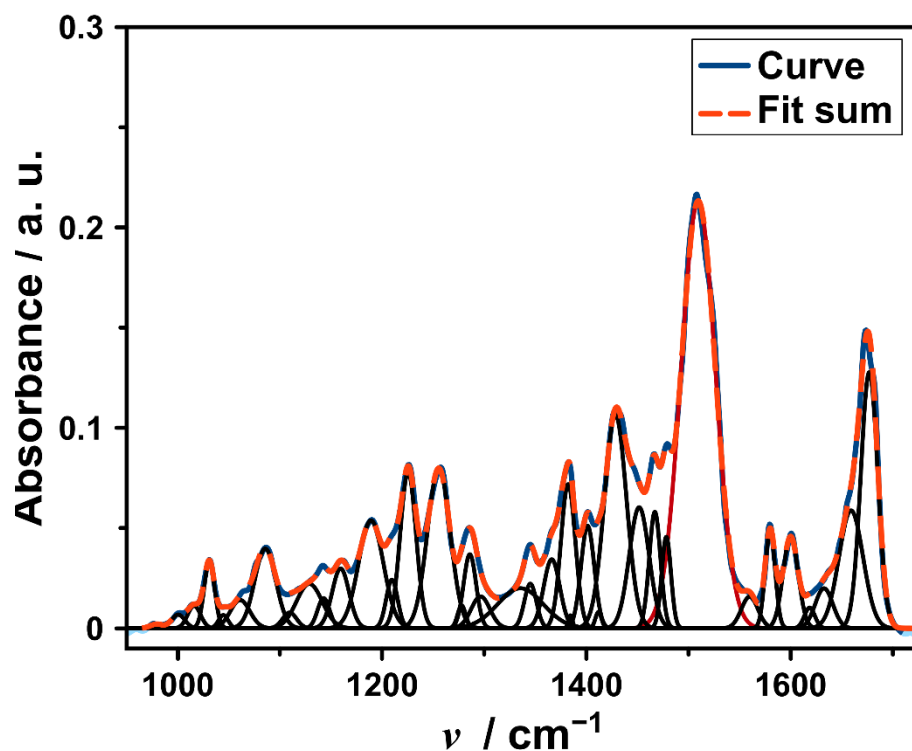


Figure A.84: Deconvoluted IR spectrum of $[\text{Co}_2(\text{L-N}_4\text{tBu}_2)_2(\text{SQ-SQ})](\text{BPh}_4)_2 \cdot 4 \text{ DMF}$ (**3b**) in KBr pellet at RT; Deconvolution was performed in the wavenumber range of 970–1710 cm^{-1} and Adj. R^2 of the fit is 0.997.

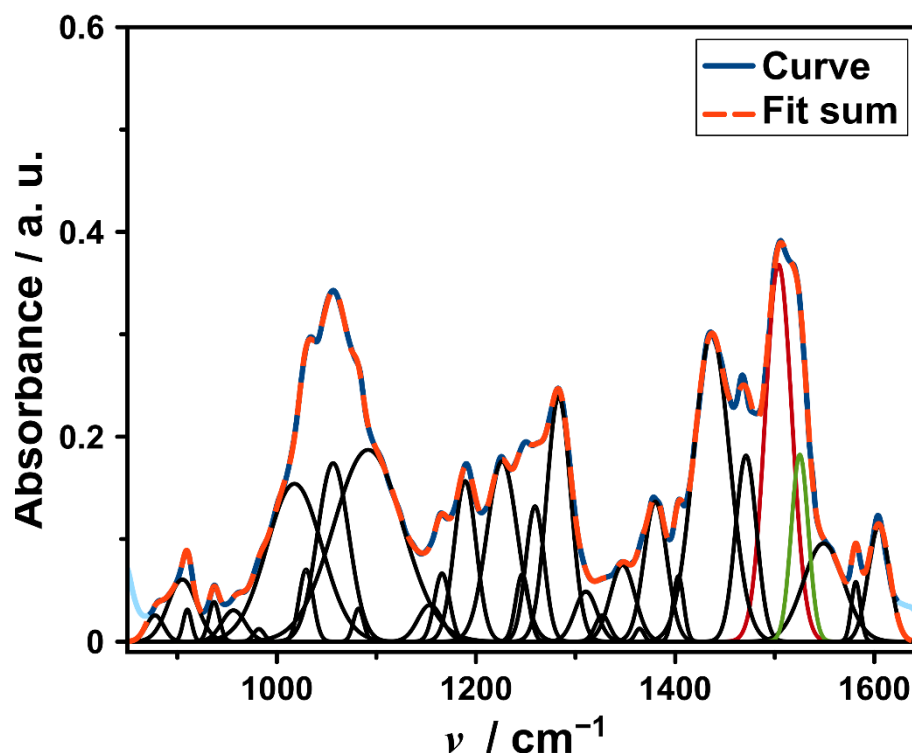


Figure A.85: Deconvoluted IR spectrum of $[\text{Co}_2(\text{L-N}_4\text{tBu}_2)_2(\text{Cat-SQ})](\text{BF}_4)_2 \cdot \text{Et}_2\text{O}$ (**3d**) in KBr pellet at RT; Deconvolution was performed in the wavenumber range of 871–1624 cm^{-1} and Adj. R^2 of the fit is 0.999.

6.2.3 NMR Spectra

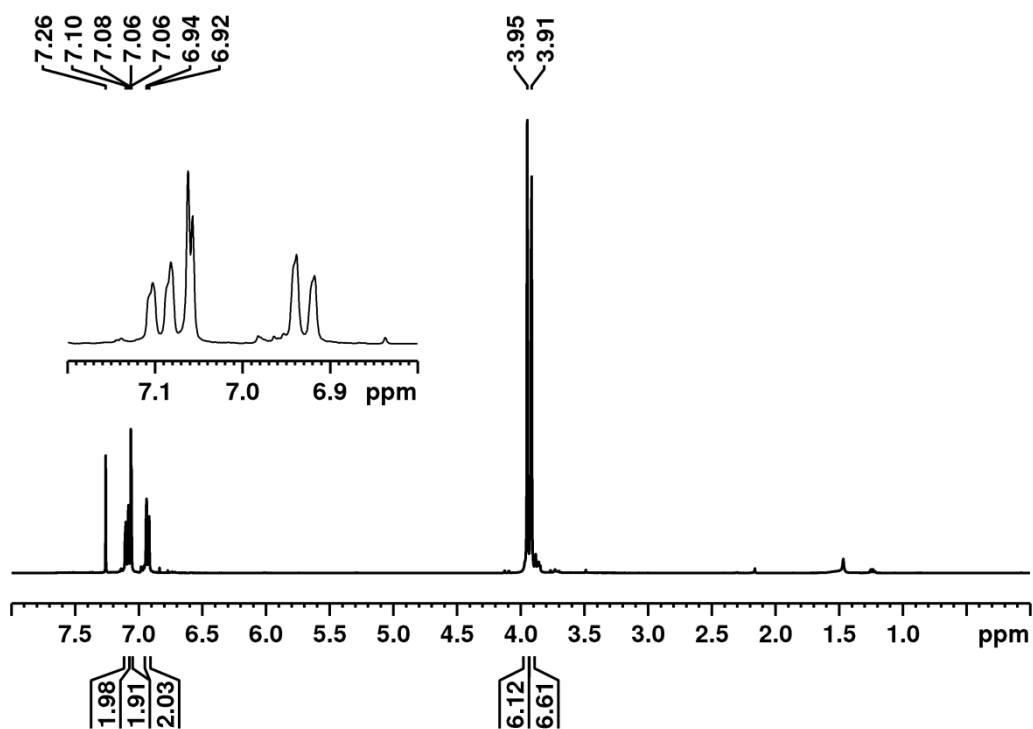


Figure A.86: ^1H NMR spectrum of 3,3',4,4'-tetramethoxybiphenyl in $[\text{D}]\text{CHCl}_3$ at RT.

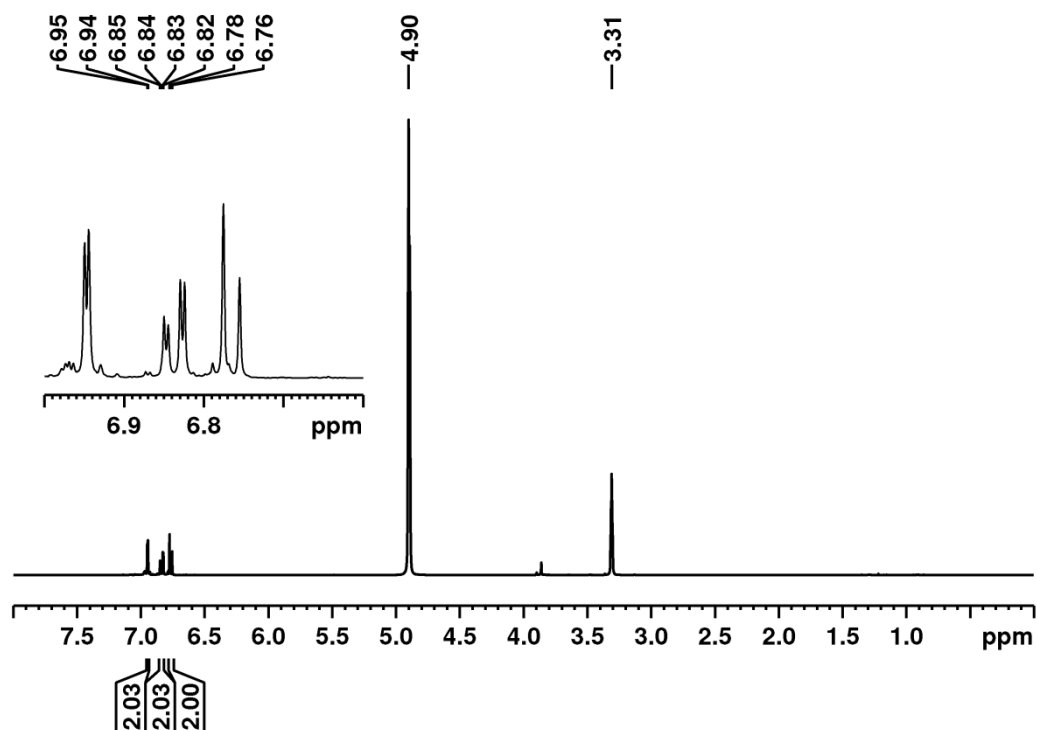


Figure A.87: ^1H NMR spectrum of 3,3',4,4'-tetrahydroxybiphenyl in $[\text{D}_4]\text{MeOH}$ at RT.

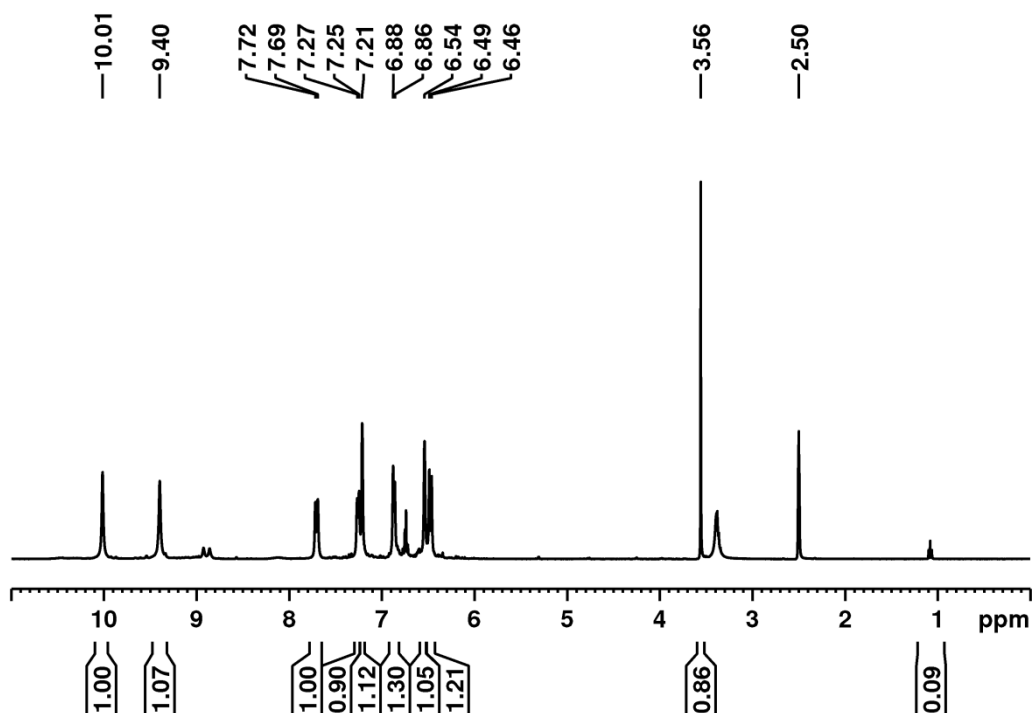


Figure A.88: ^1H NMR spectrum of 3,3'-dihydroxy-diphenylquinone-(4,4') ($\text{H}_2(\text{SQ-SQ})$) in $[\text{D}_6]\text{DMSO}$ at RT. The spectrum was measured initially from a sample of the compound.

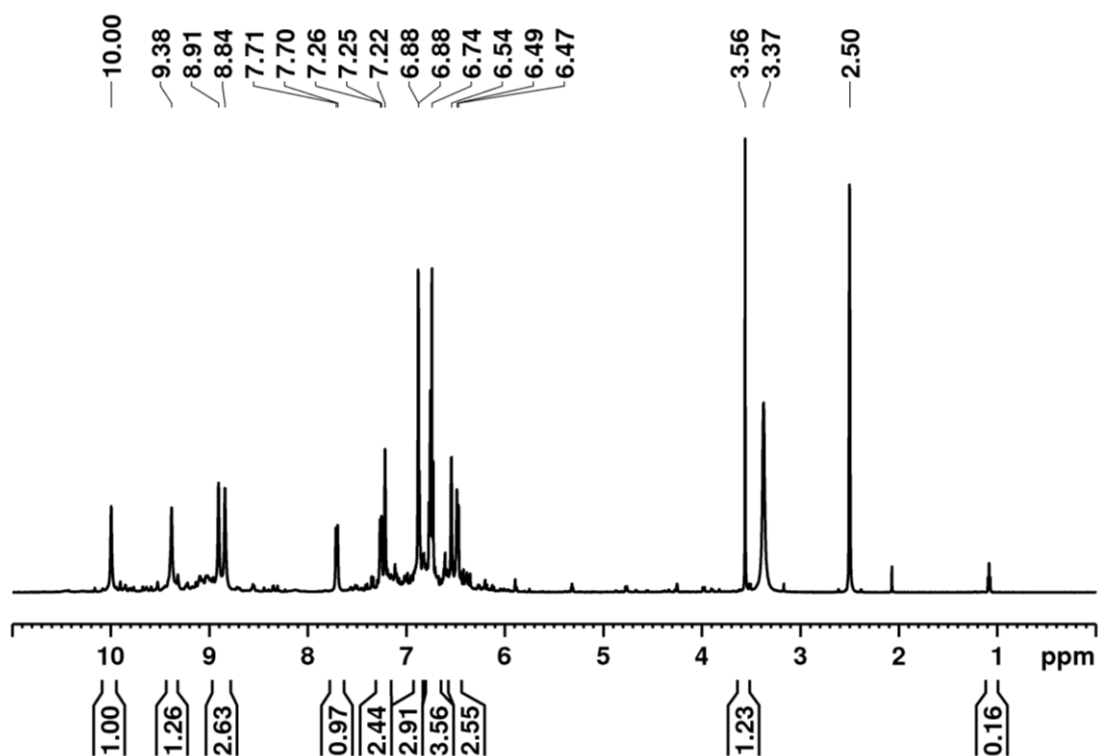


Figure A.89: ^1H NMR spectrum of 3,3'-dihydroxy-diphenylquinone-(4,4') ($\text{H}_2(\text{SQ-SQ})$) in $[\text{D}_6]\text{DMSO}$ at RT. The spectrum was measured after 1 h from the sample preparation time. This sample refers to another sample than the sample for the above spectrum.

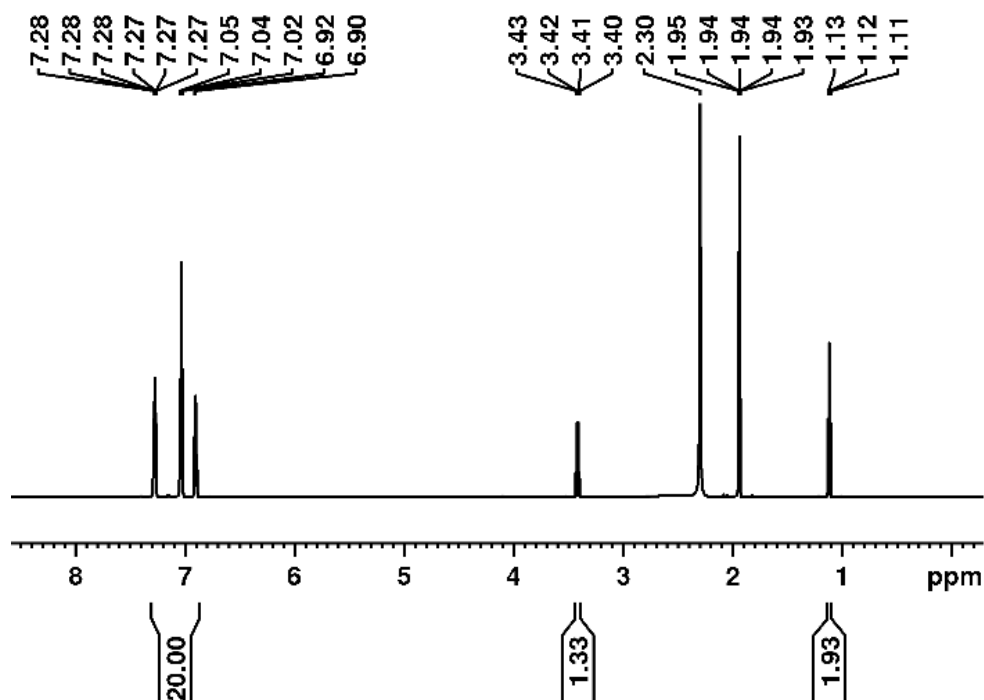


Figure A.90: ^1H NMR spectrum (diamagnetic range) of **3d** showing diethyl ether molecule signals and NaBPh_4 signals. NaBPh_4 (11 mg) was added to a solution of **3d** (13.1 mg) in $[\text{D}_3]\text{MeCN}$ to determine the ratio of Et_2O and $[\text{Co}_2(\text{L-N}_{4f}\text{Bu}_2)_2(\text{Cat-SQ})](\text{BF}_4)_2$.

Calculation of Et_2O per complex molecule of **3d**:

0.032 mmol $\text{NaBPh}_4 \equiv 0.0102$ mmol **3d**

1 mmol $\text{NaBPh}_4 \equiv 0.317$ mmol **3d**

20 protons of NaBPh_4 molecule $\equiv 3.17$ protons of Et_2O molecule

Obtained number of protons = 3.26

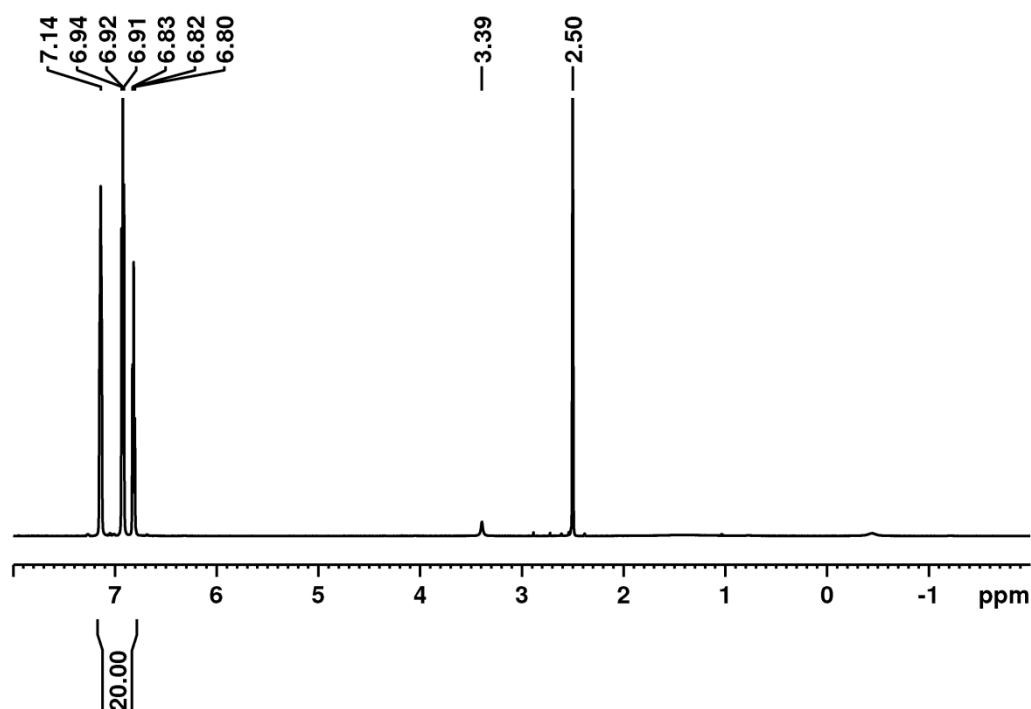


Figure A.91: ^1H NMR spectrum (diamagnetic range) of the compound $[\text{Co}_2(\text{L-N}_4\text{tBu}_2)_2(\text{Cat-SQ})](\text{BF}_4)_2$ in $[\text{D}_6]\text{DMSO}$ at RT. The sample was prepared after drying of compound **3d** in vacuum at RT.

6.2.4 UV/Vis/NIR Spectra

All the spectra showing Gaussian fit are shown in Figures A.93, A.95, A.98–A.105 and A.109–110. The orange-red dashed line corresponds to the sum of Gaussian profiles. The blue line corresponds to the data point used for the deconvolution. The Gaussian peaks are represented as black solid lines. Adjusted R^2 values for almost all the fitting are 0.999.

Table A.16: The absorption maximum (ν / cm^{-1}), molar extinction coefficient ($\epsilon / \text{M}^{-1} \text{cm}^{-1}$)^[a] and area under the Gaussian peaks (area / $\text{M}^{-1} \text{cm}^{-2}$) for the Gaussian fit of the UV/Vis/NIR spectra of **3a** in EtCN at different temperatures and $\text{H}_2(\text{SQ-SQ})$ in 1,4-dioxane at room temperature.

T/K	$\nu(\epsilon)$	$\nu(\text{area} \times 10^{-6})$
3a (LTC) ^[a]	5585 (1124), 7908 (8883), 8506 (15400), 10635 (1153), 11285 (2025), 14716 (3342), 18348 (1715), 19848	5585 (1.84), 7908 (6.10), 8506 (41.1), 10635 (1.05), 11285 (5.05), 14716 (13.4), 18348 (5.32), 19848 (2.94), 21633

	(1504), 21633 (1049), 23529 (8935), 26251 (1835), 30686 (19500)	(1.19), 23529 (37.2), 26251 (4.17), 30686 (144.9)
3a (HTC) ^[a]	9086 (3347), 14067 (22000), 17190 (1317), 18543 (3632), 21631 (13500), 25524 (6524), 27744 (741), 32052 (11600)	9086 (5.89), 14067 (108.7), 17190 (2.10), 18543 (9.10), 21631 (63.0), 25524 (41.5), 27744 (1.46), 32052 (60.7)
3a (193 K) ^[b]	5605 (815), 7901 (5857), 8484 (10700), 10814 (1062), 14155 (8715), 17648 (857), 19429 (3076), 21692 (700), 23149 (10300), 26279 (1376), 30967 (17000)	5605 (1.32), 7901 (3.98), 8484 (28.8), 10814 (1.49), 14155 (46.7), 17648 (1.58), 19429 (8.68), 21692 (0.76), 23149 (49.6), 26279 (3.23), 30967 (131)
3a (213) K ^[b]	6135 (814), 8000 (3981), 8651 (9363), 10852 (1070), 14135 (12600), 17450 (936), 18958 (2825), 21513 (283), 22372 (10800), 26643 (6324), 31674 (14800)	6135 (2.62), 8000 (2.63), 8651 (23.9), 10852 (1.34), 14135 (64.4), 17450 (1.64), 18958 (7.73), 21513 (0.30), 22372 (53.5), 26643 (34.8), 31674 (88.7)
3a (233 K) ^[b]	7891 (2386), 8741 (6259), 8925 (1960), 10817 (642), 14138 (15500), 18238 (3062), 22285 (1250015), 25943 (3570), 27702 (1770), 31754 (14200)	7891 (1.51), 8741 (14), 8925 (11.2), 10817 (0.60), 14138 (73), 18238 (9.72), 22285 (67.7), 25943 (12.8), 27702 (4.83), 31754 (100)
3a (253 K) ^[b]	7945 (2838), 8973 (3778), 9680 (3543), 14091 (17000), 18305 (5390), 22091 (12100), 25320 (5737), 27596 (2120), 31882 (13500)	7945 (2.67), 8973 (4.95), 9680 (18.8), 14091 (72.8), 18305 (23.8), 22091 (52.3), 25320 (23.5), 27596 (5.99), 31882 (90)
3a (273 K) ^[b]	7940 (1762), 8987 (3302), 9569 (2758), 14132 (18700), 17078 (1719), 18545 (3151), 22050 (13900), 25921	7940 (1.67), 8987 (4.46), 9569 (14.5), 14132 (84.8), 17078 (3.63), 18082 (18.7), 18545 (8.35), 22050 (71.8), 25921

	(4287), 27738 (1289), 32027 (13100)	(16.6), 27738 (3.02), 32027 (91.1)
3a (293 K) ^[b]	7948 (1183), 9013 (2875), 9899 (2292), 14117 (19400), 16906 (811), 18369 (4250), 22015 (14100), 25757 (4799), 27709 (1157), 32095 (13000)	7948 (1.26), 9013 (3.91), 9899 (13.3), 14117 (88.4), 16906 (1.51), 18369 (13.8), 22015 (68.6), 25757 (19.4), 27709 (2.70), 32095 (90.5)
3a (313 K) ^[b]	7913 (734), 9016 (2360), 9116 (1841), 14064 (20100), 16989 (1195), 18416 (3320), 22083 (14800), 25788 (3341), 27610 (1883), 32162 (12800)	7913 (0.73), 9016 (3.23), 9116 (9.02), 14064 (94.6), 16989 (2.29), 18416 (9.25), 22083 (79.4), 25788 (10.9), 27610 (4.74), 32162 (90.8)
3a (333 K) ^[b]	7872 (503), 8775 (1657), 9031 (1935), 14049 (20300), 16961 (1140), 18387 (3217), 22105 (15300), 25643 (2603), 27435 (2292), 32241 (12800)	7872 (0.52), 8775 (7.52), 9031 (2.65), 14049 (96.5), 16961 (2.15), 18387 (8.88), 22105 (83.7), 25643 (7.50), 27435 (6.04), 32241 (92.1)
H₂(SQ-SQ) (RT) ^[c]	20545 (10600), 24068 (8645), 27039 (6081) 36820 ^[d] (9585), 41110 ^[d] (4506)	20545 (37), 24068 (41), 27039 (44), 36820 ^[d] (69), 41110 ^[d] (15)

^[a] Wavenumber range 5000–31250 cm⁻¹. ^[b] Wavenumber range 5000–31400 cm⁻¹.

^[c] Wavenumber range 15445–42260 cm⁻¹. ^[d] These bands could be affected by the absorption of solvent peaks in this region.

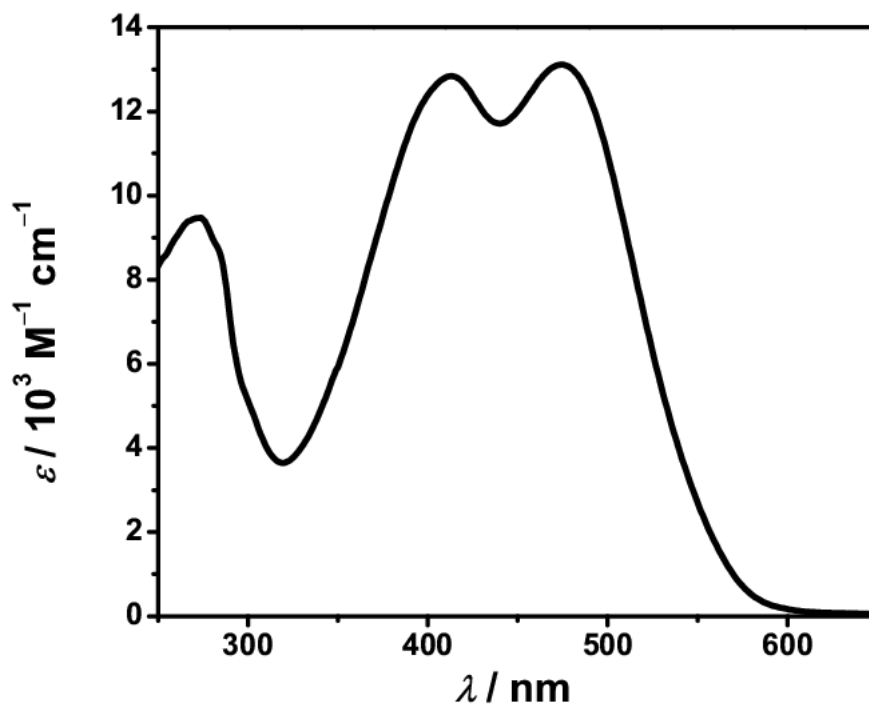


Figure A.92: UV/Vis spectrum of 3,3'-dihydroxy-diphenoquinone-(4,4') ($\text{H}_2(\text{SQ-SQ})$) in 1,4-dioxane at RT.

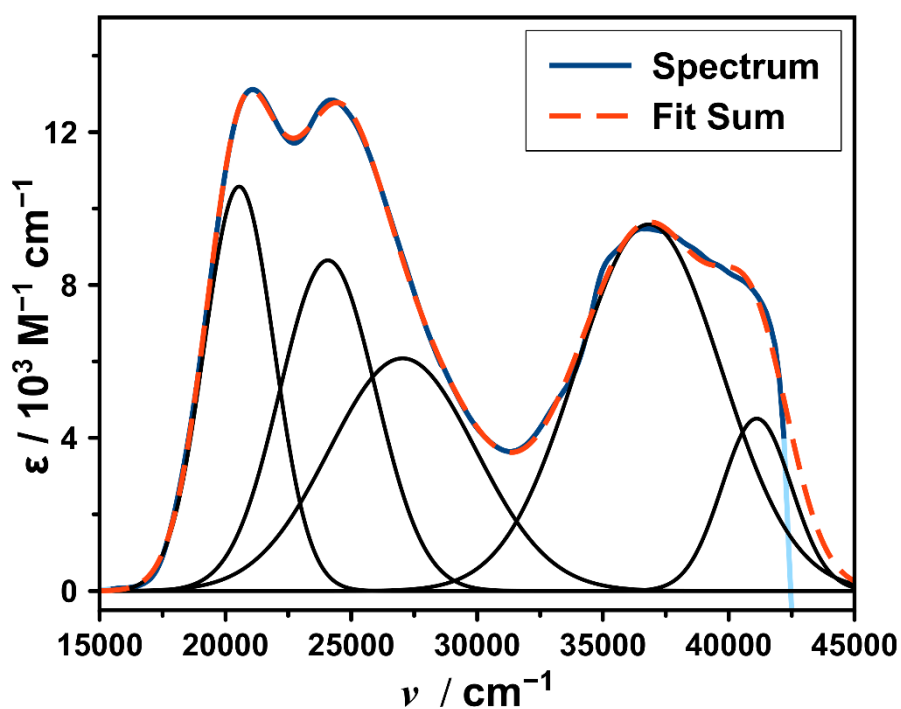


Figure A.93: Gaussian fit of the UV/Vis spectrum of 3,3'-dihydroxy-diphenoquinone-(4,4') ($\text{H}_2(\text{SQ-SQ})$) in 1,4-dioxane at RT.

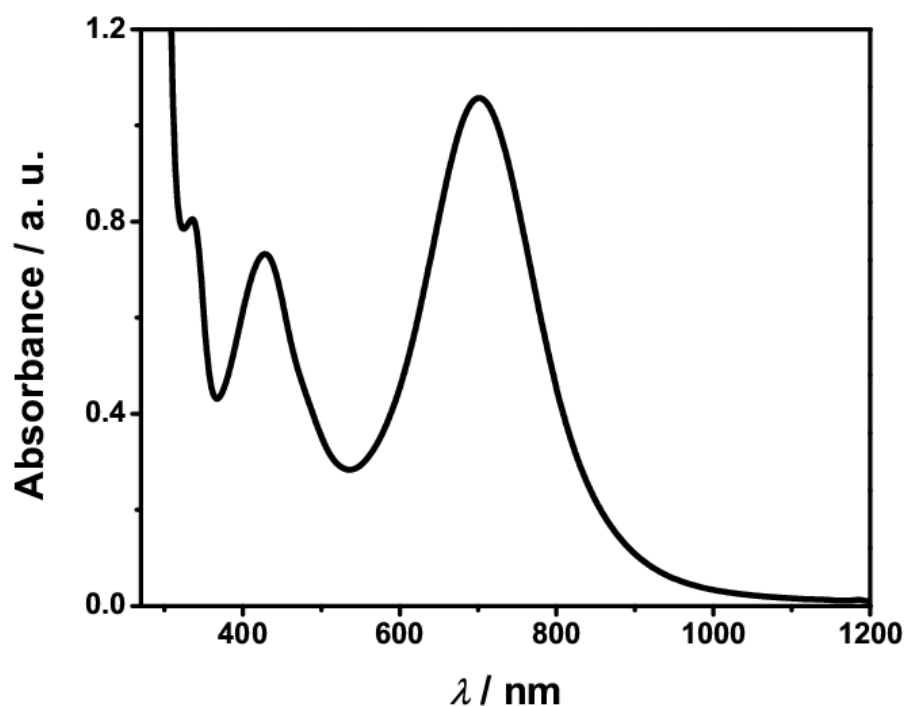


Figure A.94: UV/Vis/NIR spectrum recorded from a mixture of NaOH (excess) and 3,3'-dihydroxy-diphenylquinone-(4,4') ($H_2(SQ-SQ)$) in 1,4-dioxane/methanol (100:1) at RT.

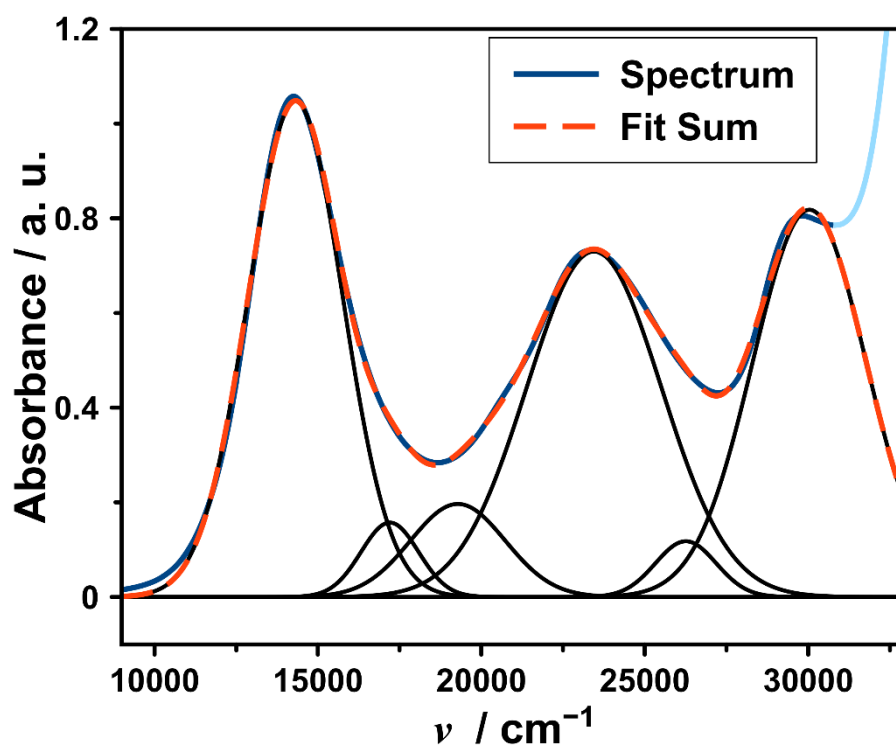


Figure A.95: Gaussian fit of the NIR/Vis spectrum recorded from a mixture of NaOH (excess) and 3,3'-dihydroxy-diphenylquinone-(4,4') ($H_2(SQ-SQ)$) in 1,4-dioxane/methanol (100:1), at RT.

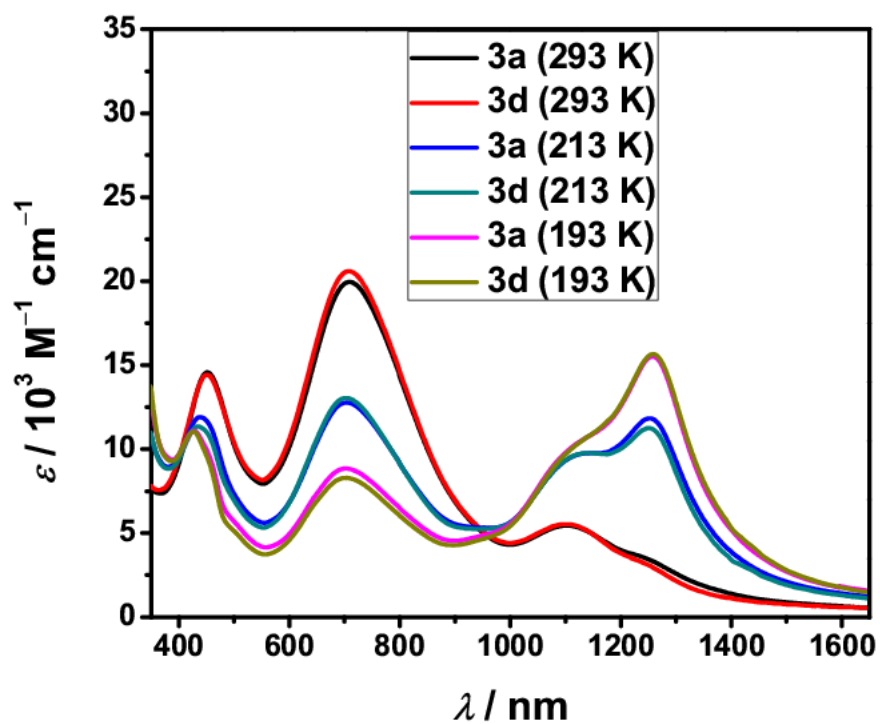


Figure A.96: Comparison among the UV/Vis/NIR spectra of **3a** and **3d** at different temperatures in EtCN.

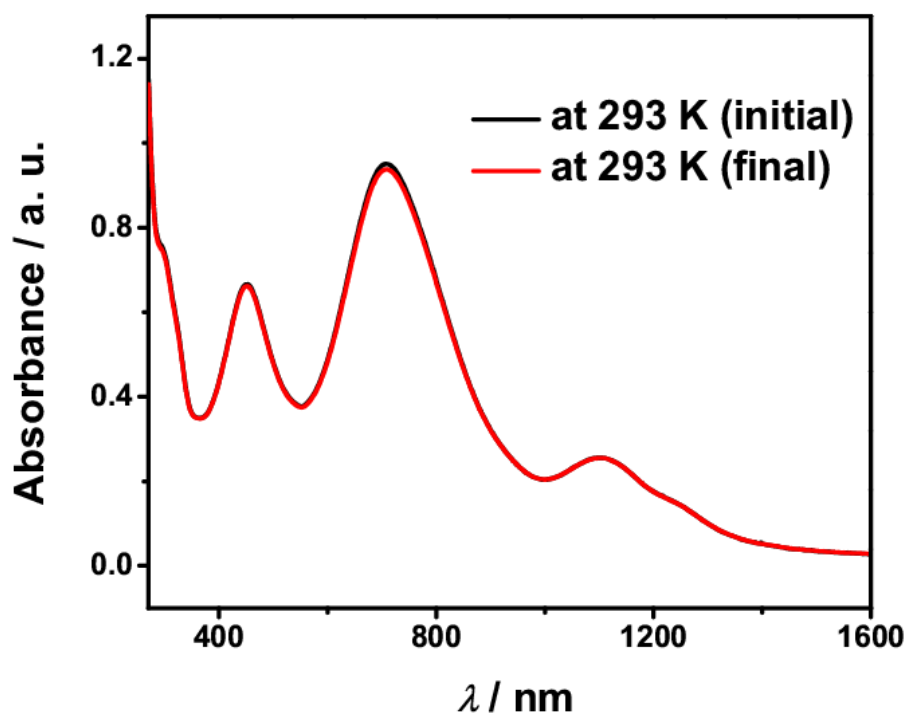


Figure A.97: Solution stability of **3d** during variable temperature UV/Vis/NIR measurement in EtCN.

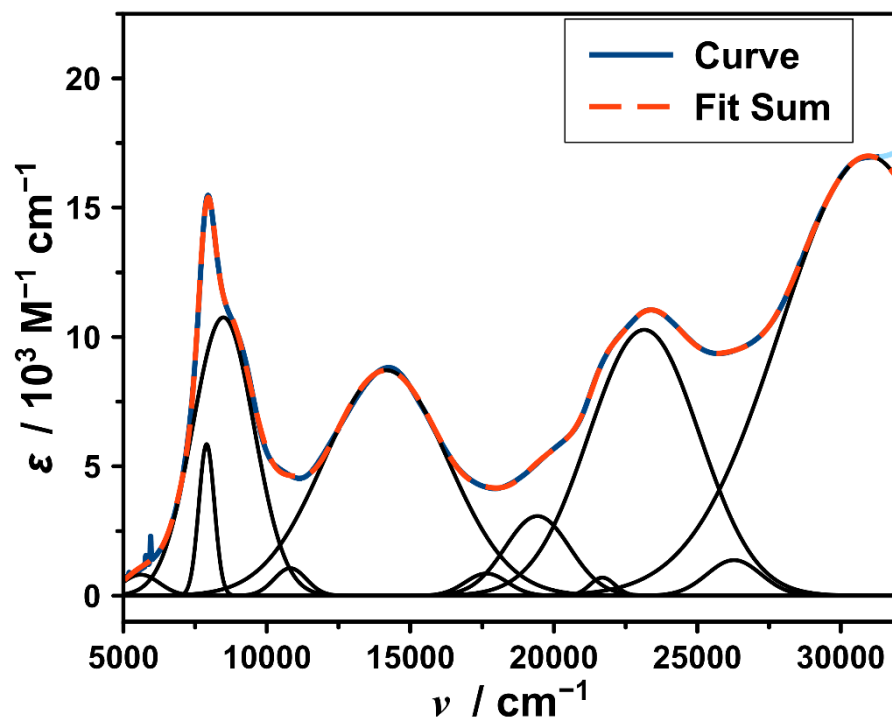


Figure A.98: Gaussian fit of the UV/Vis/NIR spectrum of **3a** in EtCN at 193 K.

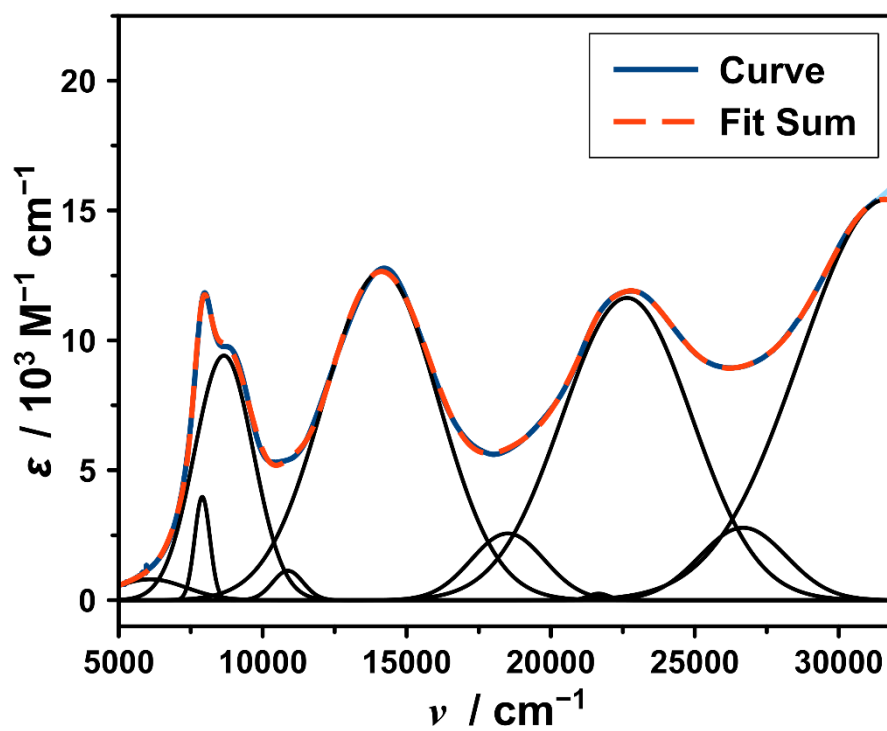


Figure A.99: Gaussian fit of the UV/Vis/NIR spectrum of **3a** in EtCN at 213 K.

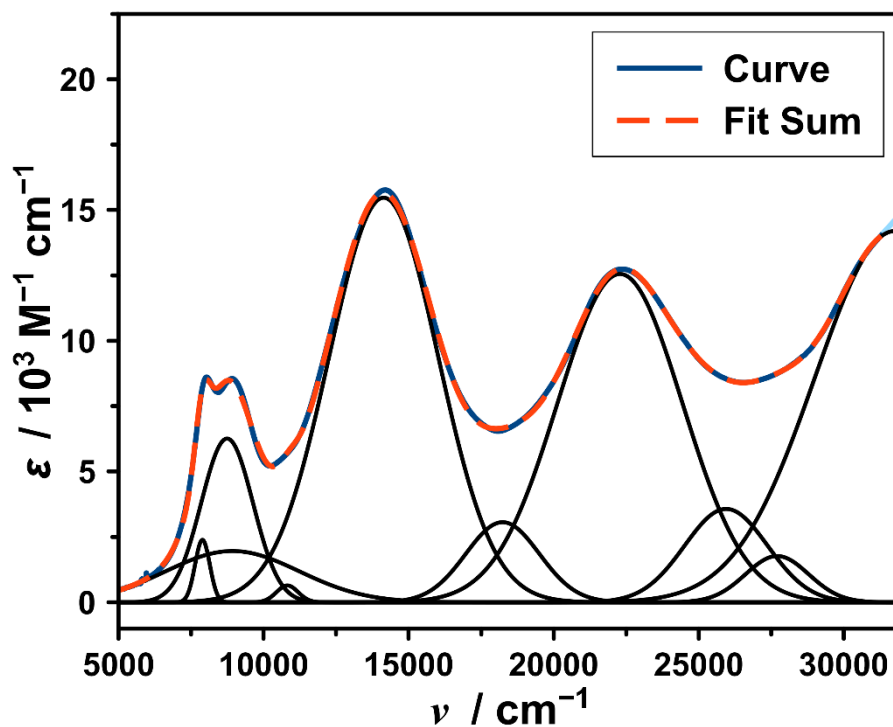


Figure A.100: Gaussian fit of the UV/Vis/NIR spectrum of **3a** in EtCN at 233 K.

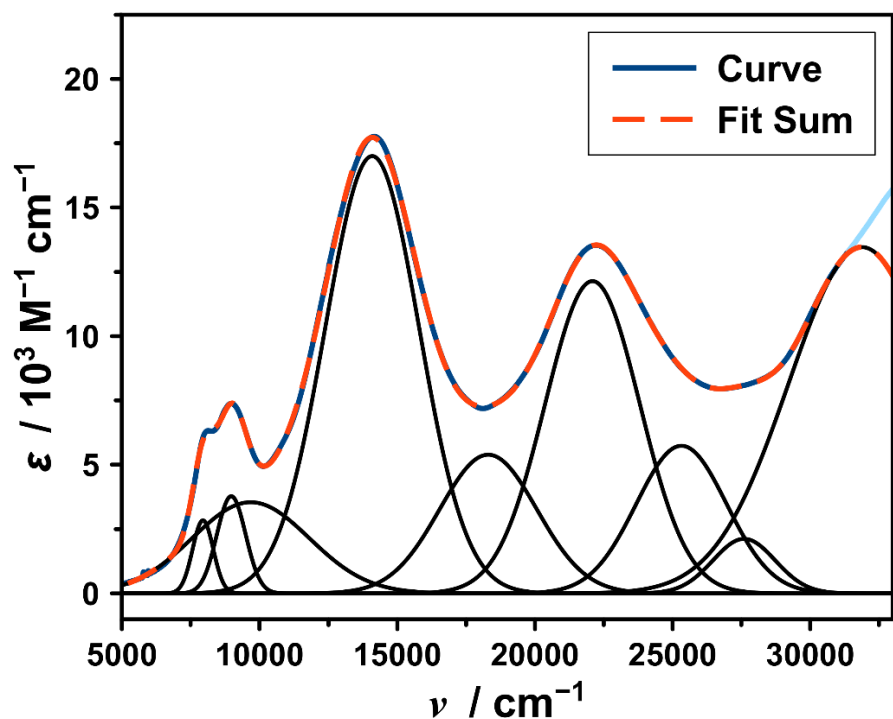


Figure A.101: Gaussian fit of the UV/Vis/NIR spectrum of **3a** in EtCN at 253 K.

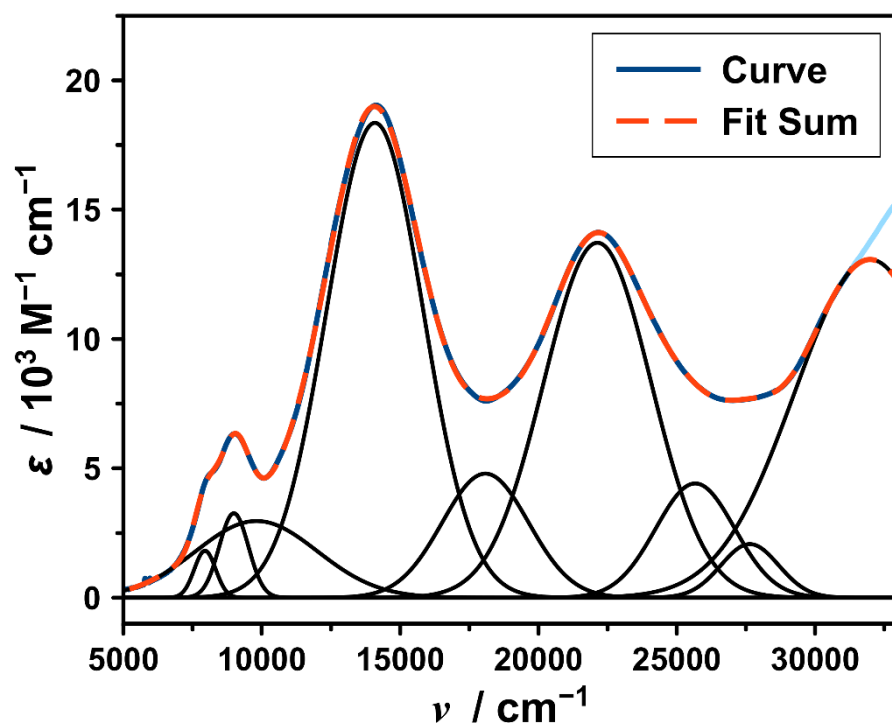


Figure A.102: Gaussian fit of the UV/Vis/NIR spectrum of **3a** in EtCN at 273 K.

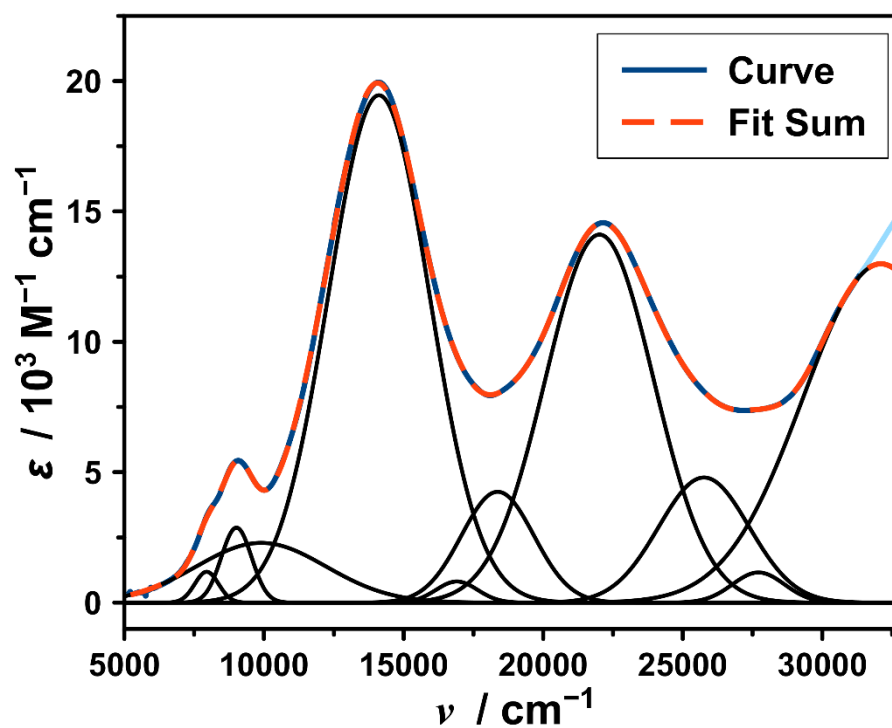


Figure A.103: Gaussian fit of the UV/Vis/NIR spectrum of **3a** in EtCN at 293 K.

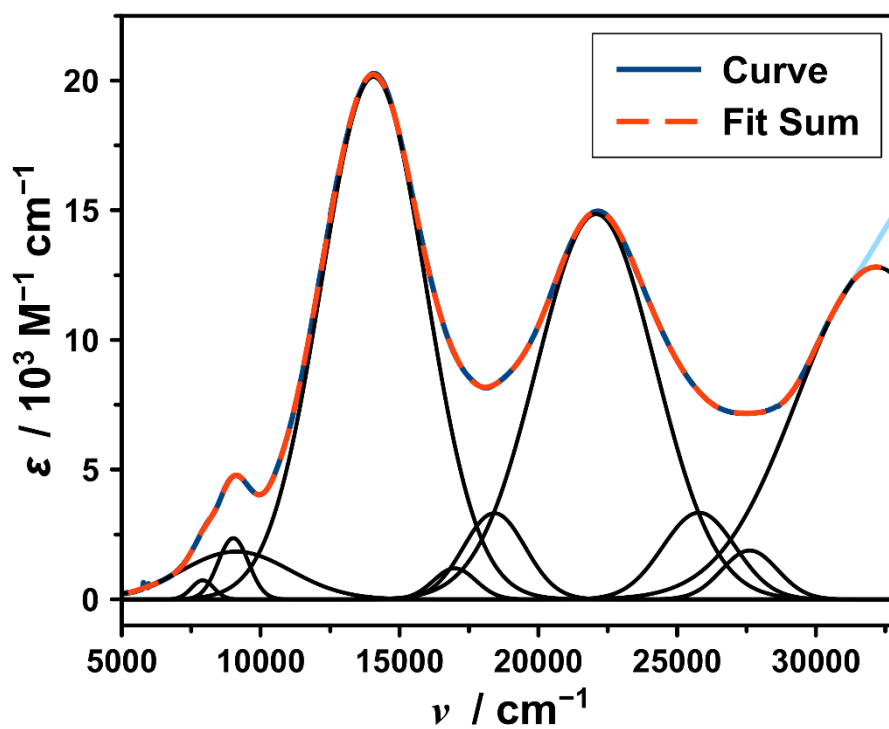


Figure A.104: Gaussian fit of the UV/Vis/NIR spectrum of **3a** in EtCN at 313 K.

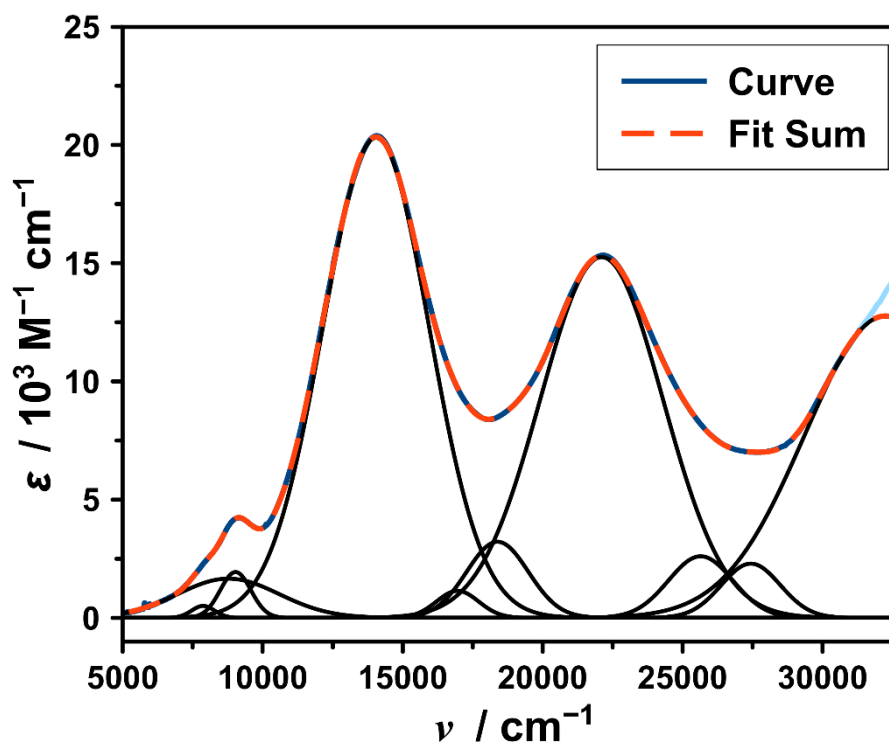


Figure A.105: Gaussian fit of the UV/Vis/NIR spectrum of **3a** in EtCN at 333 K.

Table A.17: Goodness-of-fit data for the fitting of **V** component vs. T plots, obtained from SVD of the variable temperature UV/Vis/NIR spectra of **3a** in EtCN; sum of squared residuals (SS_{res}) and root mean square error (RMSE).

V component	SS_{res}	RMSE
V component 1	1.8×10^{-4}	4.7×10^{-3}
V component 2	3.6×10^{-4}	6.7×10^{-3}

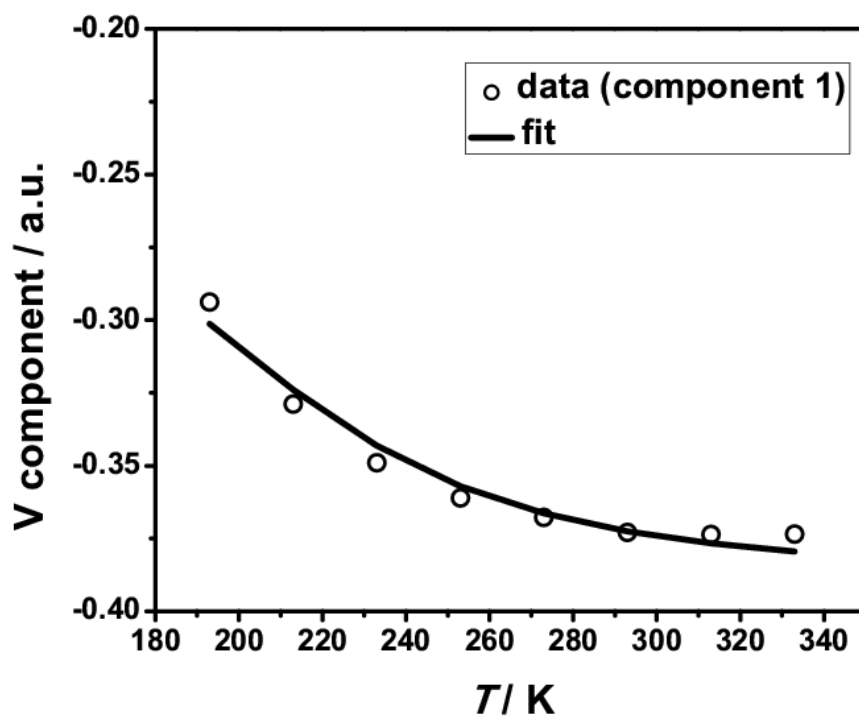


Figure A.106: **V** component (first) vs. T plot and its fit for the SVD of the variable temperature UV/Vis/NIR spectra of **3a** in EtCN.

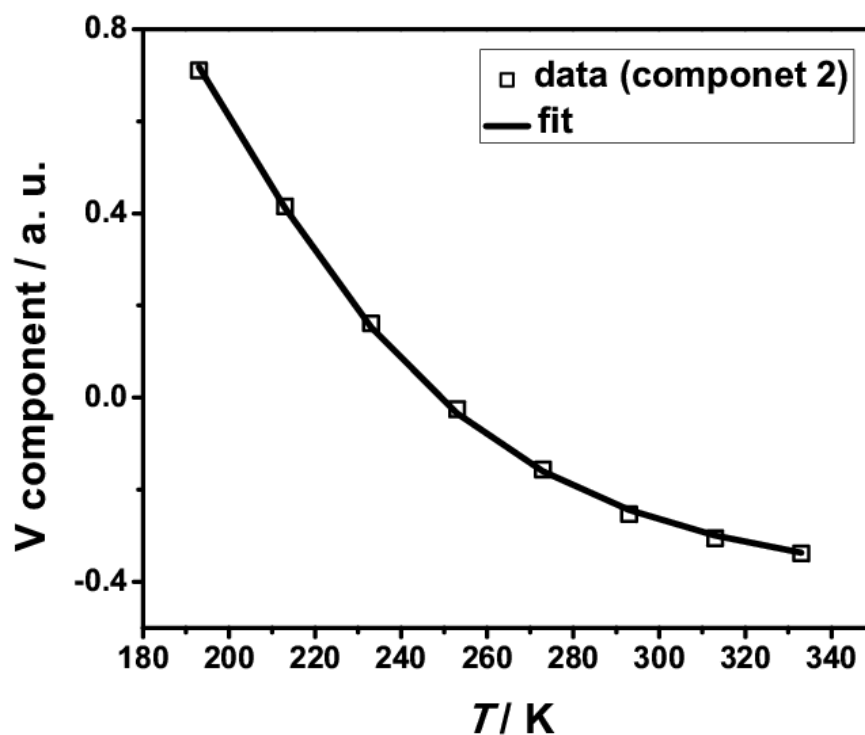


Figure A.107: V component (second) vs. T plot and its fit for the SVD of the variable temperature UV/Vis/NIR spectra of **3a** in EtCN.

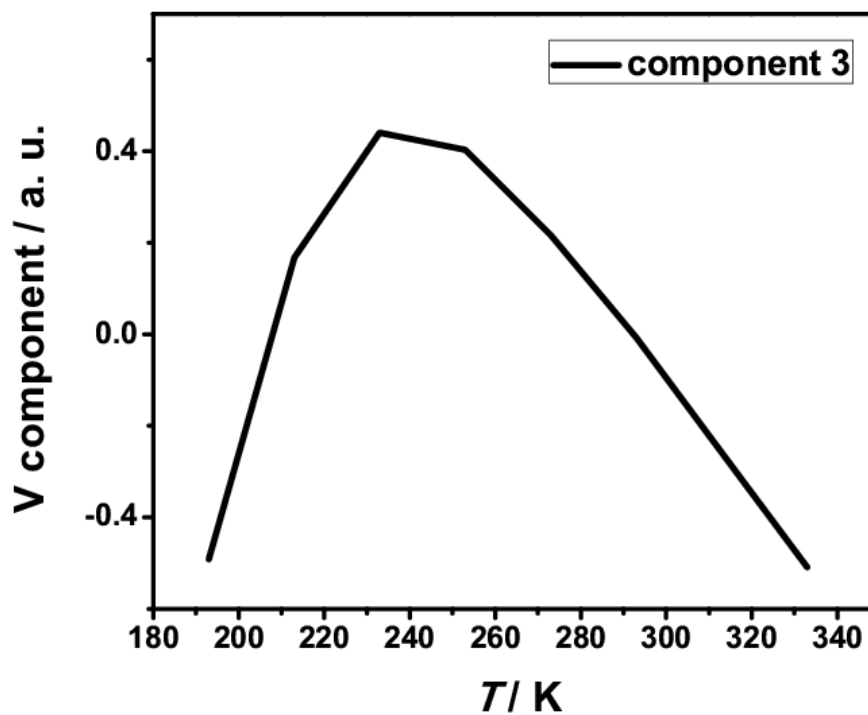


Figure A.108: V component (third) vs. T plot for the SVD of the variable temperature UV/Vis/NIR spectra of **3a** in EtCN.

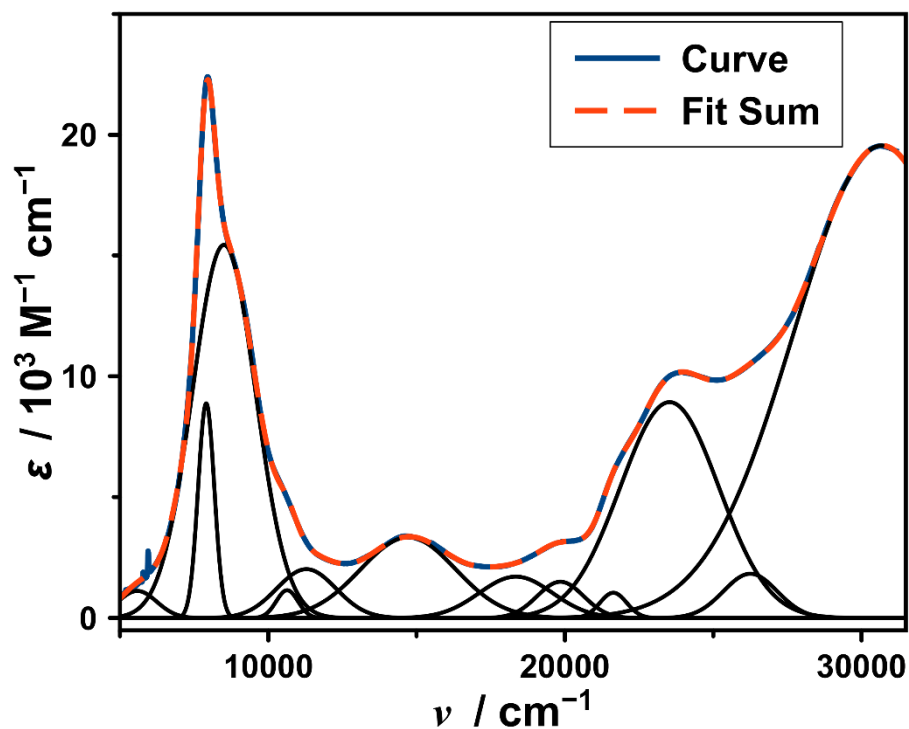


Figure A.109: Gaussian fit of the UV/Vis/NIR features corresponding to the low-temperature component in the variable temperature UV/Vis/NIR spectra of **3a** in EtCN.

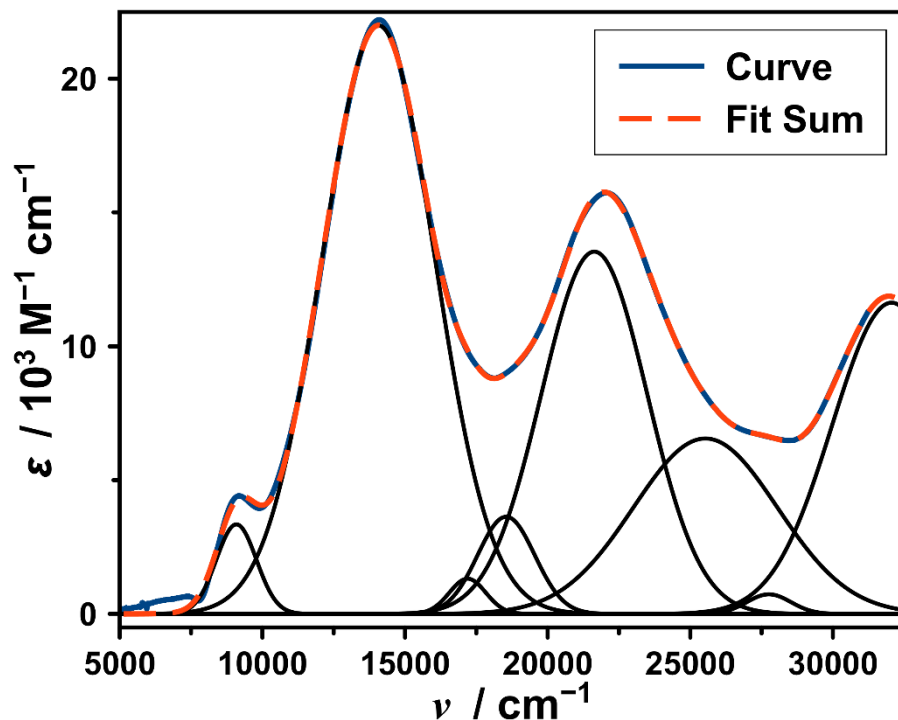


Figure A.110: Gaussian fit of the UV/Vis/NIR features corresponding to the high-temperature component in the variable temperature UV/Vis/NIR spectra of **3a** in EtCN.

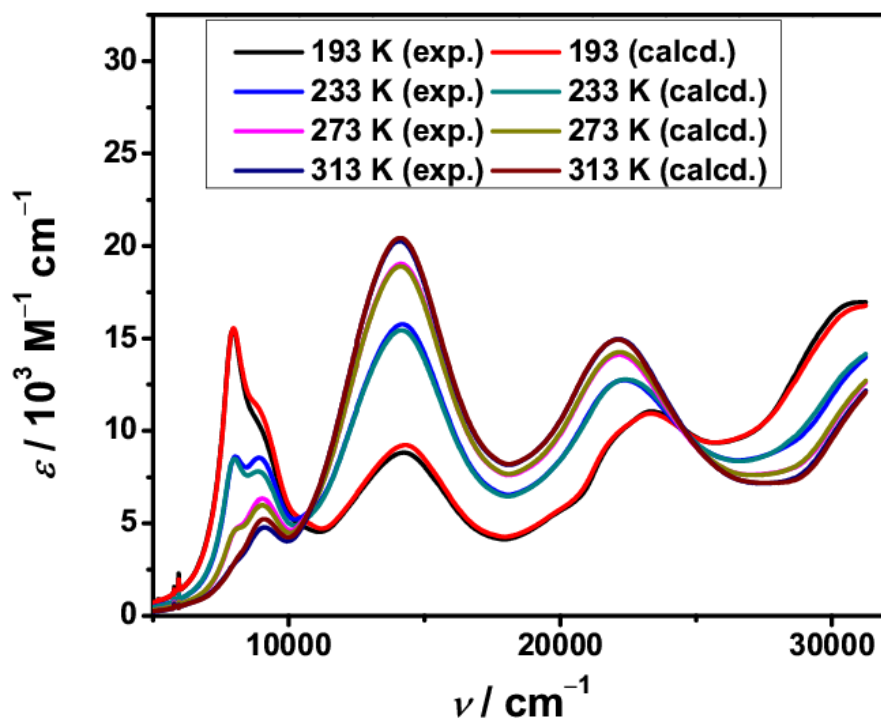


Figure A.111: Experimental and reconstructed UV/Vis/NIR spectra of **3a** in EtCN at 193, 233, 273 and 313 K.

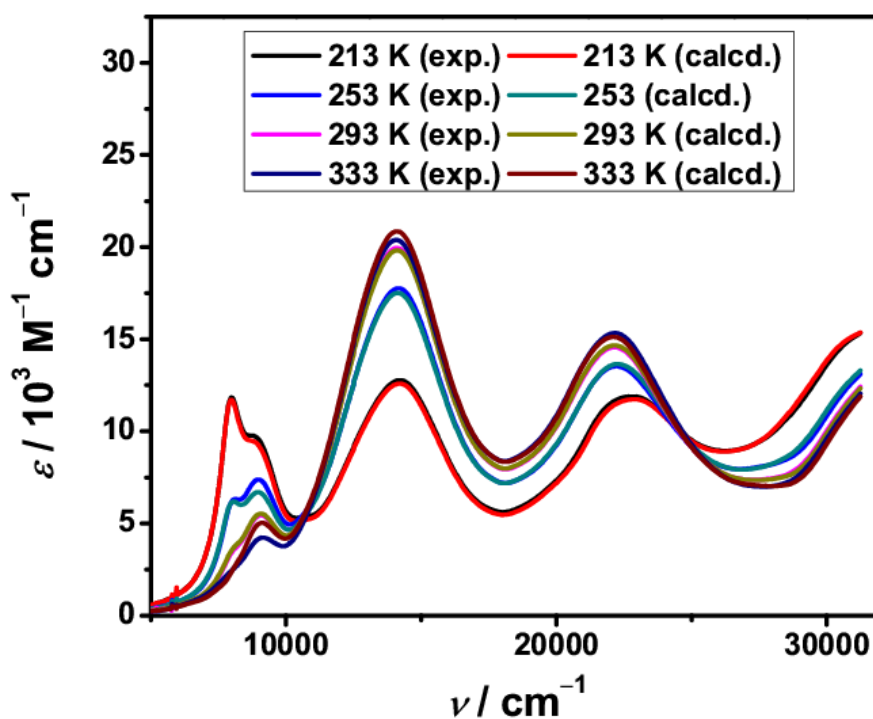


Figure A.112: Experimental and reconstructed UV/Vis/NIR spectra of **3a** in EtCN at 213, 253, 293 and 333 K.

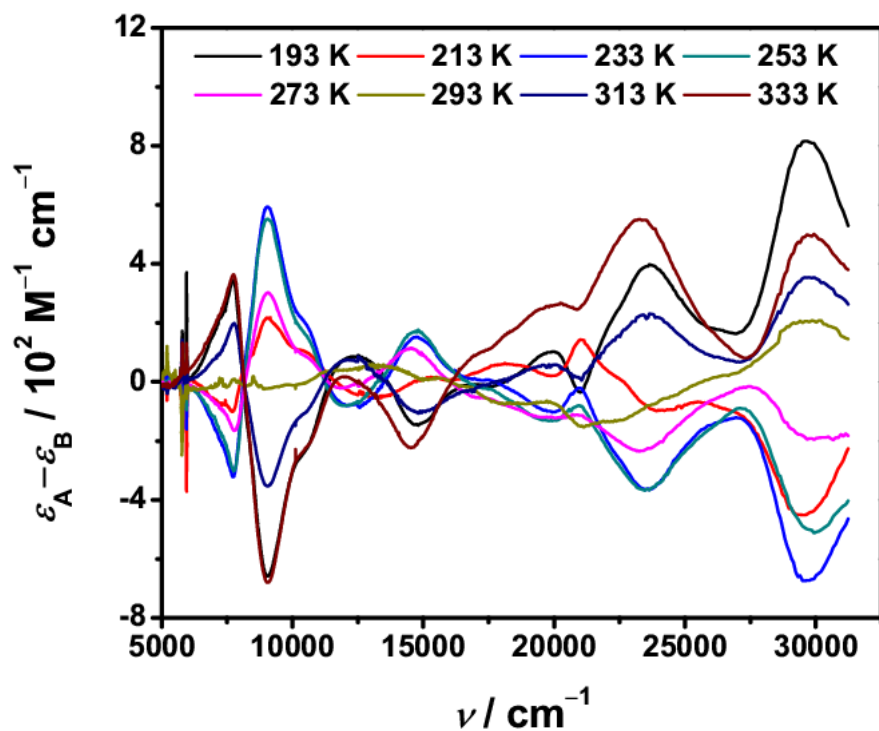


Figure A.113: Residuals between the original data matrix (**A**) and rank-defined data matrix (**B**) for the SVD of the variable temperature UV/Vis/NIR spectra of **3a** in EtCN.

6.2.5 Cyclic Voltammograms

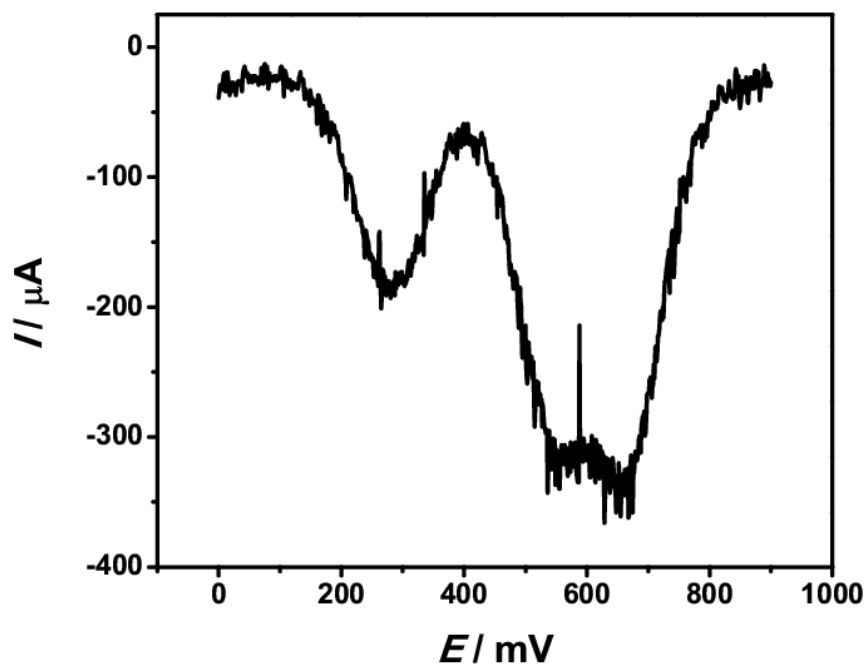


Figure A.114: Difference pulse voltammogram of **3e** in 0.2 M TBAP/MeCN at $\nu = 100$ mV/s.

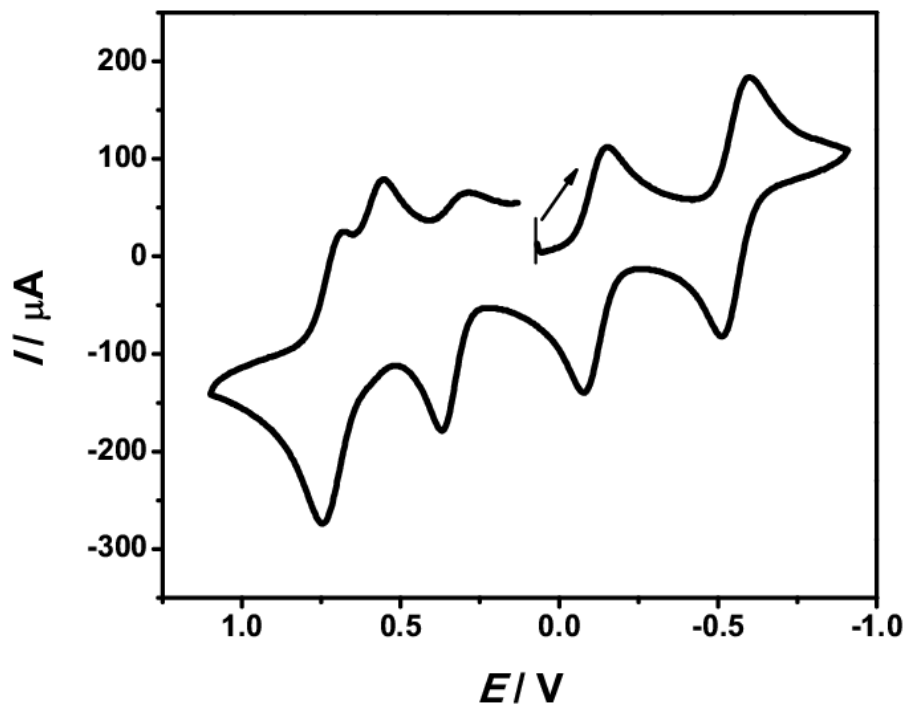


Figure A.115: Cyclic voltammogram of **3e** in 0.2 M TBAP/MeCN at scan rate $\nu = 100$ mV/s.

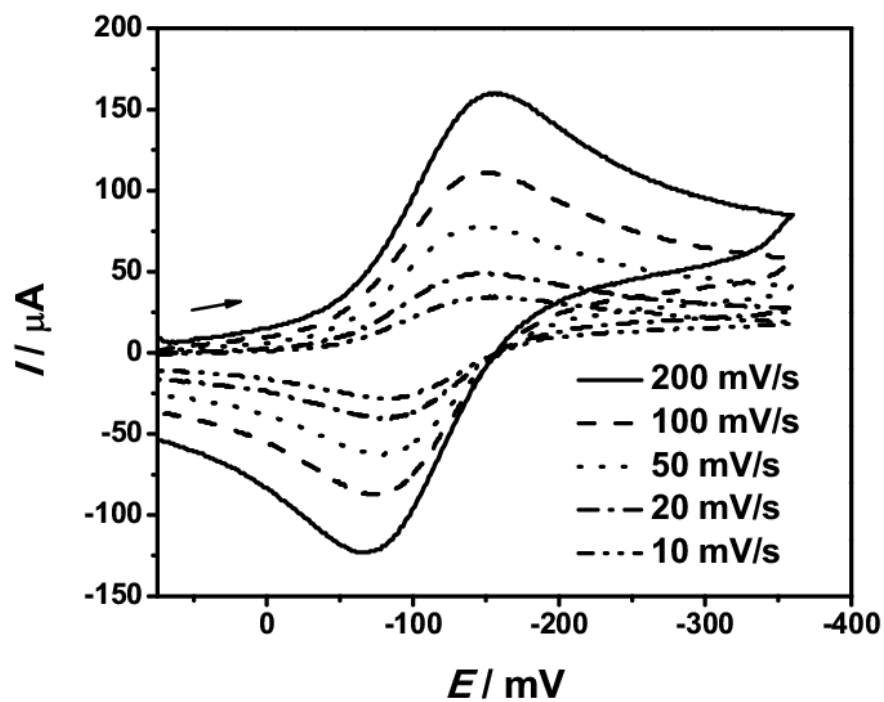


Figure A.116: Cyclic voltammograms for the first reductive processes of **3e** in 0.2 M TBAP/MeCN.

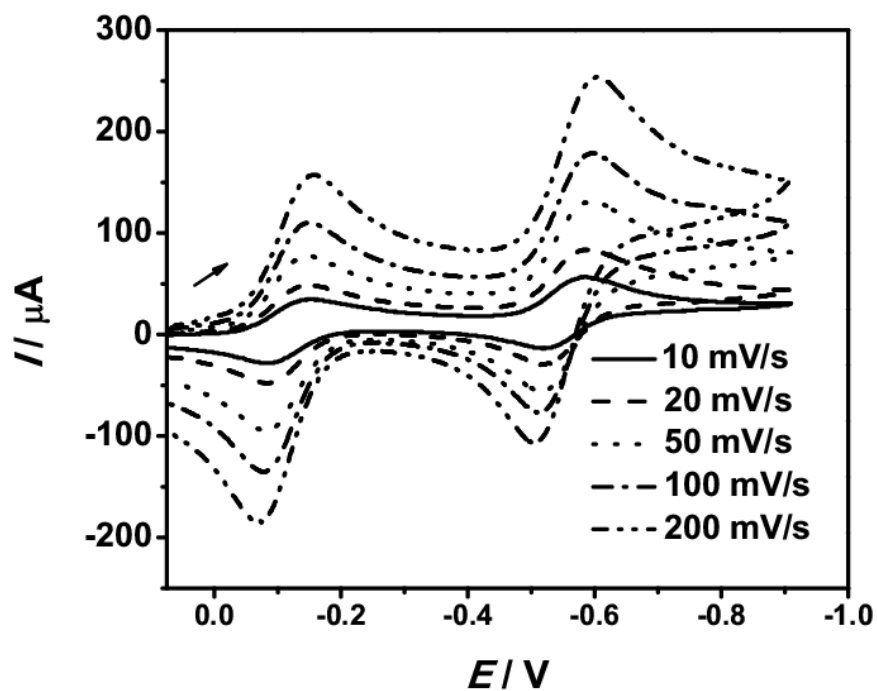


Figure A.117: Cyclic voltammograms for the two successive reductive processes of **3e** in 0.2 M TBAP/MeCN.

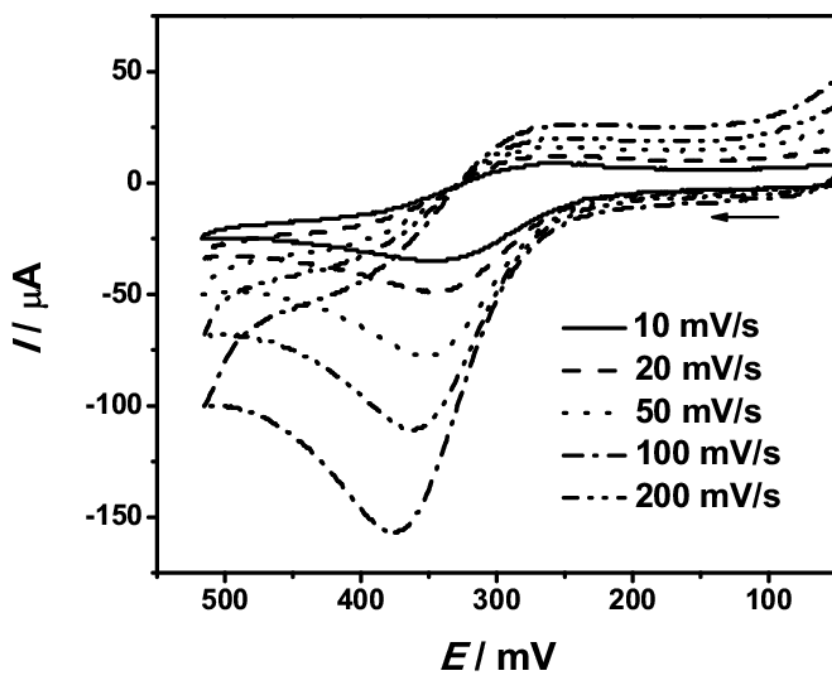


Figure A.118: Cyclic voltammograms for the first oxidative processes of **3e** in 0.2 M TBAP/MeCN.

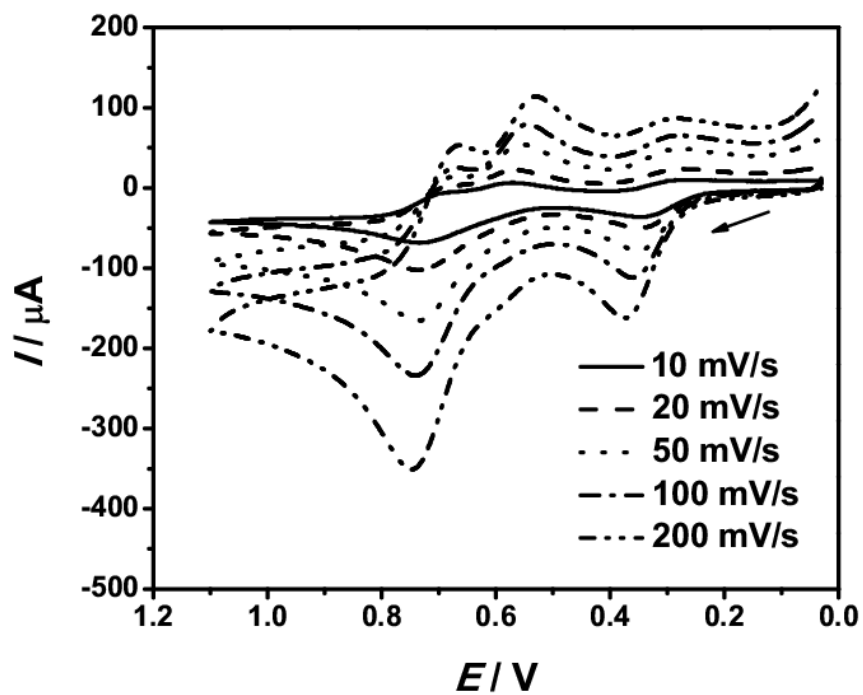


Figure A.119: Cyclic voltammograms for the three successive oxidative processes of **3e** in 0.2 M TBAP/MeCN.

Table A.18: Cyclic voltammetry data of **3e**; Scan rate ν , half-wave potential $E_{1/2}$, difference between peak potentials ΔE , peak current ratio i_{pa}/i_{pc} .

	$\nu/\text{mV s}^{-1}$	$E_{1/2}/\text{mV}$	$\Delta E/\text{mV}$	i_{pa}/i_{pc}
Reduction 1	200	-110	90	1.10
	100	-112	72	1.07
	50	-114	67	1.11
	20	-115	67	1.16
	10	-115	67	1.15
Reduction 2	200	-553	95	1.01
	100	-552	80	1.02
	50	-552	70	1.06
	20	-550	60	1.08
	10	-550	60	1.09
	$\nu/\text{mV s}^{-1}$	E_{pa}/mV	$\Delta E/\text{mV}$	i_{pa}/i_{pc}
Oxidation 1	200	374	–	–
	100	360	–	–
	50	350	–	–
	20	350	–	–
	10	350	–	–
	$\nu/\text{mV s}^{-1}$	$E_{1/2}/\text{mV}$	$\Delta E/\text{mV}$	i_{pa}/i_{pc}
Oxidation 2	200	ca. 573	ca. 76	–
	100	ca. 571	ca. 62	–
	50	ca. 570	ca. 52	–
	20	ca. 568	ca. 50	–
	10	ca. 562	ca. 51	–
Oxidation 3	200	710	86	–
	100	709	63	–
	50	710	54	–
	20	712	50	–
	10	713	54	–

6.3 Electronic States of Bis(dioxolene) Ligands and the Interactions Between Metal Ions in Nickel-, Copper- and Zinc-Bis(dioxolene) Complexes

6.3.1 Crystal Data

The X-ray crystallographic data of compounds **4a** and **6b** were collected at 100(2) and 295(2) K, and the data for compound **5a** were collected at 150(2) K. The data were collected by an Oxford Diffraction Gemini S Ultra type of instrument using graphite-monochromatized Cu- K_{α} ($\lambda = 1.54184 \text{ \AA}$) or Mo- K_{α} ($\lambda = 0.71073 \text{ \AA}$) radiation. The crystal structures were solved by direct methods implemented in the SIR 97 program package and refined using the full-matrix least-squares method on F^2 with SHELXL-97 package. The hydrogen atoms were located geometrically and refined using Riding model. As the temperature factor, 1.5 times value for hydrogen atoms of CH₃ groups and for all other hydrogen atoms 1.2 times value of the equivalent isotropic temperature factor of that atom used, to which the respective hydrogen atom is bonded. All non-hydrogen atoms were refined with anisotropic displacement parameters.

Table A.19: Crystal data and structure refinement for complex **4a** at 100 K.

Identification code	14131ocu
Empirical formula	$C_{58}H_{69}BN_6NiO_4$
Formula weight [g mol ⁻¹]	983.71
Temperature [K]	100(2)
λ [Å]	1.54184
Crystal system	triclinic
Space group	$P\bar{1}$
a [Å]	9.6455(4)
b [Å]	15.1112(4)
c [Å]	18.8295(8)
α [deg]	100.381(3)
β [deg]	96.064(3)
γ [deg]	104.678(3)
V [Å ³]	2578.25(17)
Z	2
ρ_{calcd} [g cm ⁻³]	1.267
$\mu(\text{Cu-}K\alpha)$ [mm ⁻¹]	0.955
$F(000)$	1048
Crystal size/mm ³	0.420 × 0.200 × 0.160
θ °	4.320-62.674
Reflections collected	16992
Independent reflections	8152
R_{int}	0.0196
Absorption correction	analytical
Max. and min. transmission	0.870 and 0.656
Refinement method	full-matrix least-squares on F^2
Data/restraints/parameters	8152/0/641
GOOF on F^2	1.047
Final R indices [$I > 2\sigma(I)$]	$R1 = 0.0424$, $wR2 = 0.1188$
R indices (all data)	$R1 = 0.0456$, $wR2 = 0.1219$
Largest diff. peak and hole [e Å ⁻³]	0.471 and -0.415

Table A.20: Crystal data and structure refinement for complex **4a** at 295 K.

Identification code	14132ocu
Empirical formula	C ₅₈ H ₆₉ BN ₆ NiO ₄
Formula weight [g mol ⁻¹]	983.71
Temperature [K]	295(2)
λ [Å]	1.54184
Crystal system	triclinic
Space group	$P\bar{1}$
a [Å]	9.7685(4)
b [Å]	15.2058(4)
c [Å]	19.1404(7)
α [deg]	100.399(3)
β [deg]	96.092(3)
γ [deg]	104.552(3)
V [Å ³]	2672.19(17)
Z	2
ρ_{calcd} [g cm ⁻³]	1.223
$\mu(\text{Cu-}K\alpha)$ [mm ⁻¹]	0.922
$F(000)$	1048
Crystal size [mm ³]	0.420 × 0.200 × 0.160
θ [deg]	4.274–62.796
Reflections collected	21964
Independent reflections	8488
R_{int}	0.0186
Absorption correction	semi-empirical from equivalents
Max. and min. transmission	1.00000 and 0.87604
Refinement method	full-matrix least-squares on F^2
Data/restraints/parameters	8488/0/641
GOOF on F^2	1.039
Final R indices [$I > 2\sigma(I)$]	$R1 = 0.0494$, $wR2 = 0.1387$
R indices (all data)	$R1 = 0.0543$, $wR2 = 0.1447$
Largest diff. peak and hole [e Å ⁻³]	0.448 and -0.475

Table A.21: Crystal data and structure refinement for **5a** at 150 K.

Identification code	14302o_sq
Empirical formula	C ₅₆ H ₇₀ B ₂ Cu ₂ F ₈ N ₈ O ₄
Formula weight [g mol ⁻¹]	1219.90
Temperature [K]	150(2)
λ [Å]	0.71073
Crystal system	monoclinic
Space group	<i>P</i> 2 ₁ / <i>c</i>
<i>a</i> [Å]	21.3488(18)
<i>b</i> [Å]	12.1127(8)
<i>c</i> [Å]	13.7231(11)
α [deg]	90
β [deg]	103.285(9)
γ [deg]	90
<i>V</i> [Å ³]	3453.7(5)
<i>Z</i>	2
ρ_{calcd} [g cm ⁻³]	1.173
$\mu(\text{Mo-K}\alpha)$ [mm ⁻¹]	0.681
<i>F</i> (000)	1268
θ [deg]	2.941–26.999
Reflections collected	19339
Independent reflections	7529
<i>R</i> _{int}	0.0820
Absorption correction	semi-empirical from equivalents
Max. and min. transmission	1.00000 and 0.93592
Refinement method	full-matrix least-squares on <i>F</i> ²
Data/restraints/parameters	7529/0/367
GOOF on <i>F</i> ²	0.985
Final <i>R</i> indices [<i>I</i> > 2 σ (<i>I</i>)]	<i>R</i> 1 = 0.0560, <i>wR</i> 2 = 0.1287
<i>R</i> indices (all data)	<i>R</i> 1 = 0.1004, <i>wR</i> 2 = 0.1512
Largest diff. peak and hole [e Å ⁻³]	0.935 and -0.740

Table A.22: Crystal data and structure refinement for **6b** at 100 K.

Identification code	14196o
Empirical formula	C ₅₈ H ₆₉ BN ₆ O ₄ Zn
Formula weight [g mol ⁻¹]	990.37
Temperature [K]	100(2)
λ [Å]	0.71073
Crystal system	triclinic
Space group	$P\bar{1}$
a [Å]	9.6357
b [Å]	15.1929(7)
c [Å]	18.9483(5)
α [deg]	100.093(3)
β [deg]	96.578(2)
γ [deg]	104.797(3)
V [Å ³]	2603.18(17)
Z	2
ρ_{calcd} [g cm ⁻³]	1.263
$\mu(\text{Mo-K}\alpha)$ [mm ⁻¹]	0.524
$F(000)$	1052
Crystal size [mm ³]	0.510 × 0.330 × 0.220
θ [deg]	2.819–28.999
Reflections collected	25434
Independent reflections	13808
R_{int}	0.0348
Absorption correction	semi-empirical from equivalents
Max. and min. transmission	1.00000 and 0.84356
Refinement method	full-matrix least-squares on F^2
Data/restraints/parameters	13808/0/641
GOOF on F^2	1.048
Final R indices [$I > 2\sigma(I)$]	$R1 = 0.0464$, $wR2 = 0.1110$
R indices (all data)	$R1 = 0.0560$, $wR2 = 0.1155$
Largest diff. peak and hole [e Å ⁻³]	0.794 and -0.583

Table A.23: Crystal data and structure refinement for **6b** at 295 K.

Identification code	14197o
Empirical formula	C ₅₈ H ₆₉ BN ₆ O ₄ Zn
Formula weight [g mol ⁻¹]	990.37
Temperature [K]	295(2)
λ [Å]	0.71073
Crystal system	triclinic
Space group	$P\bar{1}$
a [Å]	9.7653(4)
b [Å]	15.2813(6)
c [Å]	19.2741(8)
α [deg]	100.115(3)
β [deg]	96.570(3)
γ [deg]	104.586(3)
V [Å ³]	2702.0(2)
Z	2
ρ_{calcd} [g cm ⁻³]	1.217
$\mu(\text{Mo-K}\alpha)$ [mm ⁻¹]	0.505
$F(000)$	1052
Crystal size [mm ³]	0.510 × 0.330 × 0.220
θ [deg]	2.867–27.999
Reflections collected	25403
Independent reflections	13004
R_{int}	0.0221
Absorption correction	semi-empirical from equivalents
Max. and min. transmission	1.00000 and 0.90649
Refinement method	full-matrix least-squares on F^2
Data/restraints/parameters	13004/0/639
GOOF on F^2	1.045
Final R indices [$I > 2\sigma(I)$]	$R1 = 0.0462$, $wR2 = 0.1227$
R indices (all data)	$R1 = 0.0591$, $wR2 = 0.1312$
Largest diff. peak and hole [e Å ⁻³]	0.457 and -0.401

6.3.2 Infrared Spectra

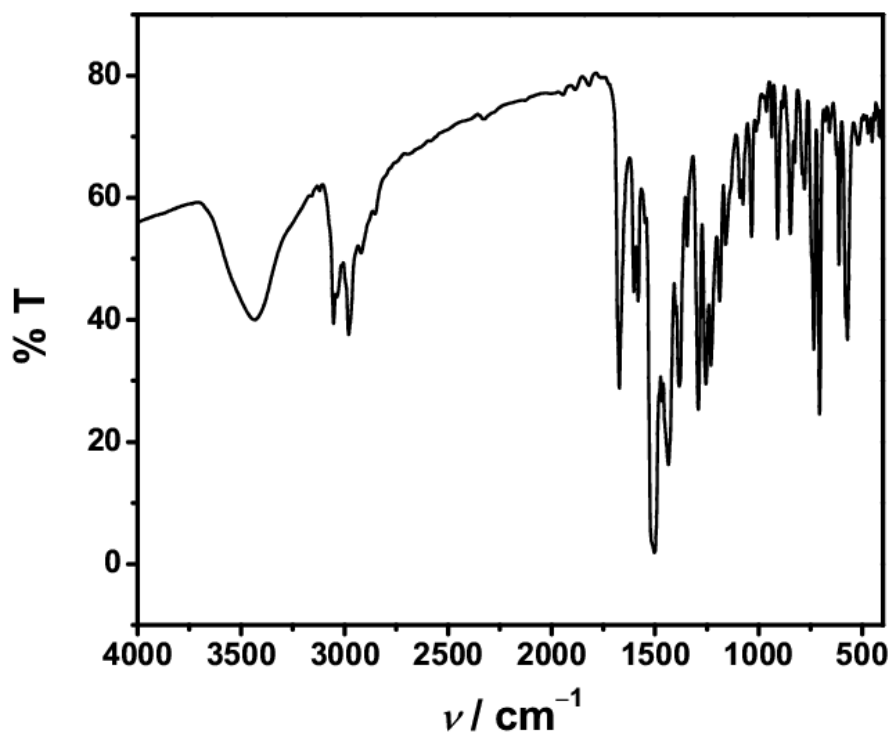


Figure A.120: IR spectrum of **4a** in KBr pellet at RT.

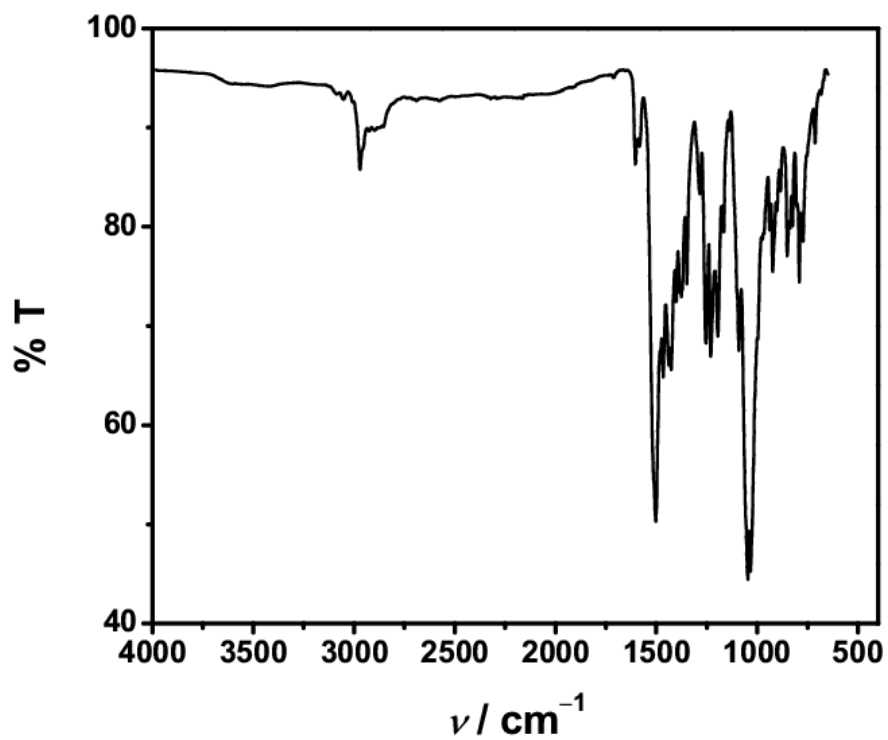


Figure A.121: ATR spectrum of **5a** at RT.

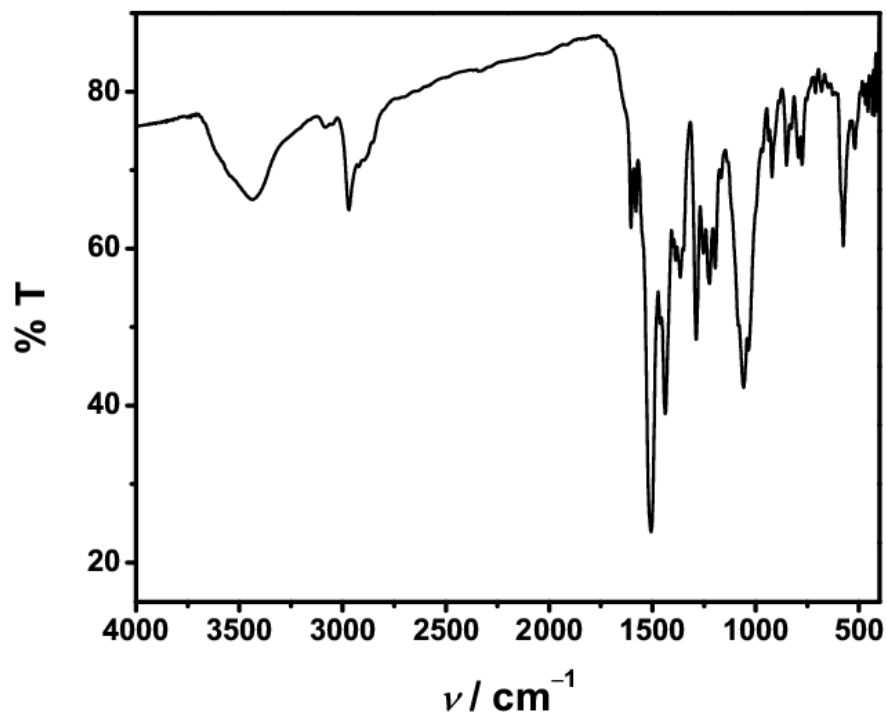


Figure A.122: IR spectrum of **5a** in KBr pellet at RT.

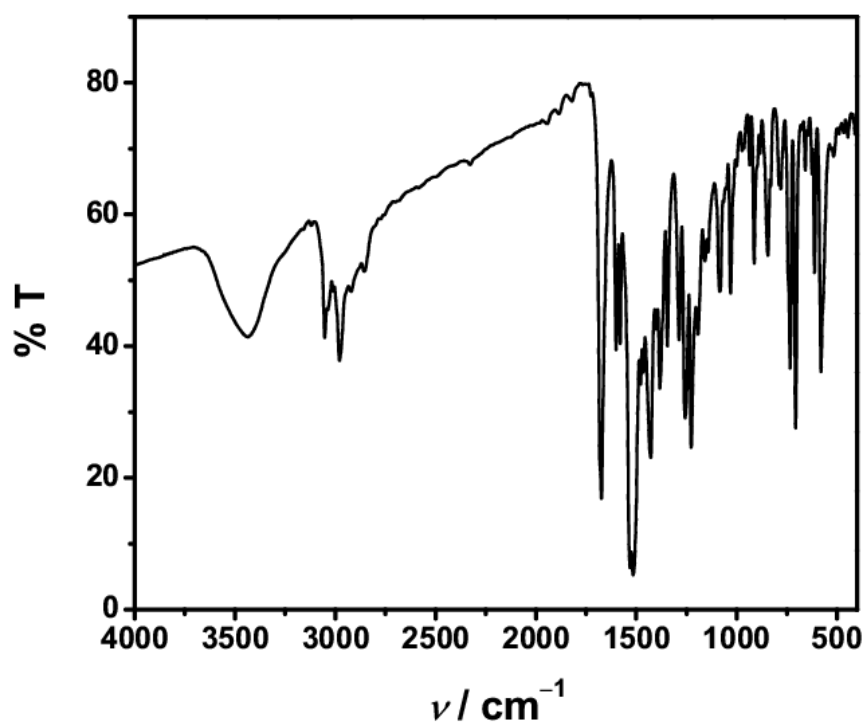


Figure A.123: IR spectrum of **6b** in KBr pellet at RT.

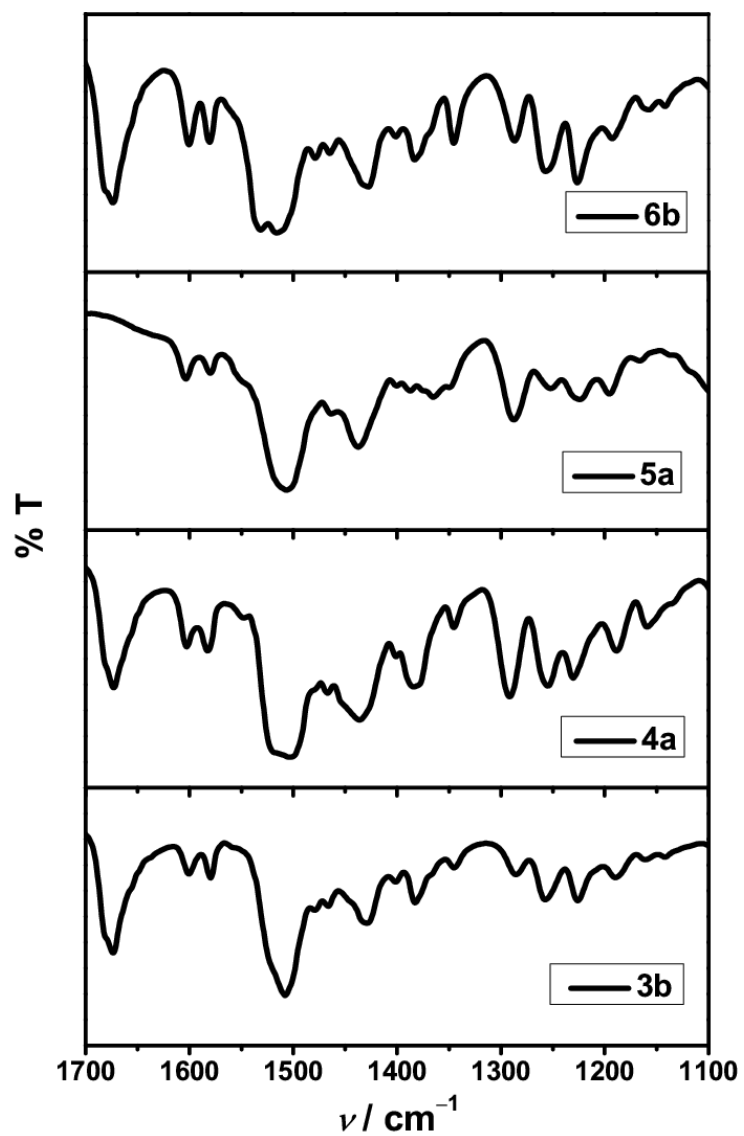


Figure A.124: KBr pellet IR spectra of **3b**, **4a**, **5a** and **6b** in the wavenumber range 1700–1100 cm^{-1} at room temperature.

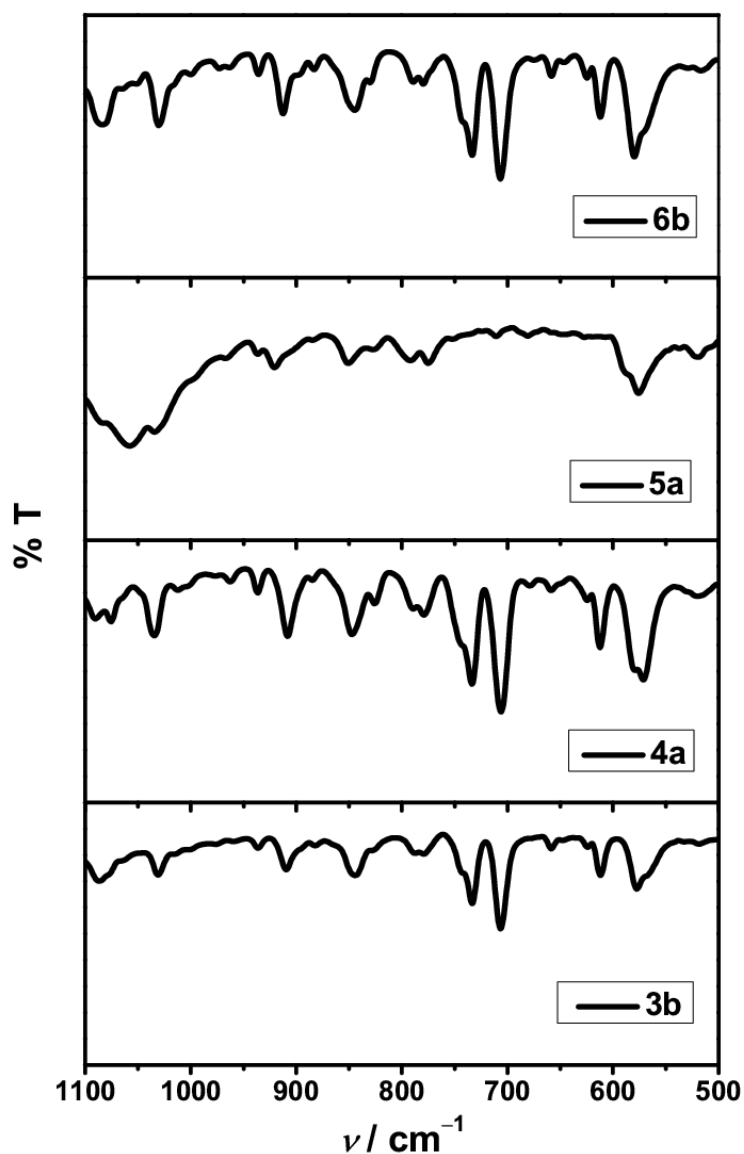


Figure A.125: KBr pellet IR spectra of **3b**, **4a**, **5a** and **6b** in the wavenumber range 1100–500 cm^{-1} at room temperature.

Table A.24: List of IR peaks of the compounds **3b**, **4a**, **5a** and **6b** in the wavenumber range of 1700–500 cm^{-1} .

	3b	4a	5a	6b
ν / cm^{-1}	1673	1673		1671
	1600	1603	1603	1600
	1580	1582	1579	1580
	1521, 1507	1519, 1504	1505	1532, 1515
	1479	1479		1478
	1465	1467	1463	1465
	1428	1435	1437	1428

	1401	1401	1400	1401
	1382	1384	1387	1382
		1377	1374, 1365	1368
	1345	1344	1349	1345
	1285	1292	1288	1286
	1257	1255	1251	1257
	1225	1231	1223	1226
	1190	1188	1195	1192
	1159	1157	1166	1157
	1142	1134		1142
	1086	1090		1084
		1075		
			1057, 1034	
	1030	1034		1030
		1011		
	936	936	938	935
	908	907	923	911
				898
	882	884	884	883
	843	847	850	844
	826	825	827	829
	787	789	791	790
	778	778	775	779
			751, 711, 687	
	743	744		742
	733	733		733
			680, 646, 587	
	706	705		
		678		
	658	658		659
	623	624		625
	612	612		611
	578	579	575	579
	567	570	537	567
	519	520	519	515
			505	

Deconvolution of the IR Spectra

The Gaussian fit of the KBr pellet IR spectra of the complexes **4a**, **5a** and **6b** are shown in Figures A.126–A.128. The Gaussian peaks are represented mainly as black solid lines. However, the peaks which are of interest are shown as red and green solid lines. The sum of the fitted spectrum is shown by orange-red dashed line. The IR spectrum in the range of the data points used for the deconvolution is shown by blue solid lines. Adjusted R^2 values for all the fitting are 0.999.

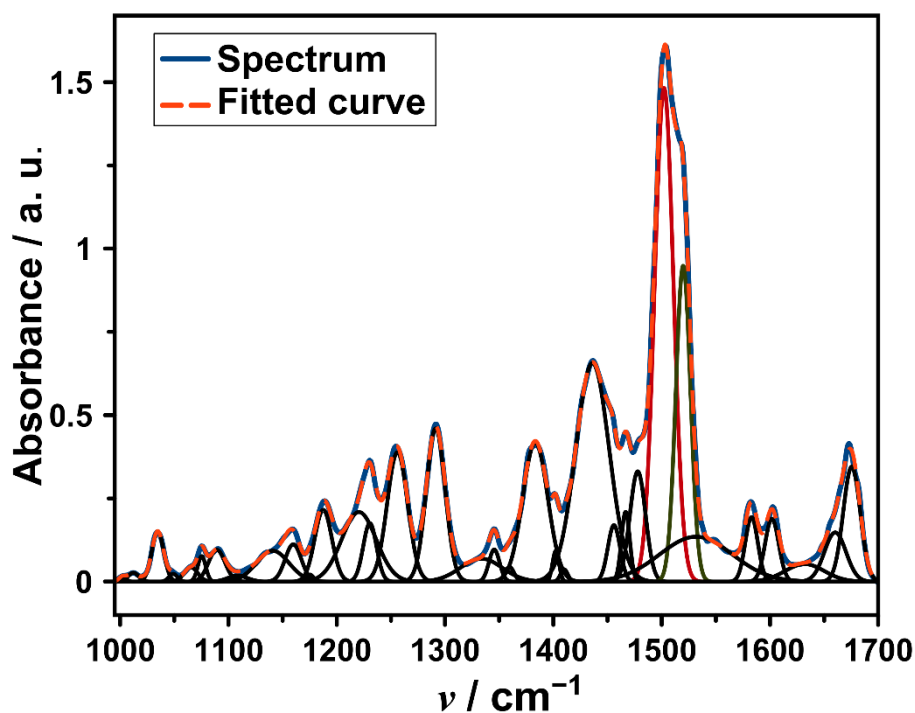


Figure A.126: Deconvoluted IR spectrum of **4a** in KBr pellet at RT; Deconvolution was performed in the wavenumber range of 995–1705 cm^{-1} .

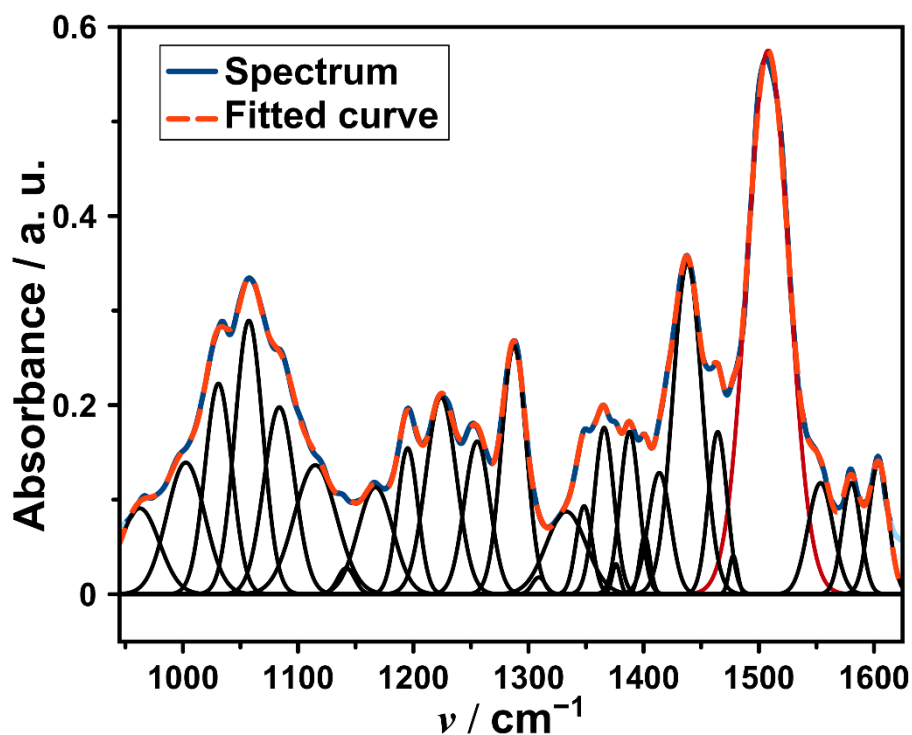


Figure A.127: Deconvoluted IR spectrum of **5a** in KBr pellet at RT; Deconvolution was performed in the wavenumber range of 950–1615 cm^{-1} .

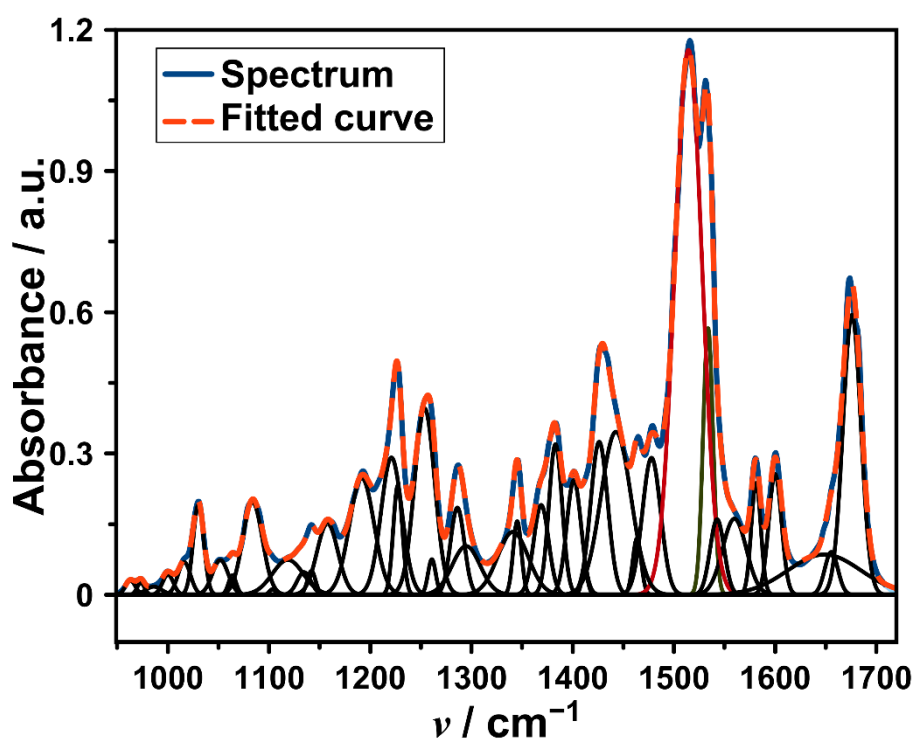


Figure A.128: Deconvoluted IR spectrum of **6b** in KBr pellet at RT; Deconvolution was performed in the wavenumber range of 947–1710 cm^{-1} .

6.3.3 UV/Vis/NIR Spectra

The spectra of compounds **4a**, **5a**, **6b** and **6^{•-}** showing Gaussian fit are shown in Figures A.129– A.135. The data obtained from the fitting are given in Table A.25. The blue line representing a UV/Vis/NIR spectrum corresponds to the data points taken for the fitting. The orange-red dashed line corresponds to the sum of Gaussian profiles. The Gaussian peaks are represented as black lines.

Table A.25: The data obtained from the Gaussian fit of the UV/Vis/NIR spectra of compounds **4a**, **5a**, **6b** and **6^{•-}**. The absorption maxima (ν / cm^{-1}), molar extinction coefficient ($\epsilon / \text{M}^{-1} \text{cm}^{-1}$), area under the curve (area / $\text{M}^{-1} \text{cm}^{-2}$) values.

Compound (solvent)	ν (ϵ)	ν (area $\times 10^{-8}$)
4a (MeCN, RT) ^[b]	13752 (27300), 16474 (3224), 18777 (4513), 21091 (12000), 24135 (3555), 29905 (2135), 32065 (11400), 35074 (11800)	13752 (0.93), 16474 (0.057), 18777 (0.107), 21091 (0.59), 24135 (0.24), 29905 (0.03), 32065 (0.54), 35074 (0.41)
5a (MeCN, RT) ^[c]	14120 (22800), 17124 (2186), 19230 (4553), 21082 (11900), 23368 (5270), 30413 (1635), 31385 (2653), 35563 (15000)	14120 (0.86), 17124 (0.038), 19230 (0.085), 21082 (0.50), 23368 (0.29), 30413 (0.021), 31385 (0.07), 35563 (1.35)
6b (MeCN, RT) ^[b]	14985 (23600), 17852 (1653), 20086 (5900), 22180 (12500), 24535 (5044), 31309 (2021), 34058 (11300),	14985 (0.933), 17852 (0.023), 20086 (0.114), 22180 (0.53), 24535 (0.29), 31309 (0.036), 34058 (0.66),
6b (DMF, 293 K) ^[d]	11284 (6940), 12176 (13900), 13911 (9063), 22122 (5208), 28130 (8780), 32011 (8455), 37953 ^[a] (33400)	11284 (0.09), 12176 (0.41), 13911 (0.46), 22122 (0.37), 28130 (0.23), 32011 (0.56), 37953 ^[a] (1.45)
6b (DMF, 213 K) ^[e]	11352 (12300), 12610 (4153), 14060 (16500), 21776 (8400), 27827	11352 (0.187), 12610 (0.048), 14060 (0.72), 17105 (0.01), 21776 (0.50),

	(5024), 33067 (8951), 37712 ^[a] (27000)	27827 (0.113), 33067 (0.88), 37712 ^[a] (0.90)
6b (DMSO, RT) ^[f]	11583 (5730), 14493 (17200), 17127 (1380), 20026 (1400), 22014 (11100), 27840 (3795), 31035 (2837), 34074 (9704), 36730 ^[a] (17700)	11583 (0.133), 14493 (0.65), 17127 (0.025), 20026 (0.021), 22014 (0.65), 27840 (0.135), 31035 (0.065), 34074 (0.58), 36730 ^[a] (0.37)
6^{•-} (DMF, RT) ^[g]	6654 (6778), 7791 (22700), 8956 (9097), 10768 (1731), 13822 (1936), 16325 (1053), 17584 (5292), 18930 (2410), 20837 (20600), 21404 (11200), 22110 (15407), 22596 (17300), 24133 (5820), 35390 (19400), 36623 ^[a] (14900)	6654 (0.09), 7791 (0.29), 8956 (0.16), 10768 (0.044), 13822 (0.26), 16325 (0.0116), 17584 (0.09), 18930 (0.029), 20837 (0.146), 21404 (0.079), 22110 (0.21), 22596 (0.45), 24133 (0.46), 35390 (1.54), 36623 ^[a] (0.21)

^[a] These bands could be affected by the absorption of solvent peaks in this region.

^[b] Wavenumber range 8000–34900 cm⁻¹. ^[c] Wavenumber range 10000–35000 cm⁻¹.

^[d] Wavenumber range 7500–32000 cm⁻¹. ^[e] Wavenumber range 8000–32000 cm⁻¹.

^[f] Wavenumber range 8000–36600 cm⁻¹. ^[g] Wavenumber range 6000–36700 cm⁻¹.

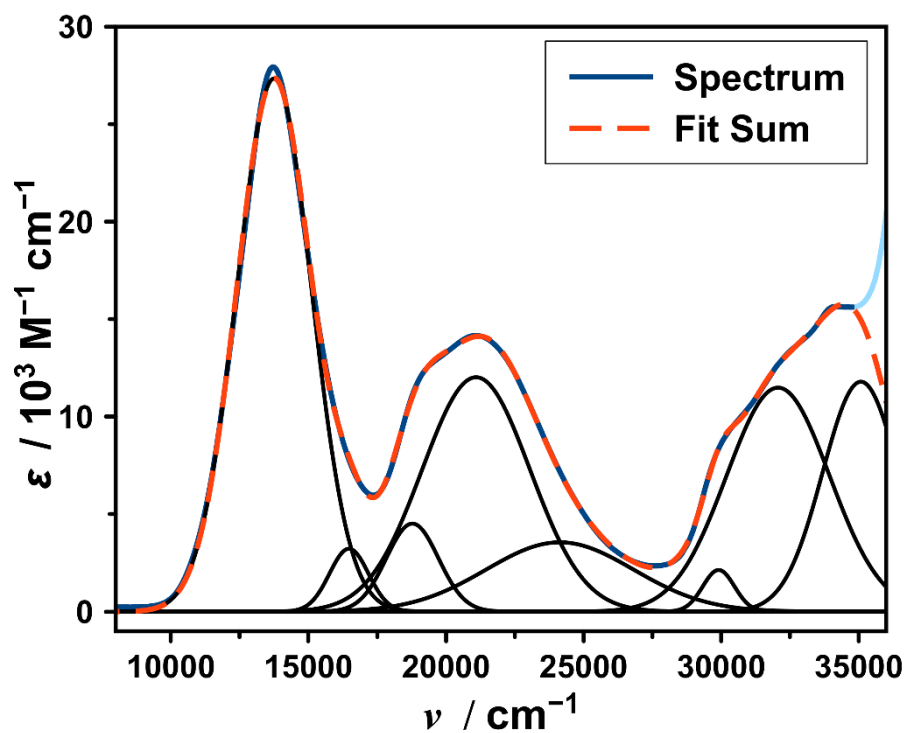


Figure A.129: Gaussian fit of the UV/Vis/NIR spectrum of **4a** in MeCN at RT. Adj. R^2 of the fit is 0.999.

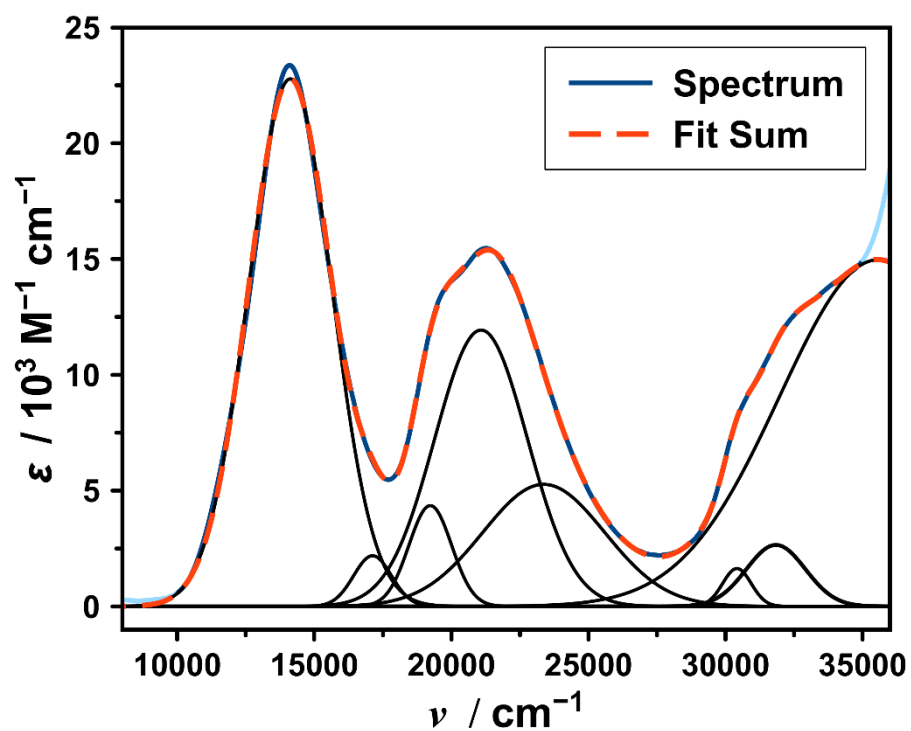


Figure A.130: Gaussian fit of the UV/Vis/NIR spectrum of **5a** in MeCN at RT. Adj. R^2 of the fit is 0.999.

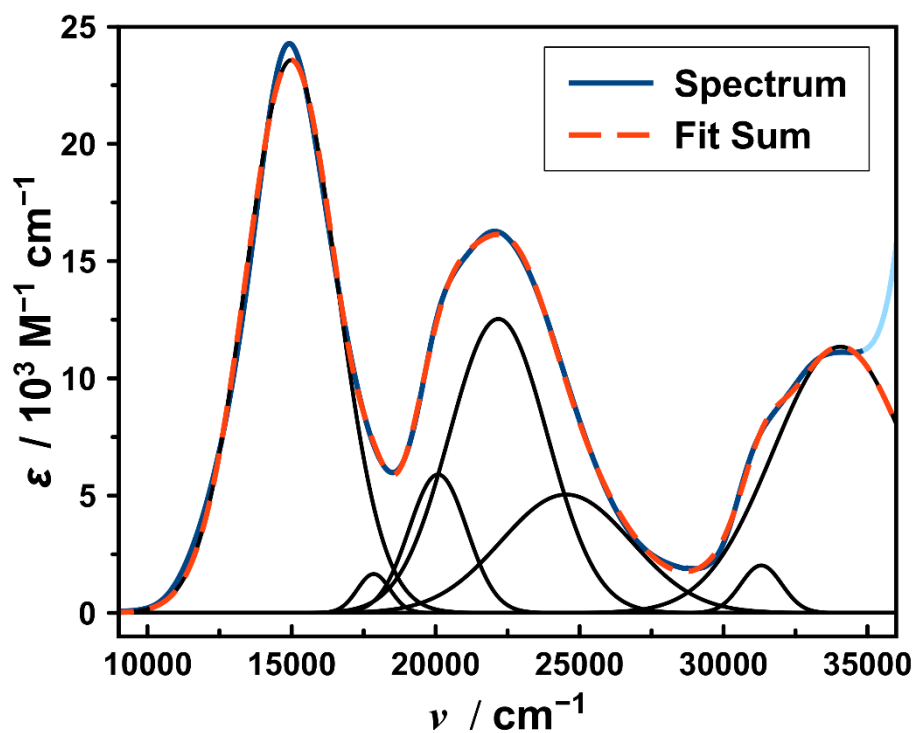


Figure A.131: Gaussian fit of the UV/Vis/NIR spectrum of **6b** in MeCN at RT. Adj. R^2 of the fit is 0.998.

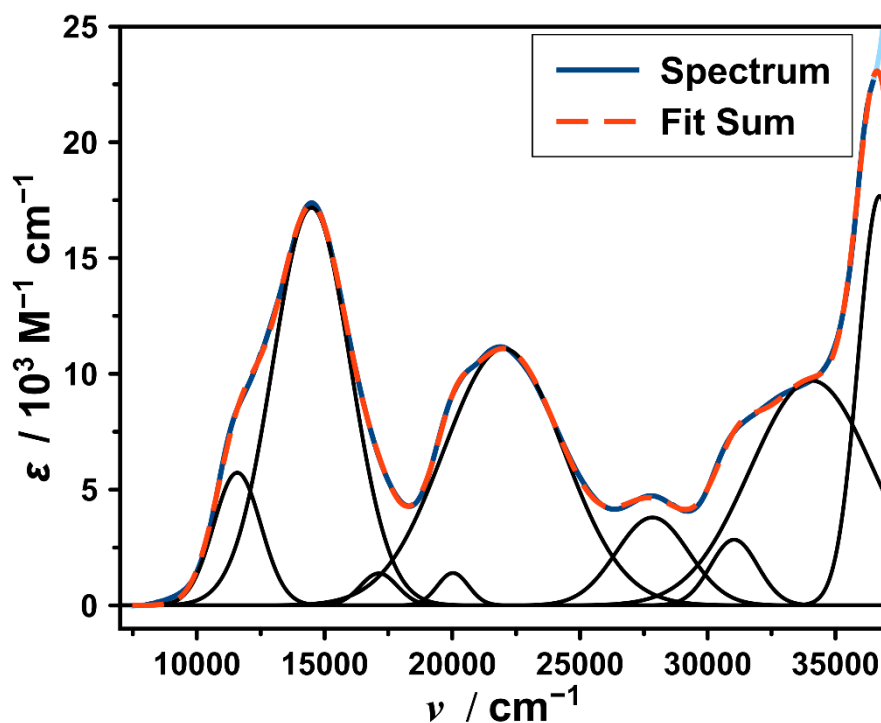


Figure A.132: Gaussian fit of the UV/Vis/NIR spectrum of **6b**, obtained by subtraction from the UV/Vis/NIR of **6^{*}-**, in DMSO at RT. Adj. R^2 of the fit is 0.999.

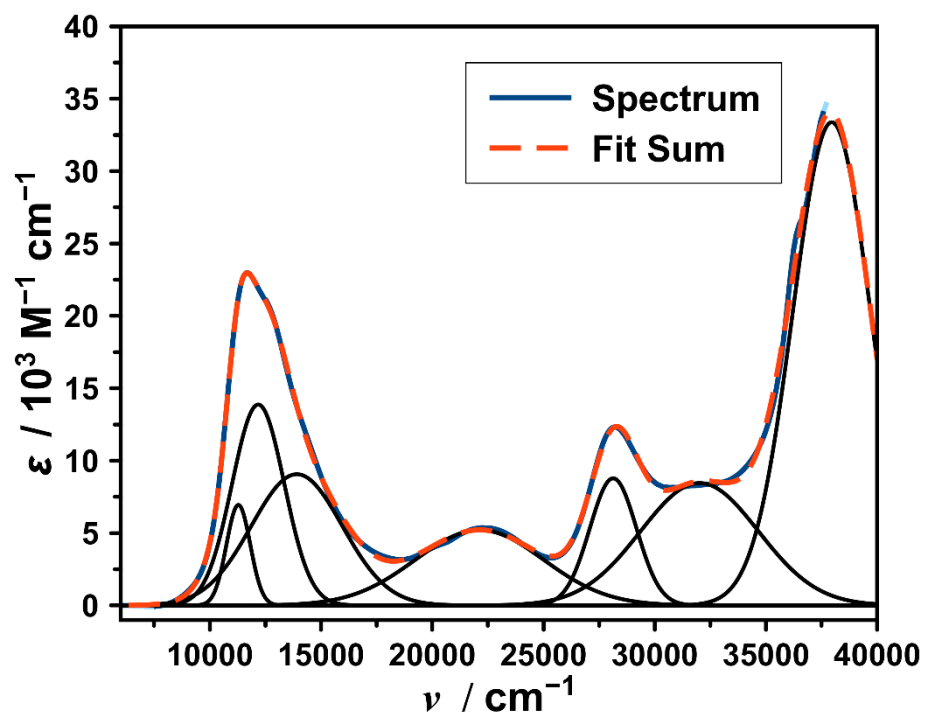


Figure A.133: Gaussian fit of the UV/Vis/NIR spectrum of **6b**, obtained by subtraction from the UV/Vis/NIR of **6***, in DMF at 293 K. Adj. R^2 of the fit is 0.999.

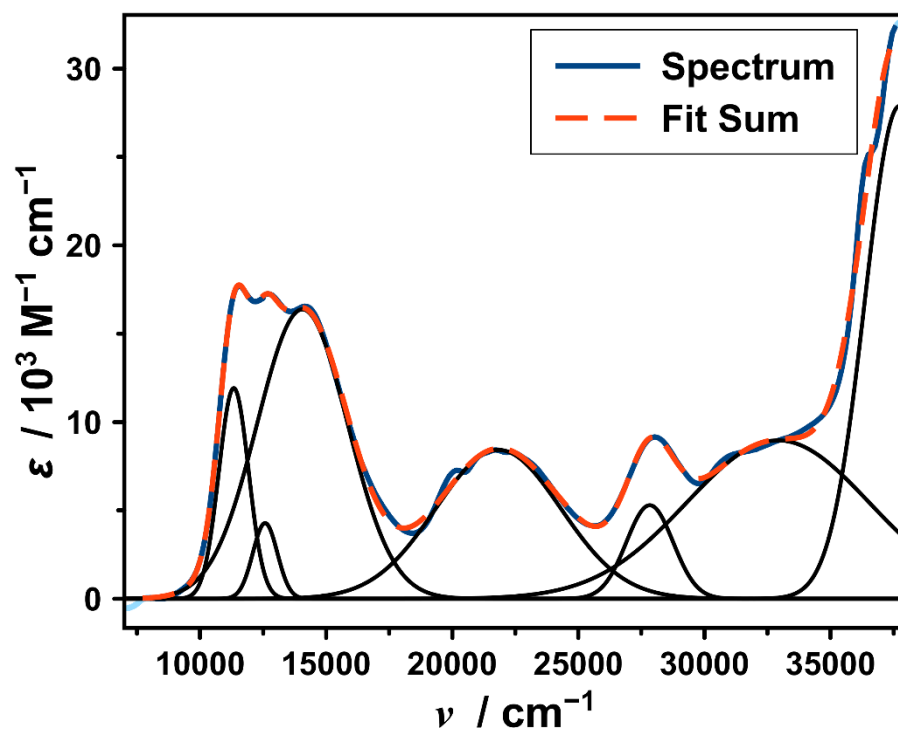


Figure A.134: Gaussian fit of the UV/Vis/NIR spectrum of **6b**, obtained by subtraction from the UV/Vis/NIR of **6***, in DMF at 213 K. Adj. R^2 of the fit is 0.999.

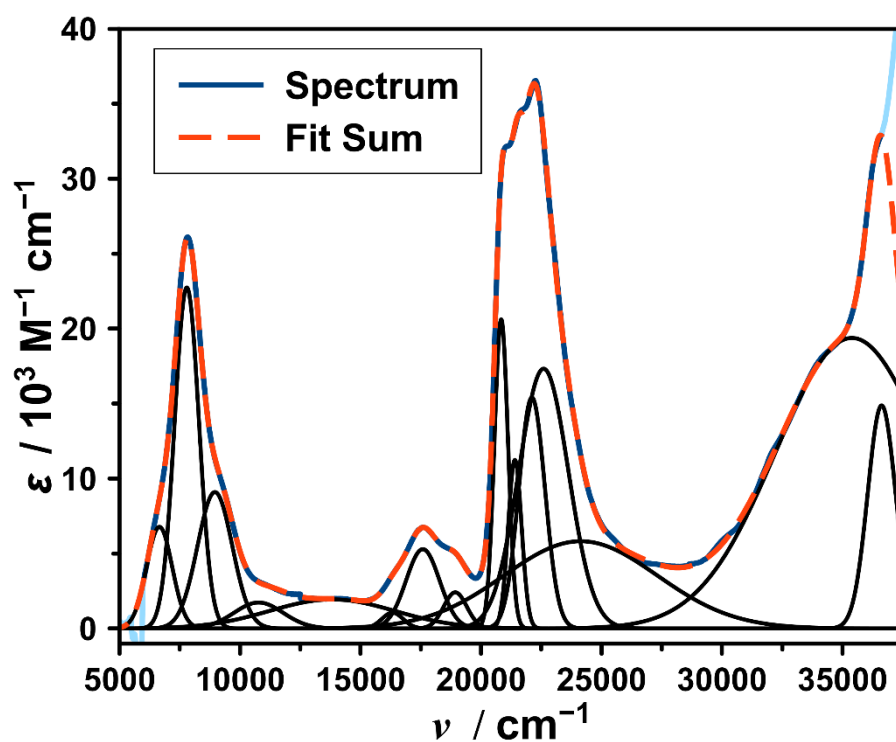


Figure A.135: Gaussian fit of the UV/Vis/NIR spectrum of $6^{\bullet-}$ in 0.2 M TBAP/DMF. Adj. R^2 of the fit is 0.999.

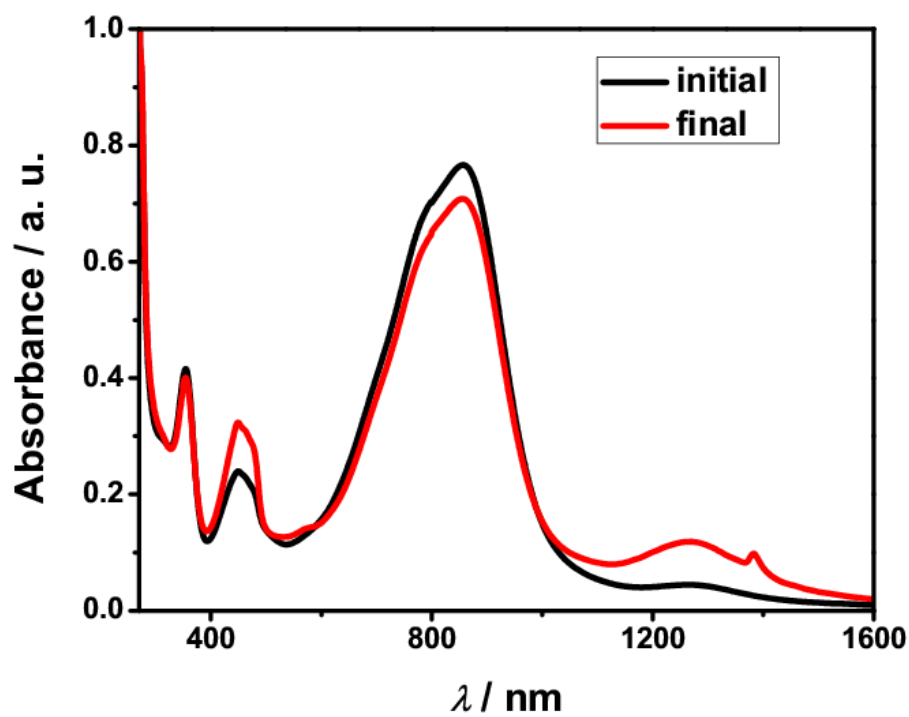


Figure A.136: UV/Vis/NIR spectra showing stability of the sample at 293 K during variable temperature UV/Vis/NIR measurement of $6b$ in DMF. The spike at around 1400 nm is due to the solvent artefact.

6.3.4 Cyclic Voltammograms

Table A.26: Cyclic voltammetry data of **4a**, **5a** and **6b**; Scan rate (ν), half-wave potential ($E_{1/2}$), difference between peak potentials (ΔE) and peak current ratio (i_{pa}/i_{pc}).

4a	$\nu/\text{mV s}^{-1}$	$E_{1/2}/\text{mV}$	$\Delta E/\text{mV}$	i_{pa}/i_{pc}
Reduction 1	200	-175	100	1.04
	100	-176	83	1.07
	50	-176	74	1.07
	20	-172	65	1.05
	10	-173	62	1.04
Reduction 2	200	-646	101	1.03
	100	-650	88	1.07
	50	-648	65	1.07
	20	-643	71	1.05
	10	-644	53	1.04
5a	$\nu/\text{mV s}^{-1}$	$E_{1/2}/\text{mV}$	$\Delta E/\text{mV}$	i_{pa}/i_{pc}
Reduction 1	200	47	97	1.01
	100	45	85	1.04
	50	41	79	1.01
	20	41	71	1.01
	10	40	70	0.98
Reduction 2	200	-455	98	1.01
	100	-450	82	1.01
	50	-450	77	1.06
	20	-450	78	1.06
	10	-445	83	0.94
6b	$\nu/\text{mV s}^{-1}$	$E_{1/2}/\text{mV}$	$\Delta E/\text{mV}$	i_{pa}/i_{pc}
Reduction 1	200	-130	186	0.89
	100	-120	163	0.91
	50	-125	142	0.90
	20	-124	121	0.88
	10	-120	106	0.87
Reduction 2	200	-527	200	1.16
	100	-526	186	1.20
	50	-525	180	1.34
	20	-530	154	1.50
	10	-530	140	1.32

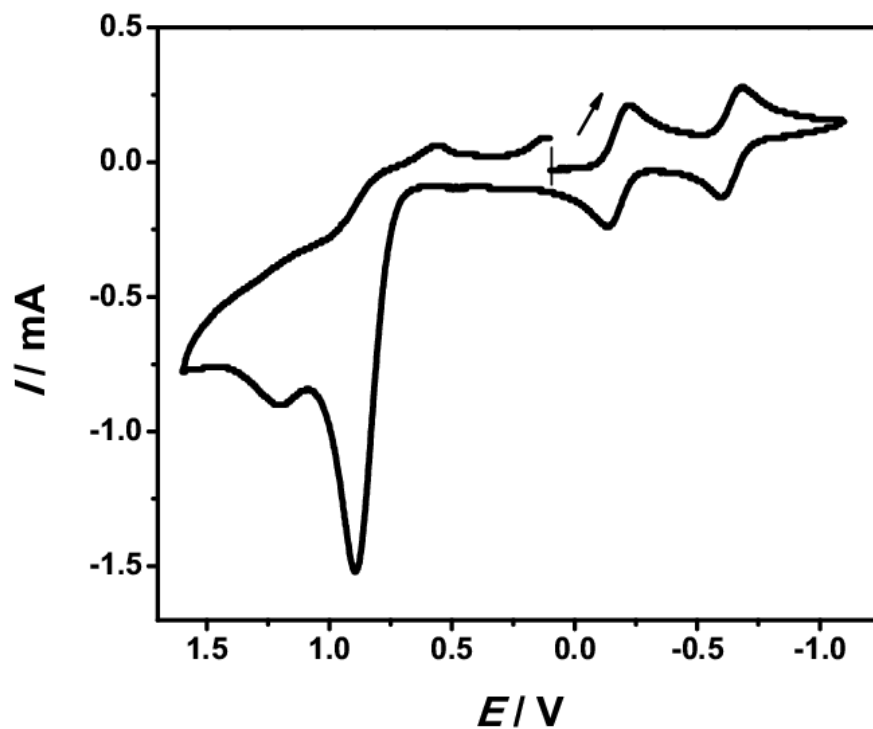


Figure A.137: Cyclic voltammogram of **4a** in 0.2 M TBAP/MeCN at scan rate $\nu = 100$ mV/s.

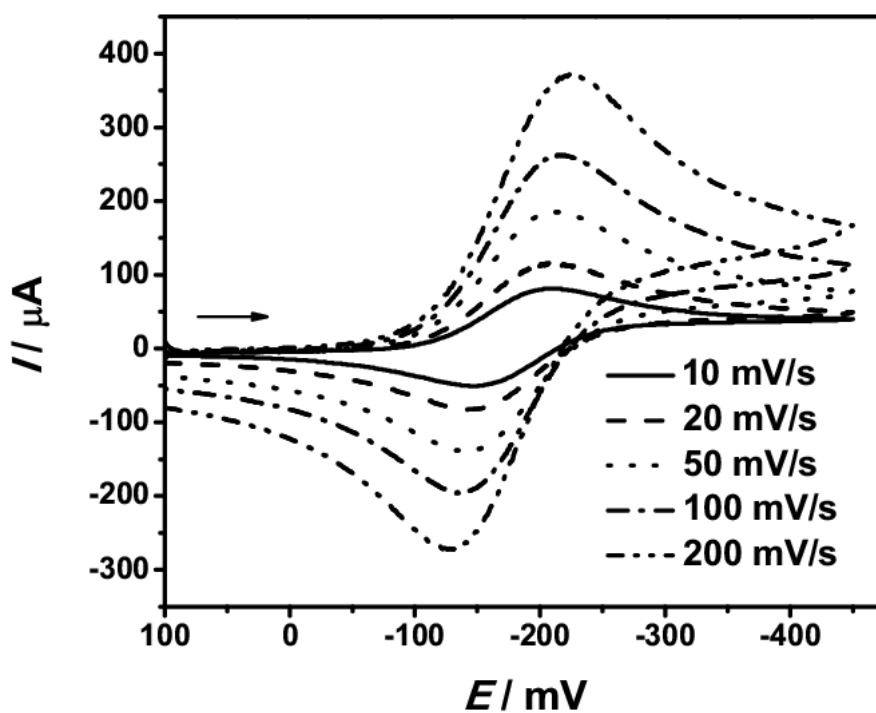


Figure A.138: Cyclic voltammograms for the first reductive processes of **4a** in 0.2 M TBAP/MeCN at different scan rates.

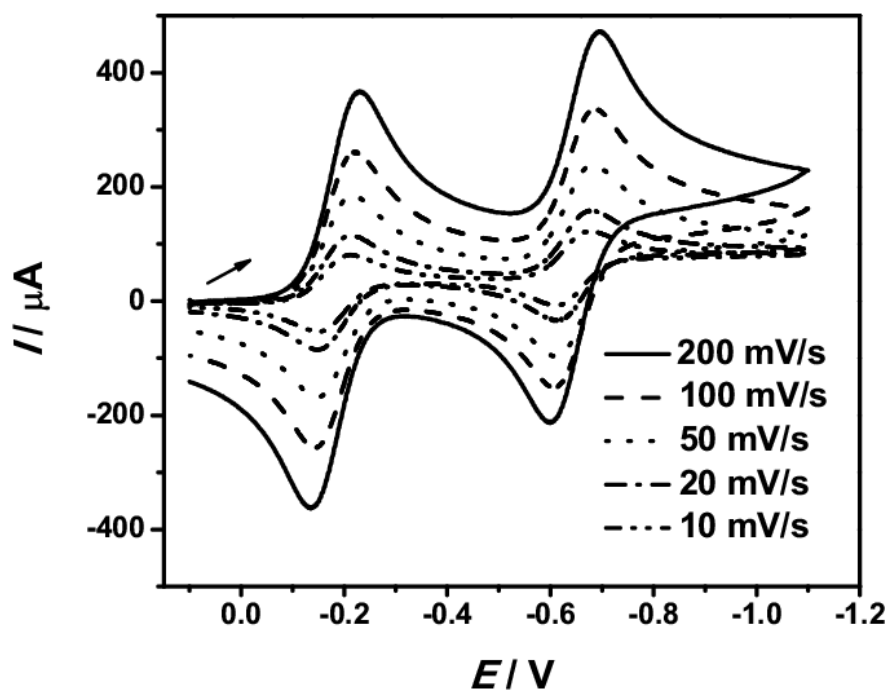


Figure A.139: Cyclic voltammograms for the two successive reductive processes of **4a** in 0.2 M TBAP/MeCN at different scan rates.

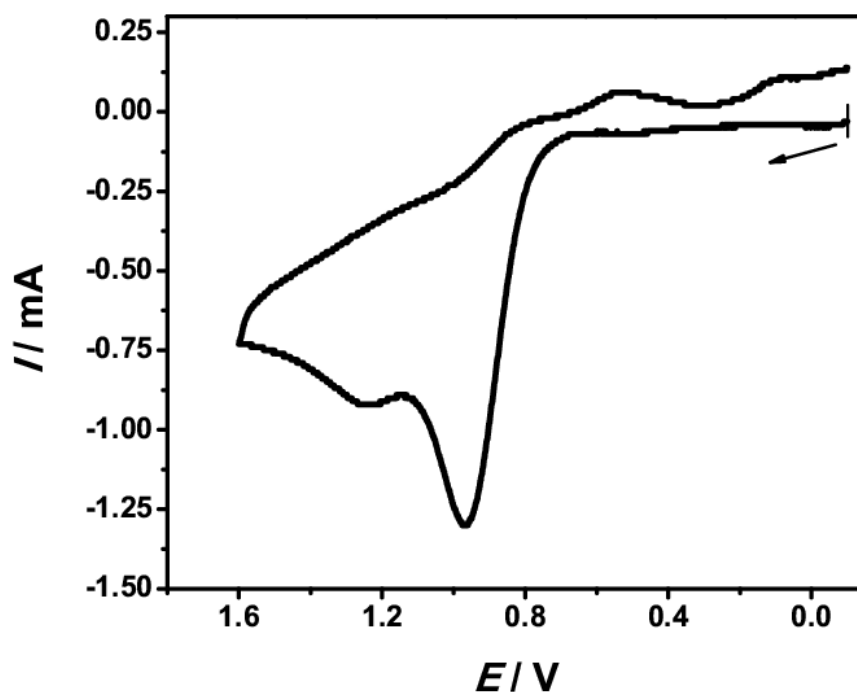


Figure A.140: Cyclic voltammogram for the oxidative processes of **4a** in 0.2 M TBAP/MeCN at scan rate $\nu = 100$ mV/s.

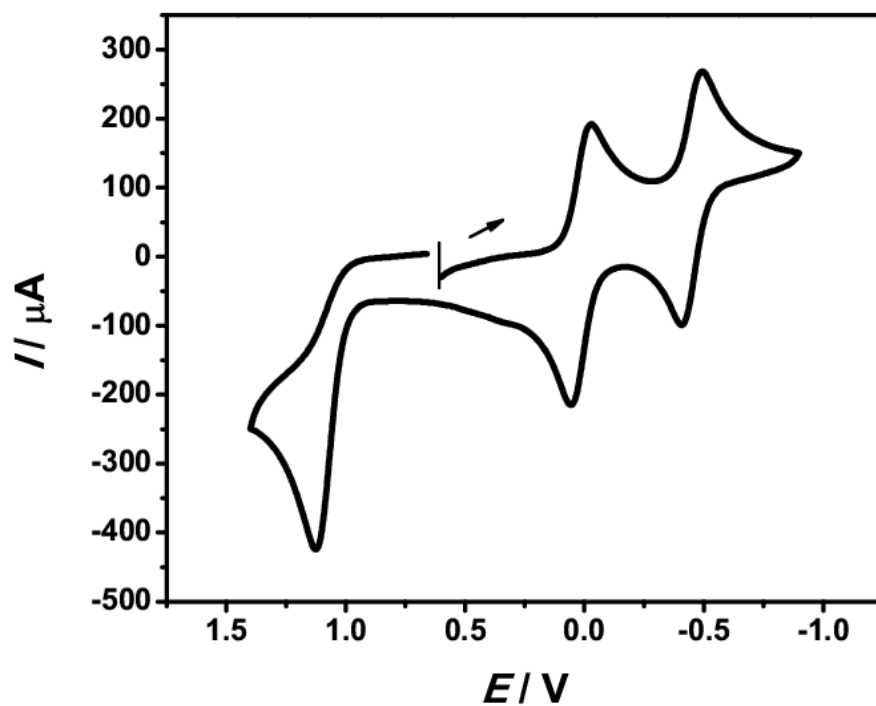


Figure A.141: Cyclic voltammogram of **5a** in 0.2 M TBAP/MeCN at scan rate $\nu = 100 \text{ mV/s}$.

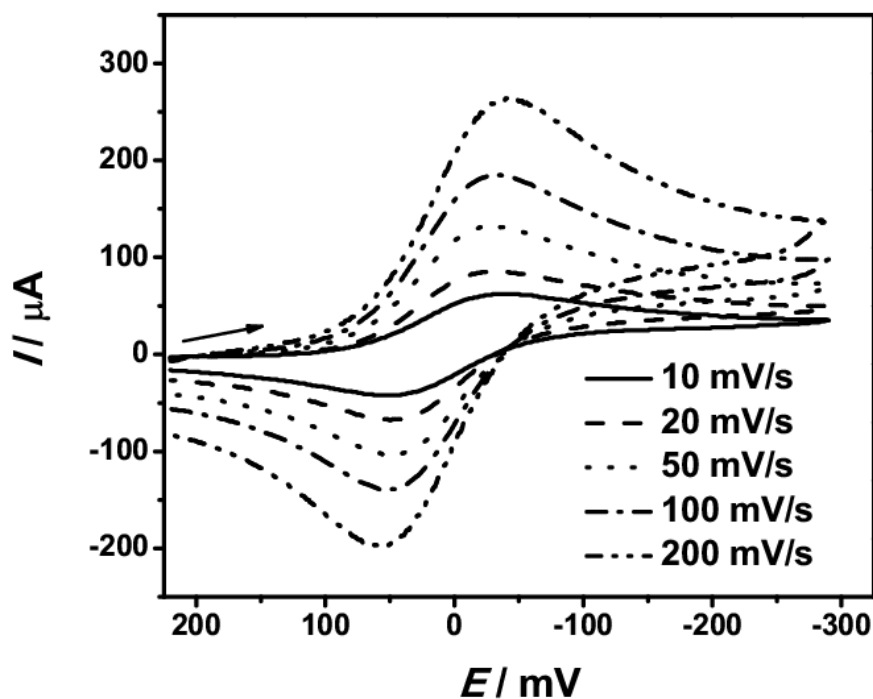


Figure A.142: Cyclic voltammograms for the first reductive processes of **5a** in 0.2 M TBAP/MeCN at different scan rates.

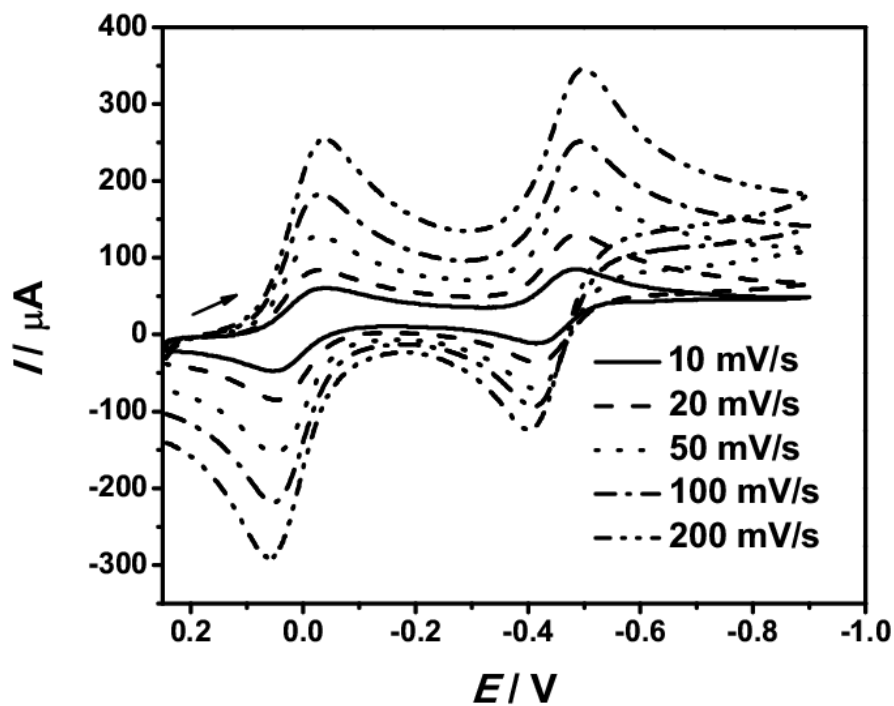


Figure A.143: Cyclic voltammograms for the successive reductive processes of **5a** in 0.2 M TBAP/MeCN at different scan rates.

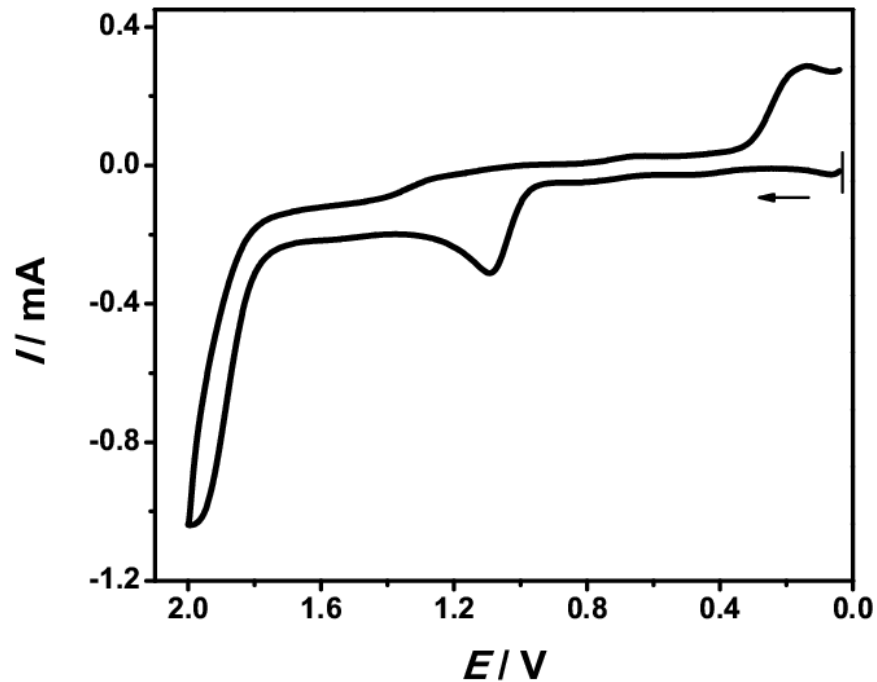


Figure A.144: Cyclic voltammogram for oxidative processes of **5a** at scan rate $\nu = 100$ mV/s.

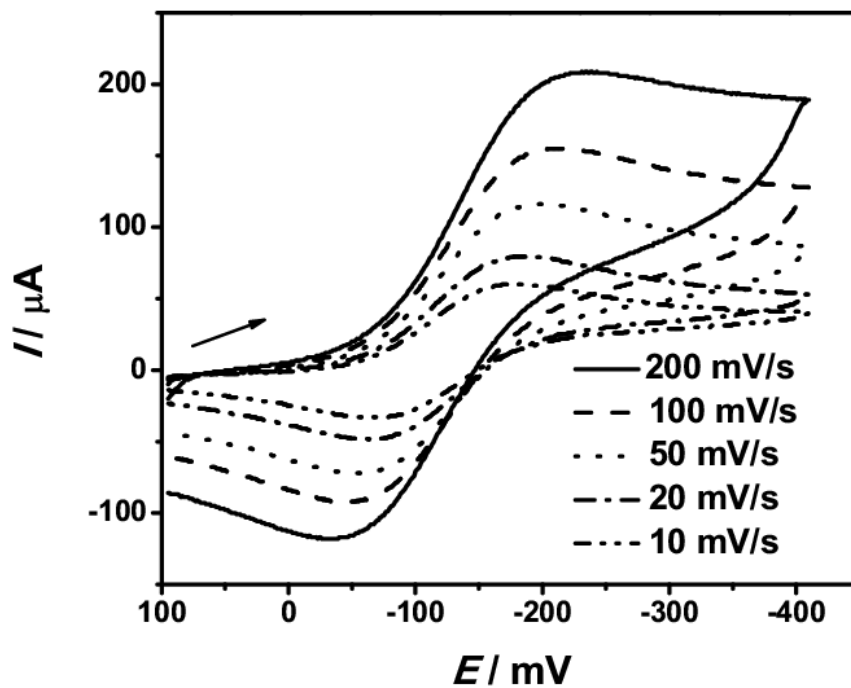


Figure A.145: Cyclic voltammograms for the first reductive processes of **6b** in 0.2 M TBAP/MeCN at different scan rates.

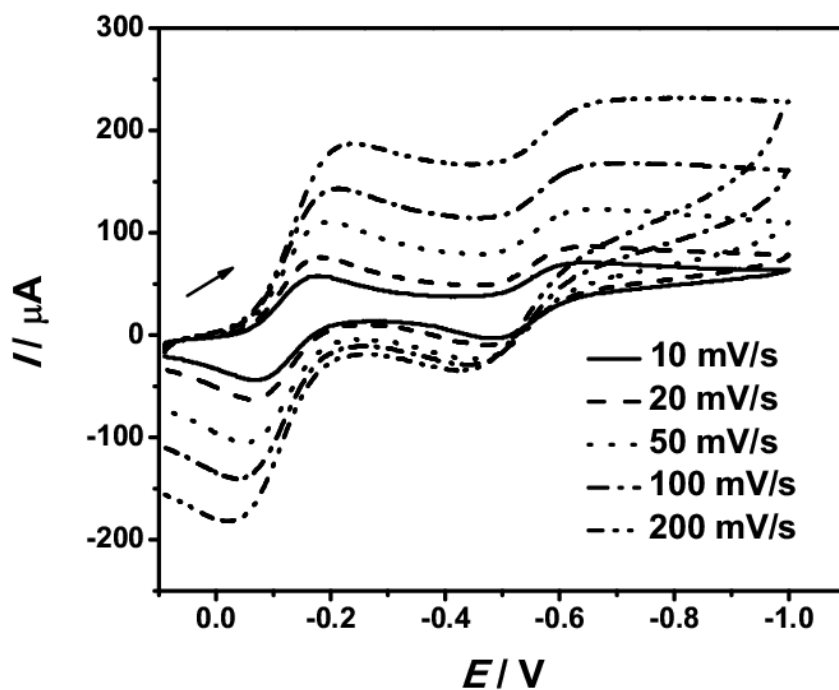


Figure A.146: Cyclic voltammograms for the two successive reductive processes of **6b** in 0.2 M TBAP/MeCN at different scan rates.

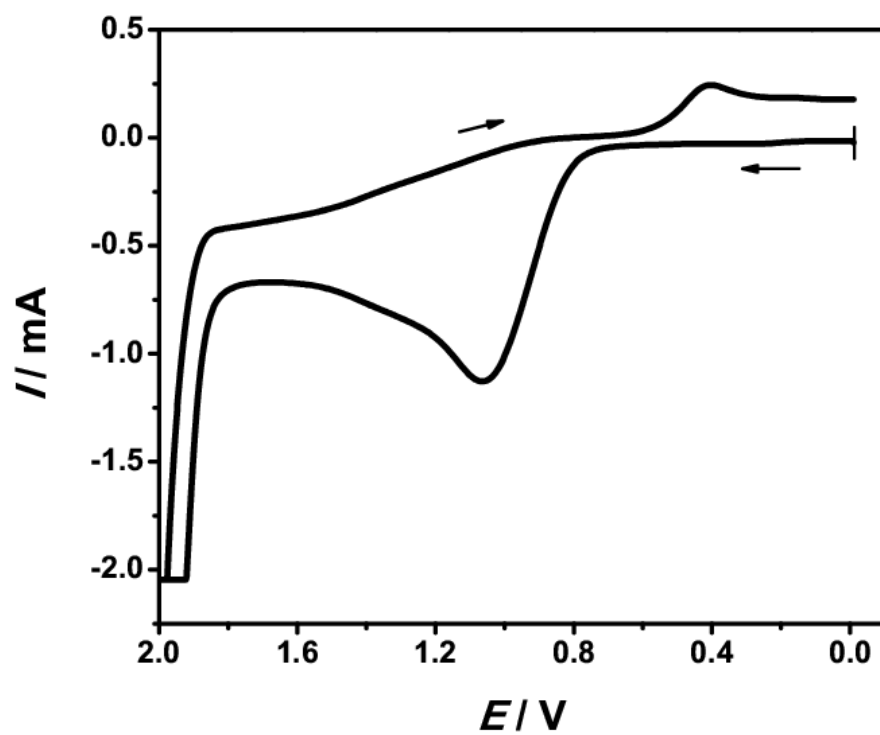


Figure A.147: Cyclic voltammogram for the oxidative processes of **6b** in 0.2 M TBAP/MeCN at scan rate $\nu = 100$ mV/s.

7 Acknowledgement

First and foremost, I would like to express my profound and sincere gratitude to my supervisor *Prof. Hans-Jörg Krüger* for his constant encouragement, guidance, valuable suggestion and support from the initial to the final level which enabled me to develop an understanding of the subject. His wisdom, knowledge and commitment to the highest standard, inspired and motivated me. He was always accessible and willing to help me throughout my dissertation which made the research life smooth and rewarding.

I would like to sincerely thank *Prof. Werner R. Thiel* and *Prof. Christoph van Willen* for being in my dissertation examination committee, their help.

My sincere thanks to *Dr. Harald Kelm* for determining the crystal structures of my compounds and NMR measurements. His valuable suggestions during my research period have helped me enormously.

My sincere thanks to *Dr. Serhiy Demeshko* of the research group of *Prof. Franc Meyer* at Universität Göttingen for performing SQUID measurements of my compounds.

I thank my M.Sc. supervisor *Prof. Sabyasachi Sarkar* of the Department of Chemistry, IIT Kanpur, India for his support and suggestions.

My sincere thanks to the working group of *Prof. W. E. Trommer* for allowing me to do EPR measurements of my compounds. Especially to *Dr. Reinhard Philipp* for helping me during my EPR measurements. I would like to thank *Ms. Annika Steiner* and *Dr. Johannes Lang* of the research group of *Prof. G. Niedner-Schatterburg* at Technische Universität Kaiserslautern for the measurement of ESI-MS.

My sincere thanks to *Mrs. Christiane Müller* from the NMR facility and *Mrs. Brigit Dusch* and *Mrs. Jana Ellmer* of CHNS-Service Elementaranalyse at Technische Universität Kaiserslautern for the measurements of Elemental Analysis.

I sincerely thank all my contemporary co-workers of the research group of *Prof. Hans-Jörg Krüger* for their suggestions and help.

I would like to thank *Mrs. Hannelore Dietrich*, *Mrs. Caro Hoffmann*, *Mrs. Heike Schramm*, *Mrs. Marion Weber* and *Mrs. Ina Berwanger* for their help regarding official works and my dissertation procedural works.

I would like to thank co-workers of *Prof. Thiel's* group and *Prof. Sitzmann's* group from whom I had received help for my dissertation purpose during my research period at Technische Universität Kaiserslautern.

My deepest sense of gratitude to my parents (*Mr. Tapan K. Dolai* and *Mrs. Basanti Dolai*) and my sister *Manasi* and brother *Shakti* for their infinite love, affection, support and constant encouragement. The same goes to my late grandparents, uncles, aunts and cousins for their love and support.

I thank my friends *Ramesh*, *Supriya*, *Soham*, *Dipankar*, *Sourav*, *Shirshendu*, *Debapriya*, *Deababrata*, *Biswajit*, *Praveen*, *Subrata*, *Avijit*, *Pratap*.

Besides, the above mentioned people, I would like to thank everybody who have helped me for my dissertation purpose.

8 Statutory Explanation

Hiermit bestätige ich, Ramapada Dolai, dass ich vorliegende Arbeit gemäß der Promotionsordnung des Fachbereich Chemie der Technischen Universität Kaiserslautern selbstständig und nur unter Verwendung der angegebenen Quellen und Hilfsmittel angefertigt habe. Ich erkläre außerdem, dass die vorliegende Arbeit weder in gleicher noch in ähnlicher Form bereits in einem anderen Prüfungsverfahren vorgelegen hat.

Kaiserslautern, den _____

Ramapada Dolai

9 Curriculum Vitae

RAMAPADA DOLAI

Education

1998–2003	Baipatna Vidyasagar High School High School
2003–2005	Baita Mahendranath High School Higher Secondary School
2005–2008	Midnapore College, W. B., India B. Sc. in Chemistry
2008–2010	Indian Institute of Technology, Kanpur, India M. Sc. in Chemistry:
2010–present	Technische Universität Kaiserslautern, Germany Ph. D. dissertation in Department of Chemistry:

Title: *“Switching of Electronic States of Cobalt Dioxolene Complexes Triggered by Spin-Crossover Process and Valence Tautomerism”*

Supervisor: Prof. Hans–Jörg Krüger, Ph. D.